

50 ~~copies~~^{or}
copies

NATIONAL AERONAUTICS AND SPACE ADMINISTRATION

Space Programs Summary 37-46, Vol. IV

Supporting Research and Advanced Development

For the Period June 1 to July 31, 1967

FACILITY FORM 802	N67-40233	_____
	(ACCESSION NUMBER)	(THRU)
	289	1
	(PAGES)	(CODE)
	CR-89567	30
	(NASA CR OR TMX OR AD NUMBER)	(CATEGORY)

JET PROPULSION LABORATORY
CALIFORNIA INSTITUTE OF TECHNOLOGY
PASADENA, CALIFORNIA

August 31, 1967

NATIONAL AERONAUTICS AND SPACE ADMINISTRATION

Space Programs Summary 37-46, Vol. IV

Supporting Research and Advanced Development

For the Period June 1 to July 31, 1967

JET PROPULSION LABORATORY
CALIFORNIA INSTITUTE OF TECHNOLOGY
PASADENA, CALIFORNIA

August 31, 1967

SPACE PROGRAMS SUMMARY 37-46, VOL. IV

Copyright © 1967
Jet Propulsion Laboratory
California Institute of Technology
Prepared Under Contract No. NAS 7-100
National Aeronautics & Space Administration

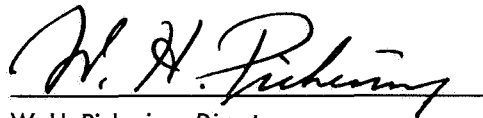
Preface

The Space Programs Summary is a six-volume bimonthly publication designed to report on JPL space exploration programs and related supporting research and advanced development projects. The titles of all volumes of the Space Programs Summary are:

- Vol. I. *The Lunar Program* (Confidential)
- Vol. II. *The Planetary-Interplanetary Program* (Confidential)
- Vol. III. *The Deep Space Network* (Unclassified)
- Vol. IV. *Supporting Research and Advanced Development* (Unclassified)
- Vol. V. *Supporting Research and Advanced Development* (Confidential)
- Vol. VI. *Space Exploration Programs and Space Sciences* (Unclassified)

The Space Programs Summary, Vol. VI, consists of: an unclassified digest of appropriate material from Vols. I, II, and III; an original presentation of the JPL quality assurance and reliability efforts, and the environmental- and dynamic-testing facility-development activities; and a reprint of the space science instrumentation studies of Vols. I and II.

Approved by:



W. H. Pickering, Director
Jet Propulsion Laboratory

Contents

SYSTEMS DIVISION

I. Systems Analysis Research	1
A. Preliminary Lunar Gravity Estimates From <i>Lunar Orbiter</i> NASA Code 814-12-02-01, J. Lorell and W. L. Sjogren	1
B. The Regularization of Optimal Trajectories NASA Code 129-04-01-01, B. D. Tapley and V. Szebehely	5
C. Neighboring Extremal Technique for Optimal Control Problems With Discontinuities NASA Code 129-04-04-02, S. R. McReynolds	9
D. A Note on Regularization Transformations in the Calculus of Variations NASA Code 129-04-01-01, H. Lass and S. R. McReynolds	13
E. Lunar Ephemeris Improvement From <i>Lunar Orbiter</i> Tracking Data NASA Code 129-04-01-02, J. D. Anderson	16
F. An Efficient Propulsion Maneuver Used to Modify Lunar Return Re-entry Latitude NASA Code 684-30-01-10, E. S. Davis	19
References	28
II. Systems Analysis	29
A. Trajectory Considerations for the Earth–Venus–Mercury Mission Opportunity, 1981–82 NASA Code 684-30-01-10, R. A. Wallace	29
References	33
III. Computation and Analysis	34
A. Numerical Solution of a Nonlinear Partial Differential Equation NASA Code 129-04-04-01, E. Ng	34
B. Integrals of Confluent Hypergeometric Functions, Part I NASA Code 129-04-04-01, E. Ng	37
References	41

PROJECT ENGINEERING DIVISION

IV. Environmental Requirements	43
A. Dry-Heat Resistance of Bacterial Spores (<i>Bacillus Globigii</i>) Upon Selected Spacecraft Surface Materials NASA Code 189-58-21-02, W. W. Paik, S. C. Michael, C. D. Smith, and J. A. Stern	43

Contents (contd)

B. Microbial Sampling Program for the <i>Mariner Venus 67</i> Flight Spacecraft (<i>Mariner V</i>) NASA Code 189-58-23-03, M. R. Christensen, R. H. Green, and J. A. Stern	48
References	55

GUIDANCE AND CONTROL DIVISION

V. Flight Computers and Sequencers	57
A. JPL STAR Computer NASA Code 125-17-04-02, A. Avizienis	57
References	62
VI. Spacecraft Power	63
A. Low-Saturation-Drop Silicon Transistor NASA Code 120-33-08-05, R. A. Booth	63
B. RCA Silicon-Germanium Air-Vac Technology NASA Code 120-27-06-08, L. Selwitz	65
C. Radiation Effects on Silver and Zinc Battery Electrodes NASA Code 120-34-01-08, G. L. Juvinal	75
D. Sterilizable Battery NASA Code 120-34-01-03, R. Lutwack	76
VII. Spacecraft Control	79
A. Investigation of Optimization of Attitude Control Systems NASA Code 125-19-04-01, B. Dobrotin	79
B. Sterilizable Inertial Sensors NASA Code 186-58-02-03, P. J. Hand	81
References	82
VIII. Guidance and Control Research	83
A. Extremely High-Density Magnetic Information Storage NASA Code 129-02-05-06, D. I. Tchernev	83
B. Curie-Point Switching in Thin MnBi Films NASA Code 129-02-05-06, G. Lewicki	84
C. Coercive Force of Thin Magnetic Films NASA Code 129-02-05-06, J. A. Baldwin, Jr.	87
D. Apparent Work Function of a Cavity Emitter NASA Code 129-02-01-07, K. Shimada	94
E. Applications of Superconductivity in Spacecraft, Part II NASA Code 129-02-05-02, P. V. Mason	97
References	102

Contents (contd)

ENGINEERING MECHANICS DIVISION

IX. Electronics Parts Engineering	105
A. Channeling in Transistors and its Detection <i>NASA Code 186-70-01-04, R. A. Summers and W. B. Bartel</i>	105
B. Analysis of Gases Contained in Transistors <i>NASA Code 186-70-01-07, E. T. Klippenstein</i>	108
X. Lunar Spacecraft Development	111
A. Advanced Mechanisms <i>NASA Code 186-68-12-05, M. B. Gram</i>	111

ENVIRONMENTAL SIMULATION DIVISION

XI. Instrumentation	115
A. Determination of Particle Size and Concentration <i>NASA Code 128-32-06-01, C. Feldstein</i>	115
XII. Aerodynamic Facilities	118
A. Initial Performance of a 6-in.-Diameter Arc Driver <i>NASA Code 124-07-01-04, J. W. Williard</i>	118
B. A Study of Molecular, Continuum, and Line Radiation from Planetary Atmospheres <i>NASA Code 124-07-01-04, W. A. Menard and G. M. Thomas</i>	122
C. Base Heating of 60-deg Half-Angle Cone <i>NASA Code 124-07-04-01, J. C. Klose</i>	122
D. Errors Associated with Atmosphere Reconstruction from Capsule Onboard Measurements <i>NASA Code 124-07-04-01, R. H. Prislín</i>	123
E. Cold-Wall Wedge-Wake Investigation <i>NASA Code 124-07-04-01, D. W. Kurtz</i>	129
References	130

PROPULSION DIVISION

XIII. Polymer Research	133
A. Structural Integrity of Solid Propellant Retrorockets, III <i>NASA Code 128-32-05-04, E. N. Duran</i>	133
B. Electron Spin Resonance Study of the Reaction Between Sodium and 2, 4-Bis-(4-Biphenyl)-Pentane <i>NASA Code 129-03-11-03, F. E. Stewart and A. Rembaum</i>	138

Contents (contd)

C. Effects of Various Sterilization Cycles on the Properties of Polymeric Products NASA Code 186-58-13-09, S. H. Kalfayan, B. A. Campbell, and R. H. Silver	139
References	141
XIV. Research and Advanced Concepts	142
A. Nuclear System Studies: Uninsulated In-Core Thermionic Diode NASA Code 120-27-06-14, J. P. Davis	142
B. Liquid MHD Power Conversion NASA Code 120-27-06-03, D. Elliott, D. Cerini, L. Hays, D. O'Connor, and G. Haskins	147
C. Radial Distributions of Enthalpy, Mass Flux and Velocity for High-Temperature Argon Flow as Determined by a Calorimetric Probe NASA Code 129-01-05-10, P. F. Massier and E. J. Roschke	153
References	161
XV. Liquid Propulsion	162
A. Liquid Propulsion System NASA Code 731-12-03-03, L. R. Toth, F. A. Rush, and O. F. Keller	162
B. The Reaction Between OF_2 and B_2H_6 : The Rate of Formation of BF_3 NASA Code 128-31-06-05, R. A. Rhein	173
C. The Reaction Between OF_2 and B_2H_6 : Further Computations on the Rate of Formation of BF_3 NASA Code 128-31-06-05, R. A. Rhein	179
References	180

SPACE SCIENCES DIVISION

XVI. Science Data Systems	181
A. Properties of Near-Maximal-Length Cycles Generated by Linear Feedback Shift Registers NASA Code 186-68-03-03, M. Perlman	181
References	185
XVII. Lunar and Planetary Sciences	186
A. Flexible-Screw Rock Sampling Device: II, First Breadboard Design and Performance NASA Code 185-42-52-01, D. Nash	186

Contents (contd)

B. Mercury's Microwave Phase Effect NASA Code 185-41-21-02, B. Gary	191
C. Retention of Water in the Martian Atmosphere NASA Code 185-41-21-01, J. E. Gunn	194
D. Emission Spectra of Silicates in the Spectral Region 8–14 μm and Application to Remote Compositional Analysis of the Moon's Surface NASA Code 185-42-52-01, J. E. Conel	194
References	195
XVIII. Physics	196
A. Low-Energy, High-Resolution Electron Impact Spectrometer NASA Code 129-02-06-01, S. Trajmar	196
B. The Determination of Chemical Mechanisms by Ion Cyclotron Resonance NASA Code 129-02-01-06, J. King, Jr. and D. D. Elleman	205
C. MOSES: A FORTRAN IV Program for Calculating Properties of Polyatomic Molecules NASA Code 129-02-07-02, M. Geller and L. M. Sachs	209
D. Reactions of O(^1D) and O(^3P) With Olefins NASA Code 129-02-01-04, W. B. DeMore	212
E. A Physical Frame for Schwarzschild Space-Time NASA Code 129-02-07-02, F. B. Estabrook	217
References	219

TELECOMMUNICATIONS DIVISION

XIX. Communications Systems Research	221
A. Combinatorial Communications: The Index of Comma Freedom for the <i>Mariner</i> Mars 1969 High Data Rate Telemetry Code NASA Code 125-21-01-01, L. D. Baumert and H. C. Rumsey, Jr.	221
B. Communications Systems Development: Acquisition and False-Lock Behavior of Phase-Locked Loops With Noisy Inputs NASA Code 150-22-11-08, R. C. Tausworthe	226
C. Communications Systems Development: Phase-Locked Loops With Externally Aided Track NASA Code 150-22-11-08, R. C. Tausworthe	234
D. Communications Systems Development: Signal Processing for Extended Frequency-Modulation Threshold NASA Code 150-22-11-08, M. J. Malone	238

Contents (contd)

E. Information Processing: Sync Error-Detecting Capability of the Deep Space Network Teletype Code <i>NASA Code 150-22-11-09, G. Solomon, E. C. Posner, and H. Fredricksen</i>	241
F. Information Processing: An Efficient Method for Estimating Noise Variance <i>NASA Code 150-22-11-09, E. C. Posner</i>	242
G. Astrometrics: An Integral Arising in Fourier Inversion <i>NASA Code 150-22-11-10, E. R. Rodemich and E. C. Posner</i>	245
H. Data Compression Techniques: Entropy of a Five-Point Space <i>NASA Code 150-22-17-08, E. C. Posner and P. Slepian</i>	247
References	249
XX. Communications Elements Research	251
A. Low Noise Transponder Preamplifier Research <i>NASA Code 150-22-17-01, S. Petty</i>	251
B. Precision Calibration Techniques: Precision Rotary Vane Attenuator Calibration <i>NASA Code 150-22-11-07, C. T. Stelzried</i>	253
C. RF Breakdown Studies <i>NASA Code 125-22-01-02, R. Woo</i>	259
D. Spacecraft Antenna Research <i>NASA Code 186-68-04-06, K. Woo</i>	260
References	266
XXI. Spacecraft Telemetry and Command	267
A. Relay Telemetry Modulation System Development <i>NASA Code 186-68-04-19, C. Carl</i>	267
References	270
XXII. Spacecraft Radio	271
A. Analyses of Certain Errors for d'Arsonval Movement Meters and Similar Instruments <i>NASA Code 186-68-04-11, M. K. Tam and C. E. Gilchrist</i>	271

I. Systems Analysis Research

SYSTEMS DIVISION

A. Preliminary Lunar Gravity Estimates From Lunar Orbiter, J. Lorell and W. L. Sjogren

The five *Lunar Orbiters* scheduled in the NASA *Lunar Orbiter* program have been successfully launched. Though the prime mission for these *Lunar Orbiters* is photographic, the analysis of the doppler tracking data is providing gravity field information for the selenodesy experiment.

The Jet Propulsion Laboratory is conducting an intensive analysis of the tracking data, under NASA sponsorship (SPS 37-43, Vol. IV, pp. 22-32), with the ultimate aim of mapping the moon's gravity field, and of obtaining other information that may be contained in the data. It is hoped that among the first results will be a resolution of the long standing question of density distribution, i.e., whether or not the moon is denser towards the center. Another early result should be the degree of north-south asymmetry. These two questions should be answered when numerical values of the second- and third-degree zonal harmonics C_{20} and C_{30} are obtained. We are presenting herewith some preliminary results which include values for these two harmonics. However, the reader is

cautioned that these results are preliminary, and are subject to revision as the work of data analysis proceeds.

The lunar gravity field is described in terms of its potential Φ through harmonic coefficients C_{nm} and S_{nm} by the formula

$$\Phi = \frac{\mu}{r} \left[1 + \sum_{n=2}^{\infty} \sum_{m=0}^n \left(\frac{R}{r} \right)^m P_n^m(\sin \phi) (C_{nm} \cos m\lambda + S_{nm} \sin m\lambda) \right]$$

in which μ is the gravity constant whose value is taken from *Mariner IV* estimates as

$$\mu = 4902.78 \text{ km}^3/\text{sec}^2$$

R is the mean radius of the moon, whose value is not critical for these computations, but which is taken as

$$R = 1738.09 \text{ km}$$

$P_n^m(z)$ is the associated Legendre polynomial in z , and r , ϕ , and λ are spherical polar coordinates.

Thus, Φ is determined when numerical values are assigned to C_{nm} and S_{nm} . We chose to limit the number of terms in the series for Φ by considering only those up to and including fourth degree and fourth order ($n = m = 4$) plus C_{50} , C_{60} , and C_{70} , i.e., 24 harmonics in all.

We present in Table 1 a list of the coefficient values and their standard deviations as obtained from the data of the first four *Lunar Orbiters*. Represented here are orbits of 12-, 18-, 21-, and 85-deg inclination, and of 2766-, 3752-, and 6148-km semimajor axes. Six separate arcs were used, the longest of which was 125 days. To show the goodness of fit, we include graphs of residuals (corresponding to the longest arc used in the analysis) of semimajor axis, eccentricity, and node (Ω) plus argument of pericenter (ω) in Figs. 1, 2, and 3, respectively. The raw data, of course, are doppler data from the NASA Deep Space Network (Refs. 1 and 2) and are extremely precise

(i.e., noise level at 1 mm/s). However, from the point of view of sampling the lunar environment, the data are rather skimpy. Additional data from orbits with inclinations between 21 and 85 deg would add considerable strength to the determinations. We feel that the statistics, in particular the standard deviations listed here, are meaningful numbers and reflect the adequacy of the data for estimating the harmonics. To be specific, we chose a weighting factor of 7000 mm/s for the doppler residuals, a factor many times larger than the 1-mm/s noise level. However, it was necessary to choose a number this large in order to be consistent with the scatter in the Kepler element residuals as shown in the accompanying figures.

Table 1. Preliminary estimates of lunar gravity harmonics based on data from Lunar Orbiters I, II, III, and IV

Harmonic coefficient	Coefficient value $\times 10^4$	Standard deviation $\sigma \times 10^4$
C_{20}	-1.9244	0.0129
C_{21}	-0.0897	0.0125
C_{22}	0.2241	0.0242
C_{30}	-0.5911	0.0145
C_{31}	0.3585	0.0024
C_{32}	-0.0421	0.0056
C_{33}	-0.0217	0.0077
C_{40}	0.1843	0.0185
C_{41}	-0.1391	0.0043
C_{42}	0.0259	0.0033
C_{43}	0.0154	0.0021
C_{44}	0.0084	0.0011
C_{50}	-0.5751	0.0198
C_{60}	0.0479	0.0091
C_{70}	0.0905	0.0107
S_{21}	0.0363	0.0135
S_{22}	0.1527	0.0331
S_{31}	0.0991	0.0028
S_{32}	-0.0071	0.0061
S_{33}	-0.0713	0.0013
S_{41}	0.0764	0.0049
S_{42}	-0.0107	0.0034
S_{43}	-0.0260	0.0015
S_{44}	0.0089	0.0011

The values of C_{20} and C_{22} derived from earth-based observations serve as a reference against which to judge the adequacy of Table 1 numbers. Jeffreys (Ref. 3) suggests values of the moment of inertia ratios corresponding to $C_{20} = (-2.093 \pm 0.020) \times 10^{-4}$ and $C_{22} = (0.210 \pm 0.004) \times 10^{-4}$ for a homogeneous moon. He also deduces from geophysical arguments that the moon is slightly denser towards the center, enough to reduce these values by about 1%. He bases his numbers on lunar libration theory, rather than on lunar orbit theory which in its present state requires a much larger value (in absolute magnitude) of C_{20} , corresponding to a moon with denser crust than interior (Ref. 4). The value of C_{20} obtained by JPL from *Lunar Orbiter* data is some 7% less in magnitude than the homogeneous moon value, and thus corresponds to a moon with interior density moderately higher than crust density. In Refs. 5 and 6 there are also results from some preliminary reductions on this data which conclude somewhat different results, indicating again that more data must be analyzed before consistent solutions are obtained.

In regard to the odd zonals, we have no nonorbiter values with which to compare. These coefficients describe the north-south asymmetry, sometimes referred to as the pear-shape. Akim (Ref. 7) has published a value of C_{30} based on a Russian orbiter equal to -0.363×10^{-4} , somewhat smaller numerically than ours, but of the same sign. Note the large numerical value of C_{50} and the high correlation between C_{30} and C_{50} . This situation could lead to radically different estimates of C_{30} if the assumed model did not include C_{50} .

Table 2 lists the pairs of coefficients with high correlations. Of course, the values of the correlations are dependent completely on the types of orbits from which the data were taken. A more complete set of orbits would yield data with smaller correlations.

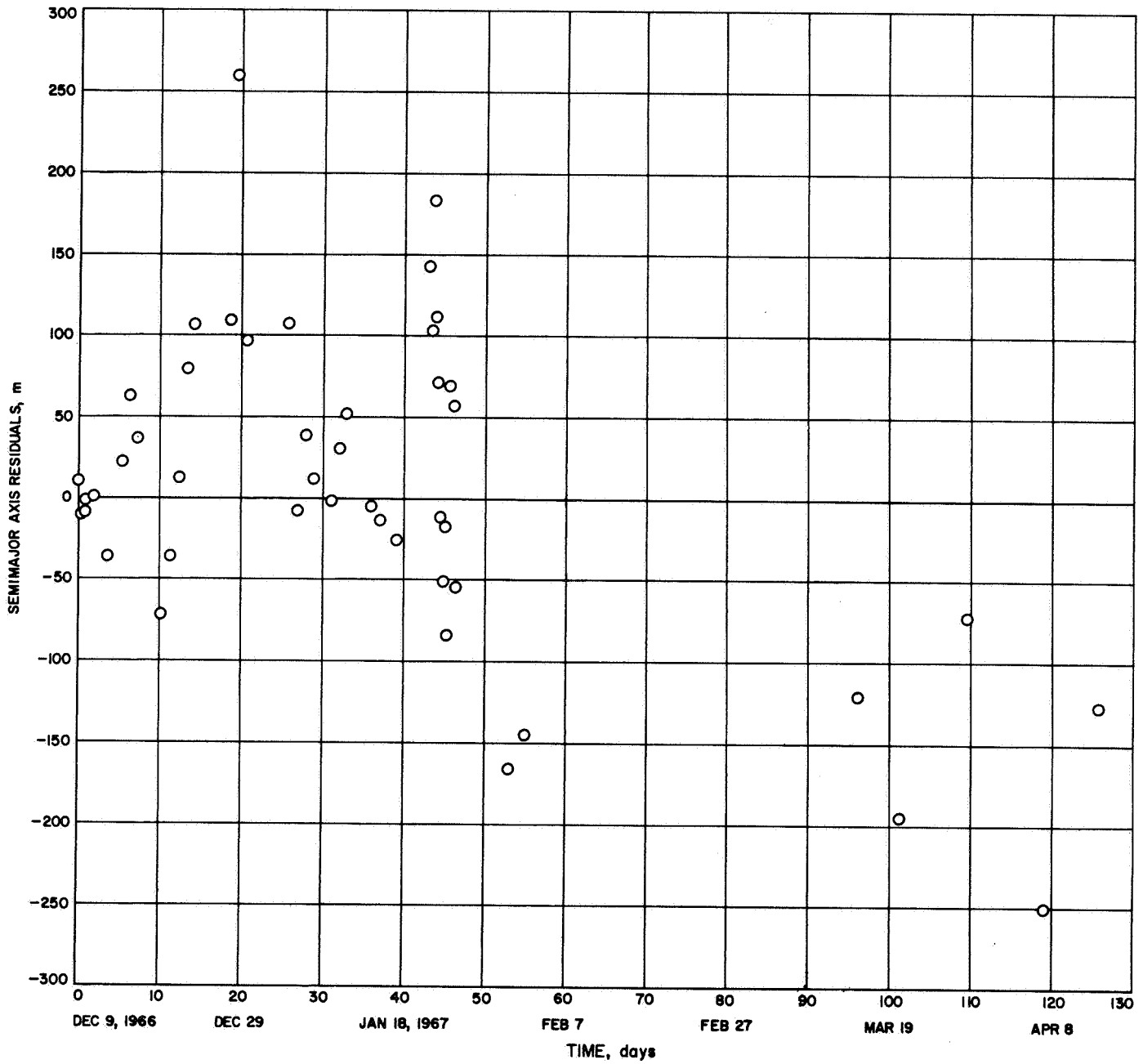


Fig. 1. Semimajor axis residuals

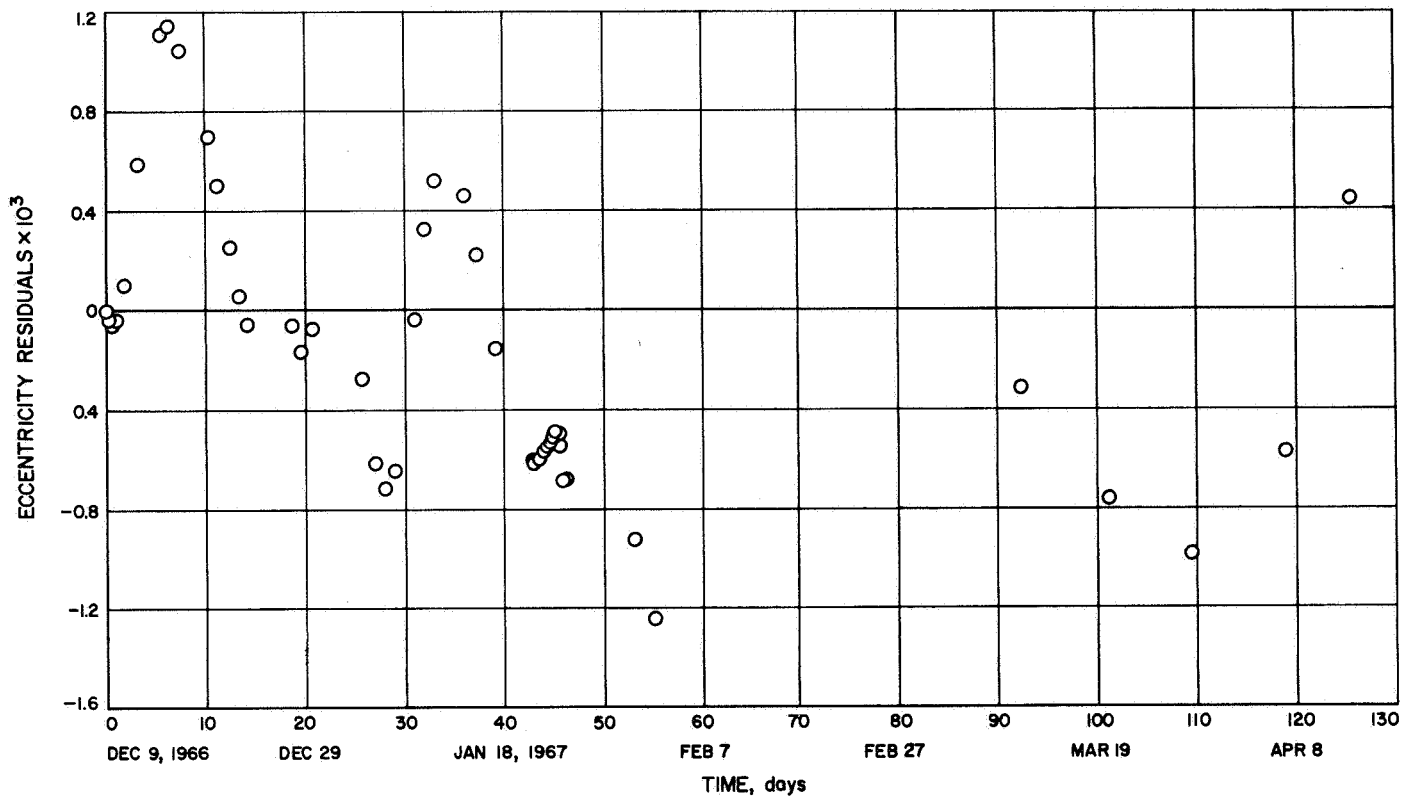


Fig. 2. Eccentricity residuals

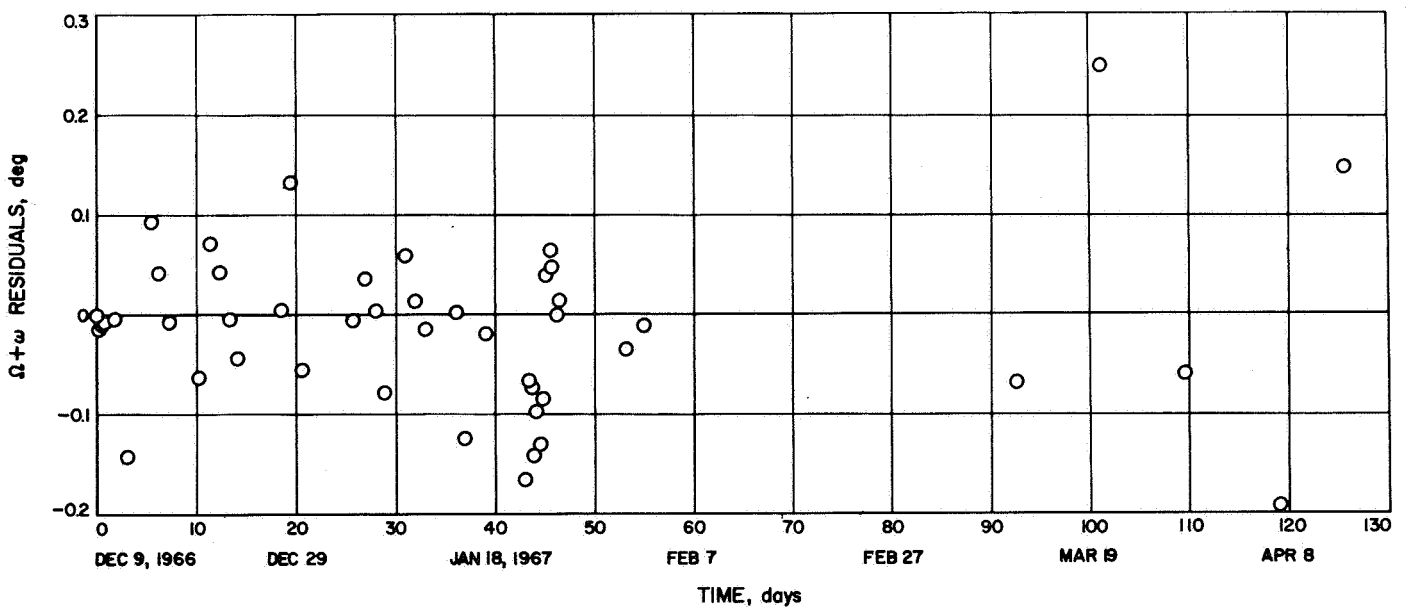


Fig. 3. $\Omega + \omega$ residuals

Table 2. Pairs of harmonic coefficients with correlation values greater than 0.8

Pair of harmonic coefficients	Correlation value
C ₂₀ and C ₄₀	+0.97
C ₂₀ and C ₆₀	+0.83
S ₂₁ and S ₃₁	+0.83
C ₃₀ and C ₅₀	+0.93
S ₃₂ and C ₄₂	-0.92
C ₃₂ and S ₄₂	+0.88
S ₃₃ and C ₄₃	-0.88
C ₄₀ and C ₆₀	+0.94
C ₅₀ and C ₇₀	+0.90

It must be emphasized here that these results are preliminary, the data are still being refined, and hopefully will submit to better fits. Furthermore, more data should soon become available from *Lunar Orbiter V*.

B. The Regularization of Optimal Trajectories,

B. D. Tapley and V. Szebehely

1. Introduction

Regularization reduces or eliminates computational and analytical problems which occur during close approaches to singularities. When the trajectory of a space vehicle connects regions of space in highly uneven gravitational fields, accuracy requirements often necessitate extreme computer times. A case in point may be a trajectory connecting the neighborhood of the earth with that of the moon.

Regularization is performed by transformations which, in general, affect both the dependent and independent variables. After such regularizing transformations, the equations of motion appear in new form and do not contain terms which attain very high values when close approaches occur.

The use of regularized variables in the computation of free-flight trajectories of space vehicles from the earth to the moon has been investigated by Szebehely, Pierce, and Standish (Ref. 8). The results of this study indicate increased computational accuracy and significant reduction in computation time when the regularization is performed.

The conditions which must be satisfied if a space vehicle trajectory is to be optimal require the solution

of a nonlinear two-point boundary value problem. There have been a number of procedures proposed for obtaining numerical solutions to this two-point boundary value problem. A survey of the characteristics of the numerical optimization procedures is given by Tapley and Lewallen (Ref. 9). It is pointed out in Ref. 9 that two of the fundamental characteristics by which a numerical optimization procedure is selected are the computation time and the accuracy with which the terminal conditions can be satisfied.

Based on the results reported in Ref. 8, it may be expected that regularization in the formulation of the optimization problem may benefit the convergence characteristics as well as reduce the computational time. In the following discussion, the equations for the optimal trajectory of a space vehicle with continuous thrust are obtained using regularized variables.

2. Formulation of the Problem

The differential equations which describe the motion of a thrusting rocket in a gravitational field may be expressed as

$$\ddot{\mathbf{r}} = -\mu \frac{\mathbf{r}}{r^3} + \frac{\mathbf{T}}{m} \quad (1)$$

where r is the distance from the force center to the vehicle, \mathbf{r} is the corresponding position vector, $\mu = GM$, G is the universal gravitational constant, M is the mass of the central body, $m = m_0 - \beta t$ is the mass of the space vehicle, $\mathbf{T} = \beta \mathbf{c}$ is the thrust force, β is the mass flow rate, and \mathbf{c} is the exhaust velocity of the propellant (Fig. 4).

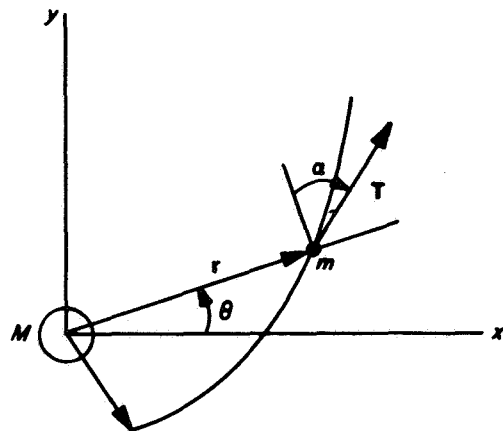


Fig. 4. Model for thrusting rocket

The transfer trajectory extends from the initial state

$$\mathbf{r}(0) = \mathbf{r}_0, \quad \mathbf{v}(0) = \mathbf{v}_0 \quad (2)$$

to the final state

$$\mathbf{r}(t_f) = \mathbf{r}_f(t_f), \quad \mathbf{v}(t_f) = \mathbf{v}_f(t_f) \quad (3)$$

where, in general, the final state will depend on the unknown final time t_f . The thrust history is unspecified, and it is to be chosen so as to minimize the transfer time.

Examination of Eq. (1) indicates that at the force center $|\mathbf{r}| = r \rightarrow 0$, and, consequently, the dominating term on the right-hand side of Eq. (1) is the gravitational force ($\mu\mathbf{r}/r^3$). As r increases, the thrust becomes the dominating term. When the probe is near the force center, the numerical integration process takes small steps in time while far from the force center large increments in time may be used.

While the limit $r = 0$ is not encountered by realistic space vehicle trajectories, situations in which the variation in r is quite large are encountered. The escape trajectory which originates near the earth is a well-known example when numerous changes in computation step size are required. In such a situation, it is desirable to introduce a transformation from the original set of variables $\{\mathbf{r}, t\}$ to another set $\{\boldsymbol{\rho}, \tau\}$ so as to reduce the variation in the relative magnitudes of the forces. Such transformations are called regularizations. The major advantage of expressing the differential equations of motion in regularized variables is that close approaches can be treated with analytical and numerical precision. A discussion of the methods for regularizing the equations of motion for bodies acted on by only gravitational forces is given, for instance, by Szebehely (Ref. 10).

As yet, the equations governing the optimal motion of a space vehicle have not been expressed in regularized form. There appear to be two approaches to this problem. In the first approach, Eq. (1) is regularized and then the problem of optimizing the motion represented by the regularized equations is attacked. In the second approach, the necessary conditions for an optimal transfer are obtained and then these equations are regularized. In other words, one may first regularize and then optimize or one may first optimize and then regularize. Using the regularizing transformation and the same optimization procedure in both approaches, the results will be identical. However, the expressions involved in optimizing the regularized equations are more formidable than those encountered

when the equations for the optimal trajectory are regularized. In the subsequent discussion, only the latter approach is used.

3. The Optimal Trajectory

Consider the problem of finding the stationary value of the integral

$$I = \int_{t_0}^{t_f} dt = t_f - t_0 \quad (4)$$

while satisfying the differential equations

$$\dot{\mathbf{r}} = \mathbf{v}, \quad \dot{\mathbf{v}} = -\mu \frac{\mathbf{r}}{r^3} + \frac{\mathbf{T}}{m}, \quad \dot{m} = -\beta \quad (5)$$

for $t_0 \leq t \leq t_f$. The geometric boundary conditions are

$$\begin{aligned} \mathbf{r}(t_0) &= \mathbf{r}_0, & \mathbf{v}(t_0) &= \mathbf{v}_0, \\ \mathbf{r}(t_f) &= \mathbf{r}_f(t_f), & \mathbf{v}(t_f) &= \mathbf{v}_f(t_f) \end{aligned} \quad (6)$$

The problem can be formulated as a Lagrange problem in the calculus of variations by introducing a set of unknown time-dependent multipliers λ and ω and the constant multipliers \mathbf{v} and \mathbf{n} . Forming the augmented functional

$$\begin{aligned} I &= \mathbf{v} \cdot [\mathbf{r}(t_f) - \mathbf{r}_f(t_f)] + \mathbf{n} \cdot [\mathbf{v}(t_f) - \mathbf{v}_f(t_f)] \\ &+ \int_{t_0}^{t_f} \left\{ 1 + \lambda \cdot \left[-\mu \frac{\mathbf{r}}{r^3} + \frac{\mathbf{T}}{m} - \dot{\mathbf{v}} \right] \right. \\ &\left. + \omega \cdot [\mathbf{v} - \dot{\mathbf{r}}] - \lambda_m [\beta + \dot{m}] \right\} dt \end{aligned} \quad (7)$$

The conditions under which I is a minimum with respect to the choice of $\mathbf{T}(t)$ are sought. For a minimum value of I , it is necessary that

$$\delta I = 0, \quad \delta^2 I \geq 0 \quad (8)$$

where δI and $\delta^2 I$ are the first and second variations of I , respectively. From Eq. (8), the following necessary conditions for an optimal trajectory are obtained in a straightforward manner

$$\begin{aligned} \dot{\mathbf{r}} &= \mathbf{v}, & \dot{\mathbf{v}} &= -\mu \frac{\mathbf{r}}{r^3} - \frac{\mathbf{T}}{m} \frac{\lambda}{\lambda}, & \dot{m} &= -\beta \\ \dot{\lambda} &= -\omega, & \dot{\omega} &= \mu \frac{\lambda}{r^3} - \frac{3\mu}{r^5} (\lambda \cdot \mathbf{r}) \mathbf{r}, & \dot{\lambda}_m &= -\frac{\mathbf{T}}{m^2} \lambda \end{aligned} \quad (9)$$

where $\lambda = |\lambda|$ and $T = |\mathbf{T}| = \beta|\mathbf{c}|$ must hold in the interval $t_0 \leq t \leq t_f$, and at the end points,

$$\left. \begin{aligned} \mathbf{r}(t_0) &= \mathbf{r}_0, & \mathbf{v}(t_0) &= \mathbf{v}_0 \\ \mathbf{r}(t_f) &= \mathbf{r}_f(t_f), & \mathbf{v}(t_f) &= \mathbf{v}_f(t_f) \\ \boldsymbol{\omega}(t_f) &= \mathbf{v}, & \lambda(t_f) &= \mathbf{n} \end{aligned} \right\} \quad (10)$$

$$1 + \lambda \cdot \left[-\mu \frac{\mathbf{r}}{r^3} - \frac{T}{m} \frac{\lambda}{\lambda} \right] + \boldsymbol{\omega} \cdot \mathbf{v} - \lambda_m \beta = 0 \quad (11)$$

Equations (9) may be reduced to the following form:

$$\begin{aligned} \ddot{\mathbf{r}} &= -\mu \frac{\mathbf{r}}{r^3} - \frac{T}{m} \frac{\lambda}{\lambda}, & \ddot{\lambda} &= -\mu \frac{\lambda}{r^3} + \frac{3\mu}{r^5} (\lambda \cdot \mathbf{r}) \mathbf{r} \\ \dot{m} &= -\beta, & \dot{\lambda}_m &= -\frac{T}{m^2} \lambda \end{aligned} \quad (12)$$

Equations (10), (11), and (12) represent conditions which must be satisfied if the trajectory is to be optimal.

It may be shown that Eqs. (12) admit the following integrals:

$$\begin{aligned} \lambda \times \dot{\mathbf{r}} - \dot{\lambda} \times \mathbf{r} &= \mathbf{h} \\ \dot{\lambda} \cdot \dot{\mathbf{r}} + \mu \frac{\lambda \cdot \mathbf{r}}{r^3} + \frac{T}{m} \lambda + \beta \lambda_m &= E \end{aligned} \quad (13)$$

where \mathbf{h} and E are analogous constants to the angular momentum and energy constants associated with the problem of two bodies.

4. The Regularized Equations

The regularization of Eqs. (12) is approached by introducing a new independent variable τ . The classical regularizing transformation, first proposed by K. F. Sundman (Ref. 11), may be generalized by writing

$$d\tau = \frac{dt}{r^n} \quad (14)$$

This transformation allows the selection of the parameter n to satisfy the requirements for regularization. It may be shown that the classical choice $n = 1$ is *not* an advantageous one for the optimal trajectory, since it will not regularize the equations for the Lagrange multipliers $\lambda(t)$.

Using primes for the derivatives with respect to τ and dots for the time-derivatives, and the relation between the derivatives

$$\frac{d}{dt} = r^{-n} \frac{d}{d\tau} \quad (15)$$

the first derivatives of $\mathbf{r}(t)$ and $\lambda(t)$ are obtained as

$$\dot{\mathbf{r}} = r^{-n} \mathbf{r}', \quad \dot{\lambda} = r^{-n} \lambda' \quad (16)$$

The second derivatives become

$$\begin{aligned} \ddot{\mathbf{r}} &= [\mathbf{r}'(-nr^{-(n+1)}) + \mathbf{r}''r^{-n}] r^{-n} \\ \ddot{\lambda} &= [\lambda'(-nr^{-(n+1)}) + \lambda''r^{-n}] r^{-n} \end{aligned} \quad (17)$$

where $\mathbf{r}' = (\mathbf{r} \cdot \mathbf{r}') r^{-1}$. Substituting these results into Eqs. (12) leads to

$$\begin{aligned} r^{-2n} r'' - nr^{-2n} \frac{(\mathbf{r} \cdot \mathbf{r}')}{r^2} \mathbf{r}' &= -\mu \frac{\mathbf{r}}{r^3} - \frac{T}{m} \frac{\lambda}{\lambda} \\ r^{-2n} \lambda'' - nr^{-2n} \frac{(\mathbf{r} \cdot \mathbf{r}')}{r^2} \lambda' &= -\mu \frac{\lambda}{r^3} + \frac{3\mu}{r^5} (\lambda \cdot \mathbf{r}) \mathbf{r} \end{aligned} \quad (18)$$

$$m' = -\beta r^n, \quad \lambda'_m = -\frac{T}{m^2} \lambda r^n \quad (19)$$

Multiplying Eqs. (18) by r^{2n} , the term $r^{(3-2n)}$ will appear in the denominators on the right-hand side. The condition of regularization is that r appears only to the 0th order in the denominator. This is satisfied if

$$\frac{3}{2} \leq n \quad (20)$$

Selecting the lowest value for n , we have $n = 3/2$. Equations (18) and (19) become

$$\left. \begin{aligned} r'' - \frac{3}{2} \frac{(\mathbf{r} \cdot \mathbf{r}')}{r^2} \mathbf{r}' + \mu \mathbf{r} &= -\frac{T}{m} r^3 \frac{\lambda}{\lambda} \\ \lambda'' - \frac{3}{2} \frac{(\mathbf{r} \cdot \mathbf{r}')}{r^2} \lambda' + \mu \lambda &= 3\mu \frac{(\lambda \cdot \mathbf{r})}{r^2} \mathbf{r} \\ m' &= -\beta r^{3/2}, & \lambda'_m &= -\frac{T}{m^2} r^{3/2} \lambda \end{aligned} \right\} \quad (21)$$

The condition used to relate the parameter τ and the time t is

$$t = \int_{t_0}^{\tau} r^{3/2} d\tau \quad (22)$$

It may be shown that Eqs. (21) are regular. First, we observe that the last two equations contain no singularities since $m > 0$ in the range $t_0 \leq t \leq t_f$. The same applies to the right-hand side of the first equation since both m and λ are different from zero. The term on the right-hand side of the second equation may be evaluated using the second of Eqs. (13) as follows:

$$\begin{aligned} 3\mu \frac{(\lambda \cdot \mathbf{r}) \mathbf{r}}{r^2} &= 3r \mathbf{r} \left[\mu \frac{(\lambda \cdot \mathbf{r})}{r^3} \right] \\ &= 3r \mathbf{r} \left[E - \dot{\lambda} \cdot \dot{\mathbf{r}} - \frac{T}{m} \lambda - \beta \lambda_m \right] \end{aligned} \quad (23)$$

From Eqs. (16)

$$\dot{\lambda} \cdot \dot{\mathbf{r}} = r^{-2n} (\lambda' \cdot \mathbf{r}')$$

or

$$\dot{\lambda} \cdot \dot{\mathbf{r}} = \frac{\lambda' \cdot \mathbf{r}'}{r^3} \quad (24)$$

In this way, Eq. (23) can be written as

$$3\mu \frac{(\lambda \cdot \mathbf{r}) \mathbf{r}}{r^2} = 3r \mathbf{r} \left[E - \frac{T}{m} \lambda - \beta \lambda_m \right] + 3 \frac{(\lambda' \cdot \mathbf{r}') \mathbf{r}}{r^2} \quad (25)$$

The remaining critical terms in Eqs. (21) and (25) are

$$\frac{(\mathbf{r} \cdot \mathbf{r}')}{r^2} \mathbf{r}, \quad \frac{(\mathbf{r} \cdot \mathbf{r}')}{r^2} \lambda', \quad \frac{(\lambda' \cdot \mathbf{r}')}{r^2} \mathbf{r}$$

The limiting value of these expressions as $r \rightarrow 0$ may be obtained from considering the problem of collision of two bodies. For this case, the energy integral gives

$$|\dot{\mathbf{r}}|^2 = \frac{2\mu}{r} - c$$

which, after the transformation given by Eqs. (16), becomes

$$|\mathbf{r}'|^2 = 2\mu r^{2n-1} - cr^{2n} = 2\mu r^2 - cr^3$$

Therefore $|\mathbf{r}'| \sim r$, or in other words, $|\mathbf{r}'|$ approaches zero as r does. The absolute value of the first critical term becomes

$$\frac{r |\mathbf{r}'|^2}{r^2} \cos \phi \sim r \cos \phi \rightarrow 0$$

where ϕ is the angle between \mathbf{r} and $\dot{\mathbf{r}}$ (or between \mathbf{r} and \mathbf{r}').

The absolute value of the second critical term is

$$\frac{r |\mathbf{r}'| |\lambda'|}{r^2} \cos \phi \sim |\lambda'| \cos \phi$$

and that of the third critical term becomes

$$\frac{r |\mathbf{r}'| |\lambda'|}{r^2} \cos \Psi \sim |\lambda'| \cos \Psi$$

where Ψ is the angle between \mathbf{r}' and λ' (or between $\dot{\mathbf{r}}$ and $\dot{\lambda}$).

Hence, it can be concluded that the previously discussed first term approaches zero and the second and third terms approach finite values as $r \rightarrow 0$.

5. Conclusions and Recommendations

This investigation establishes the fact that the equations for optimized trajectories in a central force field may be regularized, i.e., the singularity due to the gravitational potential may be eliminated. As a corollary, it is found that the optimization of the regularized trajectories presents a considerable amount of analytical and algebraic difficulties.

The model used corresponds to a space vehicle moving in the gravitational field of a single spherical planet. The vehicle is subjected to a thrust of constant magnitude. The variable direction of this thrust vector is determined so that the total travel time (and consequently the fuel used) is minimized for the mission.

The following recommendations for additional studies are offered:

- (1) The analytical findings in this article should undergo a detailed numerical evaluation to determine the merits of the equations and variables proposed.
- (2) The model used should be generalized. The first and immediate extension is to the restricted problem of three bodies. The method proposed in this article may be applied to the restricted problem and consequently to lunar and interplanetary trajectories if matching techniques are incorporated. Since such techniques often introduce additional inaccuracies and are not necessary in the restricted problem, it is conjectured that optimized lunar trajectories may be regularized by methods analogous to those described in this article.

(3) Due to the difficulties encountered in optimizing the regularized equations of motion, it is recommended that the extensions be made by first optimizing and then regularizing the resulting equations.

(4) Further extensions will be indicated as practical mission requirements appear.

C. Neighboring Extremal Technique for Optimal Control Problems With Discontinuities,

S. R. McReynolds

The "neighboring extremal technique" is used in optimal control for the purposes of computing feedback control laws and optimal trajectories (Ref. 12). Most of the existing literature treats problems where the optimal control functions are continuous functions of time. The neighboring extremal technique requires special modification for problems with discontinuities in the optimal control functions. In this article we shall extend this technique for problems with discontinuities. As a by-product a new necessary condition emerges.

1. The Problem

The optimal control problem that we shall treat takes the following form. Find the piecewise continuous function $u(t)$ over the fixed time interval $(0, T)$ to maximize

$$J = \phi[x(T)] + \int_0^T L[x(t), u(t), t] dt \quad (1)$$

subject to the constraints

$$\dot{x} = f(x, u, t) \quad (2)$$

$$x(0) = x_0 \text{ specified} \quad (3)$$

The following vector notation has been used:

$$x^T = (x_1, x_2, \dots, x_n) \text{ is the state vector}$$

$$u^T = (u_1, u_2, \dots, u_m) \text{ is the control vector}$$

Standard optimal control theory characterizes the optimal solution in terms of a solution to a two-point boundary value problem. The adjoint vector is defined

$$\lambda(T) = \phi_x^T[x(T)] \quad (4)$$

$$\dot{\lambda} = -H_x^T \quad (5)$$

where

$$H = \lambda^T f(x, u, t) + L(x, u, t)$$

is the standard Hamiltonian. In order for the control $u(t)$ to be optimum, $u(t)$ must maximize the Hamiltonian. If the Hamiltonian is continuously differentiable with respect to u , then

$$H_u = 0 \quad (6)$$

must hold along the optimal trajectory.

At points where the control is discontinuous, neither $x(t)$ nor $\lambda(t)$ will necessarily be differentiable. However, $x(t)$ and $\lambda(t)$ must be continuous at such points. If $t_i, i = 1, \dots, n$, denote the times of the discontinuities, then

$$x(t_i^-) = x(t_i^+), \quad i = 1, \dots, n \quad (7)$$

$$\lambda(t_i^-) = \lambda(t_i^+), \quad i = 1, \dots, n \quad (8)$$

$x(t)$ must be continuous for physical reasons. However, the continuity of $\lambda(t)$ requires derivation. The Hamiltonian must also be continuous:

$$H^- = H^+, \quad t_i = 1, \dots, n \quad (9)$$

Equations (2) through (9) constitute a nonlinear two-point boundary value problem which must be satisfied by the optimal solution.

2. Generation of Extremals

An extremal to the above problem is a solution which satisfies Eqs. (2) and (4) through (9). The only necessary condition that is not required to be satisfied is the initial condition specified by Eq. (3). An extremal may be generated in the following ways:

- (1) Choose $x(T)$ arbitrarily.
- (2) Choose $\lambda(T)$ to satisfy Eq. (4).
- (3) Choose $u(t)$ to maximize the Hamiltonian.
- (4) Construct functions $x(t)$ and $\lambda(t)$ by integrating the differential Eqs. (2) and (5). At points where \dot{x} and $\dot{\lambda}$ are discontinuous (because of a discontinuity in u), $\lambda(t)$ and $x(t)$ are to be continuous.

The only property of an extremal that the above-constructed solution does not obviously satisfy is the continuity of H . However, if H is a continuous function of all

its arguments, this property will naturally follow from the construction.

Since $x(T)$ determines an extremal, the field of extremals is n -dimensional. These n constants provide just enough degrees of freedom so that the initial conditions may be satisfied.

3. The Linearized Equations

A problem that often appears in guidance is as follows: An extremal solution that satisfies certain initial conditions is given, and an extremal solution that satisfies slightly different initial conditions is desired. To obtain an extremal with the desired initial conditions, the technique for solving the above problem may be iterated, starting from a generated extremal.

The neighboring extremal technique approximates neighboring extremals by solving the linearized two-point boundary value problem. The linearized equations are obtained as follows: Let (λ^*, x^*, u^*) denote a nominal extremal solution. Let (λ, x, u) be a neighboring extremal solution, and let $\delta\lambda = \lambda - \lambda^*$, $\delta x = x - x^*$, and $\delta u = u - u^*$. The expansion of Eq. (2) around a nominal solution yields

$$\delta\dot{x} = f_x\delta x + f_u\delta u + 0(\delta x^2, \delta u^2)$$

Provided that δx and δu are small, the above equation can be approximated by

$$\delta\dot{x} = f_x\delta x + f_u\delta u \quad (10)$$

Similarly, Eqs. (4) through (6) yield the linear approximations

$$\delta\lambda(T) = \phi_{xx}[x(T)]\delta x(T) \quad (11)$$

$$\delta\dot{\lambda} = -f_x^T\delta\lambda - H_{xx}\delta x - H_{xu}\delta u \quad (12)$$

$$0 = f_u^T\delta\lambda + H_{ux}\delta x + H_{uu}\delta u \quad (13)$$

Now we suppose that

$$\delta x(0) = \text{specified} \quad (14)$$

Equations (10) through (14) define a linear two-point boundary value problem which can be solved by means of several techniques (Refs. 12 and 13).

If discontinuities are present in the solution, the previous technique must be modified near the points of discontinuity. This is because a neighboring extremal will usually have its discontinuities displaced in time. Hence, near the discontinuities there will be intervals for which the change in u will be relatively large, and neither of the linearizations in Eqs. (10), (12), and (13) are valid over these intervals.

Fortunately, these effects can be approximated by impulses, superimposed on the standard perturbation equations. How this is done for trajectories is pictured in Fig. 5. The standard linearized equations are used to generate neighboring trajectories on either side of the discontinuity. However, if the discontinuity is displaced by dt , there is an apparent discontinuity given by

$$dx^+ - dx^- = -(f^+ - f^-)dt \quad (15)$$

dx^+ and dx^- denote, respectively, the right-hand and left-hand limits of the displaced trajectory at the time of original discontinuity obtained using small perturbation theory. f^+ and f^- denote, respectively, the right-hand and left-hand limits of f . The above formula is valid for $+dt$ and $-dt$.

A similar relation holds for the adjoint vector λ and the Hamiltonian H

$$\delta\lambda^+ - \delta\lambda^- = (H_x^+ - H_x^-)dt \quad (16)$$

$$\delta H^+ - \delta H^- = -(H_t^+ - H_t^-)dt \quad (17)$$

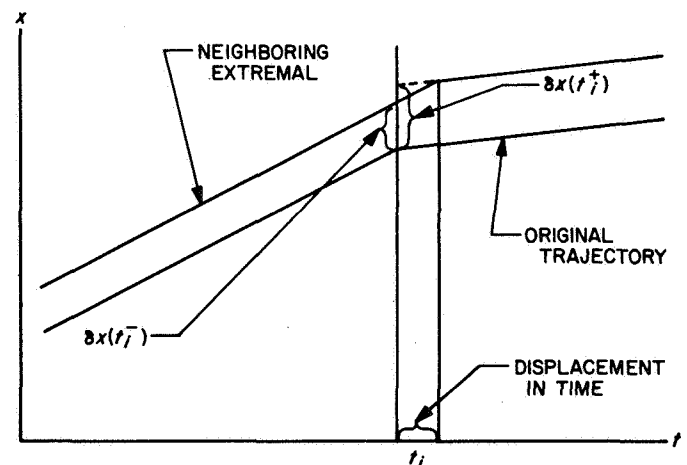


Fig. 5. Neighboring extremals near a discontinuity

In the above, we have employed the relations

$$\dot{\lambda} = -H_x, \quad \dot{H} = H_t$$

Now

$$\begin{aligned} \delta H &= H_x \delta x + f^T \delta \lambda + H_u \delta u \\ &= H_x \delta x + f^T \delta \lambda \end{aligned}$$

Hence, Eq. (17) can be written as

$$\begin{aligned} 0 &= H_x^+ \delta x^+ - H_x^- \delta x^- + f^{T+} \delta \lambda^+ \\ &\quad - f^{T-} \delta \lambda^- + (H_t^+ - H_t^-) dt \end{aligned} \quad (18)$$

Now Eqs. (15), (16), and (18) complete the linearized equations.

4. The Sweep Method

In Ref. 13 the sweep method solution is given for the above linear two-point boundary value problem for problems without discontinuities. Here, we briefly summarize those results and show what additions are necessary to handle the discontinuities.

Assuming that H_{uu} is nonsingular, one solves Eq. (13) for δu .

$$\delta u = -H_{uu}^{-1} (f_u^T \delta \lambda + H_{ux} \delta x) \quad (19)$$

This expression is used to eliminate δu from Eqs. (10) and (12), whence

$$\delta \dot{x} = A \delta x + B \delta \lambda \quad (20)$$

$$\delta \dot{\lambda} = -C \delta \dot{x} - A^T \delta \lambda \quad (21)$$

where

$$A = f_x - f_u H_{uu}^{-1} H_{ux} \quad (22)$$

$$B = -f_u H_{uu}^{-1} f_u^T \quad (23)$$

$$C = H_{xx} - H_{xu} H_{uu}^{-1} H_{ux} \quad (24)$$

Next, a matrix $P(t)$ is constructed so that

$$\delta \lambda(t) = P(t) \delta x(t) \quad (25)$$

is satisfied identically for all solutions of the differential Eqs. (20) and (21) that also satisfy the terminal boundary condition given by Eq. (11). $P(t)$ satisfies

$$P(T) = \phi_{xx}(T) \quad (26)$$

$$\dot{P} = -PA - A^T P - PBP - C \quad (27)$$

From the above construction, it is seen that $P(t)$ is symmetric. Equation (27) is a well-known matrix Riccati equation. Solutions to this equation will become unbounded at conjugate points. However, solutions to this equation may be well-behaved even though the linearized equations are unstable.

Another advantage of the relationship given by Eq. (25) is that it may be used directly in Eq. (19) to obtain a feedback law for the optimal control

$$\delta u = -H_{uu}^{-1} (f_u^T P + H_{ux}) \delta x \quad (28)$$

Storing the above relationship saves us from again integrating the linearized equations.

Now suppose that a discontinuity is encountered on the backward sweep. The matrix P^+ in the relation $\delta \lambda^+ = P^+ \delta x^+$ is known. Employing this relationship in Eqs. (16) and (18) results in

$$\delta \lambda^- = P^+ \delta x^+ - (H_x^{+T} - H_x^{-T}) dt \quad (29)$$

$$\begin{aligned} 0 &= (H_x^+ + f^+ P^+) \delta x^+ - H_x^- \delta x^- \\ &\quad - f^{T-} \delta \lambda^- + (H_t^+ - H_t^-) dt \end{aligned} \quad (30)$$

Now Eq. (15) may be used to eliminate δx^+ from Eqs. (29) and (30).

$$\delta \lambda^- = P^+ \delta x^- + [P^+ (f^+ - f) + H_x^+ - H_x^-] dt \quad (31)$$

$$\begin{aligned} 0 &= (H_x^+ - H_x^- + f^+ P^+) \delta x^- - f^{T-} \delta \lambda^- \\ &\quad + [(H_x^+ + f^+ P^+) (f^- - f^+) + H_t^+ - H_t^-] dt \end{aligned} \quad (32)$$

Now Eq. (31) may be used to eliminate $\delta \lambda^-$ from Eq. (32).

$$\begin{aligned} 0 &= [H_x^+ - H_x^- + (f^+ - f)^T P^+] \delta x^- \\ &\quad + [-(f^+ - f)^T P^+ (f^- - f) - H_x^+ (f^- - f) \\ &\quad + (H_x^+ - H_x^-) f + H_t^+ - H_t^-] dt \end{aligned} \quad (33)$$

Equation (33) may be used to solve for dt . This requires the inversion of the scalar

$$S = -(f^+ - f^-)^T P^+ (f^+ - f^-) - H_x^+ (f^+ - f^-) + (H_x^+ - H_x^-) f + H_t^+ - H_t^- \quad (34)$$

The significance of S shall be treated later. Let us also introduce the row vector

$$R_x = H_x^+ - H_x^- + (f^+ - f^-)^T P^+ \quad (35)$$

If S is not zero, Eq. (35) may be solved for dt .

$$dt = -\frac{1}{S} R_x \delta x^- \quad (36)$$

If Eq. (36) is used to eliminate dt , Eq. (31) becomes

$$\delta \lambda^- = \left(P^+ - \frac{1}{S} R_x^T R_x \right) \delta x^- \quad (37)$$

This is the relation $\delta \lambda^- = P^- \delta x^-$. Hence

$$P^- = P^+ - \frac{1}{S} R_x^T R_x \quad (38)$$

The final result is that a discontinuity in the Riccati matrix P must take place on the backward sweep. The relation Eq. (36) may be used to estimate the change in the time of the discontinuity in the forward sweep.

5. Interpretation of S

Since $(H^- - H^+)$ represents the gradient of performance index with respect to the time of the discontinuity, the quantity S represents the second derivative of the performance index with respect to the time of discontinuity. A dynamic programming derivation of this fact shall be presented.

$V^+(x, t)$ shall denote the optimal return function defined in a region to the right of the discontinuity. Let x_0 at time t_0 be left of the discontinuity from which the optimal policy is to be constructed. Let x_1 at time t_1 denote the state to the right of the discontinuity which is arrived at

from x_0 using the optimal policy. If t^* denotes the switching time, then

$$x_1 = x_0 + \int_{t_0}^{t^*} f(x, u; t) dt + \int_{t^*}^{t_1} f(x, u; t) dt \quad (39)$$

The value of the optimal return is given by

$$V^-(x_0, t_0) = V^+(x_1, t_1) + \int_{t_0}^{t^*} L(x, u; t) dt + \int_{t^*}^{t_1} L(x, u; t) dt \quad (40)$$

where t^* is chosen optimally. A necessary condition for t^* to be optimally chosen is that the right-hand side of Eq. (40) be stationary with respect to variations with respect to t^* . This implies

$$\frac{\partial V^-}{\partial t^*}(x_0, t_0) = \frac{\partial V}{\partial x_1} \frac{\partial x_1}{\partial t^*} \Big|_{x=x^*, t=t^*} + [L(x^*, u; t^*) - L(x^*, u; t^*)] = 0 \quad (41)$$

x^* denotes the value of x at time t^* . All the terms in the above expressions are evaluated at x^* and t^* . $\partial x_1 / \partial t^*$ is obtained from Eq. (39) as follows:

$$\frac{\partial x_1}{\partial t^*} = (f^+ - f^-) \Big|_{x^*, t^*} \quad (42)$$

The second partial derivative of V^- with respect to t^* is given by

$$\frac{\partial^2 V^-}{\partial t^{*2}}(x_0, t_0) = \frac{\partial}{\partial t} \left(\frac{\partial V}{\partial x} \right) \frac{\partial x_1}{\partial t^*} + \frac{\partial V^+}{\partial x_1} \frac{\partial^2 x_1}{\partial t^{*2}} + \frac{\partial L^-}{\partial t^*} - \frac{\partial L^+}{\partial t^*} \quad (43)$$

Again, all the expressions are evaluated at the discontinuity x^*, t^* . To obtain the various derivatives in the above expression, we recall

$$x^*(t^*) = \int_{t_0}^{t^*} f(x, u; t) dt + x(t_0)$$

$$\frac{\partial V}{\partial x}(x^*, t^*) = - \int_{t^*}^{t_1} \left(\frac{\partial V}{\partial x} f^+ + L^+ \right) dt + \frac{\partial V^+}{\partial x}(x_1, t_1)$$

Hence,

$$\frac{\partial x^*}{\partial t^*} = f(x^*, u, t^*)$$

$$\frac{\partial}{\partial t^*} \frac{\partial V}{\partial x}(x^*, t^*) = \left(\frac{\partial V}{\partial x} f^+ + L^+ \right)_{x^*, t^*} + \frac{\partial^2 V^+}{\partial x^2} \frac{\partial x_1}{\partial t^*}$$

Applying the above formulas to Eq. (43), one obtains

$$\begin{aligned} \frac{\partial^2 V^-}{\partial t^{*2}}(x_0, t_0) &= \left(\frac{\partial V}{\partial x} f^+ + L^+ \frac{\partial^2 V^+}{\partial x^2} \right) (f^- - f^+) \frac{\partial^2 V^+}{\partial x^2} (f^- - f^+) \\ &+ \frac{\partial V}{\partial x} [f_t^- - f_t^+ + (f_x^- - f_x^+) f] \\ &+ (L_x^+ - L_x^-) f + L_t^+ - L_t^- \end{aligned}$$

Now, let us make the following identifications:

$$H^+ = \frac{\partial V}{\partial x} f^+ + L^+$$

$$H^- = \frac{\partial V}{\partial x} f^- + L^-$$

$$P^+ = \frac{\partial^2 V^+}{\partial x^2}$$

One thus obtains the expression in Eq. (34).

A necessary condition, that, as far as the author knows, is new, is given by

$$S \leq 0 \quad (44)$$

Thus, as is typically the case, the second variation is required to be nonsingular before the neighboring extremal technique may be applied.

6. Example

Consider the following problem. Maximize

$$J = \frac{1}{2} x^2(T) + \int_0^T \frac{1}{2} (x + u)^2 dt$$

subject to the constraints

$$\dot{x} = u$$

$$|u| \leq 1$$

The Hamiltonian is given by

$$H = \lambda u + \frac{1}{2} (x + u)^2$$

u_{opt} is either ± 1 :

$$u_{opt} = \begin{cases} +1, & x + \lambda > 0 \\ -1, & x + \lambda < 0 \end{cases}$$

If $x + \lambda = 0$, the Hamiltonian is maximized by both $u = +1$ and $u = -1$. If $u^+ = 1$, $u^- = -1$, then

$$S = -4P^+ - 2x - 4$$

This is required to be negative before a switch is indicated. P^- is given by

$$P^- = P^+ + \frac{(1 + P^+)^2}{1 + P^+ + \frac{x}{2}}$$

The change in the switching time for neighboring extremals is approximated by

$$dt = + \frac{(1 + P^+)}{(2 + 2P^+ + x)} dx^-$$

D. A Note on Regularization Transformations in the Calculus of Variations, H. Lass and

S. R. McReynolds

The most elementary problem in the calculus of variations is that of determining the set of paths $q^i(t)$, $i = 1, 2, \dots, n$, which extremalizes the integral

$$I = \int_0^T \mathbf{L}(q, \dot{q}, t) dt \quad (1)$$

with specified boundary conditions at $t = 0$, $t = T$, say $q^i(0) = q_0^i$, $q^i(T) = q_T^i$, $i = 1, 2, \dots, n$. The solution is obtained by solving the Euler-Lagrange equations

$$\frac{d}{dt} \left(\frac{\partial \mathbf{L}}{\partial \dot{q}^i} \right) - \frac{\partial \mathbf{L}}{\partial q^i} = 0, \quad i = 1, 2, \dots, n \quad (2)$$

subject to the fixed boundary conditions.

In analytic dynamics, $L = T - V$, with T the kinetic energy and V the potential energy. Quite often the potential function V will contain a singularity. For the motion of a particle in the presence of a mass M located at the origin, $V = -MG/r$ yields a singularity at $r = 0$. The transformation $dt = rd\tau$ yields

$$L dt = (T - V) r d\tau = (rT - GM) d\tau$$

Thus, the singularity has been removed from the potential term.

The change of variable from t to τ is called a regularization transformation. Dr. Roger Broucke of JPL in a paper to be published in "ICARUS" makes use of Eq. (2) to obtain a set of equations for the paths under a regularization transformation. He also discusses coordinate transformations which simplify the kinetic energy term.

In this article the equations of motion will be obtained from first principles.

Let

$$dt = \psi(q^1, q^2, \dots, q^n) d\tau = \psi(q) d\tau \quad (3)$$

be a regularization transformation. Then

$$\begin{aligned} t &= \int_0^\tau \psi[q(u)] du \\ T &= \int_0^{\tau_0} \psi[q(u)] du \end{aligned} \quad (4)$$

with $q^i(0) = q_i^0$, $q^i(\tau_0) = q_i^1$, $i = 1, 2, \dots, n$. Since T is fixed, we note that τ_0 is a functional of the q^i since different paths yield different values of τ_0 , the upper limit in the integral of Eq. (4).

Equation (1) now becomes

$$I = \int_0^{\tau_0} L(q, \dot{q}, \xi) d\tau \quad (5)$$

with

$$\xi = \int_0^\tau \psi[q(u)] du$$

and $\dot{q} = dq/d\tau$, so that

$$L(q, \dot{q}, \xi) = \psi(q) L \left\{ q, \frac{1}{\psi} \frac{dq}{dt}, \int_0^\tau \psi[q(u)] du \right\}$$

Now let $Q^i(\tau)$ be the optimal set of paths which extremalize I of Eq. (5), and consider

$$q^i(\tau) = Q^i(\tau) + \varepsilon \eta^i(\tau) \quad (6)$$

as a family of nearby paths, with ε an arbitrary parameter and $\eta^i(\tau)$ arbitrary functions of τ . From $q^i(0) = Q^i(0) + \varepsilon \eta^i(0)$ it follows that $\eta^i(0) = 0$ since $q^i(0) = Q^i(0) = q_i^0$. Furthermore,

$$\begin{aligned} q_1^i &= q^i(\tau_0 + \delta) = Q^i(\tau_0 + \delta) + \varepsilon \eta^i(\tau_0 + \delta) \\ &\approx Q^i(\tau_0) + \dot{Q}^i(\tau_0) \delta + \varepsilon \eta^i(\tau_0 + \delta) \\ &\approx q_1^i + \dot{Q}^i(\tau_0) \delta + \varepsilon \eta^i(\tau_0 + \delta) \end{aligned} \quad (7)$$

so that

$$\eta^i(\tau_0 + \delta) = -\dot{Q}^i(\tau_0) \frac{\delta}{\varepsilon} \quad (8)$$

To obtain δ/ε we make use of Eq. (4). Thus

$$\int_0^{\tau_0 + \delta} \psi(Q + \varepsilon \eta) du = \int_0^{\tau_0} \psi(Q) du \quad (9)$$

Now

$$\psi(Q + \varepsilon \eta) \approx \psi(Q) + \varepsilon \frac{\partial \psi}{\partial Q^\alpha} \eta^\alpha$$

so that

$$\int_{\tau_0}^{\tau_0 + \delta} \psi(Q) du = -\varepsilon \int_0^{\tau_0} \frac{\partial \psi}{\partial Q^\alpha} \eta^\alpha du \quad (10)$$

Applying the law of the mean yields

$$\lim_{\varepsilon \rightarrow 0} \frac{\delta}{\varepsilon} = \left(\frac{d\delta}{d\varepsilon} \right)_{\varepsilon=0} = -\frac{1}{[\psi(Q)]_{\tau_0}} \int_0^{\tau_0} \frac{\partial \psi}{\partial Q^\alpha} \eta^\alpha du \quad (11)$$

assuming that $[\psi(Q)]_{\tau_0} \neq 0$.

Returning to Eqs. (5) and (6), one obtains

$$I(\varepsilon) = \int_0^{\tau_0 + \delta} L(Q + \varepsilon \eta, \dot{Q} + \varepsilon \dot{\eta}, \xi) d\tau \quad (12)$$

Thus

$$\left(\frac{dI}{d\varepsilon}\right)_{\varepsilon=0} = \int_0^{\tau_0} \left[\frac{\partial L}{\partial Q^\alpha} \eta^\alpha + \frac{\partial L}{\partial \dot{Q}^\alpha} \dot{\eta}^\alpha + \frac{\partial L}{\partial \xi} \int_0^\tau \frac{\partial \psi}{\partial Q^\alpha} \eta^\alpha du \right] d\tau + L_{\tau_0} \left(\frac{d\delta}{d\varepsilon}\right)_{\varepsilon=0} \quad (13)$$

with

$$\xi = \int_0^\tau \psi(Q) du$$

Integrating the second term of Eq. (13) by parts and making use of Eqs. (8) and (11) yields

$$\left(\frac{dI}{d\varepsilon}\right)_{\varepsilon=0} = \int_0^{\tau_0} \left[\frac{\partial L}{\partial Q^\alpha} - \frac{d}{d\tau} \left(\frac{\partial L}{\partial \dot{Q}^\alpha} \right) + \left(\frac{\dot{Q}^\beta \frac{\partial L}{\partial \dot{Q}^\beta} - L}{\psi} \right)_{\tau=\tau_0} \frac{\partial \psi}{\partial Q^\alpha} \right] \eta^\alpha d\tau + \int_0^{\tau_0} \frac{\partial L}{\partial \xi} \int_0^\tau \frac{\partial \psi}{\partial Q^\alpha} \eta^\alpha du d\tau \quad (14)$$

Now

$$\int_0^{\tau_0} \frac{\partial L}{\partial \xi} \int_0^\tau \frac{\partial \psi}{\partial Q^\alpha} \eta^\alpha du d\tau = \int_0^{\tau_0} \frac{\partial \psi}{\partial Q^\alpha} \eta^\alpha \int_{u=\tau}^{u=\tau_0} \frac{\partial L}{\partial \xi} du d\tau \quad (15)$$

so that

$$\left(\frac{dI}{d\varepsilon}\right)_{\varepsilon=0} = \int_0^{\tau_0} \left[\frac{\partial L}{\partial Q^\alpha} - \frac{d}{d\tau} \left(\frac{\partial L}{\partial \dot{Q}^\alpha} \right) + \left(\frac{K}{\psi} \right)_{\tau_0} \frac{\partial \psi}{\partial Q^\alpha} + \frac{\partial \psi}{\partial Q^\alpha} \int_\tau^{\tau_0} \frac{\partial L}{\partial \xi} du \right] \eta^\alpha d\tau \quad (16)$$

with $K = Q^\beta (\partial L / \partial \dot{Q}^\beta) - L$, the Hamiltonian associated with the Lagrangian L .

A necessary condition for an extremal is that $(dI/d\varepsilon)_{\varepsilon=0}$ vanish for arbitrary $\eta^\alpha(\tau)$. Thus, we obtain

$$\frac{d}{d\tau} \left(\frac{\partial L}{\partial \dot{q}^\alpha} \right) - \frac{\partial L}{\partial q^\alpha} = \left[\left(\frac{K}{\psi} \right)_{\tau_0} + \int_\tau^{\tau_0} \frac{\partial L}{\partial \xi} du \right] \frac{\partial \psi}{\partial q^\alpha} \quad (17)$$

for the differential equations satisfied by the $q^\alpha(\tau)$, $\alpha = 1, 2, \dots, n$, with $d\xi/d\tau = \psi(q)$.

Equation (17) involves two unknown constants, namely, τ_0 and $(K/\psi)_{\tau_0}$. An integration of Eq. (17) yields $(2n)$ constants of integration. Now there are $(2n)$ boundary conditions. Two further equations must be satisfied since

$$T = \int_0^{\tau_0} \psi(q) d\tau$$

and $K = p_\alpha \dot{q}^\alpha - L$ must reduce to $K(\tau = \tau_0)$ when $\tau = \tau_0$. Hence, in general, the $q^i(\tau)$ can be determined uniquely.

Equation (17) can also be obtained by means of a Lagrange multiplier and the transversality condition of the calculus of variations.

If L does not contain the time explicitly, then $\partial L/\partial \xi = 0$, and furthermore, $(K/\psi)_{\tau_0}$ is the energy of the conservative system. For this case, Eq. (17) reduces to

$$\frac{d}{d\tau} \left(\frac{\partial L}{\partial \dot{q}^\alpha} \right) - \frac{\partial L}{\partial q^\alpha} = E \frac{\partial \psi}{\partial q^\alpha}$$

$$\frac{d}{d\tau} \left[\frac{\partial (L + E\psi)}{\partial \dot{q}^\alpha} \right] - \frac{\partial}{\partial q^\alpha} (L + E\psi) = 0 \quad (18)$$

so that the new Lagrangian is simply $(L + E\psi)$.

As an example, let

$$L = \frac{1}{2} \left(\frac{dx}{dt} \right)^2 + \frac{\mu}{x}$$

Let $dt = x d\tau$ ($\psi = x$), so that

$$L + E\psi = x \left[\frac{1}{2x^2} \left(\frac{dx}{d\tau} \right)^2 + \frac{\mu}{x} \right] + Ex$$

and

$$L + E\psi = \frac{1}{2x} \dot{x}^2 + \mu + Ex$$

Note that the singularity has been transferred to the kinetic energy term. Let $x = y^2$ so that $\dot{x} = 2y\dot{y}$, and

$$L + E\psi = 2\dot{y}^2 + \mu + Ey^2$$

$$\frac{\partial (L + E\psi)}{\partial \dot{y}} = 4\dot{y}, \quad \frac{\partial (L + E\psi)}{\partial y} = 2Ey$$

Equation (18) yields the harmonic equation ($E < 0$),

$$\frac{d^2 y}{d\tau^2} + \left(-\frac{E}{2} \right) y = 0 \quad (19)$$

a well-known result.

E. Lunar Ephemeris Improvement From Lunar Orbiter Tracking Data, J. D. Anderson

The possibility of using range and doppler tracking data from a *Lunar Orbiter* in a program to improve the constants of the lunar motion has been investigated before (SPS 37-38, Vol. IV, pp. 6-13). However, in that analysis several simplifying assumptions were made. The most restrictive of these were that the orbiter's motion was in the orbital plane of the moon and that the eccentricities of the orbits of the orbiter and moon were zero. In addition, the geocentric motion of the tracking station was neglected. Recent studies on the information contained in a single pass of radio tracking data (SPS 37-39, Vol. III, pp. 18-23; SPS 37-41, Vol. III, pp. 47-50; SPS 37-43, Vol. III, pp. 18-24) show that the station's geocentric parallax yields important measurements of the angular position of the object being tracked. When the tracking of a *Lunar Orbiter* is considered, we would expect the station's motion to provide information on the geocentric direction of the moon.

Under the simplifying assumptions given in SPS 37-38, Vol. IV, it was shown that the orbit of the orbiter could be determined from the doppler data alone and that the range data were free to determine the lunar distance to the same order of accuracy as the range data themselves, or to about ± 15 m. Clearly, periodic measurements of the lunar distance over an interval of many months to an accuracy of a few meters are extremely important in themselves. Indeed, some ranging data have already been compared with improved sine parallax computations performed by W. J. Eckert (SPS 37-43, Vol. III, pp. 24-28). It should be remembered that the distance measurement represents the separation between the dynamical centers of the earth and moon. Thus, it is particularly appropriate for an improvement in the lunar orbital constants. Beyond this, it is necessary to investigate what other less obvious information can be obtained from orbiter tracking data, and to perform a more rigorous analysis of the observer-orbiter geometry than that considered in SPS 37-38, Vol. IV.

The approach followed here is to presume that the problem of using orbiter tracking data is primarily one of data compression. As a supporting argument we note that over the past year four orbiters have been successfully tracked with an accumulation of at least 100,000 doppler and about 10,000 range measurements. Also, the long-term reduction of these measurements for a determination of harmonic coefficients in the moon's gravity field is being accomplished with compressed data (Lorell

and Sjogren, 1967)¹. The procedure which will be used to determine the constants of the moon's motion is similar.

First of all, a recently developed double precision orbit determination program (DPODP) will be used to process *Lunar Orbiter* data in batches and from each batch, containing perhaps one full tracking pass of data, the orbital elements of the orbiter will be determined. In the same solution, the program will determine significant high-frequency gravity harmonics as well as the parameters which contain the information on the lunar motion. The orbiter's orbital elements can be used in the program described by Lorell and Sjogren to determine low-frequency terms in the moon's gravity field.

In an analogous fashion, parameters of the lunar motion can be used in a separate program designed to adjust the lunar constants to best fit the *Lunar Orbiter* compressed data as well as various types of optical observations. Even without the anticipated results of a data compression study, it would be possible to obtain lunar distances from each tracking pass of range and doppler data and to fit a numerically integrated orbit of the moon to these data alone or to a combination of them with angular observations from optical sources. Such a possibility provides motivation for studying what can be gained, if anything, from a less straightforward application of the *Lunar Orbiter* data.

As a first step in deciding what lunar ephemeris parameters should be included in the DPODP, consider the computation of the topocentric range ρ to the orbiter. Four position vectors are required. Let \mathbf{r}_ζ be the geocentric position of the moon, \mathbf{R} the geocentric position of the tracking station, \mathbf{r} the selenocentric position of the orbiter, and $\boldsymbol{\rho}$ the topocentric position of the orbiter. Then the topocentric position is given by

$$\boldsymbol{\rho} = \mathbf{r}_\zeta + \mathbf{r} - \mathbf{R} \quad (1)$$

The scalar product $\boldsymbol{\rho} \cdot \boldsymbol{\rho}$ yields the square of the range.

$$\rho^2 = r_\zeta^2 + r^2 + R^2 + 2\mathbf{r}_\zeta \cdot \mathbf{r} - 2\mathbf{r}_\zeta \cdot \mathbf{R} - 2\mathbf{r} \cdot \mathbf{R} \quad (2)$$

Both r/r_ζ and R/r_ζ are less than 0.015 in magnitude and thus we neglect terms in Eq. (2) with powers beyond

the first in r/r_ζ and R/r_ζ . Then

$$\rho = r_\zeta + \mathbf{r} \cdot \mathbf{U}_\zeta - \mathbf{R} \cdot \mathbf{U}_\zeta \quad (3)$$

where \mathbf{U}_ζ is the unit vector \mathbf{r}_ζ/r_ζ in the geocentric direction of the moon.

The scalar product $\mathbf{R} \cdot \mathbf{U}_\zeta$ is expressed in its most fundamental form, from the viewpoint of data compression, by expressing \mathbf{R} and \mathbf{U}_ζ in equatorial coordinates referred to the true equator and equinox of date.

$$\mathbf{R} = (R_s \cos \theta, R_s \sin \theta, R \sin \phi') \quad (4)$$

$$\mathbf{U}_\zeta = (\cos \delta_\zeta \cos \alpha_\zeta, \cos \delta_\zeta \sin \alpha_\zeta, \sin \delta_\zeta) \quad (5)$$

where R_s is the distance of the tracking station from the earth's axis of rotation, R is the magnitude of \mathbf{R} , ϕ' is the geocentric latitude, and θ is the local sidereal time for the tracking station. In terms of the Greenwich apparent sidereal time θ_G and the station's longitude λ , θ is given by

$$\theta = \theta_G + \lambda \quad (6)$$

We will assume that θ_G is perfectly known in order to relate the lunar positions determined from radio tracking data to optical positions taken against the stellar background. For this reason, it is advantageous to separate out the θ_G terms in the scalar product $\mathbf{R} \cdot \mathbf{U}_\zeta$ as follows:

$$\begin{aligned} \mathbf{R} \cdot \mathbf{U}_\zeta &= R \sin \phi' \sin \delta_\zeta + R_s \cos \delta_\zeta \cos (\alpha_\zeta - \lambda) \cos \theta_G \\ &\quad + R_s \cos \delta_\zeta \sin (\alpha_\zeta - \lambda) \sin \theta_G \end{aligned} \quad (7)$$

The scalar product $\mathbf{r} \cdot \mathbf{U}_\zeta$ is expressed in its simplest form in the coordinate system used in binary star problems. The x - y plane, the plane of the sky, is perpendicular to \mathbf{U}_ζ and the z -axis is directed along \mathbf{U}_ζ . In this system the product $\mathbf{r} \cdot \mathbf{U}_\zeta$ is independent of a nodal angle and is given by

$$\mathbf{r} \cdot \mathbf{U}_\zeta = r \sin i \sin u \quad (8)$$

where i is the inclination of the orbiter's orbit to the plane of the sky, and u is its argument of latitude, the angle between the position vector \mathbf{r} and the line of intersection of the orbiter's orbital plane with the plane of the sky.

A combination of Eqs. (3), (7), and (8) yields an expression for range.

¹Reported in Section I, A. Preliminary Lunar Gravity Estimates From *Lunar Orbiter*.

$$\rho = r_{\zeta} - R \sin \phi' \sin \delta_{\zeta} - R_s \cos \delta_{\zeta} \cos(\alpha_{\zeta} - \lambda) \cos \theta_G - R_s \cos \delta_{\zeta} \sin(\alpha_{\zeta} - \lambda) \sin \theta_G + r \sin i \sin u \quad (9)$$

The time varying quantity $r \sin u$ should be expressed in terms of the mean anomaly M of the orbiter so that the range can be given as an explicit function of the time. Then it will be possible to perform statistical analyses on the separation of the lunar parameters from the orbiter's orbital parameters. Unfortunately, an expansion of $r \sin u$ in powers of the eccentricity is slowly converging because the eccentricities for the first three orbiters are about 0.3, and the eccentricity for the fourth orbiter is about 0.57. However, to powers in e^7 the expansion is

$$\begin{aligned} \frac{r}{a} \sin u = & -\frac{3}{2} e \sin \omega \\ & + \left(1 - \frac{1}{2} e^2 - \frac{1}{64} e^4 - \frac{29}{1152} e^6\right) \sin(M + \omega) \\ & - \frac{1}{8} e^2 \left(1 + \frac{1}{3} e^2 + \frac{25}{128} e^4\right) \sin(M - \omega) \\ & + \frac{1}{2} e \left(1 - \frac{3}{4} e^2 + \frac{5}{48} e^4 - \frac{1}{36} e^6\right) \sin(2M + \omega) \\ & - \frac{1}{24} e^3 \left(1 + \frac{1}{4} e^2 + \frac{1}{5} e^4\right) \sin(2M - \omega) \\ & + \frac{3}{8} e^2 \left(1 - e^2 + \frac{37}{128} e^4\right) \sin(3M + \omega) \\ & - \frac{3}{128} e^4 \left(1 + \frac{1}{10} e^2\right) \sin(3M - \omega) \\ & + \frac{1}{3} e^3 \left(1 - \frac{5}{4} e^2 + \frac{43}{80} e^4\right) \sin(4M + \omega) \\ & - \frac{1}{60} e^5 \left(1 - \frac{1}{12} e^2\right) \sin(4M - \omega) \\ & + \frac{125}{384} e^4 \left(1 - \frac{3}{2} e^2\right) \sin(5M + \omega) \\ & - \frac{125}{9216} e^6 \sin(5M - \omega) \\ & + \frac{27}{80} e^5 \left(1 - \frac{7}{4} e^2\right) \sin(6M + \omega) \\ & - \frac{27}{2240} e^7 \sin(6M - \omega) \\ & + \frac{16807}{46080} e^6 \sin(7M + \omega) \\ & + \frac{128}{315} e^7 \sin(8M + \omega) \end{aligned} \quad (10)$$

where ω is the argument of the periaapsis.

An expression for range rate $\dot{\rho}$ can be obtained by differentiating Eq. (9) with respect to time and by neglecting the rates in α_{ζ} and δ_{ζ} . This is equivalent to neglecting \dot{U}_{ζ} and results in an expression for $\dot{\rho}$ where first-order terms in r/r_{ζ} and R/r_{ζ} are neglected.

$$\begin{aligned} \dot{\rho} = & \dot{r}_{\zeta} + R_s \omega \cos \delta_{\zeta} \cos(\alpha_{\zeta} - \lambda) \sin \theta_G \\ & - R_s \omega \cos \delta_{\zeta} \sin(\alpha_{\zeta} + \lambda) \cos \theta_G \\ & + a \sin i \frac{d}{dt} \left(\frac{r}{a} \sin u \right) \end{aligned} \quad (11)$$

The time rate of change of θ_G , the rotation rate of the earth, is given by ω .

It is possible to recognize at this stage compression parameters that can be applied to a statistical study of the determination of the lunar ephemeris parameters and of their separation from orbital elements of the orbiter. There are four parameters of interest. Call them m_1 , m_2 , m_3 , and m_4 and define them by

$$m_1 = \dot{r}_{\zeta_0} \quad (12)$$

$$m_2 = R_s \cos \delta_{\zeta} \cos(\alpha_{\zeta} - \lambda) \quad (13)$$

$$m_3 = -R_s \cos \delta_{\zeta} \sin(\alpha_{\zeta} - \lambda) \quad (14)$$

$$m_4 = r_{\zeta_0} - R \sin \phi' \sin \delta_{\zeta} - \frac{3}{2} a e \sin i \sin \omega \quad (15)$$

The subscript 0 refers to an epoch from which time is measured in Eqs. (9) and (11). The Greenwich apparent sidereal time in terms of this epoch is

$$\theta_G = \theta_{G_0} + \omega(t - t_0) \quad (16)$$

Now the range and range-rate expressions are written in the form

$$\begin{aligned} \rho = & m_4 + m_1(t - t_0) - m_2 \cos \theta_G + m_3 \sin \theta_G \\ & + a \sin i P(M) \end{aligned} \quad (17)$$

$$\dot{\rho} = m_1 + m_2 \omega \sin \theta_G + m_3 \omega \cos \theta_G + a n \sin i \frac{dP(M)}{dM} \quad (18)$$

where $P(M)$ contains the periodic terms in Eq. (10) and its derivative is given by

$$\begin{aligned}
 \frac{dP(M)}{dM} = & \left(1 - \frac{1}{2}e^2 - \frac{1}{64}e^4 - \frac{29}{1152}e^6\right) \cos(M + \omega) \\
 & - \frac{1}{8}e^2 \left(1 + \frac{1}{3}e^2 + \frac{25}{128}e^4\right) \cos(M - \omega) \\
 & + e \left(1 - \frac{3}{4}e^2 + \frac{5}{48}e^4 - \frac{1}{36}e^6\right) \cos(2M + \omega) \\
 & - \frac{1}{12}e^3 \left(1 + \frac{1}{4}e^2 + \frac{1}{5}e^4\right) \cos(2M - \omega) \\
 & + \frac{9}{8}e^2 \left(1 - e^2 + \frac{37}{128}e^4\right) \cos(3M + \omega) \\
 & - \frac{9}{128}e^4 \left(1 + \frac{1}{10}e^2\right) \cos(3M - \omega) \\
 & + \frac{4}{3}e^3 \left(1 - \frac{5}{4}e^2 + \frac{43}{80}e^4\right) \cos(4M + \omega) \\
 & - \frac{1}{15}e^5 \left(1 - \frac{1}{12}e^2\right) \cos(4M - \omega) \\
 & + \frac{625}{384}e^4 \left(1 - \frac{3}{2}e^2\right) \cos(5M + \omega) \\
 & - \frac{625}{9216}e^6 \cos(5M - \omega) \\
 & + \frac{81}{40}e^5 \left(1 - \frac{7}{4}e^2\right) \cos(6M + \omega) \\
 & - \frac{81}{1120}e^7 \cos(6M - \omega) \\
 & + \frac{117649}{46080}e^6 \cos(7M + \omega) \\
 & + \frac{1024}{315}e^7 \cos(8M + \omega) \tag{19}
 \end{aligned}$$

A regression analysis on the parameters m_1, m_2, m_3, m_4 and the orbital elements a, e, M_0, i, ω has not been performed at this time. Clearly, it is important to do so, because if m_2 and m_3 can be determined to a sufficient accuracy, then the present and anticipated accuracy of tracking station locations (better than ± 5 meters) would allow a corresponding determination of α_{ζ} and δ_{ζ} . Therefore, investigations will continue in the use of *Lunar Orbiter* tracking data as a source of observation of the lunar motion. In particular, for the near future, Eqs. (17) and (18) will be linearized completely, and differential coefficients relating variations in the four ephemeris parameters (m_1, m_2, m_3, m_4) and the five orbital elements

(a, e, M_0, i, ω) to variations in range and range-rate will be obtained. Then, the coefficients will be collected and combined by standard statistical methods to obtain a covariance matrix on the nine parameters. Finally, a study will be undertaken to determine the nature of the covariance matrix in terms of (1) the elements of the orbiter's orbit and (2) the interval of time over which tracking data is compressed to obtain the four ephemeris parameters. Of particular interest will be the statistical correlations among the ephemeris parameters as well as between the ephemeris parameters and the elements of the orbiter's orbit. As a result of this sort of analysis, it should be possible to decide on a definite policy for the compression of the orbiter data with an attendant understanding of what information has really been extracted from the data. A computer program to process orbiter data and adjust the constants of the lunar motion will then be required.

F. An Efficient Propulsion Maneuver Used to Modify Lunar Return Re-entry Latitude,

E. S. Davis

1. Introduction

The earth-landing-site location of a minimum re-entry g , lunar return trajectory is severely limited by the constraint on re-entry angle. Of course, any longitude, 0 to 360 deg, is accessible to a re-entry vehicle since it is simply a matter of timing the launch from the moon. On the other hand, the touchdown latitude is narrowly defined. From consideration of the desire to minimize g -level and the desire to avoid skipping out of the atmosphere, -6 deg is generally accepted as the optimum low- g re-entry angle. Figures 6 and 7 show the variation in range from re-entry point to touchdown and maximum deceleration for a ballistic re-entry from the moon.

Figure 8 shows the geometry for a typical minimum- g re-entry, lunar return trajectory. For a typical 3.5-day minimum re-entry g , lunar return trajectory where the earth-return launch operation is covered by Goldstone and the touchdown is to be in the western United States, the trajectory central angle from the moon to re-entry is very close to 163 deg. From Fig. 6 the ballistic re-entry central angle for an optimum -6 -deg re-entry angle is 15 deg. The total central angle covered by the trajectory plus ballistic re-entry is 178 deg from moon to touchdown. Therefore, the touchdown latitude is limited to ± 2 deg from the negative of the lunar declination at earth-return launch. Once flight time and launch time

are established, the locus of touchdown sites is a small circle on the earth of radius 2 deg or 120 nmi; the exact

touchdown site on the locus depends on the inclination of the trajectory plane to the earth.

The monthly range of lunar declination varies between ± 18.3 and ± 28.5 deg on an 18.61-yr cycle due to precession of the moon's orbital plane. The moon will be achieving a maximum declination of 28.5 deg on April 14,

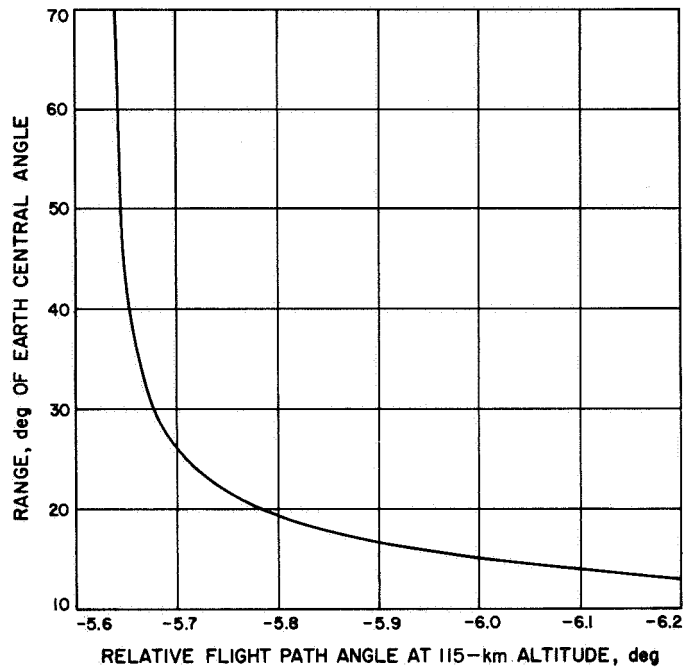


Fig. 6. Variation in range for ballistic earth re-entry

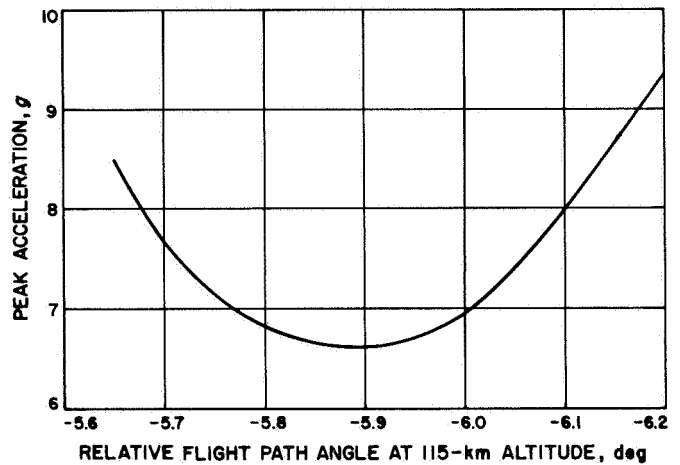


Fig. 7. Maximum value of total acceleration during ballistic earth re-entry in lunar return

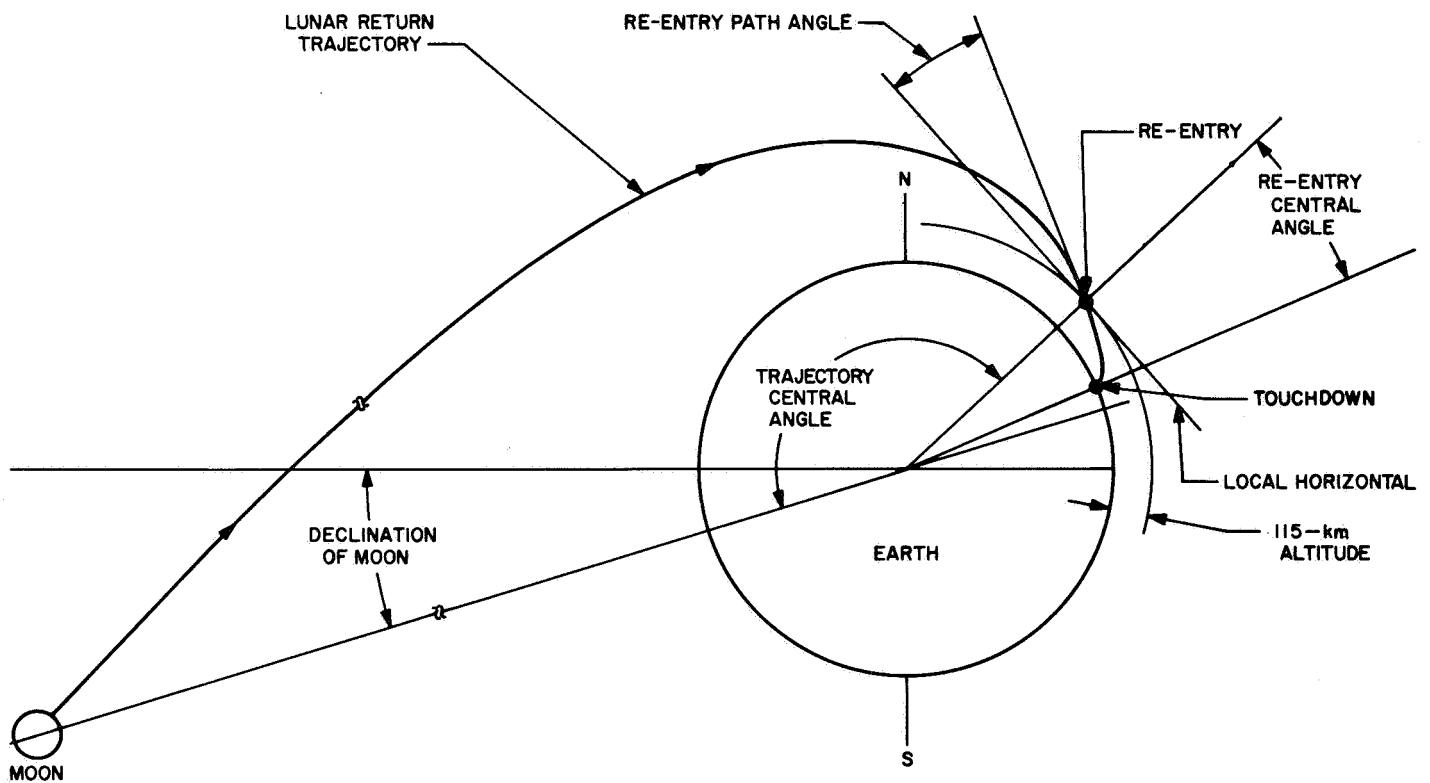


Fig. 8. Lunar-return trajectory geometry

1968. Through the next decade, the maximum declination will decrease to 18.3 deg in the middle of 1977. Earth landing sites for the simple ballistic re-entry trajectory are, thus, limited to a narrow band around the equator.

Consider the problem of landing at Edwards Air Force Base (AFB), which is approximately 34.8°N latitude. If the earth-return launch occurs at the maximum southerly lunar declination of 18.3 deg, then the touchdown latitude for a ballistic re-entry will be 20.3°N for a return over the earth's North Pole and 16.3°N for a return over the South Pole. A conventional solution to this problem would be to return over the South Pole with a lifting re-entry body, re-entry at -6-deg re-entry angle, and with the aid of a sophisticated high-speed on-board computer "glide," an additional 18.5 deg of earth central angle (1,110 nmi) to touchdown at 34.8°N latitude.

The use of propulsion to modify the impact site has been considered before. The usual result is that the cost of propulsion is quite high. For example, considerable flexibility in landing site location can be achieved by going into a low earth orbit and deboosting at the desired latitude. The ΔV required to achieve low earth orbit from a lunar-return trajectory is approximately 10,300 ft/s; adding 300 to 500 ft/s for the deboost maneuver means a total cost for this method of nearly 11,000 ft/s. Assuming an $I_{sp} = 300$ s, the initial-to-final mass ratio of the vehicle for the 10,300-ft/s ΔV can be calculated using Eq. (1).

$$\frac{m_0}{m_f} = \exp\left(\frac{\Delta V}{g_0 I_{sp}}\right) \quad (1)$$

where I_{sp} = specific impulse (s), ΔV = magnitude of velocity increment (ft/s), $g_0 = 32.2$ ft/s², m_f = final mass, m_0 = initial mass, and $m_0/m_f = 2.9$.

Therefore, almost 75% of the returning vehicle mass is fuel; quite a severe penalty considering the minor cost in weight for a lifting re-entry body.

An efficient propulsion maneuver for modifying the re-entry point latitude and, therefore, ballistic impact latitude has been discovered. The maneuver has many attractive features for a minimum- g lunar return: (1) a lifting re-entry body, with associated on-board high-speed computer, is not required, (2) a ΔV of less than 2,000 ft/s will allow an Edwards AFB landing during those years when the range of lunar declination is least favorable (i.e., years of ± 18.3 -deg declination), (3) a safe re-entry abort mode exists if the maneuver fails completely, (4) the maneuver execution accuracy required

to insure a safe re-entry is within the present state-of-the-art, (5) unique alignment of the maneuver thrust vector perpendicular to the earth-probe line may have mechanization advantages, (6) flight time is not modified by the maneuver, thus simplifying the problem of phasing operations and tracking station view periods.

Because the principal effect of this maneuver is to rotate the orbit axis, it will be called an "orbit axis rotation" (OAR) maneuver.

2. Description of the OAR Maneuver

Since the OAR maneuver is, in general, executed outside the moon's sphere of influence, it is both instructive and accurate to think in terms of the earth-centered conic properties of the return trajectory. The earth-centered conic orbits involved in a Type I OAR maneuver are shown in Fig. 9. The actual trajectory leaves the moon and asymptotically approaches the illustrated initial orbit as the probe nears the earth. The initial orbit passes over the South Polar region of the earth. At the proper range from the earth, the OAR maneuver is executed and the resulting final orbit passes over the North Polar region. The orbits shown to scale in Fig. 9 are those used to achieve an Edwards AFB landing with the moon at a declination of 18.3°S with a 3.5-day flight time. The OAR maneuver is executed at an earth range of approximately 266,000 km and requires a ΔV of 1,750 ft/s. The ΔV is applied exactly perpendicular to the earth-probe line in such a manner that the angular momentum of the probe about the earth is reversed without changing the energy, or C_3 , of the probe relative to the earth. The most obvious effect of the maneuver is the rotation of the orbit axis.

Figure 10 shows the critical point latitudes of the Type I OAR maneuver shown in Fig. 9. A -6-deg re-entry angle and a ballistic re-entry central angle of 15 deg is assumed. It is important to note that the initial orbit which passes over the South Pole would result in a minimum- g re-entry and thus provides an abort mode if the OAR maneuver fails to be executed. It is assumed that the necessary midcourse correction maneuvers are properly executed whether or not the OAR maneuver works.

Other variations of the orbit axis rotation maneuver are possible. The maneuver is not limited to be in the trajectory plane. A non-coplanar example of the OAR maneuver, which is called a Type II maneuver, is illustrated in Fig. 11. The initial orbit of the Type II maneuver is inclined to the final orbit (by 90 deg in the

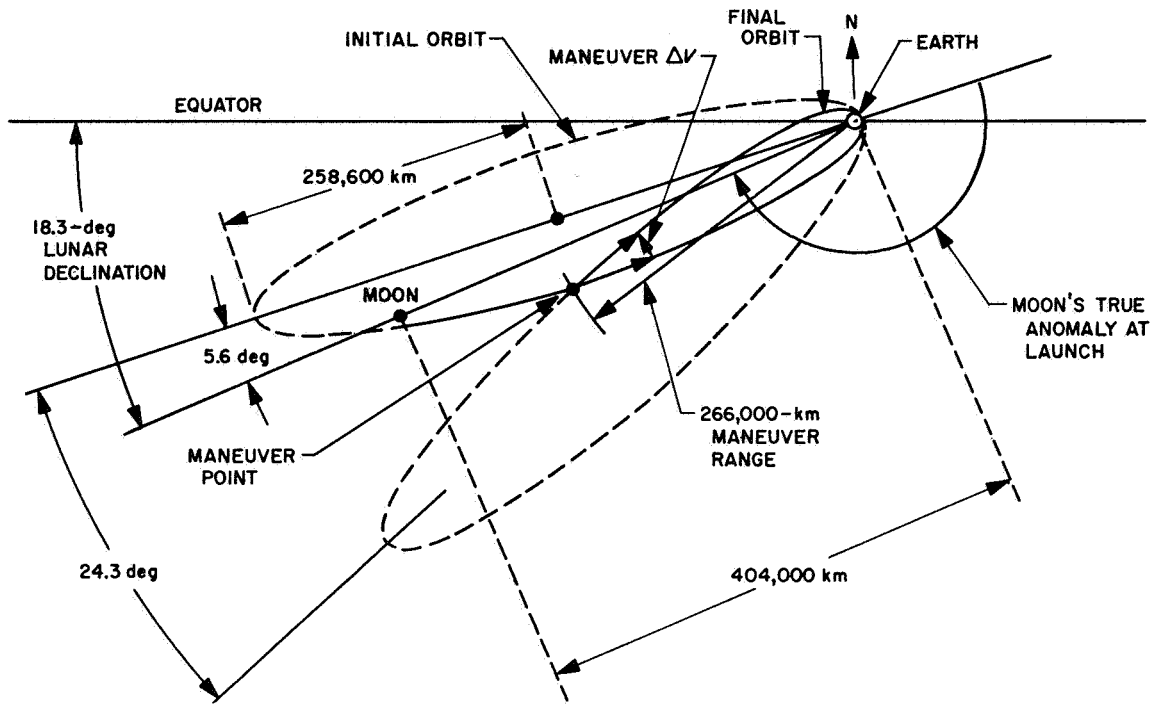


Fig. 9. Type I OAR maneuver

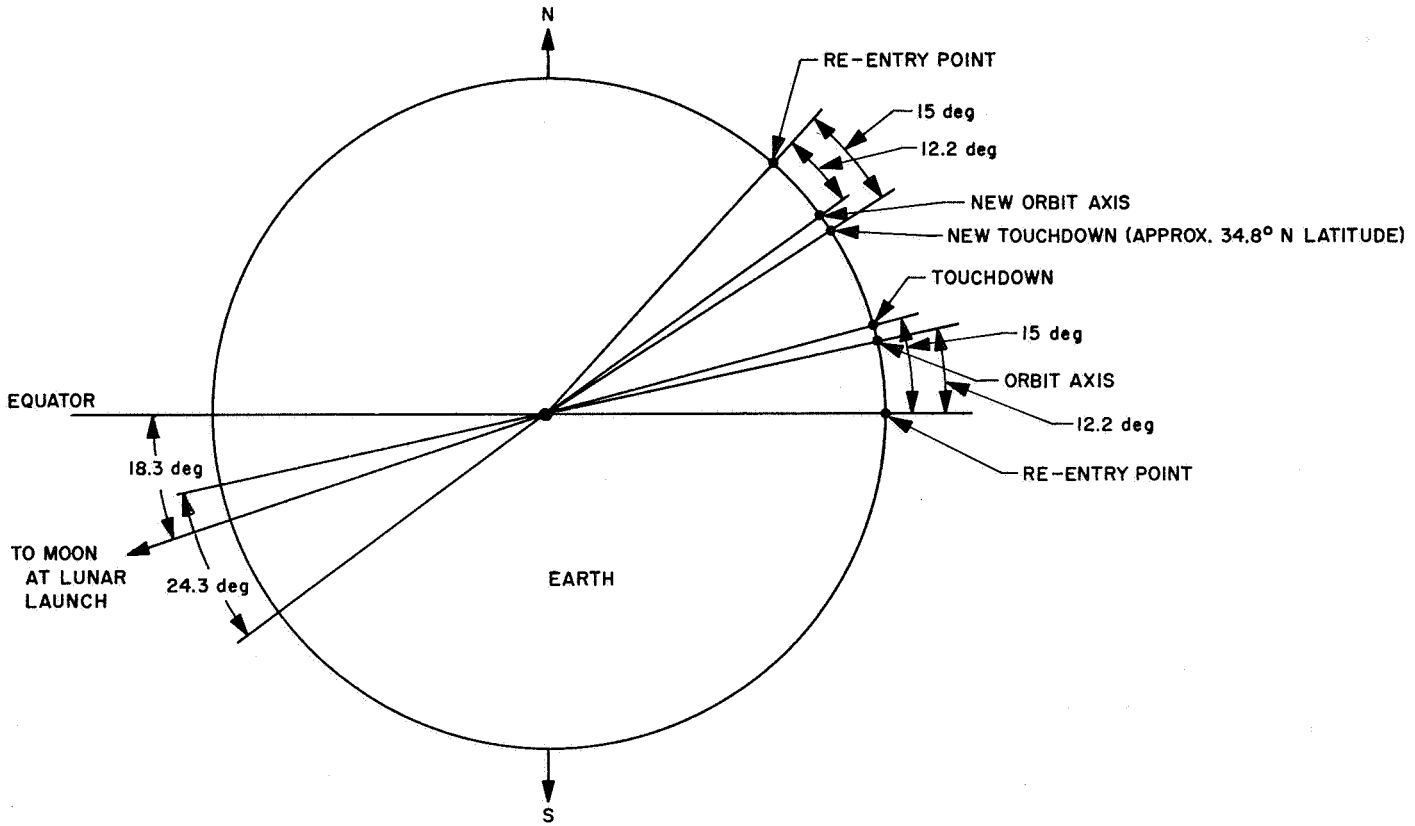


Fig. 10. Critical point latitudes of Type I OAR maneuver

example illustrated). Both the initial and final orbits have a safe re-entry path angle and, as in the Type I maneuver, the ΔV is applied exactly perpendicular to the earth-probe line. As with the Type I maneuver, the probe energy C_3 relative to the earth is unchanged, while the probe angular momentum is changed.

The initial orbit need not have a safe re-entry path angle. An extreme example of this possibility is illustrated in Fig. 12, the Type III OAR maneuver. The initial orbit is a rectilinear path from the moon to earth. At the proper earth range the OAR maneuver is executed. The final orbit is a safe re-entry orbit identical to the

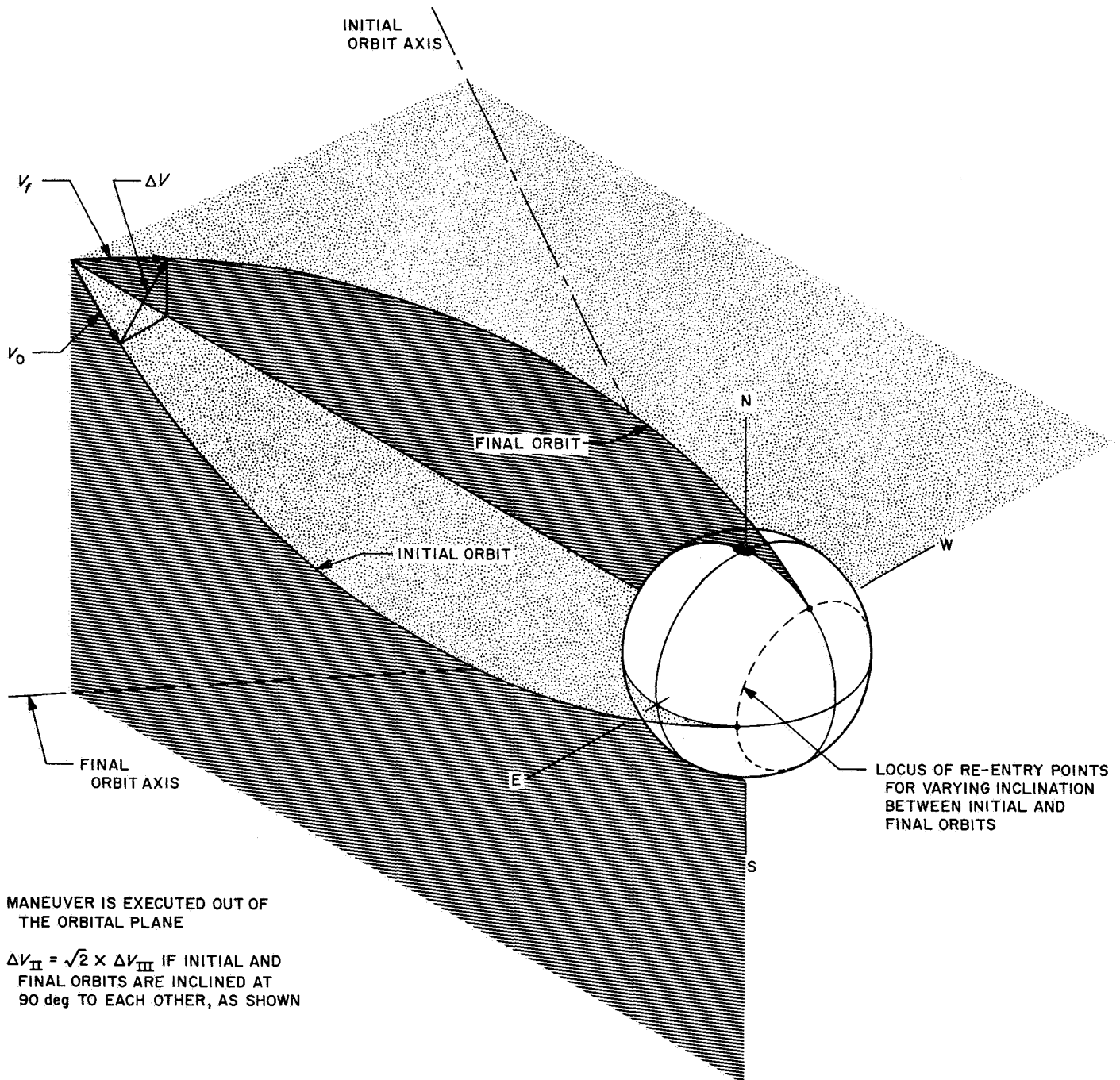


Fig. 11. Type II OAR maneuver

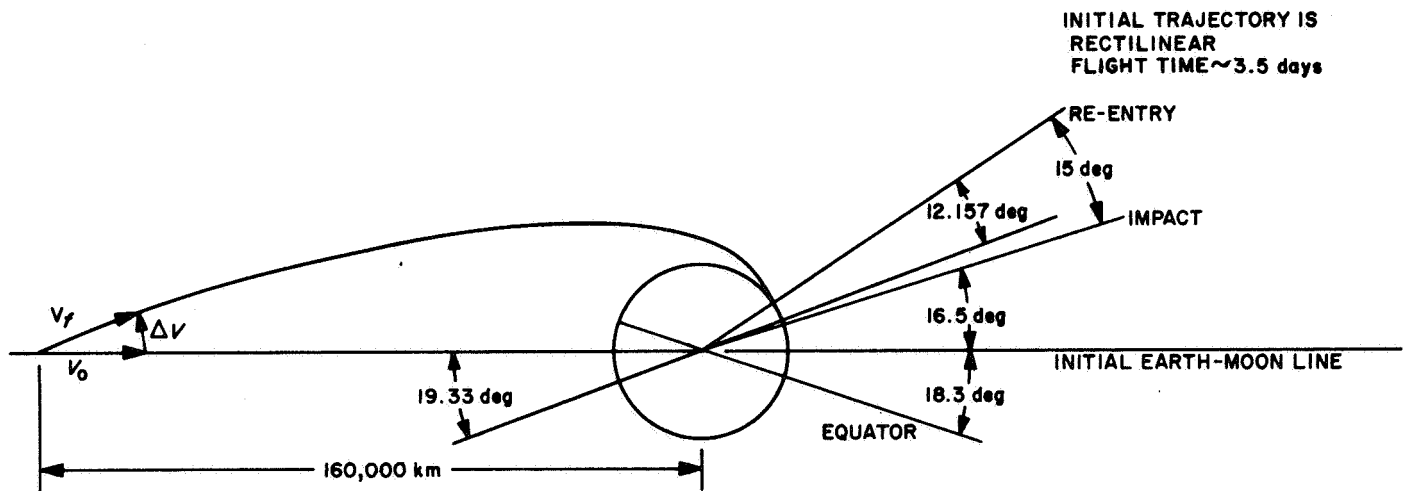


Fig. 12. Type III OAR maneuver

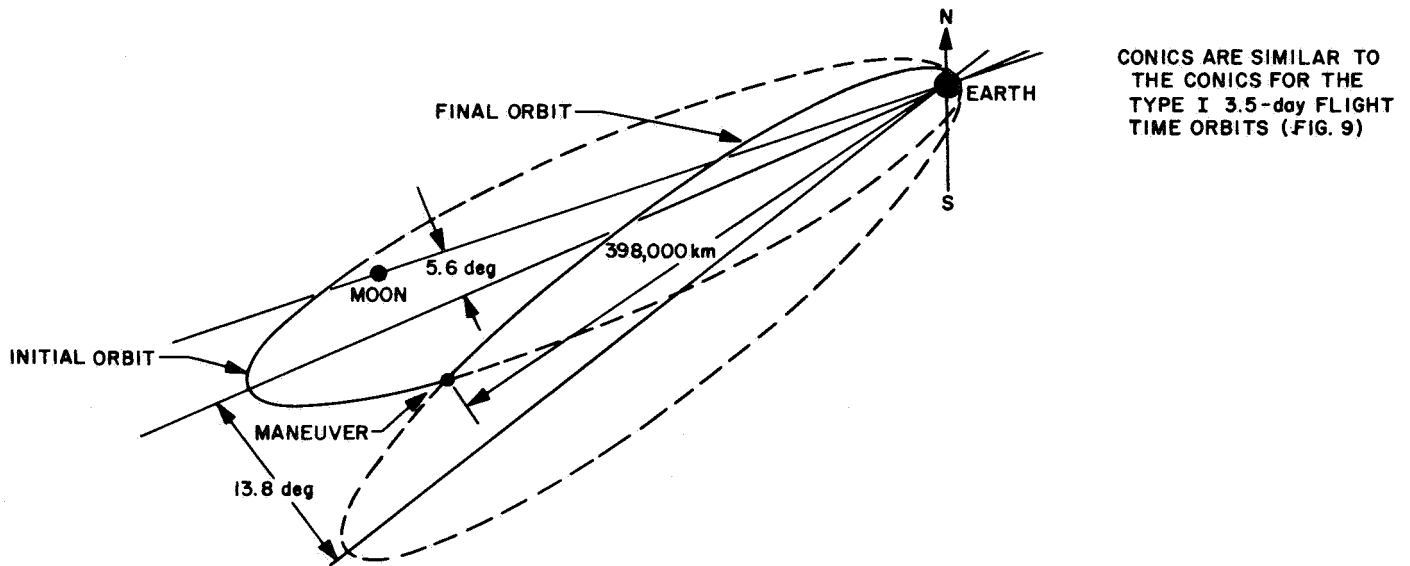


Fig. 13. Type IV OAR maneuver

Type I final orbit. If the ΔV is applied exactly perpendicular to the earth-probe line, the probe energy is increased slightly; however, the major effects are (1) the change in probe angular momentum relative to the earth, and (2) the characteristic orbit axis rotation.

The Type III maneuver is shown with the parameters required to achieve an Edwards AFB landing from the moon with $18.3^\circ S$ declination. The maneuver is executed at an earth range of 160,000 km, and the required ΔV is approximately 1,470 ft/s. It is interesting that the Type III maneuver is slightly more efficient than the

Type I maneuver. However, the abort mode capability of the Type I maneuver would seem well worth the minor cost in ΔV for a manned mission.

If flight time is not important, it is possible to achieve an even more efficient OAR maneuver. The Type IV OAR maneuver shown in Fig. 13 requires a ΔV of only 1,170 ft/s to reach Edwards AFB from a lunar declination of $18.3^\circ S$. Earth-return injection would be directed away from the earth; however, the resulting orbit has the same earth-referenced energy as the orbit for a Type I maneuver. The total flight time for the Type IV trajectory is 11.5 days.

Table 3. OAR maneuver ΔV to reach Edwards AFB^a

Maneuver type	ΔV , ft/s
I	1750
II (90-deg inclination)	2080
III	1470
IV	1170

^aLunar declination is assumed to be 18.3°S.

The fact that the OAR maneuver ΔV is always executed exactly perpendicular to the earth-probe line may be a significant factor to the mechanization of a system employing the OAR maneuver. This unique alignment is easily and accurately accomplished using a simple-body fixed earth sensor. The earth-sensor error signal may also be used to help control the spacecraft attitude during the rocket burn.

3. OAR Maneuver Performance

The ΔV required to achieve an Edwards AFB landing for each of the four maneuver types described above is summarized in Table 3.

Since the Type I OAR maneuver is the most interesting, a more detailed analysis of maneuver performance will be limited to the Type I maneuver. As long as the maneuver is executed outside the moon's sphere of influence, a 2-body conic analysis is accurate, and has the advantage of enhancing understanding. The orbit axis rotation ϕ required to achieve a given earth-landing-site latitude μ_{ls} from a given lunar declination μ_m is given by Eq. (2).

$$\phi = \mu_{ls} - \mu_m + \eta_r + \theta'_m - \theta_r \quad (2)$$

where μ_{ls} = landing site latitude (+north), μ_m = lunar declination at return launch (+south), η_r = re-entry central angle = 15 deg, θ_r = re-entry true anomaly = 12.157 deg[†], and θ'_m = 180 deg - moon true anomaly at launch = 5.55 deg[†].

The true anomaly at the time of maneuver execution, θ_{OAR} , is given by Eq. (3).

$$\theta_{OAR} = 180 - \frac{\phi}{2} \quad (3)$$

The earth-probe range at which the OAR maneuver is executed, r_{OAR} , is given by Eq. (4).

[†]3.5-day flight time is assumed.

$$r_{OAR} = \frac{a(1 - e^2)}{1 + e \cos \theta_{OAR}} \quad (4)$$

where a = semi-major axis = 258,000 km[†], and e = eccentricity = 0.975079[†].

The required maneuver ΔV is simply twice the horizontal component of velocity as given by Eqs. (5) and (6).

$$V_h = \frac{C_1}{r_{OAR}} \quad (5)$$

where V_h = horizontal velocity component, and C_1 = probe angular momentum per unit mass relative to the earth = 71220 km²/s[†].

$$\Delta V = 2 V_h \quad (6)$$

where ΔV = OAR maneuver velocity increment.

The solution to Eqs. (2) through (6), for the example trajectory with lunar distance equal to 404,000 km and 3.5-day flight time, is presented graphically in Fig. 14.

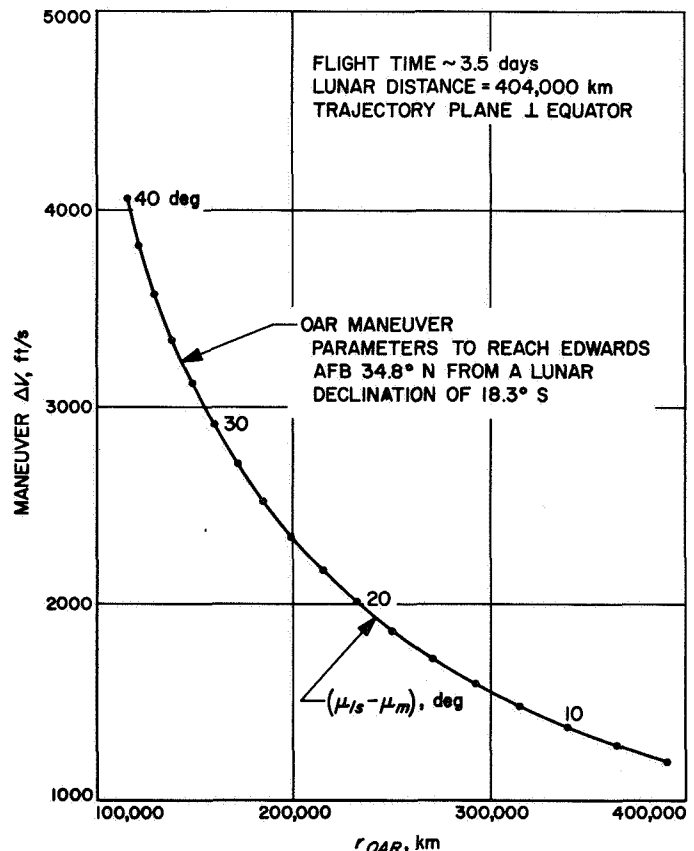


Fig 14. Parameters for a Type I OAR maneuver

For the Edwards AFB example considered above, the maneuver ΔV and execution earth-probe range are determined by selecting required $(\mu_{ls} - \mu_m)$, which = $(34.8 - 18.3) = 16.5$ deg, on the locus of possible OAR maneuver parameters plotted in Fig. 14. As stated above and indicated on Fig. 14, the maneuver occurs at a range of 266,000 km and requires a ΔV of 1750 ft/s.

Since the results shown in Fig. 14 neglect the effect of the moon, they are only valid for execution earth-probe ranges less than 360,000 km. From Fig. 14 it is apparent that the OAR maneuver is most useful when the difference $(\mu_{ls} - \mu_m)$ is less than 20 deg, with 30 deg being possible. At some point the cost of the ΔV required becomes prohibitive. For OAR maneuvers where $(\mu_{ls} - \mu_m)$ is less than 10 deg, the simple two-body solution is not valid but an OAR maneuver is still possible. One would expect the ΔV to increase as the maneuver is executed closer to the moon.

The maneuver execution error coefficients have been calculated by perturbing the maneuver and velocity vector in magnitude and direction from the nominal maneuver for the above Edwards AFB example. The post-maneuver orbit was calculated using an N -body program. The coordinate system defining the execution errors is illustrated in Fig. 15. Figs. 16 and 17 show the re-entry point errors as functions of error in execution angles. Note that 1-deg errors in maneuver direction result in re-entry angle errors less than 0.2 deg, which, from Fig. 7, keeps re-entry g within a factor of 1.5 of the minimum and avoids skip out. Execution errors of less than 1 deg should be very easy to achieve. Fig. 18 shows

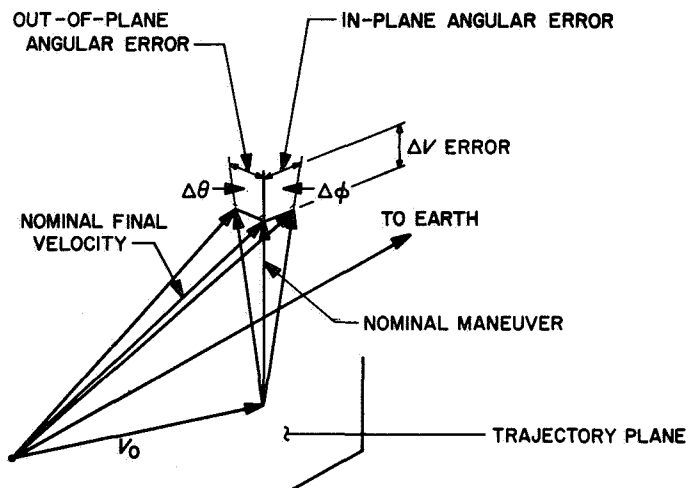


Fig. 15. Definition of coordinates for Type I OAR maneuver error analysis

the re-entry point errors for ΔV execution errors. To guarantee a 0.2-deg or less error in re-entry angle, the ΔV (1750 ft/s) must be executed to 0.3 ft/s. This shows that a quite sophisticated 0.017% accuracy is required. Commercial pendulous integrating accelerometers are capable of measurement accuracies of better than 0.01%; thus, it appears possible to obtain a safe re-entry *without a subsequent midcourse maneuver*. Capability for a subsequent midcourse maneuver, however, would still be desirable to refine the landing site and back-up the critical OAR maneuver execution dispersion. A significant feature of the OAR maneuver is that there is a reasonable chance the back-up midcourse correction might not be needed. It is also significant that the use of an OAR

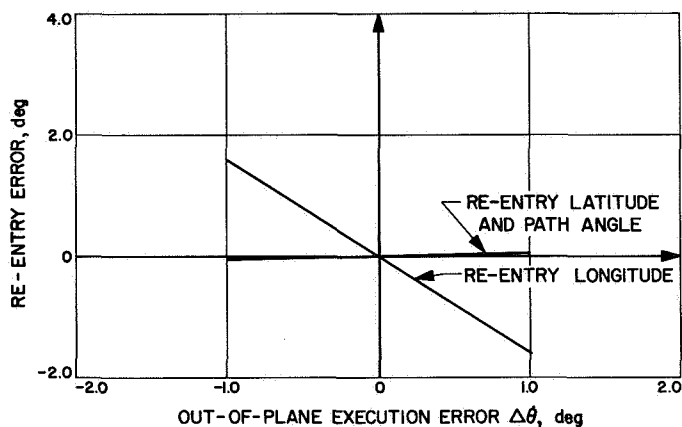


Fig. 16. Re-entry point errors for out-of-plane execution errors $\Delta\theta$

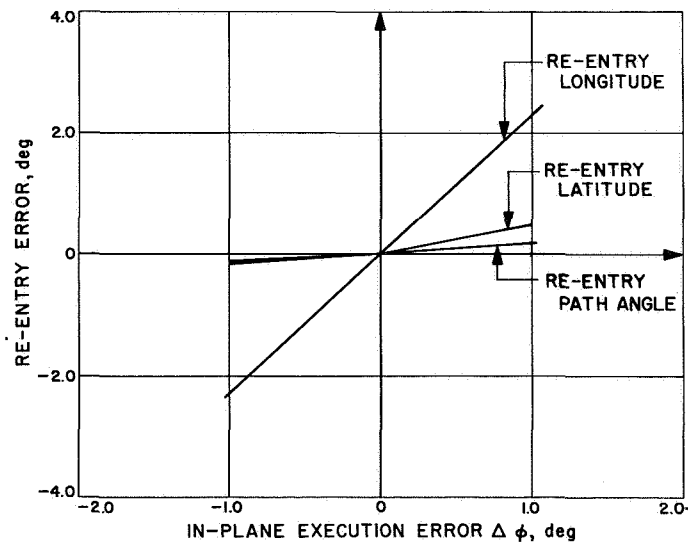


Fig. 17. Re-entry point errors for in-plane execution errors $\Delta\phi$

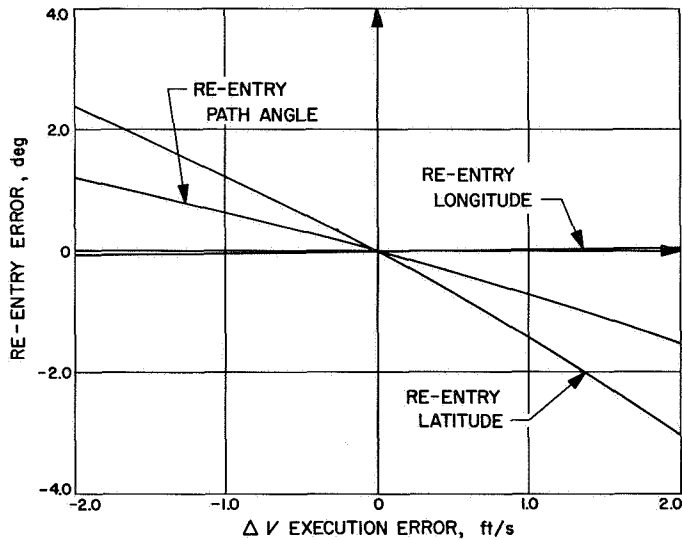


Fig. 18. Re-entry point errors for ΔV execution errors

maneuver does not require orbit determination accuracy exceeding that required by a standard lunar return mission.

4. Conclusion

The ΔV required to land at Edwards AFB from $18.3^\circ S$ using a nearly rectilinear return trajectory has been calculated as a function of earth-probe range. It turns out that the OAR maneuver is executed in a manner which nearly minimizes the ΔV required to reach a specified latitude from a given initial trajectory. The conclusion from this analysis is that the OAR maneuver is executed slightly closer to the earth and requires 5% additional ΔV than the minimum ΔV maneuver. It is likely that this conclusion is also valid for the more useful Type I OAR maneuver.

The minimum ΔV maneuver has a velocity component directed toward the earth and, thus, reduces the flight time on the post-maneuver leg of the orbit. Since it is desirable to hold total flight time constant, the earth reference energy of the pre-maneuver orbit could be reduced. Thus, some of the ΔV penalty chargeable to the optimum OAR maneuver might, in fact, be saved by the earth-return injection stage. This possibility is an important area for further study.

It may be desirable to mechanize the OAR maneuver with a fixed-velocity-increment solid motor plus a vernier impulse from the midcourse propulsion system. For a given launch window the solid motor must be sized to handle the OAR maneuver requiring the largest ΔV . Because the lunar declination varies through its minimum during the launch window, the largest ΔV is required on the first and last day of the earth-return launch window. Since less ΔV is required to achieve a desired re-entry latitude on intermediate days of the launch window, some method of expending the excess velocity of the maneuver is required on these days. One method to reduce the efficiency of the maneuver on days of near maximum lunar declination is to execute the maneuver either earlier or later than the minimum ΔV maneuver mentioned above. This method changes the flight time on the post-maneuver leg of the trajectory and may present phasing problems. A more attractive method is to vary the inclination of the pre-maneuver or post-maneuver orbit with lunar declination to hold OAR-maneuver ΔV constant. Comparison of the Type I and Type II maneuvers shows that, as the inclination of the pre-maneuver trajectory deviates from passing over the South Pole, the ΔV required to reach a given latitude increases. For a fixed ΔV maneuver, the required pre-maneuver orbit inclination is a function of lunar declination. The final orbit passes directly over the North Pole. Flight time is unaffected by this method and the maneuver is executed exactly perpendicular to the earth-probe line. Alternately, the pre-maneuver orbit can be aimed to pass directly over the South Pole. The inclination of the post-maneuver orbit, to reach a desired latitude with fixed ΔV , varies as a function of lunar declination. The post-maneuver orbit would come over the North Pole only when the maximum orbit axis rotation is required and would deviate from the North Pole if less orbit axis rotation is required.

From consideration of the Edwards AFB example, it appears that allocation of less than 2000 ft/s for an OAR maneuver would be required to handle lunar declinations of 18.3° with an adequate margin. From Eq. (1), using the same assumption as used for the earth-orbit case, 18.7% of the weight of the spacecraft injected on an earth-return trajectory would be OAR maneuver fuel. Assuming that the fuel represents 90% of the weight of the OAR maneuver propulsion system, the system weight penalty of the OAR maneuver is less than 21% of the earth-return spacecraft injected weight.

References

1. Lorell, J., Anderson, J. D., and Sjogren, W. L., *Characteristics and Format of the Tracking Data to be Obtained by the NASA Deep Space Instrumentation Facility for Lunar Orbiter*, Technical Memorandum 33-230. Jet Propulsion Laboratory, Pasadena, Calif., June 15, 1965.
2. Lorell, J., Sjogren, W. L., and Boggs, D., *Compressed Tracking Data Used for First Iteration in Selenodesy Experiment, Lunar Orbiter I and II*, Technical Memorandum 33-343. Jet Propulsion Laboratory, Pasadena, Calif., May 1, 1967.
3. Jeffreys, Sir Harold, "Dynamics of the Moon," *Proc. Roy. Soc. London, Ser. A*, No. 1446, Vol. 296, pp. 245-247, Feb. 7, 1967.
4. Eckert, W. J., "On the Motions of the Perigee and Node and the Distribution of Mass in the Moon," *Astron. J.*, Vol. 70, pp. 787-792, Dec. 1965.
5. Tolson, R. H., and Gapcynski, J. P., "An Analysis of the Lunar Gravitational Field as Obtained from Lunar Orbiter Tracking Data," presented at the IQSY/COSPAR Assemblies, London, England, July 17-28, 1967.
6. Michael, W. H., Jr., Tolson, R. H., and Gapcynski, J. P., "Preliminary Results on the Gravitational Field of the Moon from Analysis of Lunar Orbiter Tracking Data," presented at the American Geophysical Union Annual Meeting, Washington, D.C., Apr. 17, 1967.
7. Akim, E. L., "Determination of the Gravitational Field of the Moon by the Motion of AMS Luna-10," *Dok. Akad. Nauk SSSR, Mekhanika*, IOM 170, No. 4, pp. 799-802, 1966.
8. Szebehely, V., Pierce, D. A., and Standish, E. M., "A Group of Earth to Moon Trajectories with Consecutive Collisions," *Progress in Astronautics: Volume 14*, pp. 35-51. Academic Press, New York, 1964.
9. Tapley, B. D., and Lewallen, J. M., "A Comparison of Several Numerical Optimization Procedures," *Journal of Optimization Theory and Application*, Vol. I, No. 1, pp. 1-33, July 1967.
10. Szebehely, V., *Theory of Orbits*, Chapter 3. Academic Press, New York, July 1967.
11. Sundman, K. F., "Mémoire sur le Problème des Trois Corps," *Acta Math.*, Vol. 36, p. 105, 1912.
12. Breakwell, J. V., Speyer, J. L., and Bryson, A. E., "Optimization and Control of Nonlinear Systems Using the Second Variation," *SIAM Journal of Control*, Ser. A., Vol. 1, No. 2, pp. 193-223, 1963.
13. McReynolds, S. R., and Bryson, A. E., "A Successive Sweep Method for Solving Optimal Programming Problems," *Joint Automatic Control Conference, Troy, New York, June 1965*. Craft Lab Report 463, Harvard University, Cambridge, Mass., 1965.

II. Systems Analysis

SYSTEMS DIVISION

A. Trajectory Considerations for the Earth-Venus-Mercury Mission Opportunity, 1981-82, R. A. Wallace

1. Introduction

In Ref. 1, L. A. Manning has indicated that an Earth-Venus-Mercury mission opportunity exists in 1982, having a Venus pericenter altitude of 1980 km and a launch C_3^* of approximately $22 \text{ km}^2/\text{s}^2$. F. M. Sturms has investigated the 1970-80 Earth-Venus-Mercury opportunities (SPS 37-39, Vol. IV, pp. 1-5) and found that 1973 would be the last opportunity in the 1970's for a ballistic flyby with reasonable Venus altitudes using an *Atlas/Centaur*-type launch vehicle ($C_3 \leq 21 \text{ km}^2/\text{s}^2$). The 1982 opportunity, therefore, would be the first ballistic flyby opportunity after 1973. The present study is an investigation of the 1981-82 Earth-Venus-Mercury mission opportunity similar in scope to that reported in SPS 37-39.

2. Energy Matching at Venus

The first step in the investigation is to establish the minimum energy requirements for trajectories from Venus to Mercury for the Venus arrival dates of interest. In

Fig. 1 are minimum required energy curves for transfers between Venus and Mercury for Venus arrival dates between October 23, 1981 and September 5, 1982. Having constructed these curves, the second step is to match the arrival energies of Earth-Venus transfers to the minimum required departure energies shown in Fig. 1. This energy match process is accomplished by plotting over Fig. 1 the arrival energies of each Earth-Venus trajectory associated with a particular launch day. Where the two plots cross is the energy-match boundary. That is, on one side of the boundary there is not enough energy to continue to Mercury, on the other side there is. This energy match was made for launch days between September 14, 1981 and February 10, 1982.

The minimum energy trajectories between Venus and Mercury were obtained using the space research conic trajectory program (SPARC)¹ and mean planetary elements. In most cases the Earth-Venus trajectory data were obtained from tabulated conic data for the year 1973-74, i.e., the approximate 8-yr repetition cycle of Earth-Venus trajectories was assumed accurate enough for the preliminary part of this study. Where data were not available (late January and February 1982) the data were obtained from SPARC using 1981 launch dates.

* C_3 is equivalent to twice the orbital energy per unit mass, i.e., $C_3 = V^2 - 2\mu/r$ where V is the inertial velocity measured at r and μ is the gravitational constant of the central body.

¹"Space Research Conic Program," EPD 406, Jet Propulsion Laboratory, Pasadena, California, July, 1966.

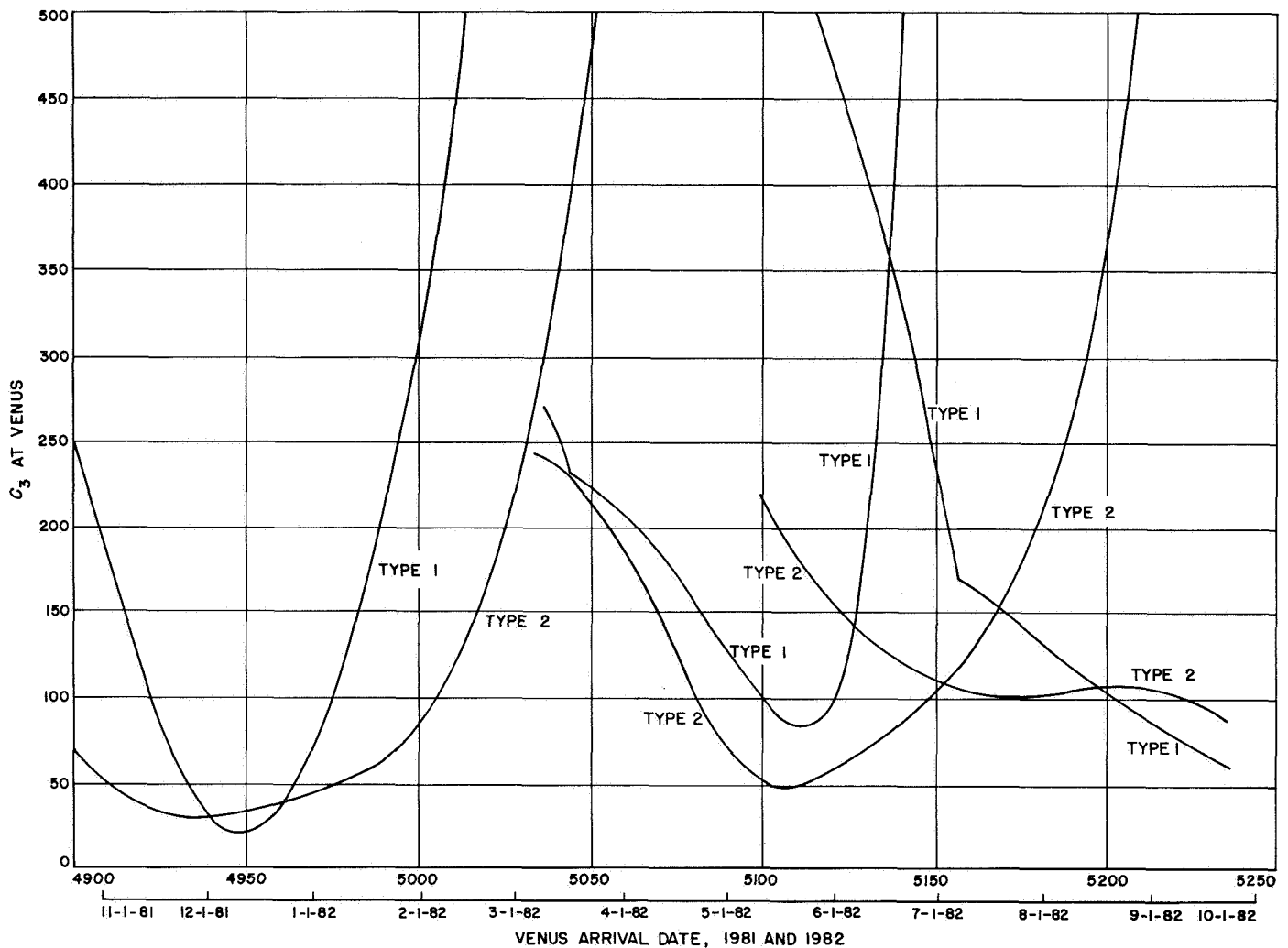


Fig. 1. Minimum energies for transfers between Venus and Mercury

3. Launch Energy Boundaries

Once the energy match at Venus has been determined, the third step is to determine the booster energy at Earth required for each launch day. This is done by transferring the energy boundary solutions obtained in the first two steps to a launch energy contour plot. This plot for 1981-82 is shown in Fig. 2 (the energy contours are also derived from the 8-yr cycle).

The boundary lines labeled *ridge* result from solutions in the vicinity of flight times for 180-deg transfers. These lines bound a narrow region outside the $23 \text{ km}^2/\text{s}^2$ curve and thus are not useful. Three other energy-match regions bear investigation, however. The trajectories between Venus and Mercury in these regions are all type 2 and, in one case, require that Mercury complete a full orbit or more (Mercury's orbital period is approxi-

mately 88 days) during the transfer from Venus to Mercury.

4. Trajectory Investigations of the Energy-Match Regions

Up to this point in the study, the goal had been to define launch regions where energy matches at Venus resulted in trajectories to Mercury with reasonable launch energies. Three such regions were found, and a detailed investigation of each region was made with the SPARC program using actual launch dates (i.e., not assuming the accuracy of the 8-yr cycle). These regions were chosen from Fig. 2 by noting where the energy boundary lines crossed the C_3 contour of $23 \text{ km}^2/\text{s}^2$. Once the regions were defined, SPARC runs were made, varying launch date and Venus arrival date over the three regions where energy matches were possible.

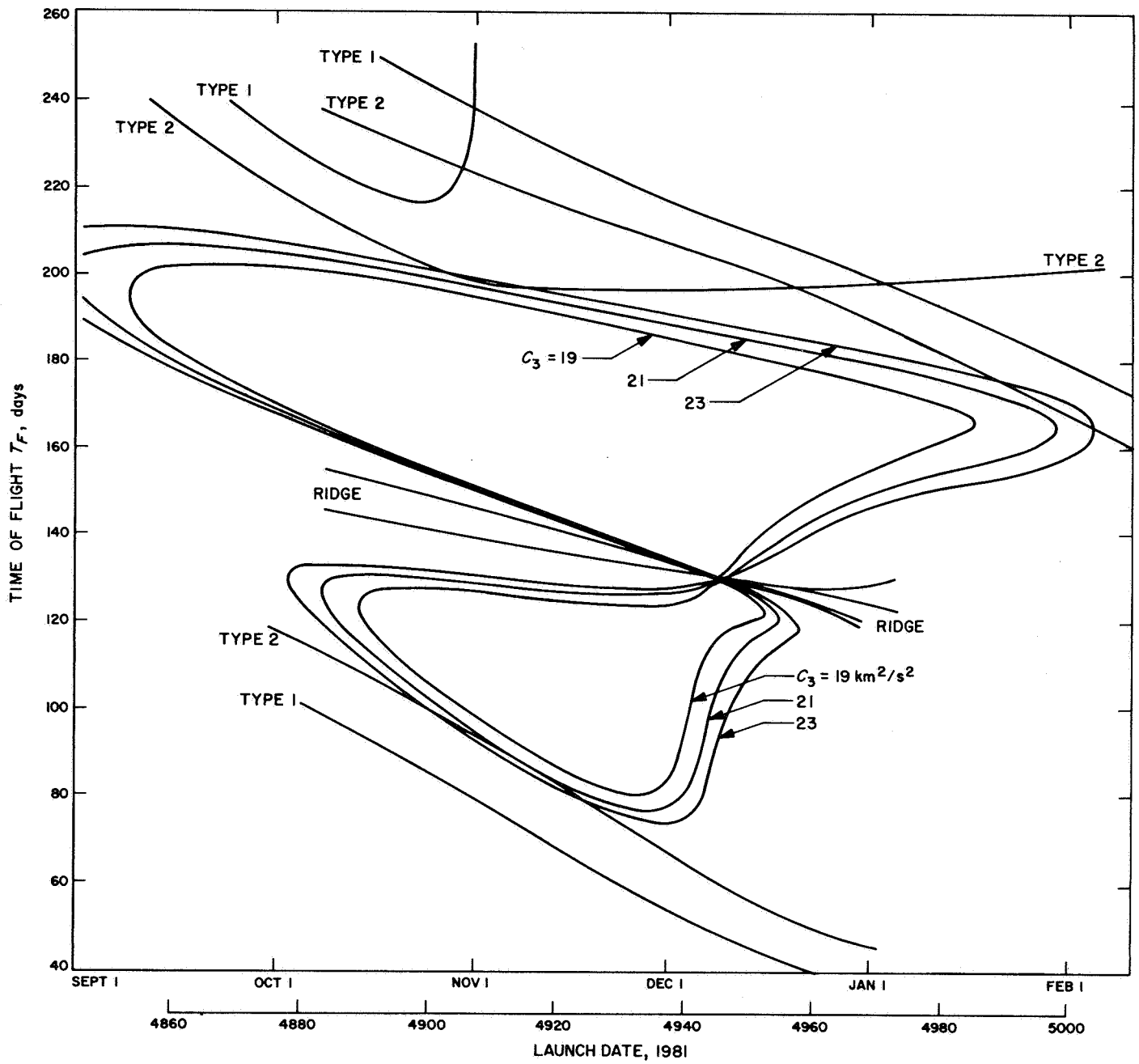


Fig. 2. Energy-match boundaries for 1981-82

The two parameters of interest in these final runs are launch energy and the flyby altitude at Venus. The launch energy variation with launch day determines the launch period. The flyby altitude at Venus determines the possibility of a ballistic trajectory mission.

5. Results and Comments

Tables 1, 2, and 3 summarize the results of the study, each table devoted to one of the energy-match regions. The following comments apply:

- (1) A C_3 of $24 \text{ km}^2/\text{s}^2$ was taken as a limiting value of the *Atlas/Centaur* performance resulting in useful payloads injected (about 1300 lb). Such performance is not available at the present time but is planned to be available by the late 1970's.

Table 1. Summary of results: region 1 of the 1981-82 Earth-Venus-Mercury opportunity

Launch between October 28 and November 19, 1981. Venus arrival between May 14 and 31, 1982
Earth-Venus trajectories: Type 1 Flight times ($C_3 \leq 24 \text{ km}^2/\text{s}^2$): 83 to 103 days Minimum C_3 : $20.8 \text{ km}^2/\text{s}^2$ Best launch period (single Venus arrival date) for $C_3 \leq 24 \text{ km}^2/\text{s}^2$: 6 days (Launch: November 2 to 8, 1981; Venus arrival: May 20, 1982) Venus-encounter: flyby altitude range, all negative Venus-Mercury trajectories: Type 2; class 1 and 2 Class 1 flight times ($C_3 \leq 24 \text{ km}^2/\text{s}^2$): 65 to 69 days Class 2 flight times ($C_3 \leq 24 \text{ km}^2/\text{s}^2$): 69 to 76 days

Table 2. Summary of results: region 2 of the 1981-82 Earth-Venus-Mercury opportunity

Launch between October 10 and November 15, 1981. Venus arrival between January 20 and February 15, 1982
Earth-Venus trajectories: Type 2 Flight times ($C_3 \leq 24 \text{ km}^2/\text{s}^2$): 193 to 200 days Minimum C_3 : $21.2 \text{ km}^2/\text{s}^2$ Best launch period (single Venus arrival date) for $C_3 \leq 24 \text{ km}^2/\text{s}^2$: 26 days (Launch: October 11 to November 6, 1981; Venus arrival: January 28, 1982) Venus-encounter: flyby altitude range, all negative Venus-Mercury trajectories: Type 2; class 1 and 2 Class 1 flight times ($C_3 \leq 24 \text{ km}^2/\text{s}^2$): 75 to 82 days Class 2 flight times ($C_3 \leq 24 \text{ km}^2/\text{s}^2$): 86 to 90 days

Table 3. Summary of results: region 3 of the 1981-82 Earth-Venus-Mercury opportunity

Launch between January 15 and February 15, 1982. Venus arrival between July 10 and 19, 1982
Earth-Venus trajectories: Type 1 Flight times ($C_3 \leq 24 \text{ km}^2/\text{s}^2$): 160 to 173 days Minimum C_3 : $22.6 \text{ km}^2/\text{s}^2$ Best launch period (single Venus arrival date) for $C_3 \leq 24 \text{ km}^2/\text{s}^2$: 15 days (Launch: January 25 to February 9, 1982; Venus arrival: July 18, 1982) Venus-encounter: flyby altitude ^a range Class 1 ^b : 0 to 1500 km Class 2 ^b : 1576 to 2304 km Venus-Mercury trajectories: Type 2; class 1 and 2 Class 1 flight times ($C_3 \leq 24 \text{ km}^2/\text{s}^2$): 126 to 136 days Class 2 flight times ($C_3 \leq 24 \text{ km}^2/\text{s}^2$): 137 to 142 days
^a Venus radius was set at 6200 km ^b Venus-Mercury trajectories (see above)

- (2) Launch periods derived using the energy-match boundary, C_3 constraint of $24 \text{ km}^2/\text{s}^2$, and single Venus arrival date, result in launch periods of 6, 26, and 15 days for each of the launch regions, respectively. Raising the launch energy ceiling to $30 \text{ km}^2/\text{s}^2$ considerably lengthens these launch periods (e.g., the region 3 launch period increases from 15 to 30 days). At the present time, 30 days is the desired length of launch period. By 1980, however, with increased reliability for launching on time, 15 days might be adequate.
- (3) Varying the Venus arrival date for region 3 (Table 3) will lengthen the launch period by only 5 days. This number of additional launch days would require the complicating features of setting up a variable date encounter package.
- (4) Regions 1 and 2, of Tables 1 and 2, respectively, result in negative altitudes at Venus. For this reason these two regions will be dropped from any further discussion in this study.
- (5) Trajectories in region 3 (Table 3) result in high positive altitudes at Venus (1500 to 2300 km). The minimum C_3 is fairly high, $22.6 \text{ km}^2/\text{s}^2$, and the launch period of 15 days for a maximum C_3 of $24 \text{ km}^2/\text{s}^2$ is somewhat low. Further, the asymptotic approach speeds at Venus are quite high, 10.1 km/s. For Venus entry probes and landers, speeds on the order of 3 to 6 km/s are desired.

(6) Compared to either the 1970 or 1973 Earth-Venus-Mercury opportunities (Refs. 2 and 3, respectively), the 1982 opportunity is not nearly as attractive from a launch vehicle, encounter conditions, and

launch period standpoint. From Manning's results (Ref. 1), the next ballistic Venus flyby mission to Mercury with fairly low launch energies does not occur until 1997.

References

1. Manning, L. A., "Comparison of Several Trajectory Modes for Manned and Unmanned Missions to Mercury: 1980-2000," *AIAA Paper 67-28*, Jan. 26, 1967.
2. Sturms, F. M., Jr., and Cutting, E., "Trajectory Analysis of a 1970 Mission to Mercury Via a Close Encounter with Venus," Paper 65-90 presented at the 2nd AIAA Aerospace Sciences Meeting, New York, Jan. 25-27, 1965.
3. Sturms, F. M., Jr., *Trajectory Analysis of an Earth-Venus-Mercury Mission in 1973*, Technical Report 32-1062, Jet Propulsion Laboratory, Pasadena, Calif., Jan. 1, 1967.

III. Computation and Analysis

SYSTEMS DIVISION

A. Numerical Solution of a Nonlinear Partial Differential Equation, E. Ng

1. Introduction

Lin's mathematical theory of galaxies has attracted much attention in the community of applied mathematics in the last few years. In a recent Society for Industrial and Applied Mathematics symposium in honor of Richard Courant, Lin (Ref. 1) presented a survey paper on the current status of his theory. This article reports some recent investigation (mainly in the context of astrophysics) of what might be considered a special case of Lin's theory. Emphasis will be mainly on the mathematical nature and method of the problem, leaving out the results and physical applications, which can be found in Ref. 2.

Consider an idealized self-gravitating, collision-free dynamical system with particles all having the same mass m and introduce a distribution function f in phase space (\mathbf{r}, \mathbf{v}) , where \mathbf{r} and \mathbf{v} are, respectively, the position and velocity vectors of the individual particles. Then the equation governing the development of $f(\mathbf{r}, \mathbf{v}, t)$ in time t is the well-known Boltzmann equation in statistical mechanics:

$$\frac{\partial f}{\partial t} + \mathbf{v} \cdot \nabla f - \nabla \Phi \cdot \nabla_{\mathbf{v}} f = 0 \quad (1)$$

where $\nabla_{\mathbf{v}}$ is the gradient in velocity space and we have replaced $\partial \mathbf{v} / \partial t$ in the last term by $-\nabla \Phi$, Φ being the

gravitational potential generated by the particles themselves. This is the familiar "microscopic" equation from which the hydrodynamic equations can be derived. For example, integrating Eq. (1) over velocity space we obtain the equation of continuity:

$$\frac{\partial \rho}{\partial t} + \nabla \cdot (\rho \mathbf{v}) = 0 \quad (2)$$

and multiplying Eq. (1) by $m\mathbf{v}$ and integrating, we obtain the equation of motion:

$$\rho \frac{\partial \mathbf{u}}{\partial t} + \rho (\mathbf{u} \cdot \nabla) \mathbf{u} + \nabla \cdot \overset{\equiv}{\mathbf{P}} + \rho \nabla \Phi = 0 \quad (3)$$

where

$$\rho = m \int \int f(\mathbf{r}, \mathbf{v}, t) d\mathbf{v} \quad (4)$$

$$\mathbf{u} = \frac{m}{\rho} \int \int \mathbf{v} f(\mathbf{r}, \mathbf{v}, t) d\mathbf{v} \quad (5)$$

$$\overset{\equiv}{\mathbf{P}} = m \int \int (\mathbf{v} - \mathbf{u})(\mathbf{v} - \mathbf{u}) f(\mathbf{r}, \mathbf{v}, t) d\mathbf{v} \quad (6)$$

are the three moments of the distribution function.

$\overset{\equiv}{\mathbf{P}}$ is a Cartesian tensor in dyadic notation.

For a self-gravitating system Φ is related to the distribution function via Poisson's equation, viz,

$$\nabla^2 \Phi = 4\pi Gm \int \int \int f(\mathbf{r}, \mathbf{v}, t) d\mathbf{v} \quad (7)$$

Equations (1) and (7) can be considered the fundamental system of equations describing a self-gravitating dynamical system, with Φ and f as the dependent variables and \mathbf{r} , \mathbf{v} and t the independent variables. To describe a dynamical system, then, one is to look for special solutions subject to specified boundary conditions.

It is well known from Poincaré's (Ref. 3) general analysis that Eq. (1) has as its special solutions functions of integrals of the equations of motions $d\mathbf{v}/dt = -\nabla\Phi$. It is also well known from classical mechanics that time-independent systems possess the energy integral, and systems with some axis of symmetry possess the angular momentum integral. In the following, we shall consider a time-independent axisymmetric disk with unit radius.

2. A Rotating Maxwellian Distribution

From here on we shall use a cylindrical coordinate system (ω, ϕ, z) with the z -axis perpendicular to the disk and as the axis of symmetry. The corresponding velocity components are v_ω , v_ϕ , and v_z . The energy and angular momentum integrals are

$$E = \frac{1}{2}(v_\omega^2 + v_\phi^2) - \Phi$$

and $J = v_\phi \omega$, respectively. Thus an analytic function of E and J will satisfy the Boltzmann equation for a time-independent axisymmetric disk. We shall assume a "rotating Maxwellian" distribution function of the form:

$$f(E, J) = \begin{cases} A \exp(-\alpha E + \beta J + \gamma J^2) & \text{for } E \leq E_0 \\ 0 & \text{for } E > E_0 \end{cases} \quad (8)$$

where A , α , β , and γ are parameters and E_0 is a cut-off energy to make the system finite. For $\beta = \gamma = 0$ this distribution reduces to the classical Maxwellian.

3. The Nonlinear Differential Equation

With the assumed form Eq. (8), the main task is then to solve for Φ in Eq. (7) which for an axisymmetric disk is:

$$\nabla^2 \Phi(\omega, z) = 4\pi mG \delta(z) \int \int_{E \leq E_0} f \left(\frac{v_\omega^2}{2} + \frac{v_\phi^2}{2} - \Phi, \omega v_\phi \right) dv_\omega dv_\phi \quad (9)$$

where $\delta(z)$ is the Dirac delta function. Since Φ does not depend on v_ω and v_ϕ , Eq. (9) is a P. D. E. of the form:

$$\nabla^2 \Phi(\omega, z) = \delta(z) F(\omega, z, \Phi; A, \alpha, \beta, \gamma) \quad (10)$$

where we have written out the explicit dependence of the parameters. The boundary condition for Eq. (10) is that $\Phi(|\mathbf{r}|) \rightarrow 1/|\mathbf{r}|$ as $|\mathbf{r}| \rightarrow \infty$. The distribution function, Eq. (8), describes circular ($\gamma = 0$) and elliptical ($\gamma \neq 0$) equidensity contours in velocity space. In Ref. 2, we have obtained numerical solutions for the circular case using Green's function method. M. L. West¹ is at present investigating the elliptical case with both Green's function method and a method employing spheroidal coordinates. In the following we shall briefly describe these methods.

Green's function is a well-known subject in mathematical physics (Ref. 4). It is essentially the kernel function of an integral operator as an inverse of a differential operator. Thus introducing the Green's function for Eq. (10) we convert it into an integral equation of the form

$$\Phi(\omega, z) = \int_0^1 \int_0^{2\pi} \int_{-\infty}^{+\infty} \delta(z') F[\omega', z', \Phi(\omega', z'); A, \alpha, \beta, \gamma] \times \frac{\omega' dz' d\phi' d\omega'}{|\mathbf{r} - \mathbf{r}'|} \quad (11)$$

From the physical context of the analyses of Ng and West, it is sufficient to consider the potential on the plane of the disk, a special case for which Eq. (11) reduces to

$$\Phi(\omega) = \int_0^1 \int_0^{2\pi} F[\omega', \Phi(\omega'); A, \alpha, \beta, \gamma] \times \frac{\omega' d\phi' d\omega'}{(\omega^2 + \omega'^2 - 2\omega\omega' \cos \phi')^{1/2}} \quad (12)$$

where we have written $\Phi(\omega)$ and $F(\omega', \Phi; A, \alpha, \beta, \gamma)$ for $\Phi(\omega', 0)$ and $F(\omega', 0, \Phi; A, \alpha, \beta, \gamma)$, respectively, and have used the well-known property for the delta function:

$$u(0) = \int_{-\infty}^{\infty} \delta(z) u(z) dz \quad (13)$$

The ϕ' -integral in Eq. (12) can be converted to a standard elliptical integral by the substitution $\psi = \pi - \phi'/2$.

¹Private communication.

We have, finally,

$$\Phi(\tilde{\omega}) = \int_0^1 F(\tilde{\omega}', \Phi; A, \alpha, \beta, \gamma) \frac{4}{\tilde{\omega} + \tilde{\omega}'} K\left(\frac{2(\tilde{\omega}\tilde{\omega}')^{1/2}}{\tilde{\omega} + \tilde{\omega}'}\right) \tilde{\omega}' d\tilde{\omega}' \quad (14)$$

where K is the complete elliptic integral of the first kind. This is a nonlinear homogeneous integral equation, similar to the Fredholm equation of the second kind. For $\gamma = 0$, and various values of the other parameters, we have solved this equation by the iterative method well known to Fredholm equation, viz, by writing Eq. (14) in the following form:

$$\Phi^{n+1} = \lambda^{n+1} L\Phi^n \quad (15)$$

where L is the nonlinear integral operator and λ^{n+1} is an eigenvalue made up of the relevant parameters. The numerical results and physical applications will be presented in a forthcoming publication.

M. L. West is currently investigating the case $\gamma \neq 0$ with the above method and also a different program due to Barbanis and Prendergast (Ref. 5). She writes Eq. (10) in the following iterative form:

$$\nabla^2 \Phi^{n+1}(\tilde{\omega}, z) = \delta(z) F(\tilde{\omega}, z, \Phi^n; A, \alpha, \beta, \gamma) \quad (16)$$

With a chosen set of parameters, at each iterative step Eq. (16) is just Poisson's equation; which written in general with spheroidal coordinates is

$$\begin{aligned} \nabla^2 \Phi &= \frac{1}{a^2(\xi^2 + \eta^2)} \left\{ \frac{\partial}{\partial \xi} \left[(1 + \xi^2) \frac{\partial \Phi}{\partial \xi} \right] \right. \\ &\quad \left. + \frac{\partial}{\partial \eta} \left[(1 - \eta^2) \frac{\partial \Phi}{\partial \eta} \right] + \frac{\xi^2 + \eta^2}{(1 + \xi^2)(1 - \eta^2)} \frac{\partial^2 \Phi}{\partial \phi^2} \right\} \\ &= \frac{\sigma(\eta, \phi)}{a|\eta|} \delta(\xi) \end{aligned} \quad (17)$$

where (η, ξ, ϕ) are related to the Cartesian coordinates (x, y, z) by

$$\left. \begin{aligned} x &= a[(1 + \xi^2)(1 - \eta^2)]^{1/2} \cos \phi \\ y &= a[(1 + \xi^2)(1 - \eta^2)]^{1/2} \sin \phi \\ z &= a\eta\xi \end{aligned} \right\} \quad (18)$$

the surface $\xi = 0$ being a circular disk of radius a . In general, to solve Poisson's equation one expands both the density and the potential in series of Legendre functions:

In the special case we are considering, the density and potential depend only on η , yielding:

$$|\eta| \sigma(\eta) = \sum_{l=0}^{\infty} A_{2l} P_{2l}(\eta) \quad (19)$$

$$A_{2l} = \frac{4l+1}{2} \int_{-1}^1 \sigma(\eta) P_{2l}(\eta) |\eta| d\eta \quad (20)$$

$$\Phi(\eta) = \sum_{l=0}^{\infty} B_{2l} P_{2l}(\eta) \quad (21)$$

where B_{2l} is related to A_{2l} via Eq. (17). To summarize this whole procedure, we see that at each iteration F in Eq. (16) is known and hence we have $\sigma(\eta)$, which gives A_{2l} in Eq. (20) and thence $\Phi(\eta)$ from Eq. (21).

From the investigation of Barbanis and Prendergast, who consider the equation

$$\nabla^2 \Phi(\tilde{\omega}, z) = \delta(z) \sigma(\tilde{\omega})$$

there is reason to believe that the method in Eqs. (17)–(21) is superior to Eq. (14). In addition, in most dynamical or electromagnetic problems where such an equation arises, there is often the need to compute the field $-\nabla\Phi$. A potential expressed in the form of Eq. (21) obviously renders the computation of the field more readily than the form of Eq. (14). There is also the intrinsic computational difficulty that, whereas the integrand for the potential (Eq. 11) behaves singularly as

$$\lim_{\Delta \rightarrow 0} \frac{1}{\Delta}$$

for the field, we have a singularity of the form

$$\lim_{\Delta \rightarrow 0} \frac{1}{\Delta^2}$$

Thus any quadrature scheme has to provide special treatment for this behavior. Therefore we strongly recommend that to solve a P.D.E. of the form of Eq. (10), the former method described is to be avoided in favor of the latter.

B. Integrals of Confluent Hypergeometric Functions, Part I, E. Ng

1. Introduction

Confluent hypergeometric functions are probably most well known in mathematical physics in the context of Schroedinger's equation, of the form:

$$\nabla^2 \psi + \frac{8\pi^2 M}{h^2} \left(E + \frac{\mu}{r} \right) \psi = 0 \quad (1)$$

By a separation of variables in spherical coordinates, one finds that

$$\psi = R(r) \Theta(\theta) \Phi(\delta) \quad (2)$$

where $R(r)$ satisfies a differential equation of the type

$$r^2 R'' + 2rR' + (ar^2 + br)R = C \quad (3)$$

of which the confluent hypergeometric functions are solutions. These functions are derivable from the more fundamental generalized hypergeometric functions. In this article we shall consider the first two kinds of confluent hypergeometric functions, often known as Kummer's functions (as distinguished from Whittaker's functions). Using Slater's (Ref. 6) notation, we define the two functions as follows:

$$M(a, b, z) = \sum_{j=0}^{\infty} \frac{(a)_j z^j}{(b)_j j!} \quad (4)$$

where

$$(a)_j = a(a+1) \cdots (a+j-1) = \frac{\Gamma(a+j)}{\Gamma(a)}, \text{ etc.}$$

and

$$U(a, b, z) = \frac{\pi}{\sin \pi b} \left[\frac{M(a, b, z)}{\Gamma(1+a-b)\Gamma(b)} - z^{1-b} \frac{M(1+a-b, z-b, z)}{\Gamma(a)\Gamma(2-b)} \right] \quad (5)$$

The series, Eq. (4), is absolutely convergent for all values of a , b and z , real or complex, excluding $b = 0, -1, -2, \dots$. One very important property of $M(a, b, z)$ and $U(a, b, z)$ is that they contain as special cases most of the commonly used special functions of mathematical physics (Ref. 6), and one can utilize this "unifying"

property to construct an integral table involving a great variety of special functions. For a description and summary of the special functions, the reader is referred to Erdelyi (Ref. 7) and Magnus, et al. (Ref. 8). Integrals of special functions occur frequently in physical problems, often in the evaluation of double or triple integrals, where one or two integrals can be expressed as a special function. Another place of occurrence is found in the context of integral transforms which usually involve integrals with infinite limits (Ref. 8).

In this investigation we shall consider the following six types of indefinite integrals:

$$\Phi_n(a, b, z) \equiv \int z^n M(a, b, z) dz \quad (6)$$

$$\psi_n(a, b, z) \equiv \int z^n U(a, b, z) dz \quad (7)$$

$$\Lambda(a, b, z) \equiv \int e^{\alpha z} M(a, b, z) dz \quad (8)$$

$$\Omega(a, b, z) \equiv \int e^{\alpha z} U(a, b, z) dz \quad (9)$$

$$\Theta_n(a, b, z) \equiv \int z^n e^{\alpha z} M(a, b, z) dz \quad (10)$$

$$T_n(a, b, z) \equiv \int z^n e^{\alpha z} U(a, b, z) dz \quad (11)$$

where a, b, z and α may be complex or real and n is a positive integer. We shall show that computationally, given a subroutine of $M(a, b, z)$, and hence $U(a, b, z)$, we can obtain all integrals considered by some derived formulae. Part I will be devoted to the investigation of Eqs. (6) and (7). Subsequent investigation will concentrate on Eqs. (8) through (11).

Here we shall summarize some well-known properties of the confluent hypergeometric functions, which will be used in subsequent sections. $M(a, b, z)$ and $U(a, b, z)$ and their contiguous functions $M(a \pm 1, b \pm 1, z)$ and $U(a \pm 1, b \pm 1, z)$ obey certain recurrence relations of which, if any two are given, the others can be deduced. We shall write down only two here. For a longer list, refer to Ref. 8.

$$(1+a-b)M(a, b, z) - aM(a+1, b, z) + (b-1)M(a, b-1, z) = 0 \quad (12)$$

$$bM(a, b, z) - bM(a-1, b, z) - zM(a, b+1, z) = 0 \quad (13)$$

$$U(a, b, z) - aU(a+1, b, z) - U(a, b-1, z) = 0 \quad (14)$$

$$= \frac{1}{(a-1)} M(a-1, a, z) \quad (23)$$

$$(b-a)U(a, b, z) + U(a-1, b, z) - zU(a, b+1, z) = 0 \quad (15)$$

$$\int e^{z\Gamma(a, z)} dz = \psi_0(1-a, 1-a, z) \quad (24)$$

$$= \frac{1}{a} U(-a, -a, z) \quad (25)$$

Two differential properties will also be found useful in this paper:

$$\frac{d}{dz} M(a, b, z) = \frac{a}{b} M(a+1, b+1, z) \quad (16)$$

$$\frac{d}{dz} U(a, b, z) = -aU(a+1, b+1, z) \quad (17)$$

2. Special Cases of $\Phi_n(a, b, z)$ and $\psi_n(a, b, z)$

To illustrate the use we shall make of the "unifying" property of the confluent hypergeometric functions, we first consider some well-known special cases. It can be shown (Ref. 6) from the differential properties of $M(a, b, z)$ and $U(a, b, z)$ that

$$\Phi_0(a, b, z) = \frac{b-1}{a-1} M(a-1, b-1, z) \quad a \neq 1 \quad (18)$$

$$\psi_0(a, b, z) = \frac{1}{1-a} U(a-1, b-1, z) \quad a \neq 1 \quad (19)$$

$$\Phi_{a-2}(a, b, z) = \frac{z^{a-1}}{a-1} M(a-1, b, z) \quad a \neq 1 \quad (20)$$

$$\psi_{a-2}(a, b, z) = \frac{z^{a-1}}{(a-1)(a-b)} U(a-1, b, z) \quad \begin{matrix} a \neq 1 \\ a \neq b \end{matrix} \quad (21)$$

Using the well-known relations of M and U to the other special functions (Ref. 6), Eqs. (18) to (21) enable us to evaluate many integrals in terms of M and U . For example,

(i) Incomplete gamma functions:

$$\int \frac{\gamma(a, z)}{z^a} dz = \frac{1}{a} \Phi_0(a, a+1, z) \quad (22)$$

(ii) Bessel functions:

$$\int e^{iz} z^{-\nu} J_\nu(z) dz = \frac{1}{i2^{\nu+1} \Gamma(1+\nu)} \times \Phi_0\left(\nu + \frac{1}{2}, 2\nu + 1, 2iz\right) \quad (26)$$

$$= \frac{2\nu}{i2^{\nu+1} \left(\nu - \frac{1}{2}\right) \Gamma(1+\nu)} \times M\left(\nu - \frac{1}{2}, 2\nu, 2iz\right) \quad (27)$$

$$\int e^z z^{-\nu} K_\nu(z) dz = (\pi)^{1/2} 2^{\nu-1} \psi_0\left(\nu + \frac{1}{2}, 2\nu + 1, 2z\right) \quad (28)$$

$$= \frac{(\pi)^{1/2} 2^{\nu-1}}{\frac{1}{2}^{-\nu}} U\left(\nu - \frac{1}{2}, 2\nu, 2z\right) \quad (29)$$

(iii) Laguerre and Poisson-Charlier polynomials:

$$\int L_k^{(\alpha)}(z) dz = \frac{(-1)^k}{k!} \psi_0(-k, \alpha+1, z) \quad (30)$$

$$= \frac{(-1)^k}{k!(1+k)} U(-k-1, \alpha, z) \quad (31)$$

$$\int z^k P_{2k}(\nu, z) dz = \frac{(1+\nu-2k)_{2k}}{[\Gamma(2k+1)]^{1/2}} \times \Phi_0(-2k, 1+\nu-2k, z) \quad (32)$$

$$= \frac{(1+\nu-2k)_{2k} (2k-\nu)}{(2k+1)^{1/2} (2k+1)} \times M(-2k-1, \nu-2k, z) \quad (33)$$

and similarly, many other integrals involving Bessel functions, exponential, logarithmic, sine and cosine integrals, Coulomb wave functions, and parabolic cylinder functions can be evaluated in terms of M and U .

3. General Cases of $\Phi_n(a, b, z)$ and $\psi_n(a, b, z)$

The evaluation of these integrals should be treated in four different cases, as follows.

(i) $a \neq \text{integer}, b \neq \text{integer}$

Integrate Eqs. (6) and (7) by parts and use Eqs. (18) and (19) to obtain

$$\begin{aligned} \Phi_n(a, b, z) &= \frac{b-1}{a-1} z^n M(a-1, b-1, z) \\ &\quad - \frac{n(b-1)}{a-1} \Phi_{n-1}(a-1, b-1, z) \end{aligned} \quad (34)$$

$$\begin{aligned} \psi_n(a, b, z) &= \frac{1}{a-1} z^n U(a-1, b-1, z) \\ &\quad - \frac{n}{a-1} \psi_{n-1}(a-1, b-1, z) \end{aligned} \quad (35)$$

Equations (34) and (35) can thus be used to obtain by recursion $\Phi_n(a, b, z)$ and $\psi_n(a, b, z)$ from $\Phi_0(a-n, b-n, z)$ and $\psi_0(a-n, b-n, z)$, which can be evaluated in terms of M and U .

(ii) $a \neq \text{integer}, b = \text{integer}$

Replace a by $(a-1)$ in Eqs. (12) and (14) and substitute into Eqs. (34) and (35) to eliminate $\Phi_{n-1}(a-1, b-1, z)$ and $\psi_{n-1}(a-1, b-1, z)$, respectively. We obtain

$$\begin{aligned} \Phi_n(a, b, z) &= \frac{b-1}{a-1} z^n M(a-1, b-1, z) - n\Phi_{n-1}(a, b, z) \\ &\quad - \frac{n(b-a)}{a-1} \Phi_{n-1}(a-1, b, z) \end{aligned} \quad (36)$$

$$\begin{aligned} \psi_n(a, b, z) &= \frac{1}{a-1} z^n U(a-1, b-1, z) + n\psi_{n-1}(a, b, z) \\ &\quad - \frac{n}{a-1} \psi_{n-1}(a-1, b, z) \end{aligned} \quad (37)$$

Again these integrals can be computed recursively from Φ_0 and ψ_0 .

(iii) $a = \text{integer}, b \neq \text{integer}$

For $a > n$, Eqs. (34) and (35) can be used as in case (i). For $0 < a < n$, the following equations are found useful.

$$\begin{aligned} \Phi_n(a, b, z) &= (b-1) \Phi_{n-1}(a, b-1, z) \\ &\quad - (b-1) \Phi_{n-1}(a-1, b-1, z) \end{aligned} \quad (38)$$

$$\begin{aligned} \psi_n(a, b, z) &= (b-a-1) \psi_{n-1}(a, b-1, z) \\ &\quad + \psi_{n-1}(a-1, b-1, z) \end{aligned} \quad (39)$$

Equations (38) and (39) are obtained from a combination of Eqs. (6) with (13) and (7) with (15), respectively. They can be used to generate Φ_n and ψ_n from Φ_0, ψ_0 , and

$$\Phi_n(0, b, z) = \psi_n(0, b, z) = \frac{1}{(n+1)} z^{n+1}$$

For $a < 0$, Eqs. (34) and (35) can be used with n, a and b replaced by $(n+1), (a+1)$ and $(b+1)$, respectively, giving

$$\begin{aligned} (n+1) \Phi_n(a, b, z) &= z^{n+1} M(a+1, b+1, z) \\ &\quad - \frac{a}{b} \Phi_{n+1}(a+1, b+1, z) \end{aligned} \quad (40)$$

$$\begin{aligned} (n+1) \psi_n(a, b, z) &= z^{n+1} U(a+1, b+1, z) \\ &\quad - a\psi_{n+1}(a+1, b+1, z) \end{aligned} \quad (41)$$

(iv) $a = \text{integer}, b = \text{integer}$

For $a > b$, Eq. (38) can be used with n and b replaced by $(n+1)$ and $(b+1)$, giving

$$\Phi_n(a, b, z) = \Phi_n(a-1, b, z) + \frac{1}{b} \Phi_{n+1}(a, b+1, z) \quad (42)$$

Repeated application of this will reduce the right-hand side to elementary integrals of the form

$$\Phi_n(a, a, z) = \int z^n e^z da$$

due to the special case $M(a, a, z) = e^z$. With $\psi_n(a, b, z)$, however, such procedure is not practical because the special case $U(a, a, z)$ is an incomplete gamma function, and hence we shall resort to another means. For $n < a$, Eq. (37) can be used to generate ψ_n from ψ_0 . For $n > a$, Eq. (37) can be applied successively to transform $\psi_n(a, b, z)$ to the form $\psi_m(\alpha, b, z)$ where $\alpha < b$, a case to be considered next.

For $0 < a < b$, Eq. (38) can be used to generate $\Phi_n(a, b, z)$ from terms of the form $\Phi_0(\alpha, \beta, z)$, $\Phi_m(\alpha, \alpha, z)$ and $\Phi_m(0, \beta, z)$. Similarly, $\psi_n(a, b, z)$ is reducible by Eq. (39) to $\psi_0(\alpha, \beta, z)$, $\psi_m(0, \beta, z)$ and $\psi_m(\alpha, \alpha + 1, z)$, the last term being obtainable from $\psi_m(0, 1, z)$ or $\psi_0(\alpha, \alpha + 1, z)$ by application of the same equation again. For $a < 0$, Eqs. (40) and (41) are to be applied as before.

With these four cases, which cover all possible combinations of the parameters a and b and the positive index n , we can form an integral table from the relations of $M(a, b, z)$ and $U(a, b, z)$ to the other special functions. For a summary of such relations the reader is referred to Ref. 8, pp. 283–287 and Ref. 6, pp. 509–510.

In the following, we shall give several examples of such integrals. With the lists of relations given by Magnus, et al., and Slater, one can express many more integrals of special functions in terms of Φ_n and ψ_n .

(i) Bessel functions:

$$\int z^n e^{iz} J_k(z) dz = \frac{(i)^{-(n+k+1)}}{2^{n+2k+1} \Gamma(1+k)} \times \Phi_{n+k}\left(k + \frac{1}{2}, 2k + 1, 2iz\right) \quad (43)$$

$$\int z^n e^z I_k(z) dz = \frac{2^{-(n+2k+1)}}{(1+k)} \times \Phi_{n+k}\left(k + \frac{1}{2}, 2k + 1, 2z\right) \quad (44)$$

$$\int z^n e^z K_k(z) dz = \frac{2^{-(n+1)}}{(\pi)^{1/2}} \times \psi_{n+k}\left(k + \frac{1}{2}, 2k + 1, 2z\right) \quad (45)$$

(ii) Laguerre and Poisson–Charlier polynomials:

$$\int z^n L_k^{(\alpha)}(z) dz = \frac{\Gamma(1+k) \Gamma(1+\alpha)}{\Gamma(\alpha+k+1)} \times \Phi_n(-k, \alpha + 1, z) \quad (46)$$

$$\int z^{n+k} P_{2k}(\nu, z) dz = \frac{(1+\nu-2k)_{2k}}{[\Gamma(2k+1)]^{1/2}} \times \Phi_n(-2k, 1+\nu-2k, z) \quad (47)$$

(iii) Hermite polynomials and parabolic cylinder functions:

$$\int z^{2n+1} H_k(z) dz = 2^{k-1} \psi_n\left(\frac{1}{2} - \frac{k}{2}, \frac{3}{2}, z^2\right) \quad (48)$$

$$\int z^{2n} H_{2k+1}(z) dz = (-1)^k \frac{(2k+1)!}{k!} \times \Phi_n\left(-k, \frac{3}{2}, z^2\right) \quad (49)$$

$$\int z^{2n} \exp\left(\frac{z^2}{4}\right) D_\nu(z) dz = 2\left[n + \frac{1}{2}(\nu-1)\right] \times \psi_n\left(\frac{1}{2} - \frac{\nu}{2}, \frac{3}{2}, \frac{z^2}{2}\right) \quad (50)$$

References

1. Lin, C. C., "Mathematical Theory of a Galaxy," *SIAM J. Appl. Math.*, Vol. 14, p. 876, 1966.
2. Ng, E. W., "Self-Consistent Models of Disc-Galaxies," *Astrophys. J.*, 1967 (to be published).
3. Poincaré, H., *Lecon sur les Hypothéses Cosmogoniques*, A. Hermann et Fils, Paris, 1911.
4. Morse, P., and Feshbach, H., *Methods of Theoretical Physics*. McGraw-Hill Book Co., Inc., New York, 1953.
5. Barbanis, B., and Prendergast, K., "Gravitational Potential," *Astron. J.*, 1967 (to be published).
6. Slater, L. J., "Confluent Hypergeometric Functions," Chapter 13 in M. Abramowitz and I. Stegun (Eds.), *Handbook of Mathematical Functions*, NBS AMS #55, U.S. Government Printing Office, 1965.
7. Erdelyi, A., et al., *Higher Transcendental Functions*, Volume I. McGraw-Hill Book Co., Inc., New York, 1953.
8. Magnus, W., Oberhettinger, F., and Soni, R. P., *Special Functions of Mathematical Physics*, Springer-Verlag, New York, 1966.

IV. Environmental Requirements

PROJECT ENGINEERING DIVISION

A. Dry-Heat Resistance of Bacterial Spores (*Bacillus Globigii*) Upon Selected Spacecraft

Surface Materials, W. W. Paik, S. C. Michael,
C. D. Smith, and J. A. Stern

I. Introduction

The established NASA planetary quarantine requirements state that the probability of a single viable organism being upon a spacecraft intended for penetration of the Martian atmosphere or for landing upon Mars shall be less than 1 in 10^{-6} (Ref. 1). To meet this requirement, a capsule designed for planetary landing must be sterilized. Several methods may be used, including the use of gaseous and liquid chemicals, various forms of radiant energy, and dry and moist heat. Moist heat has long been used in industrial applications, such as the processing of food products and the sterilization of surgical instruments. The uses of dry heat as a sterilant, while varied, have been more limited. However, dry-heat sterilization processes are now receiving critical appraisal as a possible means for terminally sterilizing spacecraft (Ref. 2).

A terminal dry-heat sterilization process for a space vehicle must take into account various factors, such as the thermal characteristics of the final assembly, the total microbial load and its distribution, and the thermal resis-

tance of the microbial population. The thermal resistance of microorganisms shall be discussed here.

The determination of the thermal resistance of microorganisms is a complex problem that must include consideration of the physiological condition of the cells, their environment, the type of heat (dry or moist) to which the cells are exposed, and other experimental factors. When considering the thermal resistance of microorganisms on space hardware, environment is of great importance. For discussion and analytical purposes, the distribution of the total microbial burden of a spacecraft can be considered in three categories: (1) those microorganisms contained within the interior of the spacecraft hardware components, (2) the microbial load existent upon exposed surfaces, and (3) those microorganisms occluded between the spacecraft's mated surfaces. The time-temperature relationships necessary to inactivate microorganisms at each of these three locations are different. To establish a terminal dry-heat sterilization cycle, each of these time-temperature relationships must be known.

This article presents the results of an effort to determine the dry-heat resistance of bacterial spores upon several different spacecraft surface materials. The materials used, their element composition, and their test heating properties are presented in Table I.

Table 1. Element composition and test heating properties of inoculated-surface materials

Material	Composition	Time required to heat test strip from 21°C to 125 ± 1°C, ^a min
Stainless steel (Type 302)	71.8% Fe, 18% Cr, 8% Ni, 2% Mn, 1% Si, 0.15% C, 0.45% P, 0.03% S	8.5
Aluminum alloy (6061-T6)	97.7% Al, 1.2% Mg, 0.6% Si, 0.2% Cr, 0.3% Cu	7.0
Conversion-coated (Dow 7) magnesium alloy	95.8% Mg, 3% Al, 1% Zn, 0.2% Mn (% MgCrO ₄ unknown)	7.5
Magnesium alloy (AZ31B-H24)	95.8% Mg, 3% Al, 1% Zn, 0.2% Mn	7.5
Titanium alloy (6Al4V)	90% Ti, 6% Al, 4% V	9.0
Cat-A-Lac black paint, (436-1-B) over stainless steel (Type 302)	Epoxy resin base, primary and secondary amines, inert pigments, talc, mica, carbon ^b	10.5
Conversion-coated (Iridite 14) aluminum alloy	Chromium hydroxide, chromium oxide, iron, aluminum hydroxide and silicone compounds ^b	11.5
24-karat gold-plated electroless nickel over aluminum (6061-T6)	24-karat gold (purity unknown)	11.5

^a 1.0- X 3.0- X 0.020-in. strips suspended from Teflon-coated aluminum support rack.
^b Percent composition of these compounds is proprietary information.

Some of the terminology used here is unique to work associated with the destruction of microorganisms by heat. Since most microbiological techniques for detecting life are dependent upon the reproduction of cells, microbial death is defined here as the inability of a cell to reproduce in appropriate biological media under favorable conditions. The ability to reproduce is not the sole criteria by which the viability of a cell may be established. Microorganisms, when exposed to adverse conditions, may become sublethally injured, resulting in their temporary inability to reproduce; yet, these microorganisms remain viable. However, a discussion of these situations is beyond the scope of this article.

The decimal reduction time, D , is defined as that time, at a specific temperature, which will result in a 90%

reduction in the number of viable cells within a single population. The thermal death time (TDT), or F value, is that time necessary at a specific temperature to reduce a given population to a particular probability level, assuming instantaneous heating and cooling. A TDT curve is the relationship between the logarithm of the D value in units of time plotted against temperature. The z value is the change in temperature, °F or °C, necessary to cause a 10-fold change in the D value. A survivor curve illustrates the log number of surviving microorganisms as opposed to the time of heat exposure. Figure 1 presents thermal destruction and sterilization time curves and their derivation.

2. Test Materials and Procedure

The test method presented here was developed to simulate the situation that may be encountered by microorganisms located on smooth exposed metallic surfaces during dry-heat sterilization of space hardware. The procedure is as follows:

- (1) The test strips are inoculated with a known quantity of *Bacillus subtilis* var. *niger* (*Bacillus globigii*)

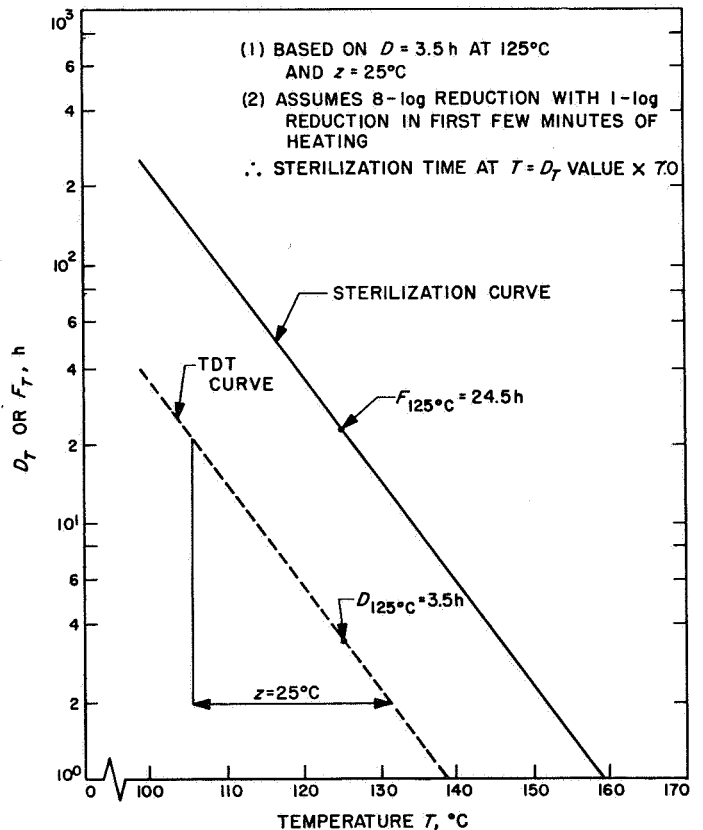


Fig. 1. Thermal destruction and equivalent sterilization time curves

spores¹ and then air-dried in a laminar-air-flow clean bench.

(2) After drying, the test strips are placed in a vacuum desiccator containing active (heated at 175°C for 2 h) silica gel. The desiccator is evacuated to 24-in. negative pressure for 16 h.

(3) The test strips are suspended from a support rod within a preheated oven (125 ± 0.8°C). A constant rate of mechanical air circulation is maintained within the oven test area. The temperature and air velocity profiles of this oven are shown in Fig. 2. The temperature of the test strips is monitored by means of a thermocouple attached to a control test strip. A sterile stainless-steel strip is also suspended from the support rack as a sterility control.

(4) Six inoculated test strips and two control strips (biological and thermal) are exposed at the test exposure time. The time necessary to heat strips of different test materials to 125°C has been quantitatively measured (Table 1). The first assay used to establish the *D* values is conducted after 13 min of heat exposure, thus ensuring that the test strips have reached 125°C. Subsequent assays are conducted at 23, 33, 43, 53, and 63 min, inclusive of the 13-min heat-up period.

(5) After the desired time of dry-heat exposure, the test strips and control strips are quickly removed from the oven and immediately placed within sterile bottles containing 22 ml of prechilled (4°C) phosphate buffer. The bottles are placed in a Branson ultrasonic bath² and treated at 25 kc/s for 12 min in accordance with NASA standard procedures (Ref. 3).

(6) Aliquots of the phosphate buffer are aseptically transferred to dilution blanks, and appropriate dilutions are made. The dilutions are plated in sterile petri dishes (100 × 15 mm) to which molten TSA is added. The metal test strips are also plated in TSA. All plates are aerobically incubated at 32°C for 48 h.

¹The *Bacillus subtilis* var. *niger* (*Bacillus globigii*) spores were chosen as the test organism since published data indicate that they are more resistant to dry heat than most other bacterial spores. These spores were grown on Trypticase Soy Agar (TSA) supplemented with manganese sulfate (20 parts/10⁶) and calcium chloride (80 parts/10⁶). A single spore suspension was utilized for all tests, thus limiting the variability that may be caused by possible differences in the heat-resistance characteristics of different spore populations.

²Branson ultrasonic bath generator, A-300; tank, LT-88; power control, PC-30.

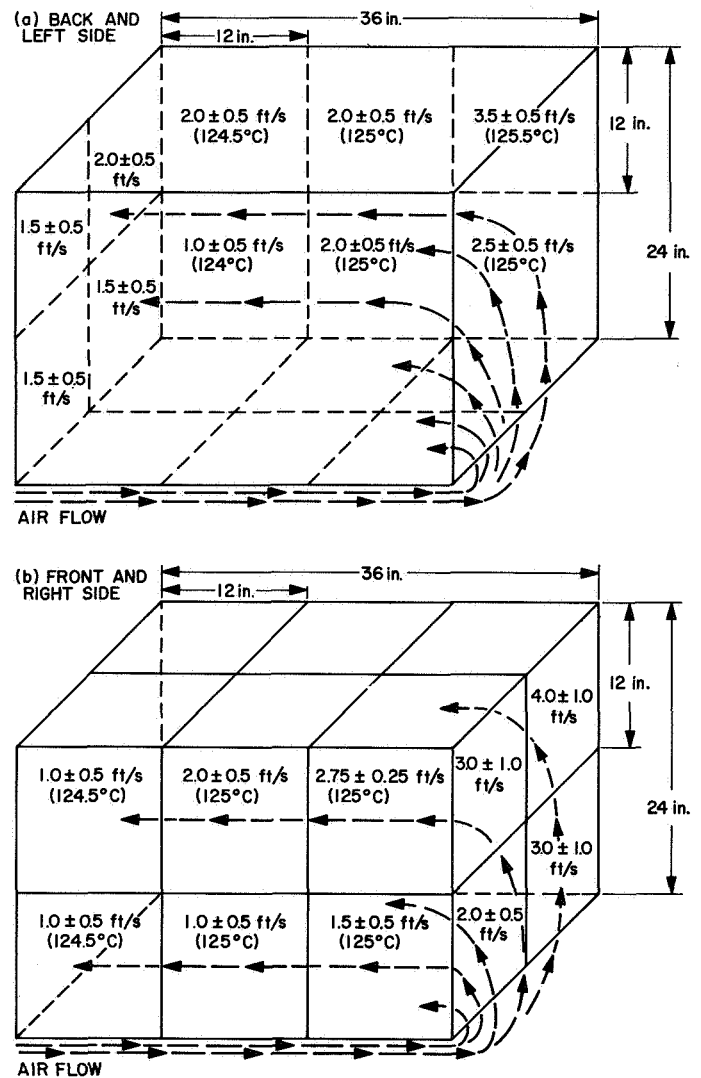


Fig. 2. Temperature and air velocity profiles of oven at 125°C (front view)

(7) Colony counts are made after 48 h, and the total number of viable particles recovered is calculated from the mean value of the various dilutions and from the number of viable particles remaining on the test strips.

3. Results

Three inoculated strips each of two different materials were exposed to the experimental conditions during each test sequence. Stainless steel was chosen as the standard reference surface material due to its previous use as a test material in dry-heat sterilization studies (Ref. 4). Figure 3 presents the results from five tests which utilized stainless steel as the inoculated surface. Figure 4 presents the results from the exposure of *Bacillus subtilis* var. *niger* spores on the other inoculated-surface materials used in this study.

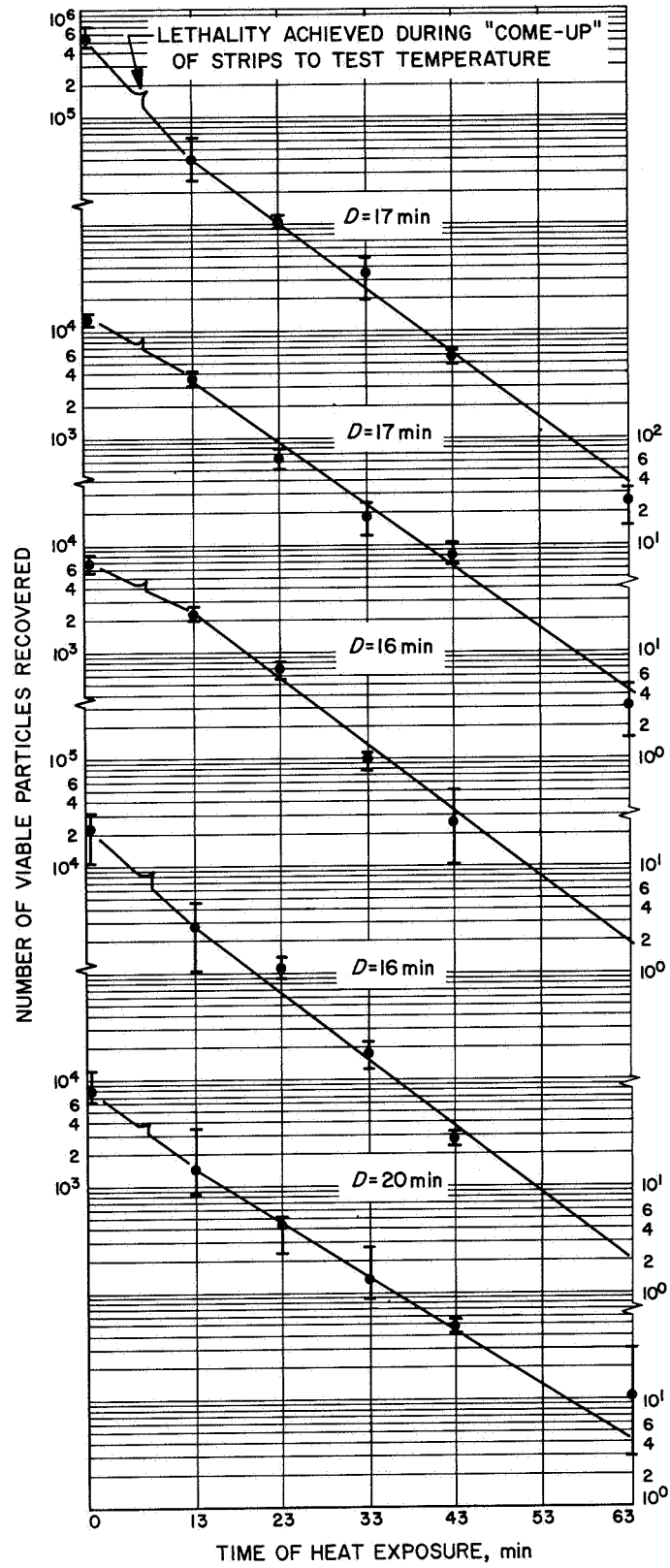


Fig. 3. Survivor curves from five tests for *Bacillus subtilis* var. *niger* spores exposed to 125°C on stainless steel

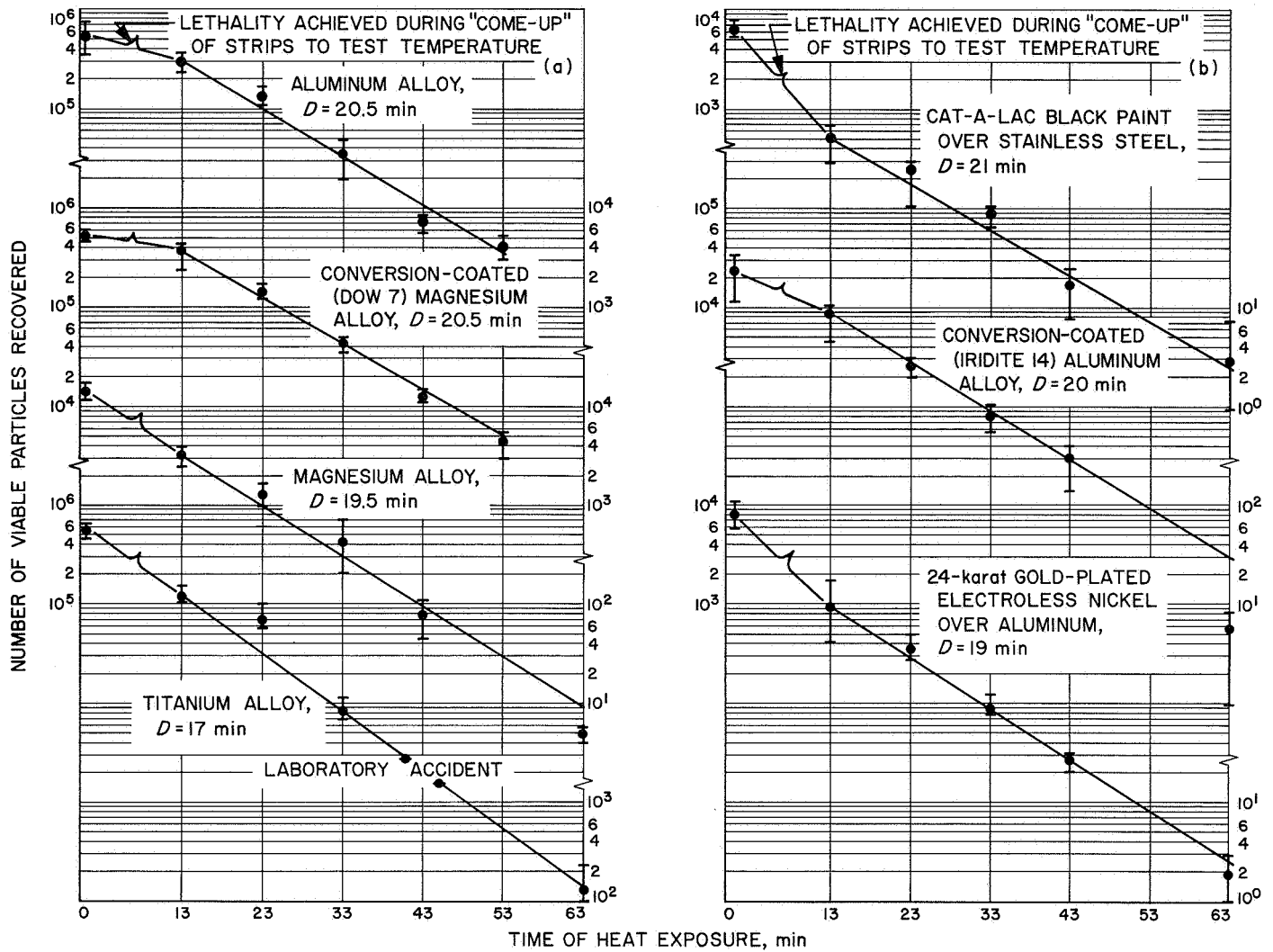


Fig. 4. Survivor curves for *Bacillus subtilis* var. *niger* spores exposed to 125°C on the other inoculated-surface materials used in this study

4. Discussion and Conclusions

There appears to be no significant difference in the *D* values for *Bacillus subtilis* var. *niger* spores on the various materials used in this study. The *D* values for the test spores varied from 16 min for one of the stainless-steel tests to 21 min for the Cat-A-Lac black paint over stainless steel test. This variation is not believed to be significant and may well be the result of slight variations in test procedure. It can be noted that the *D* values derived from the five tests of the stainless-steel reference material vary in themselves from 16 to 20 min; this variation tends to substantiate that the reported differences in thermal resistivity on different surfaces are due to procedural variations, rather than the use of different surface materials as carriers. While it appears that the type of

surface material on which the test spores are exposed to dry heat results in little, if any, difference in *D* values, it must be remembered that, with the exception of the Cat-A-Lac black paint over stainless steel, only smooth even-textured metallic surfaces have been evaluated. The accumulated data are presently being analyzed in order that confidence limits for the reported *D* values can be established and an indication of the quality-of-fit for the survivor curves can be determined.

Regardless of the varying *D* values, the survivor curves derived from all tests (Figs. 3 and 4) appear to indicate that the death of microorganisms closely follows a monomolecular type of reaction. Any major variation from a logarithmic order of death occurred during that time

necessary to bring the system to test temperature. This is in support of the most prevalent theory of microbial survival; i.e., during equal times of exposure, the number of viable microorganisms in any population will be decreased in equal percentile amounts, providing the temperature remains constant.

However, it should be noted that the *D* values for any single type of microorganism may vary according to that microorganism's environment and preconditioning. The thermal resistivity of different microorganisms may also vary considerably from species to species. Thus, considerable work remains to be accomplished before the phenomenon of death of microorganisms exposed to dry heat can be fully understood.

B. Microbial Sampling Program for the Mariner Venus 67 Flight Spacecraft (Mariner V),

M. R. Christensen, R. H. Green, and J. A. Stern³

As part of a continuing NASA/JPL effort to determine the microbial burden on spacecraft, microbial assays were performed during all phases of the assembly and test operations of the *Mariner Venus 67* Project. This program was conducted on a noninterference basis with project operations. The only NASA requirement for sampling of the spacecraft was a final swab assay for the NASA inventory of outbound contamination.

The NASA recommended sampling methods (Ref. 3) were followed throughout assembly, testing, and pre-launch operations of the M67-2 flight spacecraft (*Mariner V*). The assays were limited to sampling specific surfaces which were adaptable to the techniques being utilized. Supportive environmental fallout data were obtained from assembly and test areas in an attempt to correlate spacecraft environmental exposure to the observed burden.

The microbial sampling program was conducted during a 137-day period. The spacecraft octagon arrived in the JPL Spacecraft Assembly Facility (SAF) high-bay area on December 13, 1966; however, activity was minimal until the first part of January, at which time the microbial sampling program was initiated. Samples were obtained on a regularly scheduled basis throughout all operational

phases, terminating with the procurement of final samples just prior to shroud encapsulation of the spacecraft on May 28, 1967.

1. Environments

Most assembly and test operations at JPL were conducted in the SAF. The high-bay area was utilized for assembly and testing of the spacecraft, as well as for housing related ground and operational support equipment. Air make-up in the SAF was 80% internal and 20% external, with filtration by Farr HP-2 filters.

Whenever feasible, the spacecraft was maintained in a 168-ft², Class 100, portable, laminar-downflow, clean room housed within the SAF high-bay area. The walls consisted of plastic drop curtains with zipper corner closures. Constraints for those working on or near the spacecraft included cleaning shoes and wearing head covers, gowns, and cotton gloves. The number of personnel in the high-bay area varied between 10 and 30, while the level in the portable downflow clean room was maintained between 3 and 6.

The spacecraft was transported to the JPL environmental laboratory for vibration and space simulation tests. Air make-up, filtration, and personnel constraints were the same as those in the SAF high-bay area. The vibration laboratory is a sound-proofed area used to simulate noise, shock, and vibration spectra. During test periods, personnel levels varied between 5 and 15. The spacecraft was exposed to the vibration laboratory environment for 3 days.

Housed within a 4250-ft² area, the 10-ft space simulator was used to simulate the thermal-vacuum spectrum encountered during interplanetary cruise. Except for the pre- and post-test inversions, the spacecraft was maintained in this simulator. Air exchange between the simulator and facilities occurred during interim test periods; however, during tests the simulator was sealed, purged with dry nitrogen, and then backfilled and maintained with air that had been passed through two layers of an air-mat filtration system. The spacecraft was subjected to the thermal-vacuum environment for 15 days.

Following the completion of assembly, testing, and preshipment activities at JPL, the spacecraft was placed in a vacuum-cleaned, alcohol-decontaminated canister for shipment to the Air Force Eastern Test Range (AFETR). Upon arrival at the AFETR, the spacecraft was transferred to the JPL clean room in Hangar AO and maintained there for 14 days. Air make-up in this

³The authors acknowledge the valuable assistance and support of the *Mariner Venus 67* Project Test and Operations Team; G. Tritz, B. Moore, and R. Graves of the U.S. Public Health Service at Cape Kennedy, Fla.; and J. Fooks of NASA Headquarters.

facility was 80% internal and 20% external, with filtration through high-efficiency particulate air (HEPA) filters. Personnel constraints were similar to those employed in the SAF high-bay area at JPL. Personnel levels varied between 10 and 30; however, many of these persons were working on the *Surveyor IV* spacecraft which was housed within the same facility.

The final testing area for the spacecraft, prior to placing it on the gantry, was the north bay of the Explosive Safe Facility (ESF), where attitude-control tank pressurization, pyrotechnics, midcourse motor installation, and final shroud encapsulation were accomplished. Air make-up, filtration, and personnel constraints were the same as those listed for Hangar AO. The number of personnel was limited to a maximum of 15. The spacecraft was maintained in this environment for 16 days.

2. Sampling Procedures

The microbial profile relative to fallout contamination for all of the facilities was derived from data obtained from 1- × 2-in. stainless-steel settling strips and Reyniers air samplers. Settling-strip and swab-rinse methods (Ref. 3) were used for the burden estimation of the spacecraft.

3. Settling-Strip Samples

The settling strips were contained in Teflon-backed units that were nonmagnetic, self-contained, portable, and sterilizable. The units were attached directly to the spacecraft or its support equipment to obtain a distributive effect around, above, and below the structural octagon.

The carriers varied in shape and size according to their location on the spacecraft. Those attached to the faces of the electronic chassis (Bays 1 and 3-8) contained fifteen 1.0-in.-square strips (Fig. 5). Other carriers were attached to the top ring by means of a stainless-steel plate. The plate held six carriers, each of which contained nine 1.0-in.-square strips (Fig. 6). Additional strips were maintained on the spacecraft support ring by means of angle-iron-shaped carriers. These carriers (located below Bays 2, 4, 6, and 8) each contained nineteen (ten vertical and nine horizontal) 1.0-in.-square strips (Fig. 6). The remaining carriers were placed on the attitude-gas-control handling frames. Three (two vertical and one horizontal) carriers were attached to each of four frames. Each carrier contained nine 1.0-in.-square strips (Fig. 7).

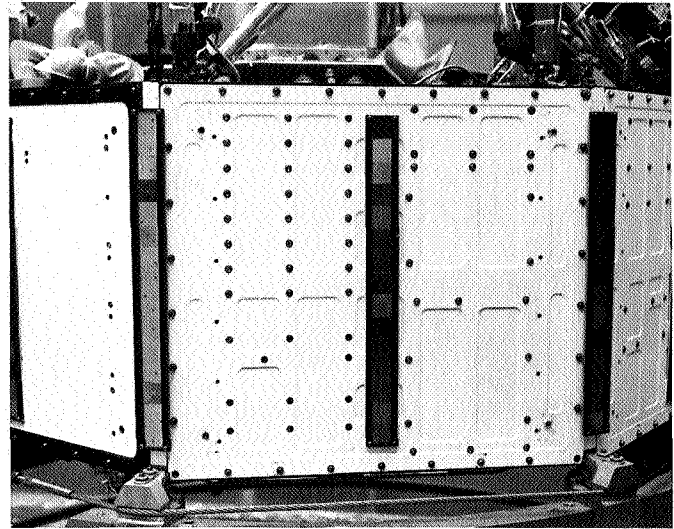


Fig. 5. Sampling carriers attached to face of electronic chassis

When the nature of a specific test dictated removal of the carriers, they were transferred to a mockup (Fig. 8) and maintained in close proximity to the spacecraft. Exposure times and positions of the carriers were correlated with the normal times and positions on the spacecraft.

All carriers contained strips which were retrieved on both weekly and monthly bases. Additionally, each carrier held strips which remained throughout the JPL or AFETR phase of the program and strips which remained throughout the entire program. At each sampling period, a minimum of 72 strips was assayed.

4. Swab-Rinse Samples

Swab samples were obtained using the techniques presented in Ref. 3. Individual surface areas of 4 in.² were sampled using templates (Fig. 9) on a weekly basis. A minimum of 45 samples was taken at each sampling period from both ground support and flight equipment. The ground-support-equipment swab-sampling sites were:

- (1) Attitude-gas-control handling frames
- (2) Pressure switches
- (3) Umbilical breakout box
- (4) Universal ring
- (5) Louver covers
- (6) Light hood, Canopus sensor
- (7) Shipping canister

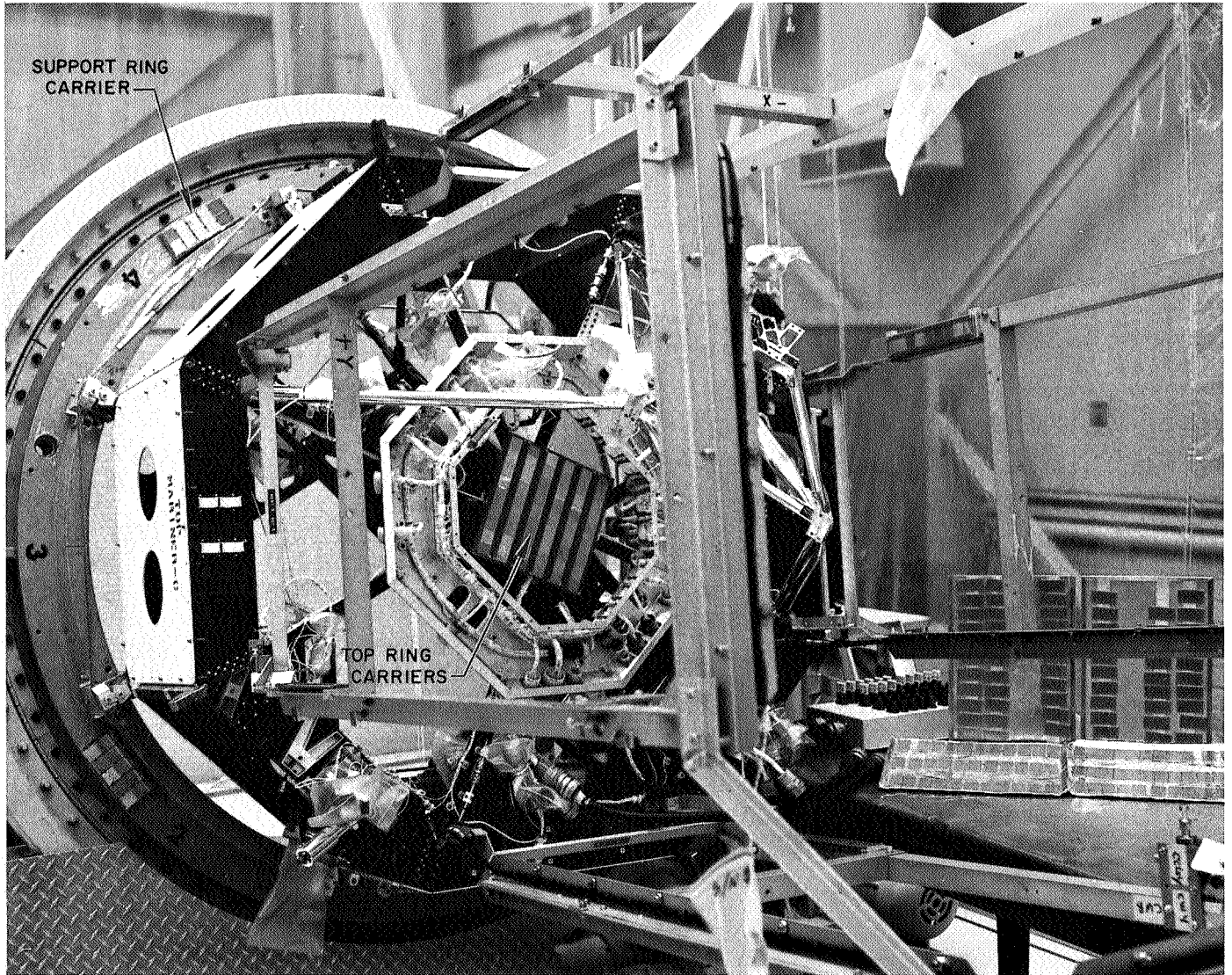


Fig. 6. Sampling carriers attached to top and support rings

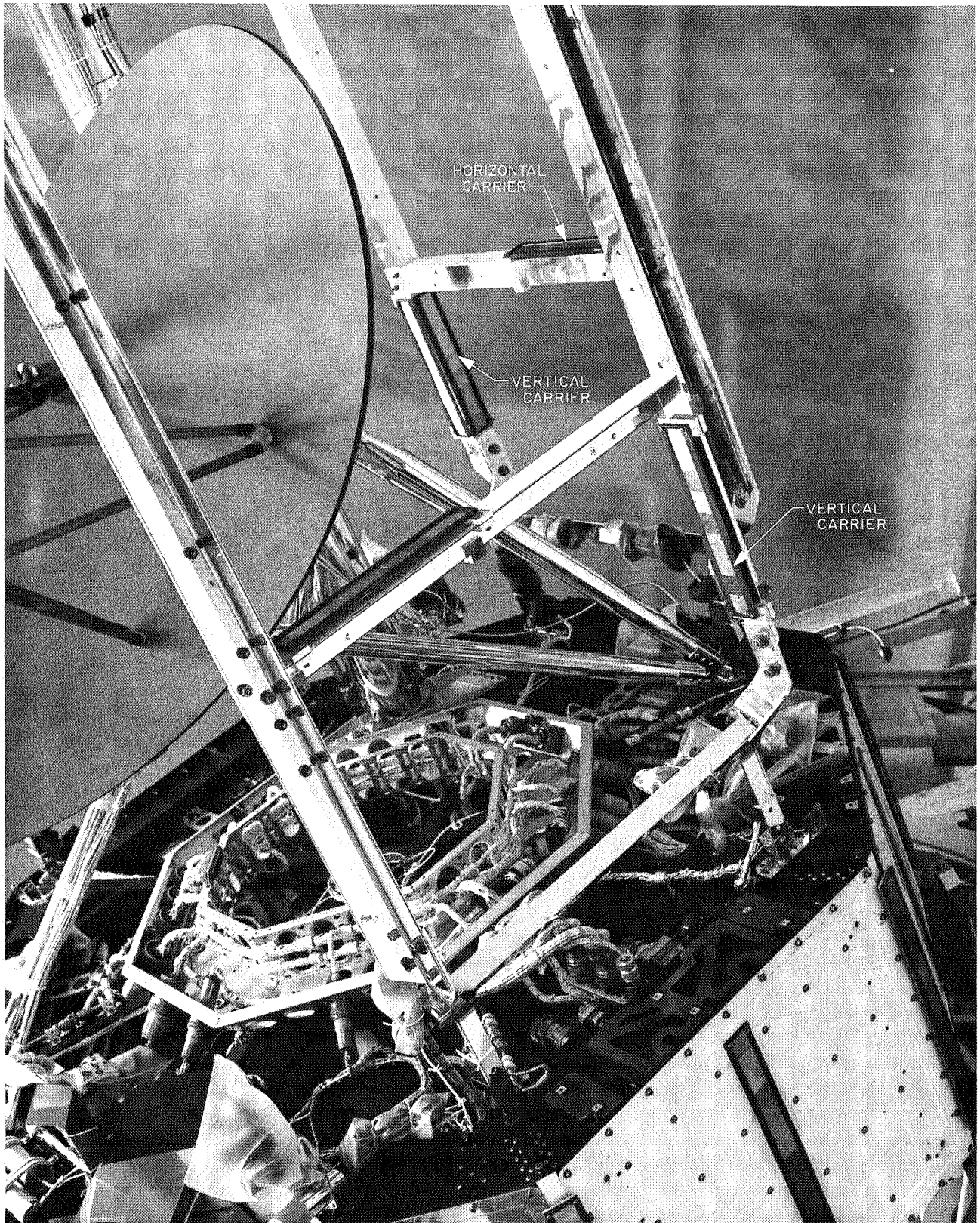


Fig. 7. Sampling carriers attached to handling frame spars

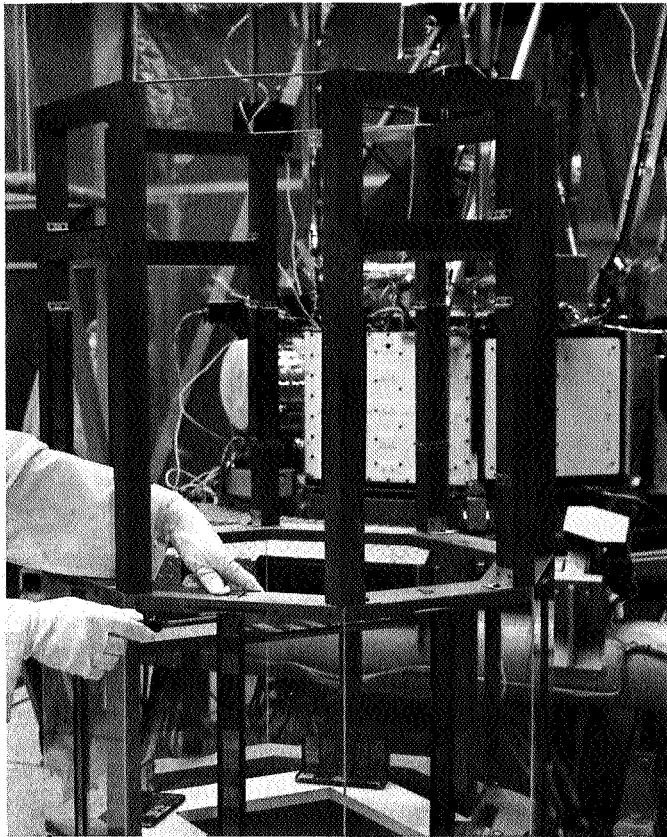


Fig. 8. Mockup used to simulate spacecraft positions

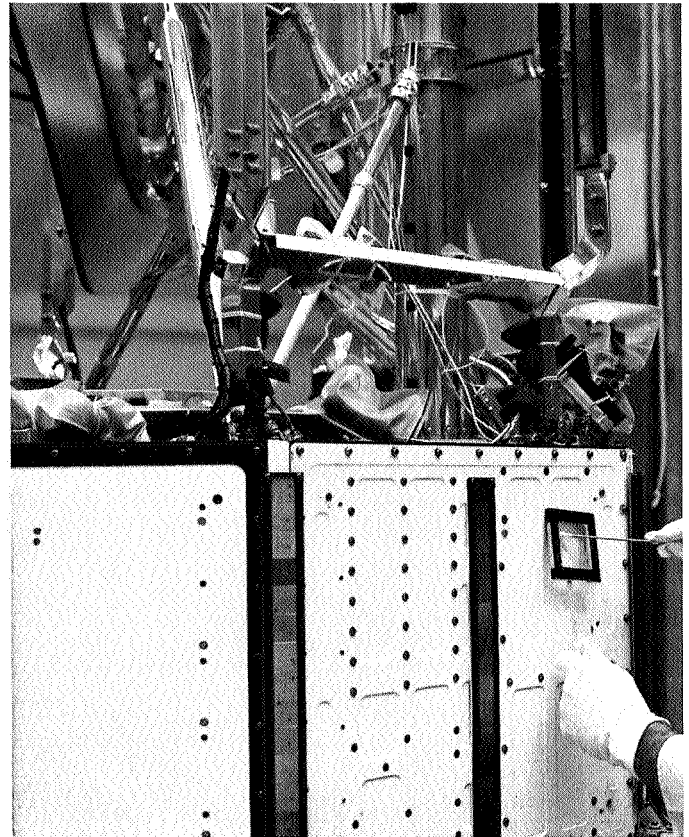


Fig. 9. Swab sampling of electronic chassis using template

The flight-equipment swab-sampling sites were:

- (1) Face, electronic chassis
- (2) Canopus sensor
- (3) Low-gain antenna (omniantenna)
- (4) Superstructure, high-gain antenna
- (5) Pedestals, secondary sun sensors
- (6) Ultraviolet photometer
- (7) Thermal blanket (TFE side)
- (8) Struts, solar panels
- (9) Flight shields
- (10) Adapter
- (11) Shroud

5. Results

The results reported here are limited to the data obtained for heat-resistant spores. The mean environmental contamination levels for the areas of spacecraft activity are presented in Table 2. Settling-strip data are presented in Fig. 10. Figure 11 shows burden levels obtained utilizing the swab technique. A 30%-efficiency recovery factor has been incorporated into the swab data. Continuity breaks in the curves represent periods when the spacecraft was unavailable for sampling.

6. Discussion

Comparison of the results from swab-rinse and settling-strip sampling indicates that the strips may be a more sensitive method for the enumeration of accumulative contamination. The lower recovery percentage observed for the swab method is probably the result of various contributing factors. The swab technique requires removal of the organisms from the spacecraft and then removal from the swab for enumeration. Additionally, large areas of spacecraft surfaces were removed from the environment for short periods and cleaned; on various occasions, the spacecraft was vacuum-cleaned and the temperature-control and polished aluminum surfaces were cleansed with isopropyl alcohol. The strips were not subjected to these procedures.

Weekly data obtained from both methods of sampling indicate that a relationship exists between personnel activity and the level of microbial accumulation (Figs. 10 and 11). Both swab and strip data reflect the higher levels of personnel activity that occurred during the spacecraft assembly operations of January 11 through 26

(as reported in the quality-assurance log). This same relationship is noted in the data from April 29 to May 12, when the spacecraft was prepared for movement to the ESF.

The effect of environmental factors in the absence of activity is indicated in Fig. 10 for March 2 through 16. At that point in the operations, the thermal-vacuum tests of the spacecraft were being performed in the space simulator, and the strips were attached to the mockup located in the laminar-downflow clean room where activity was minimal. The clean room appeared to be the

closest simulation of the space simulator environment. This procedure was repeated between March 30 and April 13, during which time the spacecraft was disassembled in the clean room following the environmental tests.

Although weekly accumulative levels fluctuated, burden estimates from monthly and long-term settling strips (Fig. 10, broken line and encircled points) indicate a leveling-off or plateauing of the microbial burden. Under the prevailing conditions, the plateau occurred at approximately 400 aerobic spores/ft².

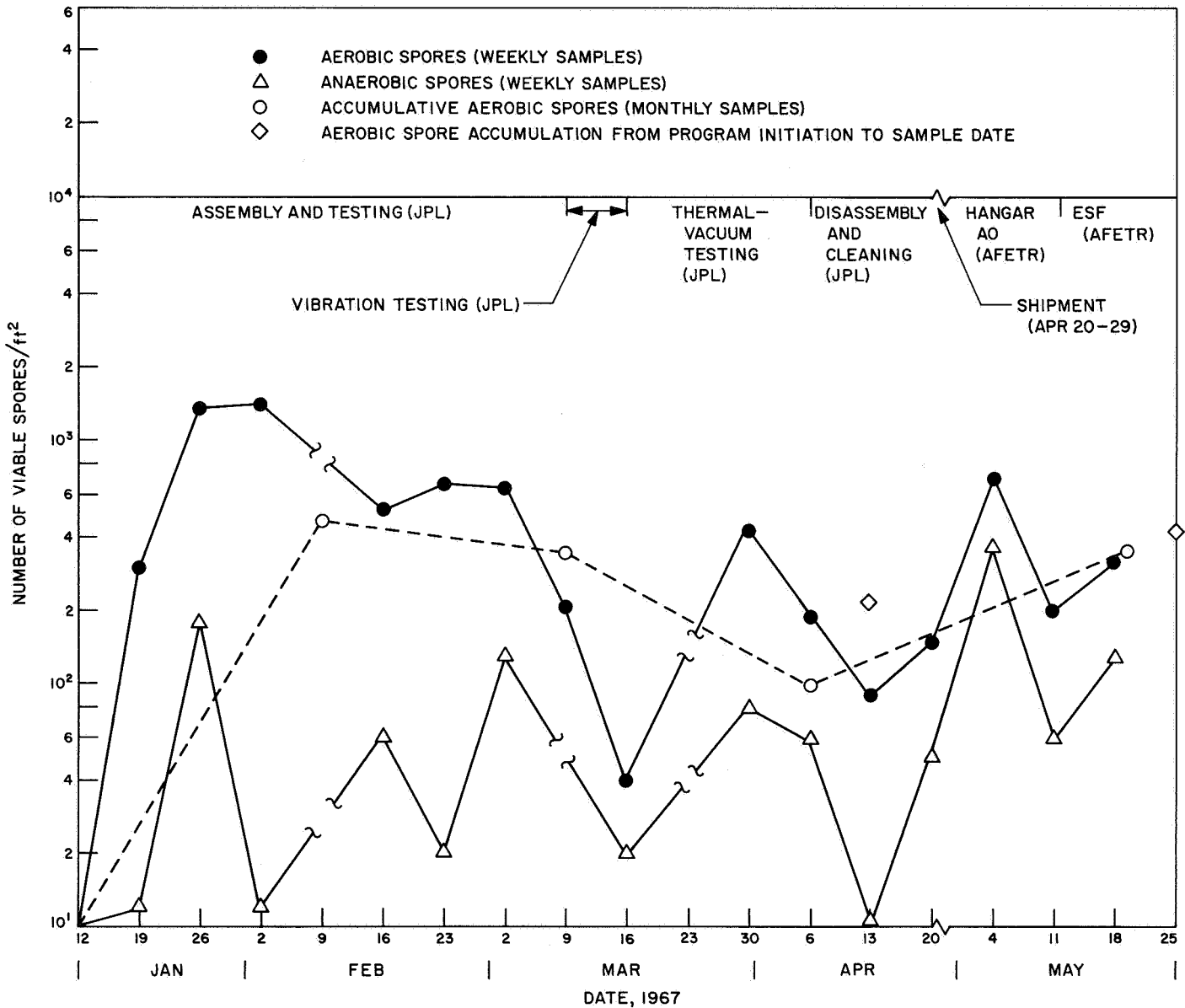


Fig. 10. Average spore burden estimates (settling-strip technique)

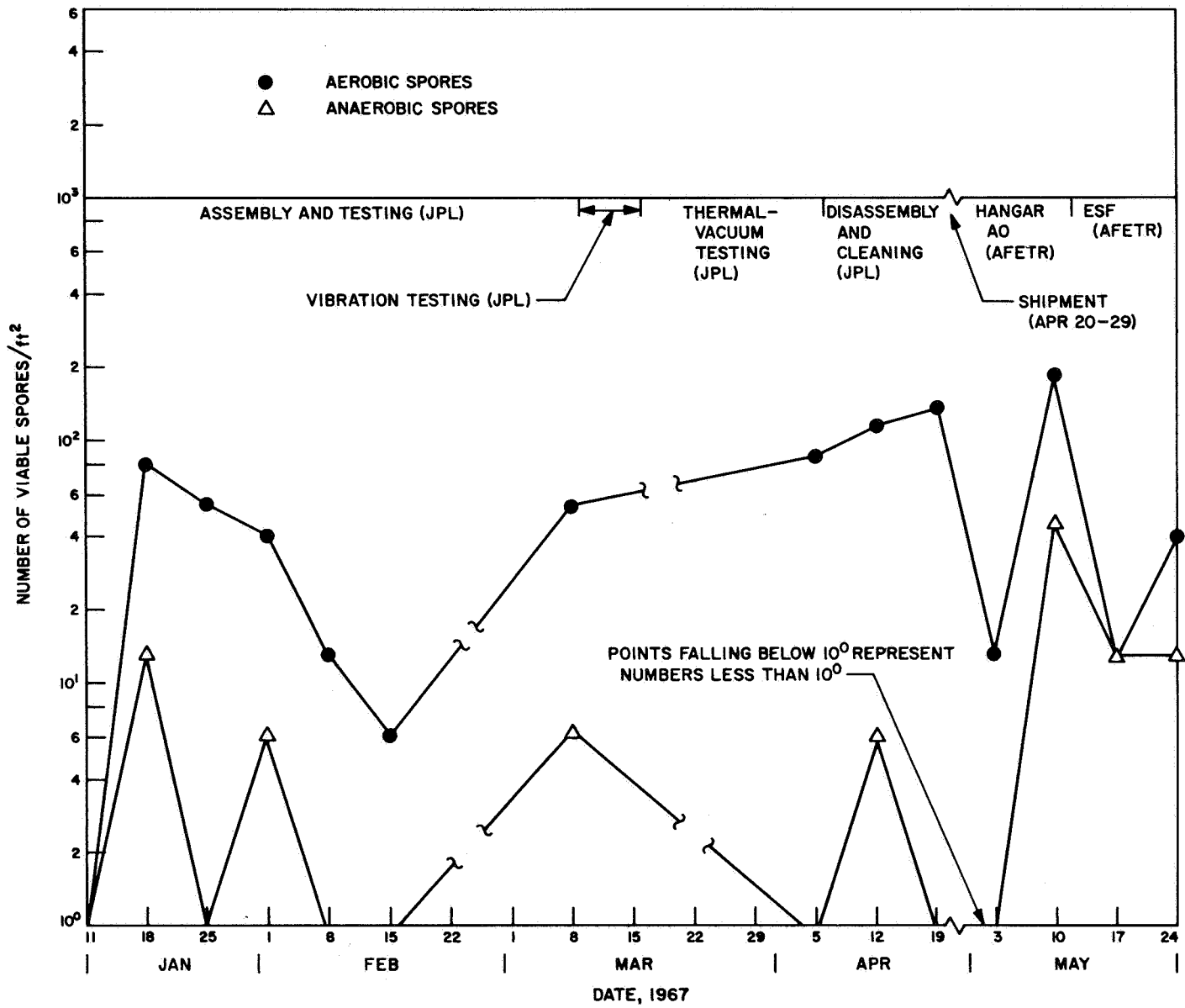


Fig. 11. Average spore burden estimates (swab-rinse technique)

Table 2. Environmental fallout: mean number of aerobic spores accumulated during various spacecraft exposure periods

Environment	Operation	Period, 1967	Mean number of aerobic spores accumulated
SAF high bay (JPL)	Assembly	Jan 15–Feb 4	520
SAF high bay and clean room (JPL)	Assembly and testing	Feb 4–Feb 16	620
		Feb 16–Feb 29	1700
Clean room (JPL)	Testing	Feb 29–Mar 9	517
Environmental laboratory (JPL)	Vibration testing	Mar 9–Mar 16	360
10-ft space simulator (JPL)	Thermal-vacuum testing, Phase I	Mar 16–Mar 25	240
	Thermal-vacuum testing, Phase II	Mar 25–Apr 6	(in chamber)
Clean room (JPL)	Disassembly and cleaning	Apr 6–Apr 20	720
Within shipping canister	Shipment	Apr 20–Apr 29	(shipment)
Hangar AO (AFETR)	—	Apr 29–May 12	1250
ESF (AFETR)	—	May 12–May 28	1990

Assuming 645 ft² of exposed surface area on the M67-2 spacecraft and an equal distribution of microorganisms on all exposed surfaces, the estimate of 400 aerobic spores/ft² represents a total burden of 2.6×10^5 aerobic spores on spacecraft surfaces. This compares to a total aerobic spore burden of approximately 6×10^3 if the data from the swab-rinse method are used. These estimates are based on averages of the data and assume an equal distribution of organisms on the spacecraft. (Distribution functions will be determined and reported with the conclusion of the data analysis.) The level of anaerobic spores has not been included in this estimate, since a high percentage of the anaerobic organisms is facultative and would be included in the aerobic count. Thus, the two are not cumulative. The anaerobic spore counts, although lower, do show the same trends.

Computer analyses (using analysis of means by variance) of all data are presently being conducted to:

- (1) Submit the data to analysis for a comparison of microbial distribution, i.e., horizontal versus vertical accumulation, and top rings versus support ring versus electronic bays, etc.
- (2) Compare levels of accumulation at various working areas with levels of personnel activity and types of work being accomplished.

The information provided by the above operation will enable a revised estimate of the burden on the spacecraft. In addition, the analyses will provide a basis for the selection of sampling areas for the estimation of microbial burden on future spacecraft.

References

1. *Planetary Quarantine Plan, Voyager Project*, Third Revision. Office of Space Science and Applications, National Aeronautics and Space Administration, Washington, June 1, 1967.
2. Bruch, C. W., Koesterer, M. G., and Bruch, M. K., "Dry Heat Sterilization: Its Development and Applications to Components of Exobiological Space Probes," *Dev. Indus. Microbiol.*, Vol. 4, pp. 334–342, 1963.
3. *Standard Procedures for the Microbiological Examination of Space Hardware*, National Aeronautics and Space Administration, Washington, June 1966.
4. Michaelsen, G. S., Ruschmeyer, O. R., and Vesley, D., *The Bacteriology of Clean Rooms*, Final Report, NASA Grant NSG-643. National Aeronautics and Space Administration, Washington.

V. Flight Computers and Sequencers

GUIDANCE AND CONTROL DIVISION

A. JPL STAR Computer, A. Avizienis

1. Design Considerations for a Fault-Tolerant Spacecraft Computer

Theoretical studies of selective redundancy, and specifically of replacement systems, indicate that a significant increase in the availability and in the mean life of a digital system may be attained without the high cost of complete replication and concurrent operation of several copies of a system. The challenge to the designer at the present time is to create computer systems which translate the theory into a working system which uses state-of-the-art components, meets current performance requirements, and attains the theoretically possible gains in reliability.

The choice of a method or a combination of methods of redundancy for a particular computing system is influenced by the intended application. The present section considers the application of protective redundancy to a guidance and control computer for an unmanned interplanetary spacecraft. The computer may also be employed for the onboard processing of scientific data when guidance computation is not in progress. The guid-

ance computer is required to survive space voyages to other planets which range up to several years in duration and to perform approach guidance and control computations at the end of the voyage. Continued control of the spacecraft after arrival, processing of scientific data collected, control of the landing and operation of a capsule, and guidance for a return voyage may also be required. Course corrections are to be computed one or more times during the mission; considerable time is available for this task. The computing at launch and in early stages of the mission may be performed or supported by computers on the ground and in the launch vehicle. The very long communication distances and possible occultation of the spacecraft make earth-based support ineffective at the destination planet. The computations which are required at a remote destination present the most demanding problem to the spacecraft guidance and control computer.

The design of a spacecraft computer must be performed within the strict constraints of the available power, weight, and volume. The existence of these constraints indicates an advantage for selective redundancy, which does not necessarily require power for the spare replicas and which offers protection with the minimum of one spare for each

operating element. An evaluation of relative advantages of the massive and selective redundancy approaches has led to the choice of selective redundancy for fault-tolerance in a spacecraft guidance computer which is being developed at the Jet Propulsion Laboratory. It will be called the JPL "Self-Testing and Repairing" (abbreviated JPL STAR) computer in this report. Performance requirements demand a certain computing capacity at the end of a long voyage, and there are no requirements for a higher computing capacity at an earlier time during the mission. Under these conditions, a fixed-configuration replacement system possessing the required capacity is preferred over a reorganizable or degradable system which has a minimal configuration of the same capacity. The replacement system is a simpler solution, since it avoids the programs, switches, and control hardware which perform the reconfiguration and resulting rescheduling of operation.

A replacement system provides to the user one standard configuration of functional subsystems which has the required computing capacity. The standard computer is supplemented by one or more spares of each subsystem. The spares are held in a standby condition and serve as replacements of operating units when permanent faults are discovered. The presence of spares imposes additional requirements on the selectively redundant system. In addition to the ordinary functions of a computer, the system must incorporate some means of fault detection, a recovery procedure for the case of transient faults, a replacement procedure and a switch for the case of permanent faults, and a checkout procedure for all spares before the mission. The standard configuration itself must be designed as an array of self-contained functional subsystems with clearly defined interfaces for replacement switching. The hardware or software which controls the recovery and/or replacement must be fault-tolerant as well.

Early in the design fundamental choices must be made between hardware and software implementations of the fault detection and recovery procedures. The current generation of aerospace computers almost exclusively uses software techniques, supplemented by hardware for parity checking of data storage and transfer. The continuing decrease in the size and in power requirements of integrated electronic circuits, as well as the vulnerability of software techniques in the case of memory failures, led to the choice of a complete hardware implementation of fault detection and recovery in the JPL STAR computer. The experimental breadboard Model I JPL STAR system is expected to provide valuable operational experience about such an extensive use of hard-

ware techniques in a replacement system. An actual hardware design rather than simulation was chosen in order to explore the circuit aspects of switching, fault detection, isolation of faulty subsystems, and recovery from externally induced transient faults.

Fault detection in digital circuits is implemented either by periodic or by concurrent diagnosis. The currently most common approach is periodic diagnosis which utilizes a diagnostic program stored in the memory. Computation is periodically interrupted, and the diagnostic program is executed. Detection of a fault initiates the replacement procedure; the program is rolled back to a point preceding the previous (successful) diagnosis period. Errors in computation which have been caused by transient malfunctions remain undetected in this approach. The diagnosis program itself is vulnerable to faults in the memory system. The cost of diagnosis consists of: storage used for the diagnostic program, the time consumed by its execution, and the time needed for repair and repeated execution of the program segment which was run after the last diagnosis. Such time costs are very severe in reentry and landing programs for guidance and control which require real-time computing.

The alternate diagnosis method is concurrent diagnosis in which error-detecting codes and monitoring circuits are employed to show the presence of faults. The execution of every instruction is checked immediately; instead of the stored diagnostic program, the cost is in hardware and consists of the logic circuits which perform the code-checking algorithm and the other monitoring circuits. Errors due to transient faults are detectable, and the immediate detection of a fault permits a relatively short rollback of the program. For these reasons concurrent diagnosis has been chosen for fault detection in the JPL STAR computer. The simplest and most costly error-detecting code (100% redundancy) is the complete duplication of program and data words. Errors are indicated by the disagreement of two words; further diagnosis is needed to pinpoint the faulty source. Parity and other more complex codes which detect errors in the transmission of digital data have a lower redundancy, but are not suitable for the checking of arithmetic operations. In order to apply a uniform code in the entire system, arithmetical error-detecting codes were selected as a means of concurrent diagnosis for the JPL STAR system. An extensive theoretical investigation of the effectiveness, cost, and applicability of arithmetic codes was conducted prior to the system design of the JPL STAR computer (Refs. 1, 2). The results showed the existence of a class of low-cost codes with sufficient effectiveness of error detection for concurrent diagnosis. The code-checking circuits

are supplemented by monitoring circuits which verify the synchronization of operation for the various subsystems. Other circuits compare duplicated critical functions of the subsystems and measure important circuit parameters (e.g., *read* and *write* currents in memory units). The monitoring circuits are included in order to detect the faults which are not always indicated by the code-checking algorithm.

Recovery and replacement procedures require both software and hardware contributions. Consistently with the choice of hardware for fault detection, the JPL STAR computer employs hardware implementation to the furthest possible degree in these procedures as well. The most fundamental hardware consideration in a replacement system is the method of switching and the nature of the switch which implements the replacement operation. The reliability of the switch is a limiting factor in the estimates of reliability for the entire system. Furthermore, the switch must provide complete isolation in the case of catastrophic failures occurring in the part of a computer which is to be replaced. The principal alternatives in the choice of a switching method are: (1) information switching and (2) power switching. A study of switching techniques (Ref. 3) has led to the conclusion that the switching of power to replaceable units offers strong isolation against catastrophic failures and minimizes the number of switches requiring extreme reliability. Furthermore, the data-transmission speed within the computer is not affected by the circuit properties of the switch. A magnetic power switch for the JPL STAR computer, which is an integral part of a replaceable unit, has been designed and is being tested at the Stanford Research Institute. The switch is a part of the unit's power supply and is designed to fail asymmetrically—in an open mode.

The use of a power switch requires that all unpowered copies of a replaceable unit should be permanently attached to the data transmission busses of the system. As a consequence, an unpowered unit is required to produce only logic signals of value *zero* on all of its output lines. Furthermore, all input and output lines of every replaceable unit must be isolated from the busses in order to prevent shorting of a bus by a short inside the unit. Methods of bus isolation for the JPL STAR computer are presently being studied and evaluated.

2. Organization of the JPL STAR Computer, Model I

The preceding section has outlined the principal alternatives which were considered in the choice of fault-tolerance techniques for the JPL STAR computer. An experimental breadboard Model I of the JPL STAR

computer has been designed and is presently being constructed. The main objectives of the Mod I STAR computer are to gain experience with the hardware aspects of a replacement system and to conduct experiments with fault detection and recovery procedures. The performance specifications of the Mod I STAR computer are similar to those of many present-generation aerospace computers; they have not been matched to any specific application. The fundamental choices in fault-tolerance techniques are as follows:

- (1) All machine words (data and instructions) are encoded in an error-detecting code.
- (2) The computer is subdivided into several replaceable functional units.
- (3) Fault detection, recovery, and replacement are carried out by special-purpose hardware; software techniques may be added later to provide additional fault-tolerance features.
- (4) Replacement is implemented by power switching: units are removed by turning power off and connected by turning power on.
- (5) The information lines of all units are permanently connected to the busses through isolating circuits; unpowered units produce only logic *zero* outputs.
- (6) The error-detecting code is supplemented by monitoring circuits which serve to verify the proper synchronization and internal operation of the functional units.

The Model I employs a 32-bit word length for its operands and instructions. Machine words are transmitted between the functional units in four-bit bytes, that is, in a series-parallel mode. The functional units contain their own sequence generators and possess identical input and output connections. A typical functional unit is shown in Fig. 1. The *information input* and *information output* lines are connected to information busses. They receive and send coded machine words, one byte at a time. The *switch control* line supplies the change position command to the power switch, while the present switch position is shown by the *switch status* line. The other control input lines supply a *clock* pulse train input, a synchronization test signal (*synch*), and a *reset* signal which places the functional unit into a standard state. There are also three more status output lines. The *active* signal indicates that at least one information output line has an active (logic *one*) output. The *complete* signal occurs at the end of every sub-algorithm being performed by the unit. The *internal fault* signal occurs when the internal monitoring circuits of the

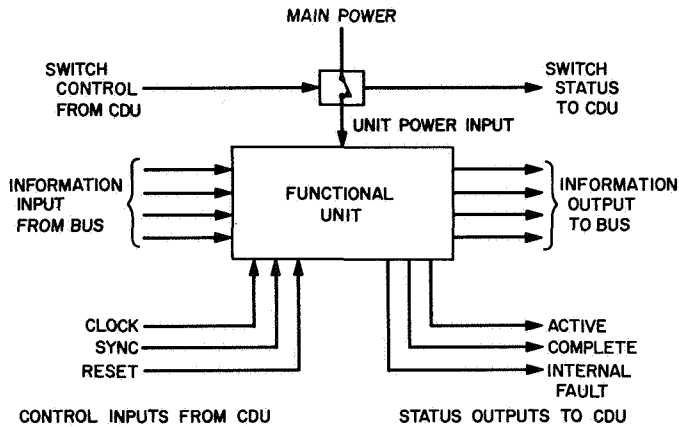


Fig. 1. Typical JPL STAR computer functional unit

unit detect an abnormal condition. All status outputs are connected to the control and diagnosis unit (CDU). The CDU also generates the four control input signals. The CDU initiates all recovery and replacement actions on the basis of the status signals received from the powered functional units in the system.

The block diagram of the JPL STAR Model I computer is shown in Fig. 2. It is a fixed-point, binary computer suitable for spacecraft guidance applications. Information words are transmitted on two busses in bytes of four bits each. The choice of the byte mode reduces the size of busses and simplifies the checkers, which are diagnostic hardware for error detection in the transmitted information words. An expansion to parallel operation is straightforward and will increase the computing speed at the cost of larger busses and more complex checkers. The replaceable functional units of Model I are:

- (1) Main arithmetic processor (MAP).
- (2) Control arithmetic processor (CAP).
- (3) 16K read-only memory unit (ROM).
- (4) Up to 12 read-write memory units, 4K each (RWM).
- (5) Input/output (buffer) unit (IOU).
- (6) Logic processor (LOP).
- (7) Interrupt unit (IRU).
- (8) System clock unit (SCU).
- (9) Two bus checkers (CH1, CH2).
- (10) Control and diagnosis unit (CDU).

All information words in the JPL STAR computer are encoded in an error-detecting code. In the case of

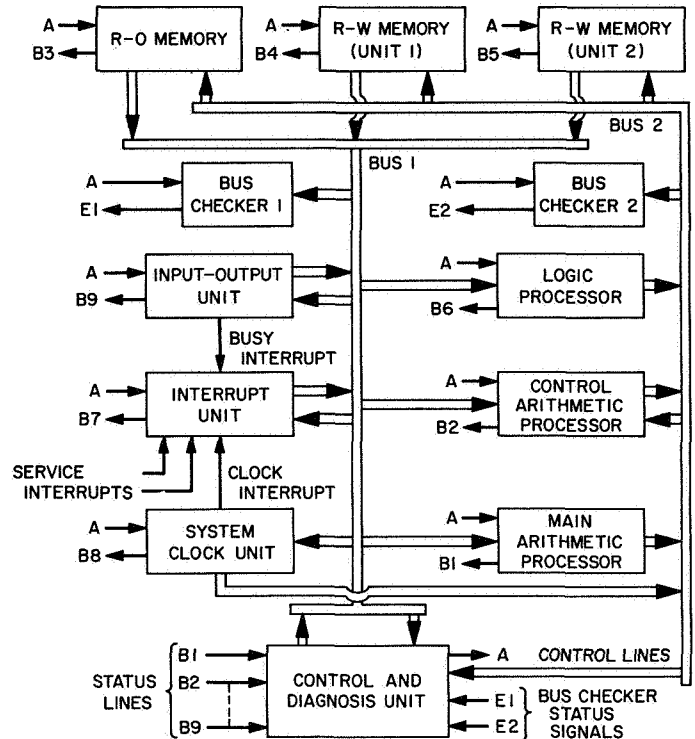


Fig. 2. JPL STAR Model I computer block diagram

numerical data words and addresses of instructions the code must be preserved during arithmetic operations. The two principal methods of arithmetic encoding are product (or An) and residue codes (Refs. 1, 2, 4, 5). In order to gain a better understanding of the relative virtues of these two methods, both are employed in the Model I: (1) product coding for numeric operands, and (2) residue coding for addresses. Figure 3 shows the formats of numeric operands and instructions.

The numeric operands (Fig. 3a) are 32-bits-long binary product-coded numbers with the check factor 15. Binary numeric operands x (28 bits long) are multiplied by 15 to obtain the product coded 32-bit operands $15x$. The check factor 15 has been found to be especially effective in the case of series-parallel transmission and computing in bytes of 4 bits length (Ref. 2).

The checking algorithm computes the modulo 15 residue of coded words which are transmitted on the busses. A *zero* residue (represented by 1111) indicates a coded word; all other values indicate a fault in the functional unit which delivered the word to the bus.

The 32-bit instruction words (Fig. 3b) consist of a 12-bit operation code and 20-bit address part. The address part is encoded in the residue code with the check

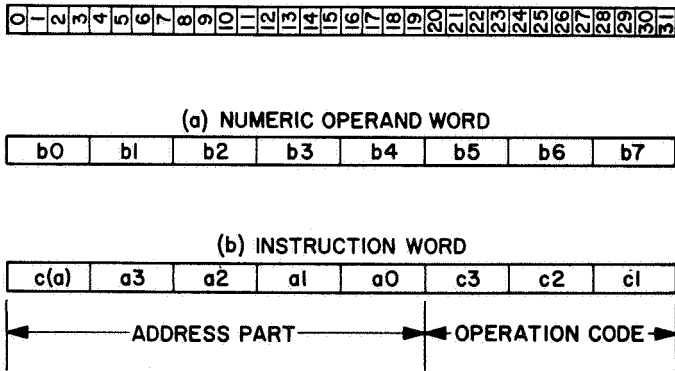


Fig. 3. JPL STAR Model I computer word formats

modulus 15. An address part consists of a 16-bit binary address a and a 4-bit check symbol $c(a)$. The check symbol $c(a)$ has the value

$$c(a) = 15 - |a|_{15}$$

where $|a|_{15}$ is the modulo 15 residue of a . The checking algorithm computes the modulo 15 residue of an address and adds it (modulo 15) to the check symbol $c(a)$. A zero sum (represented by 1 1 1 1) indicates a properly coded address part. The residue code is preferable for address parts over the product code because it is separable, and the address a is available to the memory address decoding circuits in its ordinary binary form. It is important to note that the *one's complement* $15 - |a|_{15}$ rather than the residue $|a|_{15}$ itself is used as the check symbol $c(a)$. In this case the fault-detection effectiveness in byte-serial operation remains the same as for product-coded operands, while the use of $|a|_{15}$ as a check symbol gives a lower effectiveness. Furthermore, the bus-checking algorithm is the same for product-coded operands and for address parts—it is simply a modulo 15 summation of all bytes and a test of the result for the zero value represented by 1 1 1 1.

The *operation code* is divided into three bytes of four bits each. The operation code bytes are protected by a 2-out-of-4 encoding, which leaves six valid words in a four-bit byte. Such coding is most efficient for short words and is acceptable in a computer, because operation codes are not subjected to arithmetic operations. It is evident that their validity must be tested by a separate checking circuit, since it cannot be verified by the modulo 15 checker (which is bypassed by the operation codes). The

separation of the operation code into three separately encoded bytes facilitates the decoding and validity testing of operation codes received by the functional units. The 2-out-of-4 encoding gives a total of 216 distinct combinations for operation codes. The indication of index registers which are to be used must be contained within the operation code. Since the Model I contains two index registers, every indexable operation code requires three distinct combinations, while nonindexable operations require only one each.

It is apparent that residue encoding with the check modulo 15 can be applied to the numeric operands and to the operation codes as well as to the address parts. Such use of a uniform residue code has the advantages of code separability and of identical check algorithms. In the case of operation codes, a modulo 15 residue-coded 12-bit number provides 256 distinct combinations. On the other hand, the 2-out-of-4 coding for individual bytes of the operation code permits validation and use of individual bytes. The choice of three different methods of encoding in the Model I was motivated by the need to gain detailed insight into their relative merits and shortcomings.

One instruction cycle is executed by the Model I JPL STAR system in three steps. In the first step, the address of the instruction is sent from the sequence register in the central arithmetic processor to the memory units; the transmission of the address is tested by the bus checker. In the second step, the addressed memory unit broadcasts the operation code and address to all functional units. The appropriate units recognize the code, accept the address, and initiate execution. In the third step (if needed) the instruction is executed, and a result is placed on the bus and accepted by the destination unit. The bus checkers test every word on the busses for proper encoding.

At the present time the detailed system design of the Model I JPL STAR computer is approaching completion, and logic design of the CAP, CDU, and ROM is in progress. The MAP has been constructed and is undergoing extensive testing for design verification. A description of the MAP has already been presented in SPS 37-37, Vol. IV, pp. 76-80. The magnetic replacement switch for power switching has been designed and is being tested. Detailed descriptions of the functional units will be presented in following issues of the SPS.

References

1. Avizienis, A., *A Set of Algorithms for a Diagnosable Arithmetic Unit*, Technical Report 32-546, Jet Propulsion Laboratory, Pasadena, California, March 1, 1964.
2. Avizienis, A., *A Study of the Effectiveness of Fault-Detecting Codes for Binary Arithmetic*, Technical Report 32-711, Jet Propulsion Laboratory, Pasadena, California, September 1, 1965.
3. Van de Riet, E. K., Bennion, D. R., and Yarborough, J. M., *Feasibility Study for a Reliable Magnetic Connection Switch*, Final Report—Phase I, Contract 951232 under NAS 7-100, Stanford Research Institute, Menlo Park, California, February 1966.
4. Brown, D. T., "Error Detecting and Correcting Codes for Arithmetic Operations," *IRE Trans.*, Vol. EC-9, pp. 333-337, 1960.
5. Garner, H. L., "Error Codes for Arithmetic Operations," *IEEE Trans.*, Vol. EC-15, pp. 763-770, 1966.

VI. Spacecraft Power

GUIDANCE AND CONTROL DIVISION

A. Low-Saturation-Drop Silicon Transistor, R. A. Booth

1. Introduction

A development effort currently in progress is to produce a silicon switching transistor with a maximum saturation voltage of 0.1 at 75 A collector current with an ultimate design goal of 0.07 V. The total switching time is to be less than 6 μ s (see Table 1 for transistor requirements). Possible approaches for the reduction of saturation drop for the current effort are: physical etch, ion implantation, fast dopants, and extremely thin silicon wafers.

The purpose of this development is to enable the development of power conversion circuits that operate efficiently and reliably from low voltage sources (1 to 3 V), such as a thermionic generator. The silicon transistors resulting from this effort will be used as the switching element in these converter circuits. The use of such transistors provides an almost two-to-one increase in the operating temperature margin over that which can be achieved with germanium transistors formerly used.

2. Present Status

Three different types of silicon transistors have been developed by two different contractors. ITT Semiconductors Div. has developed a 100-A, multichip, low-saturation-drop device using an epitaxial process (Fig. 1). Westinghouse Electric Corp. has developed two different types of transistors; one is made using an epitaxial process, and the other is made using a modified single diffused process (Fig. 2). Both types use a single large-area chip.

Table 1. High-power, low-saturation voltage silicon-switching transistor requirements

Absolute maximum ratings				
Collector to emitter voltage, BV_{CEO}		20 V (min.)		
Emitter to base voltage, BV_{EBO}		4 V (min.)		
Collector current, I_C		100 A (min.)		
Base current, I_B		15 A (min.)		
Collector dissipation, $T_C = 100^\circ\text{C}$, P_C		150 W (min.)		
Thermal resistance, junction to case, θ_{JC}		0.5 $^\circ\text{C}/\text{W}$ (max.)		
Junction temperature range, T_J		-65 to +200 $^\circ\text{C}$		
Electrical characteristics (100 $^\circ\text{C}$ case temperature)				
Characteristics	Test conditions	Min.	Max.	Units
Breakdown voltage, BV_{CEO}	I_C^a	20		V
Breakdown voltage, BV_{EBO}	I_{EB}^a	4		V
Collector cutoff current, I_{CEX}	$V_{CE} = 20\text{ V}$ V_{BE}^a		10	mA
Emitter cutoff current, I_{EBO}	$V_{EB} = 4\text{ V}$		10	mA
DC current gain, h_{FE}	$I_C = 75\text{ A}$ $V_{CE} = 1\text{ V}$	20		
Saturation voltage, $V_{CE, sat}$	$I_C = 75\text{ A}$ $I_B = 5\text{ A}$		0.1	V
Saturation voltage, $V_{BE, sat}$	$I_C = 75\text{ A}$ $I_B = 5\text{ A}$		1.4	V
Total switching time (including delay, rise, storage and fall time)	$I_C = 75\text{ A}$ $I_B = 5\text{ A}$ $V_{BE} = 1.5\text{ V}$ on turnoff		6	μ s
<small>^aManufacturer's standard specifying procedure acceptable.</small>				

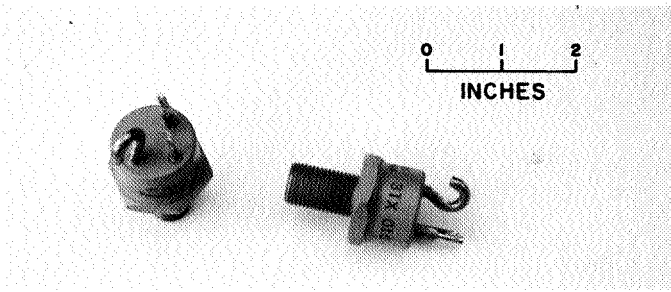


Fig. 1. An ITT Semiconductors Div. transistor

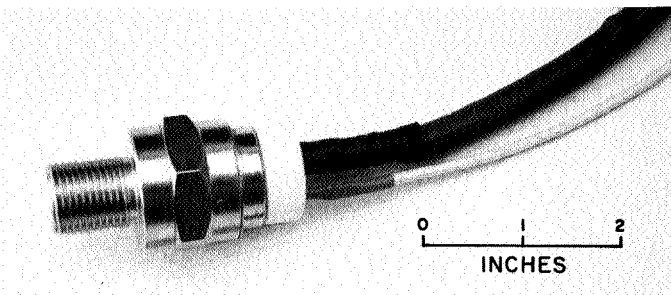


Fig. 2. A Westinghouse Electric Corp. transistor

At present, the testing of both the ITT and Westinghouse transistors is in process; the results so far are fairly satisfactory (see Tables 2 and 3 for performance data). In addition, a preliminary circuit design based on the measured transistor characteristics has been performed. The calculated efficiency is 85% for 200 W output from a 2.5-V source.

3. Future Activities

During the next 8 mo, Westinghouse Electric Corp. will pursue two approaches:

- (1) Development of an electrically symmetrical transistor.
- (2) Development of a device utilizing an ultra-thin silicon crystal.

Following the development, ten engineering samples will be submitted to JPL for evaluation. After approval, 15 devices will be manufactured, based on the better approach.

Table 2. Electrical characteristics of ITT Semiconductors Div. high-power, low-saturation voltage silicon-switching transistors

Transistor device SN	BV_{CEO} , V ($I_C = 10$ mA)	BV_{EBO} , V ($I_{BB} = 10$ mA)	BV_{CES} , V ($I_C = 10$ mA)	$VCE_{(sat)}$, V ($I_C = 75$ A $I_B = 5$ A)	$VBE_{(sat)}$, V ($I_C = 75$ A $I_B = 5$ A)	h_{FB} ($I_C = 75$ A $V_{CE} = 1$ V)
2	21	6.5	21	0.151	0.935	101
3	23	7.5	20	0.175	0.94	97
4	20.5	5.5	18	0.19	0.97	89
9	19.5	22.5	18.5	0.175	1.00	100
10	23	39	21	0.21	1.00	93
14	20.5	16	18	0.19	0.97	91
15	23.5	8	19	0.15	0.91	100
17	23.5	3	21	0.17	0.91	104
18	15.5	36	15	0.19	0.95	115
20	21.5	14	21	0.15	0.95	72
21	20.5	55	20	0.145	0.93	82
22	20.5	55	20.2	0.16	0.99	78
23	20	14	20	0.17	0.955	82
24	21.5	11.5	17.5	0.175	0.955	89
25	28.5	35	28.5	0.18	0.90	64
26	29.5	5.5	20.5	0.17	0.905	52.5
27	27.5	30	21.5	0.175	0.91	57.7
28	31	6	22	0.19	0.90	29.3
29	22	54	20.5	0.19	0.93	54.4
30	24	10.5	20	0.168	0.90	74.5

Table 3. Electrical characteristics (partial listing) of Westinghouse high-power, low-saturation voltage silicon-switching transistors

Transistor SN	I_{CB} , mA	h_{FE} ($I_C = 75$ A, $V_{CB} = 1$ V)	$V_{CE(sat)}$, V ($I_C = 75$ A, $I_B = 5$ A)	Switching time, μ s	
				($I_C = 75$ A, $I_B = 5$ A, $V_{CO} = 15$ V, $V_{BE} = 1.5$ V)	($I_C = 50$ A, $I_B = 5$ A, $V_{CO} = 12$ V, $V_{BE} = 1.5$ V)
Modified single diffusion					
JS-72-2	10	13	—	—	14
JS-65-4	1.5	12.5	—	7.0	11.0
JS-79-7	1	25	0.15	12.5	11.7
JS-79-6	1	20	0.20	9.0	8.9
JS-68-7	0.01	9	—	—	14
JS-72-4	4	19	0.2	14.9	14.5
JS-75-3	0.2	25	0.15	14	12.5
JS-81-5	0.8	21	0.2	10.7	8.6
JS-65-3	0.02	12	—	—	9.2
JS-76-2	0.5	11	—	—	8.0
JS-66-4	7.5	10	—	—	9.4
JS-72-4-1	0.2	15	0.2	8.3	12.3
JS-72-1	5	22	0.22	13.9	12.6
JS-75-2	0.05	13	—	9.0	7.5
JS-76-3	0.1	14	—	10.8	11.5
JS-72-2-1	0.8	21	0.2	—	13.8
JS-64-1	0.4	12	—	—	6.4
JS-72-3-1	3.5	13	—	12.5	10.4
JS-65-1	0.01	13	—	11.8	10.0
JS-68-2	0.01	7	—	—	11.0
Epitaxial base					
JE-33-E	8	22	0.2	16.2	15.3
JE-13-6-E	80	27	0.22	6.2	5.2
JE-2-E	1.5	22	0.18	14.4	13.1
JE-30-1	5	62	0.15	17.4	15.5
JE-110-1-E	0.01	7	—	9.7	7.4

**B. RCA Silicon-Germanium Air-Vac Technology,
L. Selwitz**

Three thermoelectric devices utilizing RCA Air-Vac couple technology have been tested at JPL: two identical four-module test units procured from RCA as complete assemblies, and one cylindrical module fabricated in-house from couples procured from RCA.

1. Four-Module Test Units

a. Description. The two test generators procured from RCA are identical in all design respects. The second unit is currently in operation as a replacement for the first

unit, which was thermally damaged due to a testing systems failure. Each test unit consists of four six-couple modules arranged in two pairs, upper and lower, sandwiched on opposite sides of planar, graphite ribbon heaters (Figs. 3 and 4). Cooling of the test unit is accomplished by means of a water-cooling-coil heat exchanger secured to the wings of the power module base plates.

Each thermoelectric power module includes a completely bonded assembly of six N-type and six P-type silicon germanium alloy thermoelectric elements, silicon-molybdenum alloy hot shoes, and stress-compensating stacks on the element cold ends (Fig. 5). The N-type alloy is phosphorous-doped and the P-type alloy is boron-

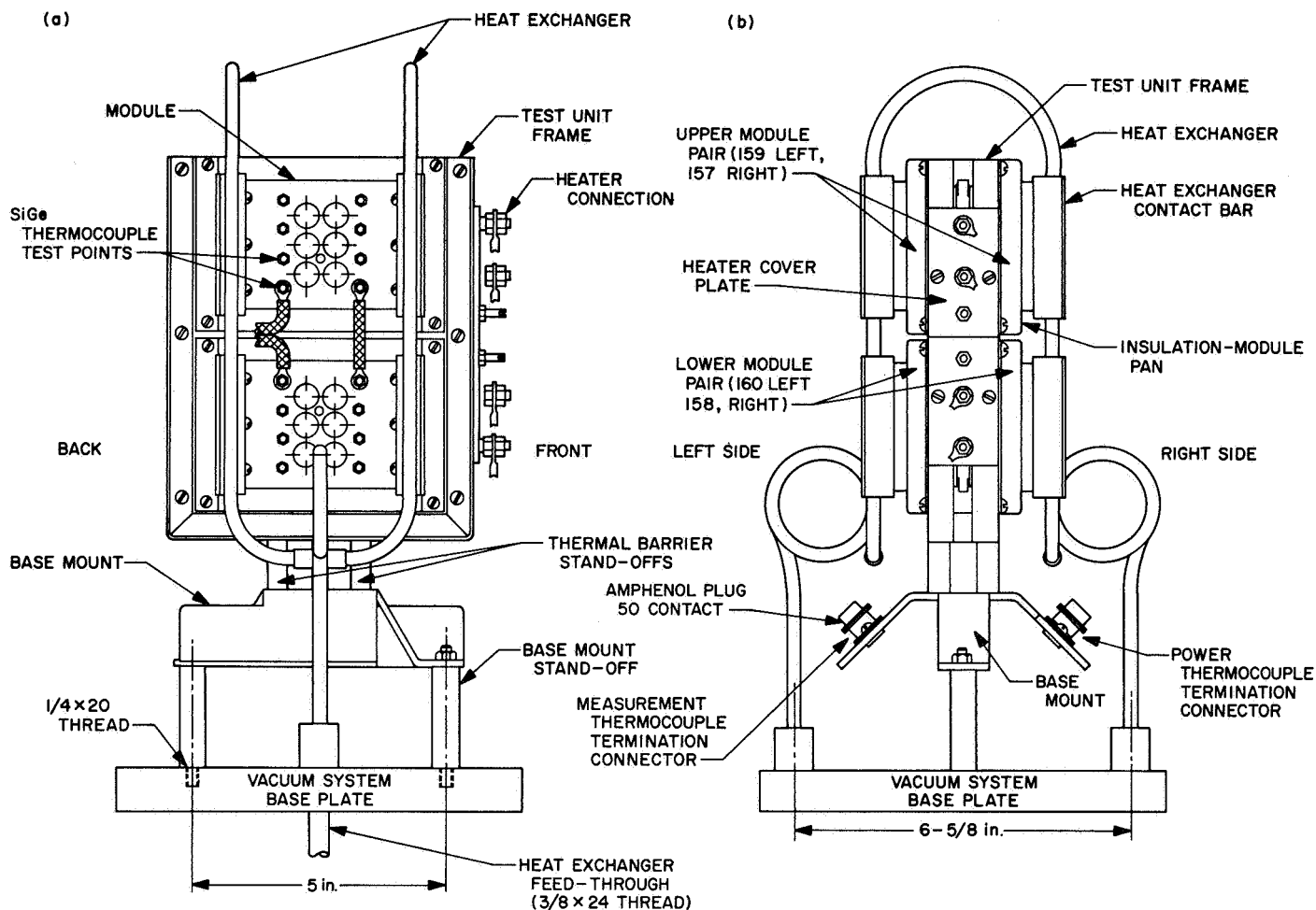


Fig. 3. Test unit assembly (a) left side view (b) front view

doped. A table of the physical characteristics of the module follows:

Thermoelectric couple weight	8.3 g
Total module weight (including couples, thermal stress compensators, electrical straps, test terminals, insulations, and radiator base plate)	226 g
Overall heat-accepting surface dimensions	1 $\frac{1}{8}$ × 1 $\frac{1}{8}$ in.
Emissivity of heat-accepting surface	Approx. 0.8
Total base-plate dimensions	5 $\frac{1}{2}$ × 2 $\frac{1}{2}$ in.
Module thickness	Approx. 1 in.

The thermoelectric couples, thermal stress-compensating pedestal, electrical connectors, ceramic insulators, and tungsten compensators are braze bonded to a copper base plate which also serves as the cold junction radiator. Eight test points, extending through the base plate and capped with screw terminals, provide individual couple readings of power output. Each module was initially supplied with three thermocouples, one each on the hot junction, cold junction, and radiator. Twenty-eight gauge chromel-alumel thermocouples were used on the cold side, one permanently attached to the electrical connecting strap near the cold junction of couple 2, and one fastened under the radiator-to-module pan-mounting screw adjacent to the same thermoelectric couple.

The planar heater used with each module pair is made of two strips of 0.5-in. wide-woven graphite ribbon supported tautly in a tantalum and ceramic frame (Fig. 6).

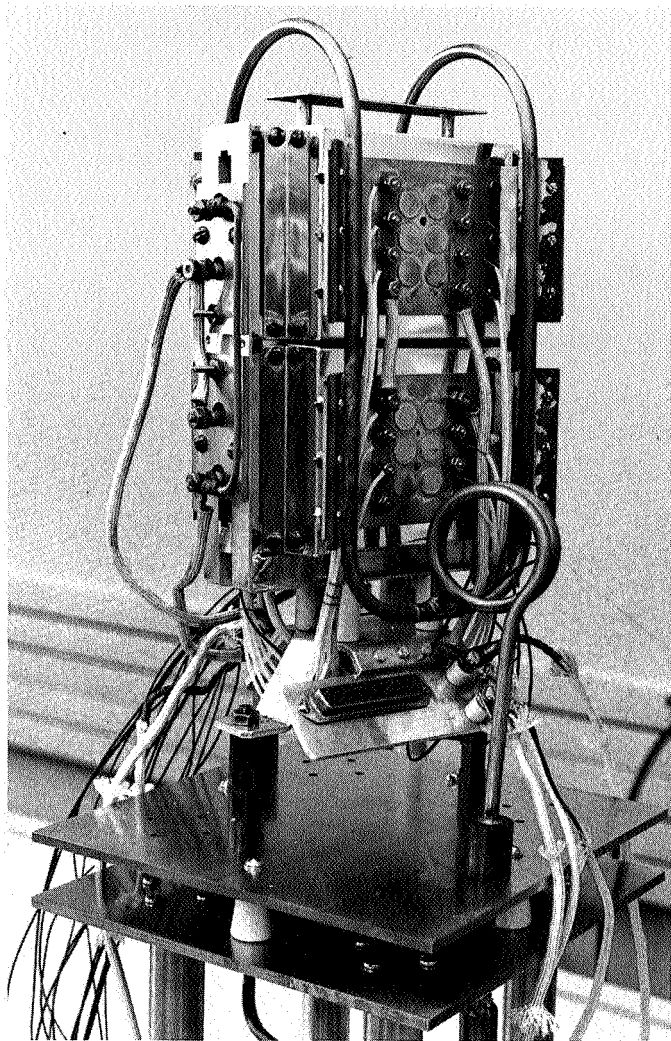


Fig. 4. Four-module test device

The nominal design input requirements of each heater are 200 to 300 W and 15 amp. Nominal extended design life of the heater is for temperatures of 1250°C or less in an atmospheric pressure of 10^{-5} torr, or less.

b. Testing, device 1. Prior to delivery, test device 1 was operated for over 300 h with six thermal cycles. A summary of the performance is presented in Table 4. Testing at JPL proved that the measured initial cold resistance of the device, 342 mΩ, was consistent with the final cold resistance reading of the device prior to delivery from RCA.

The test system used in the operation of the device included the following major components:

- (1) NRC model 3371 4-in. diffusion pumping system.

- (2) West Guardsman SCR digital set-point temperature controller.
- (3) Model 7200 Cimron digital voltmeter with plug-in ohms and ac converters.
- (4) Kiethley model 503 milliohmmeter.
- (5) Sorenson model 2000S ac voltage regulator.
- (6) Esterline Angus model E6704 24-point strip chart recorder.

The test unit was placed in an 18 × 30-in. bell jar and kept at room temperature until a vacuum of 1×10^{-5} torr was reached. Power to the heaters was increased at a low rate to minimize outgassing, the chamber never being allowed to be subjected to a pressure above 1×10^{-4} torr. A maximum heating rate of 200°C (hot junction) per hour was established for the unit.

Data were taken at random intervals during full temperature operation, and at all times where shut-down or start-up operations were required. The test unit circuitry had a safety interlock system to provide heater cut-off in the event of potential thermal hazards. This system consisted of a Shur-Flo pressure transducer that provided protection against cooling water loss or drop-off, and a limit switch programmed into the temperature recorder to provide protection against excessive hot-junction temperatures. Both safety interlock switches were connected to the circuit breaker of the electric heater circuit (Fig. 7). The control console and vacuum test station are shown in Fig. 8.

It should be noted here that the four-module test device was not optimized for efficiency; the unit was a feasibility evaluation model only, and the hot-side thermal losses from the radiant graphite tape heaters were unique to this specific piece of hardware. The test was originally intended to be at constant-temperature operation, using automatic control equipment for assured temperature stability. However, the low thermal masses of the graphite tape heater and the water-cooled Air-Vac couples caused an unstable condition of rapid, continuous thermal cycles. Rather than risk damage to the heater or couples, the controller was switched to manual operation, and power to the heaters added by means of a variable transformer.

c. Test results, device 1. In the face of numerous testing problems, the four-module Air-Vac test device showed remarkable consistency over its 4000-h life in the areas of hot internal resistance, power output, efficiency, and

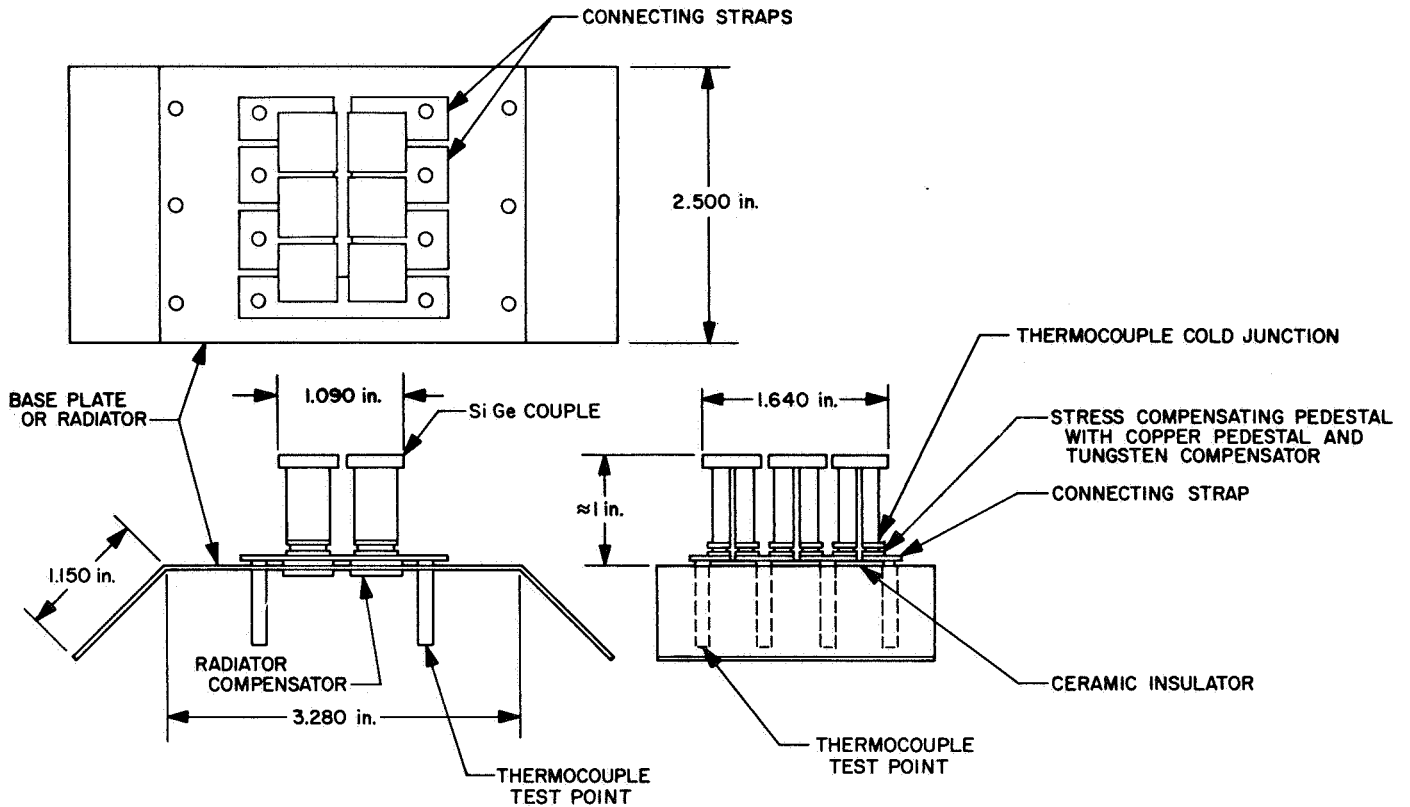


Fig. 5. Modified six-couple thermoelectric power module structure

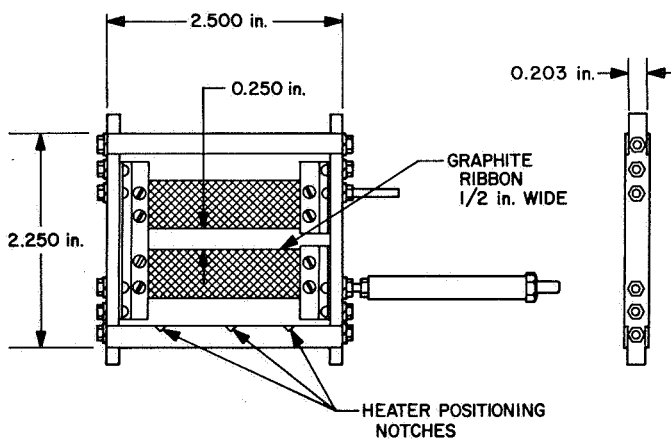


Fig. 6. Graphite ribbon heater

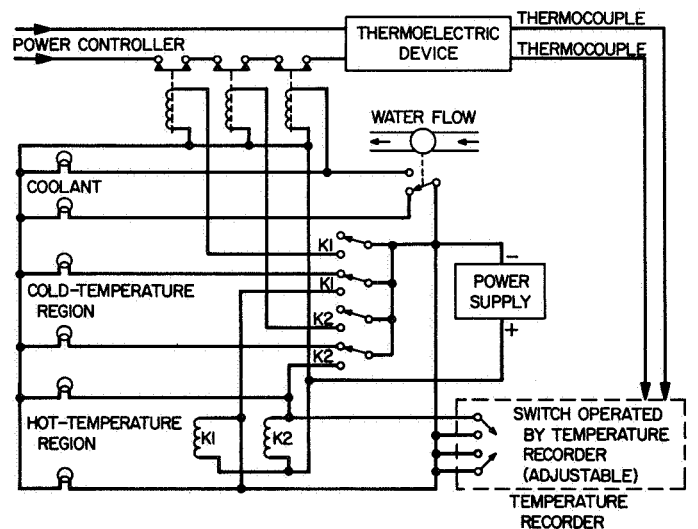


Fig. 7. Simplified schematic of interlocking safety circuit

open-circuit voltage (Table 4). The problems that occurred during the testing operation were as follows:

- (1) The original four chromel-alumel hot-junction thermocouples deteriorated between 20 and 300 h of operation, thus leaving the unit with no hot-temperature instrumentation.

- (2) Laboratory water and electricity outages resulted in eight thermal shocks (cycles from 900°C to ambient temperature in less than 5 min).
- (3) Graphite heater problems resulted in four thermal shocks.

Table 4. Performance testing summary, test device 1

	Accumulated hours ^a									
	416	574	646	846	1110	1805	1993 ^b	2384	2935	3295
	Average temperature, °C									
T_H	885	837	890	890	°	°	920	918	920	923
T_C	161	153	172	168	160	172	140	155	155	145
ΔT	724	684	718	722	°	°	780	763	765	785
Output power										
E_L , V	3.92	3.73	4.08	4.29	3.71	4.09	3.96	3.95	4.02	3.93
E_{OC} , V	7.84	7.40	8.18	8.58	7.42	8.20	7.90	8.10	8.14	8.00
R_{in} , m Ω	0.766	0.742	0.752	0.753	0.757	0.766	0.720	0.751	0.741	0.730
R_L , m Ω	0.766	0.755	0.748	0.753	0.757	0.763	0.723	0.715	0.723	0.714
I_L , A	5.12	4.94	5.45	5.69	4.90	5.36	5.47	5.52	5.56	5.58
I_{OC} , A	8.96	8.48	9.28	9.76	8.45	9.20	9.23	9.23	9.34	9.14
P , W	20.08	18.42	22.23	24.41	18.17	22.8	21.66	21.80	22.35	21.88
Input power										
E , V	22.58	20.85	23.5	24.56	20.8	24.2	23.5	23.5	23.8	24.10
I , A	26.3	24.6	26.1	26.4	27.0	25.8	28.5	27.9	27.5	26.4
P , W	593	512.9	613	648.3	567.0	608	669	656	655	636
Efficiency, % (Overall)	3.39	3.59	3.62	3.76	3.23	3.51	3.23	3.32	3.41	3.44
^a In excess of the 330 h of contractor testing. ^b New tungsten-rhenium thermocouples added; one thermocouple removed from circuit. ^c No hot-junction instrumentation.										

Following degradation and failure of the last hot-junction thermocouple, a Micro-Pyrometer¹ was used for hot-junction measurement, the device being focused on the edge of the hot shoes. The pyrometer readings were fairly consistent with the temperatures measured by the chromel-alumel thermocouples before the latter failed.

During the course of pyrometric observation, it was noticed that the graphite heater was gradually expanding over a period of time. Being restrained in rigid frames, the heater ribbons were buckling, and approaching contact with the hot shoes. At 1900 h one of the four ribbons physically contacted a hot shoe, at which point a zone of whiter incandescence was manifested, measuring approximately 1400°C. Shortly thereafter it became noticeable that separation of the buckled heater strip had occurred, electrical continuity of the heater being maintained through the hot shoe of the contacted couple. At 1967 h the heater strip opened completely, and the unit was shut down.

¹Made by Microwerck Corp.

The test device was shipped back to the contractor, where examination revealed that the couple touched by the heater strip suffered a crack in the N-leg adjacent to the hot shoe. The 23 other couples were given individual cold resistance checks, and were found to have the same internal resistances measured at the time of fabrication.

The following modifications were made by the contractor to the test unit:

- (1) The hot shoes were given a fine sand-blast treatment to remove a thin carbon film from the surfaces.
- (2) The failed chromel-alumel thermocouples were replaced with tungsten-tungsten rhenium hot junction thermocouples.
- (3) The separation distance between modules was increased by approximately 30 mils to reduce the chance of the heater ribbons' touching the hot shoes in the event of buckling.
- (4) Two new heaters, upper and lower, were supplied in place of the original heaters.

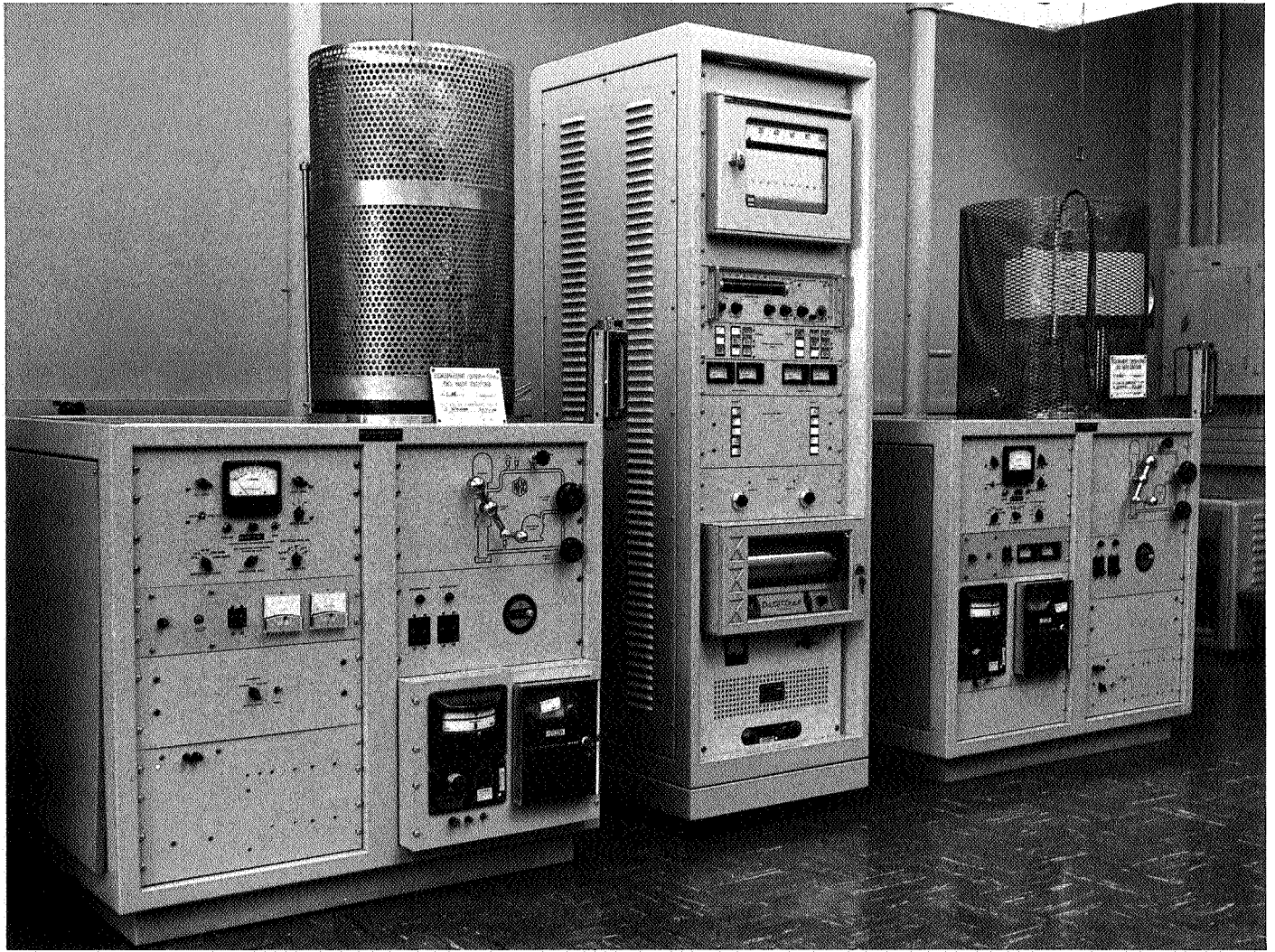


Fig. 8. Test station

The unit was returned to JPL and retested. With all four modules now possessing hot-junction instrumentation, it became possible to obtain an average hot-side temperature. A range of approximately 50°C was noted from the coldest to the hottest hot-junction temperature; with an average hot-junction temperature of 925°C, the hottest module was 950°C.

Testing continued under generally unchanged conditions to approximately 2500 h, when buckling of the graphite heater strips again became evident. By 2900 h buckling had become more pronounced and the heater strip appeared to be almost touching a hot shoe. At 3321 h physical contact between the heater strip and a hot shoe was manifested by an open circuit in the heater.

The unit was removed from test, new heaters were inserted, and the test device was brought up to temperature again. At 3334 h a short circuit in the power supply resulted in excessive heating and thermal damage to the generator. At this time the unit was permanently removed from testing.

d. Concluding remarks. The four-module silicon-germanium Air-Vac test devices exhibited outstanding ruggedness and durability under rather adverse testing conditions. For a period of approximately 4000 h the unit manifested no appreciable degradation under conditions of repeated thermal shocks, 10^{-5} torr vacuum operations, hot-junction temperatures up to 950°C, and continuous vibration transmitted to the test chamber from a roughing pump.

Two potential problem areas associated with silicon germanium Air-Vac test devices that are still in need of more definitive solution appear to be the heaters and hot-junction temperature instrumentation. Although satisfactory performance has been achieved with graphite

tape heaters and with current tungsten-tungsten rhenium thermocouples, their reliability over long (thousands of hours) periods of time does not appear to be equal to that of the thermoelectric module itself.

e. Testing, test device 2. The RCA test device 2 was tested under essentially the same conditions as the previous generator, with the following noteworthy exceptions:

- (1) The unit was delivered with tungsten-tungsten rhenium hot-junction thermocouples.
- (2) Individual thermoelectric couples were instrumented for voltage measurements to verify hot-junction temperature measurements on the basis of their Seebeck coefficients.
- (3) The safety interlock system was improved by replacement of the water-flow pressure transducer with a magnetic field switch around the flowmeter, and a high-temperature limit switch in place of the multipoint recorder with programmed alarm.

The initial cold resistance of the generator was 352 mΩ, which was consistent with the cold resistance of the unit prior to delivery. The initial thermal cycle began after the test chamber pressure had dropped below 2×10^{-5} torr. The data taken during initial start-up are given in Table 5.

The corresponding graphic relationships between power input, hot-junction temperature, and power output, are given in Fig 9. As noted earlier, the four-module test device is not optimized for efficiency; the figures quoted indicate the relative values of efficiency at various hot-junction temperatures. With 725 h of testing time accumulated on test device 2, no change in output has been noted for a constant average hot-junction temperature of 890°C.

Table 5. Test results, device 2

Input power, W	Hot-junction temperature, °C				Cold temperature, °C	Open circuit, V	Load circuit, V	Load current, A	Power output, W
	No. 1	No. 2	No. 3	No. 4					
100.7	260	310	400	450		1.19	0.559	1.3	0.727
138.2	365	405	450	505	96	1.70	0.847	1.8	1.53
230.5	550	475	575	635	103	3.16	1.58	3.0	4.75
257.6	590	510	615	665	114	3.68	1.84	3.4	6.25
339.1	705	615	680	760	122	4.98	2.46	4.24	10.45
402.2	805	690	765	840	133	6.00	2.99	4.88	14.20
497.2	930	805	885	960	160	7.45	3.74	5.72	21.40

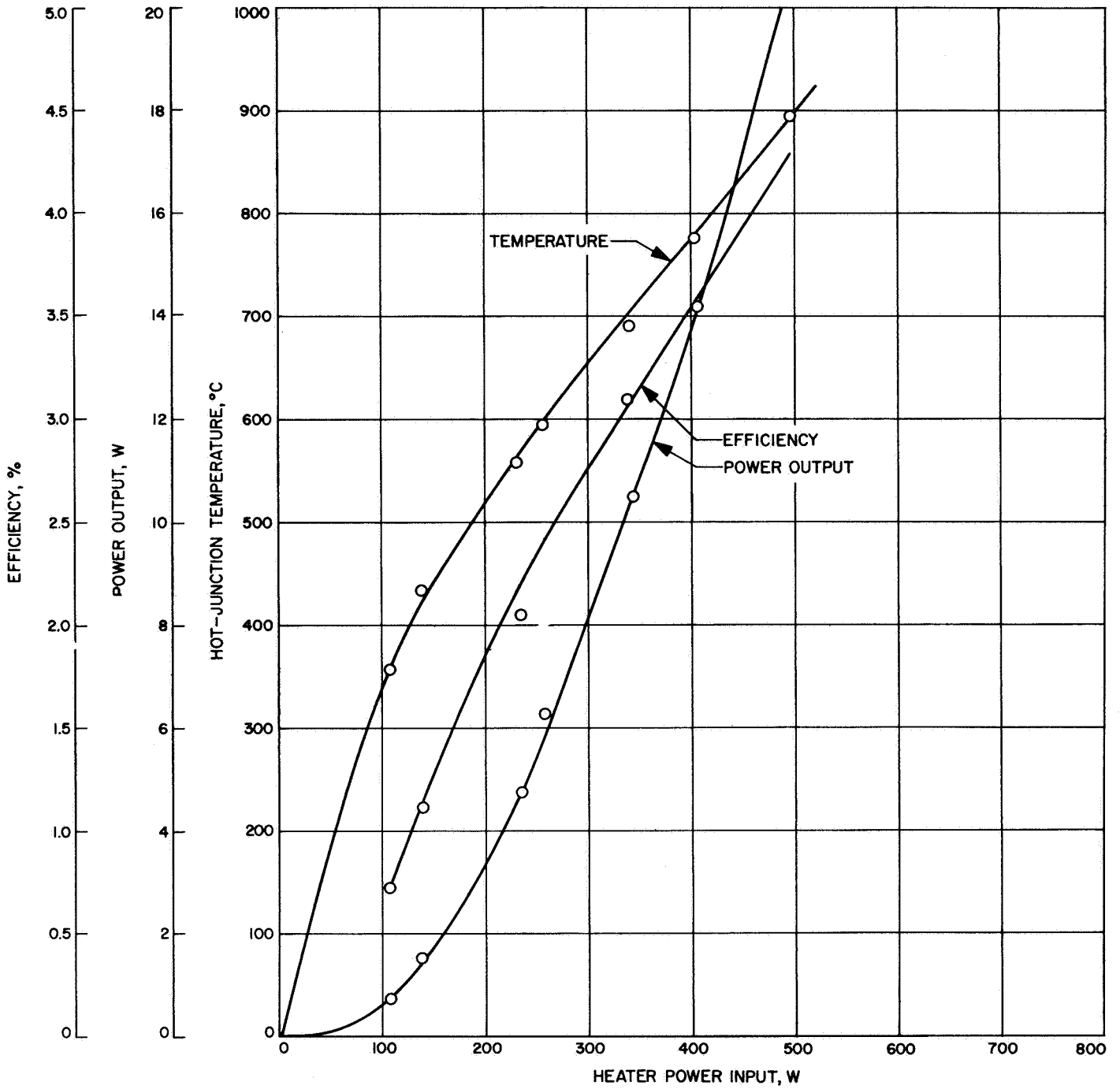


Fig. 9. Start-up characteristics of four-module Air-Vac test device 2

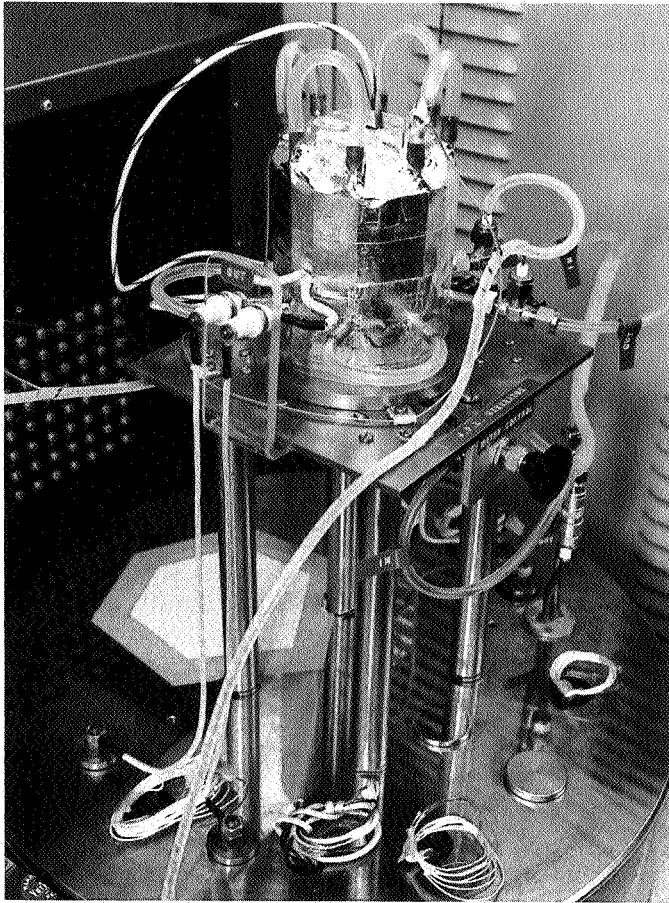


Fig. 10. In-house fabricated module

2. In-House Fabricated Module

A cylindrical thermoelectric module (Fig. 10) was fabricated in-house from 32 Air-Vac couples procured from RCA for the failure-mode testing program. The couples were similar to the couples of the four-module test devices, with the exception of having a lower l/A ratio and a different mounting configuration. The four-module test devices had couples with aspect ratios of 5.6; the in-house unit had couples with an aspect ratio of 4.0. The couples used in the four-module test devices had their cold sides bonded directly to heat-rejection plates; the failure-mode test couples had tapered bases with mounting studs (Fig. 11).

a. Construction. The cylindrical generator consisted primarily of eight copper water-cooled thermoelectric couple mounting blocks attached to a disk-shaped stainless steel base. The couples were mounted four high, with their hot shoes pointing radially in toward the center of the cylinder. Bulk and strip Dynaquartz were packed between the thermoelectric couples to provide thermal

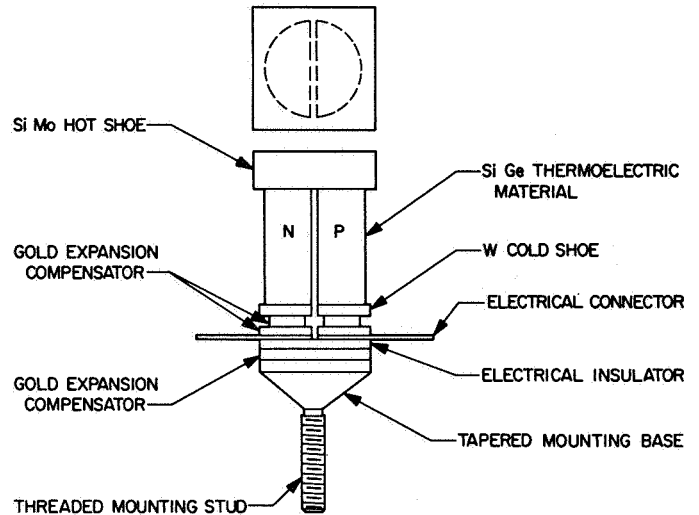


Fig. 11. Silicon germanium Air-Vac thermoelectric couple

insulation between the hot and cold sides of the module and to reduce heat shunt losses.

The generator heater was made from Kanthal heating wire wound into spiral grooves of a threaded 1-in. diam boron nitride core. To prevent the Kanthal wire from slipping out of the threads due to plasticity at operating temperatures, a quartz sleeve was placed over the boron nitride. The quartz sleeve also served the added function of preventing the heater wire from electrical shorting against the thermoelectric hot shoes.

b. Testing. A total of 700 h of air operation testing time was accumulated, which included 15 thermal cycles due to heater failures.

The total cold resistance of the generator was initially measured to be 0.33Ω across the terminals. The hottest temperature measured on the hot shoes was 755°C . This reading was made at 36 h with a tungsten-tungsten rhenium thermocouple. All three tungsten-tungsten rhenium thermocouples degraded rapidly at temperature in air and failed by 50 h. Subsequent hot temperature measurements were made with chromel-alumel thermocouples inserted into the boron nitride heater core, and into boron nitride tubes behind the hot shoes of the couples. Temperature calibrations were also made by measuring the cold-junction temperatures and calculating the hot-junction temperatures from the open-circuit voltage readings.

A summary of the power input, temperature, and output relationships is shown in Fig. 12 and Table 6.

Table 6. Parametric relations for in-house fabricated module

Input power, W	Hot-junction temperature, °C	Cold-junction temperature, °C	Open-circuit voltage, V	Load voltage, V	Load current, A	Power output, W
54	115		0.423			
94	165		0.789	0.40	1.35	0.542
184	255		1.56	0.78	2.58	1.046
284	363	33.3	3.22	1.62	3.60	5.84
371	445	40	3.70	1.84	4.05	7.45
491	550	48	5.22	2.61	5.19	13.54
585	625	51	6.63	3.55	5.79	20.55
722	755	61	8.46	4.23	7.0	29.6

The unit was taken off test at 710 h, after the last heater failure. Testing will be resumed after delivery and installation of new silicon carbide high-temperature heaters.

c. Test conclusions. Testing to date on the in-house fabricated thermoelectric device has been limited because of the nonavailability of a reliable high temperature (1200°C) heater for air ambient operation. For its brief operation, the Air-Vac module has demonstrated the following:

- (1) Ease of fabrication of nonplanar module configurations.
- (2) Air-operation capability.
- (3) Insensitivity to thermal shock.

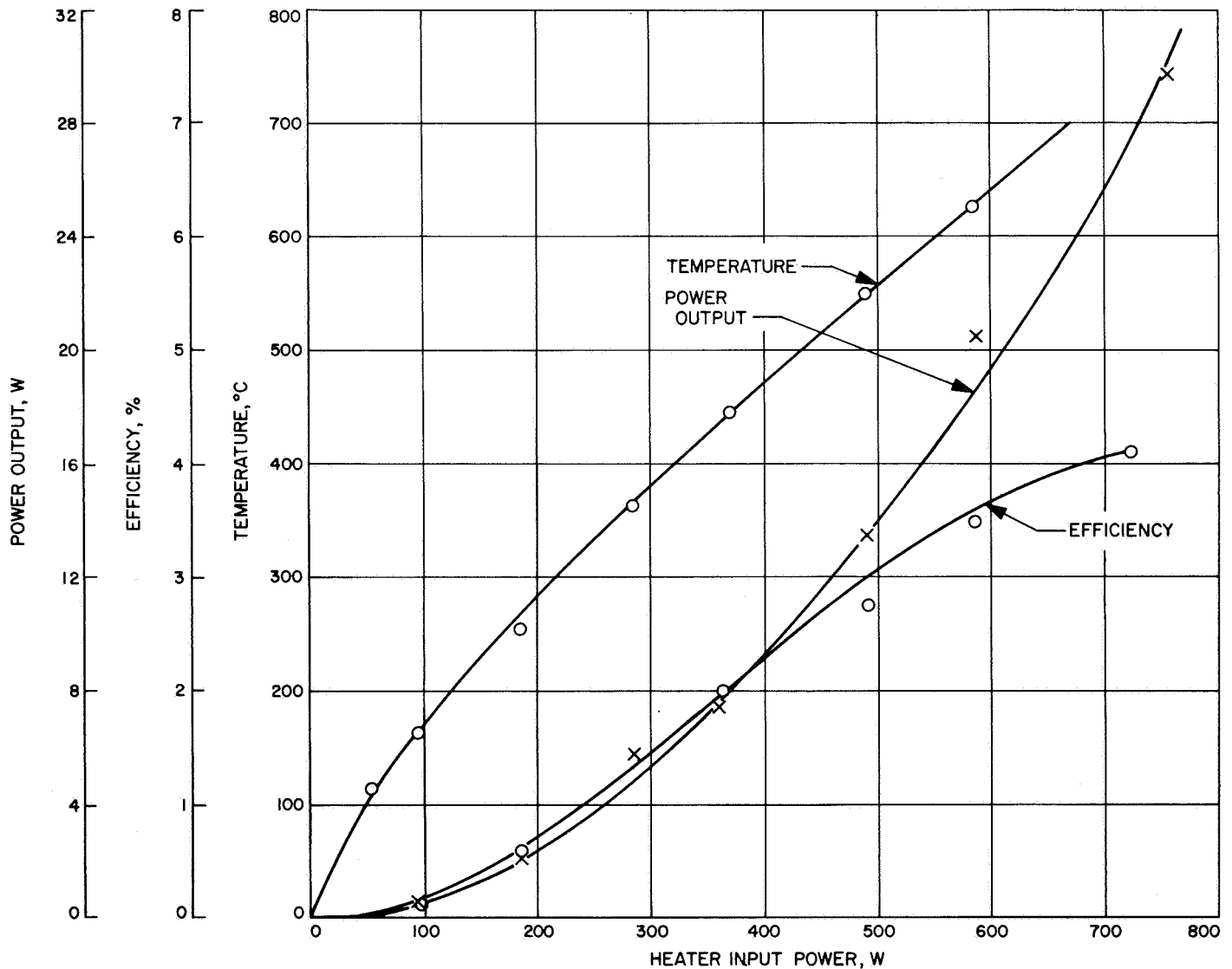


Fig. 12. Performance characteristics of in-house fabricated Air-Vac thermoelectric module

- (4) Difficulty of heating and temperature instrumenting air-operated silicon germanium devices.

C. Radiation Effects on Silver and Zinc Battery Electrodes, G. L. Juvinall

1. Introduction

The Atomic International Division of North American Aviation, Inc., has recently concluded a series of experimental studies on the effects of gamma radiation on silver and zinc battery electrodes. Earlier work at Atomic International has shown that a dose level of 10^8 rads (H_2O) is at the threshold for radiation damage for the nickel-cadmium system. The objective of the later work was to obtain comparable data for the silver-zinc system. In this study, commercial battery electrodes were irradiated in 40% potassium hydroxide with high-intensity ^{60}Co gamma rays. Gas evolution, solid material losses, and discharge capacity changes were measured.

2. Experimental Approach

Prior to irradiation the silver electrodes, cadmium counter electrodes, and electrolyte were placed in polystyrene containers which were divided into compartments by means of fritted quartz separators. The entire assembly was then placed in a stainless steel outer container which was fitted with a transducer for pressure measurement. The construction of the inner container is illustrated in Fig. 13. The silver electrodes had a nominal

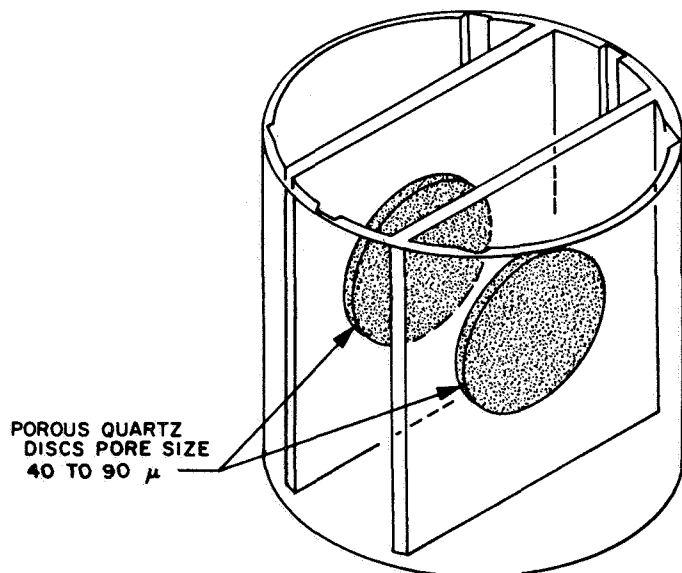


Fig. 13. Polystyrene cell liner

capacity of 1.4 A-h. Following assembly, all cells were leak-tested and filled with nitrogen.

It was necessary to develop a starved electrolyte cell in order to study the behavior of zinc electrodes. The growth of dendrites and excessive material loss on cycling precluded the use of a flooded cell. A diagram of the starved electrolyte cell configuration is shown in Fig. 14. Previously charged silver plates were used as counter electrodes in these zinc-limited cells.

The cells were preconditioned by cycling for 24 h at the desired state of charge ($Q \rightleftharpoons Q + \Delta Q$), where Q was 30, 60, or 90% of full charge, and ΔQ was 5%. During the irradiation, the cells were cycled again over these ranges. Radiation doses were in the range of 7×10^7 to 9×10^8 rads (H_2O). Subsequent to irradiation, the cells were subjected to complete charge-discharge cycling at constant current for the measurement of capacity. In all experiments, nonirradiated cells were run as controls. The zinc capacity measurements were not made with the automatic voltage-limited system because of hydrogen pressure build-up during lengthy overcharges.

After the capacity measurements, the silver electrode cells were examined for the loss of solid material from the electrodes and all cells were examined for gas evolution. Solid material losses were not directly measurable in the closely packed starved electrolyte cells.

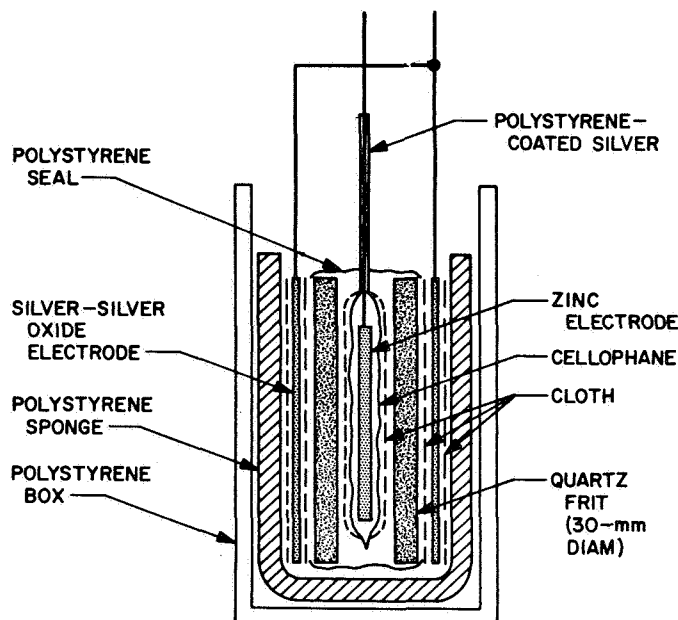


Fig. 14. Starved-electrolyte silver-zinc cell

3. Results

The discharge capacity changes of the silver electrodes due to radiation are summarized in Fig. 15. The capacity changes are uncertain by several percent at each charge level. However, there appears to be a slight capacity decrease at the 30% level, an increase at the 60% level, and essentially no change at the 90% level.

The capacity changes of the zinc electrodes were masked by changes in the physical characteristics of the cellophane separators induced by the gamma radiation.

Solid material losses from the silver electrodes averaged 1.4% of the electrode weight in the uncharged condition. The measurements were corrected for the silica which was dislodged from the fritted quartz separators. The loss consists primarily of silver, although

silver oxides were detected occasionally by X-ray diffraction methods.

Gas evolution measurements showed that substantial quantities of hydrogen were evolved in all runs. However, the results were independent of the state of charge of the silver electrode. Pressure increases up to 0.8 atm were observed.

4. Conclusions

Since the relative proportion of AgO in the electrode decreases with decreasing state of charge, it is reasonable that the effect of radiation on discharge capacity is a function of the state of charge of the electrode. Capacity changes over the charge range investigated fall between average limits of +11% and -14%. A capacity gain may result from increased surface area. Thus the depth of discharge becomes a more important design parameter when the battery is to function in a radiative environment aboard a spacecraft.

Based upon the data obtained in this study, pressure increases of 0.5 to 1 atm might be expected with doses of 10^8 rads (H_2O) and 50% ullage. Pressure containers or gas relief valves may therefore be desirable for batteries in some space applications.

The loss of solid material from the electrodes represents the most serious form of radiation damage. Material loss is cumulative and eventually must result in a real loss of capacity. This fact must also be considered in the design of a battery to operate in a radiative environment.

D. Sterilizable Battery, R. Lutwack

1. Development of Separators for Sterilizable Batteries

The research and development program for a separator for the heat-sterilizable Ag-Zn battery comprises contracts with Monsanto Research Corp., Westinghouse Electric Corp., the Southwest Research Institute and Narmco Division, Whittaker Corp. In addition, separator evaluations are being done at Electric Storage Battery Co. (ESB) and a research and evaluation program is being conducted at JPL.

a. JPL Contract 951524 with Monsanto Research Corp. This is an investigation of the efficacy of various ligand-containing polymers as heat-sterilization-resistant films. The two most promising materials are: (1) a 0.45:0.55 2-vinylpyridine/methyl methacrylate polymer and (2)

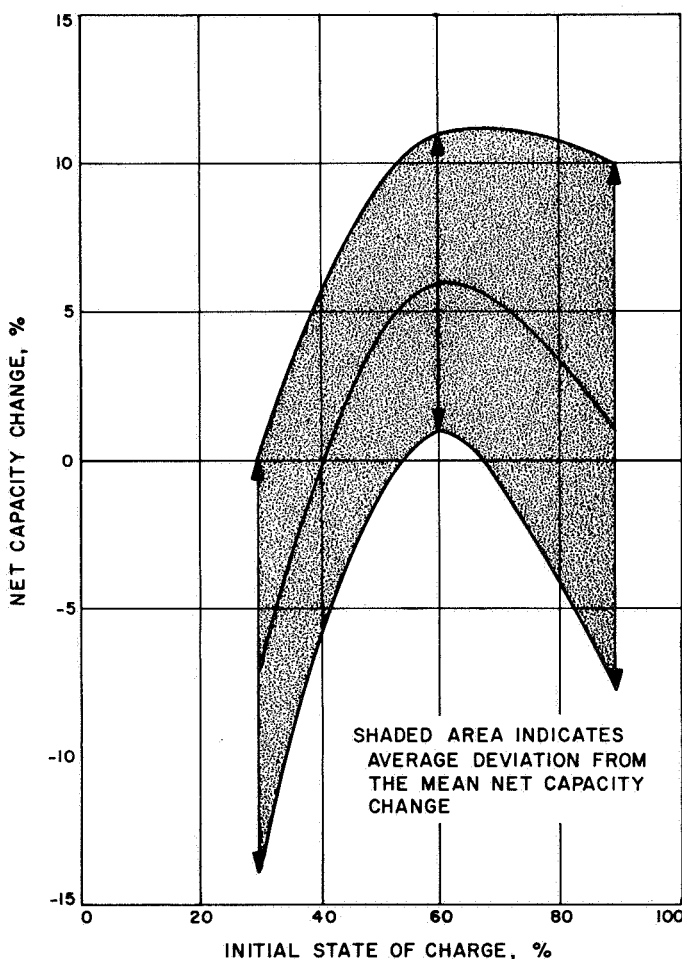


Fig. 15. Net change in silver electrode capacity with radiation dose of 7×10^7 rads (H_2O)

styrene/maleic anhydride/methyl methacrylate terpolymers. A film of the first has been prepared having a resistivity of 22 Ω -in. and a tensile strength of 1000 psi after sterilization. Films of the terpolymers have been made which have resistivities of 50 Ω -in. The contract has been extended. There will be continued efforts for the synthesis and evaluation of these systems.

b. JPL Contract 951525 with Westinghouse Electric Corp. This is a study of the utilization of composite membranes for separators in the heat-sterilizable Ag-Zn battery. The fabrication and composition variables have been extensively investigated. The most satisfactory separator was a polypropylene-reinforced, water-extracted, compressed film of polysulfone with a hydrated zirconium oxide or titanium oxide filter at a loading of 30-g filter/15-g polysulfone. These films had resistivity values of about 30 Ω -in. and a tensile strength of about 4000 psi after sterilization. This contract has been extended. There will be continued efforts for the improvement of fabrication techniques and for complete evaluations of these films.

c. JPL Contract 951718 with Southwest Research Institute. This contract is for the study of parameters affecting the grafting of acrylic acid to polyethylene film using a ^{60}Co irradiation source. The main parameters studied were irradiation dose rate, total irradiation dose, multiple irradiation in place of continuous irradiation to obtain the total dose, temperature during irradiation, effect of oxygen, and film-washing methods. A one-half replicate of a 2^5 factorial experiment was followed for studying these parameters. The conclusions from these experiments were: (1) elevated temperature and the absence of oxygen lead to low electrical resistance values; (2) the effects of dose rate and total dose in the range evaluated are minor; and (3) crosslinking after grafting has no apparent effect on electrical resistance. This contract has been extended to increase the range of study.

d. JPL Contract 951091 with Narmco Division, Whitaker Corp. This contract is for the development of poly 2,2'-hexamethylene 5,5'-bis(1- β carboxyethyl) benzimidazole as a separator material and of poly 2,2'-octamethylene 5,5'-bibenzimidazole as a case material. Since films made from the suberic acid derivative had been shown to have the characteristics necessary for a heat-sterilizable separator, the present extension is for the development of techniques such that large quantities of uniform film can be fabricated. The sebacic acid derivative has been compression molded into $4 \times 5 \times \frac{1}{8}$ -in. blocks, and various bonding techniques are being evaluated.

e. Separator evaluation programs at ESB. Polyethylene separators have been used exclusively in the development program at ESB. The divinylbenzene-crosslinked and the electron-beam-crosslinked materials (which are grafted with acrylic acid) are not apparently chemically affected by the sterilization cycles. There appear to be differences in the electrical performances of cells fabricated from the two materials, but the data are not consistent. The GX material, which is prepared by the Southwest Research Institute, is being used exclusively now in all of the Ag-Zn cell design and development. It is comparable to the previously used divinylbenzene crosslinked polyethylene, but it is more uniform, as described by electrical resistance measurements.

f. Separator program at JPL. Materials which are candidates for heat-sterilizable separators are tested and evaluated at JPL by the use of electrical resistance measurements, spectrophotometric methods, silver migration studies using radioactive tracer techniques, and in-cell testing. Resistance measurements are used for the screening of potential separator material. A large number of these measurements has been made employing consistent sampling techniques; statistical methods were used to reduce the results. The results are used to support contractors in their efforts to produce better separator materials, and they permit a measure of quality control on production runs.

Spectrophotometric methods are being investigated to develop a nondestructive test for the polyethylene-based separator materials. It is hoped that such tests will eventually permit the determination of the degree of crosslinking and grafting of the material. Being non-destructive, these methods would permit the use of tested material in spacecraft batteries.

Since the migration of silver through the separators is one of the principal failure modes of the Ag-Zn cell, a study of this phenomenon has begun. Radioactive tracer techniques will be used, since the concentrations involved are too small for conventional analytical procedures. There is some evidence that the degree of crosslinking and the separator's ability to retard silver migration are related, and it is hoped that proposed study will shed light on this relation.

In-cell testing of separator materials is a means for determining the separator's compatibility with the cell components and allows some prediction of the performance of similar cells. Ag-Zn cells are being cycled to determine how many cycles can be expected prior to

failure. A stand-test program, in which the cells are left standing in the charged state at various temperatures, is also in progress. In this test the cells are discharged and recharged at intervals to study capacity decay as a function of time, temperature, and number of cycles.

g. JPL Contract 951966 with Monsanto Research Corp. This is a new contract in which ethylene/methyl acrylate copolymers synthesized in mass at high pressures will be fabricated into films, to be tested as separator material.

2. Research and Development of the Sterilizable Battery

a. Ag-Zn and Ag-Cd batteries. Contract 951296 with ESB, is for research and development on sealed Ag-Zn and Ag-Cd cells which can provide satisfactory electrical performance after heat sterilization.

Electrochemistry task. The problem of pressure increase during the formation change of sterilized cells is being intensively studied. The pack tightness, the use of Teflon in the Zn plate, and the KOH concentration are factors in this gas generation. Lower pressures occur with looser packs and when Teflon is not used (and there are some indications that amalgamation of the Ag grid may be beneficial). The effect of KOH concentration has not yet been determined. Some cells, built by controlling these factors, have gassed very little, and the effort is concentrated on determining the cause of the gassing so that no cells will gas extensively.

Although some effort is continuing on improving the cell-to-cover seals, it has been shown that polyphenylene oxide (PPO) cells can be sealed with epoxy resin and

then sterilized and cycled. In the last attempt, twelve out of twelve cells completed sterilization without leaks.

Cell task. Cells molded from PPO 531-801 can be successfully sealed with epoxy resin. A recurring problem is the appearance of stress cracks around the terminals in the covers. This cracking has been greatly reduced by redesigning the terminal. Efforts to improve the seals continue.

Cell fabrication and test task. Nine Model 334 cells were shock-tested in three groups at average *g* levels of 4100, 7500, and 8100. Peak levels of 10,000 *g* were reached for six of the cells. The cells shocked at 4100 *g* maintained good loaded voltage readings after shock; one of these had a seal failure. Two of those shocked at 7500 *g* maintained relatively good loaded voltage readings but had cell case damage. One of those shocked at 7500 *g*, and all of those shocked at 8100 *g*, had severe loaded voltage losses due to shock. In the examination of the cells after shock it was found that: (1) movement of the cell packs was responsible for case failures; (2) the epoxy seal peeling was caused by cell failure; (3) there was no damage to the epoxy-filled top cover; (4) the PPO reinforcing struts on the Ag plate failed in all cases; (5) the reinforcing struts in the Zn plate failed in all but one case; and (6) the separators were not damaged, except where cutting by moving Ag plates took place. The plates have been redesigned and reinforced by the use of metallic struts to remove the shock weaknesses.

b. Ni-Cd battery. JPL Contract 951972 with Texas Instruments, Inc., has been let for research and development on the heat-sterilizable Ni-Cd cell.

VII. Spacecraft Control

GUIDANCE AND CONTROL DIVISION

A. Investigation of Optimization of Attitude Control Systems, B. Dobrotin

The work reported in this summary is the result of research performed by Purdue University for JPL with Dr. J. Y. S. Luh as principal investigator (Ref. 1). The objective of the research is the generation of new control concepts which are directly applicable to future JPL problems.

The problem areas being studied are the autopilot control, antenna pointing techniques, and roving vehicle control. These are three areas which are pertinent to JPL in that increased autopilot accuracy is needed for multiple planet missions; the second concerns the higher pointing requirements necessitated by the use of larger spacecraft missions; while the last is connected with the unmanned exploration of planet surfaces.

Purdue University is doing basic research in an attempt to find solutions in all three general areas described

above. The first area is the "bounded phase coordinate" problem. This consists of finding the optimal solution in a minimum time sense for bounded controls. If a feedback solution can be found, and this looks promising, it is an answer to the autopilots required for multiple planet missions. For these missions, the trajectory correction accuracy must be increased. This portion of Purdue's research should allow the errors due to misalignment and CG offset to be essentially reduced to zero.

The next case is that of optimal stochastic control where the problem is to maximize the probability of obtaining the desired terminal state in a noisy environment. This offers the possibility of providing closed loop antenna tracking without the necessity of optical trackers or lobing techniques presently proposed.

The third area is one of obtaining a feedback solution directly from the stochastic Hamilton-Jacobi equation, combined with state estimation. This would be useful in the area of radar measurements, either for soft landing or roving vehicles.

1. Problem I: Bounded Control

The first area is the minimum time problem with control inputs which have both amplitude and rate saturation. The minimum time problem is one wherein the plant, i.e. the system to be controlled, is driven from an original state to the origin (zero displacement and rates) in the minimum time:

$$\text{Performance Index (which is to be minimized)} = \int_0^T dt$$

The systems studied were linear, time invariant plants.

The unbounded problem has been extensively studied and, for most cases, requires a maximum positive or negative control force at all times, with no switching delays. The problems with saturated control have been treated with approximations such as letting the control saturate until the state variables reduce to the unsaturated control region. This does not produce a true optimal control. In other words, "better" controls exist, but the theory cannot find them.

Purdue has found optimal solutions to the bounded control problem, including limits on the rate of change of control. This is a close approximation to actual control systems where instantaneous switching is not possible in many cases. Purdue's research effort is a continuation of research contained in Ref. 2, which develops several theoretical considerations which must be met if the solution is to be time-optimal (necessary conditions). However, there are no practical applications which may be immediately derived from this work. The few examples given are for simple systems which are not meaningful.

Developments at Purdue have taken the original work and extended it to the point where practical open loop optimal control can be achieved. This work has consisted of the following steps. First, it was shown that a higher order system which is controlled by multiple independent controls may be treated as a series of independent scalar control optimization problems. The problem is then reduced to developing, from the necessary conditions, equations which will allow a computer program to be written. This is based on geometrical properties of the adjoint solution. This indicates that either the control rate or the control is saturated, which may be anticipated by engineering intuition. However, the computer program will indicate the signum function of the saturation and the switching times. This computer program has been completed and applications are in progress.

The next step Purdue intends to pursue is finding a feedback control system which will solve the above problem in real time. This is impossible with the open-loop control since the plant equations run in forward time while the adjoint equations run in backward time. Thus, for the open loop case, an iterative technique is required. This is not necessary in a feedback system where the present state determines the present control value. Thus, the feedback solution is the only practical method of implementing a control system. Purdue is studying several techniques for doing this, including one method suggested by present research. This consists of polynomial approximations in the feedback loop.

2. Problem II: Optimal Stochastic Control

The second problem Purdue is investigating is that of optimal stochastic control. The problem is essentially one of selecting the control which maximizes the probability of entering the desired terminal manifold. This is done by calculating the transitional probability density function for a particular control and then converging to the optimal control in the sense described above.

The system to be controlled has been divided into two parts: the deterministic system which is forced by the control, and the stochastic system which is forced by the noise entering the plant. An iterative technique is being developed for computing the optimal open-loop control. First, an optimal control is found for the deterministic control, with a quadratic minimum energy requirement. Next, this control is iterated upon to maximize the probability that the terminal manifold (i.e. the desired end conditions) is entered at the terminal time. This solution will then be compared with the exact theoretical solution.

The above method suffers from the drawback that the system statistics must be known beforehand, since this is an open-loop optimization problem. Therefore, to complete the problem, Purdue will develop a relationship between the current statistics, i.e. present estimate of noise and the desired control. This is obviously the feedback solution.

3. Problem III: Bounded Stochastic Control With State Estimation

This problem is in the formative stages and represents an effort to combine feedback optimal bounded state control with stochastic estimation. In the past, the estimation problem has been typically separated from the

control problem, leading to a suboptimal solution. However, particular solutions have been found for the case of a linear system with Gaussian noise. The control and estimation may then be decoupled and the optimal solution still be found. Work is being pursued on these lines, with an attempt to find a suitable performance index to minimize. While no definite results are available, this problem might be useful in cases where strong wind gust loading is found, such as in the case of a roving surface-landed system with a large parabolic antenna.

B. Sterilizable Inertial Sensors, P. J. Hand

The objective of this development task is to make available, through contracted effort, a family of miniature inertial sensors of the newest designs, which will be capable of thermal and gas sterilization. These inertial sensors have potential applications in advanced spacecraft and capsule attitude control systems. Included in this category of inertial sensors are both long-life gas bearing and ball bearing rate integrating gyros, spring-restrained rate gyros, and high-performance linear accelerometers.

The accelerometer chosen for a sterilization development effort and which will be the subject of this summary report is the Bell Aerosystems Co. model VII. This is a linear, force-balance type of instrument using a high-frequency capacitive pickoff. It is capable of either analog or digital operation, depending on the external electronic system used.

Two standard versions of the model VII were purchased by JPL for evaluation of stability and environmental capability. The first instruments received failed to pass the JPL vibration environment of 15 g rms noise. The units were returned to the vendor for minor internal design modifications, after which the vibration environment was passed with less than 10 μg shift of the bias error parameter. The next environmental test performed was shock. The levels chosen were 100 g peak terminal sawtooth of 0.5 ms duration and 200 g peak at the same duration. The latter level is equal to the *Mariner IV* and *V* type-approval test shock level. Only one of the two units was subjected to the shock environment. This unit survived 5 shocks in each of the 3 axes, one of which was the input axis at both 100 and 200 g without catastrophic failure. Very large bias error shifts were encountered, however.

The total bias shift for the 15 shocks at 100 g was 959 μg , while the shift for a similar number of 200 g

shocks was 1893 μg . These data tend to indicate that the bias shift from shock is directly proportional to the shock amplitude. It was also noted during the shock test series that damage was incurred only during those shocks applied along the accelerometer's input axis. No significant change in output was noted after shocks applied along either of the nonsensitive axes. It is logical to assume from these tests that the damage mechanism is distortion of the flexure suspension caused by bending the flexure beyond its elastic limits, in a manner in which it was never intended to be flexed. Figure 1 shows details of this abnormal flexing.

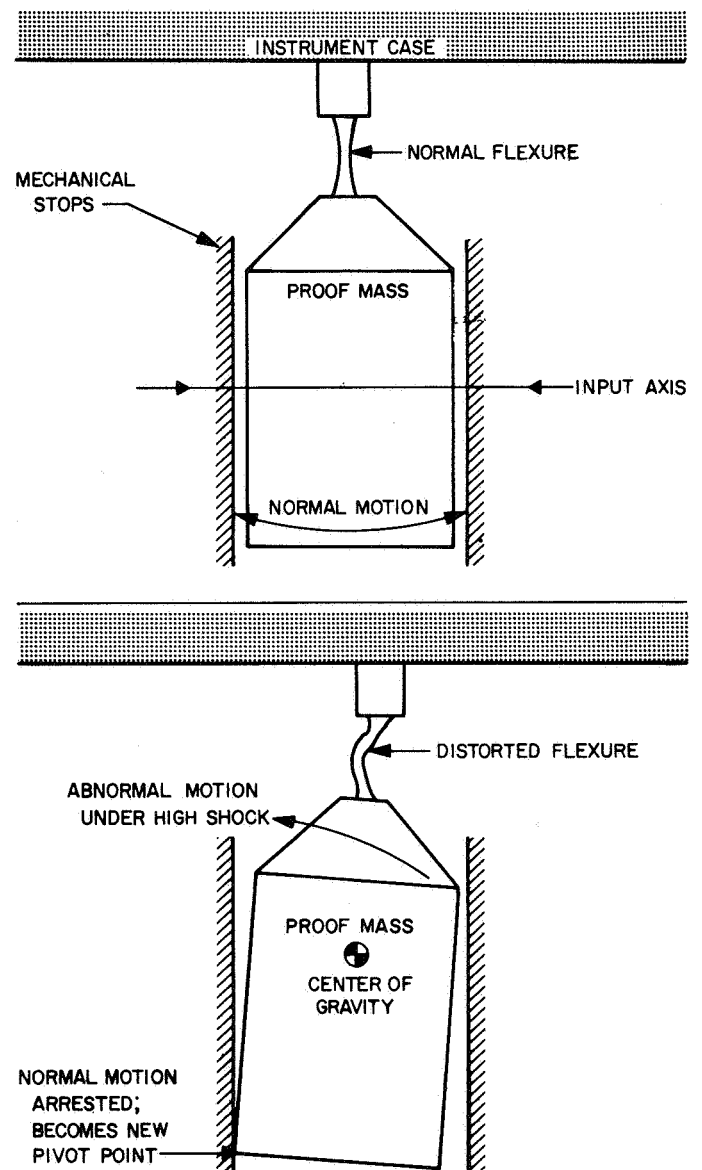


Fig. 1. Proof mass motion, model VII accelerometer

There are at least three possible ways to improve the shock capability of this instrument. One possibility would be to strengthen the flexure by making it thicker; however the penalty for this would be reduced bias stability. A second possibility would be to increase the internal damping of the instrument by fluid filling. This, however, would negate one of the principal advantages of the model VII which is, that being unfilled, it cannot leak fluid in space and does not require active temperature control. The third possibility is to increase the capture-loop capability to sufficiently constrain the proof mass to prevent it from striking the mechanical stops. The present lab test capture loop is limited to ± 7 g levels. The capture-loop bandwidth would also have to be increased to handle the fast rising 0.5-ms wave front. This implies at least 2 kHz bandwidth as against 800 Hz for the existing loop. The most probable solution would appear to be a combination of the first and third alternatives.

A contract was released to Bell Aerosystems in July 1966 for a 1-yr development program to increase the

thermal sterilization capabilities of this instrument. The present maximum nonoperating storage limit for the model VII is 93°C (200°F) while the thermal sterilization requirement is 135°C (275°F). Performance design goals for this development are shown in Table 1. These values are to apply after 6 sterilization cycles of 64 h each at 135°C, and after the vibration and shock environments described earlier. Details of this contracted effort will be discussed in subsequent SPS reports.

Table 1. Sterilizable model VII performance goals

Bias error	$\pm 300 \mu\text{g}$ maximum
Bias error stability	100 μg , 1 σ
Scale factor	1 ma/g $\pm 10\%$
Scale factor stability	0.05%, 1 σ
Input axis alignment	$\pm 15'$
Input axis stability	$\pm 30''$, 1 σ
Frequency response (analog mode)	That of a critically damped 2nd order system with cut-off frequency not less than 300 Hz

References

1. Luh, J. Y. S., "Investigation of Optimization of Attitude Control Systems," Purdue University Quarterly Report, Jan. 1 to Mar. 31, 1967.
2. "Bounded Phase Coordinate Control," NASA CR-470, May 1966.

VIII. Guidance and Control Research

GUIDANCE AND CONTROL DIVISION

A. Extremely High-Density Magnetic Information

Storage, D. I. Tchernev

Curie-point writing has been demonstrated in MnBi and other materials by electron-beam heating, hot-wire stylus heating, and laser-beam heating (Refs. 1-3). With this method of writing, a small area of a magnetic thin film, magnetized perpendicular to its surface, is heated to a temperature above the Curie point and then cooled in the demagnetizing field of the neighboring areas. The cooling process in the demagnetizing field reverses the direction of magnetization in the heated area and stores a bit of information.

In all previous experiments, the dimensions of the heated area were comparatively large (from 15 μm to over 200 μm). In the present experiment, areas smaller than 1 μm in diameter have been switched successfully by optical means, thus demonstrating the feasibility of writing densities of about 10^8 bits/cm². These are believed to be the smallest magnetic bits of information ever recorded.

Thin films of MnBi about 700 Å thick were used as the storage material. The writing was done with a biolaser,¹

¹Model 513, by TRG Inc., Melville, N.Y., a division of Control Data Corporation.

a system designed for biological and biomedical research. The instrument consists of a pulsed, high-intensity ruby laser, a flashlamp, a focusing cavity, and a pinhole aperture which is imaged on the microscope stage of a Leitz Ortholux microscope. The recorded bits of information were observed with polarized light, using the Faraday effect in MnBi.

The intensity of the laser was attenuated sufficiently to heat the spots on the MnBi films above the Curie point (360°C) without destroying the material (the decomposition temperature is 420°C). Since the biolaser produces a diffraction-limited spot of 1 μm at the 1/e point, by properly reducing the laser intensity it was possible to record spots smaller than 1 μm when using only the peak of the diffraction-limited intensity distribution to heat areas to the Curie point. Because of the diffraction limit on the smallest spot observable by the Faraday effect, it can only be estimated that the size of the smallest bits recorded is less than 0.5-0.7 μm . The limitation is in the method of observation rather than the material or the recording process.

The recorded bits of information when viewed through a set of crossed polarizers appear as dark (or light) spots against a light (or dark) background, depending on the setting of the axis of the analyzer. A sample of some recorded spots, photographed in polarized light, is shown

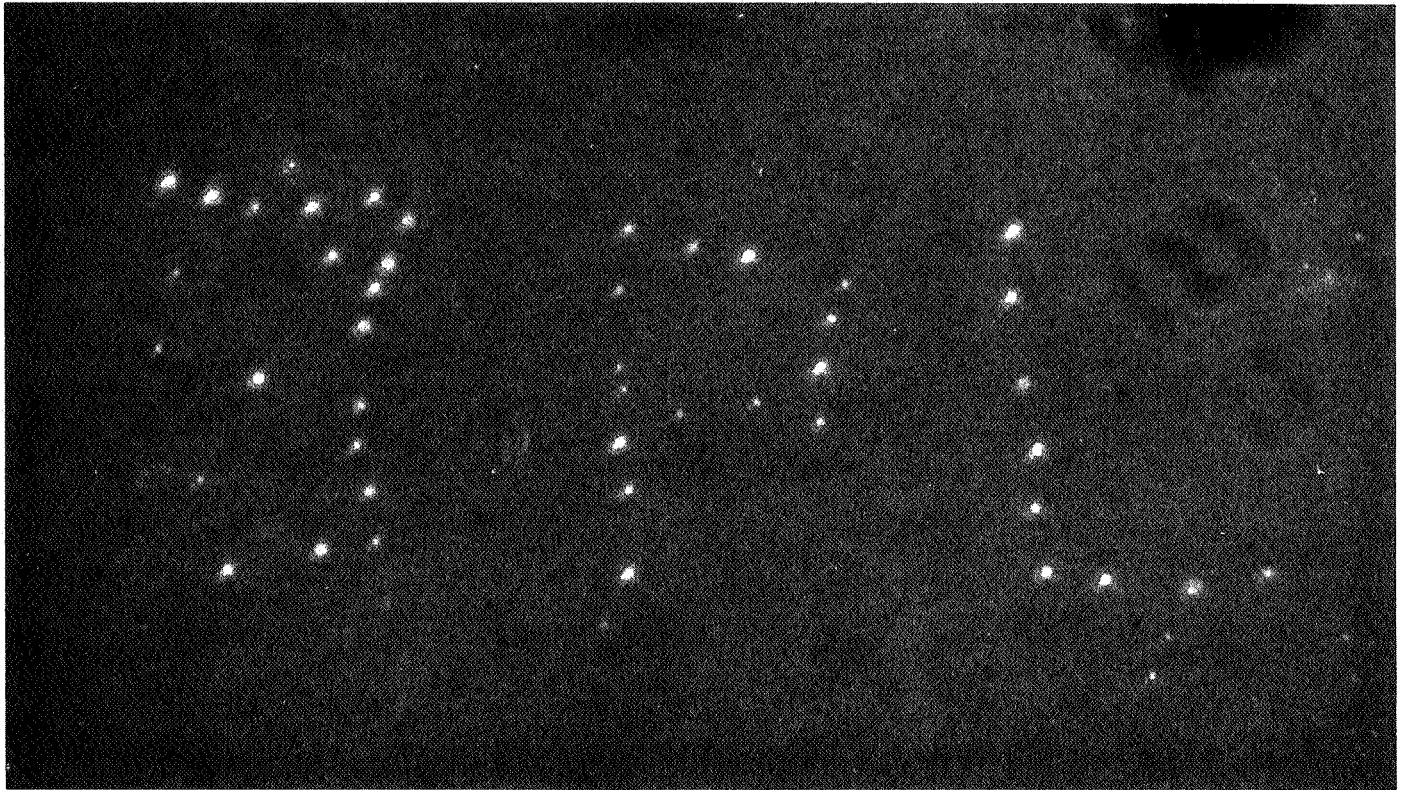


Fig. 1. Curie-point writing of diffraction-limited spots on MnBi thin films

in Fig. 1. The diameter of the small spots is below $1\ \mu\text{m}$, and the distance between spots ranges from 3 to $10\ \mu\text{m}$. The recorded information can be completely erased by saturating the film in an applied magnetic field of sufficient strength. No permanent or irreversible changes in the magnetic film are induced by heating it to the Curie temperature or by repetitive heating-and-switching of the same spot for many cycles. The closest distance between spots that will permit Curie-point writing has not been determined for any particular geometry; however, spots that were overlapping slightly have been switched without any difficulties. This seems to indicate that the density limit will be determined by the minimum average demagnetizing field that will cause switching. By leaving some unswitched areas between bits, this field can be made sufficiently large without noticeably reducing the information-storage density. This is especially easy to do in a sequential writing scheme where there is always some unswitched area ahead of the light beam while the area behind the beam is only partially switched, depending on the information content. In this case, the average demagnetizing field will always be in the required direction and of sufficient strength to ensure successful Curie-point writing.

B. Curie-Point Switching in Thin MnBi Films,

G. Lewicki

1. Introduction

The role of Curie-point switching in a proposed high-density magneto-optic memory using MnBi films has been described in SPS 37-42, Vol. IV, pp. 59-61. The present report considers the actual process of Curie-point writing in more detail.

In the Curie-point-switching process, an area of the film is heated past its Curie temperature and allowed to cool in a magnetic field having the direction desired for the magnetization. If the magnetic field is sufficiently intense, the area is successfully switched. The whole area acquires a magnetization in the desired direction. If the magnetic field is not sufficiently intense, the area becomes partially switched. Upon cooling, the area acquires a domain structure consisting of smaller areas having magnetizations parallel and antiparallel to the desired direction. Of course, there is a net magnetization in the desired direction inasmuch as the sum of the areas with magnetizations parallel to the applied field exceeds the

sum of the areas with magnetizations antiparallel to the applied field.

It is believed that the following considerations determine whether a discrete area can be completely switched with an applied field H_a . Upon cooling through the Curie temperature, a region will go into the lowest energy state possible. There are two such states: one for which the area contains domains, the other for which the area contains no domains.

If, for all temperatures between the Curie temperature and the normal operating temperature, the lowest energy state is one for which an area contains no domains, then complete switching can be achieved with the Curie-point process. On the other hand, at some temperature below the Curie temperature, the lowest energy state changes from a no-domain to a domain structure. Then a completely switched area may or may not revert to a domain structure when cooling through this temperature, depending on whether or not an energy barrier separates the two states.

A discussion relating the energies of films to the applied field and to their magnetic properties and dimensions is presented here.

2. Films With Finite Surface Dimensions

Consider an area having the dimensions shown in Fig. 2. The film is completely magnetized in a direction perpendicular to the plane of the film and is under zero applied field. The magnetostatic energy resulting from the interaction of the magnetization with its own demagnetizing field represents the total energy of the film, and is given by

$$E_s = 2\pi M_s^2 a^2 t f_s(a, t) \quad (1)$$

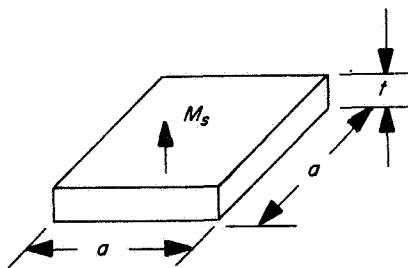


Fig. 2. Saturated film of surface dimension a and thickness t

where M_s is the saturation magnetization, and $f_s(a, t)$ is a dimensionless function of the film dimensions a and t which is always smaller than unity.

If the area acquires the domain structure shown in Fig. 3, the magnetostatic energy is reduced. However, energy stored in the domain wall separating the two domains must compensate for this reduction in the magnetostatic energy. The total energy E_d thus becomes

$$E_d = 2\pi M_s^2 a^2 t f_d(a, t) + \sigma_w a t \quad (2)$$

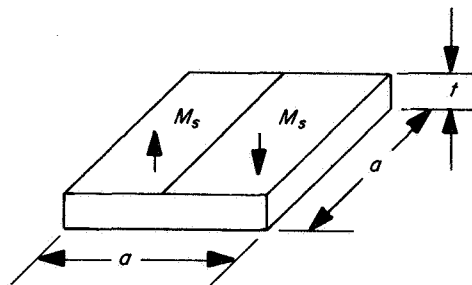


Fig. 3. Film with surface dimension a and thickness t with two domains

where $f_d(a, t)$ is a dimensionless function always smaller than $f_s(a, t)$. In Eq. (2), the first term represents the magnetostatic energy and the second the wall energy, with σ_w being the energy per unit area of the wall. If

$$\sigma_w a t > 2\pi M_s^2 a^2 t [f_s(a, t) - f_d(a, t)] \quad (3)$$

the area with no domain structure represents a lower energy state when compared with the area with a domain structure. Through a long and tedious calculation which will not be reproduced here, it can be shown that the inequality in Eq. (3) is approximately satisfied only if

$$t < \frac{\sigma_w / 2\pi M_s^2}{(2 \log_e a/t - 1)/\pi} \quad (4)$$

with $a/t \gg 1$. An MnBi film having a surface dimension of $3 \mu\text{m}$ and a thickness of 500 \AA would have to have a wall energy greater than 11 ergs/cm^2 for the no-domain configuration to correspond to the lowest energy state at room temperature. (At room temperature for MnBi, M_s is 600 G .) This is not an entirely unreasonable value for the wall energy.

If the inequality given in Eq. (4) is satisfied over a sufficiently large temperature range extending downward from the Curie temperature, the Curie-point process should achieve complete switching with very small applied fields. The area is then a bistable magnetic element; the magnetization over the whole area can only be in one of the two directions perpendicular to the plane of the film. The field applied during the cooling portion of the Curie-point process serves only to tip the magnetic spins in a desired direction rather than to prevent domain structure.

If the surface dimension of a film is so large compared with its thickness that the inequality in Eq. (4) is not satisfied, then complete switching can be achieved only with larger values of the applied field. How large these fields need be is answered below.

3. Films With Infinite or Very Large Surface Dimensions

In a film with infinite surface dimensions, the state represented by a lack of domain structure with the magnetization M_s parallel to the applied field H_a is the lower energy state only if

$$H_a \geq 2\pi M_s \quad (5)$$

For lower applied fields, the lowest energy state is the one involving domain structure.

At the Curie temperature, M_s is by definition equal to zero and increases rapidly with decreasing temperature. The major part of the increase in M_s occurs over a temperature range that is small compared with the Curie temperature. The temperature to which an area cools after switching must be one for which M_s is a large fraction of the saturation magnetization at zero temperature. The working temperature is determined in this manner because, in general, the magneto-optical effect is proportional to M_s . At working temperatures, $2\pi M_s$ is expected to be on the order of thousands of oersteds. Practical values of H_a on the order of tens of oersteds thus allow the inequality given in Eq. (5) to be satisfied only over a very narrow range of temperatures extending downward from the Curie temperature. If, at the temperature for which H_a becomes smaller than $2\pi M_s$, there is no barrier separating the single-domain and domain-structure states, a completely switched area upon cooling through this temperature will acquire a domain structure.

It is an experimental fact that an MnBi film having an infinite surface dimension in the sense that

$$t \gg \frac{\sigma_w/2\pi M_s^2}{(2 \log_e a/t - 1)/\pi} \quad (6)$$

when saturated at room temperature will not revert to a domain structure under the condition of a zero applied field. Obviously, there is an energy barrier separating the higher energy single-domain state from the lower energy domain-structure state. However, when the same film is cooled from its Curie temperature to room temperature in an applied field as high as 100 Oe, a domain structure is obtained. This indicates that at the temperature for which $2\pi M_s$ becomes larger than H_a , the barrier is not sufficiently large to prevent the saturated film from breaking up into domains. (Details of Curie-point-switching experiments now in progress will be presented in a future SPS.)

In a film with infinite surface dimension, the dimension of the unit cell containing two domains magnetized parallel and antiparallel to the applied field increases with increasing H_a . As H_a approaches $2\pi M_s$, the unit-cell dimension approaches infinity. This phenomenon is illustrated in Fig. 4, where cross-sectional views of a film with stripe domains in a zero applied field and in a non-zero applied field are shown. In Fig. 4a and 4b, x_{1a} and x_{2b} are the dimensions of the unit cell. Let the thickness, saturation magnetization, and applied magnetic field dependence on the unit-cell dimension x_2 be denoted by

$$x_2 = g(t, H_a, M_s) \quad (7)$$

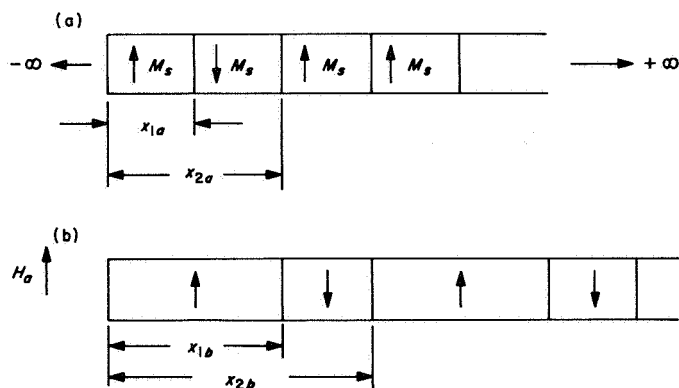


Fig. 4. Cross-sectional view of film with stripe domains: (a) appropriate to zero applied field; (b) appropriate to an applied field H_a

It is then reasonable to assume that in a film of thickness t and finite surface dimension a , the no-domain-structure state of the finite film will be lower in energy than the domain-structure state when

$$a < x_2 = g(t, H_a, M_s) \quad (8)$$

An applied field relaxes the restrictions imposed by Eq. (4) on the dimensions of a film. Nothing more specific can be said about the function $g(t, H_a, M_s)$ since at present it is not known in detail.

4. Summary

The following generalizations can be made. Films having dimensions such that the inequality in Eq. (4) is satisfied over a temperature range extending from the Curie temperature to the working temperature, or at least to a temperature for which there is an energy barrier separating the no-domain-structure and domain-structure states, should be completely switched by the Curie-point process with very small applied fields.

Films having finite dimensions such that the inequality in Eq. (4) is not satisfied can be completely switched with an applied field smaller than the largest value of $2\pi M_s$ in the temperature range described above. Films with infinite surface dimensions can be completely switched only with fields equal to this largest value of $2\pi M_s$.

C. Coercive Force of Thin Magnetic Films,

J. A. Baldwin, Jr.

1. Abstract

A simple phenomenological theory for the easy-axis coercive force H_c of thin magnetic films of thickness t is developed.² The coercive force H_c contains a term due to the surface that varies as t^{-1} , plus another term that is independent of t . This constant term is the sum of a positive term due to the bulk material plus a surface-tension term which may be either positive or negative.

Comparison with published experimental results shows the theory to fit very well, the coefficient of t^{-1} being roughly 0.2 Oe- μ m for normal films of 81% Ni and 19% Fe.

²This work was performed while the author was at JPL on leave from the University of California, Department of Electrical Engineering, Santa Barbara, Calif.

Comparison with low-scatter data shows the surface term to vary as t^{-1} , not $t^{-4/3}$. The theory also fits data taken on MnBi and gadolinium iron garnet (GdIG).

It is shown that it is possible to make a direct measurement of domain-wall surface energy in magnetic films using the technique of domain tip propagation.

2. Introduction

Study of coercive force in thin magnetic films has been confined primarily to films of NiFe because of the great commercial importance of permalloy films, especially in the area of computer memories. Other films such as MnBi (Ref. 4) and GdIG (Ref. 5) have recently shown promise of being useful as information-storage elements. It is of value to understand the mechanisms responsible for the coercive force in these films in order that this parameter may be controlled in practice. In this paper, an attempt is made to clarify this subject and, particularly, to explain how coercive force varies with film thickness.

A useful résumé on the subject of coercive force in NiFe films is given by Soohoo (Ref. 6). The question has been studied theoretically by Néel (Ref. 7), who found that the coercive force for Bloch walls should vary as the minus-four-thirds power of the film thickness. This same result was obtained by Behringer and Smith (Ref. 8), and also by Middelhoek (Ref. 9). However, the experimental situation is confused. Coercive force is extremely sensitive to the nature of the substrate surface, as well as other parameters. As a consequence, the experimental results characteristically have a great deal of scatter. Improper interpretation of the experimental data has caused further confusion, as will be shown. In summary, if it is assumed that coercive force is proportional to thickness to the power n , then experimental values of n have been found (Ref. 6) all the way from -1.4 to $+0.4$. It will be seen that the disparity is not as great as these results would imply.

3. Theory

Middelhoek (Ref. 9) has derived an expression for the easy-axis coercive force of thin NiFe films containing Bloch walls. The dependence on film thickness and domain configuration may be expressed as

$$H_c = H_{cv} + C/t^{4/3} + (\sigma_w/2M_s) \left. \frac{\partial A}{\partial V} \right|_{M=0} \quad (1)$$

where

- H_c = the wall coercive force (not a nucleation field)
- H_{cv} = the contribution due to the bulk of the material as opposed to the surface
- C = a constant depending on the magnetic properties of the material and on surface roughness
- t = the film thickness
- σ_w = the wall energy per unit area
- M_s = the saturation magnetization
- A = the total area of domain wall in the sample
- V = the total volume of the domains oriented *parallel* to the applied field

The subscript $M = 0$ means that the derivative is evaluated at the point where the overall magnetization of the sample is zero.

There is no contribution due to the gross magnetostatic energy of the sample, because it is assumed that this energy is a single-valued even function of M . Thus this contribution vanishes at $M = 0$. The last term is due to surface tension and may be either positive or negative. This is evident from Fig. 5, which shows two imaginary domain configurations. In Fig. 5a, $\partial A/\partial V$ is positive; in Fig. 5b, it is negative. If the applied field is reversed, this term changes sign because the meaning of the symbol V reverses. If the film contains Néel instead of Bloch walls, the term $C/t^{4/3}$ becomes a constant, independent of film thickness t . In examining the derivation of Eq. (1), there seems to be no reason why it should not be valid for any magnetic film, not only permalloy.

Equation (1) was derived assuming that the interaction of a wall with film imperfections was conservative. This assumption has been criticized by Rodbell and Bean (Ref. 10). It is possible to derive an equation similar to Eq. (1) using a simple phenomenological model in which the interaction is taken to be nonconservative and analogous to mechanical friction (Ref. 11). In this model an imperfection is assumed to attract a wall with a constant force f_0 . An advancing wall interacts with all imperfections within a distance d_a in front of it and a distance d_r behind it. If there are N defects per unit volume, there is a pressure P , due to imperfections, given by

$$P = -f_0 N (d_r - d_a) \quad (2)$$

acting on the wall. The minus sign indicates that this pressure is in a direction to hinder wall motion. The

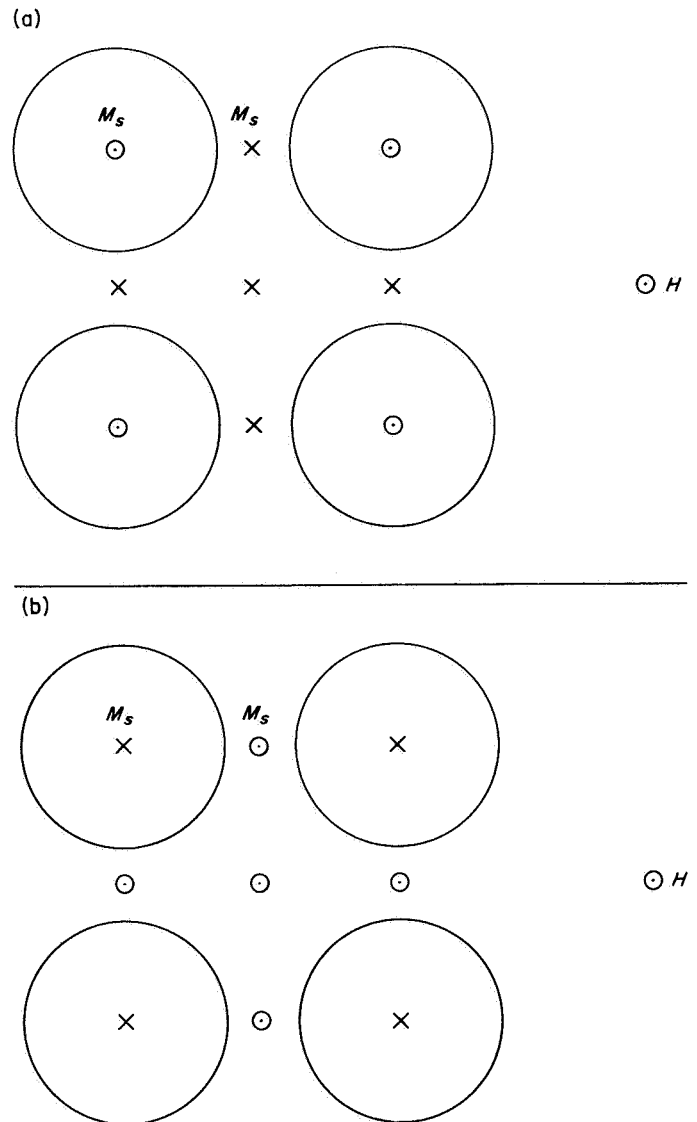


Fig. 5. Two domain configurations for which the surface-tension terms are equal but of opposite sign

coercive force may be evaluated by finding the magnetic field that will supply just enough pressure to overcome this. In the case of a thin film, surface effects become comparable to volume effects. It becomes necessary to assume that there are N_v imperfections per unit volume associated with the bulk of the material and N_s per unit area associated with the surface.

Similarly, it is necessary to distinguish between surface and volume by subscripting the other quantities in Eq. (2), thus introducing the symbols f_{0v} , f_{0s} , etc. Since the force exerted by the surface is independent of film thickness, P_s , the pressure due to the surface, is given by

$$P_s = -f_{0s}N_s(d_{rs} - d_{as})/t \quad (3)$$

Equating the sum of the pressures to zero to evaluate the coercive force, one obtains

$$2M_s H_c - f_{0v}N_v(d_{rv} - d_{av}) - f_{0s}N_s(d_{rs} - d_{as})/t - \sigma_w \left. \frac{\partial A}{\partial V} \right|_{M=0} = 0 \quad (4)$$

This may be rewritten as

$$H_c = H_{cv} + C/t + (\sigma_w/2M_s) \left. \frac{\partial A}{\partial V} \right|_{M=0} \quad (5)$$

The above derivation has implicitly assumed that all volume imperfections are identical and all surface imperfections are identical. However, the argument is easily generalized (Ref. 5) to include a distribution of defect sizes. This generalization does not change Eq. (5), but merely reinterprets the symbols occurring there. It will be noted that the only difference between Eqs. (1) and (5) is that the former predicts a $t^{-4/3}$ dependence of the coercive force on film thickness while the latter predicts a t^{-1} dependence.

4. Comparison With Experiment

In evaluating the exponent of t in the thickness dependence of coercive force, it has been customary to neglect the first and third right-hand terms of Eqs. (1) and (5), for example, by plotting H_c versus t on log-log paper. In some cases, the sum of these terms is nearly zero; in others it is not. No assumptions concerning these terms will be made here.

According to Eq. (1), if H_c is plotted versus $t^{-4/3}$, the result will be a straight line. Equation (5) predicts a straight line when the data are plotted versus t^{-1} .

Tiller and Clark (Ref. 12) have measured coercive force versus film thickness for vapor-deposited films of 81-19 NiFe. Film thickness was varied by successively etching the same films. Thus, composition and substrate were maintained constant during the experiment. The Tiller and Clark data are shown plotted versus reciprocal film thickness in Fig. 6. It is seen that, except for the two points at about 3.1 Oe, the results are well approximated by straight lines. The slopes of the two lines are about 0.21 and 0.22 Oe- μm . It is also seen that the contribution of the bulk to the coercive force of these samples is quite

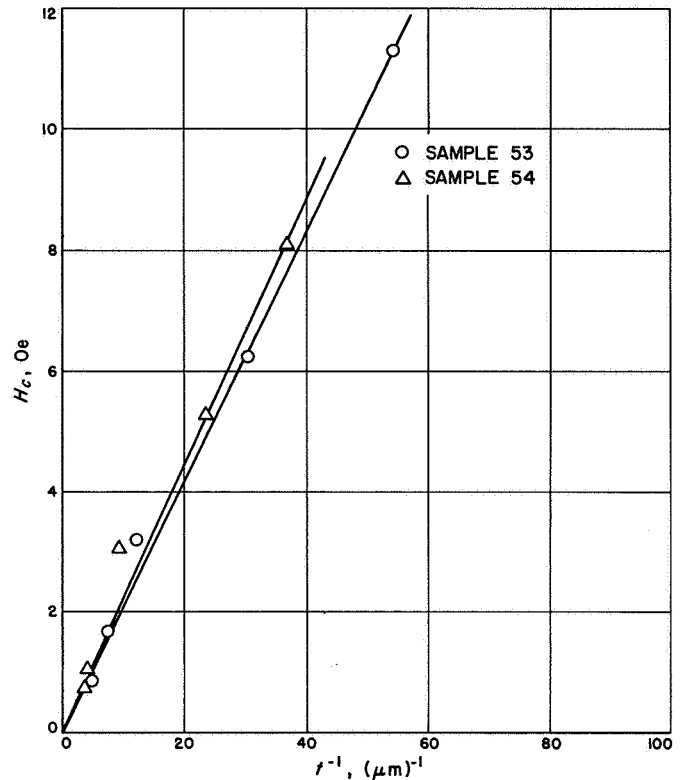


Fig. 6. Coercive force versus reciprocal film thickness for permalloy (from Tiller and Clark)

small, around 0.1 Oe. Thus, coercive force is extremely sensitive to film thickness. The same data are plotted versus $t^{-4/3}$ in Fig. 7. The fit to a straight line is poor. Therefore, it is concluded that the correct thickness dependence is t^{-1} —or perhaps more accurately expressed, it is closer to t^{-1} than to $t^{-4/3}$.

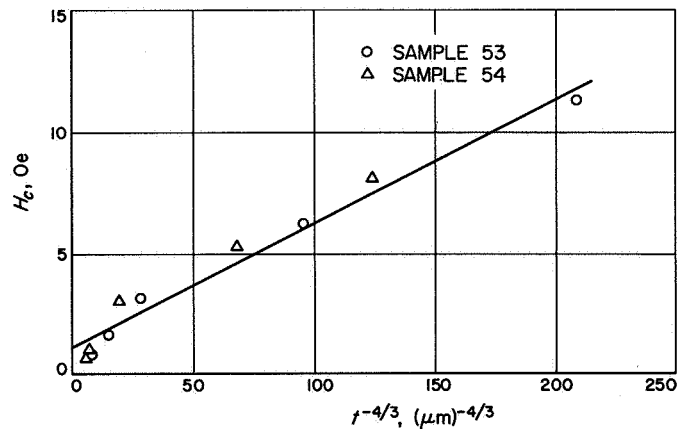


Fig. 7. Coercive force versus (film thickness) $^{-4/3}$ for permalloy (from Tiller and Clark)

With careful substrate preparation, Behrndt and Maddocks (Ref. 13) have successfully produced films of 81-19 NiFe by vapor deposition that have highly reproducible properties. They have measured the dependence of coercive force on film thickness, using separate depositions to obtain samples of different thickness. Their data are plotted versus reciprocal thickness in Fig. 8. Although there is appreciable scatter, the fit to a straight line is reasonably good. In this case, the contribution from the bulk of the film is negative because of the surface-tension

term. The slope of the straight-line fit is about $0.17 \text{ Oe}\cdot\mu\text{m}$, which is close to the value found from the data of Tiller and Clark. In Fig. 8, the fit to the Tiller and Clark data is shown as a dashed line for reference. The data of Behrndt and Maddocks are plotted versus $t^{-4/3}$ in Fig. 9. The quality of the fit is not appreciably different from that of Fig. 8, as the scatter is too great for good discrimination.

In films of NiFe having compositions other than that for zero magnetostriction, H_c does not obey either of the simple relations given above. This is because film stress interacts with the magnetostriction to modify the coercive force. This is apparent from the data of Wolf (Ref. 14), who gives H_c versus thickness and composition for electrodeposited NiFe films. For all compositions having less than 13% Fe by weight, the coercive force increases with increasing film thickness. This behavior is incomprehensible on the basis of either of the theories given above. For all compositions with more than 13% Fe, the coercive force decreases with increasing thickness. Furthermore, most of Wolf's data do not fall on straight lines when plotted versus either t^{-1} or $t^{-4/3}$. However, the

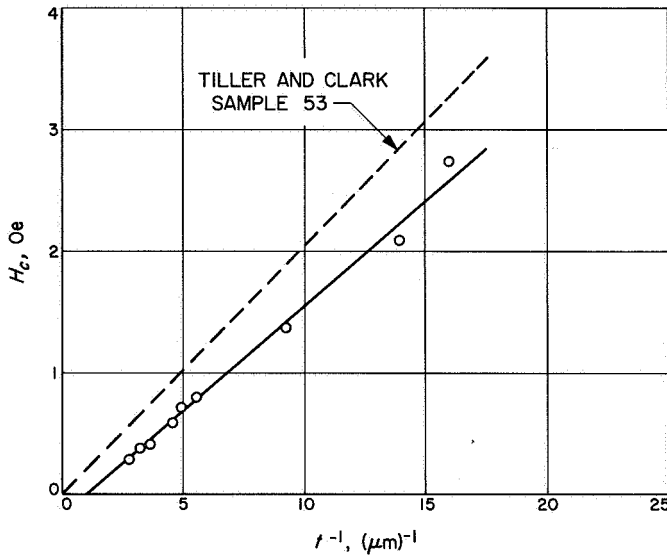


Fig. 8. H_c versus t^{-1} for permalloy (from Behrndt and Maddocks)

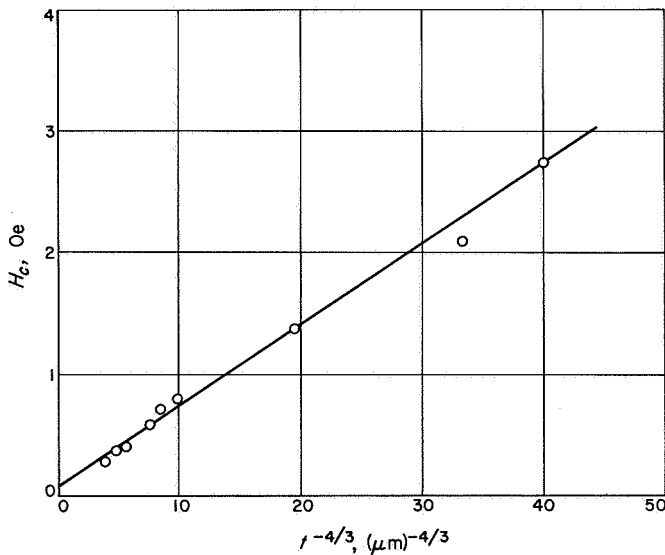


Fig. 9. H_c versus $t^{-4/3}$ for permalloy (from Behrndt and Maddocks)

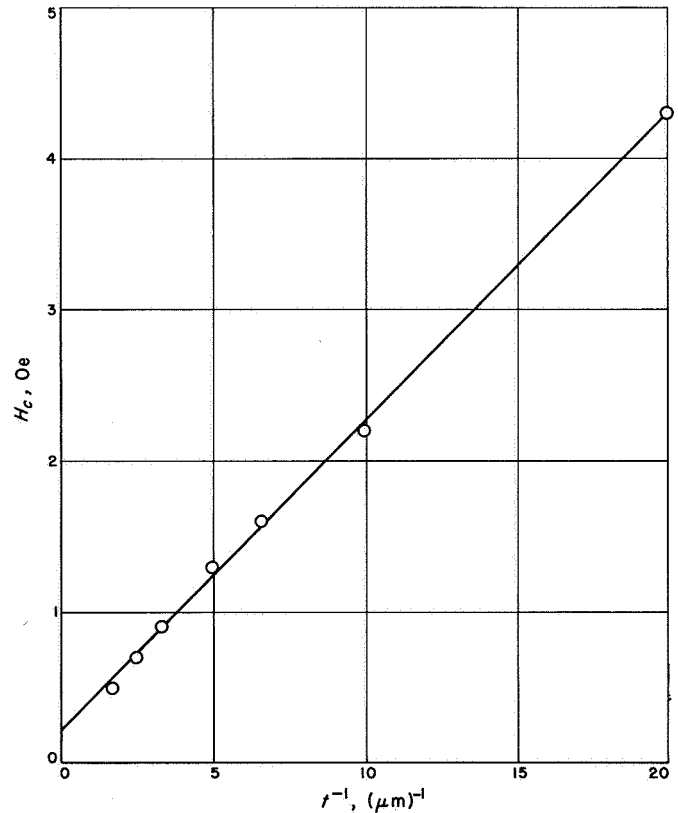


Fig. 10. H_c versus t^{-1} for electrodeposited permalloy (from Wolf)

data for 20% Fe, 80% Ni plot very nicely, as shown in Fig. 10. The slope of the straight line is about $0.20 \text{ Oe}\cdot\mu\text{m}$, which is in good agreement with values found previously. The data for the same films are shown plotted versus $t^{-4/3}$ in Fig. 11. Here it is evident that the fit is poorer, again indicating that the correct dependence is t^{-1} .

Data of Wilts³ for vapor-deposited films of 81-19 NiFe are shown in Fig. 12. In obtaining these data, no extraordinary precautions were taken in substrate preparation. The solid line is a fit to the data. The slope of this line is about $0.32 \text{ Oe}\cdot\mu\text{m}$, which indicates relatively dirty substrates. Data of Suzuki⁴ for vapor-deposited 81-19 NiFe are shown in Fig. 13. Again, substrate preparation was nominal. The straight-line fit has a slope of about $0.31 \text{ Oe}\cdot\mu\text{m}$, which is essentially the same as for Wilts' data. This is not surprising, since the two sets of data were taken in the same laboratory. An interesting feature of this figure is that H_c appears to be essentially constant for t^{-1} greater than about $12 (\mu\text{m})^{-1}$ or $t < 830 \text{ \AA}$.

³Wilts, C. H., personal communication to the author, 1967.

⁴Suzuki, T., personal communication to the author, 1967.

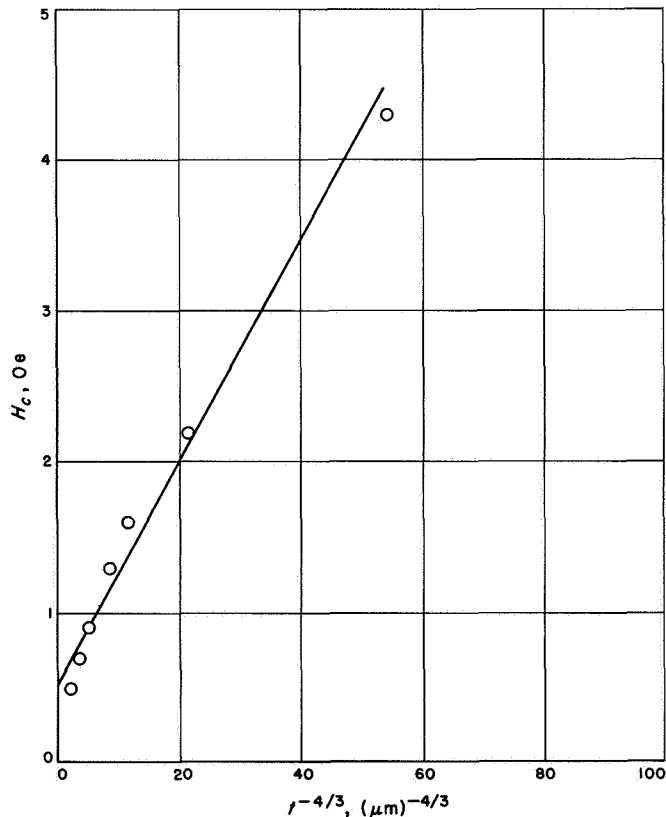


Fig. 11. H_c versus $t^{-4/3}$ for electrodeposited permalloy (from Wolf)

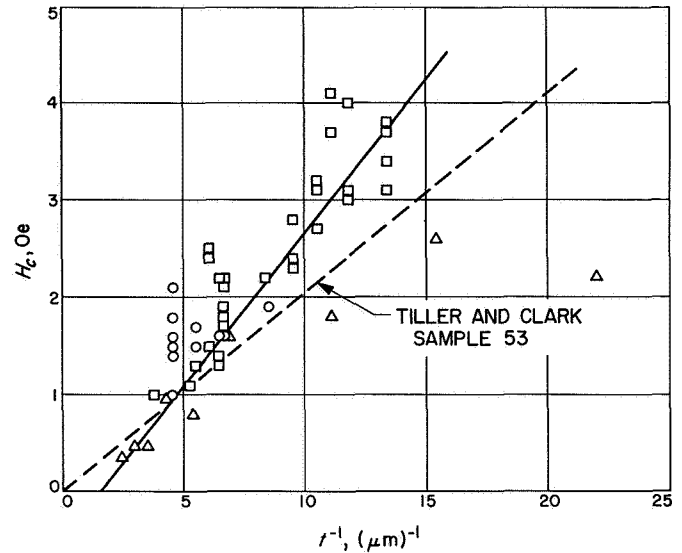


Fig. 12. H_c versus t^{-1} for permalloy (from Wilts)

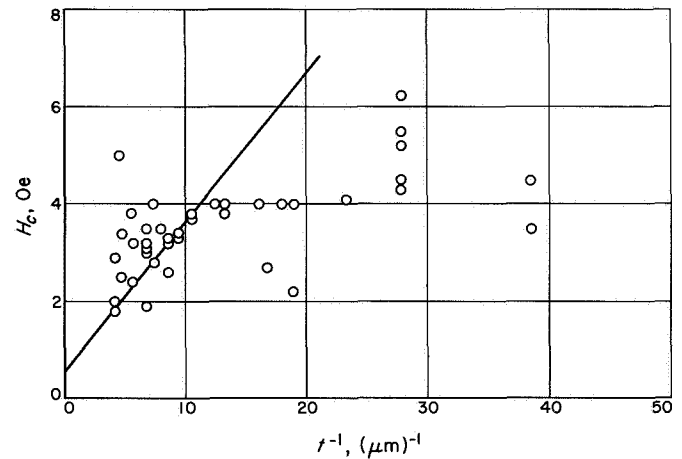


Fig. 13. H_c versus t^{-1} for permalloy (from Suzuki)

This suspicion is strengthened by the data of Middelhoek (Ref. 9) for 81-19 NiFe, shown in Fig. 14. For reasons that will become apparent, this figure is plotted to the same scale as Fig. 6. The dashed line is the Tiller and Clark data; the triangle is their highest point. The insert shows Middelhoek's first four points. It is seen that for $t^{-1} < 15 (\mu\text{m})^{-1}$ ($t > 670 \text{ \AA}$), H_c varies linearly with t^{-1} and is close to the Tiller and Clark data. The slope of this line is about $0.15 \text{ Oe}\cdot\mu\text{m}$. For films thinner than about 670 \AA , H_c is essentially constant. This is in agreement with the theory of Middelhoek, who predicts that H_c is independent of t for Néel walls. It is commonly believed that Néel walls are preferred in films thinner than 1000 \AA .

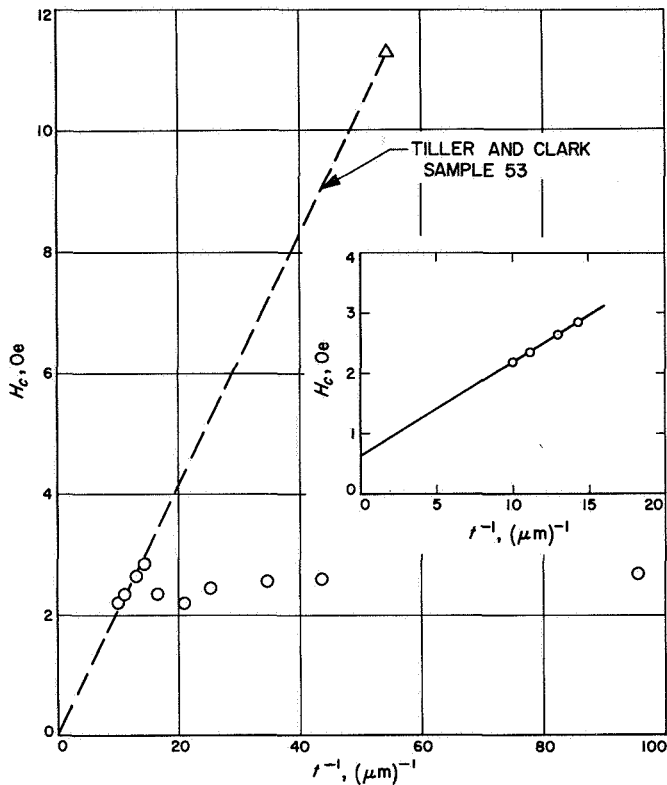


Fig. 14. H_c versus t^{-1} for permalloy showing saturation (from Middelhoek)

In order to get this result in terms of the phenomenological model presented, it would be necessary to make the plausible assumption that $f_{0s}(d_{rs} - d_{as})$ varied as t for these very thin films.

Figure 14 raises a very interesting question. The data of Middelhoek and Suzuki show that H_c varies as t^{-1} for relatively thick films, but then saturates and remains constant for the thinner films; however, the data of Tillier and Clark show no saturation. Why? Are Bloch walls stable in the thinner films prepared by etching? Or does the change in the dependence of H_c have nothing to do with the transition from Bloch to Néel walls? This would make an interesting experiment.

The effect of substrate roughness is shown by the data of Lloyd and Smith (Ref. 15). Using electrodeposited films presumably of 80-20 NiFe, they deliberately roughened the surfaces of the substrates, and then measured H_c versus t . In one set of measurements, 600 polishing paper was used; in the other, Linde B polishing compound was used. The data obtained are shown in Fig. 15; again, the dashed line is Tillier and Clark data. The slopes of the

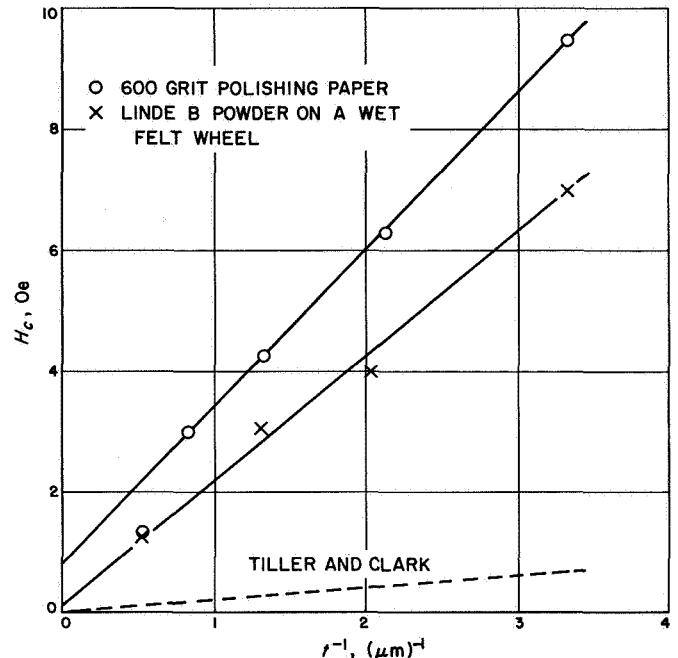


Fig. 15. H_c versus t^{-1} for permalloy on roughened substrates (from Lloyd and Smith)

straight-line fits are 2.06 and 2.58 Oe- μm , roughly ten times the value for unroughened substrates. This clearly demonstrates that the t^{-1} dependence is due to surface roughness. It also emphasizes the extreme care that must be taken with substrate preparation in order to obtain reproducible films.

Although the last term in Eqs. (1) and (5), the surface-tension term, is commonly neglected, it may be important, as has been shown. This term may be directly measured using the method of domain-tip propagation devised by Spain (Ref. 16). With this technique, a wedge-shaped domain wall is propagated down a low-coercive-force channel of width w in a high-coercive-force film by means of an externally applied field. The geometry is shown in Fig. 16. For this configuration, the coercive force for domain-tip propagation H_c is, from Eq. (5),

$$H_c = H_{cv} + C/t + \sigma_w/M_s w \quad (6)$$

This equation predicts a w^{-1} dependence of H_c on channel width. The data of Spain (Ref. 16), who has measured H_c versus w , are shown plotted versus w^{-1} in Fig. 17; the fit is good. Because the last term in Eq. (6) changes sign when the field is reversed, there are two coercive fields, one for forward and one for reverse propagation. There is also the possibility of observing a negative coercive force. This corresponds to the tip being pulled back by

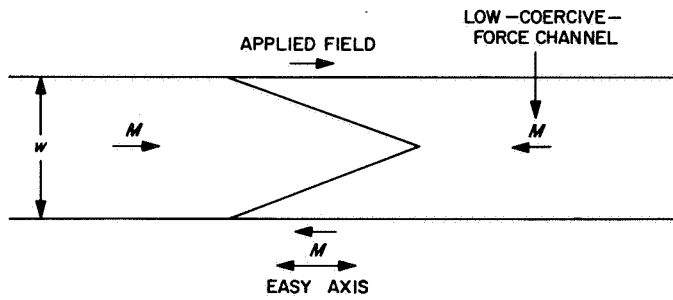


Fig. 16. Geometry for domain-tip propagation

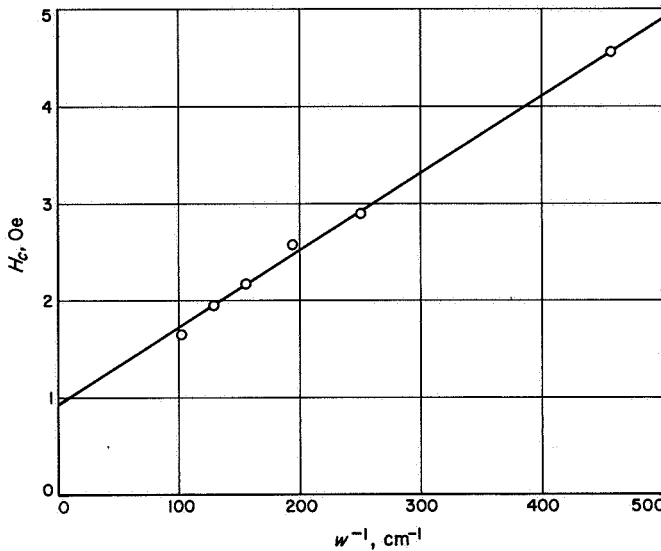


Fig. 17. Domain-tip coercive force versus reciprocal channel width

surface tension in the wall, which is left in the wake of the tip.

Although the wall is a very special type (lying on the boundary between high and low coercive-force materials), domain-tip propagation may be used to make a direct measurement of wall surface energy σ_w by means of Eq. (6). Using the measured slope of the line in Fig. 17 and the value $M_s = 800$ G, one obtains the value $\sigma_w = 6.4$ ergs/cm², which is reasonable for a 1500-Å film. To the author's knowledge, this is the only known method for measuring wall energy.

To this point, attention has been confined to films of NiFe in which the magnetization lies in the plane of the film. MnBi is a ferromagnet having a hexagonal crystal structure, very large anisotropy, and a high coercive force. The *c*-axis is the easy axis. It may be grown epitaxially on mica with the *c*-axis normal to the film.

Thus the magnetization points normal to the film. Chen (Ref. 17) has measured H_c versus t for MnBi. Figure 18 shows his data in the form of normalized coercive force H_c/H_{c0} versus reciprocal normalized thickness t/s . The straight-line fit is fairly good, and there is a large contribution from surface tension. This figure leads to the speculation that negative coercive force predicted by extrapolation of the straight line through zero H_c might be realized experimentally.

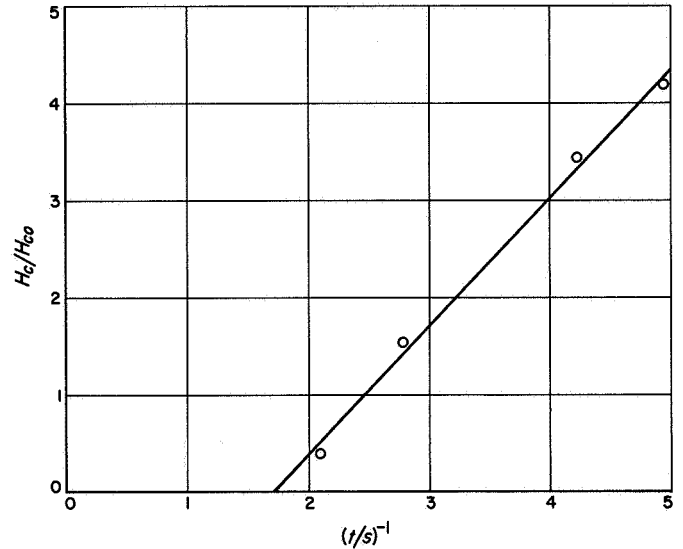


Fig. 18. Normalized coercive force versus reciprocal normalized film thickness for MnBi

Gadolinium iron garnet (GdIG) has a cubic crystal structure. Sawatzky and Kay (Ref. 18) have grown thin polycrystalline films of GdIG by sputtering. These films have large anisotropy and coercive force near the compensation temperature. The magnetization is directed normal to the film surface. The authors have measured coercive force versus film thickness. These measurements were made at temperatures that were 75°C above the compensation temperature, which was found to be a function of film thickness. All but one point of these data are plotted in Fig. 19. These points fall reasonably close to a straight line having a slope of 135 Oe- μm . The unused point, which is shown in the insert, lies nowhere near the straight-line fit. This may reflect a saturation effect such as was observed in NiFe.

5. Conclusions

The following conclusions are applicable not only to permalloy but to a large class of magnetic films. Within

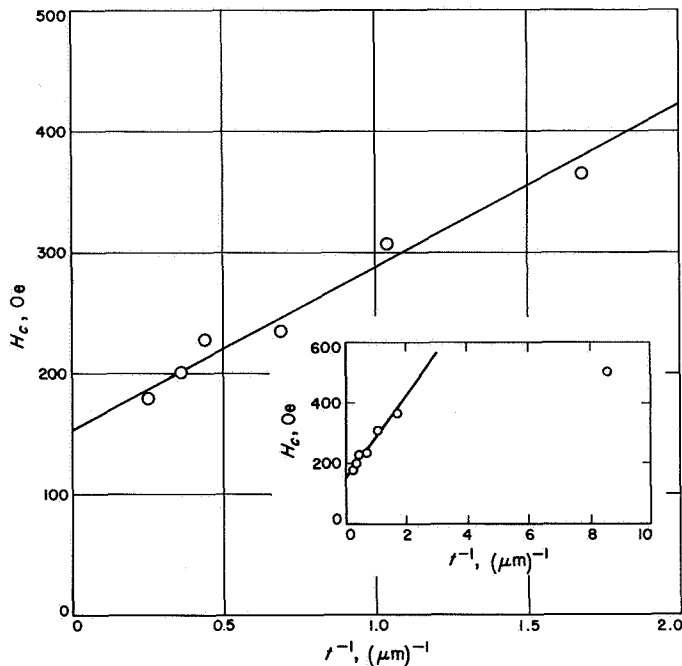


Fig. 19. H_c versus t^{-1} for gadolinium iron garnet

certain thickness ranges, the coercive force of thin magnetic films contains a term that varies as t^{-1} and not $t^{-4/3}$. The magnitude of this term depends on surface roughness. There is also a term that is independent of thickness and may be either positive or negative. In interpreting experimental results, it is necessary to take this constant term into account.

Using the method of domain-tip propagation (Ref. 16), it is possible to make a direct measurement of wall surface energy.

D. Apparent Work Function of a Cavity Emitter,

K. Shimada

1. Introduction

A thermionic cesium diode having a multiple-cavity emitter⁵ is currently being investigated as a potential means for obtaining improved power generation from thermionic diodes. The initial phase of this investigation is to determine work functions of the electrodes.

During the study, the diode was operated at relatively low cesium pressures so the saturation region in the volt-ampere curves could be clearly observed. Emitter temperatures ranged between 1200 and 2100°K, while the

cesium-reservoir temperatures were between 393 and 453°K. The work function of the cavity emitter, determined from the saturation current, was found to be nearly 0.4 eV lower than the value predicted by the Raso-Warner theory (Ref. 19). The work function of the collector, determined from the volt-ampere curves in the electron retarding (Boltzmann) region, was approximately 1.7 eV, as expected.

2. Cavity Emitter

Some years ago, several organizations⁶ made attempts to increase the total current from a thermionic emitter by drilling deep cavities into the emitter. These attempts were based upon the expectation that electron emission can be increased from the net surface area of the cavity emitter over a given projected area. However, the emitter could not have operated as expected because the dimensions of the cavity would have caused a serious reduction of collected current to result from electron space charge at the orifice of the deep cavity.

The cavity emitter designed by JPL has 19 cylindrical cavities with depths comparable to the electron-neutral mean free path. The essential features of this emitter are shown in Fig. 20. The emitter and collector materials are tantalum and molybdenum, respectively. The projected emitter area is 2 cm², 0.83 cm² of which represents the total projected area of the 19 cavities. The depth of each cavity is 0.407 mm, and the area of the cylindrical wall is 0.0302 cm². The 19 cavities, therefore, have a total side-wall area of 0.573 cm². The net surface area for electron emission is 2.573 cm², which is 29% larger than the projected area of the emitter.

3. Experimental Results

The diode under test is placed in a vacuum bell jar that operates in a pressure of approximately 10⁻⁷ torr, with the diode at elevated temperatures. The emitter temperatures T_E are observed in a blackbody hole (depth/diam = 8) with a Mikro-Werk optical pyrometer. The blackbody hole is drilled into the emitter in a direction parallel to the emitter surface. Collector temperatures T_C and cesium-reservoir temperatures T_{Cs} are measured with uninterrupted chromel-alumel thermocouples. Temperature data are acquired digitally with a four-place digital voltmeter. During those experiments that require constant T_C and T_{Cs} , temperatures are held within $\pm 0.4^\circ\text{K}$ of the desired

⁵Designed by JPL and fabricated by Thermo Electron Engineering Corporation, Waltham, Mass.

⁶Thermo Electron Engineering Corporation, Martin Company, General Motors, and others.

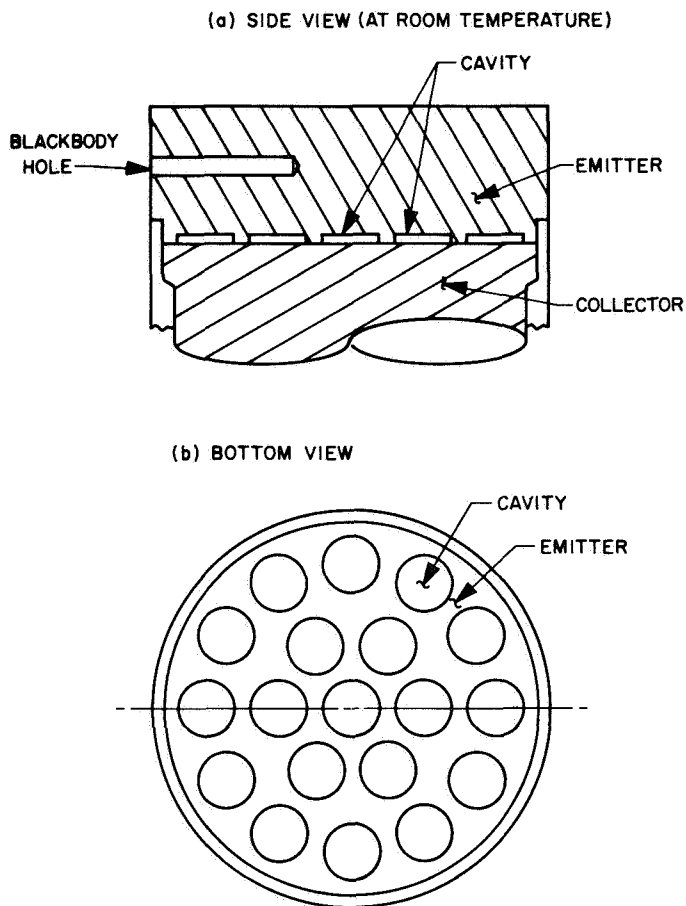


Fig. 20. Cavity emitter: (a) side view; (b) bottom view

values by proportional temperature controllers. Volt-ampere curves are drawn directly on an X-Y recorder. The diode voltage is measured across two potential terminals located on the diode.

The saturation current is determined from the intersection of two lines on the volt-ampere curve, one representing the saturation line and the other the Boltzmann line. Although the leakage current across the diode was negligible for the range of temperatures covered, it was subtracted from the measured values as required. The saturation currents thus obtained are plotted, as shown in Fig. 21, as a function of reciprocal emitter temperatures ($10^3/T_E$). The result is a family of S-curves. Straight lines representing saturation currents obtained from emitters with work functions of 4.5 and 4.3 eV are superimposed in Fig. 21 (the current values along these lines are calculated on the assumption of 2 cm^2 for the emitter area). The uncesiated emitter work function (small $10^3/T_E$) appears, from this figure, to be 4.5 eV, which is slightly higher than expected. Although values as high as 4.9 eV

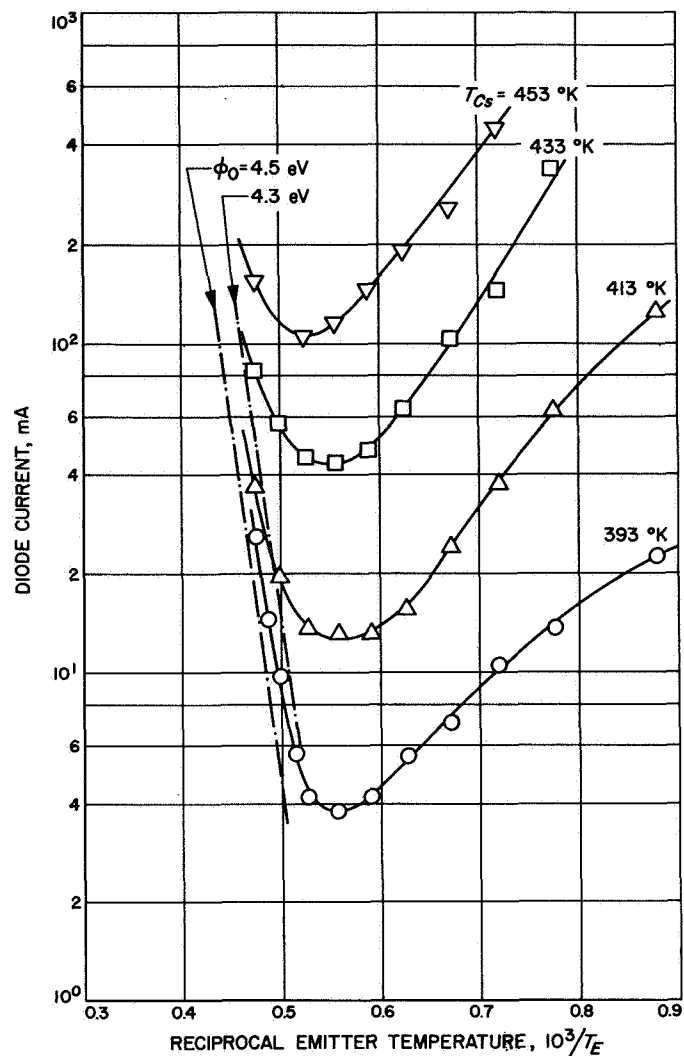


Fig. 21. S-curves for various cesium-reservoir temperatures T_{Cs}

have been reported for the [110] plane of tantalum (Ref. 20), the handbook value is 4.19 eV.

The cesiated-surface work functions were calculated from the saturation currents in Fig. 21. The current density was determined from a projected emitter area of 2 cm^2 , not from the net area 2.573 cm^2 of the cavity emitter. The Richardson constant (A -value) of $120 \text{ A/cm}^2 \cdot \text{K}^2$ was also used in these calculations. Because of the assumptions concerning surface areas and the uniqueness of the emitter construction, the work functions thus determined are the *apparent* work functions; however, these are satisfactory for comparing cavity emitters with ordinary flat emitters.

From the measured currents for various emitter and cesium-reservoir temperatures (Fig. 21), a Rasor-Warner

plot for the emitter work function is obtained. These results are shown in Fig. 22. The apparent work functions for various temperature ratios T_E/T_{Cs} fall on a well-defined curve; however, this curve deviates considerably from any one of the theoretical curves obtained from the Rasor-Warner theory. Since the uncesiated work function ϕ_0 must be 4.5 eV to be consistent with the results shown in Fig. 21, the measured emitter work function is compared with the theoretical Rasor-Warner plot for $\phi_0 = 4.5$ eV.

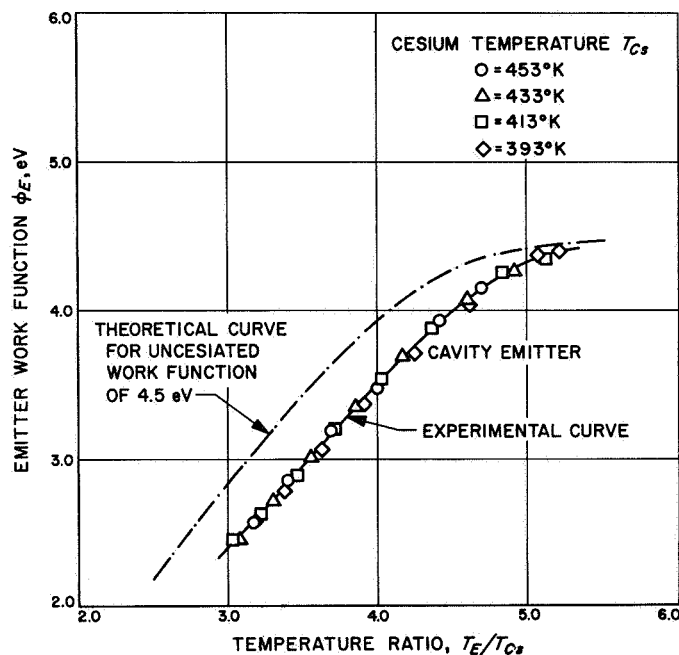


Fig. 22. Apparent work function of cavity emitter

This comparison indicates that the same emitter work function can be achieved with the cavity emitter at a temperature ratio T_E/T_{Cs} , which is significantly larger than for flat emitters. For example, the same emitter work function can be obtained at $T_E = 1800^\circ\text{K}$, $T_{Cs} = 400^\circ\text{K}$ in a diode with a flat emitter as at $T_E = 1800^\circ\text{K}$, $T_{Cs} = 367^\circ\text{K}$ in a diode with the cavity emitter. The cavity emitter thus achieves the same emitter work function (apparent) as the conventional flat emitter at a 10% lower cesium-reservoir temperature.

The work function of the collector is determined from volt-ampere curves obtained in a deeply electron-retarding region, such as those shown in Fig. 23. The diode current varies logarithmically with voltage V_0 for voltages less than -1 V. In an electron-retarding region, the current density J can be expressed by (SPS 37-28,

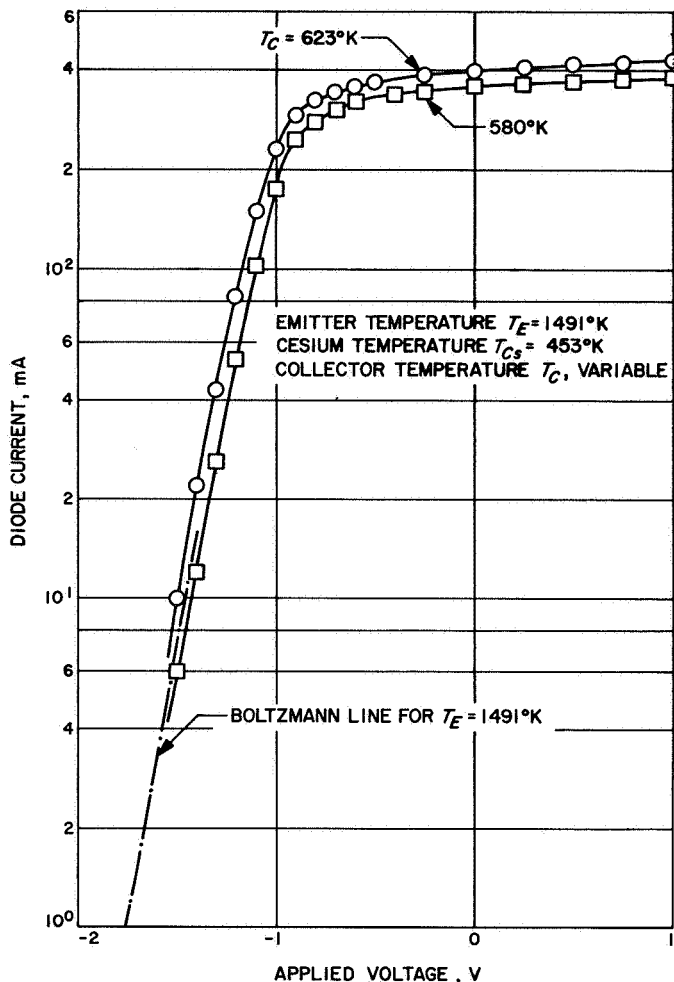


Fig. 23. Volt-ampere curves in electron-retarding region

Vol. IV, pp. 20-25):

$$J = AT_E^2 \exp[-e(\phi_c - V_0)/kT_E] \quad (1)$$

where

$$A = 120 \text{ A/cm}^2 \cdot \text{K}^2$$

$$\phi_c = \text{collector work function, eV}$$

$$k = 1.38 \times 10^{-23} \text{ J/}^\circ\text{K}$$

$$e = 1.6 \times 10^{-19} \text{ C}$$

Equation (1) may also be written as

$$\ln J = \ln(AT_E^2) - \frac{e\phi_c}{kT_E} + \frac{eV_0}{kT_E} \quad (2)$$

For $T_B = 1491^\circ\text{K}$, one obtains

$$\ln J = 19.38 - 7.78 \phi_c + 7.78 V_0 \quad (3)$$

Therefore, the log of the current density varies linearly with the voltage V_0 . Such a dependence is clearly shown in Fig. 23, where a current density of 13 mA/cm^2 (projected area of the emitter = 2.0 cm^2) at $V_0 = -1.3 \text{ V}$ is observed. This current is obtained at a collector temperature of 580°K and a cesium-reservoir temperature of 453°K . Substitution of the above current and voltage values into Eq. (3) allows calculation of the collector work function ϕ_c . The result is $\phi_c = 1.75 \text{ eV}$ at $T_c/T_{cs} = 1.28$.

Alternatively, the collector work function determined from the knee of the volt-ampere curve (Fig. 23) is found to be 1.77 eV , with $\phi_B = 2.72 \text{ eV}$ and the voltage at the knee = -0.95 . Similar calculations for $T_c = 623^\circ\text{K}$ yield comparable results. These results, together with the published molybdenum work functions (Ref. 21), are tabulated in Table 1.

Table 1. Collector work function for $T_B = 1491^\circ\text{K}$, $T_{cs} = 453^\circ\text{K}$, and for variable T_c

$T_c, ^\circ\text{K}$	Collector work function $\phi_c, \text{ eV}$		
	Retarding plot	Knee method	Published value
580	1.75	1.77	1.75
623	1.68	1.67	1.67

The collector work functions are well within the expected values. The work functions determined from the retarding plot agree remarkably well with the values determined from the knee method. Since the knee method depends on the emitter work function, as well as on the voltage at the knee, the agreement implies the validity of the emitter work-function measurement.

4. Interpretation of Results

The collector work function of approximately 1.7 eV is quite reasonable. The apparent work function of the cavity emitter is nearly 0.4 eV lower than expected for the same temperature ratio T_B/T_{cs} . Conversely, the same work function can be achieved at values of T_{cs} , which are nearly 10% smaller than expected. One should note that the projected area of the emitter (2 cm^2) is used in determining the current density. If the net emitter area is used, the work functions will be only slightly larger ($\sim 0.04 \text{ eV}$) than those shown in Fig. 22. This small difference justifies the use of either the projected or net emitter area.

The temperature ratios T_B/T_{cs} chosen for the experiments are such that the electron emission from the emitter is occurring under ion-rich conditions. Thus, the measured saturation current is indeed the temperature-saturated current of the cavity emitter. Consequently, apparent work functions determined from the saturation current are not modified by the electron-space-charge sheath adjacent to the emitter, such as exists in a diode operating under electron-rich conditions. Also, the current must not be reduced by electron scattering, since the electron mean free path λ_e is larger than the interelectrode gap d . (The mean free path λ_g of cesium atoms is also larger than d .)

The fact that the work function of the cavity emitter is 0.4 eV lower than expected for a given T_B/T_{cs} can be accounted for if the arrival rate of cesium at the emitter is considerably larger than predicted by the Rasor-Warner theory. This may be the case—since the cavity emitter is operating under a condition $\lambda_g > d$ that prevents the cesium pressure from being determined by the equilibrium vapor pressure at the cesium-reservoir temperature.

To gain further insight into the problem, similar experiments will be carried out with another diode having multiple cavities of different geometry.

E. Applications of Superconductivity in Spacecraft, Part II, P. V. Mason

1. Introduction

This report on the applications of superconductivity in spacecraft concludes the review that was begun in SPS 37-44, Vol. IV, pp. 57-59, and which will be formally documented in a technical report.⁷

The earlier portion covered (1) active and signal handling devices, including switching devices, linear amplifiers, and parametric amplifiers; (2) memories, both random active and associative; and (3) high-field solenoids for spacecraft shielding and fields for masers and other devices.

The applications as categorized here represent a slight modification of the outline given in SPS 37-44, Vol. IV. Briefly reviewed in this paper are the following:

⁷Currently being prepared for publication by the author.

- (1) High-Q circuits and transmission lines.
 - (a) Selective circuits.
 - (b) Data transmission and compression devices.
- (2) Power generation and handling.
 - (a) Generators.
 - (b) Power conditioners (called converters in Part I).
 - (c) Energy-storage devices.
- (3) Sensors.
 - (a) Magnetometers.
 - (b) Radiation detectors.
 - (c) Gyroscopes and accelerometers.
 - (d) Voltage-to-frequency converters and vice versa, and voltage detectors (the latter represents an addition to the earlier outline).
 - (e) Alpha-particle detectors.
- (4) Propulsion.

2. High-Q Circuits and Transmission Lines

a. Selective circuits. Although superconductors show ac resistance, the Qs of superconducting circuits are high enough to be of engineering interest. For a lumped inductor-capacitor circuit, an unloaded Q of 3.7×10^6 has been measured at 27 MHz and 4.2°K. A theoretical Q of 770×10^6 was calculated, indicating that the losses were due to other causes, presumably dielectric and radiation losses. Thus, large improvements seem possible by suitable redesign.

A tuner for a receiver, built for the Army Signal Corps, using a lumped circuit, was tunable over a 6- to 21-MHz range, with Q ranging from 350×10^3 to 600×10^3 . This performance could be improved considerably if wideband tuning were not necessary.

At higher frequencies, losses are higher; however, advantage may be taken of the cavity form of construction to avoid dielectric and radiation losses. As an example, one group measured a Q of 5×10^9 at 12 GHz.

Such high-Q circuits may be used in ground receivers to separate transmitted and received signals. For many purposes they must compete with the narrowband phase-locked loop now widely used in spacecraft communication. It seems unlikely, particularly on board a spacecraft, that such cavities could by themselves justify the necessary refrigeration and dewar systems. If the low-temperature environment were already present, however, superconducting cavities might well be competitive.

b. Transmission lines. Superconducting transmission lines have extremely low attenuation; however, in thin-film form the propagation velocity is a function of temperature and applied magnetic field—facts that suggest the possibility of manipulation of data.

The low attenuation makes possible the transmission of signals with large delays and little distortion. A typical result was the transmission of a pulse with 0.4 ns rise time over 30 m of 50-Ω, 0.1-in.-diam coaxial superconducting cable (about 150-ns delay), with no measurable distortion or loss. A steady-state attenuation of 6 dB over 30 m was measured at 10 GHz. In the latter case, most of the attenuation was attributed to short, connecting lengths of the line that could not be kept superconducting. Performance was much better than for a room-temperature 0.5-in.-diam Spiraline cable, a type specially designed for low loss and low distortion.

Thin-film transmission lines may also be used for pulse transmission and storage. In an experiment by the author, a 2-ns pulse stored on a 6.5-cm, 7-mΩ thin-film line decreased only 50% in amplitude after 350 round trips; i.e., 22 m and 1-μs delay. About half the loss resulted from external loading at the ends.

An advantage of thin-film lines is that the propagation velocity and attenuation depend on magnetic field, permitting manipulation of a pulse in storage. They also depend on temperature; very slow velocities—and hence, large delays—can be obtained near the critical point, but only at the expense of high attenuation.

Possible uses of transmission lines include pulse transmission over long lines, pulse storage, delay lines, shift registers, data compressors and expanders, and matched filters. Nearly lossless power transmission is also possible, but does not appear economical, except for very large amounts of power over long distances (100 GW over 1000 km).

In spacecraft application, superconducting lines appear useful primarily as components of a larger superconducting system, such as a large memory or computer.

3. Power Generation and Handling

All applications of superconductors to power systems aim at improving efficiency by reducing losses, and all face the problem that the inevitable small losses at superconducting temperatures are greatly magnified by the

refrigeration system. Typically, 500 to 1000 W of refrigeration power are required to remove 1 W at 4.2°K and reject it at 300°K. Since the ratio of saved energy to refrigeration energy increases with size, nearly all power applications are economical only for much greater powers than are needed by present spacecraft.

Three major problems limit design. First, the current lead-ins to the cold space generate and conduct considerable heat. Second, ac losses in magnetic materials preclude their use in the cold space. Third, hard superconductors exhibit ac losses which must be carefully considered in design.

a. Generators. Superconducting generators become economical in the megawatt range. Several designs for 1-MW units have been made; an experimental 50-kW unit is under construction, and several 1- to 5-kW units have been built. In one particular megawatt design, there was a factor of 10 weight and volume savings over conventional designs. Losses were 60 W at 10°K, requiring about 50 kW for refrigeration.

The most likely application of superconducting generators is in conjunction with large chemical, solar, or nuclear turboelectric power systems, where saving weight and size would be important. The availability of power at a rotating shaft, compared with that from an electric source, would also ease the refrigeration problem greatly, since a major part of the weight and power wastage of present refrigeration designs is in the electric motor drive and associated power-conditioning equipment.

b. Power conditioners. Several power-conditioning devices that use superconductors are proposed: low-loss transformers, transmission lines, inverters, converters, and rectifiers. However, because conventional methods are already efficient, the amount of power handled must be very large in order to justify the expense, size, weight, and power consumption of refrigeration and insulation involved in converting to the new devices.

Use of the proposed transformers is additionally difficult because ac hysteresis losses in magnetic materials are so high that they cannot be immersed in the cold space; hence, leakage fluxes will be high. Transformers of 15-kW size have been built, but those less than megawatt size do not appear economical.

Superconductive and related low-temperature dc-dc converters or dc-ac inverters offer some promise when used with such low-voltage devices as thermoelectric

sources, where the relatively low forward-voltage drops, compared with semiconductor devices, increase efficiency. Again, however, the refrigeration power needed makes such devices suitable only for very high power.

The devices take several forms: One is simply a high-power form of cryotron switch; another uses superconductive leads in conjunction with a magnetoresistive switching element. Problems of heat dissipation during switching are severe.

c. Energy-storage devices. Energy storage in the magnetic field of a superconducting magnet has been proposed. With fields possible at present (about 100,000 to 150,000 G), an energy-storage density of about 0.3 Wh/in.³ is possible. This number is based only on the magnetic field volume. The energy density of the entire system would be lower by at least a factor of 10. The weight of the magnet and dewar system (not including the refrigeration) would be at least 1000 lb, leading to an overall density of not more than 20 Wh/lb. Since rechargeable chemical batteries can yield figures of 6 Wh/in.³ and 60 Wh/lb, use of superconductors is not practical for the storage of large amounts of energy. Some units have been built to store energy for very quick release; e.g., for laser flash tubes (7 kJ) and for an electromagnetic hammer for smoothing sheet metal (20 kJ, 10⁶-A peak).

Overall, superconductive devices do not seem good candidates for energy storage for two reasons: (1) batteries serve better for long-term storage, and (2) capacitor banks can provide high-peak currents more economically, except for very large amounts of energy.

4. Sensors

a. Magnetometers. With superconducting point-contact and Josephson junctions, magnetic fields and field gradients can be measured far more accurately than by any other method. Relatively simple devices have been built with sensitivities of 10⁻⁹ G; those more complex can have sensitivities of 10⁻¹² G.

The basic output signal of such a magnetometer is periodic in the magnetic field, with a period inverse to the contact area. If two junctions connected by superconductors are used, the period varies inversely as the area enclosed by the superconductors. Since the devices operate when the contacts are separated by as much as 1 m, the period can be made extremely small.

By measuring the periodic changes digitally, the magnetic field can be measured in quantum units of 10^{-9} G or smaller. By placing the junction inside a solenoid, and using it as a null sensor to generate a feedback current to cancel the field at the junction, a current or voltage accurately proportional to field can be obtained. Limitations of accuracy are probably set by noise in the feedback amplifier and accuracy of voltage or current measurement, but these have not yet been thoroughly studied.

Measurements to an accuracy of 10% of a flux quantum (i.e., 10^{-10} G) have been reported, and measurements to 10^{-11} or 10^{-12} G seem quite possible. Also, measurements of 10^{-7} G in a 2000-G field have been made.

At present, possible applications of such accurate and sensitive devices in spacecraft seem to be primarily scientific; e.g., mapping of weak interplanetary magnetic fields.

b. Radiation detectors. Extremely sensitive detectors at microwave and infrared frequencies, which take advantage of the low noise of the cryogenic environment, have been proposed. The simplest of these use the rapid temperature-induced transition from superconducting to normal state. If a superconductor (usually a film for fast response) is biased to the transition region, then the addition of a small amount of radiant energy will cause a measurable change in resistance with reasonably rapid response time. An infrared detector with a noise equivalent power of 10^{-11} W/Hz of bandwidth with a response time of 10^{-8} s is feasible.

Even more sensitive devices can be made using the ac Josephson junction. A typical result is the sensing of 300- μ m infrared radiation with noise-equivalent power of 5×10^{-13} W at 1-Hz bandwidth and with a response time better than 10^{-6} s. Similar, but more complicated, detectors have been used in the microwave and millimeter range.

Superconductors appear unequalled as detectors in the millimeter and far-infrared range, down to approximately a few hundred microns. If such ranges are of scientific or engineering interest, it seems possible that fairly small, lightweight refrigeration systems could be built, since the heat load would be very small.

c. Gyroscopes and accelerometers. Both JPL and General Electric have had large research programs to

develop superconducting gyroscopes. Both used the diamagnetism of a superconductor to support a rotating mass in a magnetic field, although the design forms differed. Both demonstrated the feasibility of constructing a unit with random drifts of the order of 0.005 deg/h or better, and improvement to 0.001 deg/h seems possible. At present, however, there seems to be no requirement on a spacecraft for such accuracy; if there were, the competing electrostatically supported gyro would probably be used because of its relative simplicity.

The suggestion has been made that, since disturbance torques are acceleration dependent, a superconducting gyroscope operating in an unaccelerated spacecraft could have drifts as low as 0.001 deg/yr. Although this would allow a test of general relativity, it is still difficult to counter the argument that the stars provide the best angular reference for spacecraft guidance and control.

Some work has been done on accelerometers and gravimeters, using diamagnetic suspension of a proof mass. Gravity tides as small as 10^{-9} g have been detected. Brownian forces of 10^{-10} or 10^{-11} g probably set the limit of sensitivity. A dynamic range of 10^5 seems possible. Such an accelerometer may have application in an ion-engine-propelled spacecraft where 10^{-9} -g resolution is required. Again, however, electrostatic accelerometers would provide serious competition.

d. Voltage-to-frequency converters and vice versa, and voltage detectors. The Josephson junction is so sensitive to magnetic fields that an extremely small dc current in an adjacent superconducting wire may be detected. Since the wire has some self-inductance, a series resistor must be used to reduce the time constant. Thus, sensitivity and response time are competitive. Typically, 10^{-14} V may be detected with a series resistance of 10^{-8} Ω and a response time of 1 s.

The ac Josephson effect takes two forms. If a dc voltage is impressed across a Josephson junction, it emits radiation at a frequency of $\nu = 2eV/h$ (about 484 MHz/ μ V) within about 4 parts/ 10^6 , an accuracy limited by the present accuracy of voltage measurement. Thus, the device can be used for a voltage-to-frequency converter of unprecedented accuracy, not only for telemetering purposes, but perhaps also as an initial step in analog-to-digital conversion of data.

The inverse effect also occurs: if a Josephson junction is irradiated with a frequency ν , then dc voltages of

value $V = nh\nu/2e$, where n is an integer, appear across the junction. Thus, since frequency can be measured and stabilized to a higher accuracy than any other physical parameter, generation of highly precise voltages is possible. Indeed, it appears likely that this effect or the inverse will be used to define a new international standard of voltage.

Although many practical technological problems stand in the way, it appears that Josephson devices offer unique possibilities in voltage and frequency interconversion, and if such high accuracy is needed, superconductors must be used.

e. Alpha-particle detectors. If a narrow, superconducting, thin film is held near its critical temperature with a current flowing through it, an energetic particle hitting it can nucleate a normal region across the film, which rapidly collapses back to the superconducting state. Thus, a short voltage pulse is developed, whose length can be varied by choice of geometry and operating temperature. Such devices show promise of high resolution and high sensitivity; their primary application would be in scientific measurements.

5. Propulsion

Several schemes for propulsion involve acceleration of charged particles, as in a linear particle accelerator. The Stanford Linear Accelerator Group has made detailed studies of the use of superconducting cavities and drift tubes in high-energy accelerators which show that the savings in power and RF equipment expense far outweigh the extra expense of providing the low-temperature environment. It seems possible that a similarly detailed study of a particle acceleration engine would justify the use of superconductors. To our knowledge, no such study has been made.

6. Summary

To summarize, the various applications of superconductors are classified by the conditions under which they would be useful (see Table 2).

Table 2. Uses of superconductors

Unique properties for which superconducting devices are mandatory	
Unit	Condition
Linear amplifiers } Parametric amplifiers }	If extremely low noise amplifiers are necessary
Spacecraft shield	Probably necessary only for manned spacecraft
Magnetometers	If 10^{-9} to 10^{-12} G sensitivity and/or accuracy are needed
Voltage converters	If sensitivity of 10^{-24} V is needed
Voltage-to-frequency converters	If high accuracy is needed
Applications competitive with conventional techniques in certain areas; justified by necessary refrigeration	
Random access memories	If more than 10^9 bits are needed
Associative memories	If large amounts of associative processing are required
Applications competitive with conventional techniques; only justified if refrigeration is required for other purposes	
Switching devices	
Linear amplifiers	
Parametric amplifiers	
Fields for masers and other devices	
Selective circuits	
Data transmission and compression devices	
Radiation detectors	
Gyroscopes and accelerometers	
Alpha-particle detectors	
Application probably not justified on board spacecraft because of the high cost of refrigeration	
Generators	
Power conditioners	
Energy-storage devices	

References

1. Mayer, L., "Curie-Point Writing on Magnetic Films," *J. Appl. Phys.*, Vol. 29, p. 1003, 1958.
2. Mayer, L., "Magnetic Writing With an Electron Beam," *J. Appl. Phys.*, Vol. 29, p. 1454, 1958.
3. Chen, D., "Direct Observation of Domain-Wall Movements in MnBi Films," *J. Appl. Phys.*, Vol. 38, p. 1309, 1967.
4. Mayer, L., "Magnetic Writing With an Electron Beam," *J. Appl. Phys.*, Vol. 29, p. 1454, 1958.
5. Chang, J. T., Dillon, J. F., Jr., and Gianola, U. F., "Magneto-Optical Variable Memory Based Upon the Properties of a Transparent Ferrimagnetic Garnet at its Compensation Temperature," *J. Appl. Phys.*, Vol. 36, p. 1110, 1965.
6. Soohoo, R. F., *Magnetic Thin Films*, p. 141. Harper & Row, Publishers, New York, 1965.
7. Néel, L., "Remarks on the Theory of the Magnetic Properties of Thin Films and Fine Grains," *J. Phys. Radium*, Vol. 17, p. 250, 1956.
8. Behringer, R. E., and Smith, R. S., "The Influence of Demagnetization and Anisotropy Energy on Bloch Wall Thickness and Coercive Force in Thin Films," *J. Franklin Inst.*, Vol. 272, p. 14, 1961.
9. Middelhoek, S., *Ferromagnetic Domains in Thin Ni-Fe Films*. Drukkerij Wed. G. Van Soest N.V., Amsterdam, 1961.
10. Rodbell, D. S., and Bean, C. P., "Some Properties of the Coercive Force in Soft Magnetic Materials," *Phys. Rev.*, Vol. 103, p. 886, 1956.
11. Baldwin, J. A., Jr., "A Model for the Interaction of Magnetic Domain Walls With Crystalline Imperfections," *J. Appl. Phys.*, Vol. 38, p. 501, 1967.
12. Tiller, C. O., and Clark, G. W., "Coercive Force Versus Thickness for Thin Films of Nickel-Iron," *Phys. Rev.*, Vol. 110, p. 583, 1958.
13. Behrndt, K. H., and Maddocks, F. S., "Influence of Substrate Processing on the Magnetic Properties and Reproducibility of Evaporated Nickel-Iron Films," *J. Appl. Phys.*, Vol. 30, p. 276S, 1959.
14. Wolf, I. W., "Composition and Thickness Effects on Magnetic Properties of Electrodeposited Nickel-Iron Thin Films," *J. Electrochem. Soc.*, Vol. 108, p. 959, 1961.
15. Lloyd, J. C., and Smith, R. S., "Structural and Magnetic Properties of Permalloy Films," *J. Appl. Phys.*, Vol. 30, p. 274S, 1959.
16. Spain, R. J., "Controlled Domain Tip Propagation, Part I," *J. Appl. Phys.*, Vol. 37, p. 2572, 1966.
17. Chen, D., "Flux Reversals in Single Crystal MnBi Films," *J. Appl. Phys.*, Vol. 37, p. 1468, 1966.

References (contd)

18. Sawatzky, E., and Kay, E., "Magnetic Properties of Polycrystalline GdIG Films," presented at the IEEE International Conference on Magnetism (INTERMAG), April 5-7, 1967, Washington, D. C. (Proceedings to be published).
19. Rasor, N., and Warner, C., "Correlation of Emission Processes for Adsorbed Alkali Films on Metal Surfaces," *J. Appl. Phys.*, Vol. 35, p. 2589, 1964.
20. Webster, H., "Work Function of 110 Plane of Tantalum as a Function of Cesium Coverage," in *Thermionic Conversion Specialists Conference, Gatlinburg, Tennessee, October 7-9, 1963*, pp. 187-191 (published by IEEE).
21. Merra, S., "Test Results of Solar Thermionic Converters Using Rhenium Emitters," in *Thermionic Conversion Specialists Conference, Cleveland, Ohio, October 26-28, 1964*, pp. 350-359 (published by IEEE).

IX. Electronics Parts Engineering

ENGINEERING MECHANICS DIVISION

A. Channeling in Transistors and its Detection,

R. A. Summers and W. B. Bartel

Channeling or surface-induced inversion is the most common failure mechanism in low-level transistors. The results of channeling are manifested by large increases in leakage in PNP transistors or a large decrease in gain in NPN transistors. A typical PNP collector-to-base leakage, which is specified as 10 nA (1×10^{-8} A), can rise to the 100- μ A or 1-mA (10^{-3} A) level as a result of channeling. This high leakage is usually a saturation current increase; that is, it does not vary appreciably with voltage.

Channeling is a particularly insidious failure mechanism; a transistor which may have had a channel induced during processing or testing could have "cured" a link within the channel and met specifications during testing

or partial screening, only to fail catastrophically when placed in a circuit with a moderate impressed voltage.

Channeling is the result of the alignment of ions on the surface or within protective oxide coating of the transistor. This alignment is caused by the high field strength at the transistor junction, which is in the order of hundreds of thousands of volts per inch (Figs. 1 and 2)¹. The resulting aligned ions induce an extension of the transistor base region, which in turn moves the transistor junction with

¹P⁺ = heavily doped P; P⁻ = lightly doped P; N⁺ = heavily doped N; N⁻ = lightly doped N.

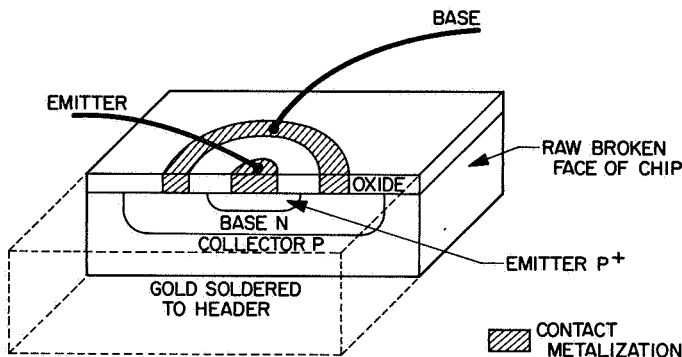


Fig. 1. Diagram of planar construction of a modern PNP transistor

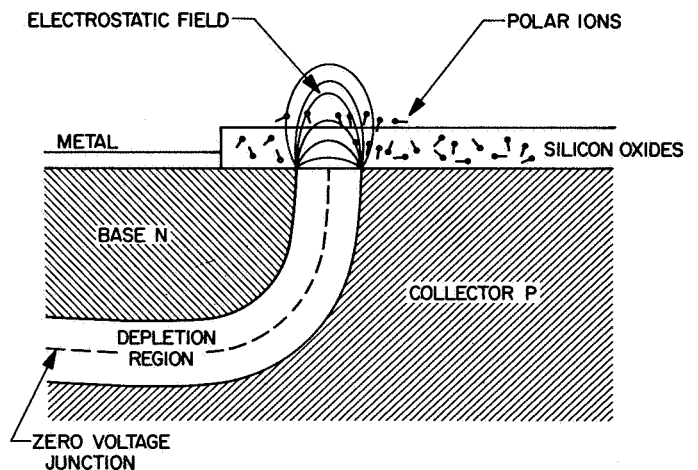


Fig. 2. Enlarged transistor collector-base junction under bias, showing ion alignment by the electrostatic field

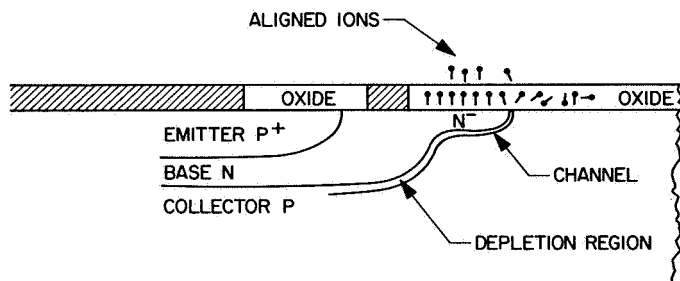


Fig. 3. Channel formation

its high field out further (Fig. 3). This progresses until the ion supply is depleted or it meets a defect in the silicon or until the junction is at the raw unpassivated edge of the transistor. At either the defect or at the raw edge, the channel is effectively shorted out (Fig. 4). The channel is usually current-limited due to the field effect nature of the thin base extension.

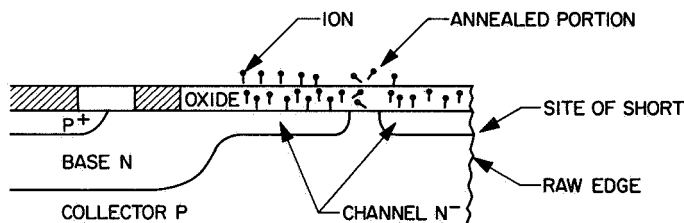


Fig. 4. Fully grown channel interrupted by spot annealing

The channel takes different forms in NPNs and PNPs because the predominant ion formation is positive, which tends to induce P material to N material. In PNPs, this results in an extension of the base region into the collector. In NPNs, the emitter tends to extend into the base region, creating a degenerate diode which shunts out the carriers; hence, a decrease in gain is obtained.

In building transistors, some ion contamination is unavoidable; however, by using good workmanship techniques the number of "clean" transistors can be raised to an economic level. There are design techniques, such as the annular process, hard oxide, and field relief electrode, which will also combat channeling (Fig. 5). The oldest technique, the annular process, does not attempt to reduce the channel formation; indeed, a channel is deliberately induced, then it is terminated by a special diffusion of a guard ring around the base of the transistor. The guard ring is a heavily doped P-type ring in the lightly doped P collector. The theory is sound; however,

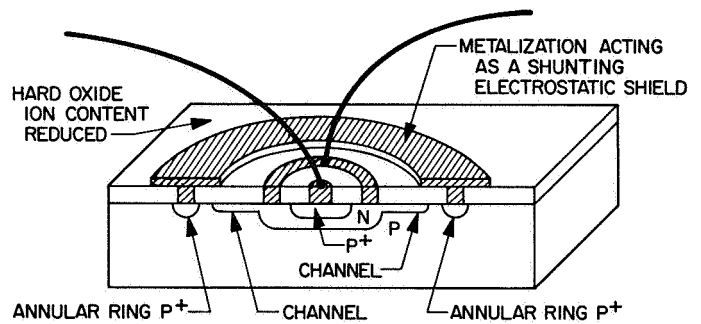


Fig. 5. Channel-stopping techniques in a PNP transistor

from 1 to 30% of the parts using only the annular ring will channel. Hard or dense oxide which reduces and immobilizes the ions is also a relatively successful technique.

The field relief electrode, which appears to be the most successful technique, depends upon a conductive surface coating to electrostatically shunt out the junction field. This conductive coating is usually the same aluminum metalization as the base and emitter contacts. The coating is usually grounded to the collector region by an annular ring.

PNP transistors made with all three processes are relatively free of destructive channels. However, a defective lot of transistors is occasionally made and does reach the customer. Because of the catastrophic nature of channeling, all low-level parts for spacecraft use should be screened specifically for channeling. The most effective means of screening for channeling is to deliberately stress the parts to accelerate the growth of channels in inherently defective transistors to the point where the existence of the channel is apparent. This is done by performing a test called high-temperature reverse voltage or high-temperature back bias. The test consists of placing a reverse voltage (normal for collector-to-base operation) as high as reasonably possible on the transistor and elevating the temperature of the transistor to 100 to 200°C. The normal test time is from 12 to 200 h. Special care must be taken during test turn-off and transistor measurement to avoid disrupting a portion of the grown channel. The transistor measurements must be made as soon as possible after test turn-off since some forms of channeling anneal rapidly without bias.

A major point of conflict about the back-bias test was the temperature at which the test should be performed. One school of thought was that the optimum temperature was about 125°C since the channels would be disrupted

by thermal agitation as rapidly as they were formed by going to a higher temperature. Another point of contention was the voltage level. It was felt by some that since the depletion region widens as the applied voltage increases, the field strength remains relatively the same or increases as a low exponential function. The thought was that some common value of voltage could be used, thereby reducing test costs.

Because of the conflicting theories about channeling, a test series was designed, a rigorous procedure was written, and a test contract was awarded through competitive bidding to Preston Scientific, Inc. The test contained a high-voltage burn-in to determine whether it would be inclusive enough to eliminate separate back-bias and burn-in testing.

Prior to writing procedures for the contracted test, a pilot test was performed at JPL on a small number of transistors. The pilot test revealed that the time required to induce a channel was a matter of minutes to a few hours at high voltage and high temperatures. A fixed step-time of 2 days or 50 h was chosen. The test turn-off procedure was verified to be essential. The decay of one channel was at a rate of losing half its leakage each 4 h until after 24 h it dropped to near its original value. The decay time varied greatly from the example mentioned to one unit which fell at the rate of about 2% per day. The pilot test yielded about 2 to 4% channeling failures, revealing that a large sample size would be needed to gain statistical value.

The contracted test was designed with four test groups. First was a control group, which was used for instrumentation verification. The control group was measured each time before a test series group was measured. The readings of the control group were examined to verify that they were within tight tolerances with respect to the previous reading, thus assuring that the automatic transistor tester was fully functional and that the proper ambient conditions were met. The control group was not exposed to any of the step stresses.

The second group was the temperature group. These transistors were tested at 50 V reverse bias for 50 h at each temperature. The temperature series ran at 125, 150, 175, and 200°C, and again at 150°C.

The third group was the voltage group. The transistors were back-bias tested at 175°C (chosen from the previously run temperature group tests) at levels of 30, 60,

and 70 V, and again at 60 V. The temperature and voltage groups were then subjected to the high voltage burn-in test.

The fourth group was a test to determine if high-voltage burn-in would be sufficient for channel detection, which would eliminate the need for separate back-bias testing. A 100°C, 50-V burn-in test was run prior to a back-bias test at 50 V and 175°C.

The transistor chosen for the test was a popular, high-voltage, general-purpose PNP Motorola 2N2907A. These transistors incorporated the annular process. A sample of 770 parts was used for this test, 20 parts for the control group and 250 in each of the other groups.

The contracted test proved that no optimum value for either voltage or temperature existed within the transistor's rating. The number of channeling units detected increased as a weak exponential function of increasing temperature and as a near-linear function of increasing voltage (Figs. 6 and 7). About 5 times the total number of units channeled at 200°C than at 125°C. About 5 times the total number of units channeled at high voltage than at the lower voltage.

The high-temperature burn-in test is not sufficiently inclusive because many channels were again detected in the back-bias test that followed the burn-in test. However, very few units were removed by the power burn-in after back-bias testing (Fig. 8).

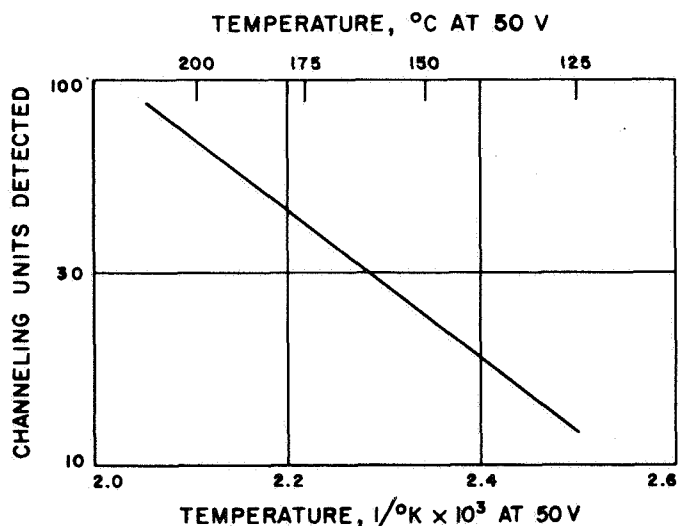


Fig. 6. Temperature vs channeling units detected

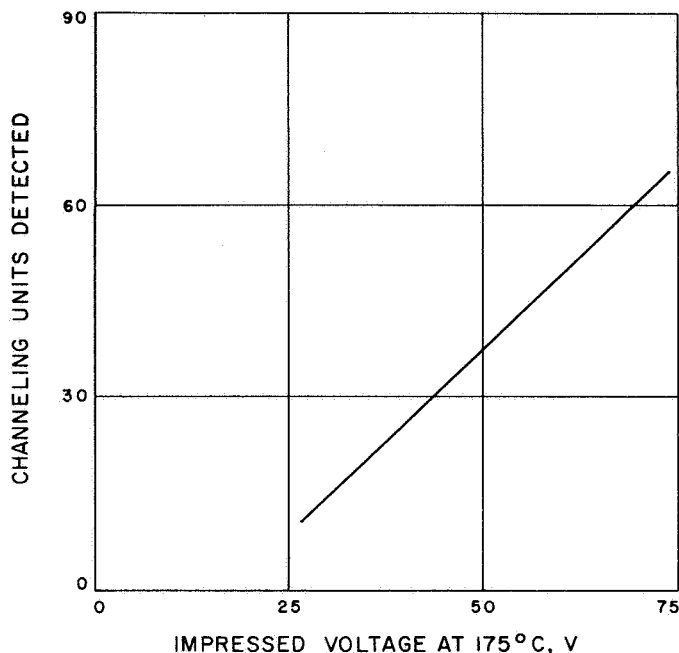


Fig. 7. Voltage vs channeling units detected

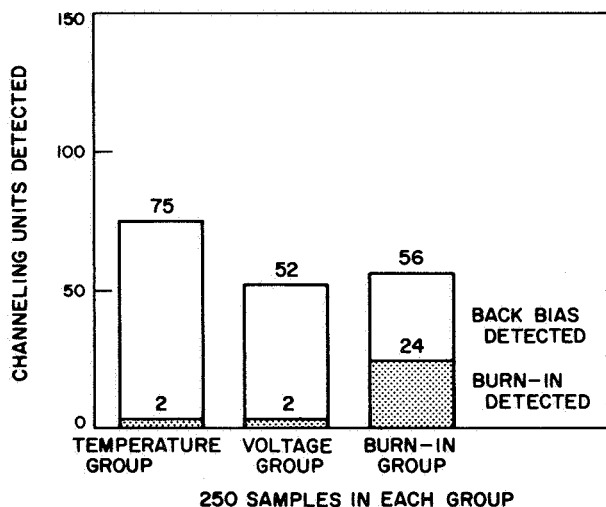


Fig. 8. Comparison of channeling units detected by 3 test groups

The results of this test series have been applied at JPL. Screening specifications, written prior to test completion, require a 100%, 150°C at 80% of maximum voltage for 48 h, high-temperature back-bias test. The back bias has replaced the 168-h (1 wk) 200°C bake. A low-voltage high-temperature power burn-in is also included.

It has been recommended that the temperature for back bias be increased to 175°C as time permits or as

specification revisions are made. It is also felt that 24 h would be sufficient test time. A drawback to this change is that most back-bias test fixtures are printed circuit boards which have a maximum temperature rating of 165°C and deteriorate rapidly if exposed to temperatures above this rating.

B. Analysis of Gases Contained in Transistors,

E. T. Klippenstein

The gases within transistors are known to affect their performance. Although the quantity of failures attributed to an undesirable gas ambient is small, nevertheless it is a problem which deserves attention. It is also one problem which can be corrected by manufacturers.

In establishing the work effort for gas analysis, the short-term goals were: (1) to design the necessary puncturing devices and mounts, (2) to develop analysis procedures, and (3) to collect data on gases contained in various transistors with various operating histories. The longer-term objectives were: (1) to have available as part of the tools of failure analysis the capability to analyze gases contained in small packages, and (2) to correlate certain gas ambients with abnormal performance and failure.

The contract for gas analysis was negotiated with Dynamic Science Corporation of Monrovia, California. Their capability included a mass spectrometer manufactured by Hitachi Perkin-Elmer and a gas chromatograph manufactured by Barber-Coleman. Their mass spectrometer is equipped with an electron multiplier for analysis of low concentration of gas constituents. The chromatograph has a porapak column which is selective for separation of water. With these instruments gases can be detected at the parts per billion level, and quantitative concentration measurements can be made in the order of 5 parts per million (ppm). The concentration of permanent gases can be measured with an accuracy of better than 1.0% of the actual concentration above the 0.1% concentration level.

An analysis scheme was devised where the gas sample contained within a transistor would be divided into two parts. One part would be run on the mass spectrometer. The mass spectrometer would quantitatively measure all gas constituents. The second half of the gas sample would be subjected to the gas chromatograph and would allow for a precise measurement of water concentration. A

special puncturing device was fabricated which allowed for releasing the gas within a transistor and allowed for expansion of the gas into two chambers. Since water is suspected to be the culprit which causes failure, special attention was given to the analysis of water. In addition, since there could be adsorbed water present, plans were made to perform analysis with the transistors and fixtures at high temperature.

1. Analysis Results

At the present time, twenty transistors have been submitted for gas analysis. Analysis of water was performed using both the mass spectrometer and gas chromatograph. The analysis of gases was performed both at room temperature and high temperature. The results are given in Table 1. It should be noted that only one value is given for water. This value is generally that which was determined on the mass spectrometer. The correlation with

the chromatograph was surprisingly good and was typically as follows:

Water concentration, mole %	
Mass spectrometer	Gas chromatograph
0.06	0.05
1.21	1.15
1.84	1.77
0.26	0.27
0.26	0.24
0.07	0.11
0.17	0.16

2. Discussion of the Results

Since the analysis of gases was for the purpose of collecting data for future work, various transistors were

Table 1. Results of analysis of gas concentration in transistors

Transistor specimen No.	Analysis temperature, °C	Gas concentration, mole %						
		Nitrogen	Oxygen	Argon	Helium	Water	Carbon dioxide	Hydrocarbons
2N2412 (518A)								
1	25	98.52	0.51	0.03	0.62	0.05	0.27	—
2	100	98.14	0.04	0.03	—	1.40	0.29	0.10
3	100	97.82	0.58	0.03	—	1.20	0.27	0.10
2N2412 (6650A)								
4	25	95.27	1.04	0.05	—	3.49	0.15	—
5	100	96.34	2.28	0.11	0.97	0.18	0.12	—
6	100	96.89	0.05	0.01	—	2.86	0.08	0.11
2N930								
7	25	98.15	0.44	0.03	—	1.15	0.22	0.01
8	25	98.38	1.01	0.06	—	—	0.39	0.16
9	25	91.85	5.58	0.28	—	1.84	0.45	—
10	100	88.56	10.60	0.30	—	0.26	0.24	0.04
11	100	89.75	7.44	0.27	—	2.15	0.34	0.05
12	100	99.40	—	—	—	0.53	0.07	—
2N1613								
13	120	99.18	0.05	0.05	—	0.26	0.44	0.01
14	120	99.04	—	0.06	—	0.26	0.63	0.01
15	120	99.68	0.01	0.06	—	0.07	0.17	—
16	130	99.07	0.52	0.07	—	0.17	0.16	0.01
17	25	99.12	0.40	0.08	—	—	0.40	—
18	25	99.53	0.02	0.05	—	0.02	0.38	—
19	25	99.58	—	0.06	—	—	0.36	—
20	25	99.52	—	0.05	—	0.01	0.42	—

analyzed and at different temperatures. The data was interesting in the amount of variation that was observed from part to part and the relatively large amount of water contained in some of the transistors—seven transistors had greater than 1.0 mole % water. With regard to temperature, there appeared to be no consistent pattern in the results. However, by calculating mean values it was observed that the average water at room temperature was 0.73 mole % while at high temperature the average water was 0.85 mole %. It appeared that some adsorbed water was observed. The helium observed in specimens 1 and 5 may have come from a sample of transistors that had been tested with a helium leak de-

tector. Specimens 9, 10, and 11 may have had defective seals, based on the relatively large amount of oxygen observed.

3. Future Work

The amount of data gathered thus far has been valuable in dispelling some *a priori* notions about gases in transistors. For the future, additional work is planned in correlating the presence of certain gases with degraded performance and failures. Analysis of gases will be performed on parts with long test histories and parts which have degraded and failed.

X. Lunar Spacecraft Development

ENGINEERING MECHANICS DIVISION

A. Advanced Mechanisms, M. B. Gram

There are currently three specific mechanism areas under investigation by the mechanisms advanced development group. These are an extendible instrument mast, an impact switch, and a chemical heater. These three devices are being studied in conjunction with the capsule system advanced development (CSAD) program and at the same time are providing research and development knowledge which is being drawn upon by various project areas.

1. Instrument Boom

Various types of extendible booms and masts have been evaluated with an eye toward the specific requirements of the CSAD program, i.e., compact size, low weight, moderate rigidity, 2-m length, and cable payout ability. DeHavilland Aircraft's "STEM" was of insufficient rigidity in the pop-up version and much too bulky in the Bi-STEM version. The Ryan boom (also manufactured by Boeing, Marquardt, and TRW Systems), although not normally designed as a self-extending boom, would have been too large and heavy for this particular application. An inflatable boom was also investigated, but internal foaming

would have been required for stiffness and as yet this is not being done satisfactorily within the framework of weight and space for this application. The unit which was finally selected is shown in Fig. 1 in its stowed configuration. It is a spring-steel ribbon element manufactured by Hunter Spring Division of Ametek, Inc. The element is a full hard 301 stainless steel strip, 0.004 in. thick and 4 in. wide, which has been formed into a spiral wound tube. The spring weighs approximately 0.7 lb, and in the stowed position it takes the form of a cylinder, 1½ in. in diameter by 4 in. long.

The boom has been assembled inside a housing, installed in a mocked-up lander package, and impacted several times at shock levels up to 2500 g at velocities above 100 ft/s. Although the housing was damaged on one such impact, the spring element itself has not been harmed.

Future plans call for integrating the instrument boom with simulated science instruments (including a rotating anemometer), a cable payout reel, and release latch pyrotechnics, thereby demonstrating total system capability.

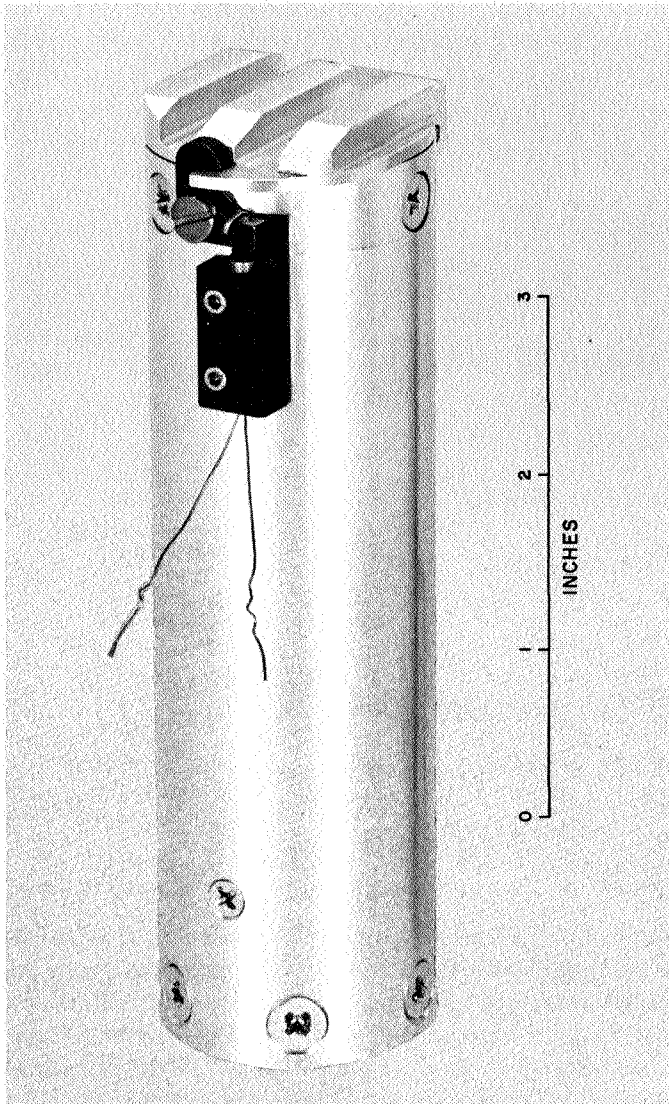


Fig. 1. Instrument boom (stowed configuration)

2. Impact Switch

Another requirement rising out of the CSAD program is that of releasing the parachute the instant that the lander touches the ground. A pyrotechnic device will be employed for the actual physical release, while the signal to initiate this device will originate from a g -actuated impact switch. Figure 2 shows the impact switch alone, while Fig. 3 is a photograph of a two-switch assembly along with a breadboard of the associated electronics as mounted in a fixture prior to being impact-tested.

The switch and its electronics have been impacted at levels ranging from 1000 to 3000 g with impact velocities of 40 to 100 ft/s. Although the electronics were not compatible with the pyrotechnic squibs, the tests indicated

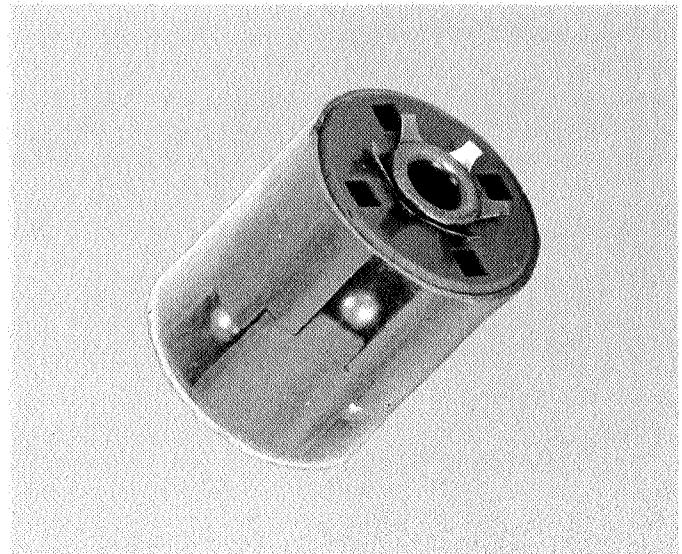


Fig. 2. Impact switch

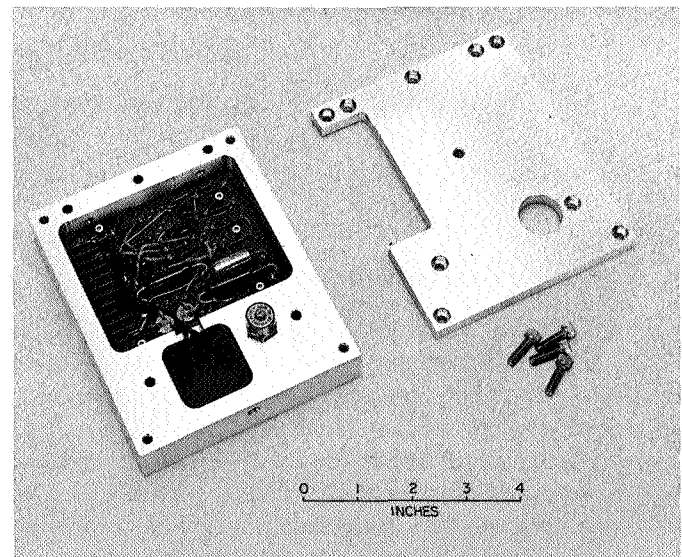


Fig. 3. Impact switch assembly mounted with associated electronics

that the impact switch was triggering the electronics as desired. Changes to the electronics are now in process such that actual squibs will be fired on future shock tests. Modifications to the impact switch itself will only be required to change its minimum- g -level actuation and to assure reliability following sterilization.

3. Chemical Heater

Requirements generally exist on every spacecraft in the area of thermal control for some means of supplying

heat. Usually on large spacecraft and lander vehicles, the heat is supplied by electric power generated by solar panels and stored by batteries. Various heating schemes were evaluated on a heat per pound basis for a small lander package, with typical results as follows:

Heating device	Heat yield
Battery power	15 W-h/lb
Chemical heater	670 W-h/lb
Nuclear heater	5 W/lb

Battery power appears very poor on this basis. The nuclear heater was not considered as a candidate because its heat yield stems from its radioactive decay and cannot be started, stopped, or controlled during operation. The yield stated for a chemical heater is based on the combination of chlorine trifluoride and elemental boron, which are the chemicals being utilized at the present time. Other combinations supply heat yields above and below this, but from a practical standpoint of storage, sterilization, materials, and operation, this appeared most favorable.

The operation of the chemical heater centers around four basic components. First, there is a pressure vessel for the storage of the chlorine trifluoride (ClF_3). It is necessary that this be a pressure vessel because during the sterilization cycle temperatures of 275°F cause the vapor pressure of the liquid to reach 470 psia. Second is a pyro-activation valve which precludes operation of the heater until commanded. The third component is a sensing and metering valve which senses the body temperature and allows the flow of ClF_3 when this temperature drops below the set point, and shuts off the flow as the temperature rises above the set point. The fourth component is a base for the storage and distribution of the boron crystals. As the ClF_3 flows through the valves and reaches the boron, the mixture immediately reacts exothermically, giving off vapor-phase BF_3 and BCl_3 reaction

products which are exhausted further on downstream. When the temperature in the area of the sensing and metering valves rises near the set point, the flow of ClF_3 is restricted, thereby terminating the reaction.

To date, considerable time has been expended in developing a suitable temperature sensing valve with a set point near 50°F which would be unaffected by sterilization temperatures of 275°F and impact loads of several thousand g 's. One such valve utilizes a bimetallic sensing disk, with no additional moving parts, which seats tightly against the valve seat when hot, yet backs completely away from the seat when cool (Fig. 4).

Test hardware has been fabricated and full-scale prototype testing of the heater will be accomplished in the near future.

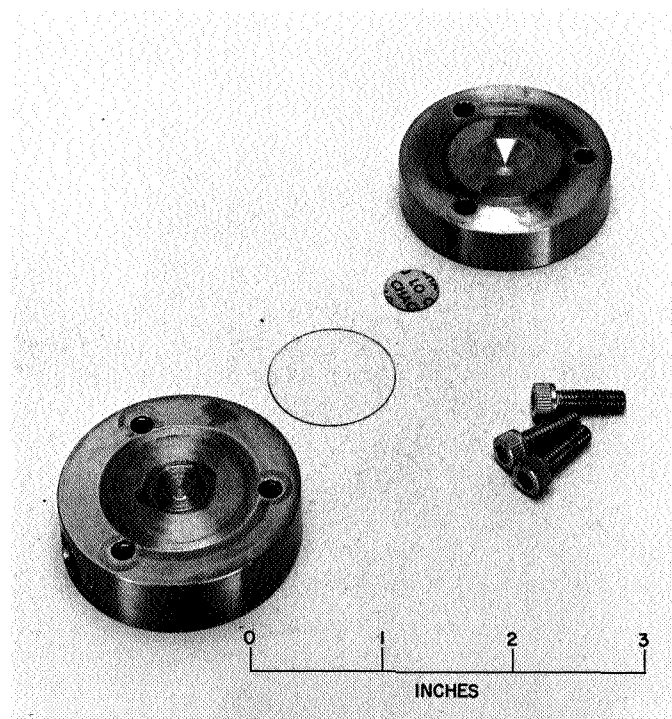


Fig. 4. Temperature-sensing-valve components

XI. Instrumentation

ENVIRONMENTAL SIMULATION DIVISION

A. Determination of Particle Size and Concentration, C. Feldstein

When metallic aluminum is added to solid propellant fuel to increase thrust, aluminum oxide particles are formed. A knowledge of the size of these solid particles occurring in the exhaust of a rocket motor is necessary in order to predict the loss in motor performance incurred as a result of the existence of these particles in the nozzle flow system. There is also the possible mechanical damage and heat transfer to space vehicle surfaces due to the impingement by exhaust particles.

Consequently, a study under contract JPL 950573 was begun in 1964 under the direction of Dr. R. A. Dobbins of Brown University. He developed and tested an emission-scattering photometer to measure the size of rocket exhaust particles using the spectrophotometric technique. The salient features of this system are:

- (1) Particle sizes can be measured when a statistically valid sample cannot be obtained.
- (2) It is more rapid than the photomicrographic method both in the collection of data and its reduction.

- (3) It is nondestructive testing; only subjected to a beam of light.
- (4) The reaction can be followed throughout the experiment as in the study of agglomeration.
- (5) The position of the sample and critical scanning can be varied during an experimental run.

The equipment has been used in the study of particles in the 2.40-, 1.01-, and 0.36-micron region. It is suggested that this equipment can be used for other types of investigations, e.g., in the study of droplets, aerosols, colloidal suspensions, and related areas.

In order to measure particle size, a necessary condition for the application of the spectrophotometric technique is the absence of absorption by molecular species at the wavelength of interest. This method has demonstrated its feasibility by tests on polydispersions of known mean diameters in an aqueous solution. Both mean size and concentration can be determined, providing the wavelengths of the optical transmission are above and below the value of the mean size. This is accomplished by the use of two of the three monochromators.

1. Description of Spectrophotometric Technique

A beam of light is generated by a tungsten filament lamp, collimated, and then subjected to a 5-Hz chopper. During the on portion, light passes through the study area; during the off portion, the subject emits or reflects light. The emitted and transmitted beams of light are then subjected to the transmittance or reflective action of narrow-beam light filters, for conditioning to their one of three individual monochromators and for measurements by photosensors and individual recording (Fig. 1).

As used in the study of particle size from rocket motors, the light beam passes through the rocket plume with the on cycle of the chopper and then allows radiation from the plume on the off portion of the cycle. Under other experimental conditions, the off beam may allow fluorescence of the particles, depending on the conditions of measurements.

2. Data Reduction

The transmission law for a polydispersion of spherical particles can be expressed as

$$\frac{B}{A} = \exp\left(\frac{-3}{2} K c_v l\right) \quad (1)$$

where B/A = optical transmission, c_v = volume of particles per unit volume of liquid, l = optical path length, K = scattering coefficient, and D_{32} = ratio of the third to second moment of the size distribution function of the volume-surface mean diameter.

To determine the value of the experimental scattering coefficient K_{ex} with a monodispersed sample of known size, the transmission law then becomes

$$\frac{B}{A} = \exp\left(\frac{-3}{2} \frac{K_{ex} c_v l}{D}\right) \quad (2)$$

This would be repeated to encompass the low and high values of sizes expected, from which K_{ex} can be calculated.

It has been found that K_{ex} can be different from the theoretical K due to the number of different sizes of particles in a polydispersion reflected in an actual measurement. More exact values of K can be found using the Mie theory in conjunction with the index of refraction of the material used.

Using a polydispersion, and since B/A , l , and c_v are known by direct measurement, a plot of K/D_{32} versus D_{32} can be prepared for specific values of wavelength and refractive index.

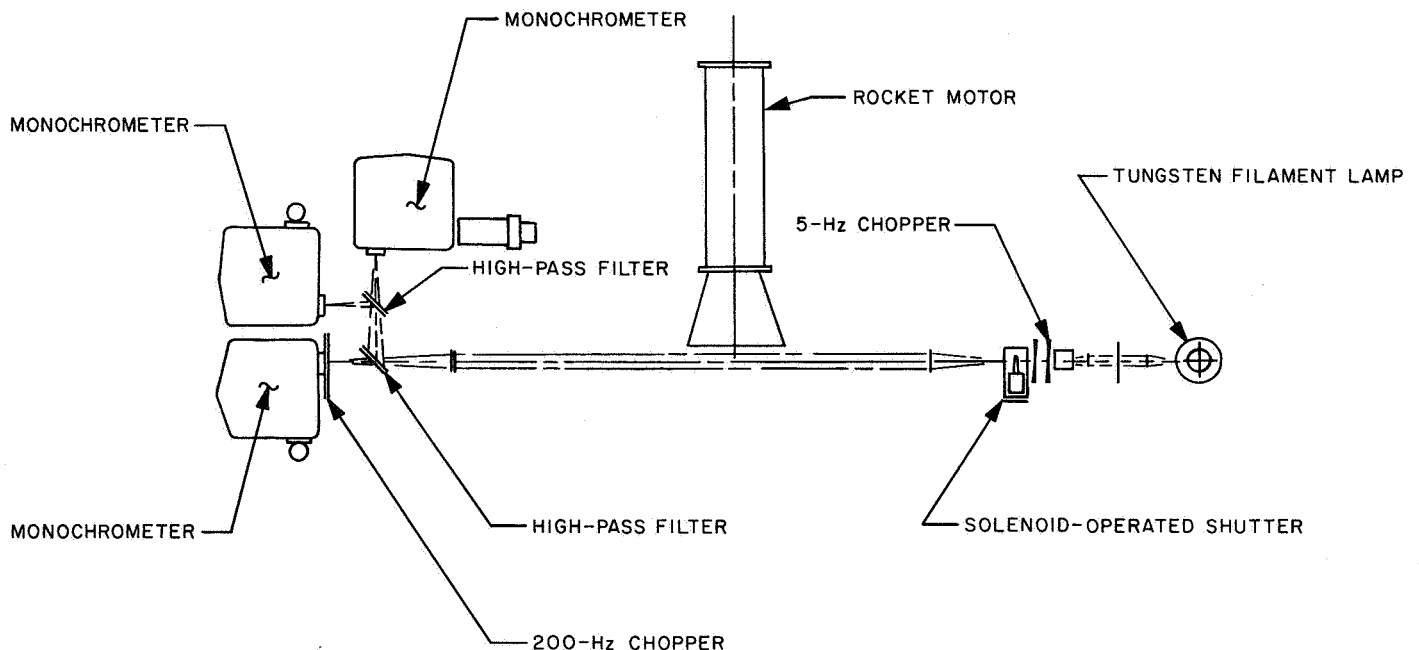


Fig. 1. Optical schematic of spectrophotometric technique

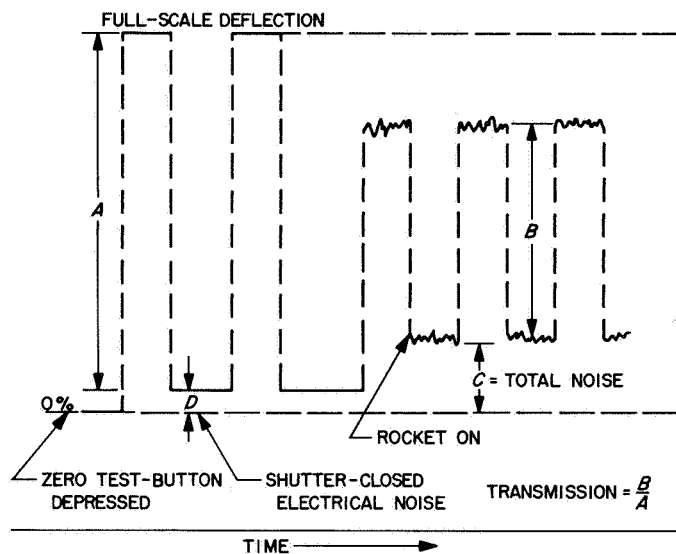


Fig. 2. Interpretation of output of recorder of one channel in terms of optical transmission

Taking the ratio of transmissions for two separate wavelengths, e.g., monochromators 2, 1 (Fig. 2),

$$r_{\gamma}(2, 1) = \frac{\ln\left(\frac{A}{B}\right)_2}{\ln\left(\frac{A}{B}\right)_1} \quad (3)$$

where γ is defined as optical depth = $\ln A/B$. A plot of $r_{\gamma}(2, 1)$ versus D_{32} is made (Fig. 3), and a similar plot is

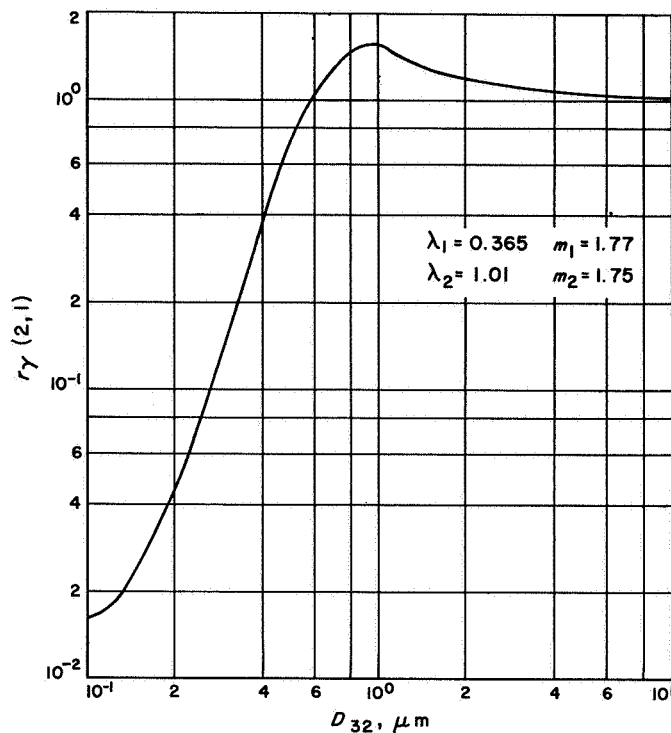


Fig. 3. Ratio of mean scattering cross section $r_{\gamma}(2, 1)$ vs mean diameter D_{32}

made of $r_{\gamma}(3, 2)$ versus D_{32} , using corresponding values of wavelength λ for various values of D_{32} . From the experimental transmission data at two specific wavelengths, the ratio of the optical depths is found. Inserting this value in Fig. 3, the mean particle size is found. Particle concentration can now be found by using Eq. (1).

XII. Aerodynamic Facilities

ENVIRONMENTAL SIMULATION DIVISION

A. Initial Performance of a 6-in.-Diameter Arc

Driver, J. W. Williard

A new electric-arc driver for the 6-in.-diameter shock tube has been installed. This driver incorporates several new design concepts and is presently being evaluated. One of the unique features of this driver is the alumina ceramic liner which has proven highly successful in eliminating liner ablation and the resulting driver gas contamination. A notable decrease in shock-speed attenuation and a corresponding increase in useable test time have also been achieved. By incorporating a variable length, i.e., volume, capability this driver should be able to produce shock speeds in excess of 45,000 ft/s. To date a shock speed of 39,800 ft/s in 0.1-mm Hg air has been obtained using the 9-in. driver length.

The driver internal diameter is 6 in. and its length can vary from 4 to 9 in. (Fig. 1). It consists of an inconel steel jacket and a 0.375-in.-thick alumina ceramic liner. There is a 0.012-in. interference fit between the liner OD and jacket ID. This puts a compressive stress of 20,000 psi on

the ceramic liner when assembled. In assembling the liner and jacket, both were heated to 1200°F, joined, and allowed to cool at room temperature.

The original driver incorporated a brass back plate and electrode stem. Initial firings indicated that a considerable amount of electrode ablation was occurring. A steel back plate with a copper insert was installed and is now being used. A ceramic backplate and tungsten alloy electrode face has been tried; the face virtually eliminated electrode ablation, although it cracked after several firings. In Fig. 2, a comparison is shown of the driver gas contamination obtained with the former driver and the contamination obtained with the new drivers that have steel and ceramic backplates.

The firing mechanism is a conventional pull-rod, insulator, coiled-wire type actuated by an air cylinder. Because of the large gap that the spider assembly must span, a replaceable 3/8-in.-diameter rod with bearing caps is now used.

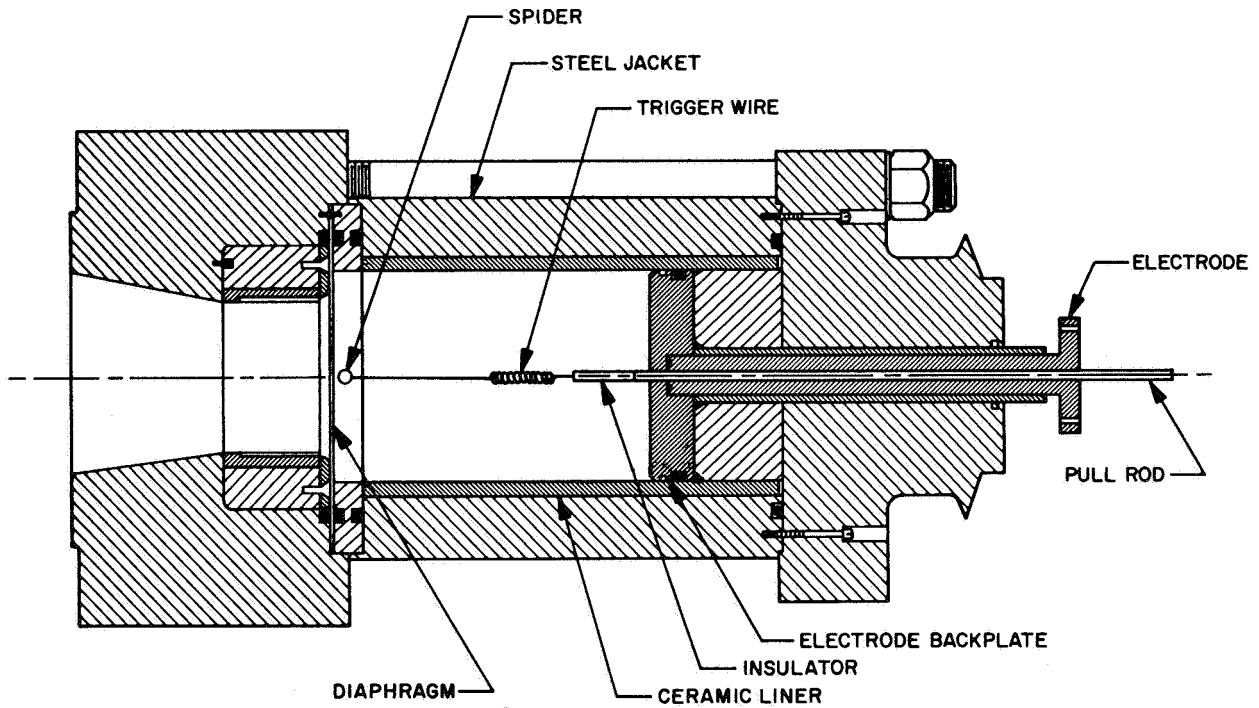


Fig. 1. Driver assembly

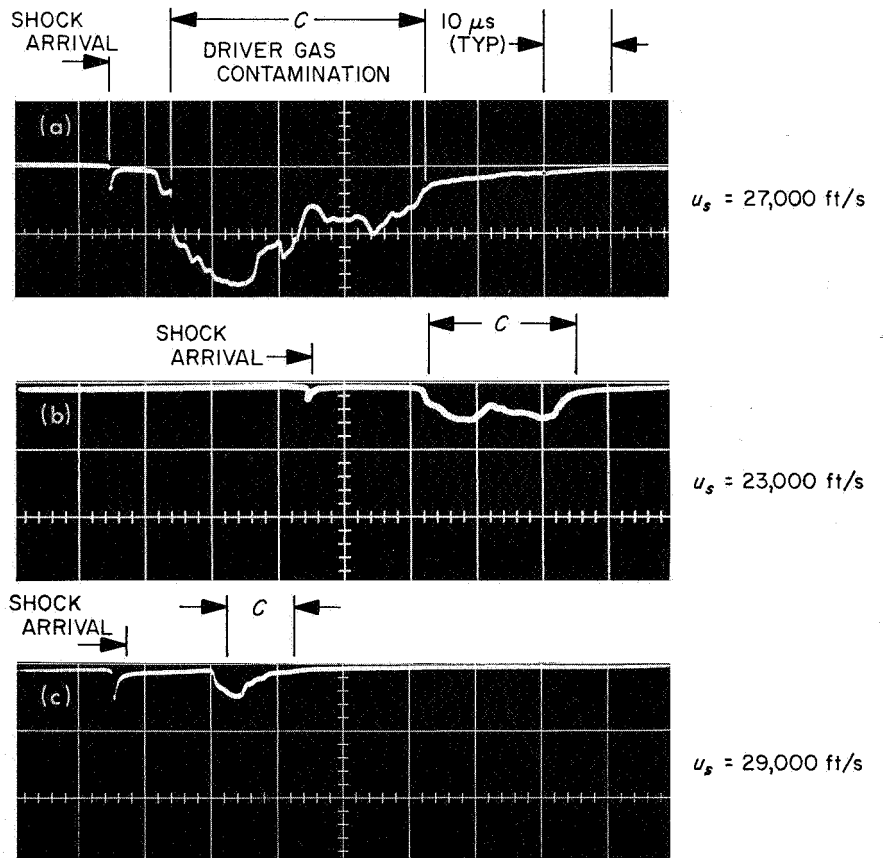


Fig. 2. Driver gas contamination: photomultiplier trace of (a) former driver with Teflon liner, (b) new driver with ceramic liner and steel backplate, (c) new driver with ceramic liner and ceramic backplate

Stainless steel diaphragms 0.125- and 0.141-in. thick are used with the driver. They span a 4.5-in.² unsupported area and open into 4 petals upon replaceable inconel inserts. These diaphragms allow driving pressures up to 10,000 psi.

The energy densities are much lower using this driver because of its large volume. The capacitor bank has a capacity of 290,000 joules. Because of the larger driver diameter and the improved area ratios between driver throat and driven tube, the overall shock tube performance has improved. In Fig. 3, it can be seen that a shock speed representing a transfer of approximately 80% of the energy available to the driver gas is produced. This is consistent with data obtained in the former electric driver. At the lower initial driver gas pressures the driver becomes radiation-limited; i.e., the driver gas radiates all additional energy to the driver walls. It is therefore necessary to find the optimum driver gas pressure which will produce maximum shock speed and test time experimentally.

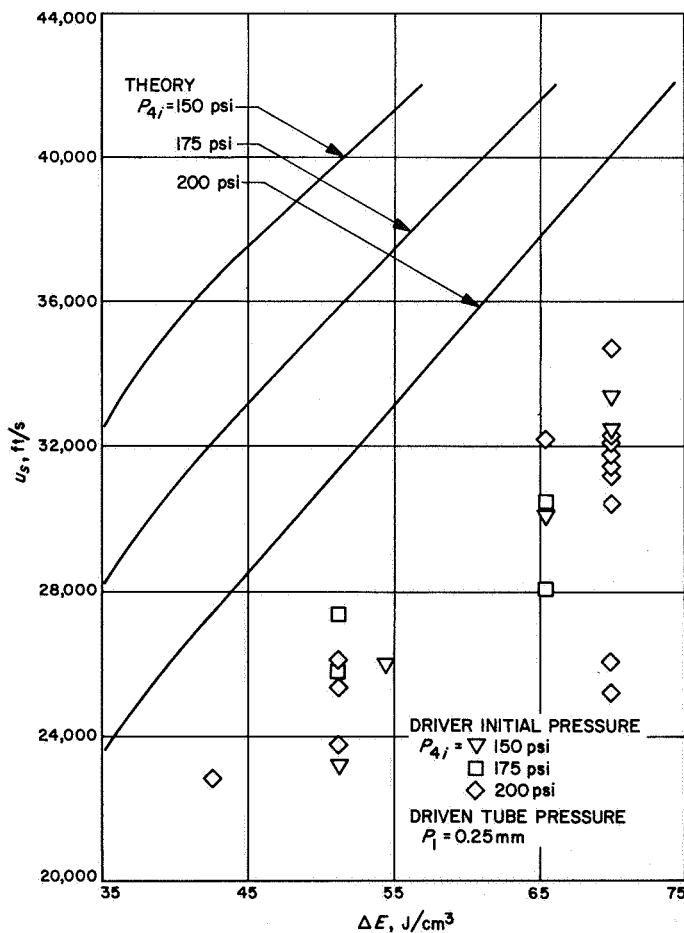


Fig. 3. Shock speed vs energy input

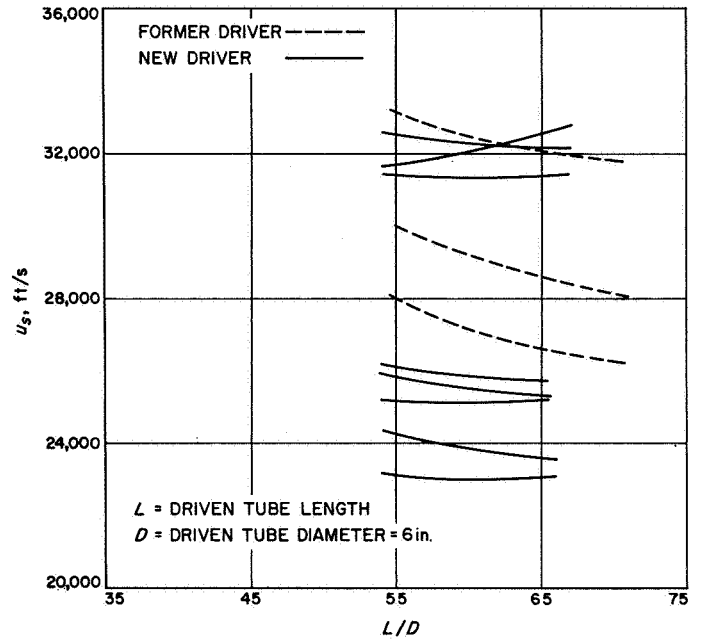


Fig. 4. Shock-speed attenuation

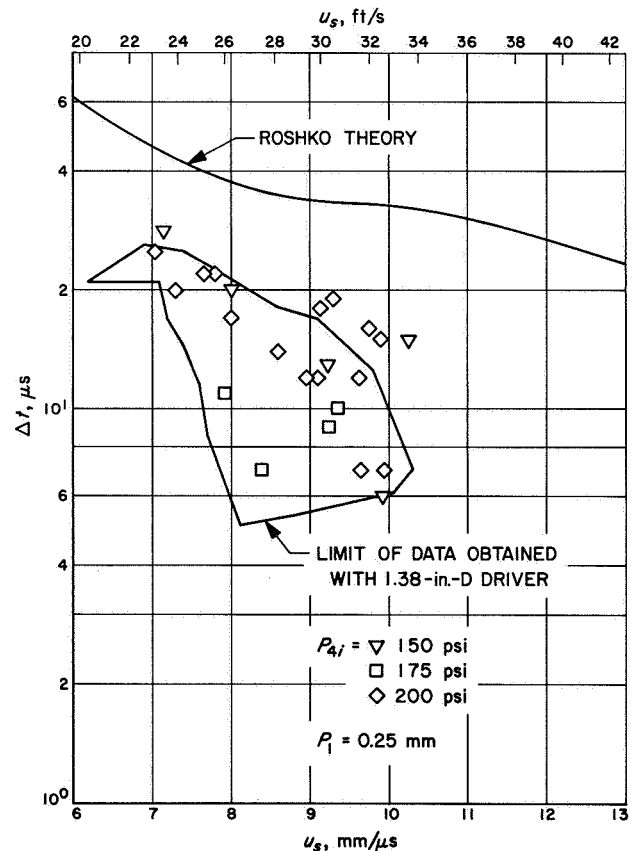


Fig. 5. Test time vs shock speed

This is being accomplished as part of the driver evaluation program.

One of the most desirable characteristics of the driver is the decrease in shock-speed attenuation. As can be seen in Fig. 4, shock-speed attenuation has been greatly reduced, especially at the higher shock speeds. It is expected that a longer driven tube can be used with this driver and even better test times can be obtained. Following current tests, these possibilities will be evaluated.

To date, the driver has been operated at the higher energy densities and shock speeds using the 9-in. driver length. As can be seen in Fig. 5, test times have been greater or equal to the previous high values obtained with the former driver (Ref. 1). In Fig. 6, test time versus driven tube length for the two drivers is compared. No increase in useable test time was obtained when testing at driven tube lengths up to 40 ft with the former driver.

So far, the new driver has been able to produce longer test times at higher shock speeds and shorter driven tube length.

The new 6-in.-diameter driver has undergone quite a few changes since its installation in January 1967. The optimum driver configuration is nearly finalized, and only minor modifications should be necessary during the remainder of the evaluation. A new ceramic electrode face will be evaluated as well as a different firing mechanism in order to eliminate electrode ablation and simplify driver operation. Modifications have also been made to the collector ring assembly and to the instrumentation ports in order to make them compatible with the new driver. Of interest is the fact that if special instrument ports are not used, what little ablation there is from the ceramic liner will ruin the windows in two or three firings. Evaluation of the new instrument ports has shown them to be highly successful in eliminating window damage and as a result improve the quality of the shock

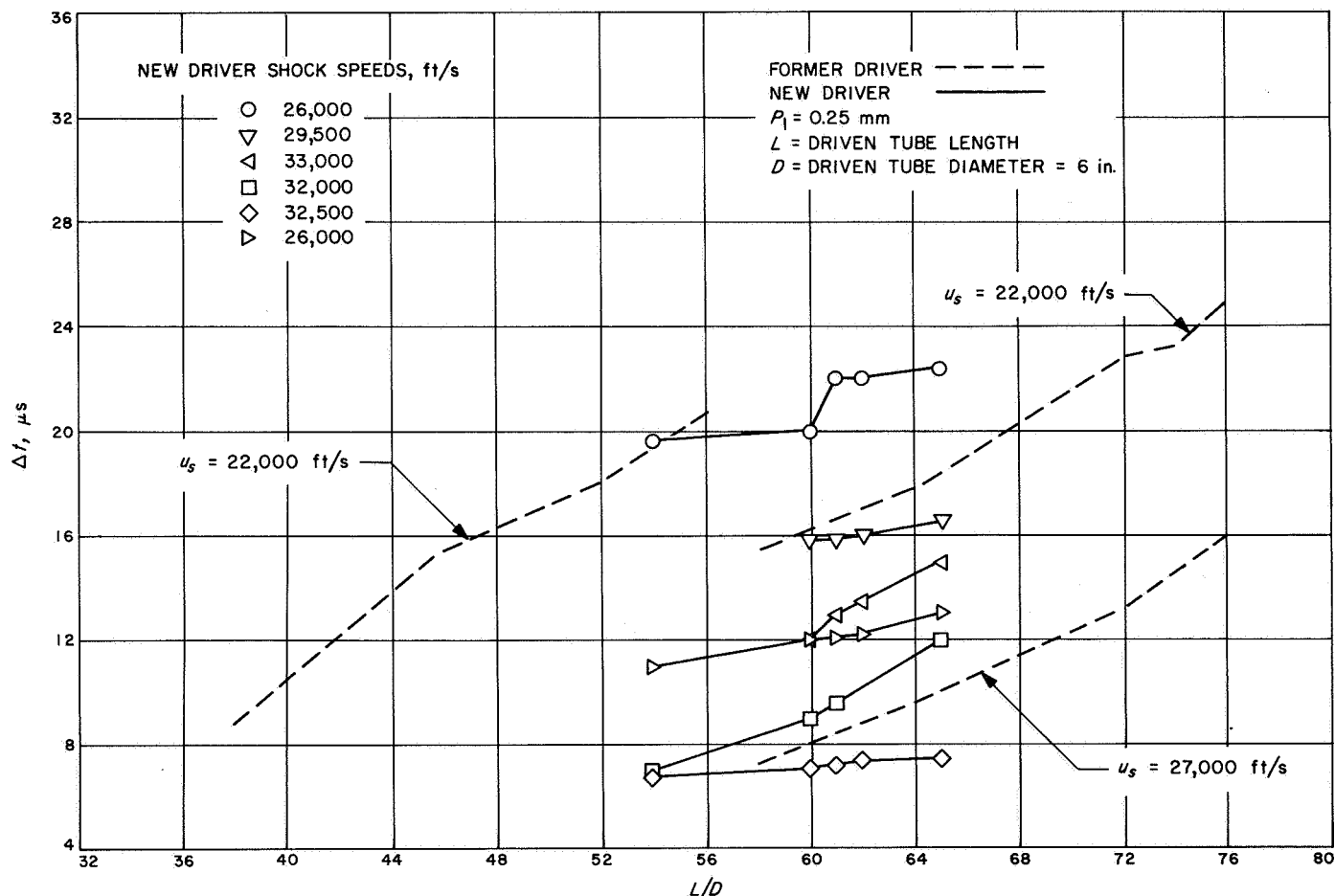


Fig. 6. Test time vs driven tube length/diameter

speed and test time data obtained. At present 181,000 joules of energy are available due to necessary modifications to the collector ring assembly. This limits shock speeds to about 35,000 ft/s unless very short driver lengths are used. Following the installation of a new collector, now being fabricated, a maximum of 290,000 joules will again be available. Evaluation of the driver to determine its maximum capability will then be undertaken.

B. A Study of Molecular, Continuum, and Line Radiation from Planetary Atmospheres,

W. A. Menard and G. M. Thomas

The various sources of equilibrium radiation important to planetary entry problems have been studied (Ref. 2). Shock tube measurements of the radiation from a mixture of 30% CO₂-40% N₂-30% A were made over the temperature range 7000-16,000°K.

Several approximate theoretical models for the molecular band structure were presented. These models were then compared with the results of spectral measurements of the CN violet band system (Fig. 7). The best fit to the data was obtained using a CN dissociation energy of 7.7 eV.

Calculations were made of the free-free (ff) and free-bound (fb) continua of singly ionized N, C, A, and O

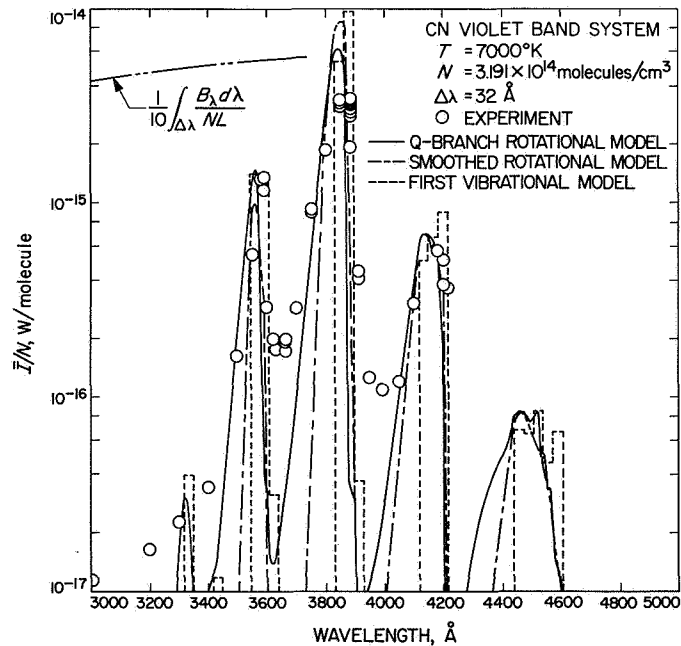


Fig. 7. Comparison of three molecular band models with experimental data

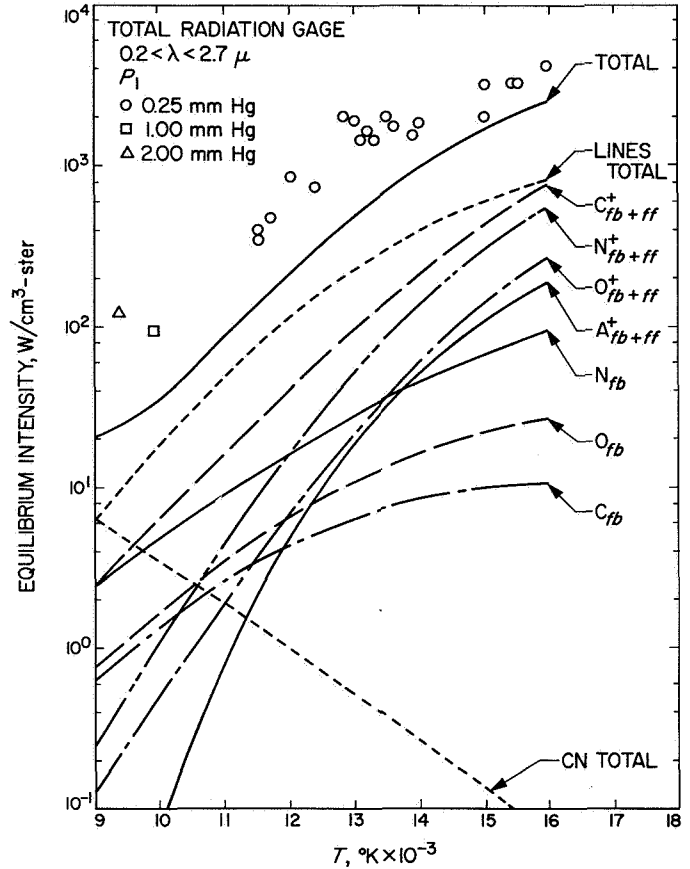


Fig. 8. Total radiation measurements in 30% CO₂-40% N₂-30% A for a flat-faced cylinder model

atoms, employing nonhydrogenic cross sections, and the electron attachment continua of neutral N, O, and C atoms, using measured cross sections. Self-absorption was accounted for in the calculation of atomic line radiation by using a statistical model that considers overlapping of the individual lines. Total radiation in the region 0.3 to 2.7 μ was measured at the stagnation point of a flat-faced cylinder model (Fig. 8). Comparison of the theoretical predictions with the data suggests that an unknown source, which was not included in the calculations, may be present.

C. Base Heating of 60-deg Half-Angle Cone,

J. C. Klose

Wind Tunnel Test 21-205 was concerned with developing a technique for using commercially available temperature-sensitive paints in wind-tunnel heat-transfer work. The paints used during this test are manufactured by U. S. Radium Corporation and are available in four

temperature ranges (65–176°F, 95–266°F, 248–536°F, and 482–752°F). When illuminated by long-wave ultraviolet radiation, the paints will retransmit varying amounts of visible light depending on their temperatures.

The principal purpose of the test was the evaluation of the temperature-sensitive paints and the test procedure. It was also hoped that useful temperature measurements might be made on the base of the model.

The model shape used in the test was a 60-deg half-angle spherically blunted cone. The nose-radius-to-base-diameter ratio was 0.10. Since the base of the cone was the region of interest, it was spread with temperature-sensitive paint and instrumented with three thermocouples. Photographic and thermocouple data were taken during the test. Approximate test conditions were: Mach number = 8.0, tunnel total pressure = 700 cm of Hg, and tunnel total temperature = 625°F.

Insufficient accuracy in calibration of temperature-sensitive paints made a quantitative reduction of the photographic data taken during the test impractical. However, visual observations of the temperature-sensitive paint indicated that the base temperature was approximately 70°F. Thermocouple readings recorded at the same time indicated a base temperature of approximately 73°F.

Even though the results from Wind Tunnel Test 21-205 were not good, it is felt that this does not disqualify temperature-sensitive paints as a useful tool in wind-tunnel heat-transfer work.

D. Errors Associated with Atmosphere Reconstruction from Capsule Onboard Measurements, R. H. Prislin

1. Determination of a Planetary Atmosphere from Acceleration Measurements

The reconstruction of a planetary atmosphere from onboard measurements of accelerations by an entry vehicle has been proposed by A. Seiff and D. E. Reese, Jr. of the NASA Ames Research Center (Refs. 3 and 4). A number of possible sources of error in atmospheric definition are associated with this method. Among these are inaccuracies of the accelerometers, validity and availability of a time versus altitude boundary condition, uncertainties in entry speed and entry angle, errors in determination of a time history of the vehicle aero-

dynamic coefficients, and effects of frequency of data measurements. Prior to an actual utilization of the technique, an assessment of the effects of these potential errors, and the corresponding applicability or limitations of the method, must be made.

The density variation with altitude will be the only relation considered in this discussion since it is the quantity with the least accurate determination from acceleration measurements. It should be noted that time is the common parameter linking the atmospheric properties and the trajectory variables. An error in a calculated density variation with altitude could be due to errors in density at given altitudes or errors in altitude at given densities or a combination of the two. The differential and algebraic equations relating the two types of variables are not independent; however, the dependence of density on altitude is not explicit and is of second order. Therefore, it is possible to have small errors in density versus time, but large errors in the altitude-time history, and hence a rather poor atmosphere definition. This very circumstance proves to be one of the major difficulties encountered in the application of the technique.

The accuracy of an accelerometer is, in general, a function of the full range of the instrument and is not dependent on a particular acceleration being measured. In practice, it may not be known which atmosphere, within postulated extremes, will be encountered on a first mission to a planet. This means that accelerometers must be designed to accommodate the maximum possible acceleration. The worst case from the standpoint of atmosphere definition would be designing for the maximum expected accelerations, but actually experiencing the minimum values. If the accelerometer error is a constant percentage bias of the instrument full range (in actual use it would probably be more of a random error within a fixed limit, and therefore not as bad as this example), this problem is equivalent to considering accelerometers of various accuracies taking measurements in a fixed atmosphere. Figure 9 shows errors in density as a function of velocity resulting from various assumed bias errors in the accelerometer. The low-velocity errors arise from the fact that in this region the accelerations are small, and even 0.1% of the maximum acceleration is a large error in terms of the measured value. One way of eliminating this difficulty is to design the vehicle to impact the surface at a velocity ratio of 0.2 or greater. However, such an alternative can seriously cut into the communication time available after blackout and prior to impact, and is, in general, not feasible. Accelerometers meeting

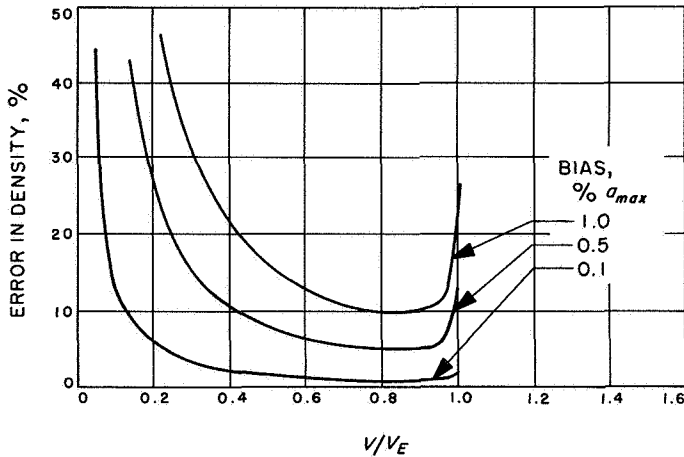


Fig. 9. Error in density vs velocity ratio

and exceeding the 0.1% accuracy specification needed for good determination down to the $V/V_B = 0.2$ point are commercially available. Any accuracy increase beyond this level would result in a further decrease of error in density determination.

The previous paragraph shows that, within communication time limitations, it is desirable to impact the planet at as high a velocity as possible. Subsequent illustrations will consider a model atmosphere of the planet Mars as proposed in Ref. 5. The so-called maximum atmosphere with a surface density of 40 mbar will be used since it constitutes a worst-case situation. Consideration of atmospheres more in line with present thought would result in less serious error restrictions. For the particular entry capsule and conditions considered, this model atmosphere results in an impact velocity ratio of less than 0.02.

The total error in a density-altitude history due to accelerometer inaccuracies can be divided into three parts: (1) errors resulting from direct use of the accelerations in the density equation; (2) errors in velocity due to integrating the acceleration errors; and (3) errors in altitude due to integrating the velocity errors. The importance of each of these is displayed in Fig. 10, assuming a constant biased accelerometer error of 0.1% of maximum acceleration. The figure shows that if velocity and altitude are measured accurately by an independent method, then the density results are excellent down to an altitude of 100,000 ft, with a subsequent error increasing to a factor of two at impact. The definition is equally good over a slightly smaller range if only the altitude is measured independently. Finally, the largest errors are shown to be a result of errors in the integrated altitude.

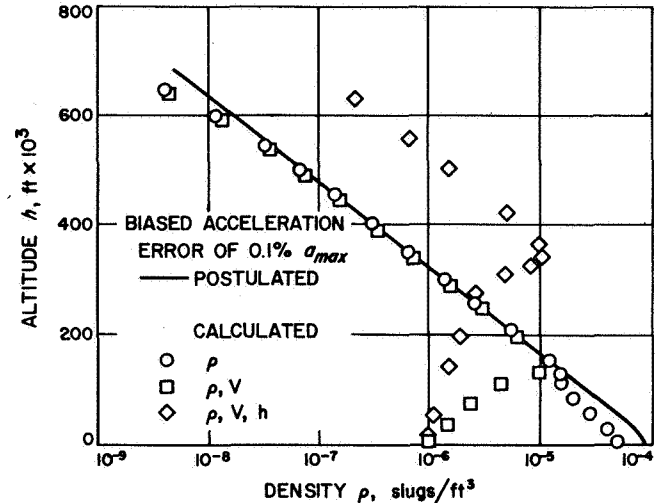


Fig. 10. Accuracy improvement due to additional measurements

This last curve is somewhat misleading in that errors are shown to be large over the entire trajectory. The altitude at entry is not known *a priori*, and therefore the boundary condition used for the differential equation describing altitude versus time is an assumed value of 0 altitude at probe impact. The majority of the error in the high-altitude values is actually accumulated over the low-speed part of the trajectory where errors in velocity are large. Since the boundary condition used is at 0 altitude, integration over this regime cannot be avoided.

The atmosphere definition, as shown in Fig. 10, determined by accelerometer readings alone is unacceptable. This may, of course, be improved by increasing the accuracy of the accelerometers. A biased error of 0.01% of the maximum acceleration would provide good agreement down to an altitude of 100,000 ft. However, this is felt to be beyond the present state-of-the-art capability. A second way to increase accuracy is to use an alternate method to measure atmospheric properties once the probe velocity is reduced to low values. This, in effect, means providing a reliable time-altitude boundary condition prior to impact. The increase in accuracy corresponding to a boundary condition given at various altitudes is displayed graphically in Fig. 11. Work by A. Seiff and D. E. Reese, Jr. (Ref. 6) indicates that velocity, altitude, and atmosphere properties can be well determined by direct measurements at subsonic speeds. Figure 11 clearly shows that, at least within present day limitations on accelerometer capabilities, this technique is only valid when used in conjunction with other measurements such as a subsonic experiment. Therefore, for the remainder of

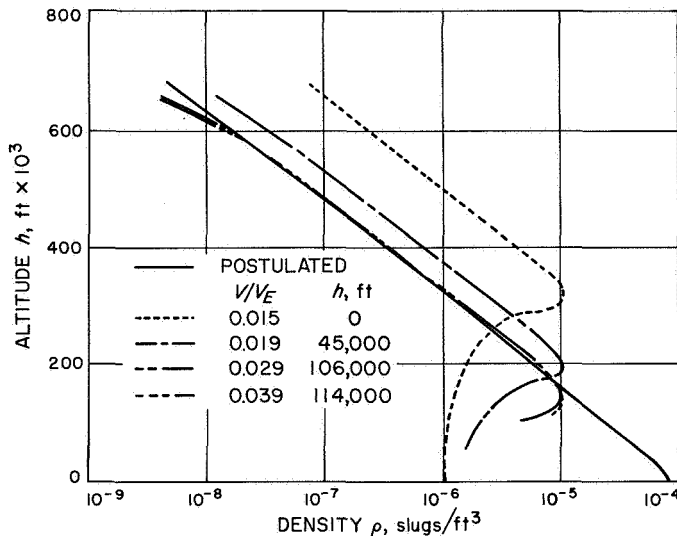


Fig. 11. Effect of experiment termination point

this discussion it will be assumed that the accelerometer experiment has been terminated at a velocity of 750 ft/s.

Three boundary conditions are required for the trajectory differential equations; these are an altitude-time correspondence as discussed in the previous paragraph and initial values for velocity and entry angle. If the time-altitude condition as determined by an independent experiment is in error, there will be a corresponding error in the density versus altitude relationship. However, the altitude affects the other variables only in the calculation of local gravity. This term is so dominated by the planet radius that even a relatively large altitude error will be of small consequence. Therefore, an initial error does not tend to magnify, but rather remains as a constant offset in the altitude versus density plot. Similarly, an error in initial entry angle does not affect the density directly, but leads to small errors in velocity and somewhat larger errors in altitude. This error is cumulative over a period of time. However, because of the gravity term, the entry angle tends to approach 90 deg independent of the initial value, thereby abating the cumulative effects. An uncertainty of ± 2.5 deg in entry angle results in a tolerable error band for atmospheric definition. An error in initial velocity also has its most pronounced effect on altitude determination. A 1% error in initial velocity again results in a tolerable error band.

The aerodynamic coefficients throughout the entry trajectory are not explicitly functions of time. They are generally functions of gas composition, Mach number,

Reynolds number, and vehicle attitude. However, the aerodynamic characteristics of most simple bodies with thin shock layers are not strongly dependent on gas composition. Furthermore, Mach number and Reynolds number variations with time can be determined approximately from the calculation of the trajectory so that these parameters do not seem to constitute a serious problem. The major difficulty results from the fact that aerodynamic coefficients can be strongly dependent on vehicle attitude and excursions in attitude from a mean can be large during a passive entry. However, the body attitude can be inferred from three-component accelerometer data. Furthermore, at least during the first portion of the entry, the combination of supersonic dynamic stability for most shapes and an increasing dynamic pressure gradient will insure a rapidly converging angular envelope. If the entry configuration is a blunt body, the aerodynamic coefficients would be nearly constant near zero angle-of-attack, so a rough determination of angular orientation is more than adequate.

As a practical necessity, the amount of data transmitted from a probe to earth must be minimized. All of the previous errors discussed were based on the assumption that the number of acceleration measurements was effectively infinite. It is difficult to assess the effects of reducing the data sampling frequency analytically. However, a numerical study done by V. L. Peterson of Ames Research Center (Ref. 7) indicates unnoticeable effects as the sampling period varies between 0 and 2 s.

In summary, the major errors in atmospheric determination by measured accelerations can be traced back to errors in the accelerometers. This difficulty is compounded by the fact that the experiment must be designed so as to accommodate a perhaps unknown maximum possible acceleration. Accuracy specification of 0.1% of the maximum value would be adequate, if it were known. Uncertainties in possible atmospheres must be accounted for by a more stringent requirement. Furthermore, assuming the accelerometer experiment constituted the only measurements taken during the entire entry trajectory, the resulting density-altitude relationship would be characterized by large errors in altitude during the high-velocity portion of the flight and large errors in density during the low-velocity regime. The actual magnitude of the errors, as well as altitudes corresponding to high- and low-velocity regimes, would depend on the particular atmosphere and entry capsule involved. The examples discussed here corresponded to engineering models for

a Mars entry vehicle and atmosphere. If the minimum atmosphere from Ref. 5 had been used rather than the maximum (10-mbar surface pressure instead of 40), the errors would have been smaller and the dividing altitude would have been 25,000 instead of 100,000 ft.

In either instance, the use of this technique alone will not produce an acceptable atmospheric definition. The most desirable single independent measurement which would increase the accuracy of the technique would be a time-altitude measurement. However, even with such an aid, there would still be large errors in density during the very-low-velocity region. Therefore, in order to insure an accurate determination of the whole atmosphere it would be necessary to adjoin a complete experiment in say the subsonic portion of the flight rather than an independent altitude measurement. Thus, the applicability of the accelerometer experiment is limited to not only a high-velocity flight regime, but also to one where atmospheric characteristics pertaining to the low-velocity region are known.

2. Subsonic Atmosphere Definition Experiment

The preceding material has discussed the determination of a planetary atmospheric structure from the acceleration-time history of an entry vehicle. The indication was that as the entry vehicle slows to subsonic speeds, significant degradation of accuracies results from integrating imperfect acceleration readings over long periods of time. Also, since a terminal condition is used as one of the boundary values for the trajectory differential equations, errors actually generated in the low-speed part of the flight affect the definition of the high-speed region. It was, therefore, concluded that the use of the accelerometer method should not only be restricted to that portion of the atmosphere traversed at speeds greater than the sonic speed, but also to a situation where atmospheric characteristics pertaining to the low-velocity region are known.

In Ref. 8, S. C. Sommer and A. G. Boissevain of the Ames Research Center discuss a subsonic experiment which could be used in conjunction with the accelerometer method in order to completely determine the atmosphere. The technique consists of onboard measurements, by the entry capsule, of pressure, temperature, and acceleration (versus time) during the latter portion of the flight. The mathematics involved in computing the atmospheric characteristics and trajectory parameters from these measurements point out several

advantages of this technique over the accelerometer method: (1) lengthy numerical integrations and corresponding cumulative errors are not required; (2) prior trajectory information, i.e., initial and/or boundary conditions for the trajectory differential equations, are not needed; (3) the average molecular weight of the atmosphere may be determined without prior knowledge of the gas properties. The restriction of this experiment to the low-speed portion of the flight insures the feasibility of the pressure and temperature measurements.

The accuracy of the resulting atmospheric definition is, of course, a function of the accuracy of the experimental measurements. However, errors are not necessarily propagated in direct proportion. The purpose of this work is to discuss the manner in which measurement errors do affect the determination of the atmosphere.

In general, stagnation conditions can be measured with greater accuracy than can free-stream conditions. Therefore, it will be assumed that the instrumentation is designed to measure stagnation temperature and pressure. The first phase of data analysis is concerned with the calculation of free-stream conditions using these measurements. The second phase is the subsequent computation of the remaining atmosphere properties and the trajectory parameters. This error discussion considers the problem in these two phases.

The measured pressures will be affected by vehicle angle-of-attack as well as flow compressibility. The angle-of-attack may be determined from the transverse and axial accelerations in conjunction with knowledge of the vehicle aerodynamics. Pressures can then be corrected to stagnation values by use of wind-tunnel pressure distributions. Stagnation temperatures may be measured directly with properly designed instrumentation. The method of converting stagnation pressure and temperature to free-stream values will be an iterative one. The dynamic pressure q can be calculated from the measured aerodynamic acceleration along the flight path and an assumed drag coefficient:

$$q = \frac{1}{2} \rho V^2 = \left(\frac{m}{C_D A} \right) a_s \quad (1)$$

Assuming an ideal gas and a value for the ratio of specific heats γ , the ratio q/p_t uniquely determines a Mach number. A new drag coefficient corresponding to the

Mach number may then be used, and the process continued until a compatible pair is produced. If the flow is supersonic, the measured pressure can be corrected for passage through a normal shock during the iteration. It is expected that in either case convergence would be quite rapid. The final Mach number which results from this iteration can be used to calculate free-stream temperature and pressure.

One obvious source of error is that γ will probably not be reliably known. However, an examination of Fig. 12 shows that within the postulated range ($1.35 < \gamma < 1.45$) γ has only minor effects, generally less than 1%. An estimate from best available information may be used and, if necessary, improved upon in an iterative fashion using the results of the complete analysis. A second source of

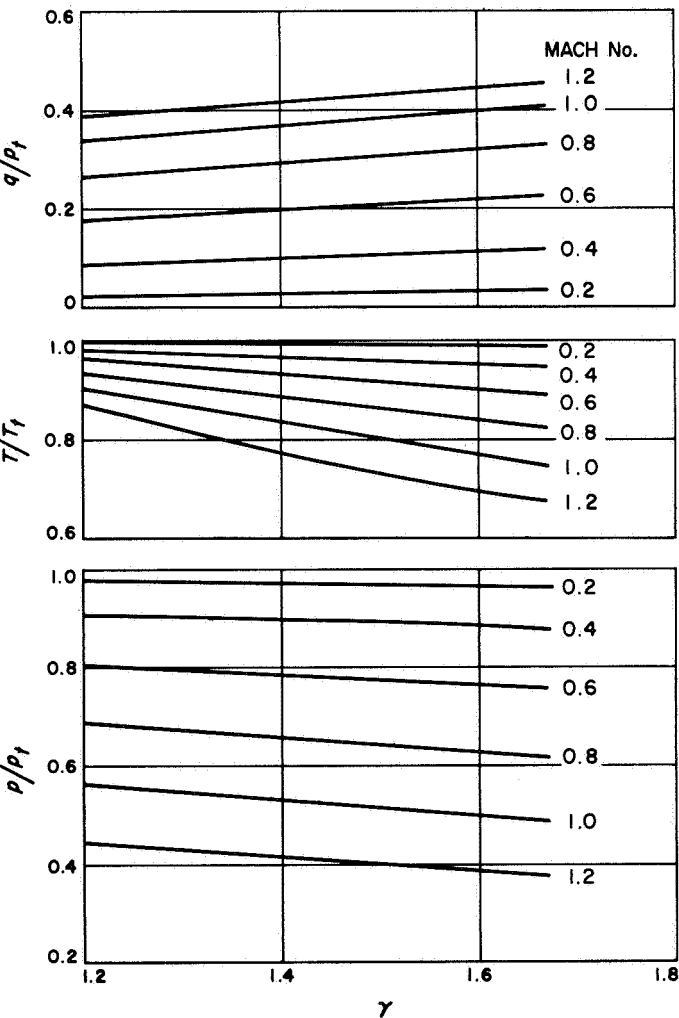


Fig. 12. Effects of γ on corrections to free-stream conditions

error arises from the actual determination of the Mach number. Figure 13 shows that the generation and influence of a Mach number error is dependent on the level at which it occurs. However, for the regime of interest, $0.2 < M < 1.0$, the three ratios of Fig. 13 can be approximated by linear functions of Mach number. The slopes of the p/p_t and q/p_t curves are about equal in magnitude, but opposite in sign. The slope of the T/T_t curve has the same sign as that of p/p_t , but is about half the magnitude. Therefore, an error in the ratio q/p_t will be related to the ratio p/p_t in a one-to-one fashion and to T/T_t in a two-to-one fashion, but with a change in direction in both cases because of the opposite algebraic signs of the slopes. Consequently, a measurement error in p_t is effectively doubled during the calculation of p ; e.g., a high p_t leads to a low q/p_t resulting in a low Mach number, which in turn leads to a high p/p_t . Error bounds expressed as percentages of the actual free-stream values may be derived in terms of error bounds on the measured values. Letting $\Delta()$ represent a signed error bound for

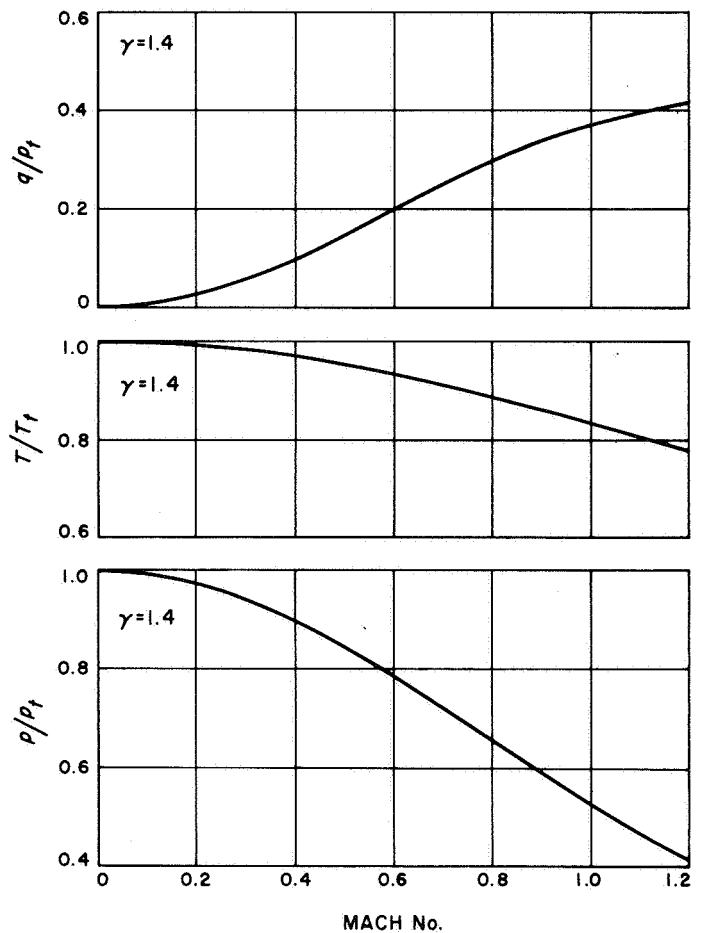


Fig. 13. Effects of errors in Mach No. determination

a measured or calculated value in terms of a percentage of the actual value, and retaining only first-order terms,

$$\begin{aligned}\Delta q &= \Delta a_s \\ \Delta\left(\frac{q}{p_t}\right) &= \Delta a_s - \Delta p_t \\ \Delta\left(\frac{p}{p_t}\right) &= -\Delta\left(\frac{q}{p_t}\right) = \Delta p_t - \Delta a_s \\ \Delta p &= \Delta\left(\frac{p}{p_t}\right) + \Delta p_t = 2\Delta p_t - \Delta a_s\end{aligned}\quad (2)$$

Since we are establishing error bounds, it should always be assumed that errors will occur with the worst possible combination of signs, i.e., that they will always be additive. This should not, however, preclude the possibility of self cancellation of errors during a calculation. The best procedure to follow is to derive equations with signed error bounds, examine the effects of all possible sign combinations of contributing factors, and determine a final result in terms of magnitudes of error bounds. Therefore, the last equation becomes

$$\Delta p = 2\Delta p_t + \Delta a_s \quad (3)$$

In a similar fashion, the signed error expression for ΔT is

$$\Delta T = \Delta T_t + \frac{\Delta p_t - \Delta a_s}{2} \quad (4)$$

This leads to the error bound,

$$\Delta T = \Delta T_t + \frac{\Delta p_t + \Delta a_s}{2} \quad (5)$$

The fact that the drag coefficient, which is a function of Mach number, was used to determine the Mach number is not considered in the error bounds given by Eqs. (3) and (5). However, for the general subsonic case of increasing drag coefficient with increasing Mach number, any error in Mach number due to other sources would be abated by an induced error from the drag coefficient. Because of this, and since measurement errors

would be expected to vary between zero and some limit, Eqs. (3) and (5), though reliable error bounds, should be regarded as very conservative error estimates.

The equation of state, the barometric equation, Eq. (1), and the trajectory equation $dh = -V \sin \theta dt$ yield

$$R = \frac{\left(\frac{2m}{C_D A}\right) g^2 \sin^2 \theta a_s \frac{p}{T}}{\left(\frac{dp}{dt}\right)^2} \quad (6)$$

$$\rho = \frac{p}{RT} \quad (7)$$

$$dh = \frac{dp}{\rho g} \quad (8)$$

The value of g changes little during the latter portion of the trajectory, and may be assumed constant for a first time through the equations. The resulting altitude-time history can then be used to correct for the variation in g . Therefore, the only unknown on the right side of Eq. (6) is the flight-path angle θ . For the purpose of error estimation, assume that θ is also known. Propagation of measurement errors may then be determined directly, and the problem of eliminating θ considered separately. Under this condition, Eq. (6) could be formulated in terms of integrals rather than derivatives. This would be advantageous for computational purposes since numerical integrations can be performed with greater reliability than numerical differentiations. For this discussion, it is sufficient to note that the denominator can be reduced to a function of

$$\int_{p_i}^p dp = p - p_i$$

Since a change in pressure can be determined more accurately than a pressure level, we can assume the denominator is exact. Therefore, at any given time

$$\Delta R = a_s + \Delta p - \Delta T$$

Substituting signed error expressions for Δp and ΔT ,

$$\Delta R = \Delta a_s + 2\Delta p_t - \Delta a_s - \left(\Delta T_t + \frac{\Delta p_t - \Delta a_s}{2} \right)$$

$$\Delta R = \frac{1}{2}\Delta a_s + \frac{3}{2}\Delta p_t - \Delta T_t \quad (9)$$

A comparison of the latter equation and the signed error expression for Δp , Eq. (2), shows that Δa_s and Δp_t cannot be cumulative in both. Similarly, comparing the latter equation and the signed error expression for ΔT , Eq. (4), shows the ΔT_t and Δp_t also cannot be cumulative in both. Though this implies that maximum errors cannot occur simultaneously in p , T , and R , it does not eliminate the possibility of a maximum error occurring independently in each sometime during the duration of the experiment. Therefore, the following three equations result from Eqs. (7), (8), and (9):

$$\Delta R = \frac{1}{2}\Delta a_s + \frac{3}{2}\Delta p_t + \Delta T_t \quad (10)$$

$$\Delta \rho = \Delta a_s \quad (11)$$

$$\Delta h \propto \Delta \rho \quad (12)$$

Again, Eqs. (10), (11), and (12) should be used as error bounds, not necessarily error estimates.

The elimination of θ from Eq. (6) cannot be handled in such a straightforward manner. Ref. 6 suggests using the differential equation describing the balance of forces normal to the trajectory along with Eq. (7), Eq. (8), and $dh = -V \sin \theta dt$ to obtain another expression for R . Equating this with Eq. (6) results in a first-order differential equation with $\cos \theta$ as the independent variable. A solution can be found in terms of numerical integrations of known quantities. However, the initial condition, $\cos \theta_i$, which is not known, also appears in this solution. Eq. (6) may be solved for $\cos \theta$, substituted for $\cos \theta$ and $\cos \theta_i$ in the solution (with the pressures and temperatures, etc., at the proper respective times), and an expression containing R , implicitly, results. However, because of the complexity of this equation, R may not be isolated, an iterative solution is necessary, and estimates of errors and convergence characteristics are difficult. An alternative approach somewhat less elegant, gives an indication of the magnitude of errors associated with the elimination of θ . In general, and especially for steep entry angles, $\theta_E > 45^\circ$, θ changes quite slowly for a large portion of the flight. This in itself indicates that θ

is of second-order influence and contributes a negligible amount to errors. A first approximation of a constant θ somewhere between the entry angle and 90° could be used to compute the atmospheric properties, including an average R , and the velocity-altitude time history. A variable θ history would then follow from the altitude-velocity information. The process could be repeated until some convergence criterion is met. A built-in check on the iteration is available since R must actually remain constant for the entire trajectory. The probable uniqueness of a θ versus time history which would satisfy both $R = \text{a constant}$ and $dh = -V \sin \theta dt$ implies a reliable solution and relegates the elimination of θ to introduction of second-order errors. Therefore, Eqs. (10), (11), and (12) are good error bounds as they stand.

This part has discussed error propagation from experimental measurements to atmosphere definition corresponding to a pressure, temperature, acceleration experiment. Under assumptions of subsonic speeds and a steep entry angle, expressions bounding errors in final results in terms of measurement accuracies have been derived. The experiment is, of course, not necessarily restricted to these cases. Note that it is necessary to have a complete knowledge of the vehicle aerodynamics and pressure distributions. Though angle-of-attack deviations are mentioned, it is tacitly assumed that they will remain small; i.e., the vehicle is dynamically stable for the majority of the flight. Furthermore, if coefficients are sensitive to Reynolds number an attempt to account for this must be made. This experiment can operate independently of the high-velocity accelerometer experiment, the converse of which is not true. As such, it becomes the more important of the two, and could feasibly be extended into the supersonic regime in order to function as a sole experiment.

E. Cold-Wall Wedge-Wake Investigation,

D. W. Kurtz

Wind Tunnel Test 20-648 was the fourth in a continuing series of detailed flow measurements in the near wake of a slender two-dimensional wedge with injection of gaseous nitrogen or helium from the base. The investigation was performed in cooperation with TRW Systems of Redondo Beach, California. The tests were run at a Mach number of 4.0 and Reynolds numbers of 3.04×10^6 , 8.78×10^4 , and 2.57×10^4 .

The model was a 6-deg half-angle wedge with a porous base through which the nitrogen or helium could be injected into the wake. Cooling passages within the

wedge allowed tests to be performed in a cold-wall condition.

Two principal types of wake measurements were made. Pitot and static probes mounted on a vertical traverse surveyed the wake area at several centerline positions during various injection rates with the model in a cold-wall condition. The data indicate that small rates of injection cause significant changes in the wake structure. This effect is most evident in the reduction of the trailing or wake-shock wave strength and in the widening of the viscous wake bucket.

Hot-wire fluctuation measurements were performed in the wake at various injection rates for the adiabatic condition. The wire was mounted on the vertical traverse in a horizontal position and had a nominal diameter of 0.00010 in. A typical survey is shown in Fig. 14.

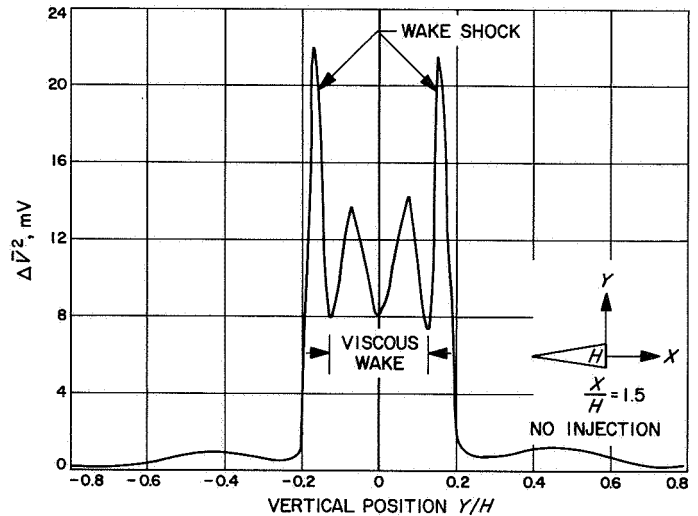


Fig. 14. Mean square voltage vs vertical wake position

References

1. Collins, D. J., et al, *Hypervelocity Shock Tube*, Technical Report 32-620. Jet Propulsion Laboratory, Pasadena, Calif., June 15, 1964.
2. Menard, W. A., Thomas, G. M., and Helliwell, T. M., "Experimental and Theoretical Study of Molecular, Continuum, and Line Radiation from Planetary Atmospheres," Paper 67-323, presented at the AIAA Thermophysics Specialist Conference, New Orleans, La., April 1967.
3. Seiff, A., *Some Possibilities for Determining the Characteristics of the Atmospheres of Mars and Venus from Gas-Dynamic Behavior of a Probe Vehicle*, NASA TN D-1770. National Aeronautics and Space Administration, Washington, D.C., 1963.
4. Seiff, A., and Reese, D. E., Jr., "Defining Mars Atmosphere—A Goal for the Early Missions," *Astronaut. Aeronaut.*, Vol. 3. No. 2, pp. 16-21, February 1964.
5. Levin, G. M., Evans, D. E., and Stevens, V., *NASA Engineering Models of the Mars Atmosphere for Entry Vehicle Design*, NASA TN D-2525. National Aeronautics and Space Administration, Washington, D.C., Nov. 1964.
6. Seiff, A., and Reese, D. E., Jr., "Use of Entry Vehicle Responses to Define the Properties of the Mars Atmosphere," Preprint 65-25, American Astronautical Society Symposium on Unmanned Exploration of the Solar System, Denver, Colorado, Feb. 1965.

References (contd)

7. Peterson, V. L., *Analysis of the Errors Associated with the Determination of Planetary Atmosphere Structure from Measured Accelerations of an Entry Vehicle*, NASA TR R-225. National Aeronautics and Space Administration, Washington, D.C., July 1965.
8. Sommer, S. C., and Boissevain, A. G., *The Structure of an Atmosphere from On-Board Measurements of Pressure, Temperature, and Acceleration*, NASA TN D-3933. National Aeronautics and Space Administration, Washington, D.C., Apr. 1967.

XIII. Polymer Research

PROPULSION DIVISION

A. Structural Integrity of Solid Propellant Retrorockets, III, E. N. Duran

1. Introduction

The study program to compare the state-of-the-art of experimental and theoretical techniques pertinent to the prediction of the structural integrity of solid propellant retrorockets is complete. Program progress and results of tasks 1, 2, and 3 were reported previously in SPS 37-35, Vol. IV, pp. 106-115, and SPS 37-36, Vol. IV, pp. 147-153. Task 1 was the construction and hydrotesting of four $\frac{1}{4}$ -scale *Surveyor* retrorocket cases. Task 2 was the three-dimensional viscoelastic stress analysis performed by Douglas Aircraft Company under Contract NAS7-392 (Ref. 1). Task 3 was the measurement of temperature-time mechanical properties of *Surveyor*-type propellant and stress-freezing epoxy (Ref. 2) for use in the viscoelastic stress analysis. This article presents the results of task 4, an experimental verification of the analytical results obtained in task 2.

2. Task 4 Results

Task 4 consisted of two parts, a photoelastic study to evaluate the stress concentration caused by embedding

the instrumentation within the $\frac{1}{4}$ -scale *Surveyor* motors and the actual stress study, using a *Surveyor*-type propellant. The general constraints for both experimental studies were the same as those used for the viscoelastic stress analysis, i.e., temperatures of 80 and 20°F, loading ramps of 250 ms, and a maximum pressure of 600 psig. These values were believed to be representative of actual flight conditions.

Miniature stress transducers (Ref. 3) were constructed and calibrated, both mechanically and thermally, for the ranges under study. Two cases were instrumented with the transducers and two were instrumented with thermocouples. In the former, a rosette, consisting of three transducers aligned along the three axes of principal stress, was placed at each of five points considered to be critical (Fig. 1). In the latter, a single thermocouple was placed at each point.

Initially, stress-freezing epoxy was cast into one thermocouple-instrumented and one stress-transducer-instrumented case. The second set of cases was cast with propellant identical to that used in task 2. All four motors were then cured, the mandrels removed, and the resulting void filled with mineral oil. Fig. 2 shows two

GAGE No.	LOCATION		
	x	y	z
1	1.474	0	4.132
2	4.360	0	-0.500
3	3.928	1.892	-0.500
4	2.314	1.114	-3.138
5	2.088	0	0

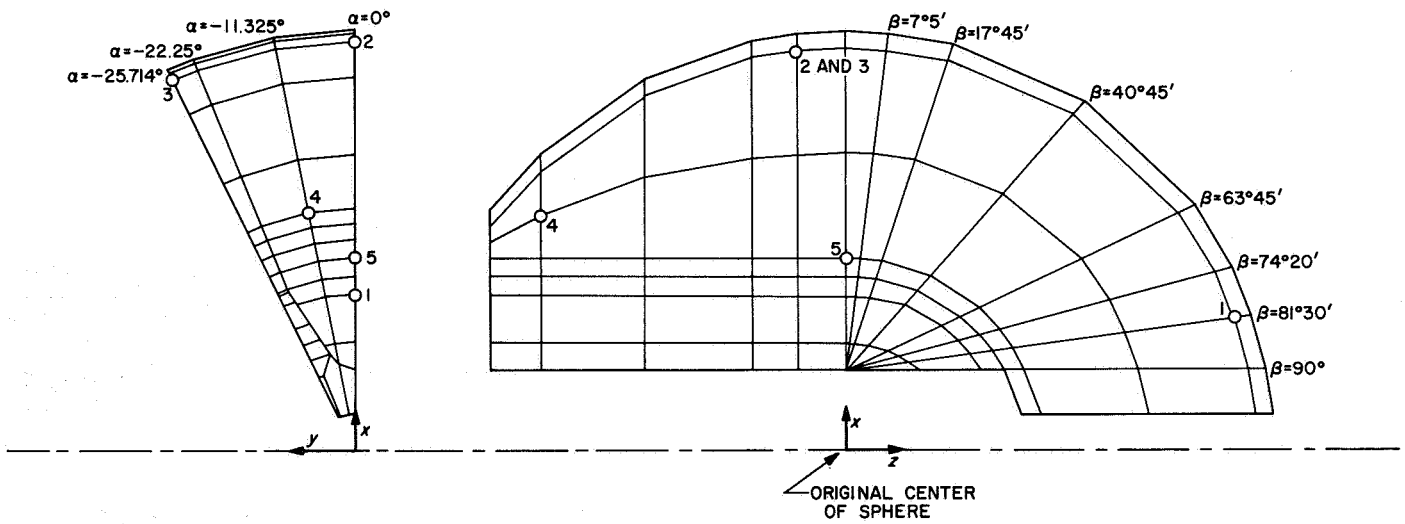


Fig. 1. Locations of the embedded miniature stress rosettes and thermocouples

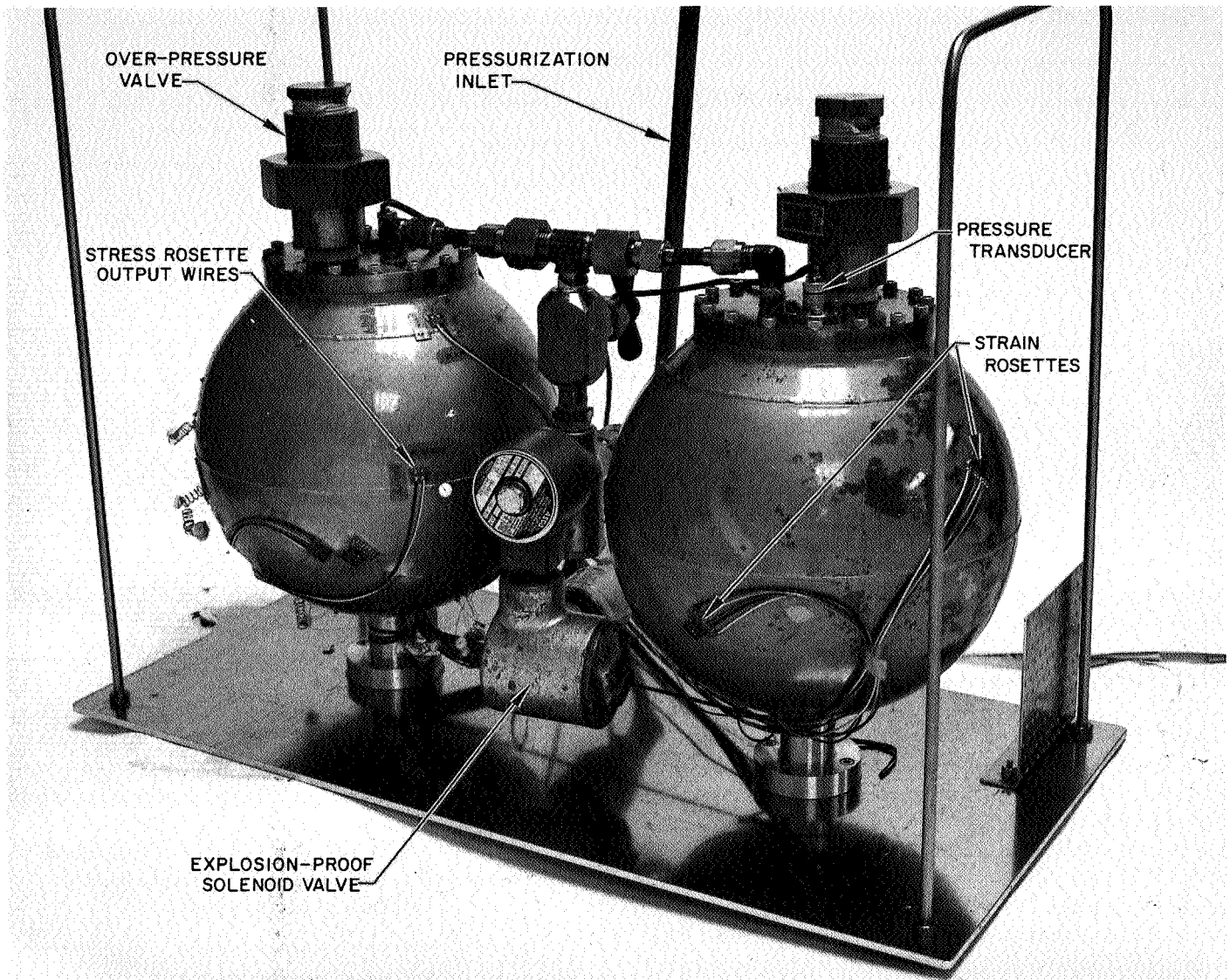


Fig. 2. Instrumented motors

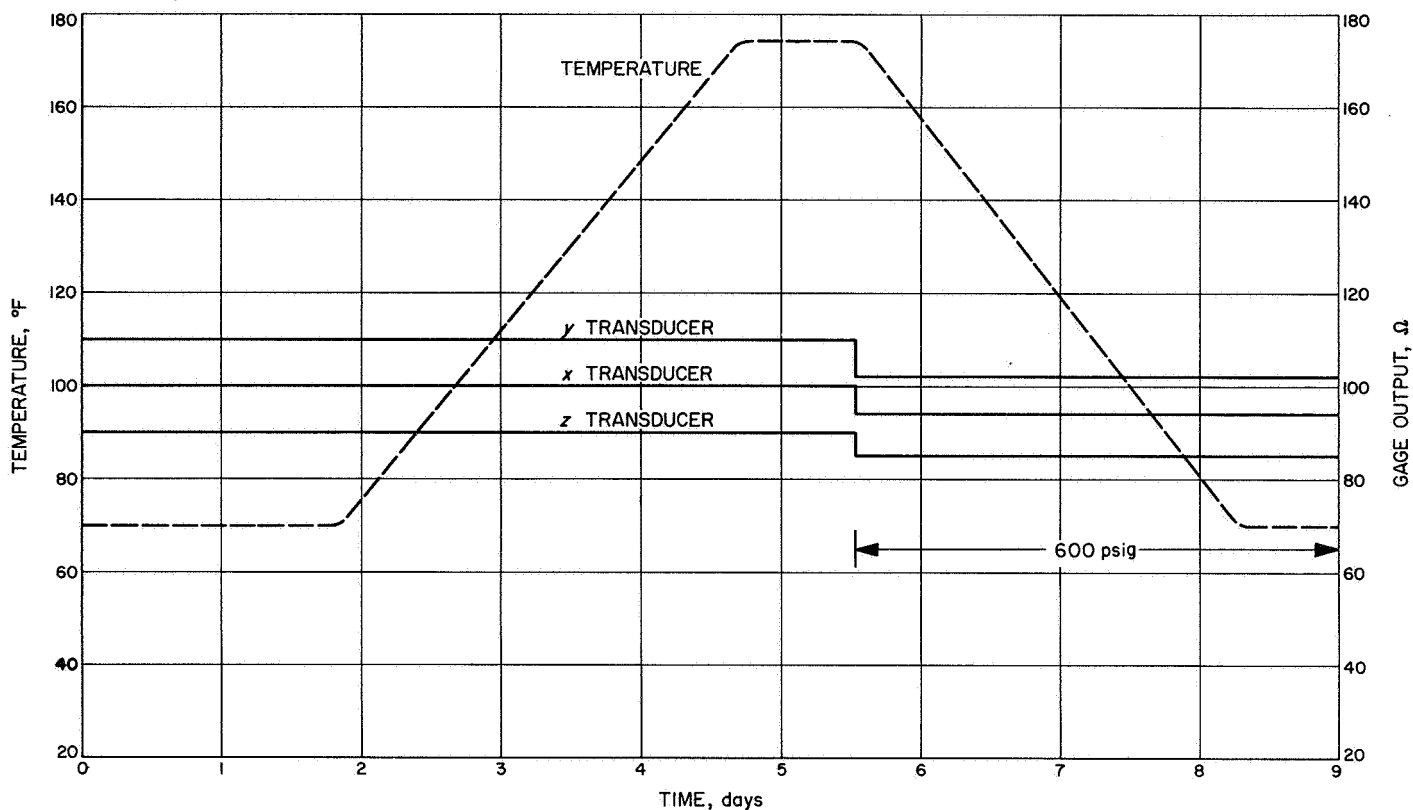


Fig. 3. Thermocouple and stress-transducer output (photoelastic model)

motors ready for pressurization. A graphical summary of the test cycles is shown in Figs. 3 and 4. The temperature-time history, from the time when the motors were cast to the end of the test, is presented.

After both motors containing *Surveyor*-type propellant were simultaneously pressurized at 80°F, an attempt was made to cycle to 20°F for the second pressurization. Due to equipment malfunction, this attempt was unsuccessful, and the low-temperature pressurization was carried out at 40°F, which was the lowest stable temperature that could be obtained. This deviation from the test schedule was not considered prejudicial to the results. The gage output-time history of one transducer rosette is included to depict the complete duty cycle. After the motors had been stabilized at 80°F, they were pressurized to 600 psig following a ramp function of 250 ms from zero to peak pressure. After cycling to 40°F, the motors were again pressurized to the same peak pressure and at the same rate. The gage temperature dependence was eliminated, and stress dependence only has been plotted. Cure shrinkage is indicated by the change in output at the cure temperature. Gage output during the two pressurization cycles is clearly indicated, and gage stability is confirmed

by lack of zero drift on pressure release. The absolute magnitude of the gage output could not be reduced to stresses of the expected level of magnitude on the basis of calibration alone. It was necessary to compensate for the hydrostatic stress field in the data reduction. When this is done, it may be observed (Table 1) that the stresses experimentally observed during the 80°F pressurization reasonably correspond to the analytically predicted stresses.

Table 1. Comparison of analytically predicted and experimentally determined stresses (propellant at 80°F, P = 600 psig)

Location	σ_r	σ_θ	σ_z	Method
1	623	633	639	Ref. 1 (analytical)
	625	625	655	Experimental
2	617	614	603	Ref. 1 (analytical)
	650	650	570	Experimental
3	617	614	603	Ref. 1 (analytical)
	679	621	575	Experimental
4	606	615	606	Ref. 1 (analytical)
	641	621	629	Experimental
5	609	625	614	Ref. 1 (analytical)
	613	617	640	Experimental

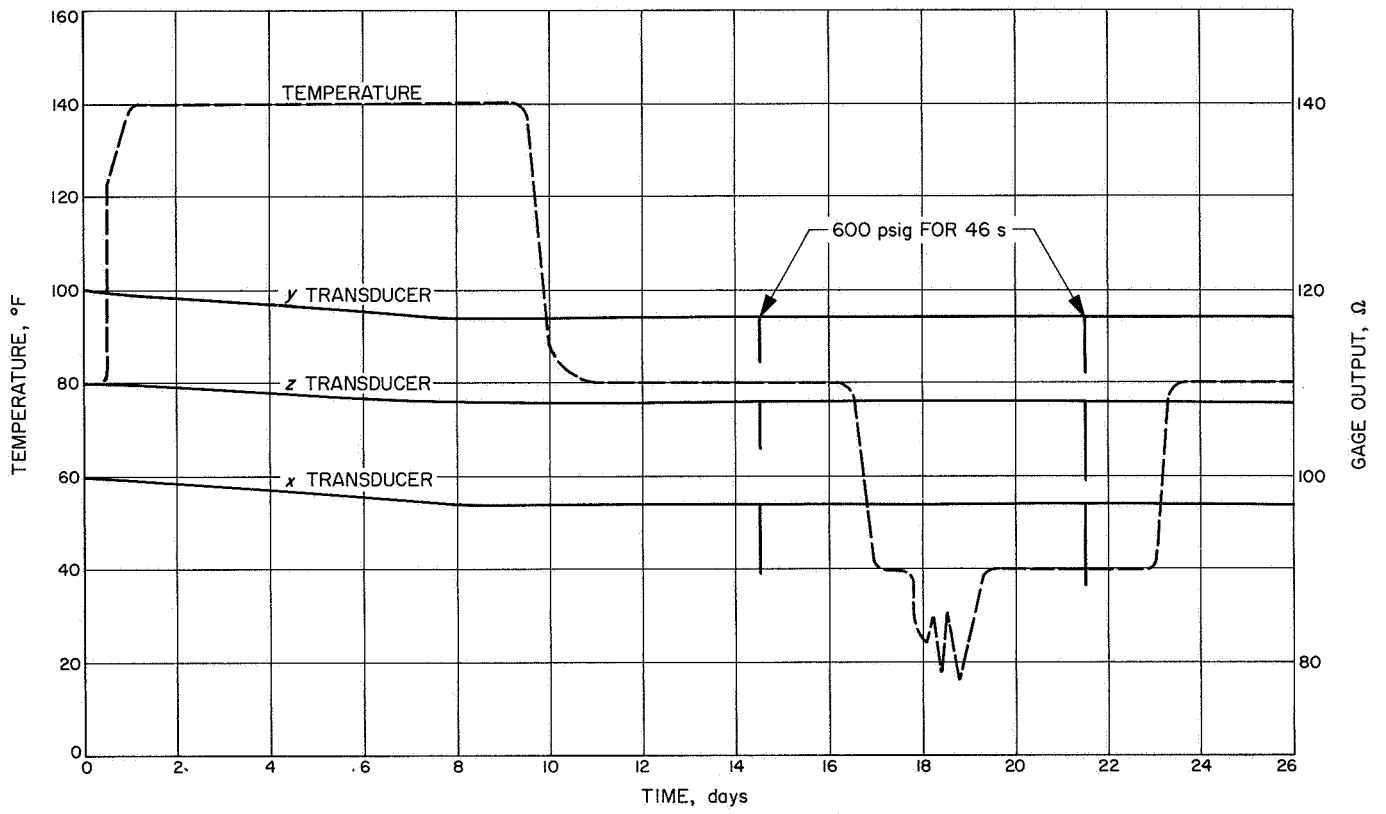


Fig. 4. One-quarter-scale Surveyor motor simulated duty cycle

B. Electron Spin Resonance Study of the Reaction Between Sodium and 2, 4-Bis-(4-Biphenyl)-Pentane, F. E. Stewart and A. Rembaum

1. Introduction

A recent study of the reaction between sodium and poly-4-vinyl-biphenyl (PVB) in dimethoxyethane (DME) has shown that electrons could be transferred from sodium to the biphenyl moieties of the polymer and that these electrons were delocalized along the polymer chain (SPS 37-43, Vol. IV, pp. 191-196). However, not all of the biphenyl moieties of PVB accepted electrons, but the extent of complexing increased as the molecular weight of the polymer decreased. Electron transfer from sodium to 4-ethyl biphenyl (EB), which represents the unit segment of the polymer chain, could be accomplished in stoichiometric proportions. The limited extent of reaction of PVB with sodium was attributed to either coulombic repulsion of electric charges, or to steric hindrance due to chain coiling.

In order to determine which of these two mechanisms predominates, the model compound 2, 4-bis-(4-biphenyl)-pentane (BBP) was investigated (Fig. 5). In this compound, the effect of steric hindrance is negligible, and it should be possible to transfer electrons to both biphenyl moieties, unless coulombic forces prevent it. Thus, the results of a simple sodium titration could distinguish between the two mechanisms. In addition, an electron spin resonance (ESR) study of the Na-BBP complex was carried out to verify the formation of BBP radical anions and to determine the extent of electron delocalization.

2. Experimental Method

BBP was prepared by J. Heller of the Stanford Research Institute. Its purity and structure were ascertained by

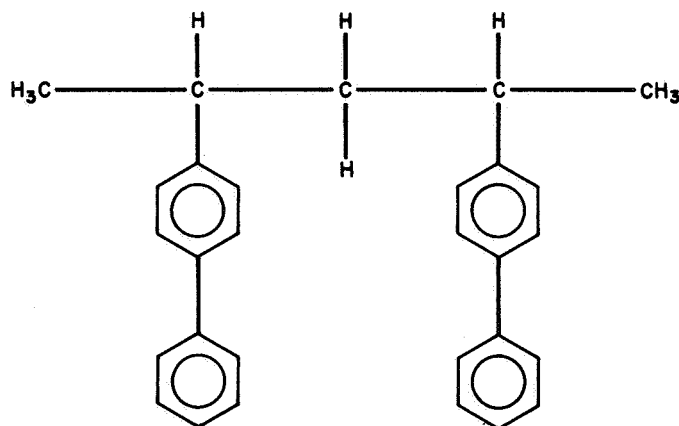


Fig. 5. 2, 4-bis-(4-biphenyl)-pentane

means of elemental and nuclear magnetic resonance analyses. The preparation of solutions of BBP radical anions over a sodium mirror, as well as the purification of DME and tetrahydrofuran (THF), were described elsewhere (Refs. 4 and 5). Sodium titrations were performed on samples which had been in contact with a sodium mirror for 20 h at -78°C (dry ice-methanol bath). Liquid-gas chromatography showed absence of any decomposition products and the absorption spectrum of the radical ion remained unchanged at room temperature over a period of 24 h. ESR measurements were made on a Varian V-4502 spectrometer equipped with the V-4540 variable temperature accessory.

3. Experimental Results and Discussion

Sodium titration results (Table 2) show that no more than one electron may be accepted by each BBP molecule, indicating that the incomplete complexing of biphenyl moieties of PVB is predominantly due to coulombic repulsion.

Table 2. Sodium titration results

Sample No.	BBP concentration, m/l	Na concentration, ^a m/l
1	0.0133	0.0132
2	0.00027	0.0002

^aAfter reaction with Na in DME for 20 h at -78°C .

The ESR spectrum of the singly-charged BBP radical anion (Fig. 6) consists of a group of seven lines and is no doubt an envelope of several hundred hyperfine lines broadened as a result of intramolecular electron exchange between the two biphenyl moieties. All attempts at further resolving the spectrum were unsuccessful. Several samples of varying concentration from 10^{-2} to 10^{-5} M in both DME and THF were prepared and examined from $+40$ to -100°C . Care was taken to insure the absence of field modulation broadening and microwave power saturation. Changes of temperature or solvent did not significantly alter the spectrum of Fig. 6, the width of which

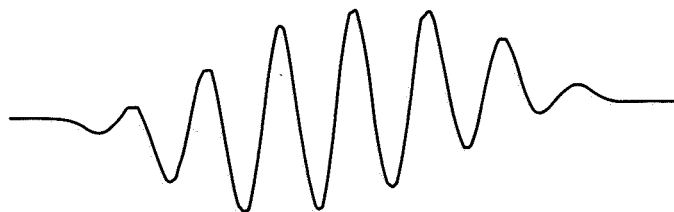


Fig. 6. ESR spectrum of BBP radical anion (5×10^{-4} M) in DME at -80°C

(17 gauss) is governed by the intramolecular exchange rate and is consistent with the fact that the BBP molecule contains two biphenyl groups. Because no intramolecular exchange occurs in 4-ethyl biphenyl, the latter yields a 486-line spectrum characterized by a total width of 25.1 gauss; in PVB of moderately high molecular weight ($M_w \approx 10^4$), extensive intramolecular exchange over several hundred biphenyl sites results in an ESR spectrum consisting of only a single narrow line (<2 gauss) (SPS 37-34, Vol. IV, pp. 191-196).

Previous investigations (SPS 37-34, Vol. IV, pp. 191-196) have shown that electron transfer to aromatic polymers leads to chain scission, the occurrence of which was attributed to repulsive interaction of unpaired electrons.

The assumption that two neighboring electrons constitute a driving force for bond scission is supported by the present study, since the BBP radical anion containing only one unpaired electron was found to be remarkably stable at room temperature.

C. Effects of Various Sterilization Cycles on the Properties of Polymeric Products, S. H. Kalfayan, B. A. Campbell, and R. H. Silver

1. Introduction

In the type-approval test procedures for the sterilization of materials, the JPL environmental specification VOL 50503-ETS calls for exposure to dry heat at 135°C for six 96-h cycles in nitrogen. Other time-temperature cycles, equivalent to the VOL 50503-ETS provisions, may also be used as effective heat sterilization conditions.

In order to study the effects of some of these other time-temperature cycles on the properties of polymeric materials, five products of interest in spacecraft application, in addition to cycling at 135°C, were also subjected to the following regimens: (1) six cycles of 250 h each at 120°C in dry nitrogen; and (2) six cycles of 59 h each at 150°C in dry nitrogen. The five products were also exposed to dry heat *in air* at 135°C, for six cycles of 96 h each, so that the effects of oxygen on these products could be assessed.

2. Experimental Method

a. Materials. The five products tested were: (1) a polyurethane encapsulant (Solithane 113); (2) a silicone encapsulant (RTV 30); (3) a butyl-rubber-based gasket material (Butyl 318-7); (4) a phenolic/glass laminate (Fiberglas 91LD); and (5) a polyimide film (Kapton 100).

b. Testing. Standard tests (ASTM) were performed on both the exposed and unexposed samples to determine the changes in the physical, mechanical, and electrical properties of the polymeric products. In all cases, the compounds subjected to the various time-temperature-atmosphere conditions were first exposed to the specified ethylene oxide/Freon 12 decontamination procedure, which consisted of six 28-h cycles of exposure to sterilant gas at 50°C and $50 \pm 5\%$ relative humidity.

3. Experimental Results and Discussion

The changes in the mechanical properties of the five compounds after exposure to dry heat in nitrogen and in air at various temperatures are given in Table 3. Values obtained for two electrical properties (volume resistivity

Table 3. Change in mechanical properties after exposure to dry heat at various conditions

Product and material type	Change in hardness (Shore or Rockwell)				Tensile strength (psi), % retained				Elongation, % retained			
	120°C 1500 h N ₂	150°C 354 h N ₂	135°C 576 h N ₂	135°C 576 h air	120°C 1500 h N ₂	150°C 354 h N ₂	135°C 576 h N ₂	135°C 576 h air	120°C 1500 h N ₂	150°C 354 h N ₂	135°C 576 h N ₂	135°C 576 h air
	Solithane No. 1 (polyurethane)	+1	-20	-13	+ 1	68	38	60	62	119	137	144
RTV 30/T-12 (silicone)	+6	+ 3	+ 3	+ 5	95	88	90	110	92	120	122	103
Butyl 318-7	-2	-12	- 4	-12	103	89	90	40	91	96	107	112
Fiberglas 91LD (phenolic/glass)	+5	+ 5	+ 8	+ 7	112	90	98	98	75	92	80	50
	Tear strength, % retained											
Kapton 100 (polyimide)	62	82	94	111	100	94	92	91	89	93	122	61

and dielectric strength) are given in Table 4. Weight loss and volume changes are reported in Table 5.

The data in Table 3 indicate that in an atmosphere of nitrogen the polyurethane-based product, Solithane 113, and the butyl-based product, Butyl 318-7, were more affected by exposure to the higher temperature (150°C) for a shorter period (354 h) than by exposure to the lower temperature (120°C) for a longer period (1500 h). At 150°C, the polyurethane showed considerable loss in hardness and tensile strength, and the butyl product showed considerable softening, but not as much loss in tensile strength.

These two products were also the more affected, among the five, by exposure to 135°C *in air*. The results of exposure to air at 135°C, however, were different with each of the two products. Solithane 113 hardened slightly and lost in elongation, suggesting crosslinking, whereas Butyl

318-7 softened, lost in tensile strength, and showed an increase in elongation: changes that suggest possible degradation.

No pronounced changes in the mechanical properties of the other three compounds tested were observed with the changes in time-temperature conditions in nitrogen. Some noteworthy changes could be observed with both Fibreglas 91LD and Kapton 100 when exposed to air at 135°C. These two products showed greater loss in elongation after exposure, indicating crosslinking. The tear strength of Kapton 100 and the tensile strength of RTV 30 increased after exposure to air at 135°C, while decreases in these properties were encountered after exposure to nitrogen at 135°C.

Table 4 shows that, in general, the electrical properties of the products tested were not affected markedly by the changes in the time-temperature-atmosphere conditions.

Table 4. Electrical properties after exposure to dry heat at various conditions

Product and material type	Volume resistivity, Ω -cm					Dielectric strength, V/mil				
	Control	120°C 1500 h N ₂	150°C 354 h N ₂	135°C 576 h N ₂	135°C 576 h air	Control	120°C 1500 h N ₂	150°C 354 h N ₂	135°C 576 h N ₂	135°C 576 h air
Solithane No. 1 (polyurethane)	8.1×10^{14}	2.3×10^{14}	2.2×10^{13}	2.59×10^{13}	3.9×10^{14}	465	480	427	471	452
RTV 30/T-12 (silicone)	3.17×10^{14}	3.7×10^{14}	1.04×10^{15}	7.32×10^{14}	3.1×10^{14}	486	456	449	491	>485
Fibreglas 91LD (phenolic/glass)	1.94×10^{14}	4.6×10^{13}	4.6×10^{13}	4.4×10^{12}	4.7×10^{13}	186	>337	337	203	>375
Kapton 100 (polyimide)	1.12×10^{17}	1.03×10^{17}	6.9×10^{16}	1.2×10^{17}	7.3×10^{16}	4630	5720	5070	5350	5255

Table 5. Percent weight and volume changes after exposure to dry heat at various conditions

Product and material type	Weight change, %				Volume change, %			
	120°C 1500 h N ₂	150°C 354 h N ₂	135°C 576 h N ₂	135°C 576 h air	120°C 1500 h N ₂	150°C 354 h N ₂	135°C 576 h N ₂	135°C 576 h air
Solithane No. 1 (polyurethane)	-0.380	-1.759	+0.825	-0.386	-0.699	Samples deformed	-0.731	-1.362
RTV 30/T-12 (silicone)	-0.357	-0.445	-0.339	-0.446	-0.912	-0.265	-0.561	+0.036
Butyl 318-7	-1.714	-2.164	-1.969	-1.946	-1.869	-2.381	-0.593	-2.271
Fibreglas 91LD (phenolic/glass)	-1.945	-1.888	-1.578	-1.840	-1.193	-2.197	-0.119	-0.882
Kapton 100 (polyimide)	-0.159	-0.131	-0.200	-0.534	-0.050	-0.569	-0.398	-0.150

References

1. Mellette, R. V., et al, *A Grain Structural Analysis on a Spherical Motor*, Report SM-52244. Missile and Space Systems Division, Douglas Aircraft Company, Inc., Santa Monica, Calif., Feb. 1966.
2. Durelli, A. J., and Riley, W. F., *Introduction to Photomechanics*. Prentice-Hall, Englewood Cliffs, New Jersey, 1965.
3. San Miguel, A., Silver, R. H., and Duran, E. N., "On the Practical Application of a Miniature Stress Rosette to Solid Propellant Grain Design," *Bulletin of the Fourth Meeting of the ICRPG Working Group on Mechanical Behavior*, The Johns Hopkins University, Applied Physics Laboratory, Silver Spring, Maryland, November 16-19, 1965.
4. Rembaum, A., et al, "Equilibria Between Metallic Sodium and Aromatic Hydrocarbons," *J. Am. Chem. Soc.*, Vol. 89, p. 1062, 1967.
5. Paul, D. E., Lipkin, D., and Weissman, S. I., "Reactions of Sodium Metals with Aromatic Hydrocarbons," *J. Am. Chem. Soc.*, Vol. 78, p. 116, 1956.

XIV. Research and Advanced Concepts

PROPULSION DIVISION

A. Nuclear System Studies: Uninsulated In-Core Thermionic Diode, J. P. Davis

1. Introduction

Two major areas of uncertainty concerning feasibility of in-core thermionic diodes are the nuclear fuels and insulator materials. For systems of 10,000-h life yielding 50 kWe net power delivered to an ion engine for propulsion application, fuel burnups are fairly low, ~ 0.3 at. %, for which fuel swelling for vented carbides, vented UO_2 , or unvented $\text{UO}_2\text{-W}$ is hoped to be tolerably small or nonexistent. Insulator performance, however, remains a distinct area of uncertainty for present thermionic reactor concepts.

Insulators are required for seals to contain the cesium interelectrode gas, and to insulate collector structure from the liquid metal coolant, thereby permitting voltage output to be increased by series connection of diodes from the base 0.7 V available for an individual diode. For the externally fueled and pancake reactor designs, this collector or sheath insulator is not exposed to cesium gas. In the flashlight design, the sheath insulator is exposed to cesium. (Basic descriptions of these concepts are given in Ref. 1). Radiation damage to insulators in the expected

range of integrated fast neutron fluxes has indicated that potential cracking problems may exist. The dielectric strength of cracked insulator, both exposed and unexposed to cesium gas, is presently not known. Several experimental programs, including one being funded by JPL, are presently under way at various facilities. Seal insulators can be located outside the core itself for both the externally fueled and flashlight designs where integrated fast neutron flux is somewhat lower than within the core. In the pancake design, seal insulators are necessarily located within the core. At the present time, therefore, the question of insulator integrity is a significant and uncertain area of concern affecting, in various degrees, all the presently contemplated thermionic reactor designs.

It is possible to conceive of an in-core thermionic reactor design which eliminates all insulator materials from the core itself and still permits series connection of diodes to build output voltage to a reasonable magnitude. The emitter-collector seals in the full core-length externally fueled diode, as proposed by Republic Aviation, are already outside the core. The collector-insulator-sheath trilayer construction could be eliminated by utilizing the liquid metal-filled coolant tube itself to carry the current out of the core. Just outside the reflector, the

desired series-parallel connections could be made by substantial busbars. These busbars would also serve as the structural members maintaining the tube-to-tube spacings. The emitter and fuel structure is basically hung from its respective coolant tube. Additional support, if required, could be obtained from pins at the top and bottom of the fuel element cladding, which are electrically insulated from grid plates above and below the core. Since temperatures are relatively low and space is not a problem, substantial insulator sections could be employed.

In a 50-kWe design, roughly 200 diodes are required. These could be connected, for example, 5 in parallel and

40 in series for about 25-V output. The paralleled diodes could have their coolant tubes manifolded to a single tube which then proceeds to the radiator. Thus 40 independent circuits would be established to form the radiator. One tube would make several loops in the radiator with appropriate finning. Finning would be electrically interrupted where one coolant loop was adjacent to another loop at a different potential. Again, inches of separation could be employed and insulated supports could be utilized for structural integrity. No current flows through these coolant tubes beyond the point of series-parallel busbar coupling; they are simply isopotential surfaces.

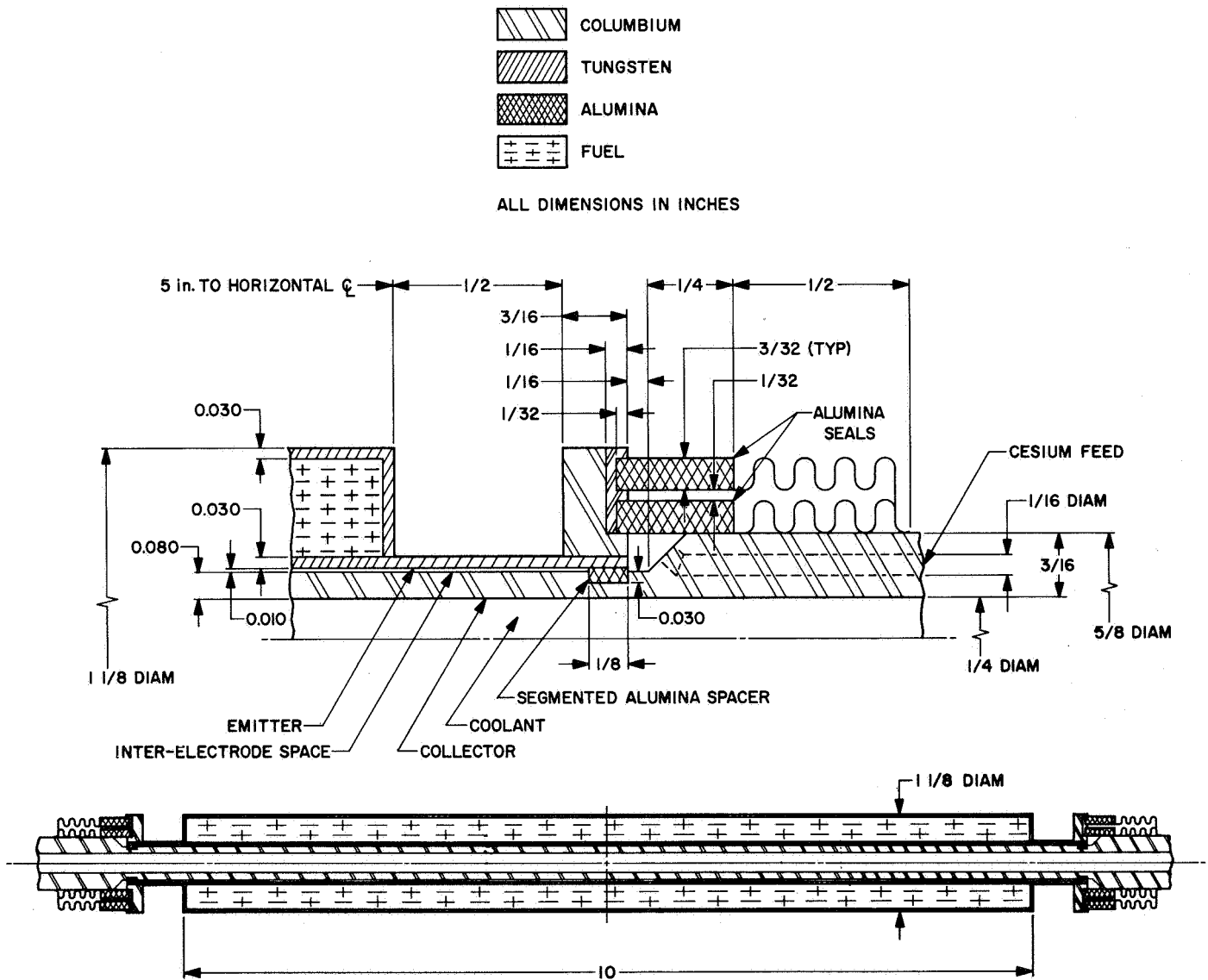


Fig. 1. Uninsulated externally fueled thermionic diode

The major drawback to the concept is that 40 separate little pumps are required, although the pump efficiency requirements are not severe. Since heat rejection is required anyway, perhaps even thermoelectric pumps could be employed for the low-pressure drop requirements of the system. Heat pipes would be another possibility and ideally suited for such an application if the heat transport capabilities and the flow area available were compatible. This possibility will be investigated.

Another significant advantage of this concept is inherent protection against potential shorts to ground. Where the coolant loop is isolated from the electrical system as in all other in-core diode concepts, insulator breakdown from collector to sheath represents a short to ground. This type of failure is intolerable and must be protected against by fusing or some other positive means. In this concept, no such grounding possibility exists within the core itself. Outside the core, massive insulation can be provided to protect against this type of failure.

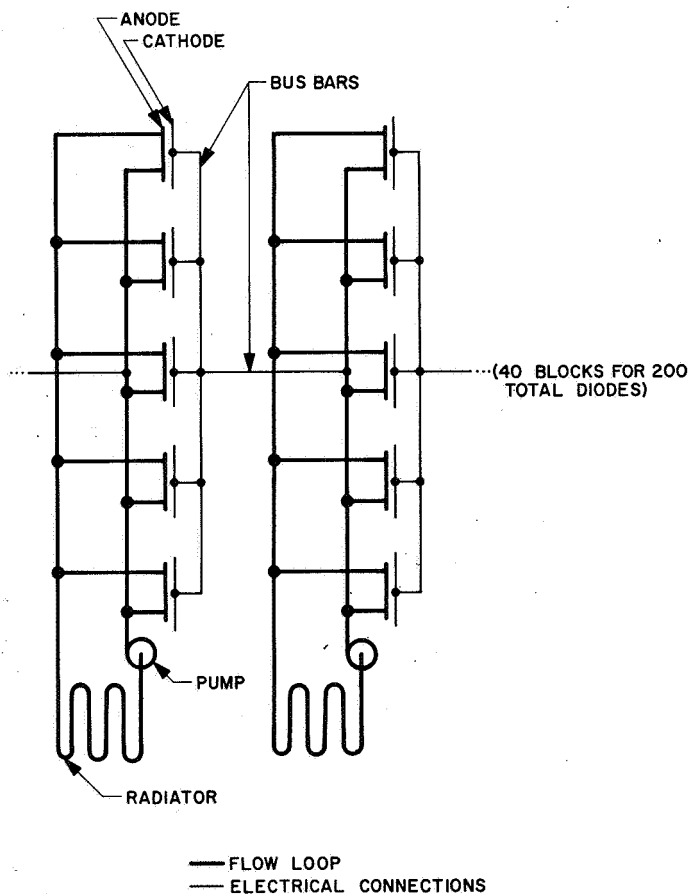


Fig. 2. Schematic flow loops and electrical connections for five parallel diode matrix (two blocks shown)

A typical diode and electrical schematic for series-paralleled coupling are shown in Figs. 1 and 2. Double seals have been incorporated for redundancy at these critical containment points.

2. Analysis

The analysis of relatively long, externally fueled diodes must consider the effect of axial voltage drops along the emitter and collector surfaces. Additionally, all diodes must optimize the lead which carries current from the emitter of one to the collector of the next when connected in series arrangement in order to minimize the combined electrical and thermal losses.

The diode is represented schematically in Fig. 3. Symbols used in the analysis are defined in Table I.

A typical diode i - V characteristic is shown in Fig. 4 (Ref. 2). A linearized characteristic over the operating

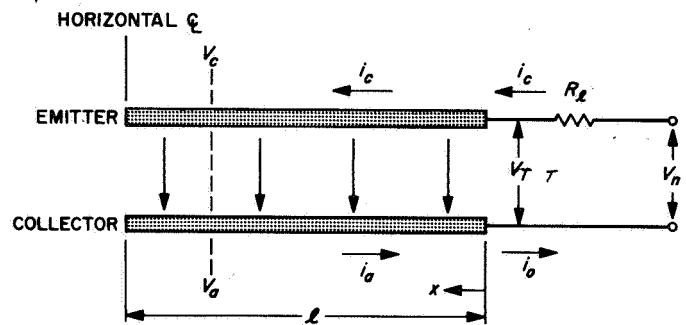


Fig. 3. Diode representation

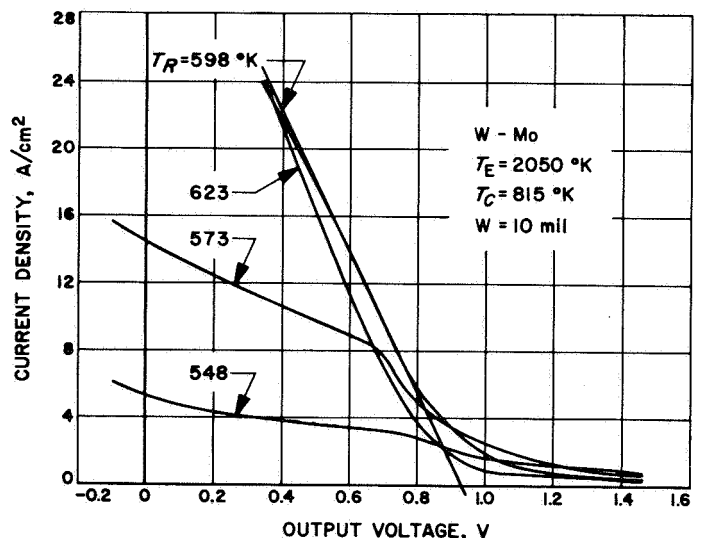


Fig. 4. Diode i - V characteristic

range of interest is taken of the form:

$$V = V_o - JAR_i = V_o - iR_i \quad (1)$$

Writing the equations for variation in voltage along the emitter and collector with the linearized i - V relation of Eq. (1) yields:

$$\frac{A_c}{\rho_c} \frac{d^2V_c}{dx^2} = \frac{1}{R_i l} (V_c - V_a + V_o) \quad (2)$$

$$\frac{A_a}{\rho_a} \frac{d^2V_a}{dx^2} = \frac{-1}{R_i l} (V_c - V_a + V_o) \quad (3)$$

Solving these relations with appropriate boundary conditions yields Eq. (4) and, solving for the terminal voltage in terms of the output current, yields Eq. (4a):

$$\Delta V(x) = V_T + (V_o - V_T) \times \left\{ 1 - \frac{e^{-x/l} \left(\frac{R_c + R_a}{R_i} \right)^{1/2} \left[1 + e^{-2(l-x)/l} \left(\frac{R_c + R_a}{R_i} \right)^{1/2} \right]}{1 + e^{-2} \left(\frac{R_c + R_a}{R_i} \right)^{1/2}} \right\} \quad (4)$$

$$V_T = V_o - i_o [R_i (R_c + R_a)]^{1/2} \times \left[\frac{1 + e^{-2} \left(\frac{R_c + R_a}{R_i} \right)^{1/2}}{1 - e^{-2} \left(\frac{R_c + R_a}{R_i} \right)^{1/2}} \right] \quad (4a)$$

where

$$R_c = \frac{\rho_c l}{A_c}$$

$$R_a = \frac{\rho_a l}{A_a}$$

if $R_a + R_c$ is expressed in terms of R_i by:

$$R_c + R_a = KR_i$$

Eq. (4) is written as

$$V_T = V_o - i_o R_i (K)^{1/2} \left[\frac{1 + e^{-2(K)^{1/2}}}{1 - e^{-2(K)^{1/2}}} \right] = V_o - i_o R_i \mathcal{F} \quad (5)$$

Table 1. Nomenclature

A	area, cm^2
\mathcal{F}	effective increase in gap resistance due to axial emitter and collector resistances
i	current, A
J	current density, A/cm^2
K	ratio of combined axial emitter and collector resistances to effective gap resistance
k	thermal conductivity, $\text{W}/\text{cm} - ^\circ\text{C}$
l	length
P	electric power, W
Q	heat power, W
R	resistance, Ω
V	voltage
x	axial position from terminals
y	length to area ratio for lead, cm^{-1}
ΔT	temperature difference, $^\circ\text{C}$
ρ	specific resistance, $\Omega\text{-cm}$
ϕ	effective electron cooling constant, V
Subscripts	
a	collector (anode)
c	emitter (cathode)
i	effective internal resistance in linearized i - V curve
l	lead
n	net
o	output or zero current intercept of linearized i - V curve
T	terminals (before optimized leads loss)

where

$$\mathcal{F} = (K)^{1/2} \left[\frac{1 + e^{-2(K)^{1/2}}}{1 - e^{-2(K)^{1/2}}} \right] \quad (6)$$

represents the "effective" increase in R_i due to the presence of emitter and collector axial resistances.

The presence of the lead carrying the output current from emitter to collector of the next diode in series results in electrical power loss and heat conduction. In the best case, heat loss normal to the lead by radiation and conduction is minimized and only axial conduction is considered. The optimum lead losses can thus never be less than those given in Eqs. (7) and (8).

$$P_l = i_o^2 \rho_l \frac{l_l}{A_l} = i_o^2 \rho_l y \quad (7)$$

$$Q_l = k\Delta T \frac{A_l}{l_l} = \frac{k\Delta T}{y} \quad (8)$$

It is desirable to maintain the emitter at the highest allowable temperature uniformly along its length to achieve maximum output. It is therefore assumed that heat input along its length is "shaped" by variable fuel loading to maintain uniform temperature. Without this shaping, temperature would vary due to both the effect of varying current density and the end effect of heat conduction down the lead. With this shaping provision, ΔT is simply the temperature difference between the emitter and collector. Heat input to the diode is composed of Q_r combined thermal radiation and cesium gap

conduction, ϕi_o electron cooling,¹ and the lead conduction given by Eq. (8).

The over-all efficiency is then given by:

$$\eta = \frac{i_o V_n}{Q_r + \phi i_o + \frac{k\Delta T}{y}} \quad (9)$$

$$\eta = \frac{i_o V - i_o^2 R_i \mathcal{F} - i_o^2 \rho_l y}{Q_r + \phi i_o + \frac{k\Delta T}{y}} \quad (10)$$

The partial derivative of Eq. (10) may now be taken with respect to y to define the optimum lead. This yields:

$$y_{opt} = \left(\frac{l_l}{A_l} \right)_{opt} = \frac{V_o - i_o R_i \mathcal{F}}{\rho_l i_o \left\{ 1 + \left[1 + \frac{(Q_r + \phi i_o)(V_o - i_o R_i \mathcal{F})}{k\Delta T \rho_l i_o} \right]^{1/2} \right\}} \quad (11)$$

The over-all efficiency may now be written, substituting y_{opt} from Eq. (11) into Eq. (10) as

$$\eta = \frac{i_o (V_o - i_o R_i \mathcal{F}) \left\{ \frac{\left[1 + \frac{(Q_r + \phi i_o)(V_o - i_o R_i \mathcal{F})}{k\Delta T \rho_l i_o} \right]^{1/2}}{1 + \left[1 + \frac{(Q_r + \phi i_o)(V_o - i_o R_i \mathcal{F})}{k\Delta T \rho_l i_o} \right]^{1/2}} \right\}}{Q_r + \phi i_o + \frac{k\Delta T i_o \rho_l}{V_o - i_o R_i \mathcal{F}} \left\{ 1 + \left[1 + \frac{(Q_r + \phi i_o)(V_o - i_o R_i \mathcal{F})}{k\Delta T \rho_l i_o} \right]^{1/2} \right\}} \quad (12)$$

The numerator term in parentheses represents the terminal voltage prior to the optimized lead. The numerator term in braces represents the net output voltage to terminal voltage ratio through the optimized lead. The last term in the denominator represents the heat loss through the optimized lead. The numerator of Eq. (12) represents the net power available. The net power per unit emitter area and efficiency are plotted in Fig. 5 using the following values:

$$V_o = 0.92 \text{ V}$$

$$R_i = 0.0236 \Omega\text{-cm}^2 \div 43.6 \text{ cm}^2 = 5.4 \times 10^{-4} \Omega$$

$$Q_r = 20 \text{ W/cm}^2 \times 43.6 \text{ cm}^2 = 872 \text{ W}$$

$$\phi = 3.0 \text{ V}$$

$$k = 1.0 \text{ W/cm} - ^\circ\text{C (tungsten)}$$

$$\Delta T = 800^\circ\text{C}$$

$$\rho_l = 0 \text{ (perfect lead), } 50 \times 10^{-8} \Omega\text{-cm (tungsten)}$$

$$\mathcal{F} = 1, 1.34, 1.65$$

Curves (1) represent the maximum attainable efficiency and power density with zero emitter and collector resistances ($\mathcal{F} = 1$) and a perfect lead (very thin zero

¹The actual electron cooling expression is complex. Direct proportionality to current is a fair first order approximation.

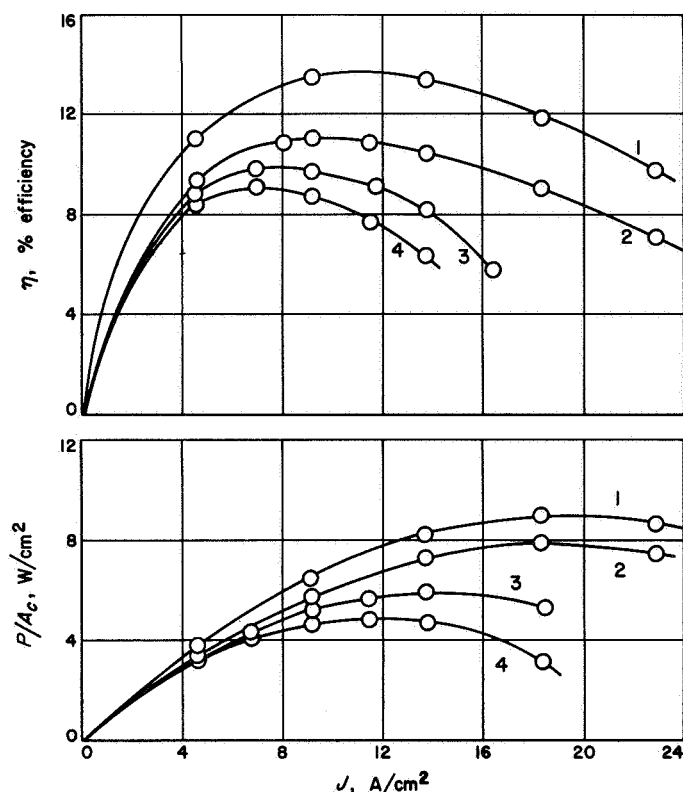


Fig. 5. Efficiency and power density versus current density

resistivity). Curves (2) represent zero emitter and collector resistances ($\mathcal{F} = 1$) and an optimized tungsten lead. Curves (3) represent a value of \mathcal{F} calculated when emitter plus collector effective axial resistance is calculated from Fig. 1 assuming $\text{UO}_2\text{-W}$ fuel. Curve (4) assumes UO_2 fuel with some tungsten webs to electrically couple the inner and outer fuel clads.

The uninsulated, externally fueled diode should suffer no performance penalties over the "conventional" externally fueled diode. For a given set of dimensions it should, in fact, improve performance somewhat due to effective reduction of the collector axial resistance by utilizing the entire coolant tube to carry current within the core.

Referring to Eq. (4a), it should be noted that if axial voltage drops are significant, the "local" operating point for the diode can vary significantly from the terminal to the center line. Lower current density and higher voltages exist as the axial location moves away from the terminals. The over-all effect on average power density and efficiency can be considerable if axial voltage drops get too high just from the above consideration

and in addition to the direct i^2R electrical power loss. This effect is, of course, taken into account in the analysis contained herein.

Refinement of the design concept and investigation of coolant pumping schemes will be pursued.

B. Liquid MHD Power Conversion, D. Elliott, D. Cerini, L. Hays, D. O'Connor, and G. Haskins

The long lifetimes required of electric-propulsion powerplants make systems without rotating parts attractive. A nonrotating Rankine cycle being investigated is the liquid-metal magnetohydrodynamic (MHD) system wherein lithium is accelerated by cesium vapor in a two-phase nozzle, separated from the cesium, decelerated in a magnetohydrodynamic generator, and returned through a diffuser and heat source to the nozzle.

Hydraulic testing of the 50-kW NaK-nitrogen conversion system is continuing. Analysis of the data on corrosion of Nb-1%Zr by lithium flowing at 20-47 m/s has been completed. A second Haynes-25 alloy corrosion loop experiment is being prepared, and assembly of the two-phase cesium-lithium loop has been resumed utilizing a new welding chamber.

1. NaK-Nitrogen Conversion System

The 50-kW, room-temperature, NaK-nitrogen conversion system is being tested with water and nitrogen to optimize the separator and diffusers and determine the flow conditions that will exist in the NaK tests. The components tested to date are the nozzle, separator, and upstream diffuser. The relationship between these components is shown schematically in Fig. 6, and the experiment is shown in Fig. 7. The nozzle is mounted on a thrust table to permit measurement of the exit velocity from each component as it is added. Knowing the velocity leaving each component, the net available fluid power existing at any station in the conversion system can be calculated from

$$P_m = \frac{1}{2} \dot{m}_a (V^2 - V_s^2) \quad (1)$$

where \dot{m}_a is the captured liquid flow rate and V_s is the velocity required at the downstream diffuser inlet at the pressure and void fraction existing at the exit of the component in question. The diffuser for the conversion

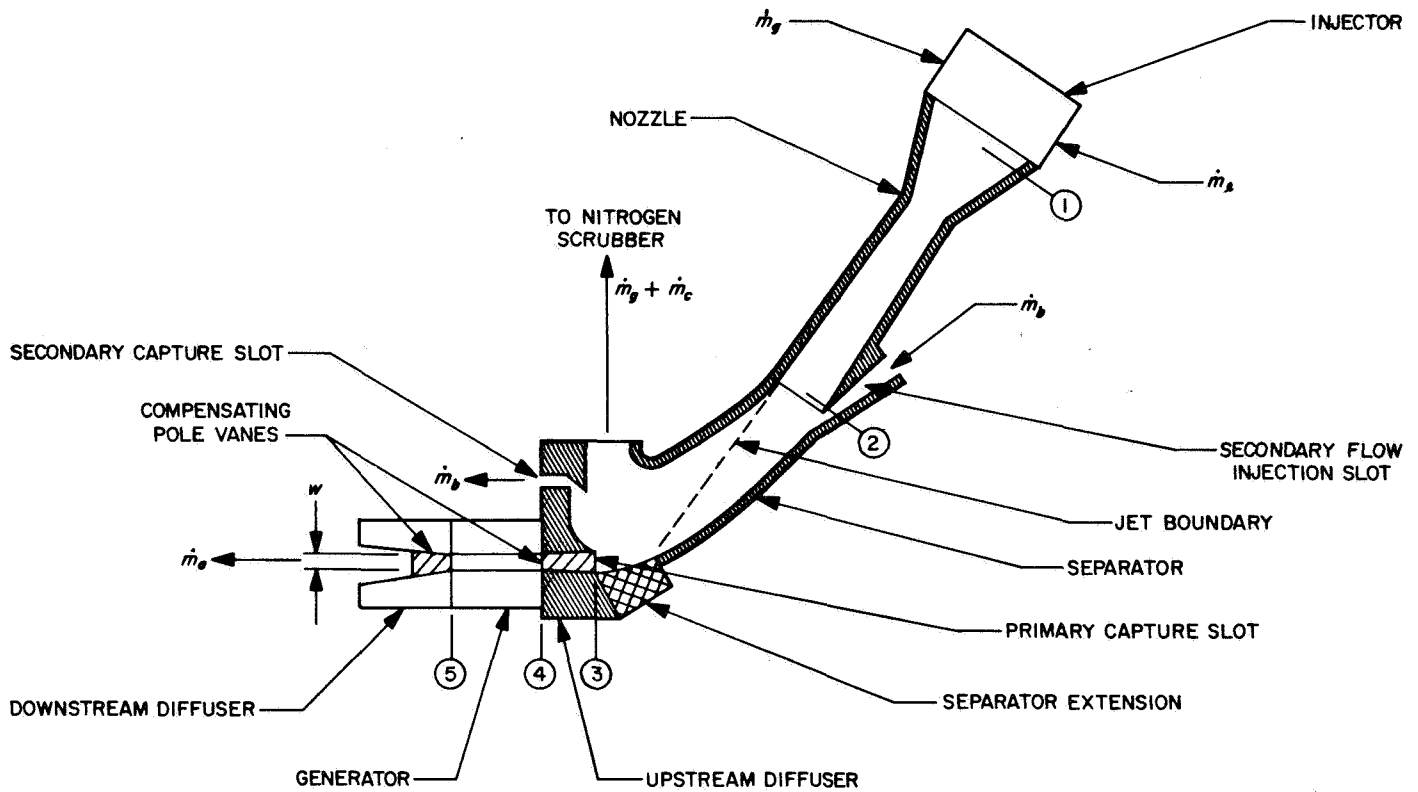


Fig. 6. Arrangement of components for conversion system hydraulic tests

system has not yet been tested, but it is expected to have an efficiency of 0.8 (actual/isentropic pressure rise) and this value is used to evaluate V_s .

In the initial tests (SPS 37-45, Vol. IV) the separator exit velocity was satisfactory, but the liquid flow bypassing the primary capture slot $\dot{m}_b + \dot{m}_c$, was an excessive 12% of the nozzle flow (at $p_1 = 230$ psia and $\dot{m}_l/\dot{m}_g = 25$). It was found possible to recover 70% of this liquid loss with the secondary capture slot, but when the liquid was reinjected at the separator inlet the flow loss increased to 17%, of which 60% was recovered by the secondary slot, and the separator exit velocity was reduced by 12%. To reduce the flow loss, the separator was extended 5 in. with a 9-in. radius of curvature, and deflecting channels were added to the side walls. These changes reduced the flow loss to 2% at the expense of a 7% reduction in separator exit velocity, without reinjection. When the secondary capture slot flow was reinjected, the flow loss increased to 3%, of which 60% was recovered by the secondary capture slot and reinjected, causing a velocity reduction of 1%. Thus, with reinjection, the separator exit velocity with the extension was 4% higher than without the extension, and the liquid loss \dot{m}_c to the scrubber was 1% instead of 7%.

The upstream diffuser was then added. Its length was 1.8 in., the length required for the upstream compensating pole of the generator. The inlet height w_s was varied from 0.4 to 0.6 in. in a series of tests, and the most satisfactory balance between liquid flow bypassing the primary capture slot and gas intake into the primary capture slot was found to occur at 0.5 in. The exit height w_4 was made 0.4 in., the value expected to provide the lowest possible exit void fraction without choking (normal shock at diffuser inlet). Fourteen 0.02-in.-thick vanes were installed in the diffuser as required for suppression of eddy currents in generator operation. The system was then operated over the range of nozzle inlet pressures and liquid/gas mixture ratios planned for the NaK-nitrogen tests, and the net fluid power values that were obtained, corrected to the density of NaK (6.7% more power at 12% lower mixture ratio than with water), are presented in Fig. 8. A maximum corrected power of 115 kW was achieved. In the three runs at mixture ratios giving subsonic exit velocity the power is below the mean data, indicating possible shock losses.

The specific fluid power at the exit of the upstream diffuser is shown in Fig. 9. The maximum value is 16 kW per lb/sec of N_2 flow, which is equivalent to 4.9%

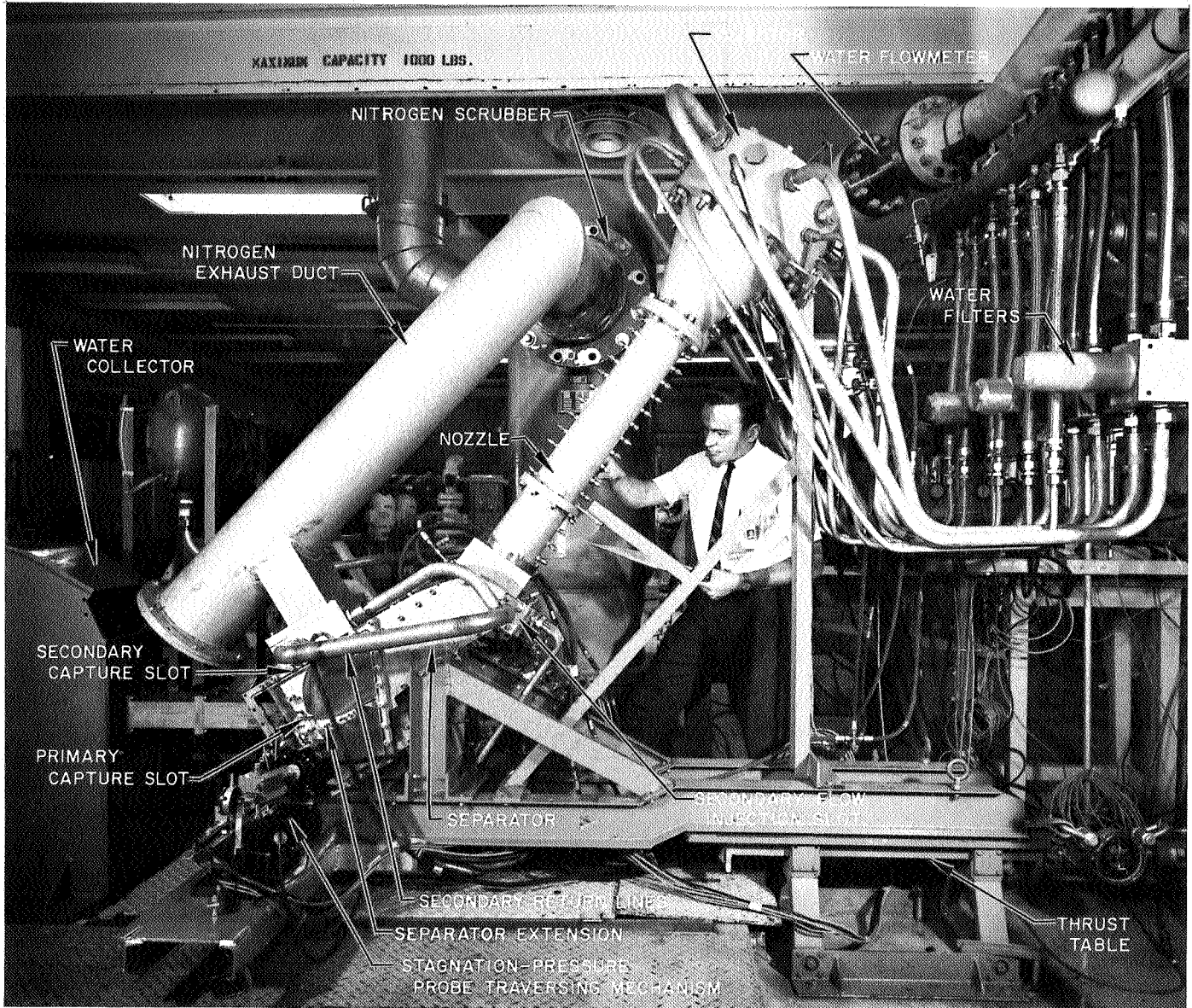


Fig. 7. Conversion system hydraulic experiment

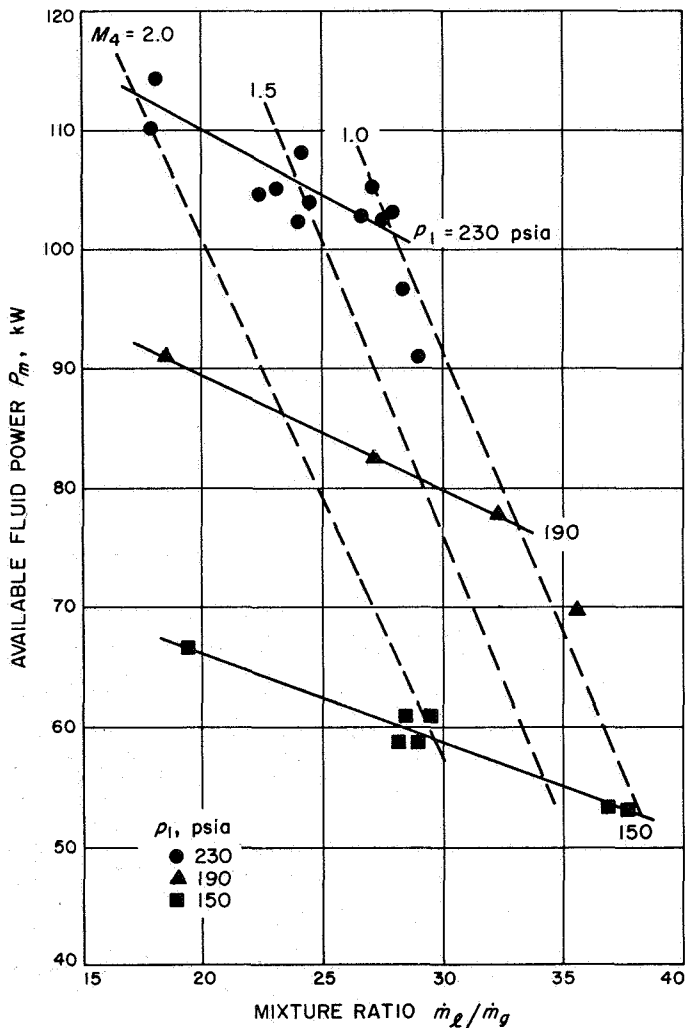


Fig. 8. Measured net available fluid power at upstream diffuser exit (corrected to NaK density and based on downstream diffuser efficiency of 0.8)

cycle efficiency at 70% generator efficiency. The measured operating conditions, corrected to NaK density, at the mixture ratio for maximum specific power, are summarized in Table 2 and compared with the predicted conditions. The differences from the design predictions are due to the lower mixture ratio at which peak specific power occurred and the lower separator velocity. The specific power is within 11% of the predicted value.

The hydraulic tests will continue with the addition of the generator channel and the downstream diffuser.

2. High-Temperature Experiments

a. Corrosion of niobium-1% zirconium by high-velocity lithium. An experiment to measure the material loss from

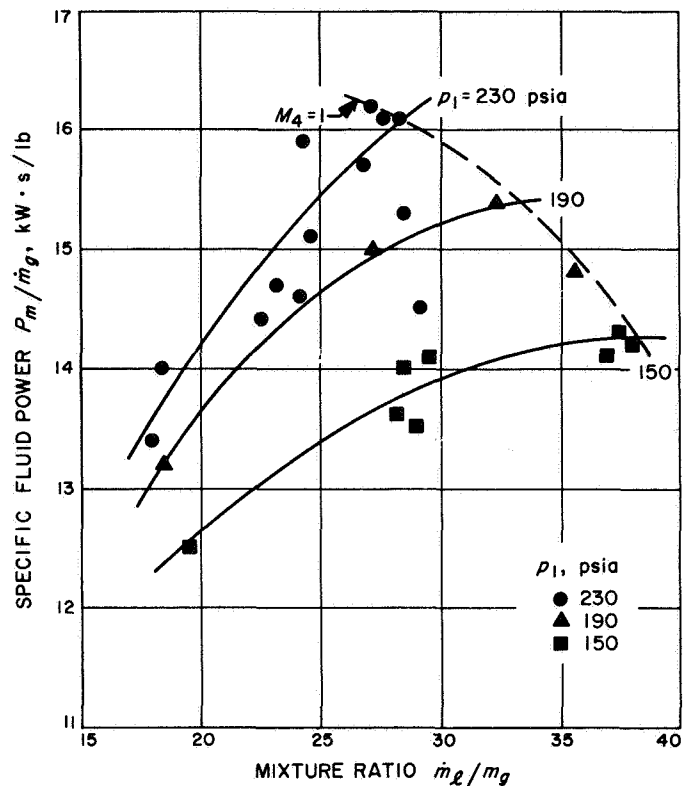


Fig. 9. Measured specific fluid power

Nb-1% Zr alloy to a high velocity lithium stream was recently completed (SPS 37-43 and 37-44, Vol. IV). The test was conducted for a 500-h period at a lithium temperature which ranged from 1073–1143°C. Preliminary results were reported in SPS 37-44, Vol. IV, and an attempt was made to compare the measured material loss with that predicted from values of solubility of niobium in lithium reported in Ref. 3. The values of solubility in that reference were summaries of the original experiment data of Ref. 4. Examination of the experimental data revealed that they were values of solubility by atomic fraction rather than weight fraction, as reported in Ref. 3. In addition, the scatter of the data appeared to be too great to warrant their representation by an empirical curve. When the data of Refs. 5–7 were also considered, experimental values for the solubility of niobium in lithium at 1000°C were found to range from less than 1 to 900 wppm.

Because of the large uncertainty in solubility values it was decided to represent the high velocity corrosion results by the value of solubility which provides the best fit to the data. Fig. 10 presents a comparison of the measured material loss at the three velocity levels of the experiment with the curve that would be calculated

Table 2. Measured flow conditions at peak specific fluid power, and comparison with predicted values

Parameter	Measured (corrected to NaK density)	Predicted (SPS 37-41, Vol. IV)
Nozzle inlet pressure p_1 , psia	230	230
Nozzle exit pressure p_2 , psia	27	22
Liquid flow rate \dot{m}_l , lb/s	174	186
Gas flow rate \dot{m}_g , lb/s	6.3	6.2
Mixture ratio \dot{m}_l/\dot{m}_g	27.5	30.0
Nozzle exit velocity V_2 , ft/s	380	385
Separator exit velocity V_3 , ft/s	317 ^a	330
Liquid flow rate entering primary capture slot \dot{m}_a , lb/s	172	185
Liquid flow rate entering secondary capture slot \dot{m}_b , lb/s	3	5
Liquid flow rate entering nitrogen scrubber \dot{m}_c , lb/s	2	1
Primary capture slot height w_3 , in.	0.5	0.6
Void fraction of flow entering primary capture slot VF_3	0.5	0.6
Mach number of flow entering primary capture slot M_3	2.1	3.7
Upstream diffuser exit height w_4 , in.	0.4	0.4
Upstream diffuser exit pressure p_4 , psia	132	94
Upstream diffuser exit velocity V_4 , ft/s	246	270
Void fraction of flow leaving upstream diffuser VF_4	0.26	0.26
Mach number of flow leaving upstream diffuser M_4	1.0	1.3
Velocity required at inlet of downstream diffuser for flow return to 260 psia, assuming 0.8 diffuser efficiency, V_5 , ft/s	179	210
Net available fluid power $P_m = \dot{m}_a(V_4^2 - V_5^2)/2$, kW	103	112
Specific fluid power P_m/\dot{m}_g , kW per lb/s	16	18
Equivalent cycle efficiency for cesium, at 0.7 generator efficiency, $\eta = 0.7 P_m / (\dot{m}_g L_{cs} + 0.7 P_m)$ where $L_{cs} = 220$ kW·sec/lb	4.9%	5.5%

^aCorrected to 27 psia; actual velocity was 304 ft/s, but liquid pressure was 87 psia due to separator curvature.

using a value of the temperature coefficient of solubility of

$$\frac{\partial S}{\partial T} = 1.2 \times 10^{-9} \text{ g Nb/g Li } ^\circ\text{C} \quad (2)$$

This value would correspond to a solubility in the 2-3 wppm range at 1100°C for a reasonable value of the heat of solution (Ref. 3).

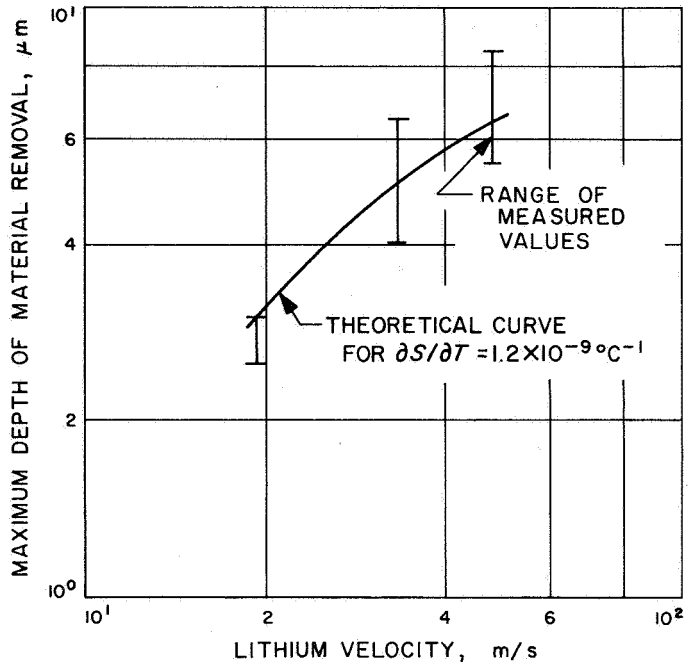


Fig. 10. Effect of lithium velocity on depth of material removal from Nb-1% Zr in 500-h test at 1073–1143°C

The theoretical material loss and concentration of niobium in the bulk lithium flow for the conditions of the experiment, corresponding to the above value of $\partial S/\partial T$, was calculated by integration of the mass transfer relations for diffusion limited dissolution around the test loop (the measured values of material loss have the same velocity dependence as the calculated values, indicating that the mass transfer process is diffusion-limited). The empirical expression for the test results produced by the detailed analysis of concentration through the loop is

$$\Delta t_w = 1.2 \times 10^{-9} k_d (\rho_s/\rho_w) (T_w - T_c) \tau \quad (3)$$

where

Δt_w = depth of material removal, cm

k_d = mass transfer coefficient, cm/s
(SPS 37-44, Vol. IV)

ρ_s = lithium density, g/cm³

ρ_w = Nb-1% Zr density, g/cm³

T_w = wall temperature, °C

T_c = effective concentration temperature, °C
(SPS 37-44, Vol. IV)

τ = time, sec

This expression is different from the preliminary relation reported in SPS 37-44, Vol. IV, by a factor of two because of the more accurate determination of T_c . The results, when applied to the example of a 300-kWe liquid metal MHD space power system in that summary, still yield acceptable values of mass transfer during 10,000 h operation.

b. Haynes-25 corrosion loop. As reported in SPS 37-45, Vol. IV, a test loop of Haynes-25 alloy was operated at 980°C (1800°F) with lithium at velocities to 64 m/s (210 ft/s) to determine the corrosion allowance which would be required to use this alloy for construction of a 300-kWe liquid MHD power system for minimum cost performance evaluation. Approximately 0.51 mm (0.020 in.) of material was lost from the high velocity location during 28 h of operation at 980°C before blockage of the pumping section occurred from mass transfer. The deposits have been removed from the pump and further operation is planned to more accurately determine the temperature variation throughout the loop so that the results can be applied to the temperature conditions of the MHD system. Although the material loss was sufficiently low to permit a minimum-duration 300-kW system, for the next loop test, the Haynes-25 alloy will have an internal vapor-deposited coating of Nb-1% Zr to determine if such a coating can provide improved corrosion protection.

c. 100-kW (thermal) cesium-lithium loop. A two-phase test system is being fabricated which will enable circulation of cesium and lithium at the temperatures, pressures, and velocities of a liquid metal MHD power system. The primary experimental objective for this facility is to evaluate long-term erosion and corrosion of Nb-1% Zr and other refractory alloys at a temperature of 1100°C and at lithium velocities to 150 m/s. Secondary objectives will be to measure the performance of a two-phase nozzle with the cesium-lithium mixture, to evaluate the solubility kinetics of cesium vapor and liquid lithium, to measure cesium condensation coefficients and to evaluate high-temperature generator duct designs.

Fabrication of this test loop had been partially completed (SPS 37-35, Vol. IV) but was interrupted to permit the construction and operation of the single-phase lithium loops. Machining and forming operations are now complete on all Nb-1% Zr components and major flow lines, and all support equipment is on hand. The NaK heat rejection system for this loop has been fabricated and is shown prior to the addition of insulation in Fig. 11.

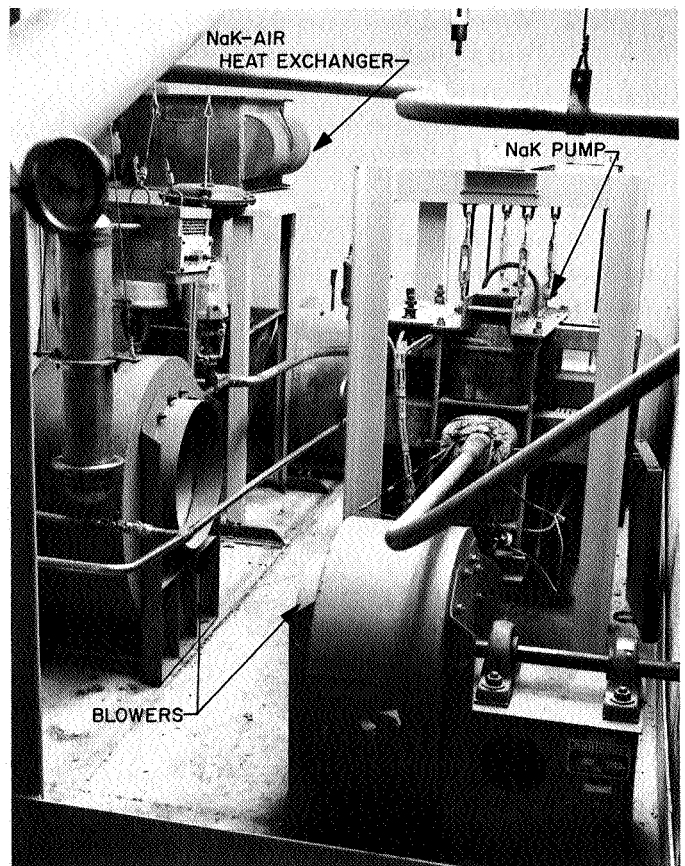


Fig. 11. NaK heat rejection system for 100-kW (thermal) cesium-lithium loop

Final welding and assembly of the niobium alloy portions of the loop have been started using a vacuum/inert gas welding facility. The controlled atmosphere chamber and gas sampling and analysis system are shown in Fig. 12. The chamber, including the interior work surface, is constructed from type 304 stainless steel. The chamber is 54 in. in diameter and 72 in. long and is equipped with 3 glove ports and 2 view ports on each side. It has a flanged and hinged head for full diameter access and a 12-in. diameter by 15-in. long air lock. The chamber is evacuated to below 5×10^{-3} torr by a 50 ft³/min 2-stage roughing pump for thorough removal of oxygen and moisture, and then filled with high-purity argon for welding. The chamber is instrumented with an argon sampling and analyzing system which is capable of monitoring water vapor and oxygen content as low as 0.5 ppm. The monitoring system consists of a Teledyne oxygen trace analyzer, a C.E.C. moisture monitor, and two small vacuum pumps for withdrawing samples of the chamber atmosphere continuously during welding.

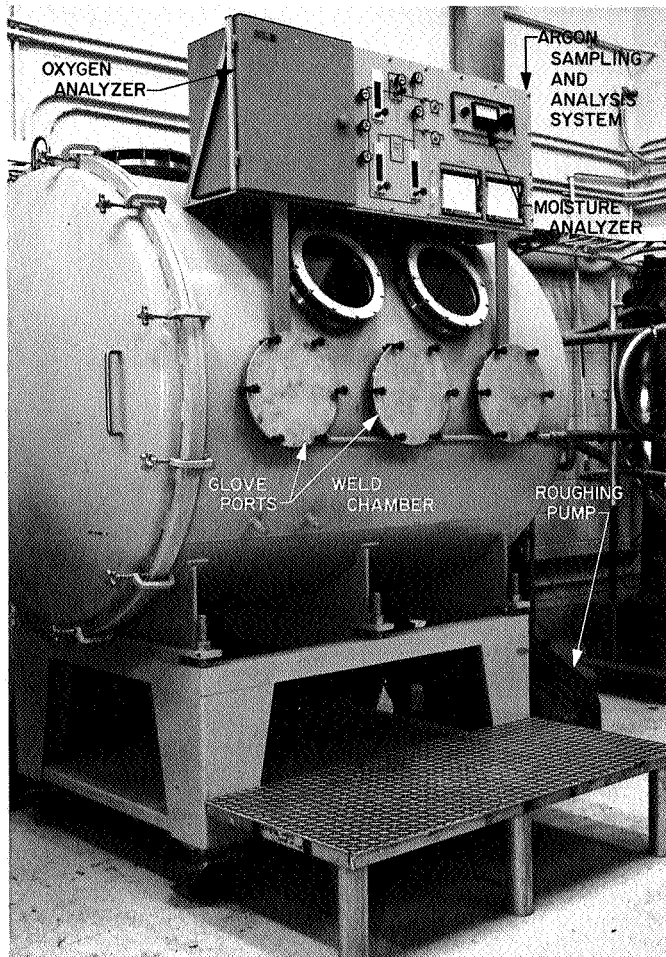


Fig. 12. Inert gas welding chamber for Nb-1% Zr loop components

C. Radial Distributions of Enthalpy, Mass Flux and Velocity for High-Temperature Argon Flow as Determined by a Calorimetric Probe, P. F. Massier and E. J. Roschke

1. Introduction

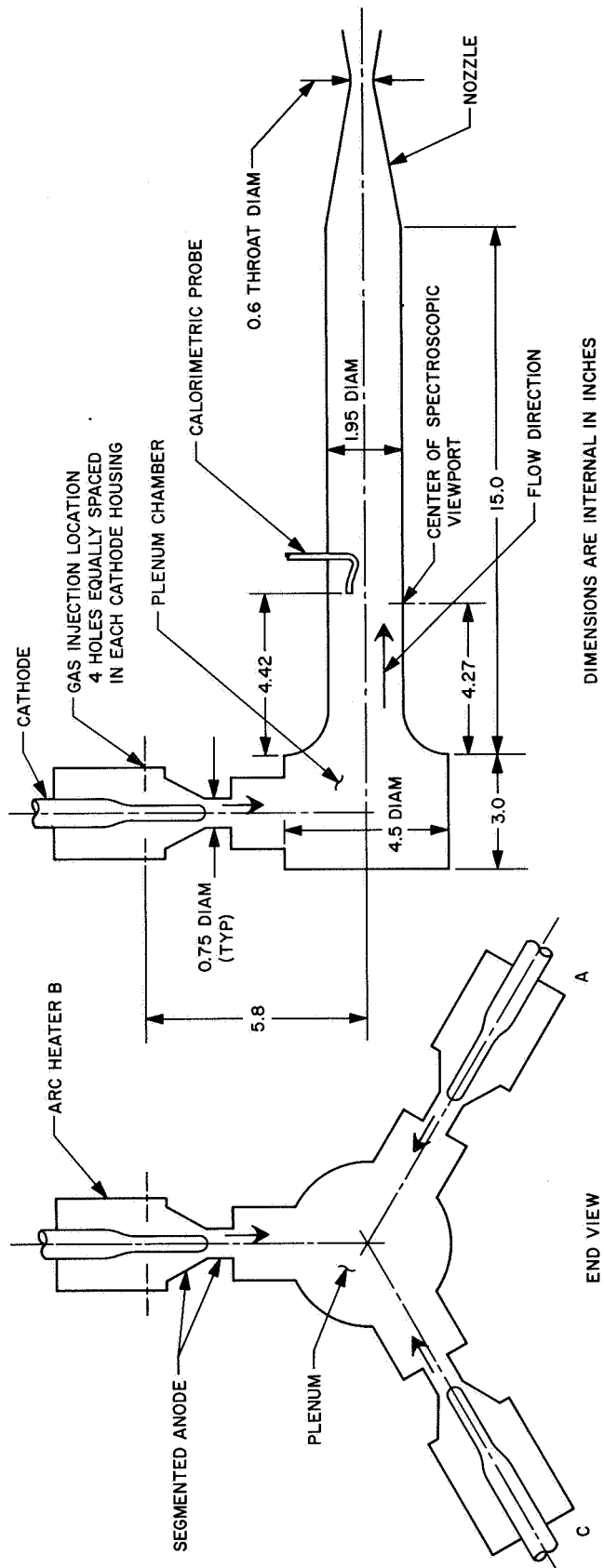
In SPS 37-45, Vol. IV, pp. 141-151, comparisons of enthalpies as determined by the use of several different instrumentation techniques are discussed for weakly ionized argon flow in a constant-diameter duct. Those enthalpies were evaluated by means of a calorimetric probe, conservation of energy, a flow meter, and spectroscopy. The results were obtained as part of a continuing investigation to expand the knowledge of heat transfer from ionized gas flows as a consequence of the current interest in electrical propulsion and power generation concepts, as well as the interest in plasma test facilities.

The purpose of this article is to supplement the information presented previously by discussing a procedure for evaluating distributions of mass flux and velocity in addition to enthalpy as deduced from calorimetric probe measurements. To obtain the mass flux and velocity, measurements of the static pressure and difference between stagnation and static pressures are required. Experimental results are shown for one test in which the stagnation pressure was approximately 4.2 psia and the ionization fraction of the subsonic flow of argon at the probe tip was approximately 0.0001. The Reynolds number based on diameter was 600 and the Mach number 0.07.

Spectroscopic results are also presented which were obtained by viewing diametrically across the duct at the axial location of the probe tip; whereas, in the previous tests the spectroscopic viewport was located downstream of the probe. The spectroscopic data is analyzed and compared using transition probabilities from two sources. A diagram of the test apparatus is shown in Fig. 13, and a sketch of the calorimetric probe is shown in Fig. 14. Symbols used in this article are defined in Table 3.

This experimental apparatus differs from the one with which the previous measurements were made primarily by the configuration of the arc heater. Three arc heaters are now used, from which the ionized gas flow discharges into a plenum chamber before entering the test section. In the past a single arc heater was employed and the flow negotiated a sharp 90-deg turn in a constant-diameter miter elbow before entering the test section. Higher maximum enthalpies are anticipated with the triple-arc heater configuration. The enthalpy probe also differs from the one used in the previous tests, but only very slightly in the bending arrangement.

With the new test apparatus, radial distributions of the velocity in the test section were obtained for room-temperature argon flow, both with swirling flow and nonswirling flow entering the plenum from the arc heaters. Those results are discussed in SPS 37-45, Vol. IV, pp. 167-175. It was found that in both instances the velocity distributions were comparatively uniform. In the present high-temperature experiments the flow in the arc heaters was swirling, although the vortices were not nearly as strong as in the cold flow tests because of the different mass flow rates at a given pressure. The maximum tangential velocity near the end wall of the arc heater for cold flow at 4 psia was between 200 and 300 ft/s, whereas in the high-temperature test it was



DIMENSIONS ARE INTERNAL IN INCHES

Fig. 13. Test apparatus configuration

Table 3. Nomenclature

A_c	cross-sectional area
c_c	specific heat of coolant
c_p	specific heat of gas
e	2.713
g	gravitational constant
H	enthalpy
I_0	ionization energy
\dot{m}	mass flow rate
p	pressure
r	radius
R	gas constant
T	temperature
u	velocity
α	ionization fraction
Δ	denotes a difference
ρ	density
Subscripts	
<i>avg</i>	average conditions
<i>b</i>	sampled (bleed)
<i>c</i>	coolant except as noted for A_c
<i>g</i>	gas
<i>t</i>	stagnation conditions except as noted
<i>w</i>	wall
<i>wb</i>	with bleed
<i>w/o</i>	without bleed

only about 80 ft/s. The radial distribution of the tangential velocity in arc heater B, as deduced from end wall pressure measurements, is shown in Fig. 15.

2. Instrumentation and Data Analysis Procedure

a. Radial distribution of the stagnation enthalpy. At each radial position of the probe, measurements of the probe coolant and sampled gas flow rates were made in addition to the coolant temperature rise and the temperature of the sampled gas leaving the probe. The

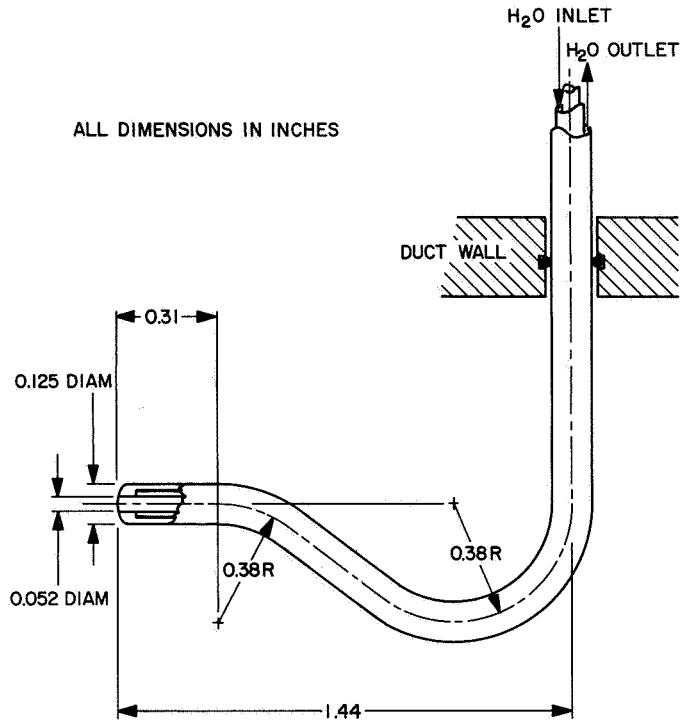


Fig. 14. Calorimetric probe

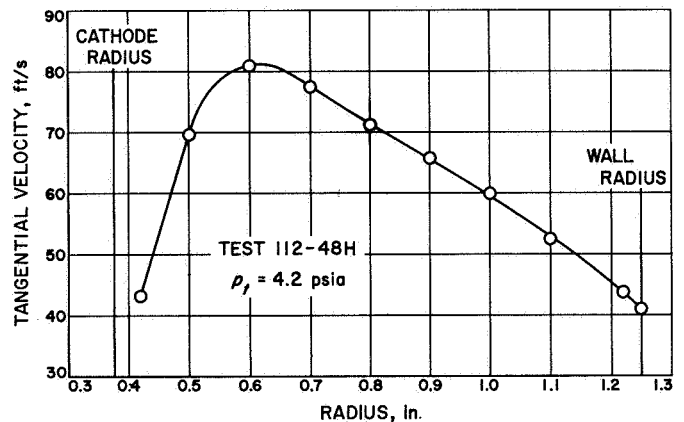


Fig. 15. Radial distribution of tangential velocity in arc heater B

stagnation enthalpy of the sampled gas was then computed using the following energy balance equation:

$$H_t = \frac{[(\dot{m}_c)(c_c)(\Delta T)_c]_{wb} - [(\dot{m}_c)(c_c)(\Delta T)_c]_{w/o b}}{\dot{m}_b} + c_{c_b} T_b \quad (1)$$

Since the magnitude of the sampled gas flow rate influences the flow field of the main gas stream surrounding the probe, and hence, the heat transferred to the

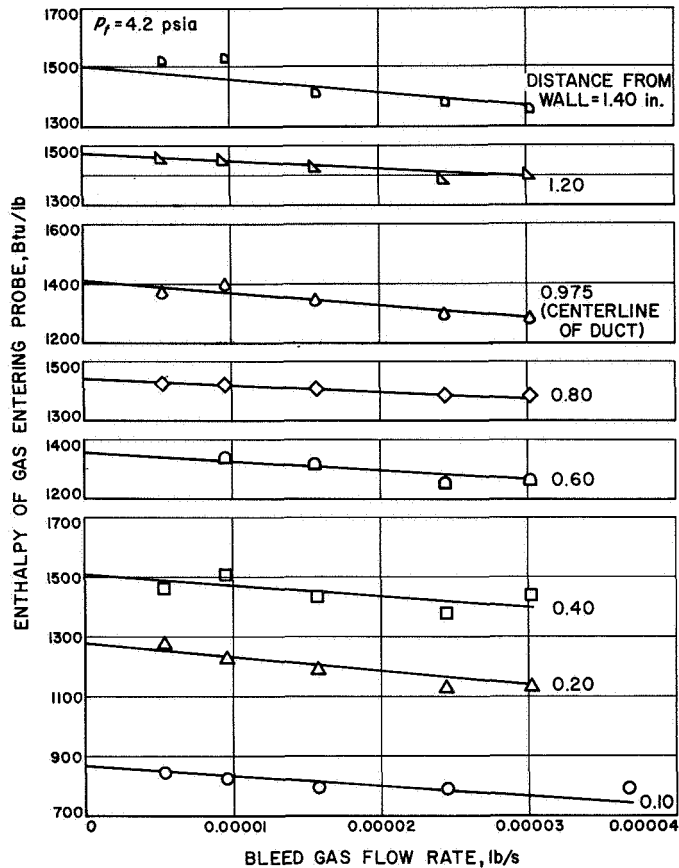


Fig. 16. Effect of bleed gas flow rate on indicated enthalpy

outer wall of the probe, measurements were acquired at several sampling flow rates at each radial position of the probe. The values of H_t versus bleed flow rate at each radial position are shown in Fig. 16. The stagnation enthalpies extrapolated to zero bleed flow rate were then used to determine the radial distribution of the stagnation enthalpy shown in Fig. 17. This procedure was used because the extrapolated value corresponds to the zero bleed flow condition at which the tare measurement was made. Small fluctuations ($\pm 0.2\%$) in the coolant flow rate passing through the probe were observed during the test. Since no effort was made to determine critically the influence of these low-frequency fluctuations on the accuracy of the results, the data points in the figures represent values that are considered to be the most realistic, based on the readability of the rotameters and on the energy balance results. Future experiments will be conducted with a modified coolant system in which an effort will be made to eliminate the fluctuations in the coolant flow rate.

b. Radial distributions of mass flux and velocity. At zero sampling flow rate the calorimetric probe was also used to determine the difference between the local stagnation pressure and the wall static pressure, in addition to the tare reading for heat transfer. The pressure difference was observed directly on an inclined manometer containing oil, and the absolute value of the wall pressure was determined by means of a second manometer

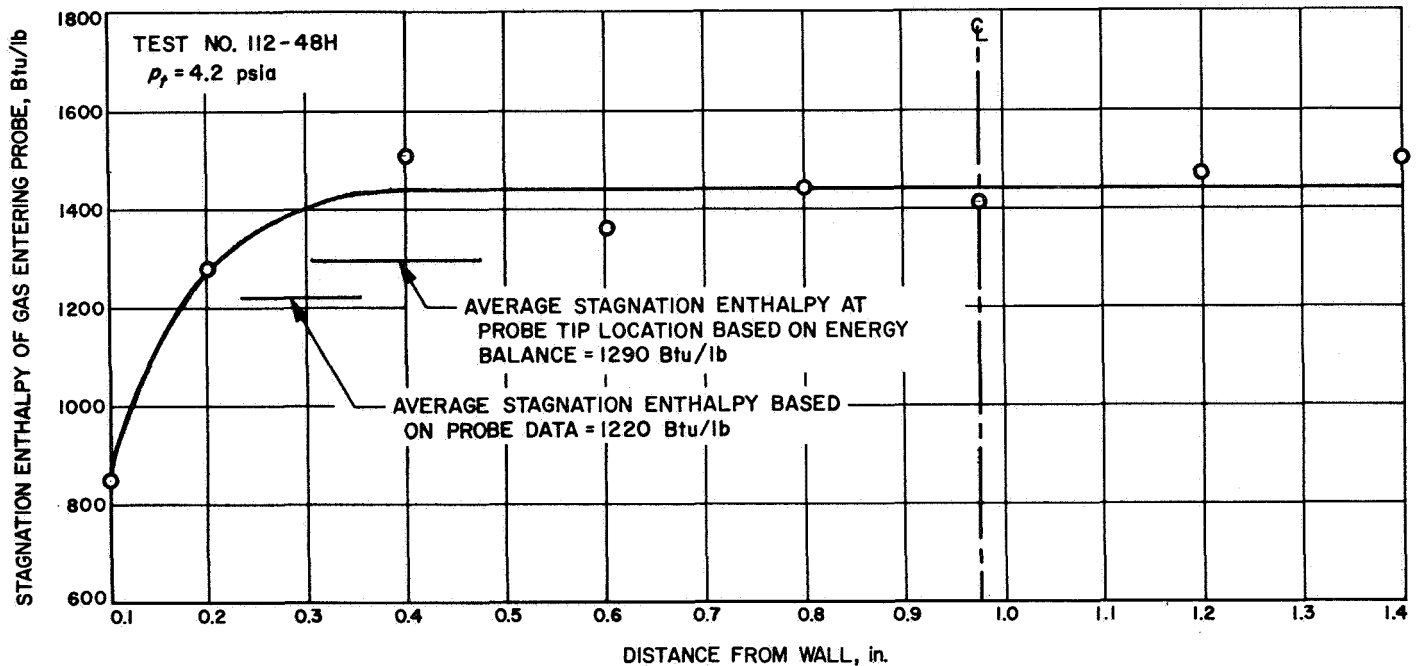


Fig. 17. Radial distribution of stagnation enthalpy

to which the wall pressure tap was also connected. From the pressure and the enthalpy data, it was then possible to compute the mass flux and the gas velocity at each radial station by use of the following procedure.

Since the average gas velocity was comparatively low (approximately 320 ft/s), as a first approximation it was assumed that the static and stagnation enthalpies were

equal. Thus, approximate static values of ionization fraction, temperature, and density could be computed and then an approximate value of the velocity could be determined. This velocity was then introduced into the equation for the definition of the stagnation enthalpy and a more accurate value of the static enthalpy computed. After that, the same procedure as above was repeated using the new value of the static enthalpy to

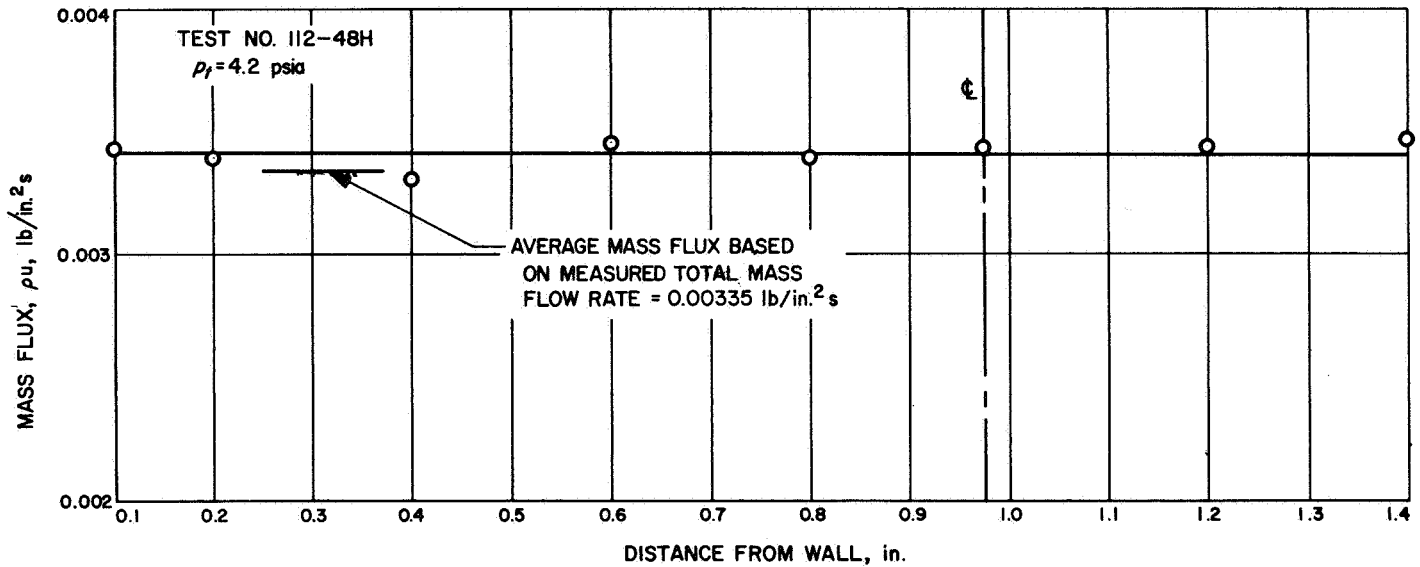


Fig. 18. Radial distribution of mass flux

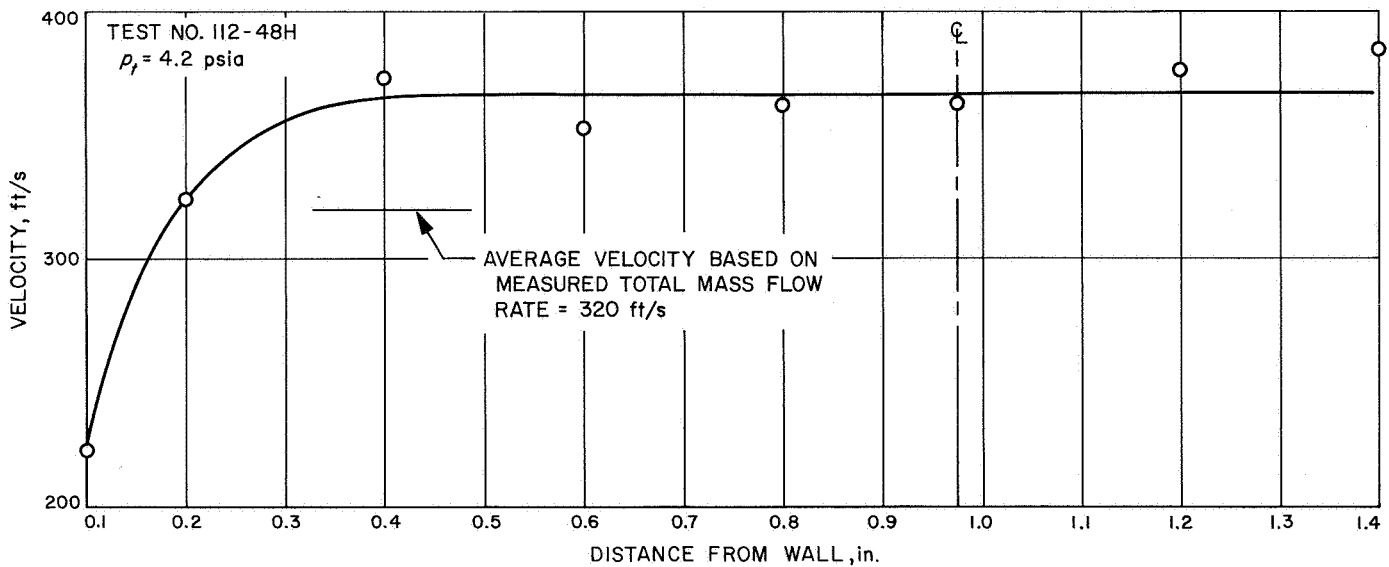


Fig. 19. Radial distribution of velocity

obtain a better value for the velocity. Only one iteration was required to achieve less than 1% change in velocity. Thus it was possible to establish the experimental mass flux (ρu) and velocity distributions shown in Figs. 18 and 19. The following equations were used:

$$\text{Energy: } T = \frac{(H - \alpha I_0)}{5/2R(1 + \alpha)} \quad (2)$$

The ionization fraction was evaluated from a Mollier chart using the experimental values of H_t and p . For the final iteration α was evaluated from the Saha equation. For this test α was negligibly small; however, the procedure is presented for situations in which α is large enough to have an effect.

$$\text{Saha: } \frac{\alpha^2}{1 - \alpha^2} = 2.228 \times 10^{-6} (4 + 2e^{-3708/T}) T^{5/2} / P e^{-329,200/T} \quad (3)$$

In Eq. (3), p is in psia and T in °R.

$$\text{State: } \rho = \frac{p}{(1 + \alpha)RT} \quad (4)$$

$$\text{Momentum: } u = \left(\frac{2g(p_t - p)}{\rho} \right)^{1/2} \quad (5)$$

Energy (definition of stagnation enthalpy):

$$H = H_t - \frac{u^2}{2g} \quad (6)$$

c. Average values of stagnation and static enthalpy. After the iteration for H , ρ and u had been completed at each radial position of the probe, the product $\rho u H$ was plotted against cross-sectional area as measured from the

duct centerline and the average static enthalpy was then computed from:

$$H_{avg} = \frac{\int \rho u H dA_c}{\dot{m}_g} \quad (7)$$

Next, the average u^2 was evaluated by plotting local values of u^2 against cross-sectional area and computing the average stagnation enthalpy from:

$$H_{t,avg} = H_{avg} + \frac{u_{avg}^2}{2g} \quad (8)$$

As shown in Table 4 and Fig. 17, $H_{t,avg}$ obtained in this manner is 1220 Btu/lb as compared to 1290 Btu/lb obtained from the energy balance method. The kinetic energy amounts to only 2.3 Btu/lb.

d. Spectroscopy. The arrangement of apparatus, and the method of acquiring and treating the spectroscopic data were similar to those previously described in SPS 37-45, Vol. IV, pp. 141-151. In the present case, however, the center of the 0.25-in. diameter circular viewport was located just 0.15 in. upstream of the calorimetric probe tip. The relative intensities of 18 argon atom lines were measured; excitation temperature was evaluated by the relative line-intensity method using the transition probabilities listed by Olsen, Ref. 8, as well as the more recent values listed by Coates and Gaydon, Ref. 9. Results are shown in Fig. 20. Measured line intensities were not corrected for absorption and the two straight lines in Fig. 20 are visual "best-fits" and not least-squares determinations.

For the tests discussed in SPS 37-45, Vol. IV, pp. 151-171, it was found that correction for absorption was to reduce the temperature by about 5%. However, it is clear from Fig. 20 that for this test the temperatures determined from the slopes of the lines are considerably different. The lower value of temperature as obtained by

Table 4. Comparison of results

Parameter	Energy balance	Calorimetric probe	Spectroscopy		From measured mass flow rate
			Coates and Gaydon transition probabilities	Olsen transition probabilities	
Average stagnation enthalpy of gas, Btu/lb	1290	1220	1210	1660	
Average stagnation temperature of gas, °R	10,370	9820	9720	13,300	
	(5760°K)	(5460°K)	(5400°K)	(7400°K)	
Average mass flux, lb/in ² s		0.00342			0.00335

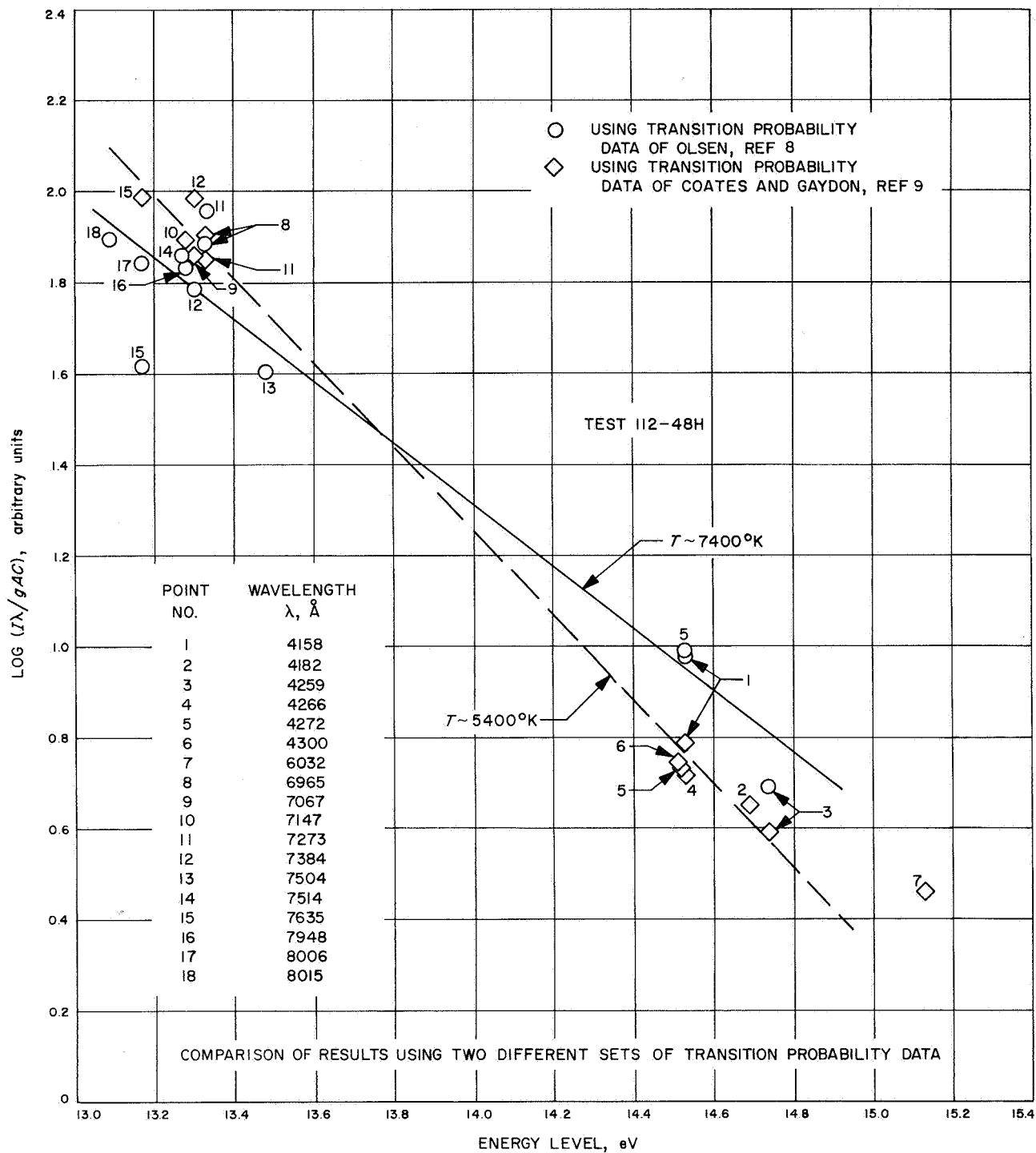


Fig. 20. Excitation temperature as determined from relative line intensities of argon atom lines

using the data of Coates and Gaydon is due to the fact that their values of transition probability are generally lower in the blue, but higher in the red, than those of Olsen. It is to be noted that Olsen's transition probability for the 7273 Å line was incorrectly listed in Ref. 8, being

high by a factor of 10; this has been amended in the present result. With the exception of the isolated 6032 Å point, the data of Coates and Gaydon yielded relatively less scatter than did Olsen's data. However, there is not yet sufficient data to form a basis for preferring one or

the other set of transition probabilities and there are other considerations beyond the scope of this article. The temperature determined by the Coates and Gaydon data agreed very well with the value of 5760°K determined near the center of the viewport section by means of the calorimetric probe, whereas, as shown in Table 4, the temperature determined by Olsen's data is much higher, as it was also for the tests reported in SPS 37-45, Vol. IV, pp. 141-151.

3. Results

One of the significant results of the probe measurements is shown in Fig. 17. The enthalpy distribution is comparatively uniform from a distance of about 0.4 in. from the wall to, and beyond, the centerline indicating an adiabatic core flow. Although, if this were the case, the thermal layer would have originated at the exit of the plenum nozzle, because, based on energy balance, the average enthalpy at that location was 1420 Btu/lb which is nearly the same as the value in the core flow at the probe tip location. Since the boundary layer, however, must certainly have originated upstream of the plenum nozzle exit, it is concluded that mixing of the main stream with the thermal layer, which undoubtedly occurred in the plenum, was still taking place in the plenum nozzle, but diminished by the time the flow reached the probe. Since the mass flux distribution is uniform, as shown in Fig. 18, the fraction of the mass flow which had been influenced by the heat transfer to the wall by the time the flow reached the probe (thermal boundary layer flow) is equal to $[1 - (r_e/r_w)^2]$ and amounts to 0.65.

An evaluation of the detailed enthalpy distribution in the thermal layer would be of interest to gain additional insight of the boundary layer structure; however, data were not acquired at a sufficient number of radial measuring stations during this test to accomplish this. It is significant, however, that the mass flux distribution was uniform across such a large part of the thermal layer. The measurements are considered to be reliable because a comparison of the average mass fluxes determined from the probe measurements and from the total mass flow rate as shown in Table 4 indicates a difference of only about 2%. The velocity distribution in the thermal layer as shown in Fig. 19 has the same shape as the enthalpy distribution; however, it will be necessary to acquire data

at more radial stations in this region to establish a good profile.

A comparison of the average stagnation enthalpies as determined from the probe data and an energy balance as shown in Table 4 indicates a difference of less than 6%. The probe results also agree within less than 1% with the spectroscopic value obtained using the transition probabilities of Coates and Gaydon. All of these comparisons are considered to be very good and establish greater confidence in carefully acquired data from the use of a calorimetric probe. It is anticipated that this confidence level will be increased when a better coolant system becomes available for the calorimetric probe.

4. Summary and Conclusion

Radial distributions of velocity and mass flux as well as of enthalpy have been evaluated from heat transfer and pressure measurements obtained in a weakly ionized subsonic flow of argon in a constant-diameter duct by use of a 0.125-in. diameter calorimetric probe. The stagnation pressure was approximately 4.2 psia, the Mach number was 0.07, the maximum value of the stagnation enthalpy was approximately 1440 Btu/lb and the Reynolds number based on diameter was 600. The enthalpy distribution indicated the existence of an adiabatic core and a comparatively thick thermal boundary layer a distance of 2.2 duct diameters downstream of the plenum chamber. The velocity distribution had the same shape as the enthalpy distribution, and the mass flux distribution was uniform across most of the thermal boundary layer. The average mass flux as determined by the probe agreed within 2% with the mass flux determined from the measured total mass flow rate. The average value of the enthalpy as determined from the probe data agreed within 6% with the average enthalpy determined from an energy balance and within less than 1% of the spectroscopic value using transition probabilities of Coates and Gaydon. The enthalpy determined from the spectroscopic data using transition probabilities of Olsen yielded a value about 36% above the average enthalpy obtained from the probe data. Comparisons with the spectroscopic results are not conclusive because the gas was viewed only along one diametral line; hence, true averages could not be evaluated. The results have established greater confidence in the use of a calorimetric probe to obtain distributions in a high-temperature internal gas flow.

References

1. Davis, J. P., Gronroos, H., and Phillips, W., *Review of Industry-Proposed In-Pile Thermionic Space Reactors*, Vol. I. General, Technical Memorandum 33-262, Jet Propulsion Laboratory, Pasadena, Calif. Oct. 15, 1965.
2. *Annual Technical Summary Report for the Thermionic Emitter Materials Research Program (July 1961-June 1962)*, Report 2-63, prepared for the Office of Naval Research by Thermo Electron Engineering Corp.
3. McKisson, R., et. al., *Solubility Studies in Alkali Metals*, Report AI-65-210. Atomics International, Canoga Park, Calif., Mar. 1966.
4. Cleary, R. E., Blecherman, S. S., and Corliss, J. E., *Solubility of Refractory Metals in Lithium and Potassium*, Report TIM-850. Pratt & Whitney Aircraft, Middletown, Conn., Nov. 1965.
5. Leavenworth, H., Cleary, R. E., and Bratton, W. D., *Solubility of Structural Metals in Lithium*, Report PWAC-356. Pratt & Whitney Aircraft, Middletown Conn., 1961.
6. Jesseman, D. S., et. al., *Preliminary Investigation of Metallic Elements in Molten Lithium*, Report NEPA-1465. Oak Ridge National Laboratory, Oak Ridge, Tenn., 1950.
7. Buchkov, Y. F., Rozanov, A. N., and Yakolev, V. B., *Determination of the Solubility of Metals in Lithium*. Translated from *Atomnaya Energiya*, Vol. 7, No. 6. Dec. 1959, by John E. Ahern. Interoffice Memo Th RD IOM 99 Marquardt Corporation, Van Nuys, Calif., May 1960.
8. Olsen, H. N., "Measurement of Argon Transition Probabilities Using the Thermal Arc Plasma as a Radiation Source," *J. Quant. Spectrosc. Radiat. Trans.*, Vol. 3, pp. 59-76, 1963.
9. Coates, P. B., and Gaydon, A. G., "Temperature Measurements in Shock Tubes; Transition Probabilities for Argon Lines," *Proc. Royal Society Series A*, Vol. 293, pp. 452-468, London, 1966.

XV. Liquid Propulsion

PROPULSION DIVISION

A. Liquid Propulsion System, L. R. Toth, F. A. Rush, and O. F. Keller

1. Introduction, L. R. Toth

The advanced liquid propulsion systems program is investigating selected problems generated by spacecraft operational requirements for propulsion systems capable of high inherent reliability; long-term storage in the space environment; multiple start in free fall (zero gravity); and engine throttling. The solutions proposed to satisfy these requirements are coordinated for practical application in a system.

Periodic reports (starting with SPS 37-8, Vol. IV) describe the progress of work on the various parts of a specific system. Recent accomplishments concerned with material compatibility and with bladder development are outlined below. These include:

- (1) Material compatibility with hydrazine and hydrazine/hydrazine nitrate mix, and dimethylhydrazine/hydrazine propellants.
- (2) Heat sterilization of ethylene-propylene-rubber (EPR) material with hydrazine.

2. Material Compatibility, F. A. Rush

A number of construction materials was subjected to long-term compatibility tests in hydrazine (N_2H_4), hydrazine/hydrazine nitrate mix (75% N_2H_4 , 24% $N_2H_5NO_3$, 1% H_2O), dimethylhydrazine/hydrazine (50% N_2H_4 , 50% UDMH).

Each material sample was sealed in a glass ampule with a lox cleaned pressure gage attached so that tests could be terminated if the internal pressure buildup from decomposition reached 40 psia. This predetermined cutoff point would preclude failure of the glass ampule. The sealed ampules were stored at $110 \pm 5^\circ F$ in the material compatibility test facility located at the Edwards Test Station.

The metal specimens were cylinders $\frac{1}{4}$ in. in diameter and 3 in. long and were one-half immersed in liquid propellant. The elastomeric specimens were typically thin sheets $\frac{1}{2}$ in. wide, $4\frac{3}{4}$ in. long and 0.03–0.06 in. thick; these were fully immersed in propellant.

All test and specimen data were fully documented for comparison with posttest analyses. This included such controlling pertinent information as: fixture internal

geometry and volume; coding; material physical measurements and properties; propellant composition and volume; and cleaning procedures involved during preparation. Evaluation of results includes: analysis for propellant decomposition; metallurgical analysis to determine effects of exposure on the basic material at the liquid interface; and significance of pitting due to material constituents. Permeation rates are measured for elastomeric specimens. Complete information will be included in a

formal report to be released at the conclusion of this phase I test program.

Fuel sample tables were presented previously in SPS 37-44, Vol. IV, p. 175. The tables were updated for this report (Tables 1-3) to include final pressure data from 51 samples removed from test June 13, 1967. These were the last of the phase I fuel samples in test. Posttest results will be reported later.

Table 1. Final results of compatibility tests with hydrazine (N₂H₄) (test terminated June 13, 1967)

Material	Sample No.	Description	Days to reach		Pressure at 200 days, psia	Total number of days in test	Pressure attained, psia
			20 psia	35 psia			
Stainless steel	20	19-9 DL SS	405	1064	12	1154	37
	19	430 SS	172	374	22	408	39
	22	440c SS	191	313	21	461	39
	16	410 SS	171	311	24	367	40
	137	310 SS	126	257	26	278	40
	136	304L SS	84	205	34	239	40
	17	416 SS	56	103	—	119	40
	135	304 SS	54	97	—	110	40
	18	420 SS	42	91	—	108	38.5
	134	303 SS	35	63	—	86	41
183	A286 SS	40	61	—	67	40	
Aluminum	244	356-T6 Al	— ^a	—	0	793	4.5
	243	356-T6 Al	— ^b	—	2	793	10
	184	7178 Al	457	773	9	835	39.5
	185	7178 Al	335	626	12	711	41.5
	24	6061-T6 Al	201	421	19	506	41.5
	186	7075-T6 Al	89	275	30	297	42
	187	7075-T6 Al	276	453	—	635	43
Miscellaneous	94	Platinum foil	1492	—	2	1502	20
	163	Teflon-aluminum laminate	663	1044	6	1198	42
	23	1018 Steel	133	210	30	286	39
	90	Gold	78	119	—	166	40
	133	6061-T6 Al (brazed)	1339	— ^d	2	1421	21
	49	6061-T6 Al and 75-A Ti (brazed)	130	288	29	343	39
	47	6061-T6 Al and 303 SS (brazed)	148	169	—	180	31
249	Vicalloy	43	85	—	100	42	
Lubricants	108	6061-T6 Al with Apiezon-L	— ^c	—	2	1417	17.5
	105	6061-T6 Al with Rulon	1182	— ^e	1	1417	27.5
	101	6061-T6 Al with Rulon	25	49	—	77	48
	107	6 AL-4V Ti with Apiezon-L	1096	— ^f	2	1417	28.5
	103	6 AL-4V Ti with Rulon	254	361	14	431	42
	106	347 SS with Apiezon-L	126	247	25	273	40
	102	347 SS with Rulon	57	95	—	121	40

^a 4.5 psia at 793 days.
^b 10 psia at 793 days.
^c 17.5 psia at 1417 days.

^d 21 psia at 1421 days.
^e 27.5 psia at 1417 days.
^f 28.5 psia at 1417 days.

Table 1 (contd)

Material	Sample No.	Description	Days to reach		Pressure at 200 days, psia	Total number of days in test	Pressure attained, psia
			20 psia	35 psia			
Ceramics and lubes	40	3/8 in. ceramic ball (Al ₂ O ₃)	482	895	9	983	40
	39	3/8 in. ceramic ball (Al ₂ O ₃)	326	483	17	571	40
	51	3/8 in. ruby ball	182	397	22	449	40
	104	Ceramic ball and Rulon	646	1059	2	1134	41.5
	146	1/4 ceramic ball and moly coat	379	1030	10	1066	39
	109	Ceramic ball and Apiezon-L	259	410	13	457	40
Butyl elastomers	194	Parker B 496-7	64	118	—	126	41
	193	Parker B 496-7	61	118	—	126	40.5
	195	Parker B 496-7	61	117	—	126	41.5
	197	Parker B 480-7	47	85	—	109	40
	198	Parker B 480-7	42	83	—	98	42.3
	196	Parker B 480-7	41	82	—	98	42
	122	Hadbar No. XB-800-71	38	79	—	97	39
	53	Stillman SR 634-70	44	73	—	77	37
	149	Stillman SR 634-70	27	47	—	56	40
	129	Stillman SR 634-70	2	9	—	16	50
	148	Stillman SR 613-75	17	24	—	36	58
	61	Connecticut Hard Rubber No. 4131	35	67	—	72	38
	57	Connecticut Hard Rubber No. 3609	32	60	—	68	40
	147	Fargo FR 6-60-26	32	61	—	74	40
	125	Fargo FR 6-60-26	<1	10	—	26	48
55	Fargo FR 6-60-27	19	44	—	49	38	
EPR elastomers	155	Parker E 515-8	— ^g	—	4	1334	19
	15	Parker E 515-8	— ^h	—	—	89	12
	200	Parker E 529-6	367	689	12	842	43
	201	Parker E 529-6	325	650	12	742	41
	199	Parker E 529-6	262	528	15	613	42
	162	Stillman SR EX 983S-75	198	389	20	476	40
	150	Stillman SR EX 983S-75	119	297	24	317	37
	164	Stillman SR 722-70	112	165	—	175	40
	165	Stillman SR 722-70	107	161	—	175	40
	168	Stillman SR 722-70	31	53	—	71	46
	63	Stillman SR EX 1004-70	16	26	—	30	41
14	Thiokol 132/54	5	8	—	9	40	
SBR elastomers	58	Connecticut Hard Rubber No. 3818	90	200	35	309	40
	123	Connecticut Hard Rubber No. 4610	54	198	35	239	40
	59	Connecticut Hard Rubber No. 3906	85	—	—	492	16
	60	Connecticut Hard Rubber No. 3954	64	114	—	124	40
	124	Connecticut Hard Rubber No. 4762	36	67	—	97	42
Miscellaneous elastomers	157	G.E. RTV-60 (silicon)	189	296	21	359	40
	62	Connecticut Hard Rubber No. 4706 (PBR)	21	42	—	49	39
	156	DuPont 5109D-590 (EPTR)	3	7	—	8	42.5
Butyl bonded to 6-4 titanium strips	120	Stillman SR 634-70	68	208	33	240	40
	121	Stillman SR 634-70	52	133	—	180	31
	119	Stillman SR 634-70	52	121	—	180	40
	118	Stillman SR 634-70	52	121	—	155	40
	171	Hadbar XB-800-71	45	74	—	86	40
	170	Hadbar XB-800-71	45	74	—	86	40
	169	Hadbar XB-800-71	42	67	—	86	44

^g 19 psia at 1334 days.

^h 10 psia at 189 days.

Table 1 (contd)

Material	Sample No.	Description	Days to reach		Pressure at 200 days, psia	Total number of days in test	Pressure attained, psia
			20 psia	35 psia			
EPR bonded to 6-4 titanium strips	203	Parker E-529-6	274	531	15	608	41
	204	Parker E-529-6	200	377	20	541	43
	181	Parker E-515-8	431	1018	13.5	1138	38.5
	182	Parker E-515-8	211	528	19	770	41
	175	Stillman SR 722-70	93	259	32	322	40
	177	Stillman SR 722-70	91	239	33	339	40
	176	Stillman SR 722-70	84	182	38	283	43
	174	Hadbar EPR 500-2	50	88	—	115	42
	172	Hadbar EPR 500-2	47	88	—	108	42
	173	Hadbar EPR 500-2	43	78	—	97	42
N ₂ H ₄ only	245	Control sample	— ⁱ	—	2	793	9
	179	Control sample	— ^j	—	4	1137	10.5
	138	Control sample	1188	— ^k	3	1421	25.5
	206	Control sample	597	786	5	854	39.5
	145	Control sample	532	1101	9	1208	42
	158	Control sample	590	1012	6	1137	42
	205	Control sample	408	677	9	741	41
	178	Control sample	326	566	15	642	41
	189	Control sample	172	337	22	433	45
	207	Control sample	86	139	—	180	40
	130	Control sample	66	220	34	277	40
	126	Control sample	44	84	—	86	40

ⁱ 9 psia at 793 days.
^j 10.5 psia at 1137 days.
^k 25.5 psia at 1421 days.

Table 2. Final results of compatibility tests with hydrazine/hydrazine nitrate mix
(75% N₂H₄, 24% N₂H₅NO₃, 1% H₂O)
(test terminated June 13, 1967)

Material	Sample No.	Description	Days to reach		Pressure at 200 days, psia	Total number of days in test	Pressure attained, psia
			20 psia	35 psia			
Stainless steel	143	310 SS	301	686	13	809	40
	231	310 SS	250	568	16	666	45
	232	310 SS	200	539	20	606	40
	142	304L SS	194	322	20	350	39.5
	236	304L SS	127	251	28	319	43
	235	304L SS	64	149	—	191	43
	233	347 SS	51	120	—	129	40
	234	347 SS	46	108	—	134	44
	95	347 SS	48	104	—	118	40
	45	347 SS	26	49	—	55	40
	141	304 SS	264	425	15	541	40
	230	304 SS	41	57	—	70	40
	97	304 SS	31	45	—	48	38
	229	304 SS	14	40	—	42	40
	96	303 SS	29	46	—	49	37
	227	303 SS	10	16	—	17	45
	228	303 SS	10	15	—	17	44
	41	416 SS	12	18	—	29	54

Table 2 (contd)

Material	Sample No.	Description	Days to reach		Pressure at 200 days, psia	Total number of days in test	Pressure attained, psia	
			20 psia	35 psia				
Titanium	212	6Al-4V Ti	— ^a	—	4	937	16	
	213	6Al-4V Ti with 6061-T6 Al	— ^b	—	3	937	10	
	214	6Al-4V Ti with 321 SS	194	414	16	594	40	
	209	6Al-4V-ELI Ti	— ^c	—	3	937	9	
	210	6Al-4V-ELI Ti with 6061-T6 Al	— ^d	—	3	937	10	
	211	6Al-4V-ELI Ti with 321 SS	237	561	21	572	44	
	215	5Al-2.5 Sn Ti	761	— ^k	5	937	27.5	
	216	5Al-2.5 Sn Ti with 6061-T6 Al	594	901	7	937	36	
	217	5Al-2.5 Sn Ti with 321 SS	213	531	19	596	41.5	
	218	5Al-2.5 Sn-ELI Ti	— ^e	—	2	937	8	
	219	5Al-2.5 Sn-ELI Ti with 6061-T6 Al	— ^f	—	3	937	19.5	
	220	5Al-2.5 Sn-ELI Ti with 321 SS	215	485	19	586	40	
	221	6Al-6V-2 Sn Ti (Annealed)	— ^g	—	3	937	11	
	222	6Al-6V-2 Sn Ti with 6061-T6 Al	— ^h	—	2	937	5.5	
	223	6Al-6V-2 Sn Ti with 321 SS	256	589	17	657	44	
	224	6Al-6V-2 Sn Ti (heat treated)	— ⁱ	—	1	937	11	
	225	6Al-6V-2 Sn Ti with 6061-T6 Al	— ^j	—	3	937	13	
	226	6Al-6V-2 Sn Ti with 321 SS	219	495	19	586	40	
	46	6Al-4V Ti	91	138	—	158	41	
	Aluminum	43	6061-T6 Al	— ^l	—	5	1553	21
		237	6061-T6 Al	734	— ^m	6	886	25
		42	6061-T6 Al	783	1437	9	1553	38
		238	6061-T6 Al	116	163	—	191	44
		139	6061-T6 Al (brazed)	— ⁿ	—	3	1421	19.5
		100	6061-T6 Al (sprayed with Rulon)	405	843	10	1030	40
	Miscellaneous metals	99	6061-T6 Al brazed to 304 SS	20	33	—	34	37
98		6061-T6 Al brazed to 303 SS	14	25	—	28	40	
250		Vicalloy	8	11	—	12	42	
52		3/8 in. ceramic ball, Al ₂ O ₃	91	173	—	190	38.5	
44		Ni—Span—C	12	20	—	29	52	
50		3/8 in. sapphire ball	138	340	27.5	383	41	
Buytl elastomers	65	FR 6-60-26 (Fargo)	23	267	30	336	40	
	127	FR 6-60-26 (Fargo)	14	34	—	39	40	
	64	FR 6-50-3 (Fargo)	68	119	—	151	45	
	131	SR 634-70 (Stillman)	12	26	—	31	43	
Fuel mix only	151	Control sample—blank	— ^o	—	2	1367	10	
	152	Control sample—blank	— ^p	—	2	1367	6	
	153	Control sample—blank	— ^q	—	2	1367	14.5	
	154	Control sample—blank	— ^r	—	2	1367	6	
	239	Control sample—blank	— ^s	—	4	886	17	
	144	Control sample—blank	766	1255	8	1317	37.5	
	241	Control sample—blank	520	783	11	886	39.5	
	240	Control sample—blank	408	606	11	668	40	
	128	Control sample—blank	31	54	—	86	48	
	132	Control sample—blank	20	54	—	86	44	
^a 16 psia at 937 days.		^h 5.5 psia at 937 days.		^o 6 psia at 1367 days.				
^b 10 psia at 937 days.		ⁱ 11 psia at 937 days.		^p 14.5 psia at 1367 days.				
^c 9 psia at 937 days.		^j 13 psia at 937 days.		^q 6 psia at 1367 days.				
^d 10 psia at 937 days.		^k 27.5 psia at 937 days.		^r 17 psia at 886 days.				
^e 8 psia at 937 days.		^l 18.5 psia at 1436 days.		^s 25 psia at 886 days.				
^f 19.5 psia at 937 days.		^m 19.5 psia at 1421 days.						
^g 11 psia at 937 days.		ⁿ 10 psia at 1367 days.						

**Table 3. Final results of compatibility tests with unsymmetrical dimethylhydrazine/hydrazine
(50% UDMH, 50% N₂H₄)
(test terminated June 13, 1967)**

Material	Sample No.	Description	Psia at no. of days to reach	Pressure at 200 days, psia	Total number of days in test	Pressure attained, psia
6 AL-4V-Ti	263	6 AL-4V-Ti ↓	20 at 536 and 25 at 653	4	653	25
	264		7.5 at 653	0	653	7.5
	265		11.5 at 653	5	653	11.5
	266		15.5 at 653	6	653	15.5
	267		10 at 653	4	653	10
	268		15 at 653	4	653	15
	269		13 at 653	3	653	13
	271		20 at 533 and 23 at 653	7	653	23
	272		8 at 653	3	653	8
	273		16.5 at 653	5	653	16.5
	274		8.5 at 653	4	653	8.5
UDMH/N ₂ H ₄ only	263A	Control sample	12.5 at 653	4	653	12.5
	269A	Control sample	20 at 417 and 33.5 at 653	7	653	33.5

3. Heat-Sterilization Compatibility Of EPR in N₂H₄

O. F. Keller

As part of the next phase of the EPR material bladder development heat-sterilization program reported in SPS 37-42, -44, Vol. IV, pp. 82 and 180, respectively, 24 additional elastomeric patch-test samples were prepared. The samples were divided into two groups for compatibility testing in hydrazine. The first group, while immersed in hydrazine, was tested at 275°F for three cycles only; the second group at 300°F for three cycles only. Prior to testing, each group was again divided into subgroups of four samples each and mounted in three type-347 stainless steel containers (Figs. 1 and 2) enclosed within an environmental test chamber. The samples were separated from each other by a type-347 stainless steel wire rack, as shown in Fig. 2. A fourth container, filled only with hydrazine, was also mounted in the environmental test chamber for use as a pressure generation reference, or control.

During previous testing (SPS 37-42, -44, Vol. IV, pp. 82 and 180, respectively) type-321 stainless steel containers of a slightly smaller diameter had been used. The purpose of this test was to investigate the heat-sterilization characteristics of the EPR patch-test samples in hydrazine at 275 and 300°F, using the larger diameter type-347 stainless steel containers. The larger containers were chosen to minimize distortion of the samples during insertion and removal. The containers, with wire racks installed,

were passivated by filling with hydrazine and allowing to stand for 20h, then draining and flushing with hydrazine, prior to testing.

The heat-sterilization cycle was nominally 60 h duration. One container with patch-test samples was removed from the environmental test chamber after each 60-h cycle. The patch-test samples were then removed from the container and the following operations performed:

- (1) Samples reweighed.
- (2) Shore hardness measured.
- (3) Permeability to hydrazine measured.¹
- (4) Shore hardness measured.
- (5) Vacuum soaked at 100 μm Hg.
- (6) Samples reweighed.
- (7) Shore hardness measured.

A few of the samples exhibited signs of attack by the hydrazine, including some spall-like marks and occasional

¹The permeability to hydrazine was measured in accordance with procedures as outlined in S. P. Vango's Technical Memorandum 33-55, "Determination of Permeability of Cast Teflon Sheet to Nitrogen Tetroxide and Hydrazine," Jet Propulsion Laboratory, Pasadena, Calif., August 25, 1961.

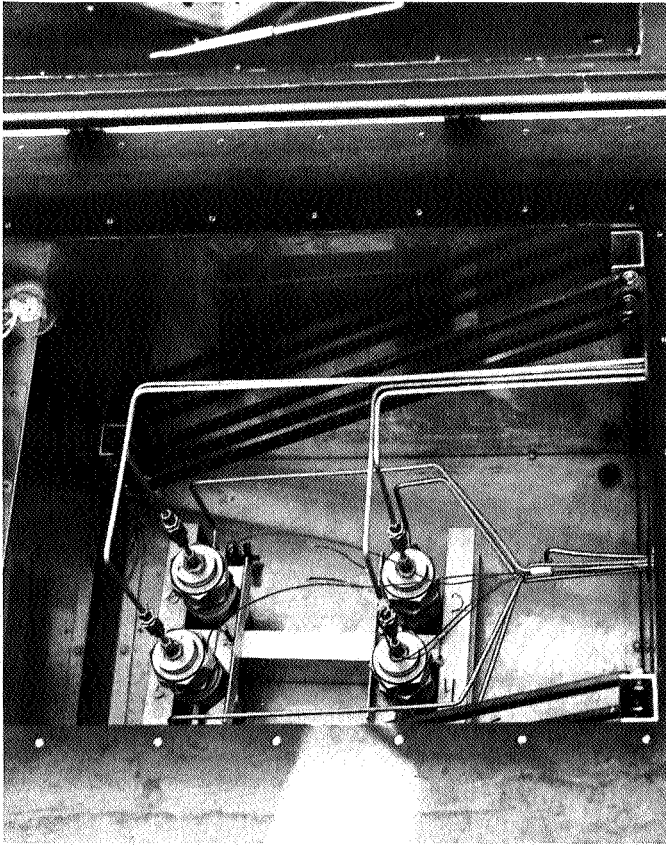


Fig. 1. Four type-347 stainless steel containers mounted in environmental test chamber

blistering, as shown in Figs. 3 and 4. Two blisters of this type were observed out of the 24 samples tested. The blisters did not appear to be critical defects; i.e., defects that could adversely affect the ability of the bladder material to perform its primary function as a barrier between the hydrazine and the pressurizing gas. Generally, the samples were in serviceable condition and still potentially capable of functioning as a bladder material.

Table 4 is a compilation of test data obtained during this series of tests. At the start of the tests the hydrazine was colorless. After the first sterilization cycle the hydrazine was light brown in color and contained fine black material in suspension, except in the reference containers.

Table 5 lists typical volumetric measurements for the containers used during these tests. Each container is filled to the vent port with approximately 305 ml N_2H_4 prior to heat-sterilization. After three 60-h cycles at 275°F, the volume of N_2H_4 remaining in a container is about 47% of the original amount. This reduction in N_2H_4 occurs during the cooling and venting of the containers between heat sterilization cycles.

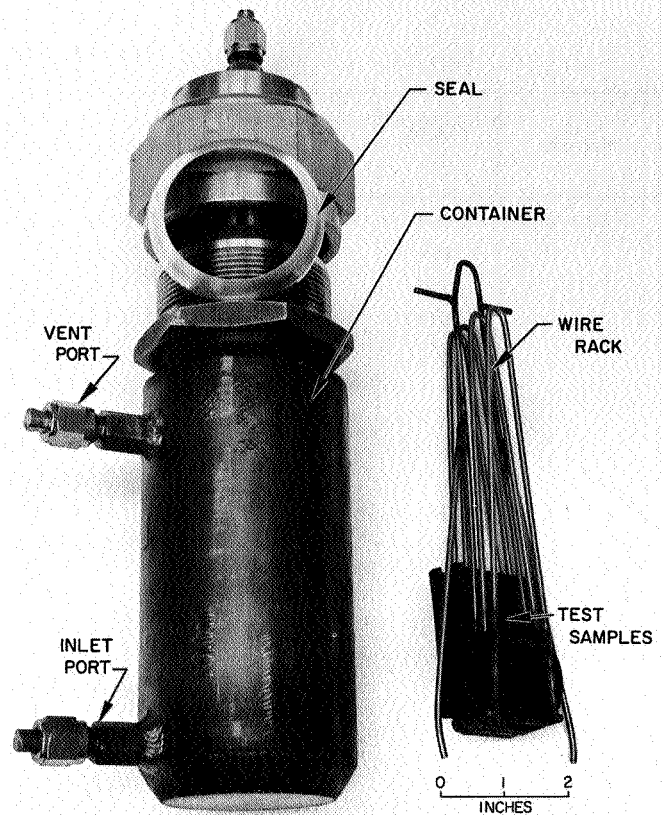


Fig. 2. Type-347 stainless steel container with wire rack

Differences in average shore A hardness and permeation rates occur because it has been necessary to use different sets of samples for each test operation. Figure 5 indicates that the shore A hardness of the test samples is relatively independent of the number of heat-sterilization cycles at 275 and 300°F. At both sterilization temperatures a slight reduction of sample shore A hardness was noted after the third heat-sterilization cycle.

Permeation rates also appear to be relatively independent of the number of heat-sterilization cycles. While Fig. 6 indicates an increase in permeation after the second and third heat-sterilization cycles at 275°F, a slight decrease in permeation after the third heat sterilization cycle at 300°F is noted.

Figure 7 by comparison indicates a marked decrease in the percentage of hydrazine, as determined by an assay of the test fluid after heat-sterilization. This relatively large decrease occurs in each case after the first heat-sterilization cycle.

Item ^a	Sample number	Initial thickness, in.	Final thickness, in.	Initial weight, g	Net increase (decrease), g	Increase (decrease), %	Initial shore A hardness ±2.0	Final shore A hardness ±2.0
1	66 × 09201-1-a ₁	0.034-0.036	0.034-0.036	1.3052	(0.0042)	(0.32)	72	72
2	66 × 09201-1-a ₂	0.035-0.037	0.034-0.037	1.3153	(0.0065)	(0.49)	73	73
3	66 × 09201-1-b ₁	0.038-0.041	0.037-0.043	3.3868	(0.0100)	(0.29)	71	72
4	66 × 09201-1-b ₂	0.039-0.041	0.038-0.041	3.3690	(0.0043)	(0.13)	71	72
5	66 × 09201-2-a ₁	0.034-0.036	0.033-0.036	1.2619	(0.0069)	(0.55)	71	73
6	66 × 09201-2-a ₂	0.035-0.037	0.034-0.037	1.3135	(0.0013)	(0.10)	—	73
7	66 × 09201-2-b ₁	0.037-0.041	0.037-0.040	3.3094	(0.0033)	(0.10)	72	74
8	66 × 09201-2-b ₂	0.038-0.042	0.038-0.042	3.5659	(0.0044)	(0.12)	72	74
9	66 × 09201-3-a ₁	0.036-0.038	0.035-0.037	1.3235	(0.0094)	(0.71)	72	71
10	66 × 09201-3-a ₂	0.034-0.037	0.034-0.036	1.2975	(0.0004)	(0.03)	73	72
11	66 × 09201-3-b ₁	0.039-0.042	0.038-0.041	3.4381	(0.0019)	(0.06)	72	71
12	66 × 09201-3-b ₂	0.036-0.040	0.036-0.039	3.2606	(0.0044)	(0.13)	71	71
13	66 × 09201-4-a ₁	0.034-0.036	0.033-0.036	1.2519	(0.0052)	(0.42)	73	73
14	66 × 09201-4-a ₂	0.033-0.037	0.033-0.036	1.2742	(0.0004)	(0.03)	72	71
15	66 × 09201-4-b ₁	0.038-0.041	0.038-0.042	3.3060	0.0012	0.04	71	72
16	66 × 09201-4-b ₂	0.038-0.041	0.038-0.042	3.3979	0.0031	0.09	71	71
17	66 × 09201-5-a ₁	0.035-0.038	0.035-0.038	1.3380	0.0148	1.11	74	69
18	66 × 09201-5-a ₂	0.033-0.034	0.032-0.034	1.2221	0.0098	0.80	74	70
19	66 × 09201-5-b ₁	0.035-0.039	0.035-0.039	3.1618	0.0225	0.71	70	68
20	66 × 09201-5-b ₂	0.036-0.040	0.036-0.041	3.2941	0.0236	0.72	72	67
21	66 × 09201-6-a ₁	0.035-0.037	0.035-0.038	1.3142	0.0038	0.29	72	72
22	66 × 09201-6-a ₂	0.035-0.038	0.035-0.038	1.3131	0.0013	0.10	71	72
23	66 × 09201-6-b ₁	0.035-0.039	0.035-0.038	3.0955	(0.0018)	(0.06)	71	72
24	66 × 09201-6-b ₂	0.037-0.041	0.037-0.042	3.4006	(0.0008)	(0.02)	71	71
← Pressure generation reference (or control) samples →								
25	66 × 09201-7-a ₁	0.036-0.037	—	1.3228	—	—	72	—
26	66 × 09201-7-a ₂	0.033-0.034	—	1.1773	—	—	73	—
^a Compound No. SR 722-70. ^b Fluid test temperature 275°F. ^c Fluid test temperature 300°F. ^d Possible leak.								

Table 4. Ethylene-propylene patch-test samples heat-sterilization test data

Shore A hardness after permeation test ± 2.0	Shore A dry hardness after vacuum ± 2.0	Permeation mg N ₂ H ₄ /h/in. ²	Time of permeation test, h	No. of cycles	Total time at test temperature, h	N ₂ H ₄ concentrate, %	Container No.	Pressure designator	Pressure after one cycle, psig	Pressure after two cycles, psig	Pressure after three cycles, psig
70	73	0.042	23 1/2	2 ^b	130.5	93.8	2	P ₁	407	270	—
70	73	0.051	23 1/2	2 ^b	130.5	93.8	2	P ₁	407	270	—
—	—	—	—	2 ^b	130.5	93.8	2	P ₁	407	270	—
—	—	—	—	2 ^b	130.5	93.8	2	P ₂	407	270	—
71	72	0.019	40	1 ^b	70.5	95.3	4	P ₂	262 ^d	—	—
71	71	0.023	40	1 ^b	70.5	95.3	4	P ₂	262 ^d	—	—
—	—	—	—	1 ^b	70.5	95.3	4	P ₂	262 ^d	—	—
—	—	—	—	1 ^b	70.5	95.3	4	P ₂	262 ^d	—	—
70	71	0.054	23 1/2	3 ^b	190.5	94.1	5	P ₃	403	296	294
69	71	0.078	23 1/2	3 ^b	190.5	94.1	5	P ₃	403	296	294
—	—	—	—	3 ^b	190.5	94.1	5	P ₃	403	296	294
—	—	—	—	3 ^b	190.5	94.1	5	P ₃	403	296	294
69	72	0.024	40	2 ^c	120	95.0	1	P ₁	426	486	—
69	72	0.028	40	2 ^c	120	95.0	1	P ₁	426	486	—
—	—	—	—	2 ^c	120	95.0	1	P ₁	426	486	—
—	—	—	—	2 ^c	120	95.0	1	P ₁	426	486	—
68	71	0.018	41	3 ^c	180	95.1	8	P ₂	470	548	762
68	70	0.022	41	3 ^c	180	95.1	8	P ₂	470	548	762
—	—	—	—	3 ^c	180	95.1	8	P ₂	470	548	762
—	—	—	—	3 ^c	180	95.1	8	P ₂	470	548	762
69	71	0.024	40	1 ^c	60	95.3	9	P ₃	558	—	—
68	71	0.020	40	1 ^c	60	95.3	9	P ₃	558	—	—
—	—	—	—	1 ^c	60	95.3	9	P ₃	558	—	—
—	—	—	—	1 ^c	60	95.3	9	P ₃	558	—	—
<div style="display: flex; justify-content: space-between; align-items: center;"> ← Reference (or control) containers → </div>											
71	72	0.026	40	3	190.5	94.7	6	P ₄	498	494	314
73	73	0.028	40	3	180	94.7	10	P ₄	792	740	620

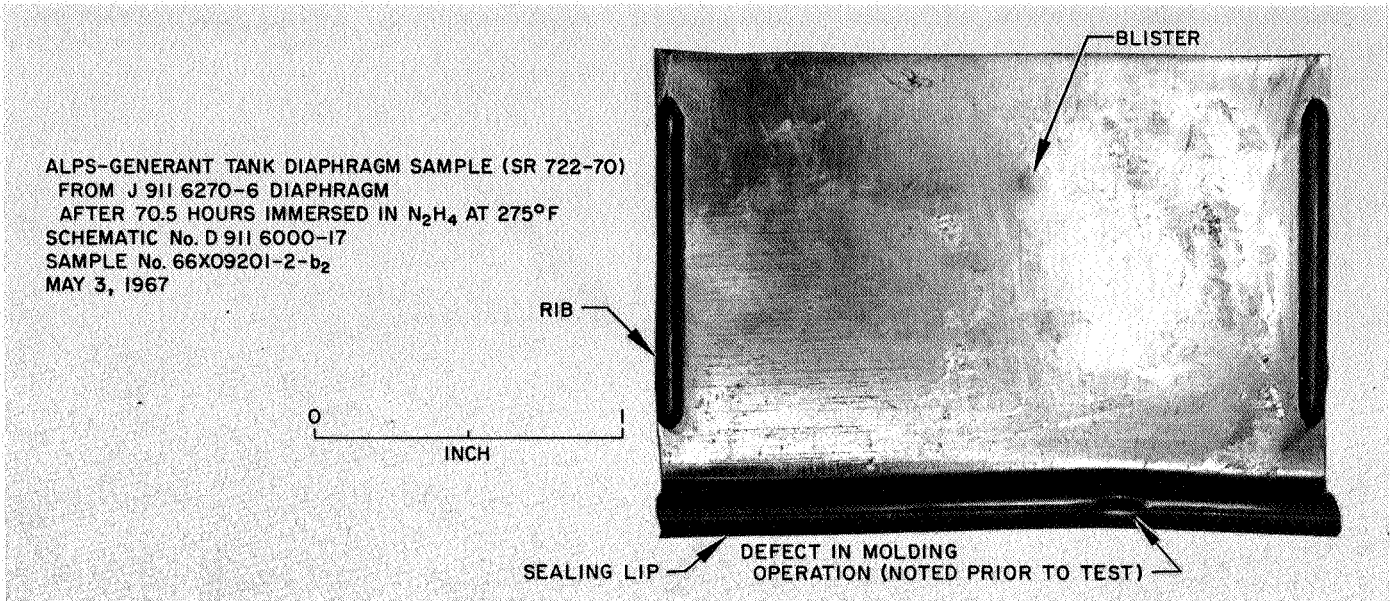


Fig. 3. Diaphragm sample of EPR (SR 722-70) after 70.5 h in hydrazine at 275°F (outside, or liquid-side, surface)

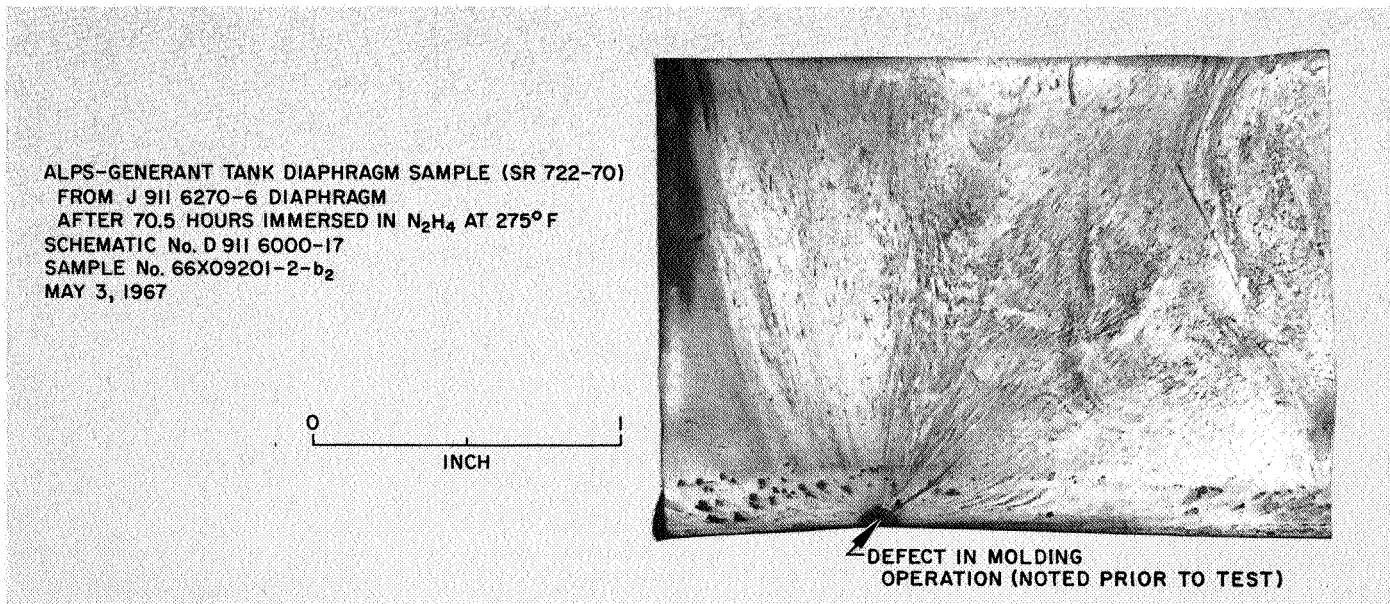


Fig. 4. Diaphragm sample of EPR (SR 722-70) after 70.5 h in hydrazine at 275°F (inside, or gas-side, surface)

Table 5. Typical volumetric measurements of test containers

Container No.	Volume less sample, ml	Volume to pressure port, ml	Volume to vent port, ml	Volume N ₂ H ₄ after test, ml	N ₂ H ₄ Volume after test, %	Volume samples, ml	No. of cycles	Fluid test temperature, °F
2	502	475	309	—	—	7.7	2	275
4	497	470	302	190	63	7.7	1	275
5	504	473	309	145	47	7.7	3	275
6	503	473	301	270	90	N/A	1	275
Average container	502	473	305	—	—	7.7	—	275

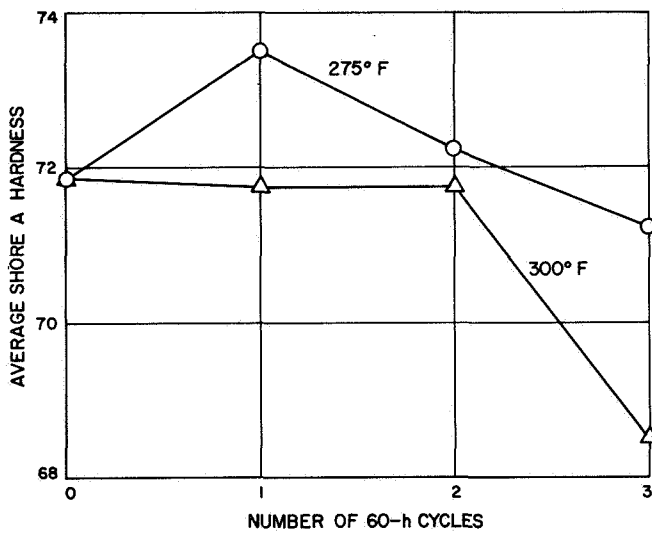
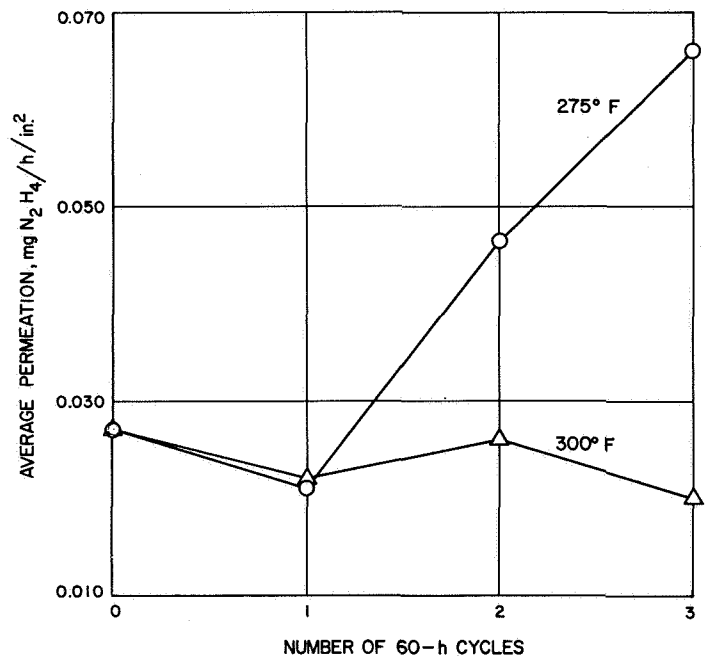


Fig. 5. Shore A hardness of EPR (SR 722-70) after heat sterilization cycles

Fig. 6. Permeation rates of EPR (SR 722-70) by hydrazine after heat-sterilization cycles



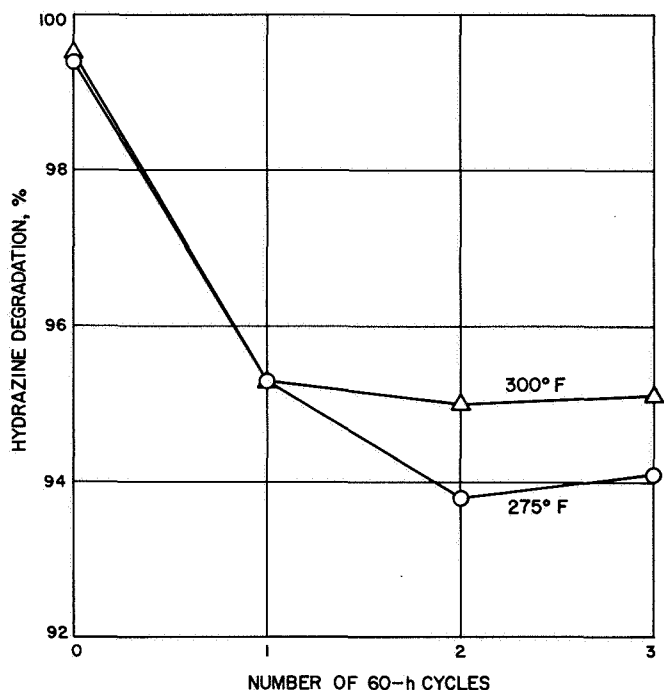


Fig. 7. Hydrazine degradation after heat-sterilization cycles (assay results)

From the test data, as shown in Table 4, an average rate of pressure generation has been computed for each heat-sterilization temperature. This information is shown graphically in Fig. 8. The dashed lines of the two curves

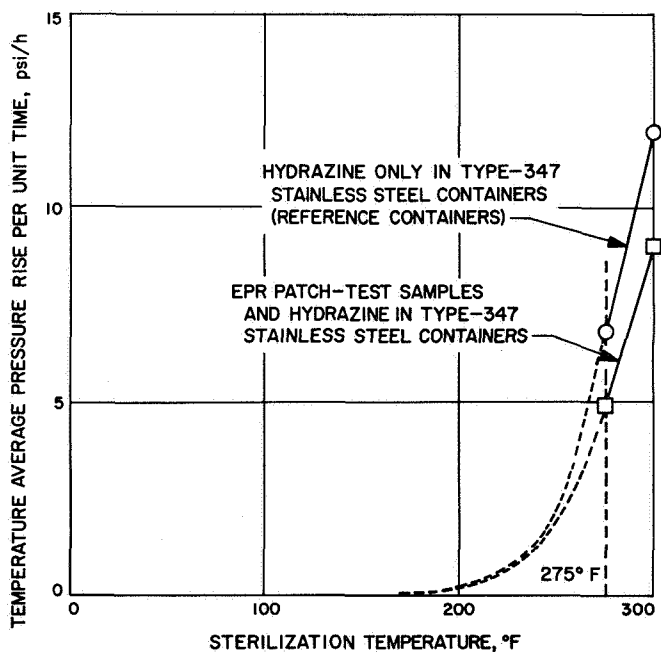


Fig. 8. Temperature sensitivity of EPR patch-test samples immersed in hydrazine

are based on heat-sterilization test data previously reported in SPS 37-44, Vol. IV, p. 180. These data indicate that the average pressure rise in the reference containers was greater than the average pressure rise in the containers with EPR patch-test samples. Also noted, as previously reported in SPS 37-44, Vol. IV, p. 180, that the rate of pressure generation is very sensitive to changes in the heat-sterilization temperature.

The next phase of this program will include additional cycling at sterilization temperatures of 275 and 300°F until six sterilization cycles at each temperature have been completed. A detailed posttest analysis will be carried out on the EPR patch test samples, the hydrazine propellant, and the type-347 stainless steel containers.

B. The Reaction Between OF_2 and B_2H_6 : The Rate of Formation of BF_3 , R. A. Rhein

1. Introduction

The object of this research program (of which this article is one portion) is to measure the rate of reaction of OF_2 with B_2H_6 . In order to determine the reaction rates, it is necessary to measure the partial pressure of the OF_2 and of the B_2H_6 continuously as the reaction proceeds. Infrared spectroscopy was chosen as the method for making these measurements.

To determine the partial pressure of OF_2 in the presence of B_2H_6 by infrared spectroscopy, it is necessary to know the pressure-broadening effect² of the B_2H_6 on the infrared absorption of the OF_2 . But since the OF_2 reacts with B_2H_6 , it is difficult to determine the pressure-broadening effect unless one knows the reaction rate and uses it to calculate the partial pressures of the OF_2 and the B_2H_6 for any time interval after they were mixed. This rate can be estimated by using the rate of formation of BF_3 . The same reasoning holds for determining B_2H_6 in the presence of OF_2 .

As neither OF_2 nor B_2H_6 reacts with BF_3 , it was relatively easy to measure the pressure-broadening effect of

²Each compound absorbs infrared radiation reasonably strongly at one or more frequencies. The amount of absorption of infrared radiation at any of these frequencies for a gas depends primarily on the path length through which infrared radiation passes and the concentration of the gas. For a gas mixture, however, because of a pressure-broadening effect, the presence of other gases increases the absorption of infrared radiation to a value greater than would be observed for a pure gas.

B_2H_6 and of OF_2 on the infrared absorption of BF_3 . By making continuous measurements of BF_3 partial pressure versus time for various initial values of the partial pressure of OF_2 and of B_2H_6 , the initial rates of formation of BF_3 were determined.

It was assumed that the initial rate of formation of BF_3 is a good indicator for the initial reaction rate of OF_2 with B_2H_6 . As BF_3 was the predominant fluorine-containing

product of the reaction of OF_2 and B_2H_6 (SPS 37-42, Vol. IV, pp. 73-80), the assumption is probably valid.

As a result of this study, it was found that OF_2 reacts with B_2H_6 in an interesting and very unexpected manner. The initial rate of formation of BF_3 from this reaction was found to be proportional to the square of the OF_2 partial pressure and to the inverse square root of the B_2H_6 partial pressure.

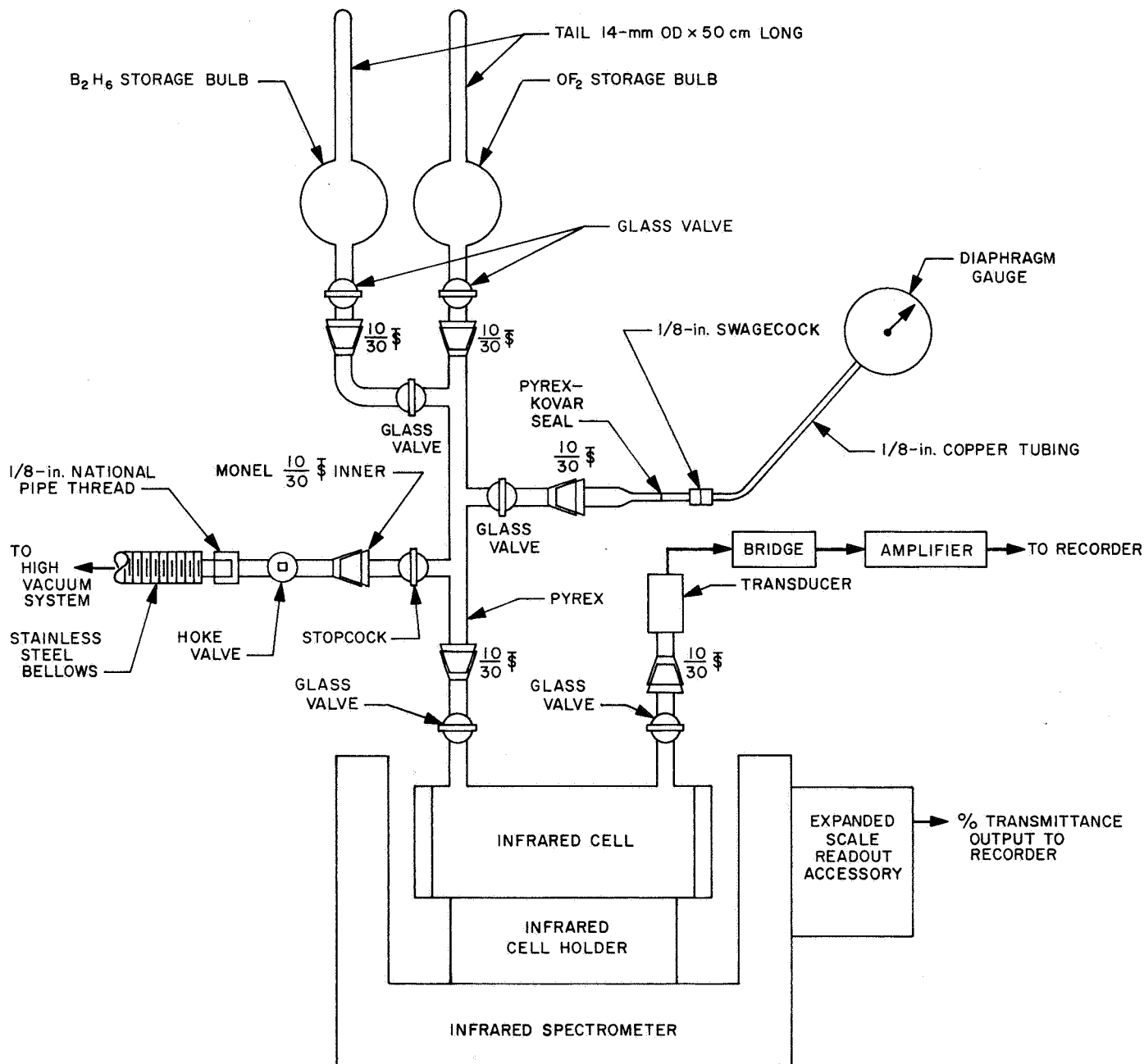


Fig. 9. Schematic of the experimental setup

The results of the experiments described in this article indicated that the initial rate of formation of BF_3 at ambient temperatures corresponded to the rate expression

$$\left[\frac{d}{dt} (P_{\text{BF}_3}) \right]_0 = 0.0082 (P_{\text{OF}_2})_0^2 (P_{\text{B}_2\text{H}_6})_0^{-0.5} \quad (1)$$

where the subscript 0 indicates initial conditions; time and pressure were expressed in minutes and torr.

2. Experimental Procedure

The experimental setup is shown in Fig. 9. The OF_2 and the B_2H_6 were purified by the method described in SPS 37-42, Vol. IV, pp. 73-80, and were stored in the pyrex bulbs shown. In the bulbs, the pressure of the OF_2 and of the B_2H_6 was ordinarily held between 400 and 800 torr.

The infrared cells were constructed of either pyrex or 316 stainless steel; the design for the stainless steel cell is shown in Fig. 10. The cell windows were made of NaCl, AgCl, or IRTRAN-2 (pressed polycrystalline ZnS).

Although the experiments were conducted using either cell with any of the windows, there was no observable difference in the reaction rate due to the cell or window materials of construction.

The pressure of gases in the cells was measured by an electronic transducer, attached directly to the cell. The pressure could also be measured by the diaphragm gage shown on the gas handling system attached to the cell. This system was connected to a standard high vacuum apparatus through the metal bellows, as shown. It was through the bellows that the cell and assembly were evacuated.

The following procedure was used to conduct each experiment:

- (1) The cell and the attached system were evacuated to a pressure of approximately $1 \mu\text{m}$.
- (2) The B_2H_6 was added, to both the cell and the system, to the desired pressure, as registered by the diaphragm pressure gage. The stopcock between the cell and the system was closed and the system was evacuated.

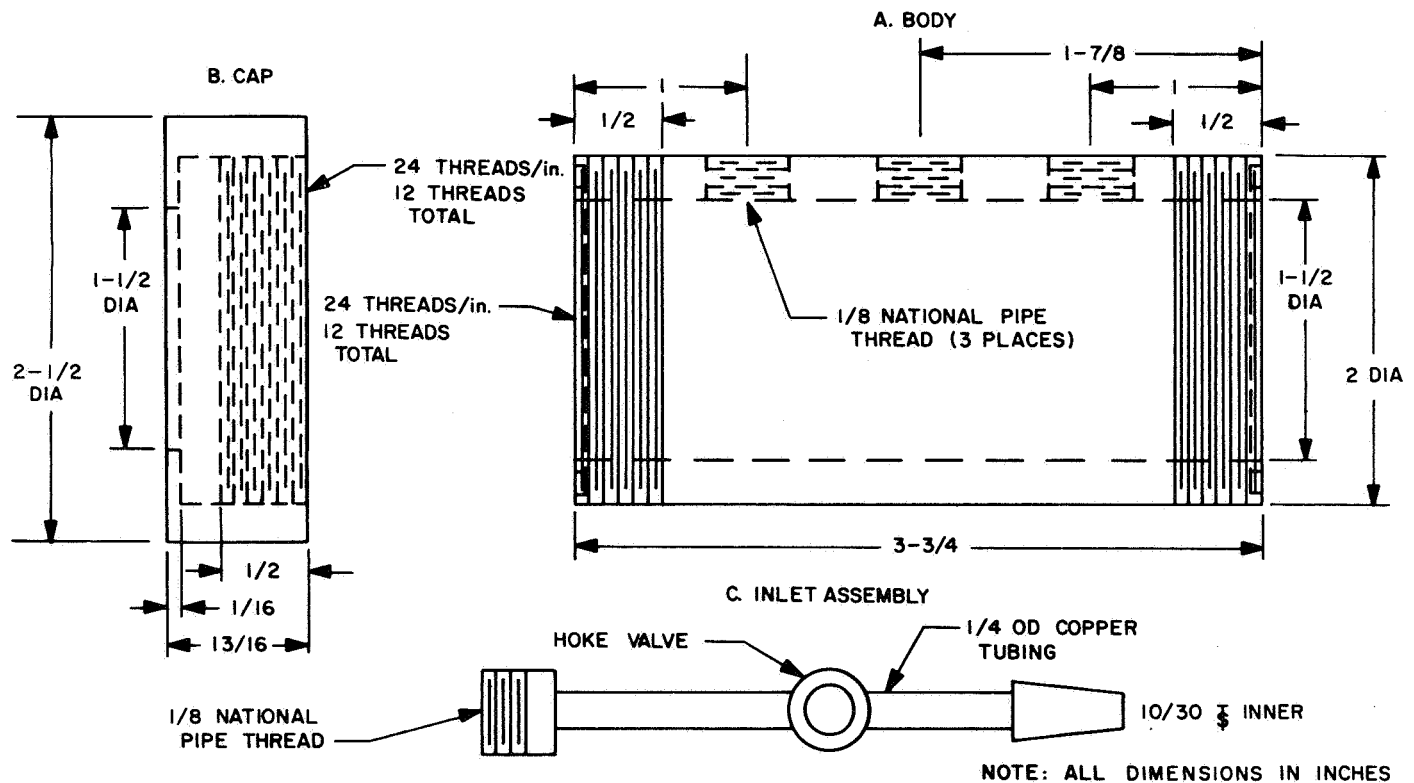


Fig. 10. Stainless steel infrared cell design

(3) The OF_2 was added to the system until its pressure was equal to the B_2H_6 pressure in the cell; the stopcock between the cell and the system was then opened, and the OF_2 pressure was increased until the final desired pressure was achieved; the addition of OF_2 to the B_2H_6 generally took about 1 min. Then the stopcock between the system and the cell was closed.

(4) The voltage output from the electronic equipment associated with the transducer was impressed on a strip chart recorder. This voltage output was calibrated by the pressure measured by the diaphragm gage immediately after the OF_2 was added to the B_2H_6 .

(5) The transmittance output from the infrared spectrometer was impressed on one strip-chart recorder; and, simultaneously, the output from the electronics associated with the transducer was impressed on another strip-chart recorder for the duration of the experiment.

(6) The experimental duration was approximately 10 min. After that, the cell was evacuated.

3. Results

Perhaps the most important finding of this work was that the initial rate of formation of BF_3 from the reaction of OF_2 and B_2H_6 could be represented fairly well by Eq. (1), derived from experimentally measured values of

$$\left[\frac{d}{dt} (P_{\text{BF}_3}) \right]_0$$

which are listed in Table 6. Because the BF_3 rates depend upon the initial partial pressures of OF_2 and of B_2H_6 , these BF_3 rates, along with their rms deviations, are shown in Table 6 for a series of selected pairs of values of initial partial pressures of OF_2 and of B_2H_6 . Each value for the BF_3 rate shown in Table 6 represents an average value from several experiments. Also listed are values for the BF_3 rates calculated from Eq. (1).

The BF_3 partial pressure was determined from measurements of the transmittance of infrared radiation at the $6.88\text{-}\mu\text{m}$ absorption band of BF_3 . All infrared measurements were conducted at a 10-cm path length. For

Table 6. Initial rates of formation of BF_3 from the reaction of OF_2 and B_2H_6 ^a

$(P_{\text{OF}_2})_0$, torr	$(P_{\text{B}_2\text{H}_6})_0$, torr	$\left[\frac{d}{dt} (P_{\text{BF}_3}) \right]_0$ (experimental), torr/min	σ (rms)	$\left[\frac{d}{dt} (P_{\text{BF}_3}) \right]_0$ (calculated), torr/min	$\left[\frac{d}{dt} (P_{\text{reactor}}) \right]_0$, torr/min	σ (rms)
5.0	1.0	0.0227	0.0038	0.0205	0.0100	0.0000
5.0	2.5	0.0124	0.0004	0.0129	0.0287	0.0018
5.0	5.0	0.0149	0.0017	0.0092	0.0228	0.0042
10.0	1.0	0.0805	0.0013	0.0820	0.1184	0.0065
10.0	2.5	0.0361	0.0031	0.0519	—	—
10.0	5.0	0.0418	0.0008	0.0367	0.0854	0.0140
10.0	10.0	0.0353	0.0048	0.0259	0.0901	0.0059
10.0	20.0	0.0223	0.0042	0.0183	0.0741	0.0061
10.0	30.0	0.0182	0.0026	0.0150	0.0710	0.0128
20.0	5.0	0.1578	0.0079	0.1467	0.2578	0.0386
20.0	10.0	0.1047	0.0068	0.1037	0.1800	0.0142
20.0	20.0	0.0566	0.0035	0.0733	0.1785	0.0258
20.0	30.0	0.0770	0.0067	0.0599	0.1133	0.0054
30.0	5.0	0.434	0.194	0.3300	—	—
30.0	10.0	0.325	0.032	0.2334	-1.12	0.49
30.0	20.0	0.182	0.013	0.1650	0.120	0.027
30.0	30.0	0.190	0.024	0.1347	0.1973	0.1171
40.0	20.0	0.510	0.004	0.2934	0.0564	0.0252

^aTabulated values are for those observed experimentally and those calculated from Eq. (1); the rate of change of pressure of the gases in the reactor (consisting of OF_2 , B_2H_6 , and their gaseous products) are tabulated for values of the initial partial pressures of OF_2 and of B_2H_6 .

pure BF_3 , the absorbance³ as a function of pressure is shown in Fig. 11. Because of the pressure-broadening effect described above, the presence of another gas mixed with BF_3 increases the infrared absorbance to a value somewhat greater than that for BF_3 alone. This pressure-broadening effect must be taken into account when the BF_3 partial pressure in the presence of OF_2 and B_2H_6 is determined from measurements of its infrared absorbance. The pressure-broadening effect is called here the differential absorbance, i.e., the increase in absorbance due to the presence of another gas mixed with the BF_3 .

For a particular partial pressure of BF_3 , the differential absorbance is a function of the partial pressure of the

³The absorbance is defined as $(\text{absorbance}) = -\log_{10}(\text{transmittance})$; the transmittance is the fraction of infrared radiation passing through a substance in an infrared cell. The transmittance (which depends on the infrared frequency) is the quantity measured by the infrared spectrometer, and ranges in value from 0 to 1.0 (or 100%). For an empty infrared cell, the transmittance is 100%.

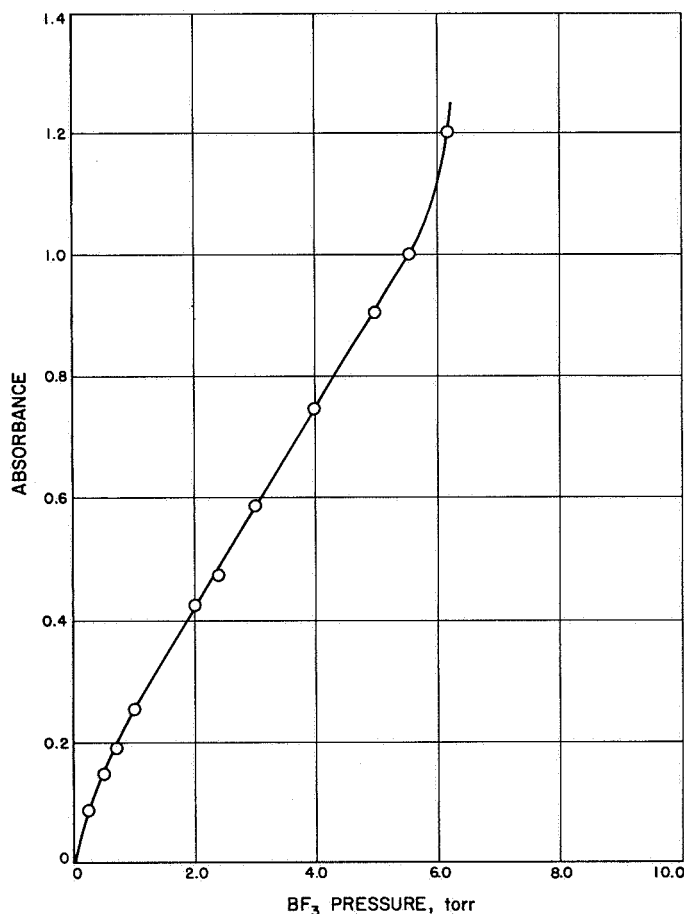


Fig. 11. Infrared absorbance vs pressure of BF_3 , 10-cm cell, 6.88- μm wavelength

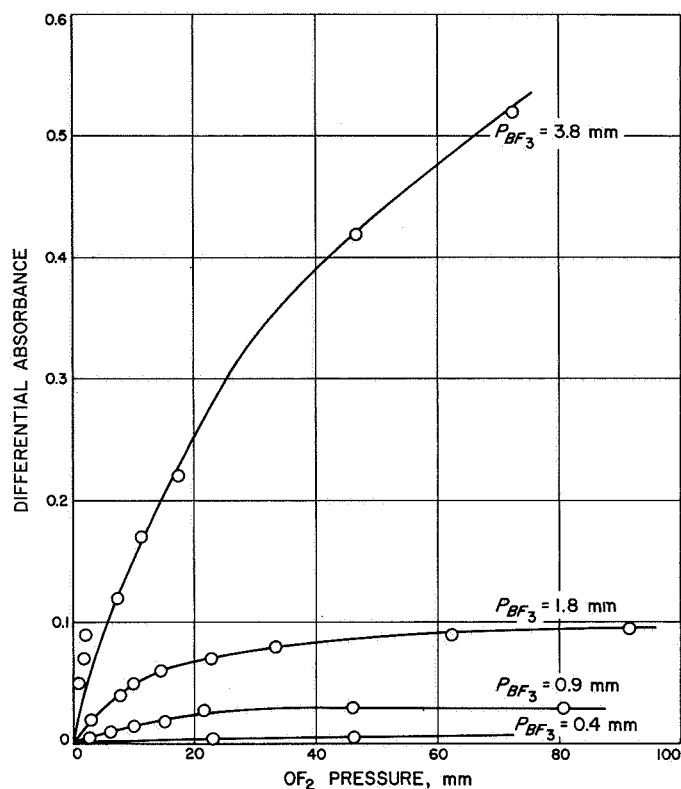


Fig. 12. The increase in absorbance, or differential absorbance, on the 6.88- μm absorption band of BF_3 vs pressure of OF_2 added to BF_3 at various initial pressures (10-cm path length)

added gas. In Fig. 12, the differential absorbance, as a function of the OF_2 pressure, is presented for a series of values of BF_3 partial pressures. In Fig. 13, the differential absorbance, as a function of the partial pressure of B_2H_6 , is presented for a series of values of the BF_3 partial pressure.

In each experiment involving the reaction of OF_2 with B_2H_6 , the total pressure was measured as a function of time. The slope of the total pressure versus time curve was determined, immediately after the OF_2 was added to the B_2H_6 . The average initial total pressure rate of change, with time, and the rms deviation, for each pair of OF_2 and B_2H_6 initial pressures are listed in Table 6. No attempt was made to determine the significance of these rates, however.

To convert absorbance to BF_3 partial pressure, it was necessary to know the absorbance of pure BF_3 , the differential absorbance from the OF_2 present, and the differential absorbance from the presence of the B_2H_6 . The total absorbance is the sum of the absorbance due to BF_3

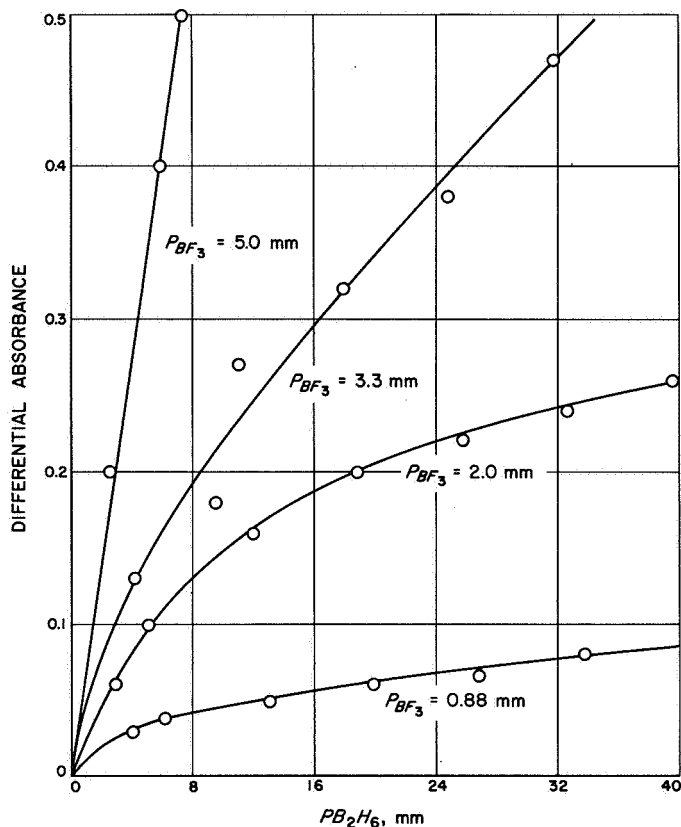


Fig. 13. The increase in absorbance, or differential absorbance, on the 6.88- μ m absorption band of BF_3 vs pressure of B_2H_6 added to BF_3 at various initial pressures (10-cm path length)

alone (Fig. 11), the differential absorbance from OF_2 , and the differential absorbance from B_2H_6 .

The differential absorbance from OF_2 depends upon the pressures of both OF_2 and BF_3 . For a given OF_2 pressure, therefore, the differential absorbance due to OF_2 is a function of BF_3 partial pressure. This likewise holds true with the differential absorbance of B_2H_6 . The differential absorbance from a constant partial pressure of OF_2 with variable partial pressure of BF_3 can be determined from the information presented in Fig. 12. Likewise, the differential absorbance for variable BF_3 and constant B_2H_6 partial pressures can be determined from the information on Fig. 13.

The initial rate of formation of BF_3 is equal in value to the slope of the BF_3 partial pressure-time curve, measured at that time where the reaction was assumed to have begun, that is, immediately following the addition of OF_2 to the B_2H_6 . It is true that the total pressure would be equal to the sum of the pressures of the OF_2

and B_2H_6 only if there were no reaction between them. It was assumed here that the reaction between OF_2 and B_2H_6 is negligible while the OF_2 was being added to the B_2H_6 . As it turns out, the assumption was a fairly good one, as the rate of formation of BF_3 was generally < 1 torr/min under these experimental conditions, and the length of time required to add the OF_2 was generally < 1 min.

In order to find an algebraic expression from which one could calculate the BF_3 rate for a given initial partial pressure of OF_2 and of B_2H_6 , the following form was used:

$$\left[\frac{d}{dt} (\text{BF}_3) \right]_0 = A (P_{\text{OF}_2})_0^a (P_{\text{B}_2\text{H}_6})_0^b \quad (2)$$

The following procedure was used to obtain values for the constants A , a , and b :

(1) An experimental condition was specified by the initial partial pressures of OF_2 and of B_2H_6 ; for each, several experiments were performed. For each initial partial pressure of B_2H_6 there were several experimental conditions, specified by that value of the B_2H_6 partial pressure and by one of several values of the OF_2 partial pressure. For each of these sets of experimental conditions, defined by a particular value of initial partial pressure of B_2H_6 , a graphical plot was made of the logarithm of the BF_3 rate plotted against the logarithm of the initial partial pressure of OF_2 . These plots were shown to be a family of approximately straight lines, and the slope of each of these lines was found to be closely equal to two. Consequently, the OF_2 pressure exponent a , was chosen to be two.

(2) To get A and b , the rate equation was expressed in the form

$$\frac{d}{dt} (P_{\text{BF}_3})_0 = A (P_{\text{OF}_2})_0^2 (P_{\text{B}_2\text{H}_6})_0^b \quad (3)$$

or

$$\frac{\frac{d}{dt} (P_{\text{BF}_3})_0}{(P_{\text{OF}_2})_0^2} = A (P_{\text{B}_2\text{H}_6})_0^b \quad (4)$$

A and b could be found by plotting \log_{10}

$$\frac{\left[\frac{d}{dt} (P_{\text{BF}_3})_0 \right]}{(P_{\text{OF}_2})_0^2}$$

versus $\log_{10} (P_{B_2H_6})_0$. This was done and the slope of this log-log plot was found to be approximately equal to -0.5 . Consequently, the exponent b for the BF_3 concentration was presented as -0.5 . From the intercept of this curve, the value of A was found to be 0.0082 .

(3) Therefore, as expressed before, Eq. (1) fits the experimental data reasonably well.

4. Discussion

It was noted that the relationship between the BF_3 rate and the initial partial pressures of OF_2 and B_2H_6 could be expressed by Eq. (2). The experimental values of the BF_3 rate, and the values of BF_3 rate calculated from that expression (shown in Table 6) compare reasonably well over the range of partial pressures of OF_2 and of B_2H_6 used in this study. It is likely that the algebraic expression is only an approximation to whatever the correct expression is. It may not apply at very low partial pressures of B_2H_6 , for example.

The experimental finding that the initial rate of formation of BF_3 is inversely proportional to the square root of the B_2H_6 partial pressure is interesting. If, indeed, the initial rate of formation of BF_3 corresponded to the reaction rate between OF_2 and B_2H_6 , then the mechanism for this reaction would be different from the mechanisms for either the oxidation of diborane (Ref. 1) or for the decomposition of B_2H_6 (Ref. 2). This is so because (in the references cited) the reaction rate of B_2H_6 with O_2 was proportional to the $3/2$ -power of the value of the diborane partial pressure and was independent of the O_2 pressure. The rate of decomposition of diborane was found to be also proportional to the value of the partial pressure of diborane raised to the $3/2$ -power.

5. Future Work

The rate of formation of BF_3 from the reaction of OF_2 with B_2H_6 , determined as described in this article, was assumed to be an indicator for the rate of reaction of OF_2 with B_2H_6 . This rate will be used in the next part of this research program, concerned with finding the initial rate of change of partial pressure of OF_2 and of B_2H_6 in the OF_2 - B_2H_6 reaction. From this information, it should be possible to devise a reaction mechanism that accounts for the initial rate of formation of BF_3 , as well as the initial rate of change of partial pressure of OF_2 and of B_2H_6 .

C. The Reaction Between OF_2 and B_2H_6 : Further Computations on the Rate of Formation of BF_3 , R. A. Rhein

BF_3 is one of the products resulting from the reaction of OF_2 and B_2H_6 . The initial rate of formation of BF_3 has been measured for various values of the initial partial pressures of OF_2 and B_2H_6 . The relationship between the initial rate and the initial reactant partial pressures was found to follow an equation of the form

$$\left[\frac{d}{dt}(P_{BF_3}) \right]_0 = A(P_{OF_2})_0^b (P_{B_2H_6})_0^c$$

where the units were in torr for pressure and minutes for time. The constants A , b , and c were found by a graphical method to be: $A = 0.0082$; $b = 2.0$; and $c = -0.5$. (Refer to the previous subsection B of this SPS.)

This article discusses the results of the calculation of the constants A , b , and c by a stepwise multiple regression of the matrix

$$\begin{vmatrix} \ln(\text{rate})_1 & \ln(P_{OF_2})_1 & \ln(P_{B_2H_6})_1 \\ \ln(\text{rate})_2 & \ln(P_{OF_2})_2 & \ln(P_{B_2H_6})_2 \\ \vdots & \vdots & \vdots \\ \ln(\text{rate})_n & \ln(P_{OF_2})_n & \ln(P_{B_2H_6})_n \end{vmatrix}$$

The first column represents the dependent variable, the second and third columns the independent variables. From the regression, the constants A , b , and c were found to be: $A = 5.2 \times 10^{-4}$; $b = 2.15$; and $c = -0.43$. For the regression, the multiple correlation coefficient was found to be 0.982 . The matrix elements were calculated from the data presented in Table 7, the first four columns of which are taken from the previous subsection B of this SPS.

The average measured rates, along with their standard deviations, were each computed from the results of several experiments.

The rate expression obtained from the regression is, then,

$$\left[\frac{dt}{d} (P_{BF_3}) \right]_0 = 5.2 \times 10^{-4} (P_{OF_2})_0^{2.15} (P_{B_2H_6})_0^{-0.43}$$

Table 7. Measured and calculated values of the initial rate of formation of BF_3 resulting from the reaction of OF_2 and B_2H_6

Reactant initial partial pressure, torr		Average measured rate, torr/min	Standard deviation	Calculated rate, torr/min	Residual
OF_2	B_2H_6				
5.00	1.00	0.023	0.005	0.017	0.006
5.00	2.50	0.012	0.001	0.011	0.001
5.00	5.00	0.015	0.003	0.008	0.006
10.00	1.00	0.080	0.002	0.074	0.006
10.00	2.50	0.036	0.005	0.050	-0.014
10.00	5.00	0.041	0.001	0.037	0.004
10.00	10.00	0.035	0.010	0.028	0.008
10.00	20.00	0.022	0.008	0.020	0.002
10.00	30.00	0.018	0.005	0.017	0.001
20.00	5.00	0.158	0.012	0.165	-0.006
20.00	10.00	0.104	0.010	0.122	-0.019
20.00	20.00	0.057	0.005	0.091	-0.034
20.00	30.00	0.076	0.012	0.076	-0.000
30.00	5.00	0.434	0.274	0.394	0.040
30.00	10.00	0.320	0.057	0.292	0.028
30.00	20.00	0.182	0.026	0.217	-0.035
30.00	30.00	0.190	0.034	0.182	0.008
40.00	20.00	0.511	0.004	0.403	0.109

In Table 7 are shown the rates computed from this expression, for the listed values of the initial partial pressures of OF_2 and of B_2H_6 . The residual column shown in Table 7 is the difference between the measured and the calculated rates.

The values of the residuals are small compared to those of the rates, and generally are of the same magnitude as the values for the standard deviations. Consequently, the calculated rates, based on the rate expression, compare favorably with the measured rates. We could also conclude that the calculated and measured rates compare favorably from the fact that the regression correlation coefficient was 0.982.

Before attempting to propose a mechanism for the $\text{OF}_2/\text{B}_2\text{H}_6$ reaction, it will be necessary to find the relations between

$$\left[-\frac{d}{dt} (P_{\text{OF}_2}) \right]_0$$

and

$$\left[-\frac{d}{dt} (P_{\text{B}_2\text{H}_6}) \right]_0$$

as a function of $(P_{\text{OF}_2})_0$, $(P_{\text{B}_2\text{H}_6})_0$, and $(P_I)_0$, where I represents an inert gas, i.e., one that does not enter the reaction. These relations will be described in future articles.

References

1. Goldstein, M. S., *The Oxidation of Diborane*, PhD thesis. Rensselaer Polytechnic Institute, Troy, N.Y., 1960.
2. Adam, R. M., *Boron, Metallo-Boron Compounds, and Boranes*. Interscience Publishers, New York, 1964.

XVI. Science Data Systems

SPACE SCIENCES DIVISION

A. Properties of Near-Maximal-Length Cycles Generated by Linear Feedback Shift Registers, M. Perlman

1. Introduction

In SPS 37-44, Vol. IV, pp. 209-216, it was shown that cycles of length $2^s - 2$ and $2^s - 4$ can be realized with s -stage linear feedback shift registers (FSRs). An odd number of feedback taps is needed for each s -stage shift register. For values of s from 4 through 21, a near-maximal-length cycle can be realized with a 3-tap feedback function which satisfies the linear recurrence relationship

$$\begin{aligned} a_n &= 1 \oplus a_{n-i} \oplus a_{n-j} \oplus a_{n-s} \\ &= a_{n-i} \oplus a_{n-j} \oplus a'_{n-s} \end{aligned} \quad (1)$$

The generating function for characterizing the sequence $\{a_n\}$ emanating from a near-maximal-length linear FSR was discussed in SPS 37-45, Vol. IV, pp. 225-228. In this summary, the autocorrelation properties of $\{a_n\}$ and methods for altering its periodicity are presented.

2. Complementary Structure of $\{a_n\}$

The sequence $\{a_n\}$ over one period consists of two subsequences and each is the one's complement of the other.

EXAMPLE 1:

$$a_n = a_{n-1} \oplus a_{n-2} \oplus a'_{n-4} \quad (2)$$

For the initial conditions $a_{-1} = a_{-2} = a_{-3} = a_{-4} = 0$,

$$\begin{aligned} \{a_n\} &= a_0 a_1 \cdot \cdot \cdot a_7 \cdot \cdot \cdot a_{13} \cdot \cdot \cdot \\ &1 \ 0 \ 0 \ 1 \ 1 \ 1 \ 1 \ 0 \ 1 \ 1 \ 0 \ 0 \ 0 \ 0 \cdot \cdot \cdot \end{aligned}$$

Note that $a_0 = a'_7$, and $a_k = a'_{k+7}$.

EXAMPLE 2:

$$a_n = a_{n-1} \oplus a_{n-3} \oplus a'_{n-4} \quad (3)$$

For the initial conditions $a_{-1} = a_{-2} = a_{-3} = a_{-4} = 0$,

$$\begin{aligned} \{a_n\} &= a_0 a_1 \cdot \cdot \cdot a_6 \cdot \cdot \cdot a_{11} \cdot \cdot \cdot \\ &1 \ 0 \ 1 \ 1 \ 1 \ 1 \ 0 \ 1 \ 0 \ 0 \ 0 \ 0 \cdot \cdot \cdot \end{aligned}$$

In example 2, $a_0 = a_6$, and $a'_k = a'_{k+6}$.

Sequence lengths of $2^s - 2$ and $2^s - 4$ are illustrated in examples 1 and 2, respectively.

The results of examples 1 and 2 are apparent when examining the characteristic polynomials of the transformation matrices associated with the linear FSRs. In example 1,

$$\theta(\lambda) = (\lambda + 1)^2(\lambda^3 + \lambda + 1) = (\lambda^2 + 1)(\lambda^3 + \lambda + 1)$$

The linear combination of outputs of FSRs associated with $\lambda^2 + 1$ and $\lambda^3 + \lambda + 1$ appears as follows:

$$\begin{array}{l} \lambda^2 + 1 \quad 1 \ 0 \ 1 \ 0 \ 1 \ 0 \ 1 \ 0 \ 1 \ 0 \ 1 \ 0 \ 1 \ 0 \ 1 \ \cdots \\ \lambda^3 + \lambda + 1 \quad 1 \ 0 \ 1 \ 1 \ 1 \ 0 \ 0 \ 1 \ 0 \ 1 \ 1 \ 1 \ 0 \ 0 \ 1 \ 0 \ 1 \ \cdots \\ \{a_n\} \quad 0 \ 0 \ 0, 1 \ 0 \ 0 \ 1 \ 1 \ 1 \ 1 \ 0 \ 1 \ 1 \ 0 \ 0 \ 0 \ 0, \cdots \end{array}$$

The resulting sequence $\{a_n\}$ has a length that is the least common multiple (LCM) of the lengths of the sequences associated with $\lambda^2 + 1$ and $\lambda^3 + \lambda + 1$. Two periods of the latter combine with seven of the former to form one period of $\{a_n\}$.

Similarly, in example 2,

$$\begin{aligned} \theta(\lambda) &= (\lambda + 1)^3(\lambda^2 + \lambda + 1) \\ &= (\lambda^3 + \lambda^2 + \lambda + 1)(\lambda^2 + \lambda + 1) \end{aligned}$$

The linear combination of outputs of FSRs associated with $(\lambda + 1)^3$ and $\lambda^2 + \lambda + 1$ appears as follows:

$$\begin{array}{l} (\lambda + 1)^3 \quad 1 \ 1 \ 0 \ 0 \ 1 \ 1 \ 0 \ 0 \ 1 \ 1 \ 0 \ 0 \ 1 \ 1 \ 0 \ \cdots \\ \lambda^2 + \lambda + 1 \quad 1 \ 1 \ 0 \ 1 \ 1 \ 0 \ 1 \ 1 \ 0 \ 1 \ 1 \ 0 \ 1 \ 1 \ 0 \ \cdots \\ \{a_n\} \quad 0 \ 0 \ 0, 1 \ 0 \ 1 \ 1 \ 1 \ 1 \ 0 \ 1 \ 0 \ 0 \ 0 \ 0, \cdots \end{array}$$

The initial conditions of the component FSRs of both examples were assumed to be $00 \cdots 1$ (i.e., a binary 1).

In general, the maximal-length component sequence appears twice per period for $2^s - 2$ lengths and four times per period for $2^s - 4$. The components associated with $(\lambda + 1)^2$ and $(\lambda + 1)^3$ account for the two subsequences in each $\{a_n\}$ being complementary.

3. Complementary Sequences Resulting From Complementary Initial States

In SPS 37-45, Vol. IV, the generating function associated with an s -stage FSR with NOT EXCLUSIVE-OR feedback was shown to be

$$G(x) = \frac{1 + (1+x) \left[\sum_{i=1}^s C_{s-i} x^i (a_{-i} x^{-i} + a_{-i+1} x^{-i+1} + \cdots + a_{-1} x^{-1}) \right]}{(1+x) \left(1 + \sum_{i=1}^r C_{s-i} x^i \right)} \quad (4)$$

The initial state $00 \cdots 0$ where $a_{-1} = a_{-2} = \cdots = a_{-s} = 0$ yields

$$G(x) = \frac{1}{(1+x) \left(1 + \sum_{i=1}^r C_{s-i} x^i \right)} \quad (5)$$

Note that modulo 2 rules of arithmetic are used. Also, $C_{s-i} = 1$ if the i th stage is in the feedback (see Fig. 1).

For $C_{s-i} = C_{s-j} = C_0 = 1$ (as in Eq. 1),

$$G(x) = \frac{1}{(1+x)(1+x^i+x^j+x^s)} \quad (6)$$

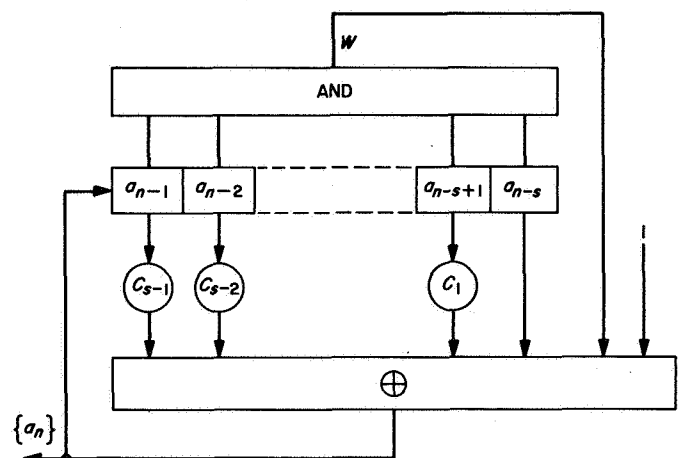


Fig. 1. An s -stage FSR sequence generator

When the initial state is $11 \cdots 1$, Eq. (5) reduces to

$$G(x) = \frac{x^i + x^j + x^s}{(1+x)(1+x^i+x^j+x^s)} \quad (7)$$

The sum modulo 2 (linear combination) of the right-hand side of Eqs. (6) and (7) equals

$$\frac{1}{1+x} = 1 + x + x^2 + \cdots$$

Thus, the sequences associated with Eqs. (6) and (7) are complementary. They emanate from the same linear FSR with initial states of $00 \cdots 0$ and $11 \cdots 1$, respectively. Successors to these initial states will also be complementary. The successive contents of the FSR of example 1 for both sets of initial states are shown below with minor cycles added.

n	a_{n-1}	a_{n-2}	a_{n-3}	a_{n-4}	a_{n-1}	a_{n-2}	a_{n-3}	a_{n-4}
0	0	0	0	0	1	1	1	1
1	1	0	0	0	0	1	1	1
2	0	1	0	0	1	0	1	1
3	0	0	1	0	1	1	0	1
4	1	0	0	1	0	1	1	0
5	1	1	0	0	0	0	1	1
6	1	1	1	0	0	0	0	1
7	1	1	1	1	0	0	0	0
8	0	1	1	1	1	0	0	0
9	1	0	1	1	0	1	0	0
10	1	1	0	1	0	0	1	0
11	0	1	1	0	1	0	0	1
12	0	0	1	1	1	1	0	0
13	0	0	0	1	1	1	1	0
	0	1	0	1	1	0	1	0
	1	0	1	0	0	1	0	1

Note that corresponding states of both cycles are complementary when initialized with complementary states.

For cycle lengths of $2^s - 2$ and $2^s - 4$, both the $00 \cdots 0$ and the $11 \cdots 1$ states appear.

4. The Autocorrelation of Near-Maximal-Length Sequences

The autocorrelation of a sequence is defined (Ref. 1) as

$$C(\tau) = \sum_{n=0}^{p-1} b_n b_{n-\tau} \quad (8)$$

where $b_n = 1 - 2a_n$ and p is the period of the sequence. The zeros and ones of $\{a_n\}$ correspond to plus one and minus one, respectively.

Note that $C(\tau)$ is the sum of the agreements minus the sum of the disagreements that a sequence has over one period, with the same sequence delayed τ digit periods. The autocorrelation of the sequence in example 1 is enumerated for various values of τ .

$\{a_n\}$	1	0	0	1	1	1	1	0	1	1	0	0	0	0	
$\{a_n\}$	1	0	0	1	1	1	1	0	1	1	0	0	0	0	
	+	+	+	+	+	+	+	+	+	+	+	+	+	+	$C(0) = +14$
$\{a_n\}$	1	0	0	1	1	1	1	0	1	1	0	0	0	0	
$\{a_{n-1}\}$	0	1	0	0	1	1	1	1	0	1	1	0	0	0	
	-	-	+	-	+	+	+	-	-	+	-	+	+	+	$C(1) = +2$
$\{a_n\}$	1	0	0	1	1	1	1	0	1	1	0	0	0	0	
$\{a_{n-2}\}$	0	0	1	0	0	1	1	1	1	0	1	1	0	0	
	-	+	-	-	-	+	+	-	+	-	-	-	+	+	$C(2) = -2$
$\{a_n\}$	1	0	0	1	1	1	1	0	1	1	0	0	0	0	
$\{a_{n-7}\}$	0	1	1	0	0	0	0	1	0	0	1	1	1	1	
	-	-	-	-	-	-	-	-	-	-	-	-	-	-	$C(7) = -14$

A complete tabulation of $C(\tau)$ for the sequence in example 1 appears in Table 1; $C(\tau)$ for the sequence in example 2 is given in Table 2.

Table 1. $C(\tau)$ versus τ for $a_n = a_{n-1} \oplus a_{n-2} \oplus a'_{n-4}$ and $p = 2^4 - 2$

τ	$C(\tau)$	τ	$C(\tau)$
0	+14	7	-14
1	+ 2	8	- 2
2	- 2	9	+ 2
3	+ 2	10	- 2
4	- 2	11	+ 2
5	+ 2	12	- 2
6	- 2	13	+ 2

Table 2. $C(\tau)$ versus τ for $a_n = a_{n-1} \oplus a_{n-3} \oplus a'_{n-4}$ and $p = 2^4 - 4$

τ	$C(\tau)$	τ	$C(\tau)$
0	+12	6	-12
1	0	7	0
2	+ 4	8	- 4
3	0	9	0
4	- 4	10	+ 4
5	0	11	0

In general, $C(\tau)$ for near-maximal-length sequences is as follows:

CASE 1:

$$p = 2^s - 2$$

$$C(0) = 2^s - 2$$

$$C(2^{s-1} - 1) = -(2^s - 2)$$

$$C(\tau) = \pm 2 \text{ for } \tau \neq 0 \text{ or } 2^{s-1} - 1$$

$$C(\tau) = -C(\tau + 2^{s-1} - 1)_{\text{mod } p} \text{ for all } \tau$$

CASE 2:

$$p = 2^s - 4$$

$$C(0) = 2^s - 4$$

$$C(2^{s-1} - 2) = -(2^s - 4)$$

$$C(\tau) = 0, \pm 4 \text{ for } \tau \neq 0 \text{ or } 2^{s-1} - 2$$

$$C(\tau) = -C(\tau + 2^{s-1} - 2)_{\text{mod } p} \text{ for all } \tau$$

5. Altering the Periodicity of Near-Maximal-Length Sequences

In Ref. 2, it was shown that a maximal-length cycle of $2^s - 1$ from an s -stage linear FSR could be altered to

realize every cycle length l where $1 \leq l \leq 2^s$. The same method can be applied to near-maximal-length sequences. When the recurrence relationship of a near-maximal-length sequence is simpler than that of a maximal-length sequence, less combinational logic is required for the former.

EXAMPLE 3:

$$a_n = a_{n-1} \oplus a_{n-3} \oplus a'_{n-5} \oplus W \quad (9)$$

Table 3. Cycle lengths versus W for $a_n = a_{n-1} \oplus a_{n-3} \oplus a'_{n-5} \oplus W$

a_{n-1}	a_{n-2}	a_{n-3}	a_{n-4}	a_{n-5}	l
0	0	0	0	0	1
1	0	0	0	0	7
0	1	0	0	0	11
1	0	1	0	0	—
1	1	0	1	0	27
0	1	1	0	1	9
1	0	1	1	0	19
1	1	0	1	1	3
1	1	1	0	1	25
0	1	1	1	0	23
0	0	1	1	1	13
1	0	0	1	1	21
1	1	0	0	1	17
1	1	1	0	0	5
1	1	1	1	0	29
1	1	1	1	1	1
0	1	1	1	1	7
1	0	1	1	1	11
0	1	0	1	1	—
0	0	1	0	1	27
1	0	0	1	0	9
0	1	0	0	1	19
0	0	1	0	0	3
0	0	0	1	0	25
1	0	0	0	1	23
1	1	0	0	0	13
0	1	1	0	0	21
0	0	1	1	0	17
0	0	0	1	1	5
0	0	0	0	1	29
0	1	0	1	(0) ^a	32
1	0	1	0	(1) ^a	32

^aContent of fifth stage is not sensed.

The first three terms of the recurrence relationship are associated with a sequence length $p = 2^5 - 2$; W is a nonlinear term which senses the content of the five-stage shift register. The successor to that state (i.e., state or states for which $W = 1$) is changed because the bit fed back is complemented. This results in skipping or annexing states to the cycle.

$$W = a_{n-1}^{\alpha_1} a_{n-2}^{\alpha_2} a_{n-3}^{\alpha_3} a_{n-4}^{\alpha_4} a_{n-5}^{\alpha_5} \quad (10)$$

where

$$\begin{aligned} a_{n-i}^{\alpha_i} &= a_{n-i} \text{ when } \alpha_i = 1 \\ &= a'_{n-i} \text{ when } \alpha_i = 0 \end{aligned}$$

The cycle lengths resulting for each W are shown in Table 3.

When the content of all stages is sensed, states that are not in the desired cycle branch into the desired cycle (see Ref. 3). If the content of all stages but the last (i.e., a_{n-5}) are sensed, the cycle is split into branchless cycles or expanded into a single branchless cycle. From Table 3 it can be seen that there are two distinct W s associated with every realizable length.

For $W = a_{n-1} a_{n-2} a'_{n-3} a_{n-4} a'_{n-5}$, a cycle length of 27 results. This is also true for $W = a'_{n-1} a'_{n-2} a_{n-3} a'_{n-4} a_{n-5}$. The cycle length can be expanded to 32 for $W = a_{n-1} a'_{n-2} a_{n-3} a'_{n-4}$ or $W = a'_{n-1} a_{n-2} a'_{n-3} a_{n-4}$.

Note that, except for 15, all odd cycle lengths less than p are realizable with a W of the form shown in Eq. (10).

Even cycle lengths equal to or greater than 16 can be realized by detecting two words. For example,

$$\begin{aligned} W &= (a_{n-1} a'_{n-2} a_{n-3} a_{n-4} a'_{n-5} \oplus a'_{n-1} a'_{n-2} a'_{n-3} a'_{n-4} a_{n-5}) \\ &= (a_{n-1} a'_{n-2} a_{n-3} a_{n-4} a'_{n-5} + a'_{n-1} a'_{n-2} a'_{n-3} a'_{n-4} a_{n-5}) \end{aligned}$$

where the symbol $+$ denotes a logical sum (i.e., OR).

The first term shortens the cycle to a length of 19, and the second term shortens the 19-length cycle to 18. By this procedure, an even length of 18 is realized.

In general, the following shortened cycle lengths can be realized with a W consisting of a single term:

CASE 1: $p = 2^s - 2$

All odd lengths l , except $l = 2^{s-1} - 1$, are realizable where $1 \leq l < 2^s - 2$.

CASE 2: $p = 2^s - 4$

All odd lengths l , except $l = 2^{s-2} - 1$ and $3(2^{s-2} - 1)$, are realizable where $1 \leq l < 2^s - 4$.

In both cases, the cycles may be lengthened to 2^s by sensing the content of the leftmost $s - 1$ stages such that a jump is made into one of the states in the minor cycle (see Ref. 1).

Values of s for which $\frac{1}{2}(2^s - 2)$ or $\frac{1}{4}(2^s - 4)$ are Mersenne primes (Ref. 4) result in shortened cycles (when W is of the form shown in Eq. 10) with lengths relatively prime to $2^s - 2$ or $2^s - 4$, respectively.

References

1. Golomb, S. W., and Welch, L. R., *Nonlinear Shift-Register Sequences*, Technical Memorandum 20-149. Jet Propulsion Laboratory, Pasadena, Calif., Oct. 1957.
2. Golomb, S. W., Welch, L. R., and Goldstone, R. M., *Cycles From Nonlinear Shift Registers*, Progress Report 20-389. Jet Propulsion Laboratory, Pasadena, Calif., Aug. 1959.
3. Baumert, L. D., *Table of Period Generators*, Technical Report 32-564. Jet Propulsion Laboratory, Pasadena, Calif., Nov. 1, 1962.
4. Le Veque, W. J., *Topics in Number Theory: Vol. 1*. Addison-Wesley Publishing Company, Inc., Reading, Mass., 1956.

XVII. Lunar and Planetary Sciences

SPACE SCIENCES DIVISION

A. Flexible-Screw Rock Sampling Device: II, First Breadboard Design and Performance, D. Nash

Described in SPS 37-38, Vol. IV, pp. 136-139 were the operating characteristics of the Stockwell-Imus rotating-helix conveying mechanism (Ref. 1). It also set forth the design criteria for incorporating this mechanism as the principal component of a simple, single-motored sample acquisition device to be used to supply particulate rock samples to the X-ray diffractometer or other remotely operated analytical instruments. This article describes the first breadboard model of the sampler, discusses its performance, and outlines required modifications.

The essential mechanical components of the sampling device are shown in Fig. 1:

- (1) A flexible helical transport screw which is wound from 0.035-in. square cross section Be-Cu wire into a helix (Archimedean screw) with an OD of 0.090-0.095 in.

- (2) A triple-curved rigid transport tube made of thin-walled (0.010 in.) stainless steel with an ID of 0.105 in. and length of 21.75 in. (from acquisition end to discharge vent)
- (3) A swivel joint in the transport tube near the discharge end
- (4) A housing for the swivel joint, swivel-torque spring, discharge vent, and drive shaft
- (5) A gear box with 1:1 spur gears with 1-in.-pitch diameter
- (6) A 24-V, dc gearmotor which has a rated shaft torque of 6-in.-oz at 1120 rev/min

The weight of the sampling device is 0.9 lb.

The operating mode of the sampler is as follows. The transport screw rotates inside the transport tube at 1120 rev/min. When released, the curved transport tube swivels on the discharge axis until the acquisition end of the tube (and the exposed portion of the helical screw) contacts the

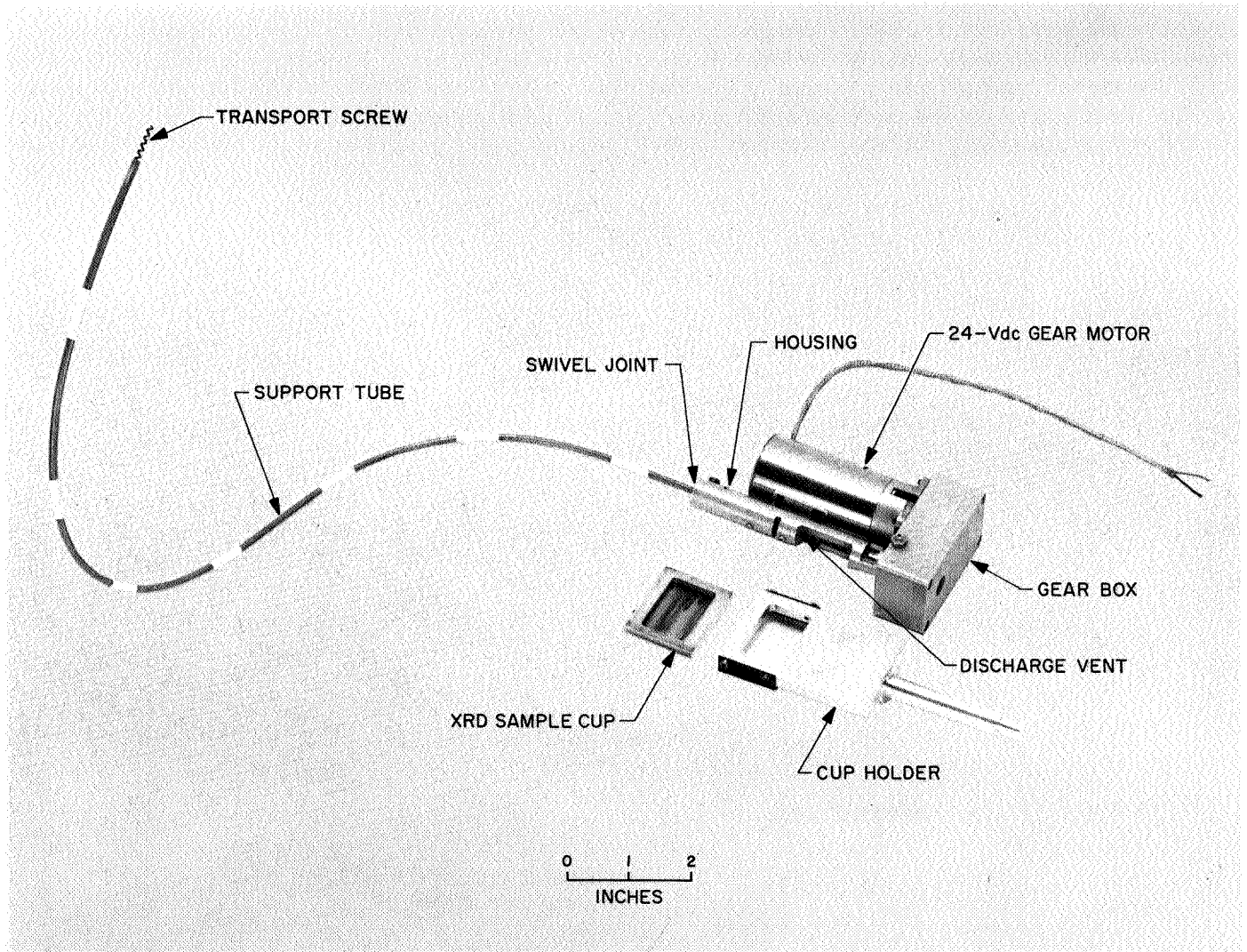


Fig. 1. Essential mechanical components of sampling device

powdered rock surface (Fig. 2). Frictional torque (developed by friction between the helix and the wall of the tube), as well as torque from the helical spring inside the swivel joint-housing, force the acquisition end into the rock powder. Acquisition of the powder by auger action commences as the screw rotates and is driven forward; the powder is transported up the inside of the curved transport tube and is discharged through the discharge vent (Fig. 1) in the lower side of the transport tube. During acquisition the acquisition end slowly progresses (i.e., bores a hole) through the powder; the leading 5-in. section of the curved transport tube is curved to a radius such that the tube does not broach during initial circumferential motion (broaching inhibits penetration of the

tube into the powder); during this initial 5-in. travel, enough powder is acquired to fill the sample cup which is mounted in the cup holder of the X-ray diffractometer (XRD). Essentially, all powder acquired at the acquisition end is discharged, provided the screw continues to rotate, even though the acquisition end stops penetrating or continues swiveling on out of the powder.

The performance of the sampler in air at room temperature was determined for sample material composed of pulverized basalt powder of particle size $< 37\mu\text{m}$ and bulk density approximately 1.0 g/cm^3 (Fig. 3). The maximum depth of penetration of the transport tube was set

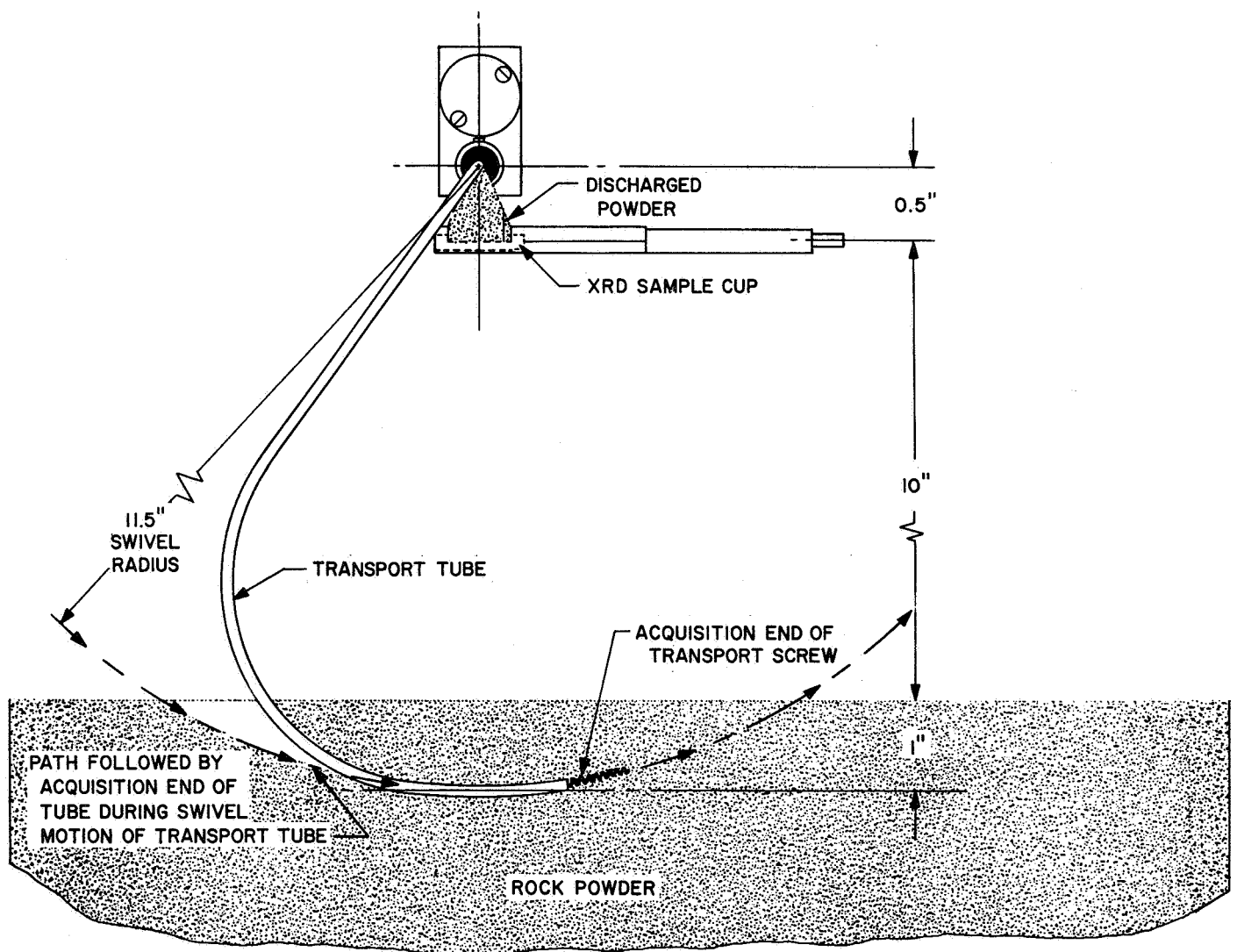


Fig. 2. Schematic showing deployment of transport tube of sampling device through rock powder sample

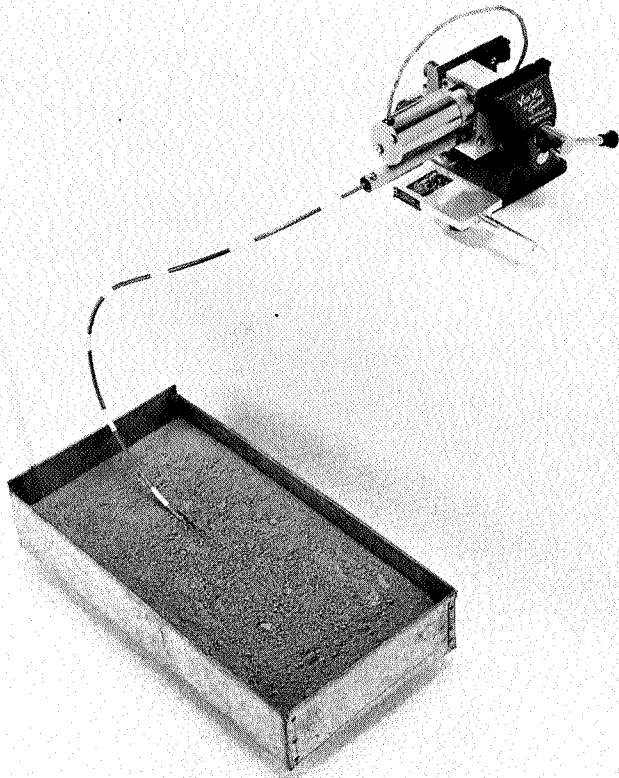


Fig. 3. Sampling device with transport tube deployed in box of rock powder. Note material that has been delivered into XRD sample cup

for 1 in.; the vertical transport distance was 11.5 in., as shown in Fig. 2. The test results were as follows:

Time required to start discharge	19 s
Discharge rate	4.5 cm ³ /min
Discharge time required to fill XRD cup (2 cm ³)	28 s
Total operating time required to fill XRD cup	47 s
Power (at 24 V dc input)	
Prior to acquisition (tube empty)	0.35 A (8.4 W)
During acquisition (tube full, < 37 μm)	0.45 A (10.8 W)
Weight	0.9 lb

During operation it was observed that best spreading action of the discharged powder occurred when the height of the discharge vent above the bottom of the XRD-cup was set at 0.5 in. At that height, the powder poured out of the discharge vent and initially built a conical pile

on the cup bottom; when the top of the growing pile contacted the turning screw, discharge continued down the forward slope of the pile and the pile grew laterally, parallel to the feed direction, until the whole cup was covered (or until the drive motor was stopped). A slight vibratory motion applied to the cup (by gently tapping it) caused the loose powder to collapse, increasing its bulk density about 20%. (High bulk density is favorable for optimum XRD data provided no preferred orientation of mineral grains results during compaction; Ref. 2.) It was also found that acquisition was most efficient when the acquisition end of the transport tube penetrated the powder at a low angle (e.g., ~30 deg) and to a shallow depth (e.g., ~1 in.; Fig. 2) as opposed to vertical downward penetration.

A second test was run under the same environmental conditions but with sample material composed of basalt rubble containing a mixture of particles ranging in size from fine dust, less than 5 μm, to pebbles 2 cm in diameter. In this material, the acquisition end would not penetrate by the force of the swivel spring alone, and penetration was therefore achieved by forcing the acquisition end into the rubble by hand.

Upon penetration of the acquisition end into the rubble, transport action commenced and continued for about 5 s, whereupon the screw jammed due to lodgment of millimeter-sized particles, and the motor stalled. The transport mechanism was then dismantled, cleaned, and reassembled, and another penetration performed using a ¼-in. drill motor for power (as in the preliminary tests reported earlier in SPS 37-38). Acquisition and discharge commenced and continued for about 30 s, whereupon the device failed due to twist-rupture of the helical screw at the driven end.

An analysis was made of the particle size distribution of the discharged rubble powder and the powder acquired but left in the transport tube at failure; the data are shown in Fig. 4. It is notable that the maximum particle size acquired was 800 μm and that there was a considerable increase in the finer size fraction of the acquired sample due to pulverization and particle size reduction during the acquisition and transport action.

Chemical analyses (Table 1) of the rubble powder showed measurable amounts of contamination from abrasion of the screw and tube material (Be-Cu and stainless steel, respectively). About 1% of metallic copper and lesser amounts of the metals beryllium, chromium, nickel, and cobalt were added to the discharged powder. The contamination was visibly evident in the darkening of the

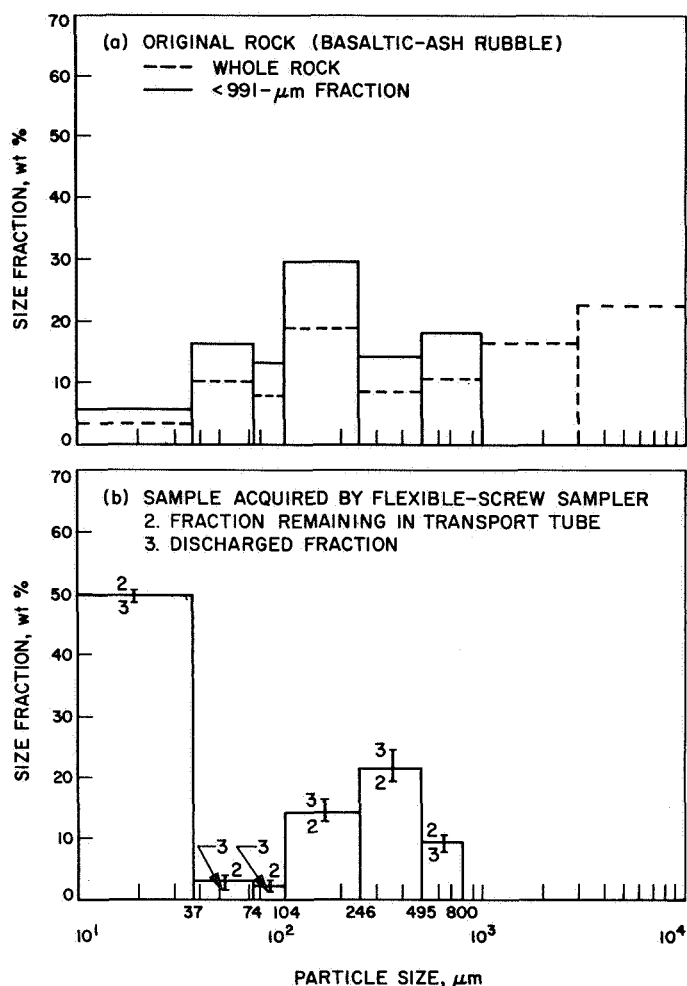


Fig. 4. Particle size analyses

discharged powder compared to the color of the original powder.

The contamination levels, although large in relative terms, were sufficiently small in absolute magnitude so as to present no interference in either diffraction or

fluorescence analyses of the sample. The major contaminant was Cu, which is not excited by CuK radiation (used in the XRD), and, furthermore, not among the elements for which fluorescence analyses will be attempted (Ref. 3). Also, the Ni contamination was below the expected minimum detectable limit for Ni.

No chemical analysis was made of the <37-μm basalt powder sample, although it was noted that no darkening of the powder occurred during transport and discharge, suggesting that no substantial contamination occurs when the device operates in fine powder in air.

The principal conclusions drawn from these tests are:

The 0.9-lb sampling device that was tested performed satisfactorily in fine basalt powder; acquisition and transport were efficient and rapid, requiring only 47 s running time at a power drain of 11 W to fill the 2-cm³ XRD sample cup located 10 in. above the sampled surface.

The device failed in rubble because of jamming of the transport screw by 800-μm particles. Two basic design changes are planned to overcome this problem: (1) the motor size will be increased to prevent stalling when the transport screw is loaded with coarse particles; (2) the transport screw will be reinforced with a flexible braided wire (speedometer cable) core within the helix. The sampler will then be tested in a variety of rock types and under vacuum at simulated lunar and Martian temperatures.

The swiveled-flexible-screw sampler concept provides a simple, lightweight, low-power, single-motored, self-deploying device capable of acquiring, transporting, and presenting finely particulate rock samples to the X-ray diffractometer and other analytical instruments for geological and biological experiments performed aboard unmanned lander spacecraft.

Table 1. Chemical analysis of rubble powder showing amount of bias contamination of acquired powder by abrasion from transport screw and transport tube

Contaminant source	Metal	Metal concentration, wt %			
		Sampler components (approx)	Original sample powder	Acquired sample	
				Powder remaining in tube	Discharged powder
Transport screw	Cu	97.5	0.003	0.60	0.93
	Be	2.5	0.014	0.018	0.030
	Fe	73	1.7	2.0	1.7
Transport tube	Cr	18	0.019	0.096	0.15
	Ni	8	0.004	0.002	0.046
	Co	1	0.003	0.014	0.028

B. Mercury's Microwave Phase Effect, B. Gary

Recent measurements at λ 3.4 mm (Ref. 4) and λ 19 mm (Ref. 5) of the phase dependence of Mercury's microwave thermal emission are incompatible with each other according to a simple model for the thermal behavior of the planet's surface. The model employed here was first formulated by Piddington and Minnett (Ref. 6) for application to the moon, and can be described briefly as a vertically and horizontally homogeneous and temperature-independent surface model. Conditions on Mercury seem to meet the requirements of the model and justify its use about as well as those on the moon. Figures 5 and 6 show the discrepancy between the two sets of Mercury observations. Although the amplitudes and phases of the variation in Mercury's brightness disk

temperature are nearly the same at the two wavelengths of observation, the model lines predict large differences. For example, in Fig. 5 the observed variation in λ 3.4 mm brightness temperature of $(35 \pm 4 \text{ SE})\%$ corresponds to a model-predicted variation at λ 19 mm of $(9 \pm 2)\%$, versus the $(27 \pm 3)\%$ observed value.

The model lines in Figs. 5 and 6 were constructed by adopting a Mercury sidereal rotation period of 59 days (the recent radar value), a sunlight intensity at local noon corresponding to Mercury's mean orbital distance to the sun, a local midnight temperature of 100°K , and a $\pi/4$ conversion factor to allow for the disk temperature versus center-of-disk temperature effect on the amplitude of the phase variation. When allowance is made for the

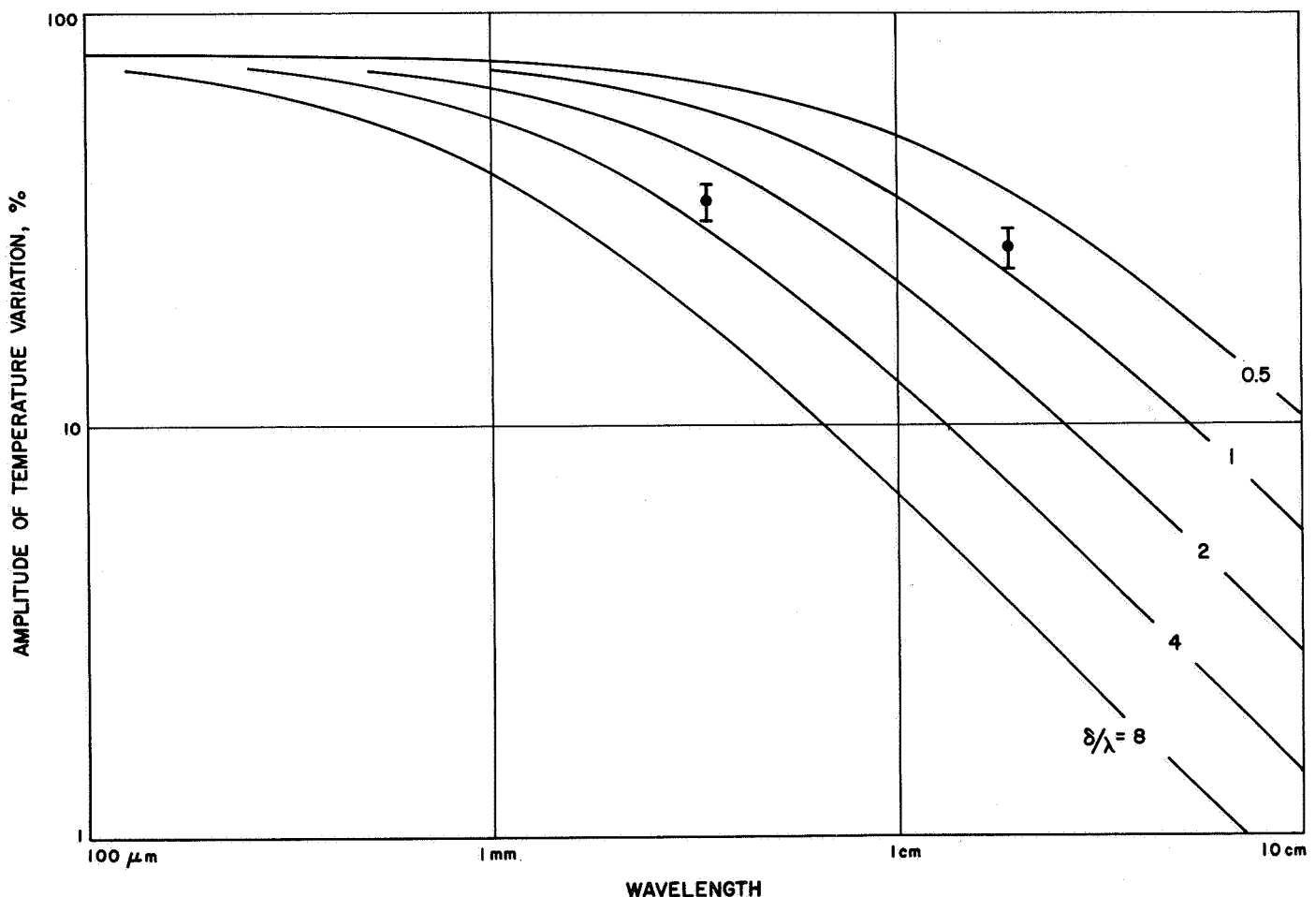


Fig. 5. Amplitude of Mercury's microwave phase effect at λ 3.4 mm and λ 1.9 cm. The lines are predicted by a vertically homogeneous, temperature-independent thermal model for Mercury's surface, where δ is the ratio between the depth of microwave emission to the depth of penetration of the surface temperature variation

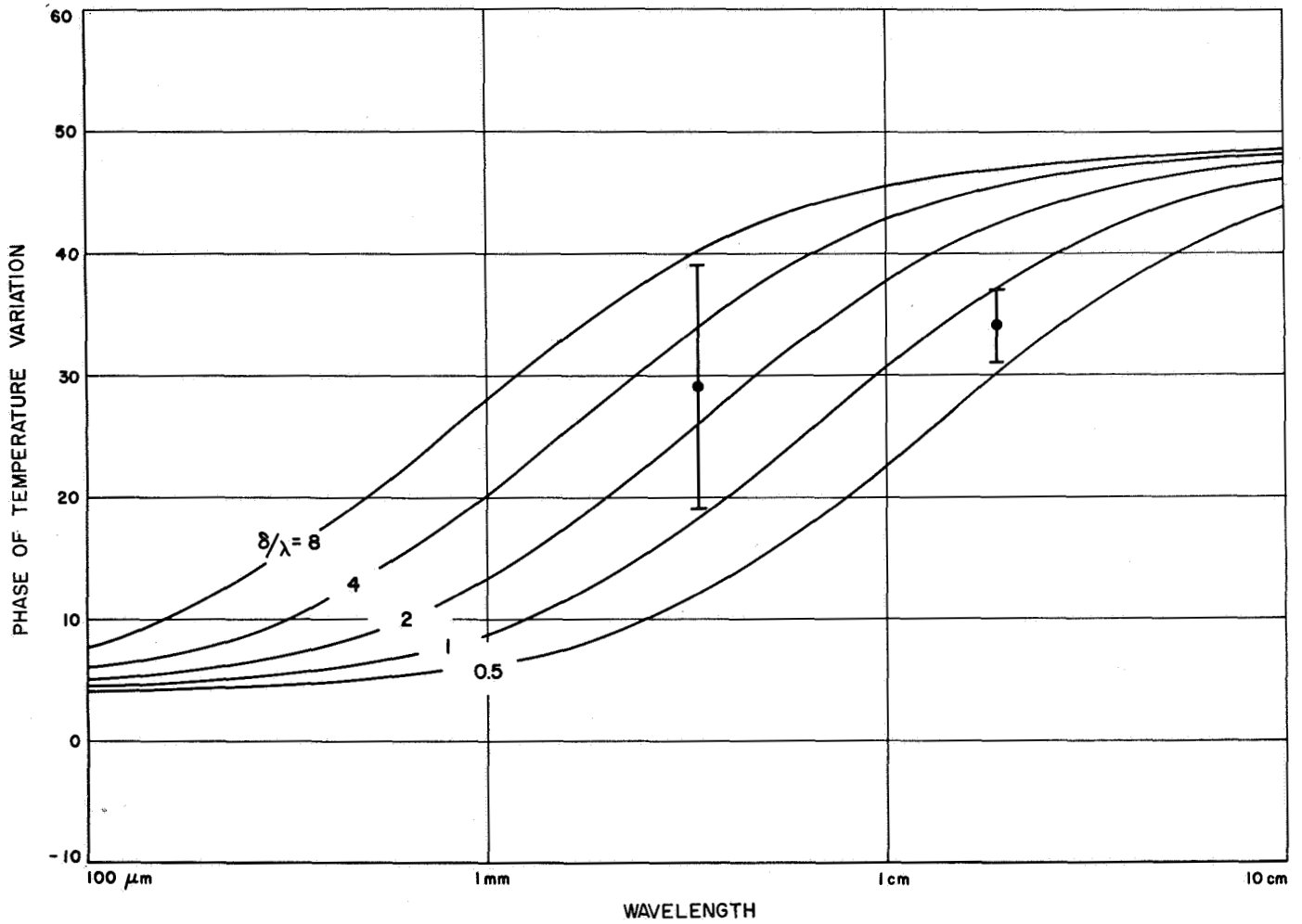


Fig. 6. Phase of Mercury's microwave phase effect at λ 3.4 and λ 1.9 cm. The lines are predicted by a vertically homogeneous, temperature-independent thermal model for Mercury's surface

uncertainties in the above parameters, the model versus observations discrepancy still exists.

Moon observations are in much better agreement with a similarly constructed set of model lines, as shown in Figs. 7 and 8. Recent high-resolution measurements of the moon's center-of-disk brightness temperature (Ref. 7) have permitted a comparison to be made between observation and model for the higher harmonics of the lunar phase effect. Agreement is poor, and Linsky (Ref. 8) and Gary (Ref. 7) point out that this constitutes evidence for the need to incorporate in any future surface models a temperature dependence of the moon's thermal conductivity (caused by the porosity-associated radiative component superseding the conductive component at high temperatures). Although the observations of Mercury are incapable of providing the same accuracy and spatial

resolution as those of the moon, the more extreme thermal conditions on Mercury may be affecting the observed first harmonic of the planet's phase effect.

Peculiar differences in thermal conditions exist on Mercury due to its high orbital eccentricity and the apparent 2:1 ratio between its solar day and orbital period. A cursory examination of the effect this might have on an observed phase effect predicts a maximum amplitude of variation discrepancy of 36%, whereas the observed discrepancy is $(200 \pm 90/60)\%$.

Further speculation might produce a mechanism to account for the existing measurements, but perhaps an investment of time in observation to verify the discrepant phase effects would be more fruitful.

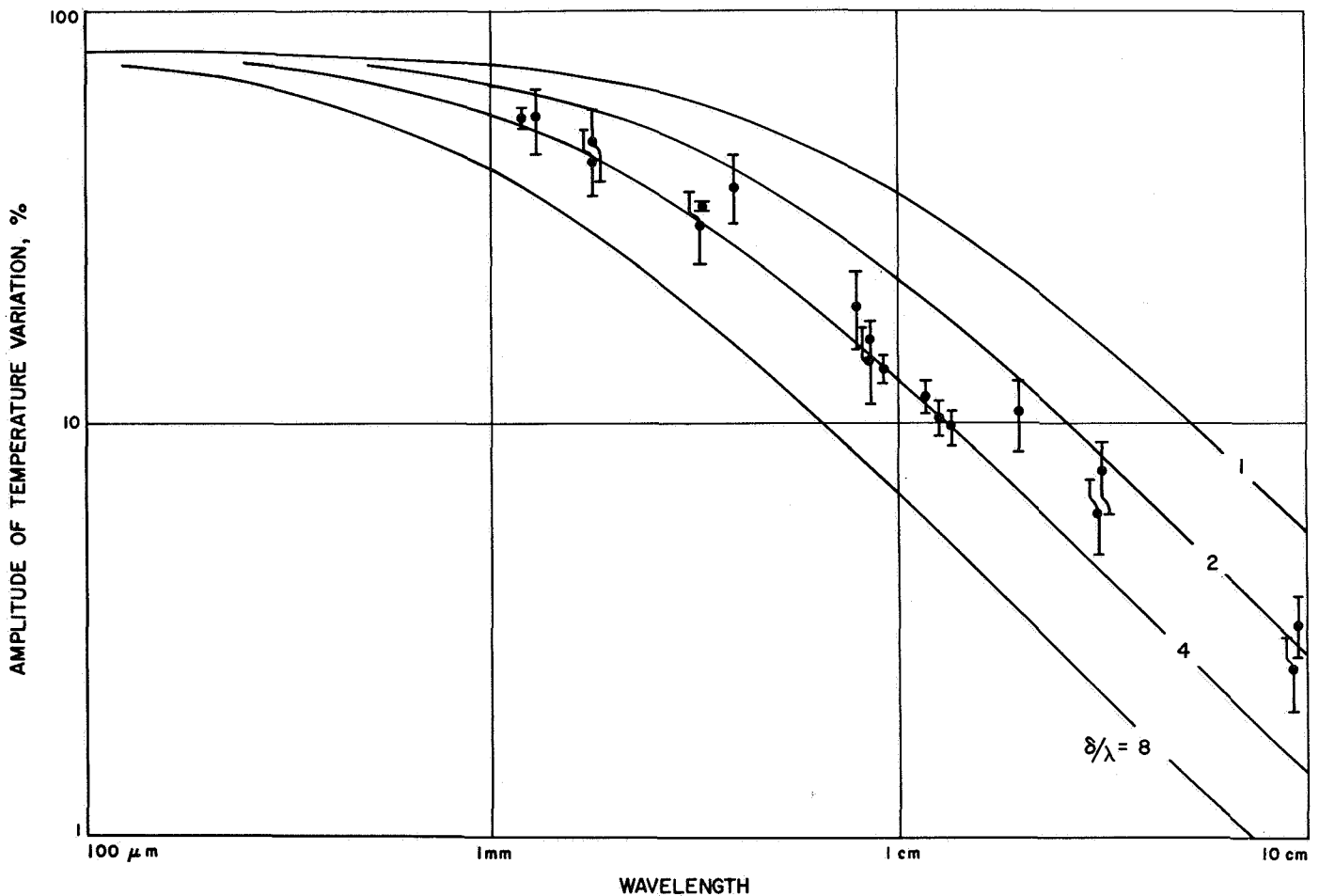


Fig. 7. Amplitude of the moon's microwave phase effect

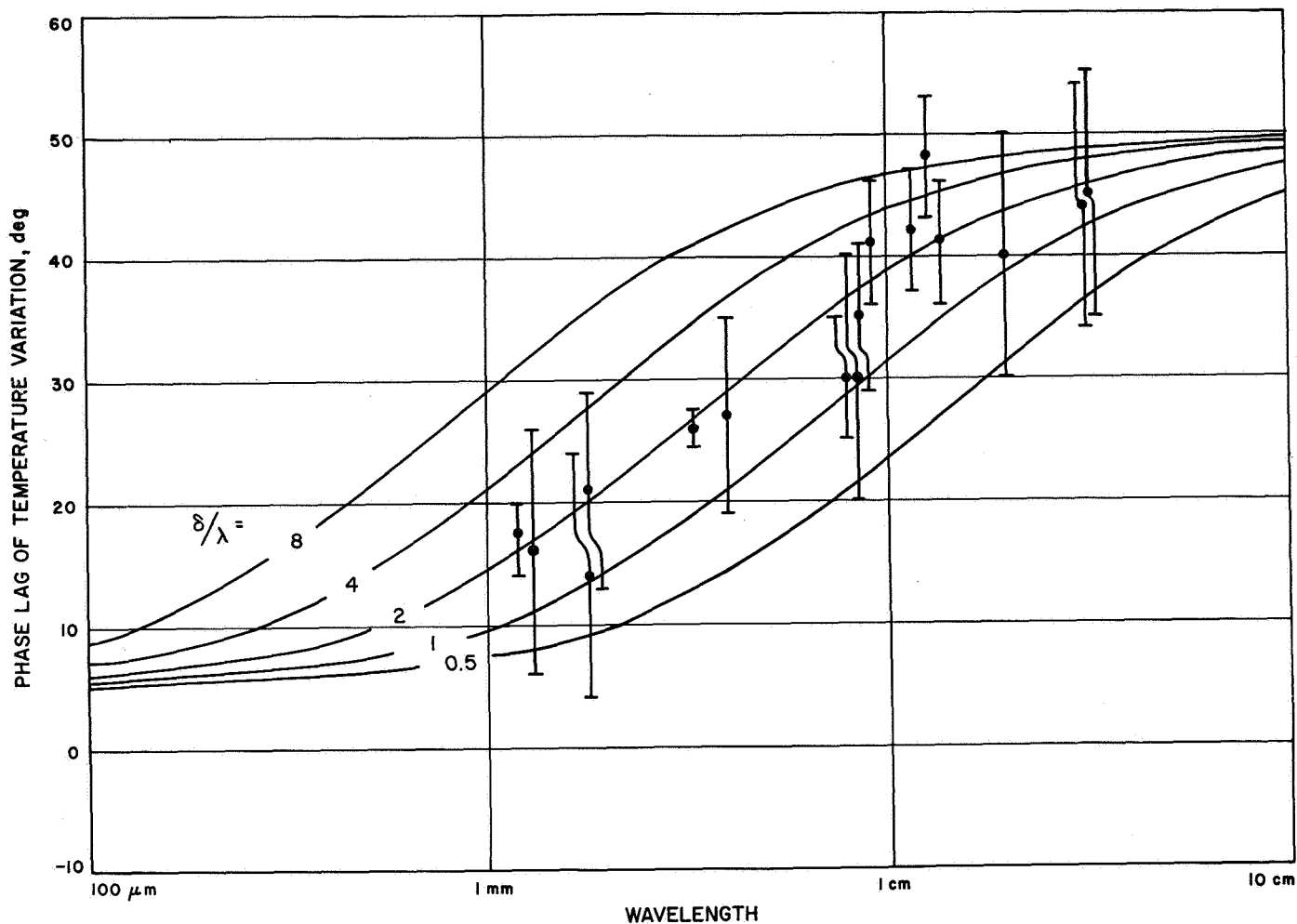


Fig. 8. Phase of the moon's microwave phase effect

C. Retention of Water in the Martian Atmosphere, J. E. Gunn

Photochemical-diffusion equilibrium studies have been carried out in order to estimate the lifetime of water molecules in the Martian atmosphere. Using the troposphere-stratosphere models of Prabhakara and Hogan (Ref. 9), which predict a temperature minimum of about 150°K, it is found that water is effectively cold-trapped at an altitude of approximately 20 km, though the vapor pressure is sufficiently high that a few percent of the water mixes to levels at which significant photochemical action can occur. Though heavily shielded by the relatively transparent but overwhelmingly abundant carbon dioxide component, the destruction rate is still high, of the order of $10^9/\text{cm}^2\text{-s}$.

For a total abundance of $10 \mu\text{m}$, this corresponds to a mean life of 1000 yr. The dissociation components mixed downward, however, can recombine, so that this need

not represent the characteristic life of water in the atmosphere. For an eddy-diffusion coefficient corresponding to a mixing time of 1 day per scale height, the hydrogen produced in the destruction of water diffuses upward to the escape level (Ref. 10) with a characteristic time of the order of 10^4 yr, and this does represent a real retention time. The time scales are two orders of magnitude too short to explain the origin of the water in terms of hydrogen from the solar wind.

D. Emission Spectra of Silicates in the Spectral Region 8–14 μm and Application to Remote Compositional Analysis of the Moon's Surface, J. E. Conel

Thermal emission spectroscopy in the spectral region 8–14 μm has been examined as a method of remote compositional analysis of planetary surfaces. Laboratory

emission spectra of a wide variety of common igneous rocks, rock-forming minerals and meteorites, both solid and granulated, show that surface roughness and granulation induce gray spectral behavior in silicates which otherwise contain mineralogically diagnostic emission features. Spectral contrasts are never removed by granulation alone, but may be reduced to a few percent for particle sizes near the wavelength. Spectral emissivities of size-fractionated particulate samples generally follow patterns similar to emissivities of corresponding solid samples until particle sizes are reduced to the order of the photon mean free path in silicates (tens of microns).

When particle size is small, new diagnostic features may be added to those normally present. Spectral emissivities of polyminerallic samples having mixed particle sizes may differ significantly from the emissivities of well-sorted or solid material of identical mineralogy. This method is useful for distinguishing gross differences in composition. Precise identification of rock types appears difficult unless a single mineral phase is very abundant or the sample is not particulate or rough.

These experimental results have been compared with available lunar observations. Goetz (Ref. 11) has noted small spectral contrasts in region 8–9 μm between the (source/reference) areas Plato/Tycho and Plato/Copernicus.

The laboratory data suggest the following possible interpretation:

- (1) Surface material in Plato is enriched in ferromagnesian silicates relative to the reference areas
- (2) Surface material in Plato is granulated to particle sizes the order of the wavelength
- (3) The reference areas are nearly black emitters in this spectral region

These conditions are generally compatible with inferences made from other infrared, photometric, and visible spectroscopic data for the moon.

References

1. Hotz, G., Office of Space Science and Applications-Supporting Research and Technology, Science Review Meeting Summary, JPL, May 3–5, 1965; and Semi-annual Progress Report, Geo-sampling Task Group, January 1–June 30, 1965.
2. Nash, D. B., *Guidelines for the Development of a Lunar Sample Preparation System*, Technical Memorandum 33-218, pp. 51–69. Jet Propulsion Laboratory, Pasadena, Calif., June 1, 1965.
3. Dunne, J. A., and Nickle, N. L., *Balanced Filters for the Analysis of AL, Si, K, Ca, Fe, and Ni*, Technical Report 32-1134. Jet Propulsion Laboratory, Pasadena, Calif., Aug. 1, 1967.
4. Epstein, E. E., et al., *Science*, 1967 (in preparation).
5. Kaftan-Kassim, M. A., and Kellermann, K. I., *Nature*, Vol. 213, p. 272, 1967.
6. Piddington, J. H., and Minnett, H. C., *Australian J. Sci. Res.*, Vol. 42, p. 63, 1949.
7. Gary, B., *Ap. J.*, Vol. 147, p. 245, 1967.
8. Linsky, J. L., *Icarus*, Vol. 5, p. 606, 1966.
9. Probhakara, C., and Hogan, J. S., *J. Atm. Sci.*, Vol. 22, p. 97–109, 1965.
10. Spitzer, L., "The Atmosphere Above 120 KM," *The Atmosphere of the Earth and Planets*, p. 211, 1948.
11. Goetz, A. F. H., *Infrared 8–13 μ Spectroscopy of the Moon and Some Cold Silicate Powders*, Ph.D. thesis. California Institute of Technology, Pasadena, Calif., 83 pp., 1967.

XVIII. Physics

SPACE SCIENCES DIVISION

A. Low-Energy, High-Resolution Electron Impact Spectrometer, S. Trajmar

1. Introduction

Recent developments in high-vacuum techniques, particle counting, and energy analyzing equipment, as well as theoretical advances in the field of low-energy electron scattering, made it feasible to design and build an electron impact spectrometer for attacking problems that were not amenable for investigation up to the present. Some of these are the vibrational (and in limited cases the rotational) structure of electronic excitations by electron impact, resonances in elastic and inelastic channels, differential cross sections (nonzero angle scattering), near-excitation threshold phenomena, optically forbidden electronic transitions, and excitations in the far-ultraviolet and above-ionization limit.

Low energy is defined here as the 0- to 100-eV region that corresponds to the binding energy of electrons in atoms and molecules. This energy range is therefore of greatest interest in atmospheric and plasma physics, in chemistry, and in spectroscopy.

The design and operation of a low-energy, high-resolution electron impact spectrometer¹ are briefly re-

¹Designed and built in cooperation with A. Kuppermann and J. Rice of California Institute of Technology, Pasadena.

ported here and will be described in more detail in a forthcoming technical report.²

2. General Description

The spectrometer is designed to investigate the following process: molecule (n_i) + electron (E_i, θ_i) = molecule (n_f) + electron (E_f, θ_f), where n represents all the quantum numbers characterizing the molecular state before and after scattering, and E and θ refer to the energy and direction of the electron.

The apparatus is of the same type as described by Purcell (Ref. 1), Simpson (Ref. 2), and Kuyatt and Simpson (Ref. 3), and consists of an electron gun, two hemispherical electrostatic energy selectors (monochromator and analyzer), a scattering chamber, and a detector system. It is shown schematically in Fig. 1. The electron gun forms an intense ($1 \mu\text{A}$) well-collimated beam (half-angle ~ 0.5 deg), which is then decelerated and focused into the monochromator. The beam leaving the monochromator is reaccelerated to the required impact energy and focused into the scattering chamber which contains the static gaseous sample. Electrons that are scattered into the θ_f direction within a small solid angle are then collected, energy-analyzed, and focused into the detector system.

²Now in preparation by the author.

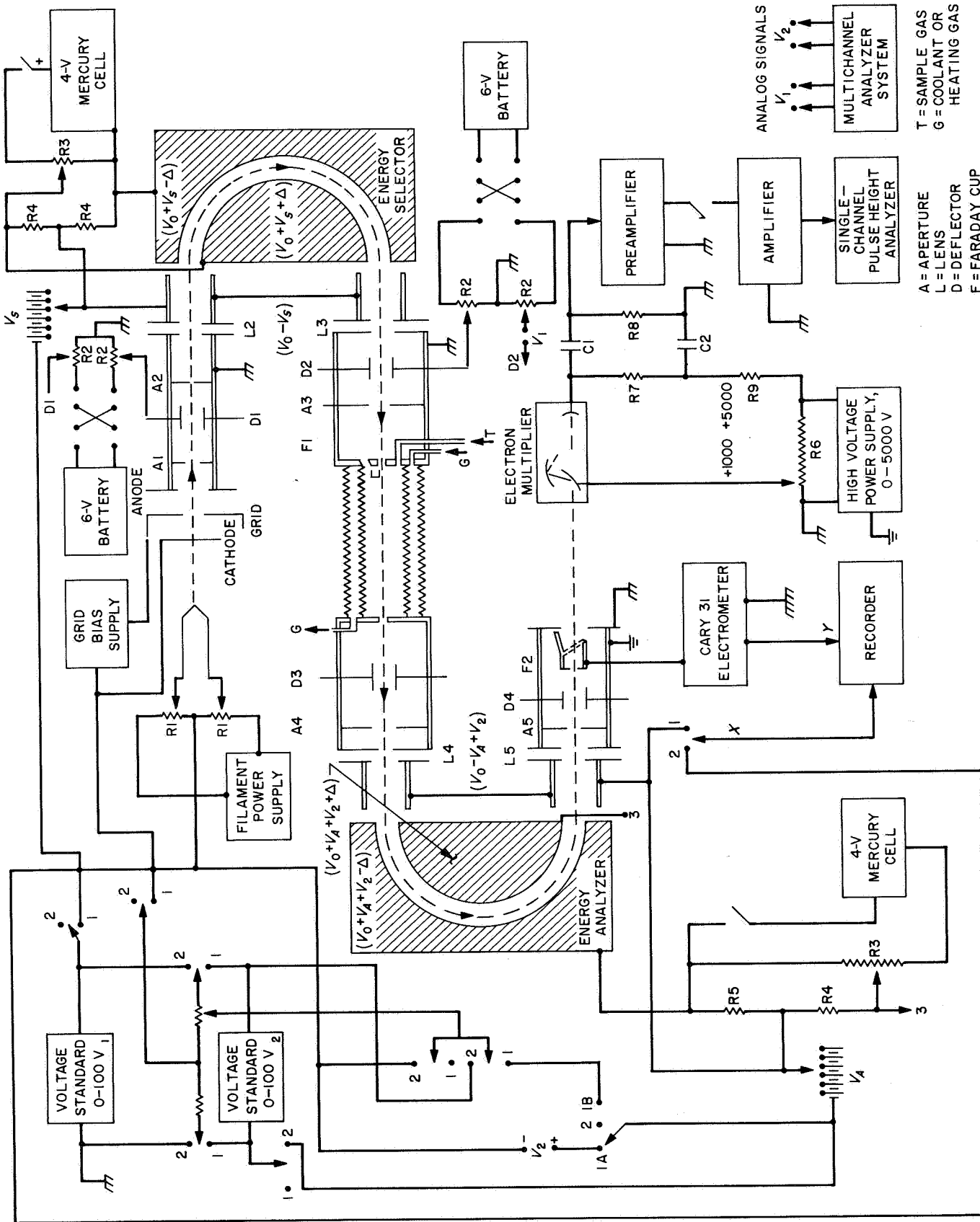


Fig. 1. Schematic diagram of electron impact spectrometer

There are three parameters (in addition to pressure and temperature) that can be varied in different types of experiments:

- (1) The impact energy of the electrons (E_i).
- (2) The energy loss during the collision ($E_i - E_f$).
- (3) The scattering angle (θ_f).

These three variables are extremely important in recognizing the type of scattering processes and in gaining insight into the details of the phenomenon. In the present apparatus, the target is a gas in the 10^{-5} - to 10^{-2} -torr region. The temperature is controllable from -180 to $+300^\circ\text{C}$. The energy range covered is from 0 to 100 eV, in both impact energy and energy loss, and the angle θ_f can be varied from -30 to $+90$ deg.

An ideal beam of highly directional low-energy electrons represents a compromise between two incompatible requirements:

- (1) High current density.
- (2) Low angular divergence.

High energy resolution by the hemispherical analyzers and high efficiency of both the energy selectors and the scattering chamber require that the electron beam be launched with a low divergence angle. This angle (and electron energy), however, sets an upper limit to the achievable current density.

In designing a low-energy electron impact spectrometer, it is of basic importance to understand the limitations that determine the flow patterns, the beam profile, and the density of the low-energy electron beam. These limitations are due to space charge and thermodynamic effects. Three basic restrictions must be satisfied:

a. The beam current intensity must be below space-charge limit. The maximum current that can flow through a tube of length l and diameter $2r$ against the dispersive forces of space charge is

$$I_{max} = 38.5 V^{3/2} \left(\frac{2r}{l} \right)^2 = 38.5 V^{3/2} \tan^2 \alpha$$

where

I_{max} = the space charge limited current, μA

V = kinetic energy of the electrons, eV

α = half-angle of divergence

This relationship applies all along the beam path and determines the saturation current one can put through the given space. In order to achieve this maximum current throughput, the beam must enter the volume so that in the absence of space charge the beam would focus to a point at the center of the volume.

b. The law of Helmholtz and Lagrange:

$$V_1 d\Omega_1 dA_1 = V_2 d\Omega_2 dA_2$$

where

$d\Omega$ = differential solid angle

dA = differential area

This equation expresses the conservation of current along the beam path or conservation of electron brightness. If this relationship is applied to conjugate image and object or to object and crossover planes, one obtains (Ref. 4)

$$V_1^{1/2} \sin \alpha_1 = M V_2^{1/2} \sin \alpha_2$$

where M is the Gaussian magnification.

c. Langmuir's equation (Ref. 5):

$$J_{max} = J_{cathode} \left(1 + \frac{V}{kT} \right) \sin^2 \alpha$$

This equation relates the maximum achievable current density J_{max} in an electron beam to the current density and other parameters at a thermionic cathode.

3. Electron Energy Analysis

The electron beam generated by the gun has a half-width of ~ 0.5 eV. In order to resolve vibrational structure of electronic transitions in a spectrum, a resolution of about 0.050 eV is required. To achieve this resolution, hemispherical electrostatic electron energy selectors were chosen for the monochromator and analyzer.

The equation of motion for this system can be rigorously solved, and the trajectory equation for an electron in the sphere is given by

$$R(\theta) = \frac{2R_i^2 \cos^2 \alpha X}{\cos \theta (2R_i - \cos^2 \alpha X - R_0) - 2R_i \cos^2 \alpha \tan \alpha \sin \theta X + R_0}$$

where

$$X = \frac{E}{2E_0} - \frac{R_0}{R} - 1$$

R = the position of the electron measured from the center of the spheres; i index refers to initial value at the entrance, and 0 to the center of the gap

θ = the angle measured from the entrance face of the hemisphere

α = half-angle of the beam divergence

E = kinetic energy of the electron in the sphere

E_0 = kinetic energy of the electron that will make a circular orbit if $\alpha = 0$ and $R_i = R_0$

Typical trajectories are shown on Figs. 2, 3, 4, and 5.

Electron-optical properties of the analyzer and the question of line shape, resolution, and external field effects will be discussed in a JPL report now in preparation.

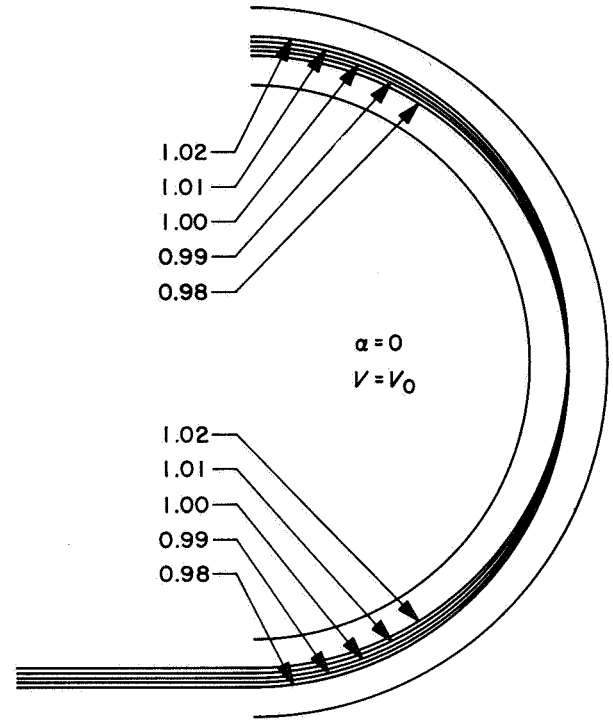


Fig. 3. Dependence of trajectory on entrance position

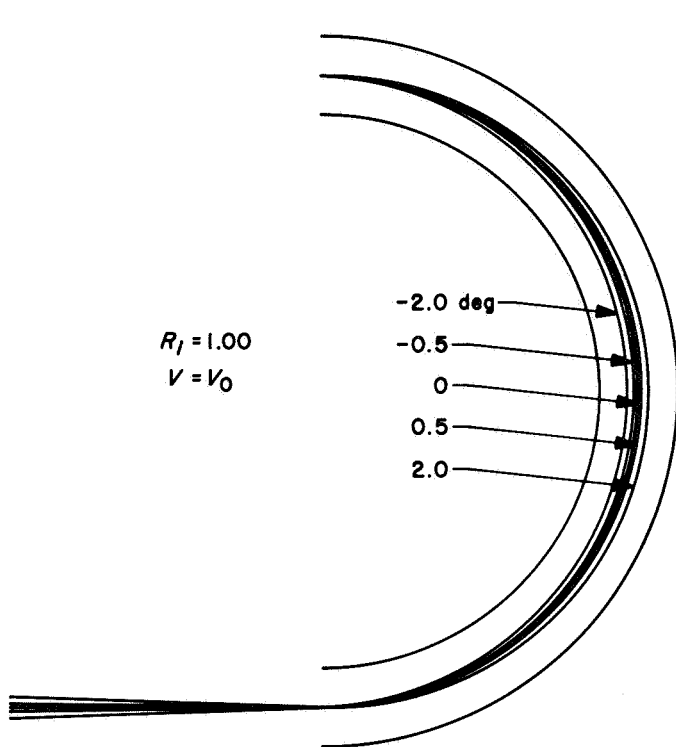


Fig. 2. Dependence of trajectory on entrance angle

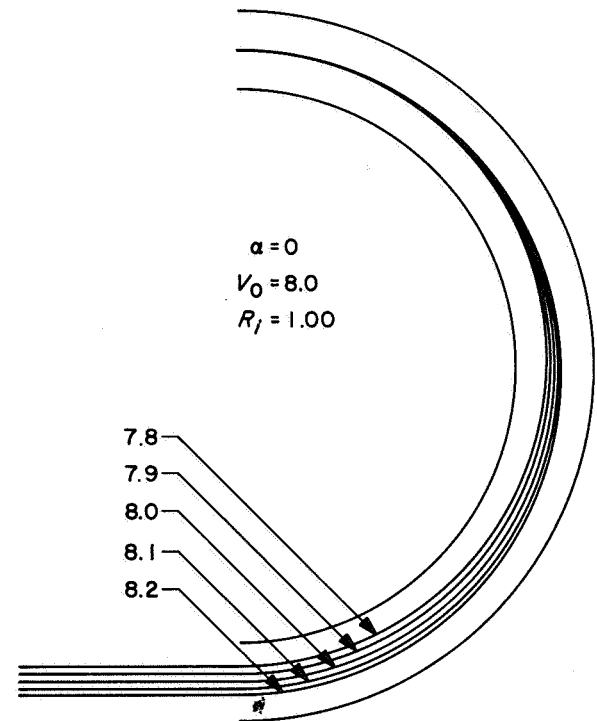


Fig. 4. Dependence of trajectory on entrance energy (8 V)

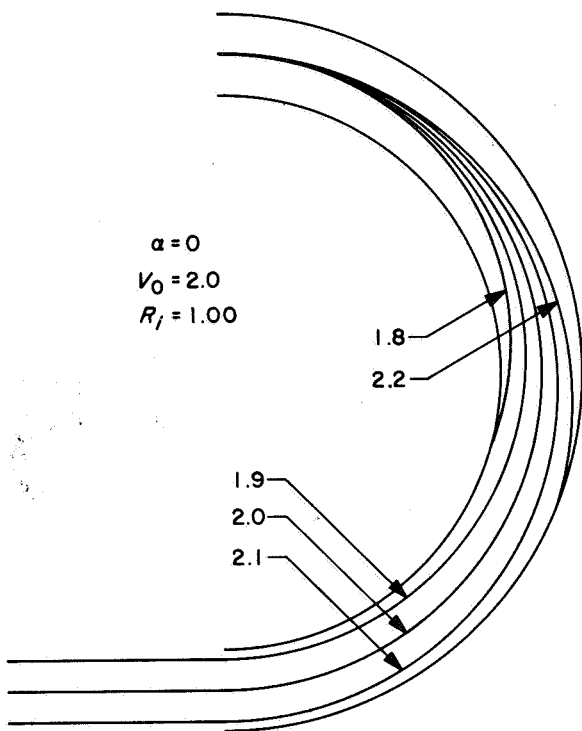


Fig. 5. Dependence of trajectory on entrance energy (2 V)

4. Scattering Chamber

The scattering chamber (shown in Fig. 6) consists of a double bellows, entrance and exit electron optics, sample inlet and pressure monitoring elements, and a retractable Faraday cup. Cooling or heating media can be introduced into the space enclosed by the double bellows. Continuous rotation of one end of the scattering chamber and the

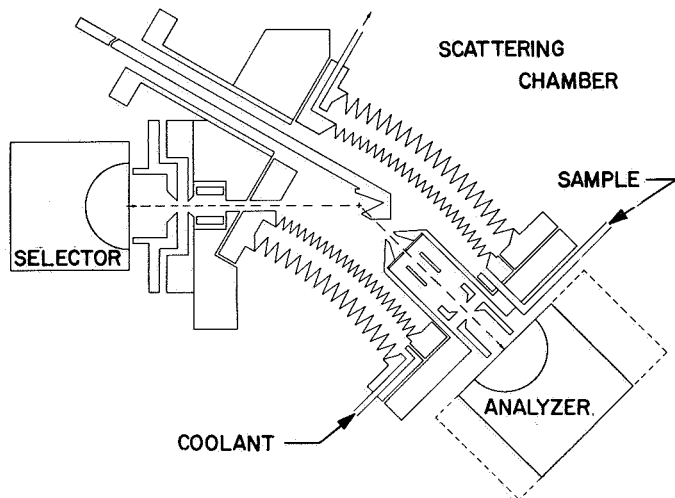


Fig. 6. Scattering chamber

incoming electron beam is possible from -30 to $+90$ deg with respect to the detector.

The electron gun and the entrance end of the chamber are mounted on a gear wheel which can be driven from outside the vacuum chamber. The Faraday cup is used to monitor the beam intensity entering the scattering chamber, and is retracted when not in use. The sample gas flows continuously from a temperature-controlled sample-handling system through a variable leak, thus maintaining the required pressure in the scattering chamber in spite of the leakage through the entrance and exit apertures. The pressure is monitored by either a miniature GE ionization gauge or an RCA-1946 thermocouple gauge, both of which are calibrated against a McLeod gauge specifically designed for this region (10^{-2} to 10^{-5} torr). It is expected that the pressure will be known to within 5%.

The entire apparatus is enclosed within a stainless-steel vacuum chamber which is bakeable up to 400°C . A background vacuum of 10^{-6} torr or better is required for the efficient operation of the gun.

5. Detector System

When the scattered beam intensity permits, the signal is detected by a vibrating reed electrometer which is useful down to 10^{-16} A, or about 600 electrons/s. In case of low signal levels, counting techniques are used. The counting system used operates up to 10^6 counts/s. It

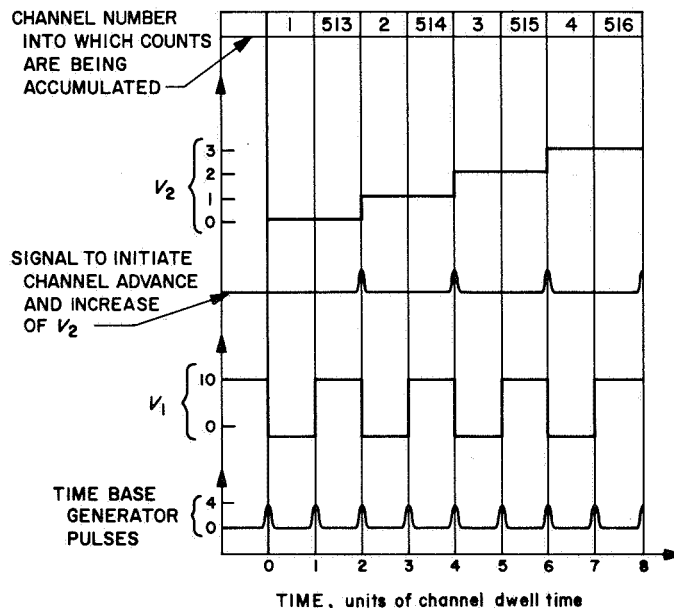


Fig. 7. Time signal relations for MCS-II mode

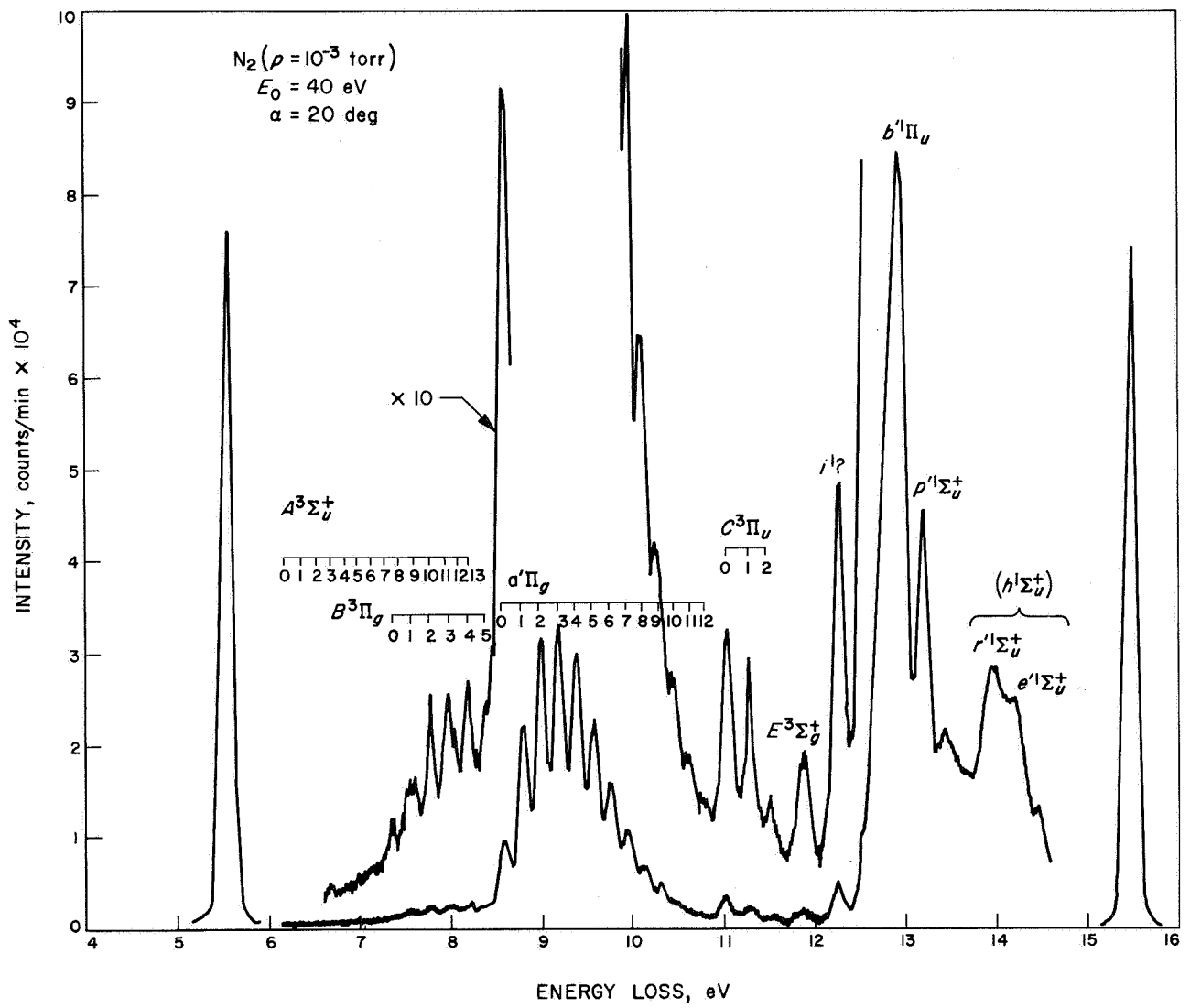


Fig. 8. Electron impact spectrum of N_2 at 20 deg

consists of the following elements: electron multiplier, preamplifier, amplifier, single-channel pulse height analyzer, trigger, and a count rate meter or a Nuclear Data (ND) 181 system.

The ND system is a 1024-channel analyzer with some custom-built-in features. The multichannel scaling (MCS) mode is specifically designed for electron scattering experiments. In these experiments, the 1024-channel memory is divided into halves: Into the first half, signal plus noise is counted; into the second half, only noise. The electron beam is chopped by a signal (V_1) which is supplied by the counting system and which is synchronized with the jumps from the first to the second half of the memory. The memory channel number is decoded, and an analog signal (V_2) is produced by a digital-to-analog converter. It is used for reaccelerating the electrons after scattering (i.e.; for the energy loss sweep). This analog signal is proportional to the channel number into which the counting occurs, and can change in steps 1, 2, 4, 6, 8,

10, 20, 30, 40, or 50 mV when going from one channel to the next. The time relations of the different signals are shown in Fig. 7.

A complete sweep is repeated as many times as set on a preset counter. Channel dwell times can be varied from 50 μ s to 2 s. The memory can be read by an X-Y recorder, scope, punch tape, or typewriter.

6. Performance

The operation and performance of the spectrometer according to design and expectations have been demonstrated. Energy loss spectra of He, N₂, and C₂H₂ have been obtained in the impact energy range of 20 to 50 eV and the angular range of -30 to +80 deg.

The advantage of electron impact spectroscopy over optical spectroscopy has been shown in two areas:

- (1) The study of optically forbidden transitions.

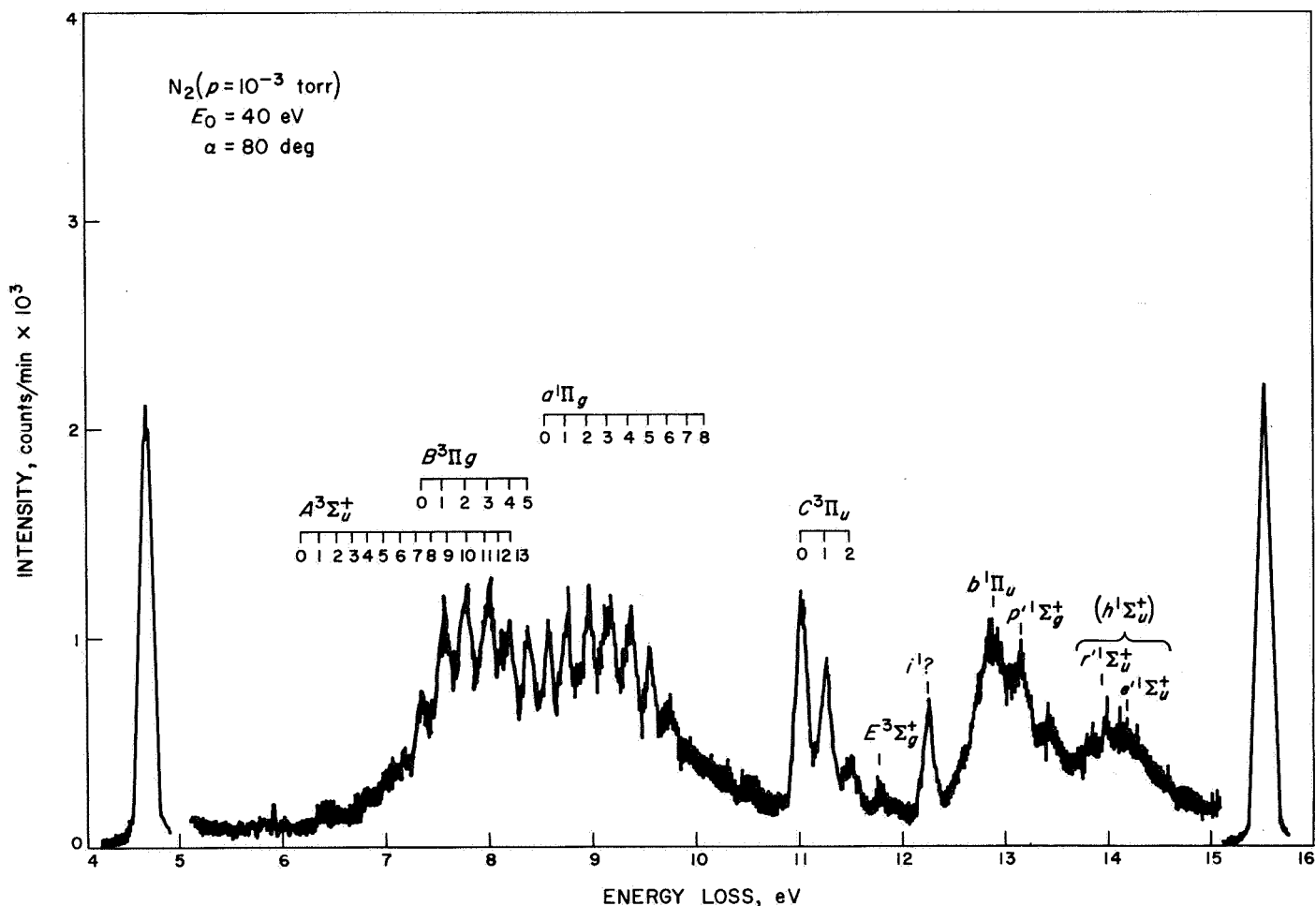


Fig. 9. Electron impact spectrum of N₂ at 80 deg

(2) The observation of highly excited states (far UV).

The angular and energy dependence of electron excitation cross sections presents an extremely powerful tool for identifying the type of excitation process. (There are no analog variables corresponding to energy and angle in optical spectroscopy.) At present, there is no theory available to properly describe these dependences for low-energy electron excitation of molecules (or even atoms). The experimental information is also very scarce. In order to establish general patterns for assisting the assignment of unknown transitions and developing adequate theories, this information will be obtained systematically, starting with He as the simplest system. Several examples are presented here to demonstrate the performance of the instrument as well as the angular dependence of cross sections.

Figure 8 shows the energy loss spectrum of the nitrogen molecule in the 6.0- to 15.0-eV region ($\alpha = 20$ deg, $E_0 = 40$ eV, $p_{N_2} = 10^{-3}$ torr). Transitions from the $X^1\Sigma_g^+$ ($v = 0$) ground state to the different excited electronic and vibrational levels are shown and marked at the corresponding peaks. In addition to the strong optically allowed transitions (e.g., $X^1\Sigma_g^+ \rightarrow b^1\Pi_u$), levels associated with symmetry-forbidden ($a^1\Pi_g$), spin-forbidden ($A^3\Sigma_u^+$, $C^3\Pi_u$), and both symmetry- and spin-forbidden ($B^3\Pi_g$, $E^3\Sigma_g^+$) systems can be observed. The vibrational structure of several electronic transitions are resolved. (Resolution can be further improved by sacrificing intensity.) The elastic peak is shown before and after scanning the spectrum. It defines the zero on the energy loss scale, and serves as a check on the stability of the instrument. In Fig. 9, the same spectral range is shown for $\alpha = 80$ deg. The intensity of the triplet transitions does not change appreciably from 20 to 80 deg, while the intensity of the singlet systems is reduced by about a factor of 100.

Figure 10 shows the electron impact spectrum of acetylene. Most of the features (2 to 14) are optically allowed, belong to two Rydberg series, and have been seen in optical spectroscopy. Peak 1 is a yet unidentified system; 2 is the first member of one of the Rydberg series. This spectrum is far superior to any published electron impact spectrum of C_2H_2 in both resolution and intensity.

Figures 11a and b show the 3- to 9-eV energy loss region at 60 and 20 deg, respectively, with a factor of about 10^3 increased sensitivity. The bands indicated as *a* and *b* do appear on these figures at 5.2- and 6.2-eV energy loss. They have been studied by Wilkinson (Ref. 6) and Ingold and King (Ref. 7) by means of optical spec-

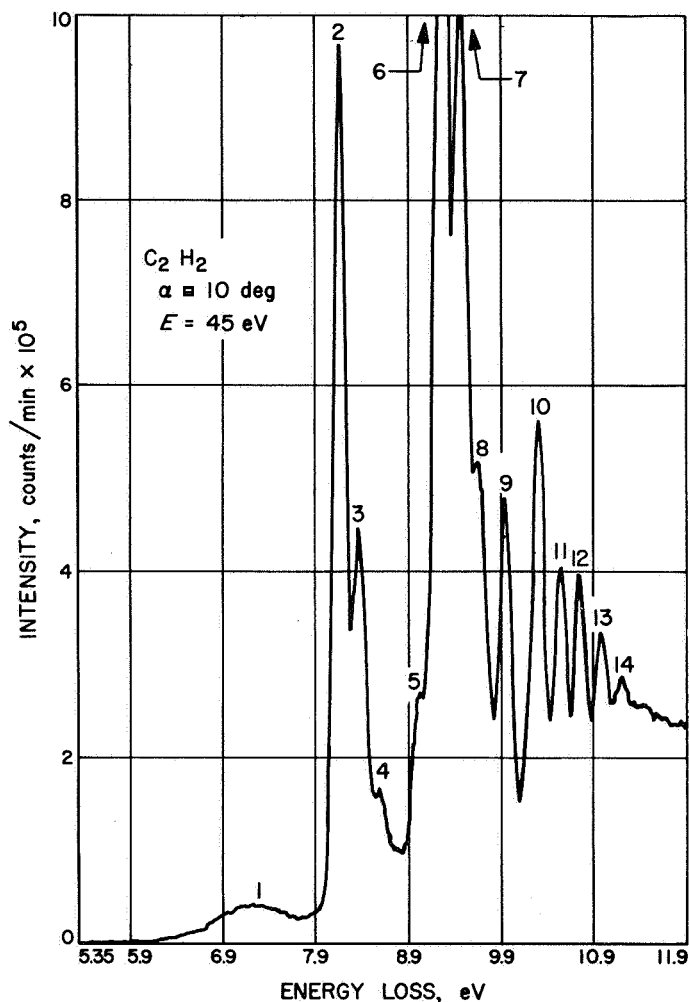


Fig. 10. Electron impact spectrum of C_2H_2 .

troscopy, using long path absorption, and were assigned to transitions from a linear $^1\Sigma_g^+$ ground to the *trans* bent 1A and 1B states. The low intensity of the bands was attributed to the low Frank-Condon overlap factor.

Preliminary data on angular and energy dependence of the *a* and *b* transitions indicate that they are not singlet-singlet transitions. The intensities of peaks *a*, *b*, 1, 6, and 10 were normalized to peak 2; the angular dependence of each peak is shown in Fig. 12. Transitions of the same types should have similar angular dependence. Peaks 6, 10, and 2 behave similarly, while *a*, *b*, and 1 have different characters.

The energy and angular dependence of these and other features of molecules of atmospheric and of general interest are being studied. The findings will be reported in later publications.

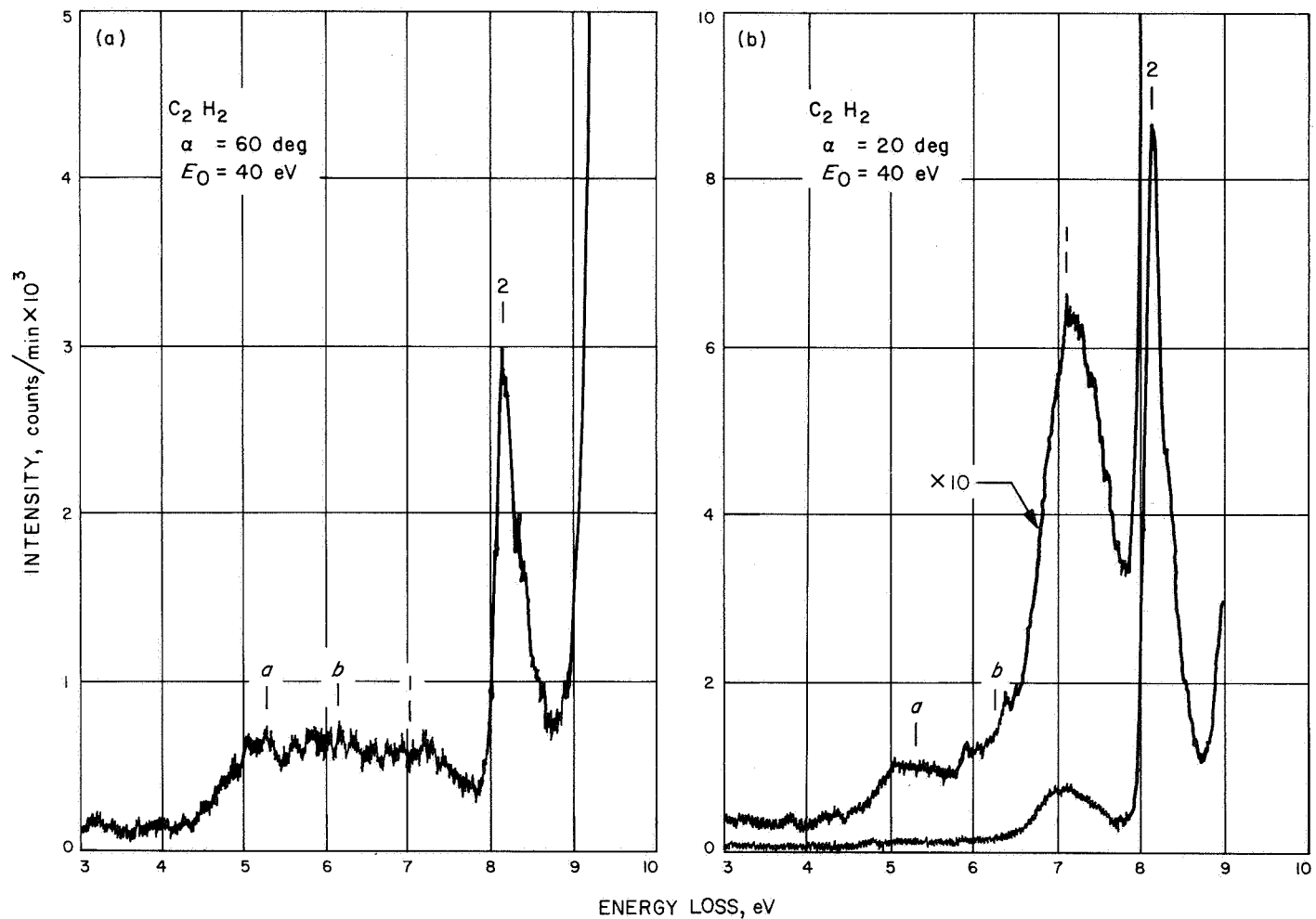


Fig. 11. Electron impact spectrum of C_2H_2 at 20 and 60 deg

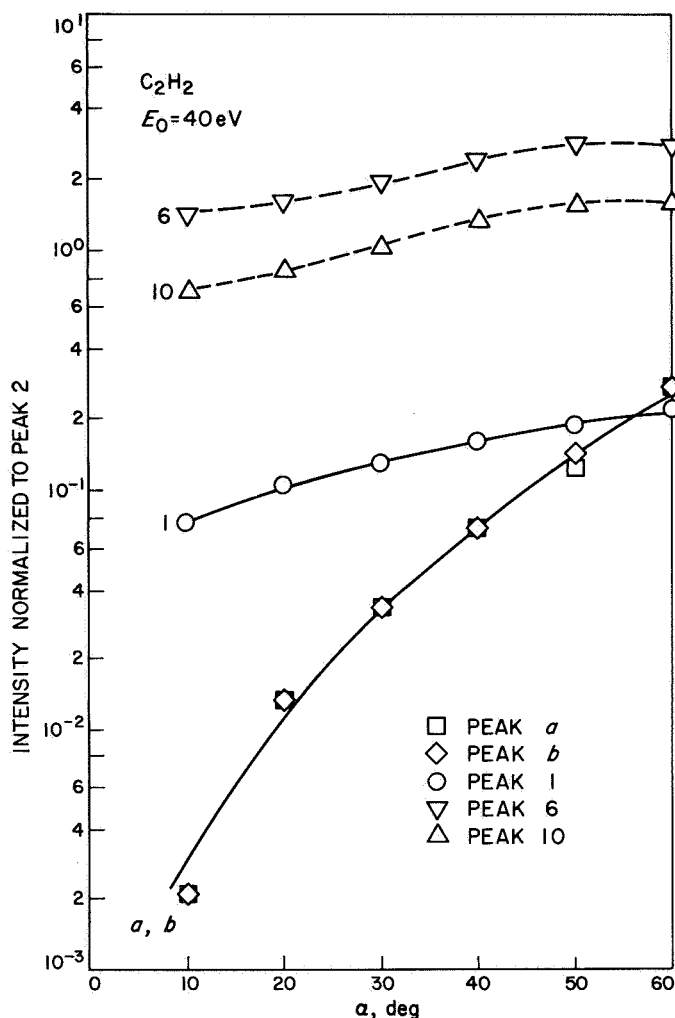


Fig. 12. C_2H_2 electron impact excitation cross section versus angle

B. The Determination of Chemical Mechanisms by Ion Cyclotron Resonance,

J. King, Jr. and D. D. Elleman

1. Introduction

The reaction of ions with atoms and molecules has generated great interest during the past few years. This type of reaction is not only important in the study of planetary atmospheres but also plays an important role in thermonuclear and plasma research. Recent interest in ion-molecule reactions has been sufficient to warrant the publication of the first monograph on the subject (Ref. 8).

In the past, conventional mass spectrometers have been used for most of the experimental investigations of ion-molecule reactions. For example, tandem mass spectrom-

eters have provided a wealth of data on various aspects of ion-molecule reactions, but the methods are not suitable for the study of complex, high-order reaction sequences.

A new instrument, the ion cyclotron resonance (ICR) spectrometer, provides a straightforward method for obtaining the mechanism of complex ion-molecule reactions. In this spectrometer, ions of differing masses are detected by the absorption of energy from an oscillating electric field. The charged particle moving in a uniform magnetic field H describes a circular orbit in a plane perpendicular to H , with an angular frequency, or cyclotron frequency, ω_c . When an alternating electric field $E(t)$ is applied normal to H at ω_c , the ions absorb energy from the electric field and are accelerated to larger velocities and orbital radii. A mass spectrum is obtained by sweeping the magnetic field so that the cyclotron frequency of ions of differing masses is brought to the operating frequency of the spectrometer and energy is absorbed (resonance).

2. Experimental Apparatus and Conditions

The ion cyclotron resonance spectrometer was patterned after an instrument designed and constructed by Varian Associates,³ and consists of a resonance cell, a high vacuum system, an inlet system, and a 12-in. magnet with its associated power supply. The cell is enclosed in a 4-in. OD \times 36-in. cylindrical vacuum chamber which was constructed to fit between the pole faces of the 12-in. magnet.

There are three compartments in the cell. In one compartment, electrons from a rhenium filament are accelerated in the direction of the magnetic field by a negative bias on the filament and enter the source region of the cell through a side plate. Ions formed in the source region are caused to drift into the resonance region by the application of static voltages. The top and bottom plates of the resonance region form part of the capacitance in the tank circuit of a marginal oscillator. The irradiating oscillator leads are also attached to these plates. The output of the marginal oscillator-detector is amplified and fed to a phase-sensitive detector. The phase-sensitive detector is referenced to a modulation oscillator which allows field modulation methods, common in nuclear magnetic resonance (NMR) and electron paramagnetic resonance (EPR) techniques (Ref. 9), to be employed.

The third region of the resonance cell is the collector region in which the total ion current is measured with an electrometer. The feature of the instrument that makes it

³Syrotton Mass Spectrometer, Varian Associates, Palo Alto, Calif.

unique is the separation of the regions where the ions are formed and where analysis takes place. This separation allows double-resonance techniques to be used to ascertain chemical mechanisms. The double-resonance technique involves the simultaneous RF heating of one type of ion while a second type is being observed under resonance conditions. Any coupling of the species, through charge transfer or other types of ion-molecule reactions, is easily detected, since ion-molecule collision cross sections are strongly dependent on the relative ion-molecule velocity (Ref. 10). Thus, if one type of ion is heated with a strong RF electric field, $E_2(t)$ at frequency ω_2 , substantial changes should occur in the concentrations and temperatures of other ions in equilibrium with the irradiated ion. These changes are detected with a weak RF electric field, $E_1(t)$ at frequency ω_1 , through changes in the line shape and intensity of the observed ion spectra.

In the present investigation, the marginal oscillator operated at 76.6 kHz, which corresponds to 50 G/amu. The magnetic field was swept from 2000 to 7000 G, covering the mass range from 40 to 140 amu. The double-

resonance experiments were performed with 60-eV electrons. The instrument was equipped with an automatic pressure controller which maintained the pressure at a preset value.

3. Results

In order to check out the ICR spectrometer and to obtain useful scientific information, a study was made of the ion-molecule reactions occurring in hexafluoroethane (C_2F_6). This compound was chosen because very little is known in general about the decomposition processes of perfluoroalkane ions, and very recently speculations (Ref. 11) have been made about the reactions occurring in C_2F_6 . Smith and Kevan (Ref. 11), in their study of the dissociative charge exchange of rare gases with C_2F_6 , interpreted the various charge-exchange mass spectra as portraying the dissociation of $C_2F_6^+$ as a function of its excitation energy.

In reactions with Kr^+ , Ar^+ , Ne^+ , and He^+ , Smith and Kevan observed the production of $C_2F_5^+$, CF_3^+ , and CF_2^+ .

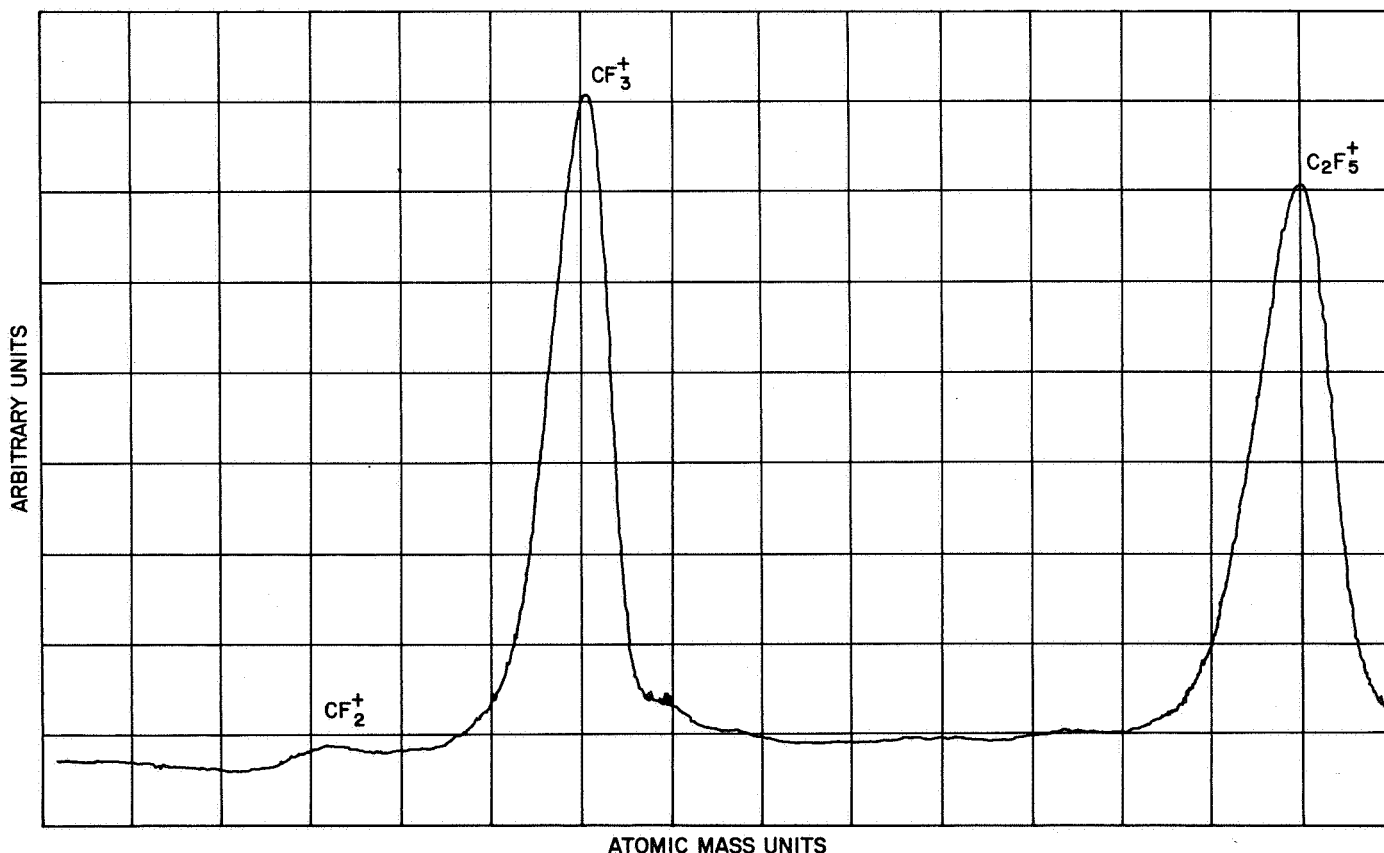


Fig. 13. The ion cyclotron resonance spectrum of C_2F_6

The presence of two maxima in CF_3^+ formation was attributed to at least two separate processes. To account for an unexpected increase in CF_2^+ production, Smith and Kevan suggested that $C_2F_5^+$ could possibly dissociate to give CF_2^+ instead of CF_3^+ . However, the charge should appear on CF_3 instead of CF_2 , since CF_3 has the lower ionization potential (Ref. 12).

These apparent irregularities prompted the use of the ion cyclotron resonance technique to ascertain the mechanism of CF_2^+ and CF_3^+ formation in the decomposition scheme of C_2F_6 .

When C_2F_6 is subjected to electron bombardment, it fragments into three major ionic components, $C_2F_5^+$, CF_3^+ , and CF_2^+ . These components can be seen in the single-resonance ion cyclotron spectrum of C_2F_6 in Fig. 13.

In the double-resonance experiments, one component is detected at frequency ω_1 , while the other two components are heated, in turn, with $E_2(t)$ at ω_2 . The field E_2 was modulated at 39 Hz, and the signal at ω_1 was detected with a phase detector referenced to the modulating frequency. This setup allowed the difference between the single- and double-resonance spectra to be directly displayed so that only those products that are coupled to the irradiated species by chemical reaction produced a spectrum. The double-resonance spectra in Fig. 14 were taken under the condition of ω_1 set at the resonance frequency of $C_2F_5^+$ while first CF_2^+ and then CF_3^+ were heated by sweeping the frequency. The positive results show that both CF_3^+ and CF_2^+ are reactants in $C_2F_5^+$ formation. The results of all the double-resonance experiments are shown in Table 1. A minus sign indicates that no spectrum was observed.

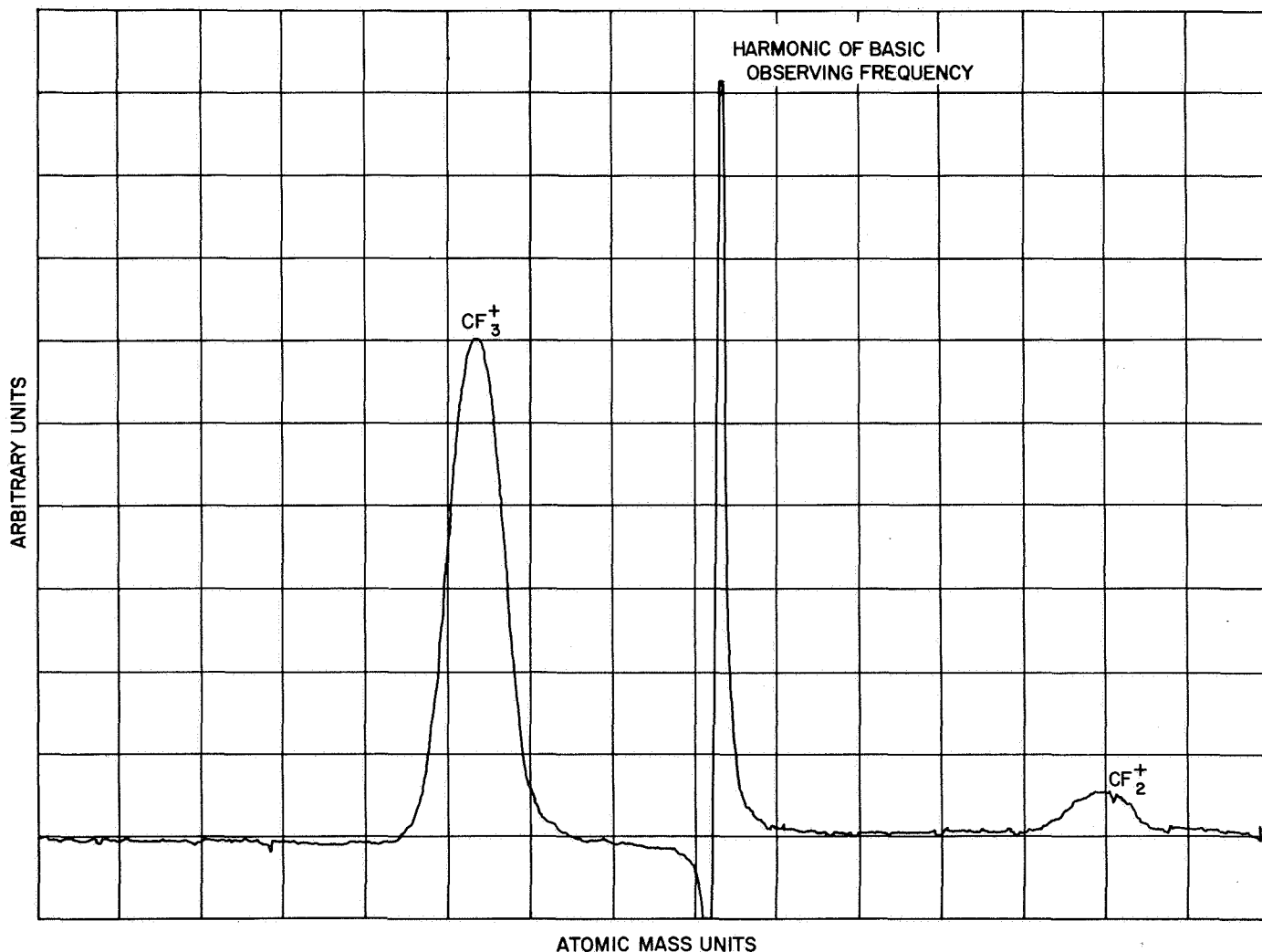


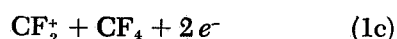
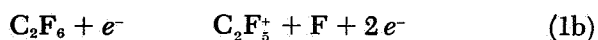
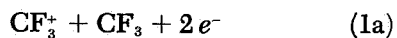
Fig. 14. Double-resonance spectra of C_2F_6 (the $C_2F_5^+$ was monitored while CF_3^+ and CF_2^+ were irradiated, in turn)

Table 1. Double resonance experiments in C₂F₆

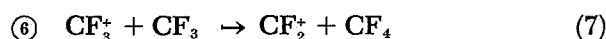
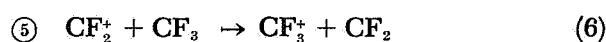
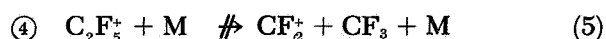
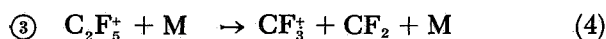
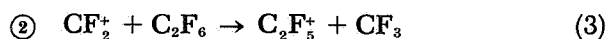
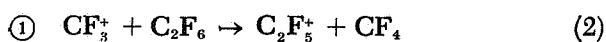
Experiment number	Observed ion	Irradiated ion	Results
1	C ₂ F ₅ ⁺	CF ₃ ⁺	+
2	C ₂ F ₅ ⁺	CF ₂ ⁺	+
3	CF ₃ ⁺	C ₂ F ₅ ⁺	+
4	CF ₂ ⁺	C ₂ F ₅ ⁺	-
5	CF ₃ ⁺	CF ₂ ⁺	+
6	CF ₂ ⁺	CF ₃ ⁺	+

4. Discussion

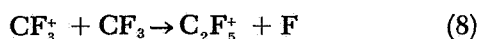
The following mechanism is proposed to explain the electron impact decomposition of hexafluoroethane with 60-eV electrons:



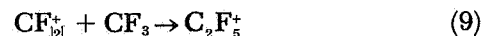
By varying the electron energy, it was found that reaction (1a) occurred at low electron energy (~12 eV), while (1b) and (1c) occurred at much higher energies. This energy dependence agrees with that found by Smith and Kevan (Ref. 11). The following set of secondary reactions is compatible with the data in Table 1, where the encircled number refers to the experiment number of Table 1.



Although this set of secondary reactions explains the experimental observations, it is, obviously, not all inclusive. For example, the reaction



could explain experiment ① as well as reaction (2). Similarly, the reaction



is compatible with experiment ②. However, reaction (9) competes with reaction (6), and the latter is chosen because of its greater exothermicity.

The charge-transfer reaction (6) is compatible with the ionization potentials *I* of the species (Ref. 13), provided the *low* value for the ionization potential of the CF₃ radical is correct (Ref. 12).

Reaction (7) proceeds contrary to the ionization potentials, since *I*(CF₂) > *I*(CF₃) (Ref. 12). With both reactants in their ground state, reaction (7) is endothermic by approximately 25 kcal/mole. Thus, its occurrence suggests that one of the reactants is in an excited state. It is quite probable that CF₃⁺ is formed with enough excess energy in reaction (1a) to permit reaction (7) to occur. The nonionic reaction



is known to occur (Ref. 13) and is exothermic by approximately 25 kcal/mole. The investigation of reaction (7) is continuing.

The results offer an explanation for some of the discoveries of Smith and Kevan. The second maximum in CF₃⁺ formation could be explained by reactions (4) and (6), which allow CF₃⁺ to be formed at the expense of C₂F₅⁺ and CF₂⁺, respectively.

The increase in the CF₂⁺ formation at high energies could be accounted for if its rate of production by reaction (1c) is greater than its disappearance by reactions (3) and (6). This would cause an increase in its rate of rise with energy. This point requires further quantitative study. The suggestion of Smith and Kevan that C₂F₅⁺ could possibly dissociate to give CF₂⁺ instead of CF₃⁺ is incompatible with experiment ④ in Table 1.

5. Conclusion

These experiments show the potential of the ion cyclotron double-resonance technique for deciphering complex mechanisms in ion-molecule reactions. It should become a very useful tool in the study of ion-molecule reactions occurring in planetary atmospheres. The investigation of these and other potential applications is continuing.

C. MOSES: A FORTRAN IV Program for Calculating Properties of Polyatomic Molecules, M. Geller and L. M. Sachs⁴

1. Introduction

A new computer program has been designed for the computation of approximate wave functions for polyatomic molecules. The program has been named MOSES, which is an abbreviation for Molecular Orbital Self-Consistent Field Energy System. It is a flexible system of programs of high speed and accuracy that permit extensive variation of given basis sets in a finite time. The program has been written completely in FORTRAN IV language, so that only minor changes are needed to switch from one computer installation to another, and is designed to function in a 32K memory. The use of a larger core storage would result in a decrease in computation time, although exact time estimates are unavailable. There are no stops in the program, and no special operator action is required during running.

2. General System Layout

As presently constituted, MOSES is restricted to single-configuration self-consistent field (SCF) calculations. The main program sequentially initiates calls to the three major subprograms; this is done automatically from a few input specifications. Each of the subprograms is completely independent of the others, with the proviso that certain information is available at all times via block common or the peripheral storage units. The three major subprograms are:

GPACKG—produces the necessary one- and two-electron integrals from the raw input data. These input data are a basis of Gaussian atomic orbitals. Gaussian functions have been chosen so that all integrals can be analytically evaluated (Ref. 14).

SCF—solves the Roothaan self-consistent field equations (Ref. 15), thereby generating the following:

- (1) Molecular orbitals (MOs) formed by the appropriate linear combination of the Gaussian atomic orbitals.
- (2) The total energy of the system.
- (3) The individual orbital energies.
- (4) The level ordering.

⁴Martin Co., Research Institute for Advanced Studies (RIAS), Baltimore, Md.

Control is switched either to SCF 1 for closed-shell systems or SCF 2 for open-shell systems. (SCF 2 is not yet completely operational.)

PROPTY—utilizes the MOs formed above in SCF to calculate specific properties of the system such as population analysis, dipole and higher multipole moments, and others.

At the beginning and end of each major section, the run is identified, and the clock (if one exists) prints out the time in seconds. The symmetric matrices used in the SCF process are stored lower-triangularly and the MOs are stored as a one-dimensional array. This storage makes efficient use of the core and avoids a great deal of tape handling. No special tape searching routines are necessary.

MOSES is capable of handling any number of runs successively, with up to 72 basis functions.⁵ The input data have been kept to a minimum to avoid errors and time consumption in making up the input cards.

3. Integral Subprogram—GPACKG

A schematic of the integral subprogram GPACKG is presented in Fig. 15. Unnormalized Gaussian functions

⁵This restriction is based on the use of a 32K capacity machine. In testing this program on a GE-625 with a 128K core, 100 basis functions can easily be handled.

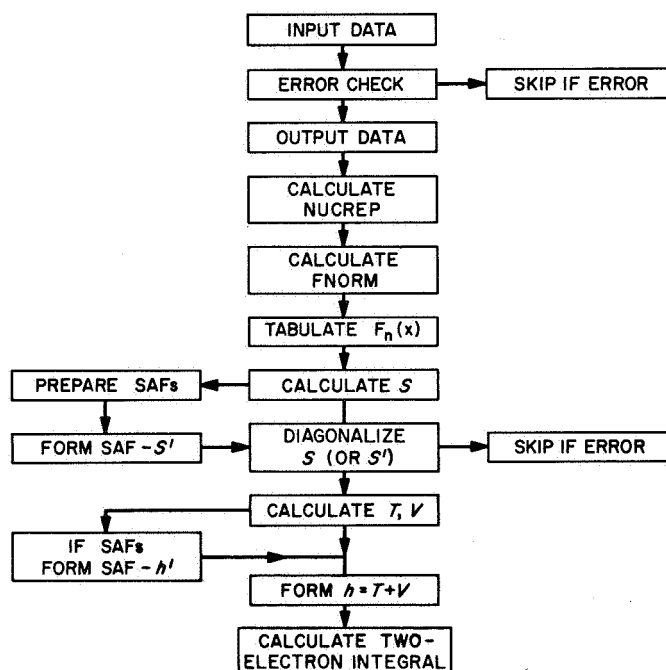


Fig. 15. Flow diagram of integral subprogram GPACKG

on different centers are read in. These can be of S-type [$\exp(-ar^2)$], P-type [x , y , or $z \exp(-ar^2)$], or D-type [x^2 , xy , xz , y^2 , yz , or $z^2 \exp(-ar^2)$]. An input card also gives the total number of input Gaussians, the number of symmetry types, whether or not symmetry-adapted functions (SAFs) will be constructed, an option to print out the one-electron integrals, all the integrals, or none of the integrals, and an integral-changing option. This latter option is extremely important in making variations on the bases. A new integral tape is generated from the integral tape of the original basis, with only the new two-electron integrals being recalculated, while preserving the old tape in its original form. Further input cards specify the names of the symmetry types and the number of SAFs belonging to each symmetry.

The input specifications are then checked for errors; if any are found, that case is abandoned and control proceeds to the next case. If no errors are detected, the specifications are printed out. Next, the total nuclear repulsion energy of the system (NUCREP) is calculated, and then the Gaussian functions are normalized (FNORM).

The only auxiliary function needed in the complete analytic evaluation of all the integrals is the error function (Ref. 16)

$$F_n(x) = \int_0^1 t^{2n} e^{-xt^2} dt \quad (1)$$

For $x \leq 9.8$, we make use of an interpolation scheme⁶ based on

$$F'_n(x) = -F_{n+1}(x) \quad (2)$$

from which we can derive, by a Taylor expansion,

$$F_n(x + \Delta x) = \sum_{p=0}^{\infty} \frac{1}{p!} (-\Delta x)^p F_{n+p}(x) \quad (3)$$

We first construct a table of $F_n(x)$; $x = 0(.1)9.9$ and $n = 0(1)13$. The table entries are calculated in double

⁶This method was suggested to the authors by Professor S. Huzinaga, Kyushu University, Japan. It apparently originated with A. D. McLean of IBM, San Jose, Calif.

precision from the series

$$F_n(x) = \frac{1}{2} e^{-x} \Gamma\left(n + \frac{1}{2}\right) \sum_{i=0}^{\infty} \left[\frac{x^i}{\Gamma\left(n + i + \frac{3}{2}\right)} \right] \quad (4)$$

with a tolerance of 10^{-11} , and then stored in single precision. For any value of x in this range, six terms in the series of Eq. (3) guarantee an accuracy of, at worst, 10^{-10} . On the IBM 7094/2 computer, about 0.2 ms is needed to obtain a value by this interpolation scheme. For $x > 9.8$, we use the asymptotic series

$$F_n(x) = \frac{1}{2} x^{-n-\frac{1}{2}} \Gamma\left(n + \frac{1}{2}\right) - \frac{1}{2} e^{-x} \sum_{i=1}^M x^{-i} \left[\frac{\Gamma\left(n + \frac{1}{2}\right)}{\Gamma\left(n - i + \frac{3}{2}\right)} \right] \quad (5)$$

We have obtained empirical expressions for the number of terms in the series M as a function of n and x . Calculation time on the 7094/2 ranges from 0.2 to 1.0 ms, with an error of at most four in the eighth figure.

After the error function table is prepared, the one-electron integrals are calculated: first, the overlap integrals S ; then the kinetic energy integrals T ; and last, the potential energy integrals V . The latter two are combined to form h integrals, since they are never needed separately; thus, a savings in core storage can be effected. If SAFs are being employed, the coefficients of the SAFs are read-in via the NAMELIST input, and S is transformed to S' (overlap matrix over SAFs) and h to h' ($T+V$ matrix over SAFs), the transformation matrix being stored for later usage. The overlap matrix is then diagonalized (S or S'), and the eigenvalues and determinant of the overlap matrix are printed out.

Finally, the two-electron integrals are computed. They are written on the integral tape(s), one record at a time, as they are computed. We have chosen the logical record size equal to the physical record size, so that no wasted space appears on the tape. All zero integrals are written out. This is the most time-consuming part of GPACKG, as the number of two-electron integrals is proportional to N^4 , where N is the number of basis functions. We have taken advantage of all special cases of the formulas resulting from the equality of indices, centers, and exponents. Further, wherever possible, specific expressions for

every type of integral arising is programmed individually. The time to produce the integrals ranges from 0.3 to 1.5 ms for $\langle SS|SS \rangle$; from 1.0 to 5.5 ms for $\langle PP|PP \rangle$; and from 3.0 to 45.0 ms for $\langle DD|DD \rangle$ on a 7094/2. Table 2 gives the number of integrals arising and an estimate of the time needed to calculate these integrals (for an S, P basis) for a few different size bases. From the table it can be seen that, at present, with the 7094/2, bases of greater than 72 functions are unfeasible.⁷

Table 2. Number of integrals and estimated computation time on IBM 7094/2 for different size bases

Number of basis functions	Number of integrals	Estimated time for integral evaluation
18	14,706	40 s
24	45,150	2 min
33	157,641	7 min
54	1,103,355	50 min
72	3,454,506	2½ h
100	12,753,776	10 h

The accuracy of most integrals is about ± 5 in the eighth *significant* figure, with the exceptions happening when the value of the integral is very small. In no case do the errors run into the sixth *decimal* figure.

4. Self-Consistent Subprogram—SCF

The workings of the Roothaan SCF programs have been described in detail many times (Ref. 17) and will not be repeated here. SCF 1 and SCF 2 do no calculation, but merely monitor the flow and shift control to the appropriate subsections. Basically, the Fock F matrix is formed, diagonalized, and checked for self-consistency by means of an iterative procedure. With the exception of the contraction of the two-electron integrals to form the coulomb and exchange matrices, *all* products are accumulated in double precision and then truncated to single precision, thereby guaranteeing accuracy. Contractions could not be done in this manner on the 7094/2 because of the shortage of core storage. With the availability of a larger core machine, this feature will be added. The input data to SCF are the option parameters for open or closed shell, the convergence criteria, the molecular orbital occupancy, and an initial guess of the eigenvectors. Several other options have been included:

⁷The integral package presented here has been tested on the CDC-6600 at NYU, and the integral times appear to be roughly a factor of 5 faster, thus making the use of larger size bases practicable.

- (1) An option to either read-in zero eigenvectors, any starting guessed set, or the set generated in the previous calculation.
- (2) An option to freeze one or more vectors and then let the remaining vectors approach self-consistency before unfreezing (although this has been found to be unnecessary with the use of SAFs).
- (3) A Newton-Raphson-type procedure to extrapolate the eigenvectors from three successive runs to generate a new starting set.

The diagonalization of the Fock matrices are done by the Jacobi method, using a slightly modified version of HDIAG.⁸ The eigenvalues and eigenvectors are then ordered algebraically. A single-vector diagonalization option has also been included to increase convergence speed when the energy has stabilized to one part in 10^6 . After the occupied eigenvectors of the Fock matrices are obtained, they are checked for self-consistency with the eigenvectors from the previous iteration, subject to the convergence criteria. When self-consistency has been reached, the output program is called into use, and the final vectors are printed out in splendid fashion and are then punched out on cards for future employment.

5. Physical Properties Subprogram—PROPTY

After the completion of an SCF run, the main program calls in the physical properties subprogram PROPTY. At present, PROPTY contains only the routines needed for calculating the electronic population analysis, as outlined by Mulliken (Ref. 18), and the dipole moment.

6. Future Plans

Among the areas of improvement scheduled for MOSES are the following:

- (1) Replacement of the Jacobi diagonalization routine by the faster, more accurate and efficient Wilkinson-Householder routine (Ref. 19).
- (2) Completion of SCF 2—the open-shell SCF subprogram.
- (3) Programming of additional one-electron property subroutines, such as quadrupole moments, susceptibility, field-gradient, etc.
- (4) Major subprogram to do multiconfiguration SCF calculations, with the ultimate aim of chemical reality.

⁸MIHDI3, SHARE distribution number 705.

At present, the systems being investigated include BeH_2 , BH_2 , NF_2^+ , NF_2^- , and O_3 , with the aim of quantitatively elucidating the geometry, energy-level orderings, total energy, binding energy, and molecular properties. In a future issue of this volume, the use of MOSES for study of these systems will be considered.

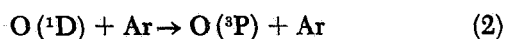
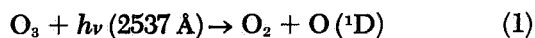
D. Reactions of $\text{O}(^1\text{D})$ and $\text{O}(^3\text{P})$ With Olefins,

W. B. DeMore

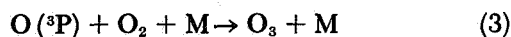
1. Introduction

Previous reports (SPS 37-35, Vol. IV, pp. 222-227; SPS 37-43, Vol. IV, pp. 287-290) have described experiments on the reactions of $\text{O}(^1\text{D})$ with saturated hydrocarbons, including CH_4 , C_2H_6 , C_3H_8 , and $i\text{-C}_4\text{H}_{10}$. The experiments involve photolysis of mixtures of O_3 and hydrocarbons dissolved in liquid Ar at 87.5°K. A principal result of the earlier work was that C—H bonds in alkanes were found to be attacked indiscriminately by $\text{O}(^1\text{D})$, without regard to bond type (primary, secondary, or tertiary) or bond strength. The present work extends the investigations to compounds containing the carbon-carbon double bond, and permits a determination of the relative rate of attack by $\text{O}(^1\text{D})$ on C—H and C=C bonds.

An additional feature of the present work is that the corresponding reactions of ground state (^3P) atomic oxygen with several olefins have also been studied. The sequence of reactions that produce $\text{O}(^3\text{P})$ is



where reaction 2 represents deactivation of $\text{O}(^1\text{D})$ by the solvent. Conditions can be chosen such that reactions of $\text{O}(^1\text{D})$ are slow compared with the $\text{O}(^3\text{P})$ reactions, provided that the $\text{O}(^3\text{P})$ reactions have low activation energies. Reactions with activation energies greater than 1 or 2 kcal/mole cannot compete detectably with the association reaction

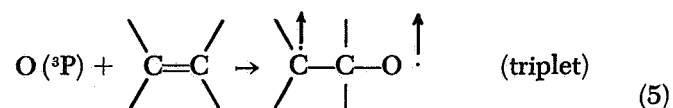
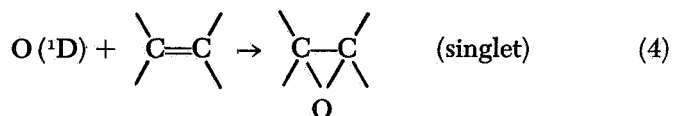


The reason for the foregoing limitation can be illustrated as follows: At 87.5°K, a 1 kcal/mole activation energy effectively lowers the rate of a reaction by a factor of 300, compared with a competing reaction that has no energy barrier but is otherwise equivalent. By the same

token, the method should be particularly useful in detecting small activation energy differences among competing reactions that have low activation energies, owing to the high sensitivity as shown above. The present experiments demonstrate the utility of the method by yielding new information on the activation energies for addition of $\text{O}(^3\text{P})$ to a series of olefins, a topic about which there has been much disagreement in the literature.

2. Review of the Literature

The only previous work on the reaction of $\text{O}(^1\text{D})$ with olefins is that of Sato and Cvetanovic (Ref. 20) who studied the addition of $\text{O}(^1\text{D})$ to 1-butene. An increased yield of α -butene oxide, relative to the $\text{O}(^3\text{P})$ case, was taken as evidence that $\text{O}(^1\text{D})$ adds directly to the C=C double bond to form the epoxide, as opposed to $\text{O}(^3\text{P})$ which is believed to add first to give a triplet biradical in accordance with the spin conservation rule:



There is extensive literature on the $\text{O}(^3\text{P})$ addition to olefins, most of which supports the biradical mechanism represented by Eq. (5). (For a review, see Ref. 21.) The principal disagreement is in the area of activation energies and Arrhenius A-factors for addition of $\text{O}(^3\text{P})$ to the various olefins. For instance, Cvetanovic and co-workers (Ref. 21) find an activation energy E_a for the $\text{O}(^3\text{P})$ - C_2H_4 reaction of 2.6 kcal/mole, whereas Elias and Schiff (Ref. 22) and Elias (Ref. 23) report a value of 1.6 kcal/mole. The difference, though small, is considered by each group to be outside the experimental uncertainties of their own measurements. Avramenko and co-workers (Ref. 24) not only reported different activation energies than the other groups, but also found a different trend in activation energy with increasing substitution at the C=C bond. The foregoing uncertainties have to some extent frustrated attempts to correlate rate parameters with molecular structure (Ref. 24).

3. Results

a. Rates of $\text{O}(^1\text{D})$ reactions with olefins. In order to study the $\text{O}(^1\text{D})$ reactions with olefins without interference from $\text{O}(^3\text{P})$ reactions, it is necessary to scavenge the $\text{O}(^3\text{P})$ with added O_2 . As shown in later sections, the

scavenging reaction (3) is sufficiently rapid so that at an O_2 /olefin ratio of 7:1 the $O(^3P)$ reaction is nearly completely suppressed. The $O(^1D)$ experiments were carried out under these conditions; where necessary, a correction was made for the slight residual $O(^3P)$ contribution.

Ozonolysis of the olefin is an additional complication in the present experiments. Rate measurements, which will be reported separately, show that ozonolysis of C_2H_4 and C_2F_4 is negligibly slow compared with the photochemical reaction. However, for C_3H_6 and higher olefins, the ozonolysis process prevents a quantitative study of the $O(^1D)$ reactions; therefore the experiments were limited to C_2H_4 and C_2F_4 .

As discussed previously (SPS 37-43, Vol. IV, pp. 287-290), quantum yields of O_3 disappearance in low-temperature solutions can be correlated with the rates of $O(^1D)$ reactions by the following equation:

$$\frac{1}{\Phi_{O_3} (^1D)} = \frac{k_r + k_d}{k_r} + \frac{k_{Ar}}{k_r [\text{substrate}]} \quad (6)$$

In Eq. (6), k_d denotes the rate constant for $O(^1D)$ deactivation by the added substrate, k_{Ar} represents solvent deactivation, and k_r is the rate constant for $O(^1D)$ reaction with the solvent. The notation $\Phi_{O_3} (^1D)$ indicates that the quantum yield refers only to the 1D reaction.

The results for C_2H_4 and C_2F_4 are shown in Fig. 16; for comparison, data from previous work on other sub-

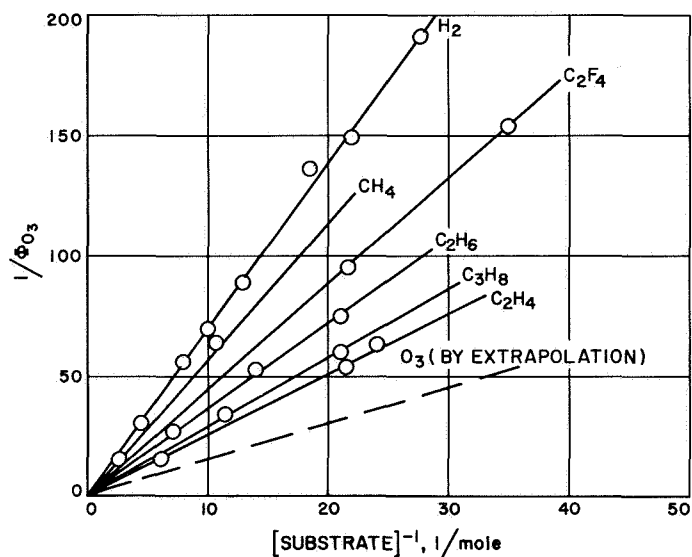


Fig. 16. Quantum yields of O_3 decomposition for $O(^1D)$ reactions

strates are included. The implications of these results are discussed in a later section.

b. Rates of $O(^3P)$ reactions with olefins. Two methods were employed in these experiments. The first was based on quantum yield measurements and involved competition between an olefin and O_2 for $O(^3P)$. For O_3 photolysis at a given olefin/ O_2 ratio, the quantum yield of O_3 disappearance due to the $O(^3P)$ reaction with the olefin is given by

$$\frac{1}{\Phi_{O_3} (^3P)} = \frac{1}{\Phi_{O_3} (\text{tot}) - \Phi_{O_3} (^1D)} = \frac{1}{\phi} + \frac{k_3 [O_2]}{\phi k_4 [\text{olefin}]} \quad (7)$$

In Eq. (7) $\Phi_{O_3} (\text{tot})$ refers to the total observed quantum yield, including the 1D contribution $\Phi_{O_3} (^1D)$. The latter quantity, obtained from the data of Fig. 16, was small compared with $\Phi_{O_3} (\text{tot})$, and was subtracted to obtain $\Phi_{O_3} (^3P)$. The quantity ϕ is the limiting quantum yield of O-atom production in the primary photochemical process (Eq. 1).

Results for experiments of the above type for C_2H_4 and C_2F_4 are shown in Figs. 17 and 18, respectively. In most cases, the O_2 concentration was taken as equal to the O_3 decomposed. The validity of the latter calculation is shown by the data of Fig. 17, which show good agreement between points determined by the method of O_3 decomposed and by points determined from experiments in which O_2 was added initially.

The intercepts in Figs. 17 and 18 are equal, and give a value of ϕ equal to 0.8. The latter quantity is in good agreement with a previous measurement of ϕ made by an exchange technique (SPS 37-31, Vol. IV, pp. 225-228).

The slopes in Figs. 17 and 18 are 38 and 33, respectively, and, combined with $\phi = 0.8$, indicate that $O(^3P)$ reacts with O_2 30 times faster than with C_2H_4 and 25 times faster than with C_2F_4 . Within the experimental error, these values may be taken as equal; therefore $O(^3P)$ reacts with C_2H_4 and C_2F_4 at nearly the same rate.

The second method used for relative rate measurements was based on product analysis and involved competition between olefin pairs for $O(^3P)$. As shown later, the major products of the $O(^3P)$ addition to olefins are the corresponding epoxides and isomeric carbonyl compounds, which are suitable for accurate determination by gas chromatography. Mixtures were photolyzed containing C_2H_4 and a second olefin at a known ratio

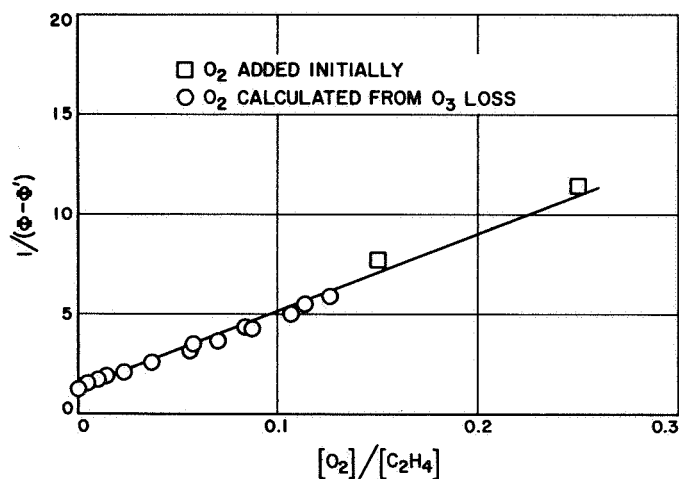


Fig. 17. Quantum yields of O_3 decomposition by the reaction of $O(^3P)$ with C_2H_4

C_2H_4 /olefin, and the product ratios were measured. A correction was made for chromatographic sensitivities. The rate constant ratios could then be calculated by the expression

$$\frac{k_{olefin}}{k_{C_2H_4}} = \frac{[C_2H_4]}{[olefin]} \times \frac{olefin\ products}{C_2H_4\ products} \quad (8)$$

Results for the above measurements are listed in Table 3; experiments at 87.5°K and 77.4°K are included. At 87.5°K, the relative rates for C_2H_4 , C_3H_6 , and 1- C_4H_8 are in the ratio 1:16:20.

c. Products of the $O(^3P)$ reactions. With the exception of C_2F_4 , the major products for each olefin were the corresponding epoxides and isomeric carbonyl compounds. In addition, aldehydes formed by scission of the double bond were found; for example, the formation of propanal

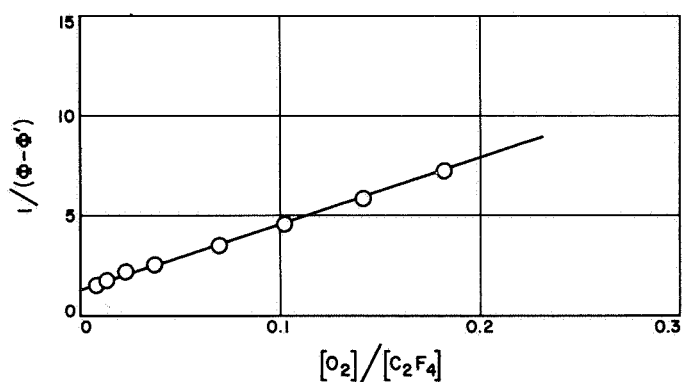


Fig. 18. Quantum yields of O_3 decomposition by the reaction of $O(^3P)$ with C_2F_4

in the reaction of $O(^3P)$ to 1-butene. Table 4 lists products and product ratios for C_2H_4 , C_3H_6 , and 1-butene. Also in Table 4, the observed ratio of epoxide to total isomeric carbonyl compounds is compared to the same ratio obtained by Cvetanovic (Ref. 21) in the gas phase in the high pressure limit. It may be noted that the product distributions from the gas phase work are quite similar to those of the present work.

In addition to the products listed in Table 4, small amounts of H_2 were also found, corresponding to approximately 1–2% of the total products. Carbon monoxide, which is formed in fairly high yields in the gas phase, would not have been detected by the analytical methods of the present experiments.

The material balance was satisfactory since the total oxygen-containing product yields accounted within experimental accuracy (about 15%) for the O_3 decomposed.

In the case of C_2F_4 , the chromatographic analysis was not applicable, since the expected products decompose

Table 3. Rate of $O(^3P)$ addition to C_3H_6 and 1- C_4H_8 relative to addition to C_2H_4

Temperature, °K	$[C_2H_4]$ ($M \times 10^3$)	$[C_3H_6]$ ($M \times 10^3$)	$[1-C_4H_8]$ ($M \times 10^3$)	$[C_2H_4]$ / [olefin]	Product ratio ^a (olefin products / C_2H_4 products)	Ratio $k_{olefin} / k_{C_2H_4}$
87.5	11.6	1.53	—	9.35	1.86	17.4
87.5	12.4	1.53	—	10.4	1.96	20.4
87.5	6.3	2.10	—	3.6	5.55	20.0
87.5	19.2	1.05	—	22.5	0.89	20.0
77.4	12.6	1.26	—	12.6	1.90	23.9
77.4	14.4	1.26	—	14.0	1.87	26.2
87.5	12.6	—	1.26	13.0	1.94	19.1
87.5	15.8	—	0.99	20.3	1.34	20.8

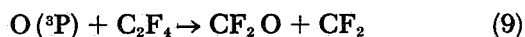
^aChromatographic peak area ratios of products corresponding to $C_nH_{2n} + O$ (aldehydes, ketones, and epoxides) relative to C_2H_4 products (acetaldehyde and ethylene oxide).

Table 4. Major products of O (³P) addition to olefins

Olefin	Products	Ratios	Ratio epoxide/isomeric carbonyls	
			This work	Gas phase (Ref. 21)
Ethylene	Ethylene oxide	0.39	0.75	—
	Acetaldehyde	0.52		
	Formaldehyde	0.09		
Propylene	Propylene oxide	0.50	1.25	1.0
	Propanal } ^a	0.40		
	Acetone }			
Butene-1	Acetaldehyde	0.10	1.29	1.1
	α-Butane oxide	0.53		
	n-Butanal }	0.41		
	Methylethylketone }			
	Propanal	0.05		

^aNot resolved.

on the columns. Therefore, the analysis was made by infrared spectroscopy, and the only product which could be found was CF₂O. The possible products perfluoroethyleneoxide and CF₃CFO were not present in detectable amounts. Evidently, the initial reaction of O (³P) with C₂F₄ is



as is the case in the gas phase (Ref. 25). Unfortunately, the CF₂O analysis was not quantitative, so that it is not clear whether the CF₂ produced by reaction (9) appeared as CF₂O in the final products. Cyclo-C₃F₆, which would be formed by addition of CF₂ to C₂F₄, could not be detected among the products. Further evidence bearing on the fate of CF₂ is the fact that the limiting Φ_{O₃}(³P) from Fig. 18 was 0.8, and not a higher value. If CF₂ reacted quantitatively with O₃ according to



the limiting Φ_{O₃}(³P) would have been about 1.6; i.e., 2 φ. There is thus no evidence for the occurrence of reaction (10), and the fate of CF₂ is not known at the present time.

d. Products of the O (¹D) reactions. In preceding sections, it has been shown that addition of O₂ in the photolysis of O₃-olefin mixtures scavenges O (³P), so that in the limit of high O₂/olefin ratios the residual reaction is due entirely to O (¹D). Figure 19 shows the effect of increasing O₂/C₂H₄ ratio on the total yield of addition products and on the ratio C₂H₄O/CH₃CHO. The yield of C₂H₄O and CH₃CHO decreased from a maximum of

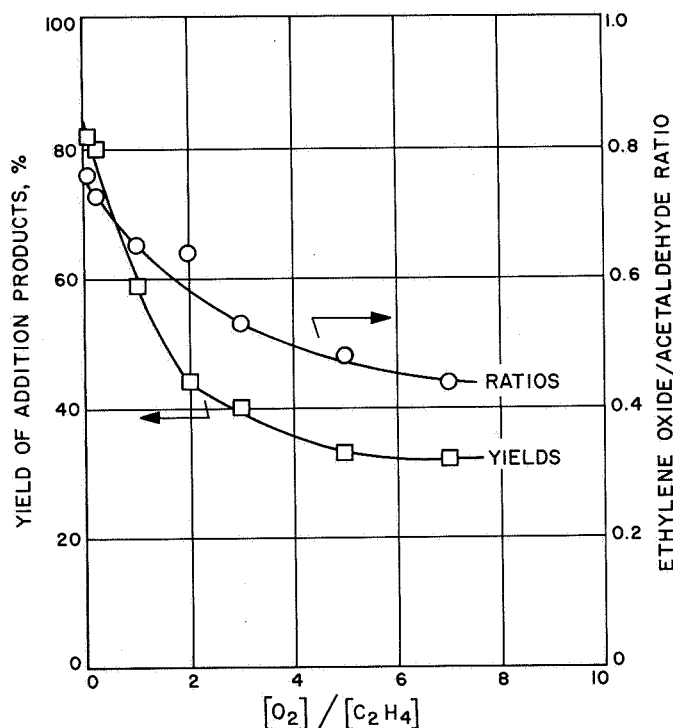
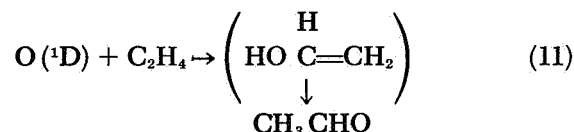


Fig. 19. Effect of the ratio O₂/C₂H₄ on products in the reaction of O (³P) with C₂H₄

about 0.85 for the O (³P) reaction to a minimum of about 0.32 in the limit of pure O (¹D) reaction. The ratio C₂H₄O/CH₃CHO decreases from 0.75 to 0.44 in the same sequence.

In comparing the relative C₂H₄O yields from the O (³P) and O (¹D) reactions, account must be taken of the fact that O (¹D) attacks both C—H and C=C bonds, whereas

O(³P) adds only to the double bond. The probable reaction of O(¹D) with C—H bonds is



where the intermediate vinyl alcohol is unstable and rearranges to acetaldehyde. Therefore, it is necessary to correct the CH₃CHO yield for the amount arising by reaction (11). As shown in Section 4, reaction of O(¹D) with the CH bonds of C₂H₄ accounts for about 40% of the overall reaction. When the latter amount is deducted from the observed CH₃CHO yield, it is found that the C₂H₄O/CH₃CHO ratio resulting from attack of O(¹D) on the C=C bond is approximately unity. It appears, therefore, that for O(¹D) there is a slight increase in the C₂H₄O/CH₃CHO ratio compared with that for O(³P).

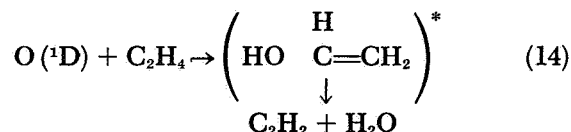
The observed decrease in yield of addition products is accompanied by an increase in the relative CH₂O yield, suggesting increased importance of the reaction



There is some evidence, unfortunately not conclusive, that cyclopropane is formed in trace amounts, particularly in the O(¹D) experiments, by the reaction



The most striking difference in the O(¹D) reactions is the appearance of HC≡CH as a product of the O(¹D) reaction with C₂H₄. The yield was about 1–3%, which is similar to the amount of C₂H₄ formed in the reaction of O(¹D) with C₂H₆. Acetylene is undoubtedly produced by attack of O(¹D) on the CH bonds

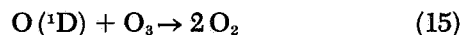


It is not clear at the present time whether both H atoms are removed from the same carbon or from adjacent carbons.

Hydrogen was also observed in the O(¹D) reactions, in somewhat higher yield than for O(³P).

4. Discussion

a. Relative rates of the O(¹D) reactions. The data of Fig. 16 summarize the relative rates of O(¹D) attack on a variety of substrates. The most rapid reaction observed is that with O₃:



For purposes of discussion, it is convenient to express the other rates relative to the O₃ reaction, as in Table 5. An important question then arises as to what factors determine the reactivity of a given substrate. One possibility would be that the reaction rate depends entirely on the dimensions of the reactant molecule, through influence of the cross-sectional area of the molecule on the collision rate. In Table 6 the significant molecular parameters are tabulated on absolute and relative bases. From the latter data, it is clear that the observed relative reaction rates cannot be correlated with the collision cross sections, since, for example, C₂H₄ is smaller than C₃H₈ but is nevertheless more reactive. It is necessary, therefore, to introduce a dependence on bond type to account for the relative reactivities.

In regard to the concept of bond reactivities, two significant relationships can be pointed out on the basis

Table 5. Rates of O(¹D) reactions relative to O₃

Substrate	Relative rate (normalized to O ₃ = 1)
H ₂	0.232
CH ₄	0.267
C ₂ H ₆	0.445
C ₂ F ₄	0.370
C ₃ H ₈	0.570
C ₂ H ₄	0.610
O ₃	1.000

Table 6. Molecular dimensions and collision cross sections

Molecule	σ _r ^a Å	σ ₁₋₂ ^b Å	σ ₁₋₂ ² Å ²	σ ₁₋₂ ² (relative)
H ₂	2.9	2.9	8.4	.73
CH ₄	3.8	3.3	10.9	.94
C ₂ H ₆	4.4	3.6	13.0	1.12
C ₂ F ₄	—	—	—	—
C ₃ H ₈	5.1	3.9	15.2	1.32
C ₂ H ₄	4.2	3.5	12.3	1.07
O ₃	~4.0	3.4	11.6	1.00

^aMolecular diameter.
^bDefined by (σ₁ + σ₂)/2.

of Table 5. First, if the relative reactivity *per C—H bond* is determined from the results for CH₄, C₂H₆, and C₃H₈, an average value of 0.071 ± 0.004 is found. It is shown, therefore, that the reactivities of the saturated hydrocarbons depend, to a close approximation, only on the number of C—H bonds present in the molecule, regardless of the bond types and bond strengths. Second, it may be shown that if the observed reactivity of C₂F₄ is taken to represent the C=C reactivity, since CF bonds are inert to O(¹D), then the relative reactivity of C₂H₄ can be represented quite accurately as the sum of the reactivities of four C—H bonds and one C=C bond. These calculations are summarized in Table 7, and are based on R(CH) = 0.071 and R(C=C) = 0.37. These results show that the C=C is five times more reactive to O(¹D) than a C—H bond.

Table 7. Bond additivity of reaction rates

Compound	Bonds	Relative reactivity	
		Calculated	Observed
CH ₄	4 CH	0.28	0.27
C ₂ H ₆	6 CH	0.43	0.44
C ₃ H ₈	8 CH	0.57	0.57
C ₂ H ₄	4 CH + 1 C=C	0.65	0.61

b. Rates of O(³P) addition to olefins. The data of Figs. 16 and 17 and Table 3 indicate that the relative rates for addition of O(³P) to C₂H₄, C₂F₄, C₃H₆, and 1-C₄H₈ are 1:1:16:20 at 87°K. The different rates are apparently due largely to activation energy differences. For example, the C₂H₄ and C₃H₆ rates point to an activation energy difference $E_a(\text{C}_2\text{H}_4) - E_a(\text{C}_3\text{H}_6) = 0.52$ kcal/mole. The relative rate increases from 16.0 to 20.2 in going from 87.5°K down to 77.4°K, and from this change the calculated value is $E_a(\text{C}_2\text{H}_4) - E_a(\text{C}_3\text{H}_6) = 0.31$ kcal/mole. Thus the relative rates at 87.5°K can probably be used to calculate relative activation energies with an uncertainty of only a few tenths of 1 kcal.

Table 8. Activation energies for addition of O(³P) to olefins

Olefin	E_a , kcal/mole				
	This work ^a	Refs. 22, 23	Ref. 21 ^b	Ref. 26 ^c	Ref. 24
C ₂ H ₄	1.4	1.6	2.6	1.5	1.35
C ₂ F ₄	1.4	—	—	0.6	—
C ₃ H ₆	0.9	—	—	0.6	3.00
1-C ₄ H ₈	0.85 (assumed)	0.85	1.4	—	—

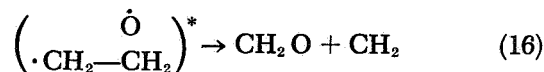
^aAssuming $E_a(1\text{-C}_4\text{H}_8) = 0.85$ kcal/mole.
^bAssuming $E_a(\text{tetramethylethylene}) = 0$.
^cAssuming $E_a(1\text{-C}_4\text{H}_8) = 1.2$ kcal/mole.

The relative values can be placed on an absolute scale provided that any one of the activation energies is shown. The most reliable absolute E_a measurement seems to be for 1-butene, the result being 0.85 kcal/mole (Refs. 22 and 23). In Table 8 the calculated values are tabulated and compared with the results of other workers.

Those values in Table 8 that are greater than 2 kcal/mole are almost certainly in error, since they are completely incompatible with the present low temperature results.

c. Reaction mechanisms. The similar product distributions obtained for O(³P) reactions in the present work and in the gas phase (Ref. 21) attest to the exceedingly short lifetimes of the biradical intermediates of these processes. The effective collision rate in liquids is approximately 10¹² s⁻¹, and therefore the lifetimes of the biradical intermediates must not be greater than 10⁻¹¹ to 10⁻¹² s. It would be difficult to explain the unchanged product ratios if extensive deactivation of the biradical intermediates occurred.

Fragmentation processes of the biradical such as



would be particularly sensitive to the energy loss by the biradical, yet comparison with the gas phase work shows that these processes occur with undiminished efficiency in the liquid.

E. A Physical Frame for Schwarzschild Space-Time, F. B. Estabrook

The Schwarzschild line element is the best known, and also the most studied, exact solution of the Einstein field equations of general relativity. It describes the space-

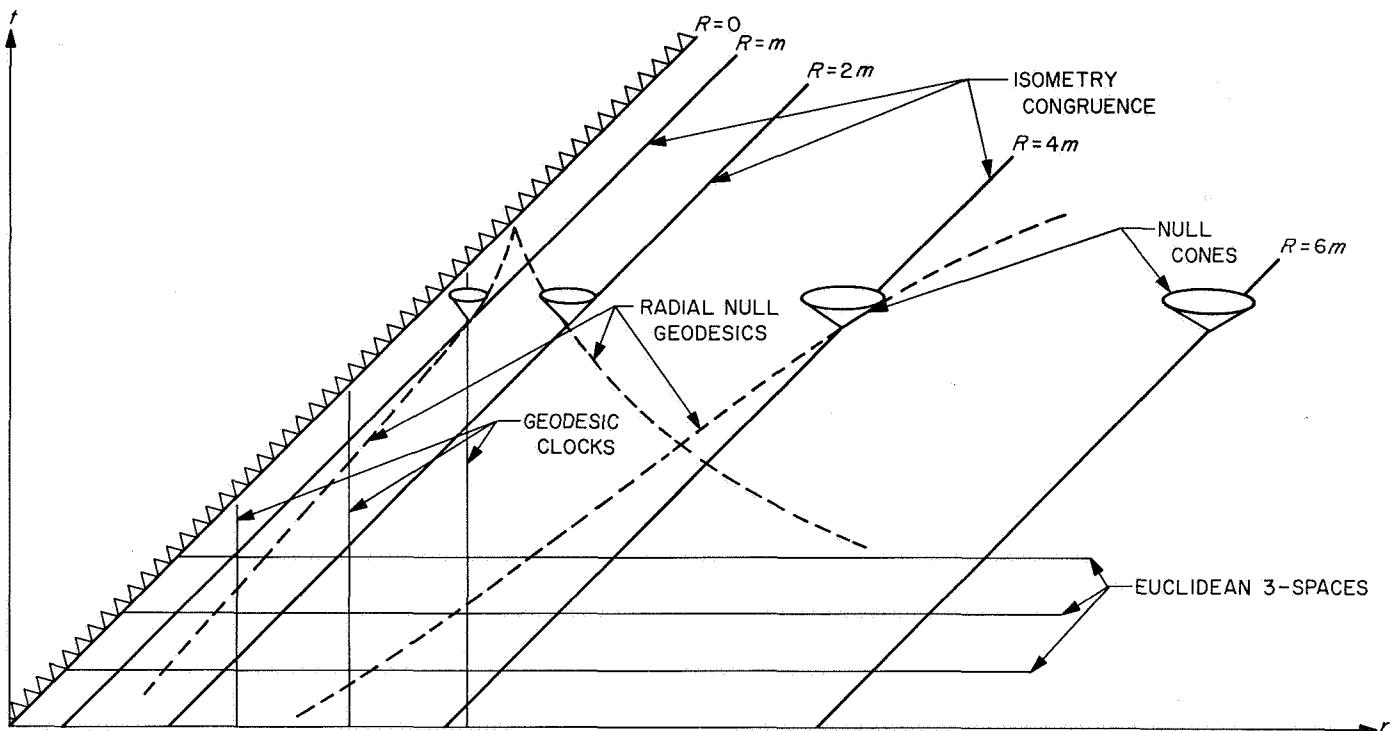
time metric of the empty space around a spherically symmetric distribution of matter. The small deviations from Newtonian theory which it predicts for the motion of planets and light rays about the sun are the basis for the few present local experimental verifications of the theory.

It appears that detailed experimental understanding of solar space-time, as well as careful verification of the general theory through the Schwarzschild solution, will result when the presently achievable accuracy of radar tracking of small transponding interplanetary space probes is fully utilized.

The physical understanding of the predictions of the general theory is often, at first sight, obscure because of the plethora of possible coordinate systems that may be used. Although covariant formulation allows *any* sufficiently well-behaved coordinates to be used, it is always best, in practice, to seek, in a given solution, for intrinsically determined frames. As a facet of a general investigation of this problem, a new and interesting frame for the Schwarzschild metric has been discovered.

The coordinates used by Schwarzschild in the original exact solution were based on an isometry congruence which can be shown to be immersed in the space-time. The Schwarzschild coordinate R and the two angular coordinates θ and ϕ are constant along the lines of this congruence. The Schwarzschild coordinate T is then taken so as to diagonalize the line element. For values $R > 2m$ (m is the mass of the central body in appropriate units) the isometry is timelike, and this region of Schwarzschild space-time is called "static." For values $R < 2m$ the isometry is spacelike; in fact, R is then a timelike coordinate, and T spacelike—a conceptually confusing situation. Moreover, at $R = 2m$, the metric appears to be singular—a result of the use of these particular coordinates. At $R = 0$, the metric is indeed singular, as may be shown by computation of curvature scalars from the Riemann tensor.

It has been discovered that there exists in Schwarzschild space-time a geodesically parallel family of Euclidean 3-spaces. When coordinates t, r, θ, ϕ based on this family are used, the line-element takes the form shown in Fig. 20. The three-dimensional surfaces $t = \text{const.}$ are Euclidean;



$$ds^2 = -dt^2 + \left(\frac{4}{3} \frac{m}{r-t}\right)^{2/3} dr^2 + \left(\frac{9m}{2}\right)^{2/3} (r-t)^{4/3} d\Omega^2$$

Fig. 20. Schwarzschild space-time

in each of these, ordinary spatial geometry obtains. The timelike congruence $r = \text{const.}$, $\theta = \text{const.}$, $\phi = \text{const.}$, normal to the Euclidean spaces, is geodesic: coordinate time, in our frame, is read directly by this family of radial freely falling clocks. The Schwarzschild isometry appears as a family of straight lines along which the metric may

be moved into itself. The *true*, or essential, singularity at $R = 0$ is shown with a saw-tooth. The coordinate singularity at $R = 2m$ now is not present, although by inspection of the paths of light rays it may be seen how this is an event horizon. This coordinate chart covers one-half of a geodesically complete Kruskal diagram.

References

1. Purcell, E. M., "The Focusing of Charged Particles by a Spherical Condenser," *Phys. Rev.*, Vol. 54, p. 818, 1938.
2. Simpson, J. A., "High Resolution, Low Energy Electron Spectrometer," *Rev. Sci. Instr.*, Vol. 35, p. 1698, 1964.
3. Kuyatt, C. A., and Simpson, J. A., "Electron Monochromator Design," *Rev. Sci. Instr.*, Vol. 38, p. 103, 1967.
4. Sturrock, P. A., *Static and Dynamic Electron Optics*, p. 93. Cambridge University Press, Cambridge, England, 1955.
5. Langmuir, D. B., "Theoretical Limitations of Cathode-Ray Tubes," *Proc. IRE*, Vol. 25, p. 977, 1937.
6. Wilkinson, P. G., "Absorption Spectra of Acetylene and Acetylene- d_2 in the Vacuum Ultraviolet," *J. Mol. Spectrosc.*, Vol. 2, p. 287, 1958.
7. Ingold, C. K., and King, G. W., "Excited States of Acetylene: Parts 1-5," *J. Chem. Soc. (London)*, p. 2702, 1953.
8. *Ion-Molecule Reactions in the Gas Phase (Advances in Chemistry Series 58)*. Edited by R. F. Gould. American Chemical Society, Washington, 1966.
9. *NMR and EPR Spectroscopy*. Pergamon Press, New York, 1960 (prepared by Varian Associates Staff).
10. Wobschall, D., Graham, J. R., and Malone, D. P., "Ion Cyclotron Resonance and the Determination of Collision Cross Sections," *Phys. Rev.*, Vol. 131, p. 1565, 1963.
11. Smith, D., and Kevin, L., "Disassociative Charge Exchange of Rare-Gas Ions With C_2F_6 and C_3F_8 ," *J. Chem Phys.*, Vol. 46, p. 1586, 1967.
12. Fischer, I. P., Homer, J. B., and Lossim, F. P., "Free Radicals by Mass Spectrometry. XXXIII. Ionization Potentials of CF_2 , CF_3 , CF_2 , CF_3 , CH_2 , $n-C_3F_7$, and $i-C_3F_7$ Radicals," *J. Am. Chem. Soc.*, Vol. 87, p. 957, 1965.
13. *Formation and Trapping of Free Radicals*, p. 33. Edited by A. M. Bass and H. P. Broida. Academic Press, New York, 1960.

References (contd)

14. Boy, S. F., "Electronic Wave Functions. Part I. A General Method of Calculation for the Stationary States of Any Molecular Systems," *Proc. Roy. Soc. (London)*, Vol. A200, p. 542, 1950.
15. Roothaan, C. C. J., "New Developments in Molecular Orbital Theory," *Rev. Mod. Phys.*, Vol. 23, p. 69, 1951; "Self-Consistent Field Theory for Open Shells of Electronic Systems," *Rev. Mod. Phys.*, Vol. 32, p. 179, 1960.
16. Shavitt, I., "The Gaussian Function in Calculations of Statistical Mechanics and Quantum Mechanics," in *Methods of Computational Physics: Volume II. Quantum Mechanics*, p. 1. Edited by B. Alder, et al. Academic Press, New York, 1963.
17. Roothaan, C. C. J., and Bagus, P. S., "Atomic Self-Consistent Field Calculations by the Expansion Method," in *Methods of Computational Physics: Volume II. Quantum Mechanics*, p. 47. Edited by B. Alder, et al. Academic Press, New York, 1963.
18. Mulliken, R. S., "Electron Population Analysis on Linear Combination of Atomical Orbital-Molecular Orbital Molecular Wave Function," *J. Chem. Phys.*, Vol. 23, pp. 1833, 1841, and 2338, 1955.
19. Wilkinson, J. H., *The Algebraic Eigenvalue Problem*. Oxford University Press, London, England, 1965.
20. Sato, S., and Cvetanovic, R. J., "Photooxidation of Buetenes by Nitrogen Dioxide at Different Wave Lengths," *Can. J. Chem.*, Vol. 36, p. 1668, 1958.
21. Cvetanovic, R. J., "Addition of Atoms to Olefins in the Gas Phase," in *Advances in Photochemistry: Volume 1*, p. 115. Edited by W. A. Noyes, Jr., et al., Interscience Publishers, New York, N.Y., 1963.
22. Elias, L., and Schiff, H. I., "Absolute Rate Measurements of O-Atom Reactions With Ethylene and With Butane," *Can. J. Chem.*, Vol. 38, p. 1657, 1960.
23. Elias, L., "Reinvestigation of Some Absolute Rate Measurements of O-Atom Reactions With Olefins," *J. Chem. Phys.*, Vol. 38, p. 989, 1963.
24. Avramenko, L. I., Kolesnifova, R. V., and Savinova, G. I., "Reaction Rate Constants and the Mechanism of Reactions Between O-Atoms and C₂H₄, Propylene, and Isobutylene," *Izv. Akad. Nauk SSSR, Otd. Khim. Nauk*, Vol. 17, p. 36, 1963.
25. Saunders, D., and Heicklen, J., "The Reaction of Oxygen Atoms With Tetrafluoroethylene," *J. Am. Chem. Soc.*, Vol. 87, p. 2088, 1965.
26. Saunders, D., and Heicklen, J., "Some Reactions of Oxygen Atoms, Part I," *J. Phys. Chem.*, Vol. 70, p. 1950, 1966.

XIX. Communications Systems Research

TELECOMMUNICATIONS DIVISION

A. Combinatorial Communications: The Index of Comma Freedom for the *Mariner Mars 1969* High Data Rate Telemetry Code, L. D. Baumert and H. C. Rumsey, Jr.

1. Introduction

Orthogonal and biorthogonal codes and their indices of comma freedom have been extensively studied (Refs. 1, 2). In this article Stiffler's upper bound for the comma-free index of a general biorthogonal code is improved slightly. Further, a method of Stiffler (Ref. 2) is used to compute an exact value for the index of comma freedom achievable by any coset of the *Mariner Mars 1969* high data rate telemetry code. For this code Stiffler's bound on the comma-free index is 13, whereas our improved formula gives the value 11. Actually, we are able to show that the exact value is 7, and we determine all cosets achieving it; the best value previously achieved was 6. For each of these cosets we give the complete distribution of the correlation values occurring between code words and overlaps of code words.

2. Coding Preliminaries

A Hadamard matrix is a square matrix of 1's and -1 's, whose rows are orthogonal. These rows, considered as code words, constitute an *orthogonal code*. The associated code consisting of these rows and their negatives form a *biorthogonal code*.

It is often convenient to use symbols other than 1 and -1 in the code words. If we define the correlation of two n -tuples to be the number of times they agree less the number of their disagreements, we can preserve the important property of code word orthogonality in any binary representation. (We use both 1, -1 , and 0,1 as our alphabets below, each notation being standard for the computations in which they occur.)

If every overlap $b_2, \dots, b_n, a_1; \dots; b_n, a_1, \dots, a_{n-1}$ possible in a coded message disagrees with every code word of the code in at least i positions, then the code is called *comma-free of index i* . Some receiving systems can distinguish only between agreement and disagreement but

cannot say which is which. For such systems it is convenient to insist that every overlap agree as well as disagree with every code word in at least i positions before one calls the code comma-free of index i . For our purposes (dealing with biorthogonal codes exclusively) there is no distinction between these definitions.

Given a code in 0,1 notation, the code derived from it by adding modulo 2 a fixed 0,1 vector to every code word is a *coset* of the original code. Clearly, such a coset has the same correlation properties as the original code; however, it may have a different index of comma freedom. Thus, if the comma-free index of a code is important, one would like to find a coset code having maximum such index. (A much more comprehensive and leisurely presentation of these definitions and their consequences appears in Ref. 1.)

3. General Upper Bound

The code words of a binary orthogonal code (in 1, -1 notation) form an orthogonal basis for the N -dimensional vector space which they span over the real field. Any m -tuple of ± 1 's ($m \leq N$) will have a correlation of maximal absolute value with one of these coded words. (If $m < N$ we adjoin $N - m$ zero components to our m -tuple.) We wish to compute the minimal such maximal correlation as a function of m . Let x_i, ρ_i denote the code words and the correlations our modified m -tuple y achieves with them. Then

$$\begin{aligned} y \cdot y &= \|y\|^2 = m = \left(\sum_{i=1}^N \frac{\rho_i}{N} x_i \right) \cdot \left(\sum_{j=1}^N \frac{\rho_j}{N} x_j \right) \\ &= \frac{1}{N^2} \sum_{i=1}^N \rho_i^2 (x_i \cdot x_i) = \frac{1}{N} \sum_{i=1}^N \rho_i^2 \end{aligned}$$

Thus, the correlations are such that the average value of their squares is m , i.e.,

$$m = (\rho^2)_{av}$$

Note that in dealing with a biorthogonal code this maximal correlation can be assumed to be positive. So we have

Lemma 1. Let $m \leq N$ and let an N word orthogonal code (in 1, -1 notation) be given. Then, any 1, -1 m -tuple has a correlation in absolute value at least ρ with some word of the code, where $\rho > 0$ is the least integer, such that $\rho^2 \geq m$ and ρ, m have the same parity.

Consider an overlap of two words from a biorthogonal code which consists of the last three symbols of the first

word and the first $N - 3$ symbols of the second word. The $m = N - 3$ symbols give a positive correlation of at least ρ with some word w of the code, where ρ is given by the lemma above. Since N is necessarily even, ρ can be expressed by the formula

$$\rho = 1 - 2 \left[\frac{1 - (N - 3)^{1/2}}{2} \right]$$

where $[x]$ indicates, as usual, the greatest integer $i \leq x$. Since the code is biorthogonal, we may assume that the last three symbols of the first word agree with the first three symbols of the maximal correlation word w , (provided $N \geq 8$). Thus, some overlap has correlation

$$\rho + 3 = 4 - 2 \left[\frac{1 - (N - 3)^{1/2}}{2} \right]$$

with a code word. Hence, an upper bound for the index of comma freedom ($N \geq 8$) is given by

$$\frac{N - \rho - 3}{2} = \frac{N - 4}{2} + \left[\frac{1 - (N - 3)^{1/2}}{2} \right]$$

The first few values of this function are given in Table 1. Except for a few early irregularities, this upper bound improves the previous bound (Ref. 1) by at most 2.

4. The Reed-Muller (32,6) Code

We are interested in computing an exact upper bound for the index of comma freedom achievable by any coset of the Reed-Muller (32,6) code. This code is biorthogonal with 32 symbols per word and is distinguished among all such codes by its unique algebraic structure over GF(2).

Table 1. Upper bounds for the comma-free indices of biorthogonal codes

N	Bound
8	1
12	3
16	4
20	6
24	8
28	10
32	11
64	26
128	56

Much of the work below would be prohibitively harder for any other biorthogonal code of word length 32. This unique algebraic structure facilitates not only our computations but also encoding and decoding of this code. As a consequence, extremely efficient decoding schemes have been worked out for this code (SPS 37-39, Vol. IV, pp. 247-252), whereas nothing comparable is known for other biorthogonal codes of word length 32. Indeed, this algebraic structure is so important for efficient decoding, that it may well be that no comparable decoding algorithms are possible for the other biorthogonal codes of word length 32. Consequently, it is not surprising that this Reed-Muller code has been selected for use in the *Mariner Mars 1969* high data rate telemetry system.

The computation below is nothing more than an exercise in linear algebra; but because it deals with matrices of fairly high dimension, almost every step of the process had to be done by digital computer (SDS 930). Furthermore, high speed memory limitations forced the computation to be broken into many segments. In order to distinguish among these segments they shall be referred to as computer programs A, B, C, ... We recall from linear algebra the concept of *row reduction*. The matrix A is said to row reduce the matrix M if A is nonsingular and AM has the following properties:

- (1) The first nonzero entry in each row is 1, and it is the only nonzero entry in its column.
- (2) Each zero row comes below all nonzero rows.
- (3) Of two nonzero rows the one whose first nonzero entry has the smaller column index also has the smaller row index.

We use a method of Stiffler's (Ref. 2) to compute the desired bound. First note that the Reed-Muller (32,6) code has generator matrix G, where

$$G = \begin{bmatrix} 1 & 0 & 0 & 0 & 0 & 0 \\ 1 & 0 & 0 & 0 & 0 & 1 \\ & & & & & \cdot \\ & & & & & \cdot \\ & & & & & \cdot \\ 1 & 1 & 1 & 1 & 1 & 0 \\ 1 & 1 & 1 & 1 & 1 & 1 \end{bmatrix}$$

That is, G is a 32×6 matrix whose n th row is the binary representation of $n + 31$. The code words arise by matrix

multiplication of G into the 6-tuple of information symbols [arithmetic here is that of $GF(2)$]. Thus, the general form of a word of a coset code is $Gx + c$, where the 32-tuple c is the so-called *coset leader*.

Let G_e^l denote the $l \times 6$ matrix, consisting of the *last* l rows of G, and G_f^l denote the $l \times 6$ matrix, consisting of the *first* l rows of G. Then

$$M_k u + (c + c_k) = \left[G \left| \begin{array}{c} G_e^{32-k} \\ 0 \end{array} \right| \begin{array}{c} 0 \\ G_f^k \end{array} \right] \begin{bmatrix} x \\ y \\ z \end{bmatrix} + (c + c_k) = e \quad (1)$$

is the general form of a vector e whose weight (= number of 1's) is the number of disagreements of the k th overlap of $Gy + c$, $Gz + c$ with $Gx + c$. (Here c_k denotes the k th cyclic shift of c .) Let A_k be a matrix which row reduces M_k . Then

$$A_k M_k u + A_k (c + c_k) = A_k e \quad (2)$$

and, restricting attention to the rows of A_k which annul all columns of M_k (call this submatrix \tilde{A}_k), one has

$$\tilde{A}_k (c + c_k) = \tilde{A}_k e \quad (3)$$

We computed (PROGRAM A) A_k , and, hence, \tilde{A}_k for $k = 1, 2, \dots, 31$. \tilde{A}_{13} is 18×32 , and, when e was allowed to range over all 32-tuples of weight 8 or less, (PROGRAM B) $\tilde{A}_{13} e$ exhausted all possible 18-tuples. Thus, for any c , there is a vector e of weight 8 or less satisfying Eq. (3). This implies that there is a u satisfying Eq. (2); multiplying through by A_{13}^{-1} produces a solution to Eq. (1). Thus, there is, for every coset leader c , at least one vector u such that Eq. (1) is satisfied with an e of weight 8 or less. That is, the maximum index of comma freedom possible for any coset of this Reed-Muller code is 8.

In order to decide whether this bound was attained, we attempted to construct a coset leader which achieved it. \tilde{A}_k is 18×32 for $k = 11, 13$. For $k = 11$ there are 216 18-tuples which do not satisfy Eq. (3) when e is limited to be of weight less than 8 (PROGRAM B). Similarly there are 360 such 18-tuples for $k = 13$. Let v denote a generic member of the 216 and let w be generic for the 360 18-tuples. Then

$$\left[\begin{array}{c|c} \tilde{A}_{11} & 0 \\ \hline 0 & \tilde{A}_{13} \end{array} \right] \begin{bmatrix} c + c_{11} \\ c + c_{13} \end{bmatrix} = \begin{bmatrix} v \\ w \end{bmatrix} \quad (4)$$

Let J be the matrix which corresponds to a cyclic shift of 1 position; i.e., let

$$j_{12} = j_{23} = \cdots = j_{n-1,n} = j_{n1} = 1$$

and $j_{ik} = 0$ otherwise. Then letting $H_k = \tilde{A}_k (I + J^k)$, Eq. (4) becomes

$$\begin{bmatrix} H_{11} \\ H_{13} \end{bmatrix} \begin{bmatrix} c \end{bmatrix} = \begin{bmatrix} v \\ w \end{bmatrix} \quad (5)$$

Let S be the row reduced form under R of the H matrix in Eq. (5); then

$$R \begin{bmatrix} H_{11} \\ H_{13} \end{bmatrix} \begin{bmatrix} c \end{bmatrix} = S \begin{bmatrix} c \end{bmatrix} = R \begin{bmatrix} v \\ w \end{bmatrix} \quad (6)$$

R and S were computed (PROGRAM C). The last 13 rows of S are zero; thus, the last 13 rows of R are constraints on the v, w pairings. (Indeed, only 17 of the $216 \cdot 360$ v, w pairs satisfied these constraints: PROGRAM D.) Since S is 36×32 with rank $36 - 13 = 23$, S has a null space of dimension $9 = 32 - 23$. Thus, for each of the 17 satisfactory v, w pairings, there were $2^9 = 512$ solutions to Eq. (6). These can be derived from any one solution by adding all vectors of the null space of S .

We can reduce these 512 solutions to just $2^3 = 8$ significant ones by noting that if c is a satisfactory coset leader, then so is $c + g$, where g is an arbitrary word of our Reed-Muller code. Thus, any basis for the null space of S (one such can be read off directly from S , since S is in reduced form) can be transformed into another basis for this null space, where 6 of the new basis vectors form a basis for the code (i.e., they may be assumed to be the column vectors of the generator matrix G). The remaining 3 basis vectors generate all significant solutions to Eq. (6). (The fact that this actually happened, PROGRAM E, served as a check on the calculations to this point.)

There were, thus, 8 coset leaders for each of the 17 v, w pairings (PROGRAM D). By means of PROGRAM F, their images $\tilde{A}_9 (c + c_9)$ were generated. These were compared with the table of 18-tuples which did not satisfy Eq. (3) for e 's of weight less than 8 (PROGRAM B). Only 4 coset leaders remained, none of which survived the corresponding test for $k = 15$. Thus, there are no coset leaders which required e 's of weight greater than 7 for $k = 9, 11, 13, 15$. That is,

Lemma 2. Every coset of the Reed-Muller (32,6) bi-orthogonal code has an index of comma freedom less than or equal to 7.

5. Lower Bound

The upper bound for the Reed-Muller code given in the preceding subsection is actually achieved. To show this, we used the same process as above. However, the computations became harder because of the larger number of things which had to be considered. This forced us to modify our approach somewhat.

We computed for $k = 11$ the 31,644 18-tuples which do not satisfy Eq. (3) when e is limited to be of weight less than 7 (PROGRAM B). Similarly, we computed the more than 31,000 such 18-tuples for $k = 13$. As it would have been extremely time consuming to solve Eq. (6) for each of the more than $(31,000)^2$ pairs of v, w so obtained, we were forced to analyze Eq. (6) more closely. Since the last 13 rows of R annul all valid v, w pairs, by restricting attention to these rows, we have

$$\tilde{R}_v v = \tilde{R}_w w \quad (7)$$

For a fixed v , this equation can be solved for all compatible 18-tuples w . In fact, since the null space of \tilde{R}_w is of dimension 5, there are exactly $2^5 = 32$ 18-tuples w which satisfy Eq. (7) when a particular v is used. Not all these 18-tuples belong to the set of $\sim 31,000$ w 's computed by PROGRAM B. Another program (PROGRAM G) was used to solve Eq. (7) for each of the 31,644 possible v 's; it selected for each v those of the 32 possible solutions which were legitimate w 's. This same program then solved Eq. (6) for these 153,098 selected v, w pairs.

As pointed out previously, the matrix S of Eq. (6) has an associated null space of dimension 9, which implies that there are 512 solutions to Eq. (6) for each v, w pair. We can restrict attention to 8 solutions for each valid v, w pairing, as noted above. Thus, there were precisely 8(153,098) coset leaders which satisfied Eq. (6).

These 8(153,098) coset leaders were compared (PROGRAM F) with the table of 18-tuples which did not satisfy Eq. (3) for e 's of weight less than 7 (PROGRAM B), for all other ($\neq 11, 13$) shift values k . In the process, it was observed that one of the 8 vectors from the null space of S had no effect on the calculations. That is, denoting the vector by \mathbf{h} , then $c + \mathbf{h}$ and c were interchangeable insofar as these tests were concerned. This fact was used to shorten the computation. (The vector \mathbf{h} is 0001000100010001000100010001; its behavior is explained below.)

Sixteen coset leaders passed the tests for all cyclic shifts k . Thus, these coset leaders generate cosets of the Reed-Muller (32,6) code which have index of comma freedom 7. Adjoining the vector \mathbf{h} to these yields sixteen more such cosets.

Thus, we have

Lemma 3. There are exactly 32 distinct cosets of the Reed-Muller (32,6) code which have comma-free index 7.

Any coset of this code is generated by $c + g$ as well as by c for all code words g of the code. Hence, there are 64 different coset leaders which generate the same coset. Thus, there are $64(32) = 2048$ coset leaders which can be used to generate a coset of the Reed-Muller (32,6) code with comma-free index 7. These are all vectors of the form $(a_i = 0,1)$

$$c + a_1g_1 + a_2g_2 + \dots + a_6g_6 + a_7\mathbf{h} \quad (8)$$

where

$$g_1 = 010101010101010101010101010101$$

$$g_2 = 00110011001100110011001100110011$$

$$g_3 = 00001111000011110000111100001111$$

$$g_4 = 00000000111111110000000011111111$$

$$g_5 = 00000000000000001111111111111111$$

$$g_6 = 11111111111111111111111111111111$$

$$\mathbf{h} = 00010001000100010001000100010001$$

and c is one of

```

10101100100111000101000000000000
00010011111011101100101101010110
00000000101011111001110001010011
11100010111011101010010101010110
01011111010111010011101001010011
00110101101000110100010100000101
10000100101101001001100101010110
01100110100100111010000001010011
01111010111111001010001000000000
01111110011110010101111100000101
01110010110101110100110001010011
10010011010110000001000000000000
11001010110001100000101000000000
01110111001100101011011111010110
11001100001110110010100100000101
10001011001100100110100111010110

```

If we examine Eq. (1), we can see why the vector \mathbf{h} behaves so curiously. For $(c + \mathbf{h}) + (c + \mathbf{h})_k = (c + c_k) + (\mathbf{h} + \mathbf{h}_k)$ and $\mathbf{h} + \mathbf{h}_k$ is a code word for all values of k . Thus, the effect of replacing c by $c + \mathbf{h}$ is equivalent to changing x in Eq. (1). Since our results depend upon all 64 values of x and not just on particular ones, this has no noticeable effect in Eq. (1) or in any of the subsequent calculations.

Table 2. Correlation distributions

c ρ	1 or 8	2 or 16	3 or 13	4 or 7	5 or 6	9 or 14	10 or 11	12 or 15
± 18	2304	1824	1072	1952	2352	4576	2176	2368
± 16	22896	20272	18928	28368	18976	19824	16640	19904
± 14	39392	41152	41360	37696	38576	39104	39104	41920
± 12	151360	157632	173888	154560	154624	152384	155392	156672
± 10	198048	196448	198496	208736	200896	189984	202432	198272
± 8	551872	533952	496064	527680	550272	549824	556544	544000
± 6	522720	521760	521888	504352	518592	525920	512576	506240
± 4	1044672	1101888	1128640	1025088	1084416	1092800	1089792	1076224
± 2	810400	811680	810048	820128	812448	813280	816576	824064
0	1439136	1353248	1345696	1509344	1364160	1351072	1344000	1387136

6. Correlation Distributions for the Reed-Muller Cosets of Index 7

Index 7 implies that all correlations ρ of code words with overlaps lie in the range $-18 \leq \rho \leq 18$, since $32 - 2 \cdot 7 = 18$. We have computed the distribution of correlation values for each coset of index 7 found in the previous subsection. (For fixed c , all coset leaders of the form $c + \sum a_i g_i + a_7 \mathbf{h}$ have the same correlation distribution.) Only 8 distinct distributions arise, each associated with a pair of c 's. Numbering the c 's according to their position in the list of subsection 5, the distributions are given in Table 2. That is, Table 2 records for each c the number of times the correlation ρ occurs when all code words are compared with all overlaps.

B. Communications Systems Development: Acquisition and False-Lock Behavior of Phase-Locked Loops With Noisy Inputs, R. C. Tausworthe

1. Introduction

It is a well-documented fact that first- and second-order loops are stable and lock onto the incoming carrier, provided the carrier frequency is not separated too far from the voltage-controlled oscillator (VCO) rest frequency. The practical implementation of such loops is seldom ideal because there are usually other time-constants in the loop besides those designed into the loop filter $F(s)$. However, it can be argued that this extraneous characteristic will have little effect on the form of the in-lock loop-equations so long as its bandwidth w_H is much larger than that of the loop w_L . But there are practical limitations on how wide w_H may be made before noise begins to saturate amplifiers, phase detectors, etc., and there is a theoretical limitation on how narrow w_H may be made before the formulas for loop performance are affected.

As w_H is narrowed, the first effect one may notice is not a departure from the performance formulas when the loop is locked, but a degradation in loop frequency-acquisition range known as *false-lock*. This anomaly results when the beat-note between the incoming carrier and the VCO, appearing at the phase-detector output, causes frequency-modulation of the VCO in such a way that one of the frequency-modulated (FM) sidebands of the VCO lies precisely at the carrier frequency. When this occurs, there is a dc voltage out of the phase detector which tends to force the VCO to remain at that particular frequency, falsely phase-locked to a VCO sideband. There are both stable and unstable false-lock frequencies,

just as there are stable and unstable phase-lock points in the normal loop behavior.

The second-order loop phase-plane diagram shown in Fig. 1 exhibits a limit cycle to which trajectories from both above and below converge. In this article we will see analytically what causes such behavior. The treatment is essentially an extension of the methods of Develet (Ref. 3) and Gruen (Ref. 4).

The problem in its most rigorous form is one much too difficult to solve. There are a myriad of possible harmonics of the VCO to which the loop could lock; hence, rather than to enumerate these and give conditions for false-lock in each case, we shall focus our attention mainly on deriving a condition whereby false-lock may be avoided altogether and examine the effect of input noise on this condition.

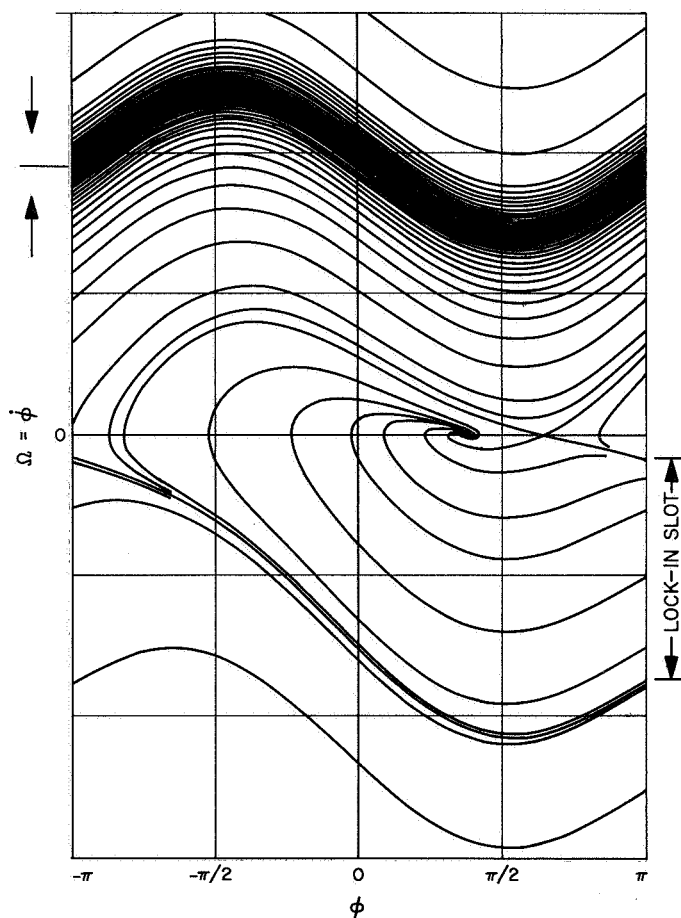


Fig. 1. Lock-in behavior of a second-order loop with imperfect integrator, $F(s) = (1 + \tau_2 s)/(1 + \tau_1 s)$, for $\Omega_0/AK = 0.9$ and $AK\tau_2^2/\tau_1 = 2$

2. Limit Cycles in the Loop

Suppose a phase-locked receiver is in a false-lock condition, and assume that a frequency offset ($\theta = \Omega_0 t + \theta_0$) is incident to the loop. Then in order to produce a stable condition, the VCO input must be a periodic function of time. When noise is incident to the loop, it is also then clear that for a suitable choice of the time origin, the phase error ϕ takes the form

$$\phi = \psi + \nu t + \phi_0 + a_1 \sin \omega t + \dots \quad (1)$$

for appropriate nonrandom ν , ϕ_0 , $a_1 \geq 0$, and $\omega \geq 0$, each to be determined, and for a low-frequency zero-mean random process ψ . We may also consider $\Omega_0 > 0$, as a completely symmetric argument will account for $\Omega_0 < 0$. We shall suppose that the higher harmonic terms of Eq. (1) are negligible as, indeed, a more detailed analysis will verify. The phase error must satisfy the usual loop equation

$$\Omega_0 = \dot{\phi} + AKF(p) \left\{ \sin \phi + \frac{n(t)}{A} \right\} \quad (2)$$

where A is the incoming rms signal voltage; K the open-loop gain; $F(s)$ the loop-filter transfer function; p the Heaviside operator; and $n(t)$ the baseband equivalent input noise process with spectral density N_0 . Thus we must have

$$\begin{aligned} \Omega_0 = & \dot{\psi} + \nu + a_{1\omega} \cos \omega t + AKF(p) \\ & \times \left\{ \sin [\psi + \nu t + \phi_0 + a_1 \sin \omega t] + \frac{n(t)}{A} \right\} \quad (3) \end{aligned}$$

The solution of Eq. (3) is effected by equating the coefficients of each harmonic zone in the series to zero. [Higher harmonic terms may fail to vanish because of the simplified form we assumed for ϕ in Eq. (1); nevertheless, these terms should be very small.]

The loop filter function $F(s)$ represents the total open-loop response of the output frequency to the phase detector error; this nominally contains IF filters, system delays, VCO output filtering, etc., in addition to the normal design loop filter. The actual loop function $F(s)$ over the frequency range of interest often can, for example, be approximated by

$$F(s) = \left(\frac{1 + \tau_2 s}{1 + \tau_1 s} \right) e^{-s\tau} \quad (4)$$

in which τ is the loop *excess delay*. The expression in parentheses is the ordinary second-order loop filter.

The assumption necessary to carry out a simple analysis is that

$$\omega \gg AK |F(j\omega)| \quad (5)$$

For the usual first- and second-order loops, this condition reduces to $\omega \gg 2\omega_L$. The hypothesis is a reasonable one, as it merely requires¹ that if there is a false-lock its offset frequency lies outside the bandwidth of the loop.

It is evident in Eq. (3) that the cosine coefficient $a_{1\omega}$ must be related to a term in the expansion of $\sin \phi$, and therefore

$$a_{1\omega} \leq AK |F(j\omega)| \quad (6)$$

This bound can be combined with our assumption to reveal that

$$a_1 \leq \frac{AK |F(j\omega)|}{\omega} \ll 1 \quad (7)$$

Since a_1 is so small, we can approximate $\cos a_1 \approx 1$ and $\sin a_1 \approx a_1$ with excellent accuracy to produce the equation

$$\begin{aligned} \Omega_0 = & \dot{\psi} + \nu + a_{1\omega} \cos \omega t + AKF(p) \left\{ \sin (\nu t + \psi + \phi_0) \right. \\ & \left. + a_1 \sin \omega t \cos (\nu t + \psi + \phi_0) + \frac{n(t)}{A} \right\} \quad (8) \end{aligned}$$

from which it is clear that either $\nu = 0$, or $\nu = \omega$. But $\nu = 0$ leads to the conclusion that $\omega < AK |F(j\omega)|$, contrary to our hypothesis. One equation relating the various parameters can be gotten by averaging Eq. (8) with respect to sample functions of the input noise $n(t)$

$$\begin{aligned} \Omega_0 = & \nu + a_{1\omega} \cos \omega t + \delta AKF(p) \{ \sin(\nu t + \phi_0 + \psi_0) \\ & + a_1 \sin \omega t \cos(\nu t + \psi_0 + \phi_0) \} \quad (9) \end{aligned}$$

¹It is interesting to note that in a more detailed analysis this same condition also insures that the second harmonic coefficient a_2 of ϕ is much smaller than a_1 . Such a condition thus also insures that the representation of ϕ given in Eq. (1) is a sufficient one for the analysis here.

in which $\psi_0 = \arctan [E(\sin \psi)/E(\cos \psi)]$ and $\delta = E(\cos \psi)/\cos \psi_0$. It is evident in Eq. (9) that $\omega = \nu$, and that a_1 , ϕ_0 , and ω must satisfy the conditions

$$\Omega_0 = \omega - \frac{\delta AK F a_1}{2} \sin(\phi_0 + \psi_0) a_{1\omega} \cos \omega t + \delta AK |F(j\omega)| \times \sin[\omega t + \psi_0 + \phi_0 + \arg F(j\omega)] = 0 \quad (10)$$

with $F = F(0)$. Obviously, the latter of these two equations can be satisfied only when

$$\psi_0 + \phi_0 = (4k - 1)\pi/2 - \arg F(j\omega) \quad (11)$$

$$a_1 = \frac{\delta AK |F(j\omega)|}{\omega}$$

and these, along with the first equation in (10) produce the false-lock condition

$$\Omega_0 - \omega = \frac{(\delta AK)^2 F |F(j\omega)|}{2\omega} \cos[\arg F(j\omega)] \quad (12)$$

As a special case, for example, the approximate loop characteristic given by the $F(s)$ in Eq. (4) produces the noise-extended Develet equation

$$\Omega_0\tau - \omega\tau = \left(\frac{r^2\tau_1\tau^2\delta^2}{2\tau_2^3} \right) \frac{\cos \omega\tau}{\omega\tau} \quad (13)$$

in terms of the parameter $r = AK\tau_2^2/\tau_1$. Solutions to this equation are readily obtained graphically, as in Fig. 2, or by iteration, and correspond to stable and unstable false-locks.

The effect of the noise is clearly displayed in the factor δ multiplying AK : the behavior is the same as one would notice if no noise were present and the loop gain reduced by a factor δ .

3. Loop Acquisition Range

Since we are looking for a way to avoid false-locks, let us seek the largest Ω_0 for which Eq. (12) has no solutions. This value we will define as the *acquisition range*. It is the largest frequency offset for which the loop will lock, regardless of the VCO initial conditions. As indicative of the method, we shall limit our attention, for the present, to the simplified example of Eq. (4). Referring to Fig. 2, one can readily see that the critical case occurs when the line $y_1 = \Omega_0\tau - \omega\tau$ is just tangent to the curve

$y_2 = \lambda (\cos \omega\tau)/\omega\tau$, λ taking the value in parentheses of Eq. (13). Since there is a multiple root involved at the point of tangency, both the equation $\omega\tau(\Omega_0\tau - \omega\tau) - \lambda \cos \omega\tau = 0$ and its derivative can be solved simultaneously for $\Omega_0\tau$ and $\omega\tau$, but the roots are transcendental. It is, of course, clear that the smaller τ is, the wider the frequency-acquisition interval is.

When λ is small, the corresponding $\omega\tau$ is less than $\pi/2$ where, in fact, $\cos \omega\tau \approx 1 - (\omega\tau)^2/2$. This approximation yields a quadratic equation for $\omega\tau$, which must then have two equal roots because of the point of tangency. The two roots are equal when the quadratic discriminant is zero, a condition which requires $(\Omega_0\tau)^2 = 4\lambda(1 - \lambda/2)$. As a final result, the condition under which no false-locks occur for such λ is

$$\Omega_0\tau < 2[\lambda(1 - \lambda/2)]^{1/2} \quad (14)$$

For the usual second-order loop with $r\tau_1 \gg \tau_2$ and in terms of the in-lock loop bandwidth ω_L , this condition is

$$\frac{\Omega_0}{\omega_L} < \frac{4r\delta}{r+1} \left(\frac{\tau_1}{2\tau_2} \left[1 - \frac{\tau_1}{\tau_2} \left(\frac{\delta r \omega_L \tau}{r+1} \right)^2 \right] \right)^{1/2} \quad (15)$$

which, as $\tau \rightarrow 0$, reduces to the case

$$\frac{\Omega_0}{\omega_L} < \frac{4r\delta}{r+1} \left(\frac{\tau_1}{2\tau_2} \right)^{1/2} \quad (16)$$

Except for the factor δ , this result is the same as that found in Gruen, Develet, and Viterbi (Refs. 4, 3, and 5, respectively).

Of special note in Ineq. (14) is the fact that λ cannot be made too large without seriously degrading the loop lock-in range. According to Ineq. (14), there is an optimum value of λ somewhere around unity. This is not a particularly good approximation of λ_{opt} because it corresponds to $\omega\tau = 2$, a value too large for our estimation of $\cos \omega\tau$.

When the condition (14) is violated, both stable and unstable lock-frequencies are contained in the transcendental solutions of Eq. (13). Physical reasoning based on small perturbations away from the intersection in Fig. 2 indicates that the only stable solutions are those in which the angle from the line to the curve has a *clockwise* rotation. Since stable and unstable points alternate, it is obvious that the system will eventually drive to one of the stable points.

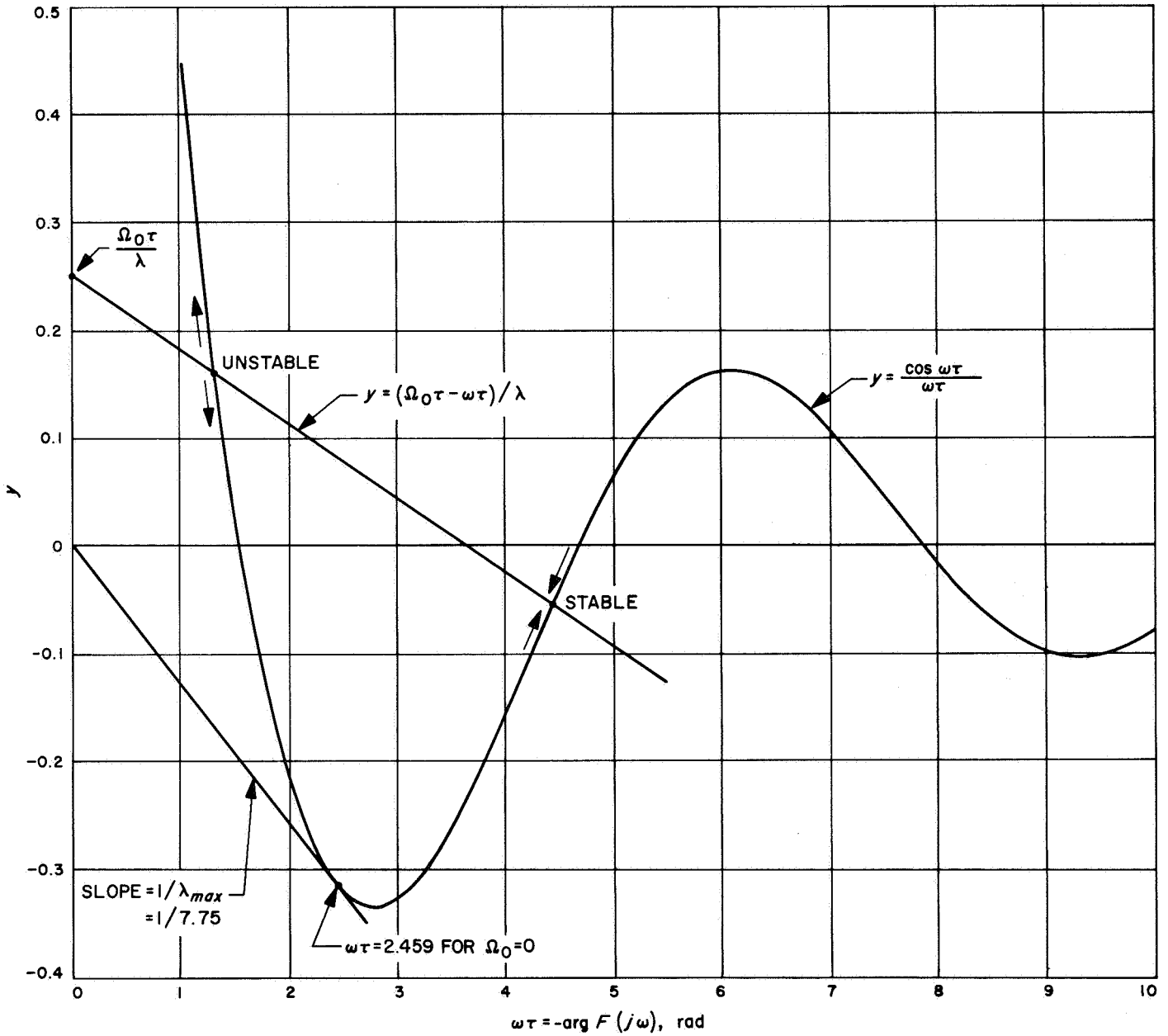


Fig. 2. Graphical method for solutions to the false-lock condition $\Omega\tau - \omega\tau = \lambda \cos(\omega\tau)/\omega\tau$

It is interesting and significant that the first solution (intersection), when one exists, is always unstable. If the VCO initial condition produces an initial $\omega\tau$ somewhat larger than this solution, the loop will be driven away from signal lock to a stable point at higher $\omega\tau$; if $\omega\tau$ is less, the loop is driven to the stable solution $\omega\tau = 0$, and the loop locks to the incoming signal phase. It should be remembered that solutions to Eq. (13) are only valid when the restriction $\omega \gg AK|F(j\omega)|$ is met; hence, $\omega\tau = 0$ does not appear as one of the solutions in Fig. 2, although there is always a stable lock there.

As λ increases to the degree at which the critical value of $\omega\tau \rightarrow \pi/2$, the approximation $\cos \omega\tau \approx \pi/2 - \omega\tau$ is a better one than $1 - (\omega\tau)^2/2$, in which case Ineq. (14) would be replaced by

$$\Omega_0\tau < (2\pi\lambda)^{1/2} - \lambda \quad (17)$$

or for the usual case $r\tau_1 \gg \tau_2$,

$$\frac{\Omega_0}{\omega_L} < \frac{2r\delta}{r+1} \left(\frac{\pi\tau_1}{\tau_2} \right)^{1/2} \left[1 - \frac{r\omega_L\tau\delta}{r+1} \left(\frac{\tau_1}{\pi\tau_2} \right)^{1/2} \right] \quad (18)$$

Again we see that λ cannot be made too large without seriously degrading the lock-in range. The optimum λ according to Ineq. (18) is at $\lambda_{opt} = \pi/2$ for $\omega\tau = \pi/2$, a point accurately given by the cosine approximation.

$$\lambda_{opt} = \frac{2\tau_1}{\tau_2} \left(\frac{r\tau\delta\omega_L}{r+1} \right)^2 = \pi/2 \quad (19)$$

Finally, when λ is still larger, the critical $\omega\tau \rightarrow \pi$, so the proper approximation is $\cos \omega\tau \approx -1 + (\omega\tau - \pi)^2/2$, leading to

$$\Omega_0\tau < -\lambda\pi + [\lambda(2+\lambda)(\pi^2-2)]^{1/2} \quad (20)$$

These approximations are very good for algebraic evaluation of the lock-in range; the actual lock-in range as a function of λ is shown in Fig. 3, with each of the approximations.

With a fixed value of excess loop delay τ , the curve in Fig. 3 puts an upper bound on the ratio τ_1/τ_2 (and thus the loop gain) which can safely be used. In fact, if λ is ever greater than 7.75, the lock-in range drops to zero so the loop will not acquire lock for all initial conditions of

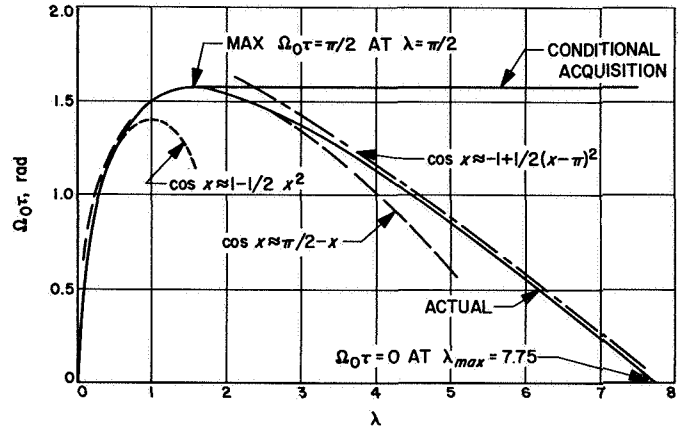


Fig. 3. Value of $\Omega_0\tau$ producing marginal acquisition as a function of the parameter $\lambda = \frac{1}{2} (\delta AK\tau)^2 F |F(j\omega)|$, along with approximate curves to show their region of applicability

the VCO. The maximum excess loop delay must, therefore, not exceed

$$\tau < \frac{r+1}{\omega_L r \delta} \left(\frac{3.875\tau_2}{\tau_1} \right)^{1/2} \quad (21)$$

if the loop is to acquire lock unconditionally. One startling conclusion which may be reached at this point is that a perfect-integrator loop ($\tau_1 \rightarrow \infty$) will always have false-lock points, but a loop with an imperfect-integrator in the loop filter may not.

One must be careful not to interpret the optimum λ in Fig. 3 wrongly; while it is true that $\Omega_0\tau$ is maximized at $\lambda = \pi/2$, Ω_0 itself is always maximized when $\tau = 0$. As illustrated in Fig. 4, which shows how Ω_0 and τ are interrelated at the critical false-lock condition, the acquisition range is monotonically decreasing in τ . The figure also implicitly shows how the lock-in interval is related to the loop parameter

$$\mu = \delta AK \left[\frac{F|F(j\omega)|}{2} \right]^{1/2} = \frac{r\delta}{\tau_2} \left[\frac{\tau_1}{2\tau_2} \right]^{1/2}$$

which simultaneously stretches the ordinate and shrinks the abscissa.

The way $\omega\tau$ at critical false-lock varies as a function of $\lambda = \mu^2\tau^2$ is depicted in Fig. 5, and $\Omega_0\tau$ and $\omega\tau$ are cross-plotted in Fig. 6.

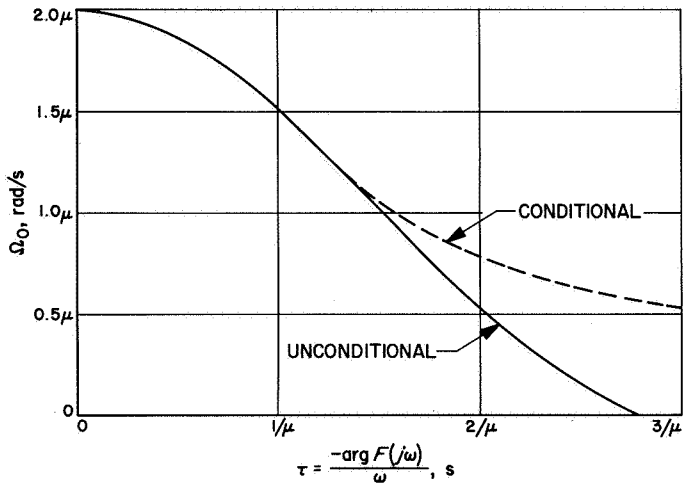


Fig. 4. Acquisition range as a function of loop-filter time delay at critical false-lock frequency, normalized by the parameter $\mu = \delta AK(F | F(j\omega) | / 2)^{1/2}$

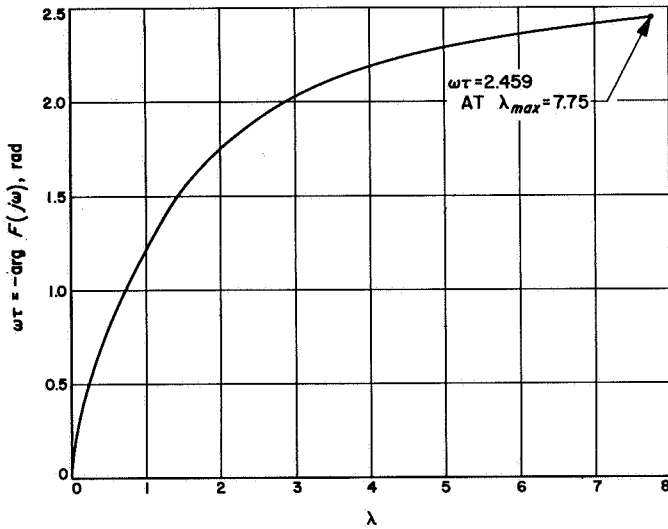


Fig. 5. Variation of loop-filter phase angle at critical false-lock as a function of the parameter

$$\lambda = \frac{1}{2} (\delta AK \tau)^2 F | F(j\omega) | = \mu^2 \tau^2$$

4. Conditional Acquisition Range

Under the restriction that the initial VCO offset is $\omega_{init} = \Omega_0$, as will be the case when the loop is open prior to acquisition, we can see from Fig. 2 that the loop will lock provided $\Omega_0 \tau$ is less than the first (unstable) false-lock solution. Since the line y_1 intersects the abscissa at $\Omega_0 \tau$, and since y_2 intersects first at $\omega \tau = \pi/2$, it is clear that this conditional acquisition will take place whenever $\Omega_0 \tau < \pi/2$ for $\lambda > \pi/2$. With $\lambda < \pi/2$ there is no conditional lock-in: if the loop locks in with $\omega_{init} = \Omega_0$, it will lock for all conditions of the VCO.

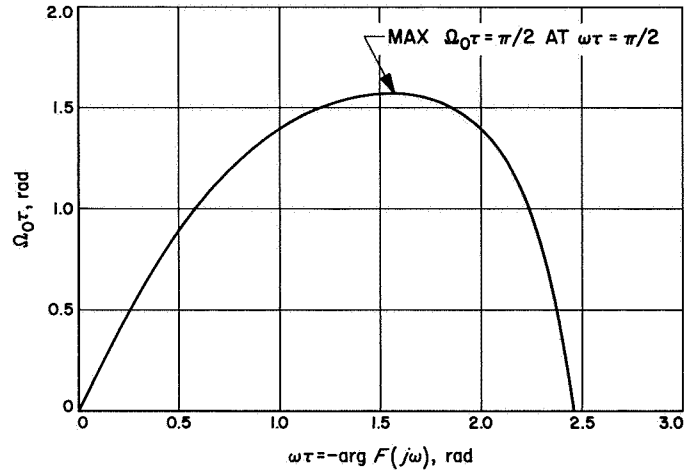


Fig. 6. Value of $\Omega_0 \tau$ producing critical acquisition as a function of loop-filter phase angle $\omega \tau$ at critical false-lock frequency

One aspect worth noting whenever $\lambda > \pi/2$ is that the conditional acquisition range $\Omega_0 = \pi/2\tau$ is not a function of the loop gain, bandwidth or damping factor, but depends only on the value of excess loop delay. Figure 3 indicates the conditional acquisition range as a function of λ , and Fig. 4 translates the behavior to a function of τ .

5. The Effects of Extraneous Time Constants

The analysis for the example in subsection 3 was carried out under the assumption that the effect of extraneous time constants internal to the loop could be approximated by $e^{-\tau s}$. This assumption is clearly valid over a certain frequency range, but it cannot extend beyond the band-edge of the extraneous filter characteristic, for example. In a more detailed analysis, these extraneous effects should be represented by their true response, call it $F_x(s)$

$$F(s) = \left(\frac{1 + \tau_2 s}{1 + \tau_1 s} \right) F_x(s) \quad (22)$$

We still assume $F_x(0) = 1$, but in addition to the phase lag $\xi (= \omega \tau$ in the previous analysis), there is also an attenuation $F_x = |F_x(j\omega)|$

$$F_x(j\omega) = F_x e^{-j\xi} \quad (23)$$

The largest value that the excess phase shift $\xi = -\arg F_x(j\omega)$ can reach is limited by the number of poles and zeros in the extraneous filter $F_x(s)$. Specifically, if the order of $F_x(s)$ at infinity is n (i.e., there are n more poles than zeros), then

$$\xi \leq n\pi/2 \quad (24)$$

The true response $F(s)$ when inserted in the false-lock condition (12) modifies the previous condition (13) only slightly to read

$$\Omega_0 - \omega = \left(\frac{F_x r^2 \tau_1 \delta^2}{2\tau_2^3} \right) \frac{\cos \xi}{\omega} \quad (25)$$

Each side of Eq. (25) is conveniently plotted whenever F_x and ξ are known or measured functions of ω . Such a plot reveals the false-lock character of the receiver. However, by defining $\tau = \tau(\omega) = \xi/\omega$, we produce an equation analogous to Eq. (13) from which much insight is available.

$$\begin{aligned} \Omega_0 \tau - \omega \tau &= \left(\frac{F_x r^2 \tau_1 \tau^2 \delta^2}{2\tau_2^3} \right) \frac{\cos \omega \tau}{\omega \tau} \\ &= \lambda' \frac{\cos \xi}{\xi} \end{aligned} \quad (26)$$

relative to the restriction $\omega \tau \leq n\pi/2$. The only difference between Eqs. (26) and (13) is that λ' and $\Omega_0 \tau$ are functions of ω , so even the simplified bounds, Ineqs. (14), (17) and (20), we derived for Ω_0 are transcendental in ω . It is usually the case that $F_x < 1$ and that $\lambda' < \lambda_{opt}$. As a result, the value of the maximum allowable Ω_0 is degraded whenever $F_x(s)$ departs significantly from unity. What this means, insofar as loop design is concerned, is that the frequency acquisition interval can be limited, perhaps very severely, whenever the $F_x(s)$ is too narrow or has too many poles.

Whenever a false-lock condition exists, it can sometimes be broken by slowly tuning the VCO to reduce Ω_0 until a solution of Eq. (26) no longer exists. For loops with $\lambda' > 7.75$, this requires tuning until Ω_0 goes *negative* (we assumed it was positive to start with). That is, to acquire an incoming signal higher in frequency than the VCO, it may be necessary to tune the VCO to a frequency *above* that coming in just to break false-lock. But then the loop may false-lock again because of the negative Ω_0 seen by the loop. In such cases the operator must open the loop, tune the VCO near enough the incoming frequency that the initial $\omega \tau$ lies below the first (unstable) false-lock, then close the loop. Such acquisition is conditional, as it will not occur for all initial conditions of the VCO.

6. Calculation of δ

It thus remains only to evaluate δ . The subtraction of Eq. (9) from Eq. (8), evaluated only in the low-frequency zone, shows that the false-lock phase error ψ must satisfy

$$\dot{\psi} + \frac{1}{2} a_1 AKF(p) \left\{ -\sin(\psi + \phi_0) + \delta \sin(\psi_0 + \phi_0) + \frac{2n(t)}{a_1 A} \right\} = 0 \quad (27)$$

which, with ϕ_0 removed by Eq. (11), reads

$$\dot{\psi} + \frac{1}{2} a_1 AKF(p) \left\{ \cos[\psi - \psi_0 - \arg F(j\omega)] - \delta \cos[\arg F(j\omega)] + \frac{2n(t)}{a_1 A} \right\} = 0 \quad (28)$$

This equation is almost the same as the normal in-lock phase error, except that A has been replaced by $\frac{1}{2} a_1 A$ and the sinusoidal phase-detector characteristic by

$$g(\psi) = \cos[\psi - \psi_0 - \arg F(j\omega)] - \delta \cos[\arg F(j\omega)] \quad (29)$$

We shall approximate ψ by a zero-mean gaussian process with variance c^2 and use the linear spectral method (Ref. 6) to compute c^2 . Straightforwardly, one may then verify that $\psi_0 = 0$, because $E(\sin \psi) = 0$; and, as a result,

$$\delta = E(\cos \psi) \equiv e^{-c^2/2} \quad (30)$$

For simplicity it is necessary at this point to restrict $F_x(s) = 1$ (i.e., have no extraneous effects in the loop). With this done,

$$\begin{aligned} \eta &= 0 \\ \gamma^2 &= \frac{1}{2} \left[\frac{1 - e^{-c^2}}{c} \right]^2 \approx \frac{1}{2} c^2 \end{aligned} \quad (31)$$

The variance c^2 has been tabulated in terms of the parameters of the second-order loop as [Eqs. (9-28) and (9-29) of Ref. 6]

$$c^2 = \frac{N_0 \omega_L}{A^2 \gamma^2} \frac{(1 + r\gamma)}{(1 + r)(1 + \tau_2/r\tau_1\gamma)} \left[1 + \frac{2(1 - \tau_2/\tau_1)}{r\gamma(1 + \tau_2/r\tau_1\gamma)^2} \right]^{1/2} \quad (32)$$

Further, at the marginal false-lock [i.e., the double-root condition for Eq. (12)] we find

$$\begin{aligned} \omega &= \frac{\Omega_0}{2} = \frac{\delta r}{\tau_2} \left(\frac{\tau_1}{2\tau_2} \right)^{1/2} \\ a_1 &= \frac{\delta r}{\tau_2 \omega} = \left(\frac{2\tau_2}{\tau_1} \right)^{1/2} \end{aligned} \quad (33)$$

Substitution of $\frac{1}{2}a_1A$ for A , along with η , γ , and a_1 above, produces the estimate

$$c^2 = \frac{4(1 + \frac{1}{2}a_1r\gamma)}{\rho a_1^2 \gamma^2 (r+1) [(1 + a_1/r\gamma)^2 + 2/r\gamma]^{1/2}} \quad (34)$$

in terms of the linear-theory in-lock signal-to-noise ratio (SNR), $\rho = A^2/N_0\omega_L$, following the assumption $\tau_1 \gg \tau_2$. A solution can be found by inserting the receiver parameters into Eq. (34), assuming a particular value of c^2 , and solving for the loop SNR required. Figure 7 illustrates then how c^2 and δ vary as a function of ρ for various loop configurations.

7. Lock Detection and Automatic Gain Control Readings

Most receivers are fitted with quadrature detectors to detect lock, calibrate signal strength, and provide automatic gain control. The synchronously-detected automatic gain control (AGC) waveform is $AK_D \cos \phi$, which, with no false-lock in effect, would deliver AK_D volts dc into the AGC system; with a false-lock, however, the dc component is only a fraction of this, namely

$$E(\cos \phi) = -\frac{a_1 \delta}{2} \sin [\arg F(j\omega)] \quad (35)$$

as large. Thus, depending on $\arg F(j\omega)$, the AGC detector reading may be negative or positive. The incoming signal level is often known or predictable to a certain degree *a priori*, in which case false-locks can be detected by comparing the false-lock AGC reading with that predicted.

Whenever $E(\cos \phi)$ is positive, the false-lock AGC voltage will be the same as that produced by another input signal only $[E(\cos \phi)]^2$ as strong, but *in lock*. Thus, even

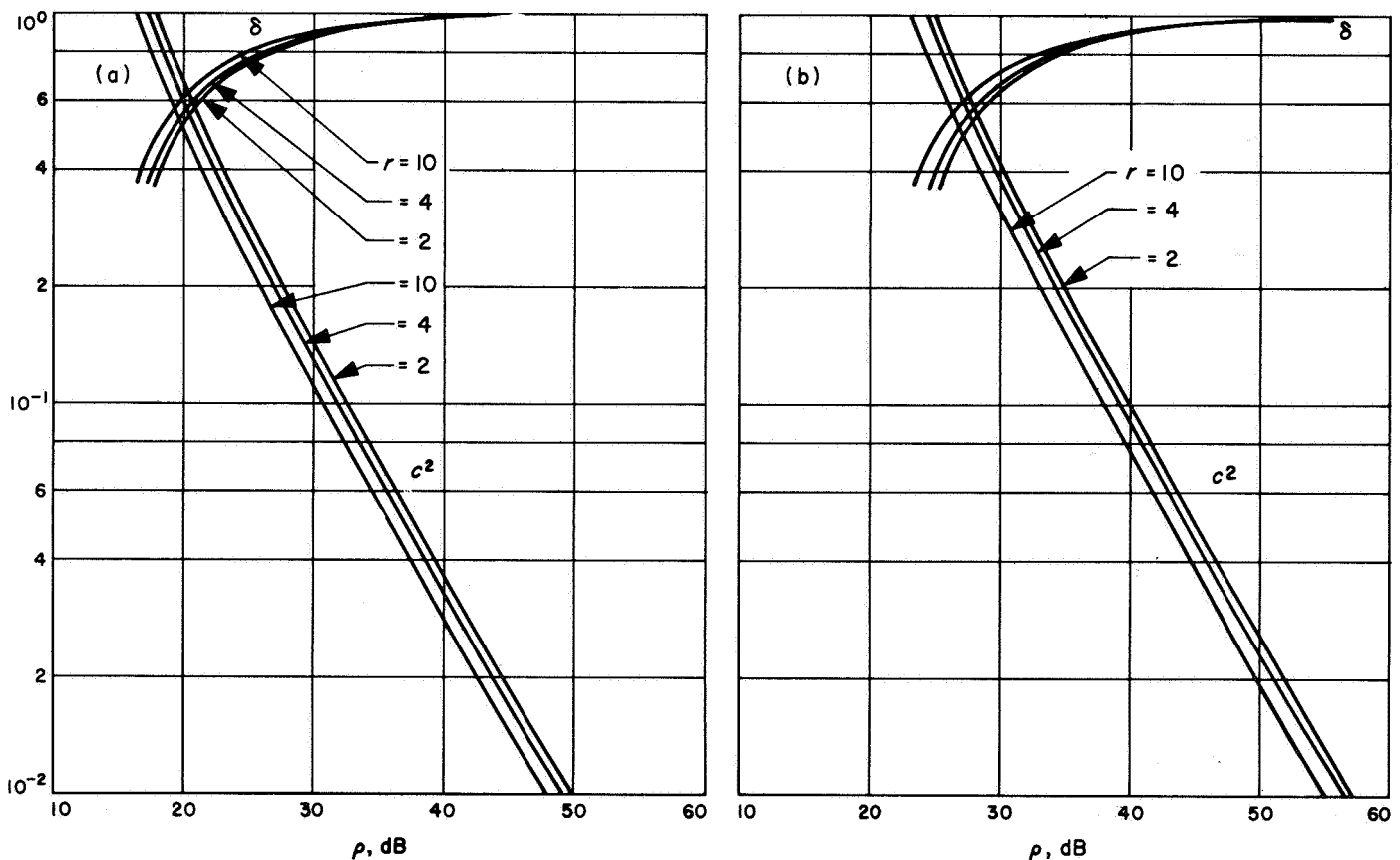


Fig. 7. Variation of false-lock phase error c^2 and signal degradation factor $\delta = E(\cos \psi)/\psi_0$ as a function of loop SNR: (a) $\tau_2/\tau_1 = 0.01$; (b) $\tau_2/\tau_1 = 0.001$

though a_1 is relatively small, a sensitive receiver may indicate that lock has been achieved on a signal many dB below the actual signal level.

Whenever $E(\cos \phi)$ is negative, however, the receiver gain drives to its maximum—normally a no-signal indication—and hangs up. It is not unusual in such cases for the receiver IF amplifier, etc., to be severely overdriven. Since amplifiers often have phase-delay characteristics different when overdriven than when operating linearly, it is usually difficult to predict accurately what the false-lock frequency will be in such a case.

Some false-locks will thus be strong enough to give an AGC voltage sufficient to indicate that a lock is in effect; others produce a negative or very small AGC voltage, a no-signal indication when in truth it is in a false-lock condition. The latter situation is sometimes very difficult to detect, for an oscilloscope connected to the detector output will show the presence of a beat note, but only if noise is small enough. It can also be very confusing, as for example, when the operator, not seeing a lock indication, attempts to tune the VCO until a lock is indicated, but finds that the tuning control is inoperative—that is, that there is not enough VCO voltage range to break the false-lock. It is also possible for an indicating false-lock to go completely undetected until later reduction of doppler data comes up with some ridiculous doppler shift. For these reasons the importance of proper acquisition procedures and adequate design measures are self-evident.

C. Communications Systems Development: Phase-Locked Loops With Externally Aided Track, R. C. Tausworthe

1. Introduction

One of the most fundamental concepts of communication theory is that no system has been optimized until it makes full use of known or predictable variations in the system parameters. This concept applied to a receiver says, for one thing, that its best operation will be obtained only when the known or predictable part of the incoming signal phase function is removed, so that the loop is only required to track unpredictable variations in signal phase. To a certain extent, the optimized loops in Jaffee and Rechtin (Ref. 7) do precisely this, as, for example, pointed out by the fact that a loop required to follow a doppler offset has an integration in the loop filter in order to tune its voltage-controlled oscillator (VCO) output to the actual incoming frequency automatically. Had the doppler offset been known *a priori*,

the loop could have been pretuned to the correct frequency, so the integrator would not have been needed. Had the offset been known only approximately, the lesser-order loop could still have been pretuned to the expected arrival frequency, and then, once the loop was locked, tuned to remove steady-state phase error.

What the foregoing discussion shows is that the loop's complexity, or bandwidth, or both can be reduced by an external tracking-aid. Sometimes this can be supplied by an operator tuning the VCO manually, as we described above; sometimes it can be automatic, programmed tuning according to a doppler ephemeris; and sometimes the external aid can be derived from a signal whose phase variations are correlated with the phase we desire to track, as would be the case if carrier-loop information is used to aid a subcarrier track.

This article treats the performance and design of loops with such external aid.

2. Predict-Aided Track

The simplest type of externally-aided loop is depicted in Fig. 8. There is a voltage inserted into the VCO by an operator or by an automatic device of some sort, attempting to tune the VCO to an expected incoming frequency offset $\hat{\Omega}_0$. The prediction must be converted to a voltage $\hat{\Omega}_0/K_{VCO}$ to do this. But the VCO constant K_{VCO} is not really constant—it is a function of temperature, drifts, and the VCO operating point; hence the predictor, at best, uses a value somewhat in error, \hat{K}_{VCO} . The equation describing the loop operation, [Eq. (4-2) of Ref. 6] in the present context, shows that the equivalent input phase function can be replaced by

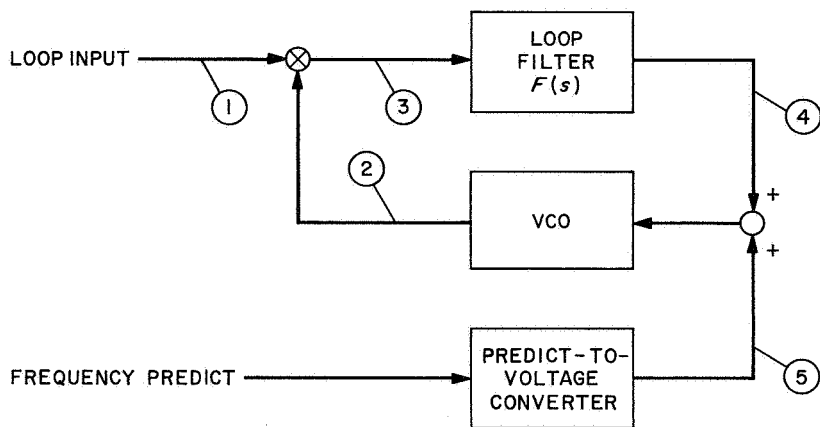
$$\dot{\theta}_{eq} = \dot{\theta} - \frac{K_{VCO}}{\hat{K}_{VCO}} \hat{\Omega}_0 \quad (1)$$

insofar as the loop error is concerned.

For example, if $\theta = \Omega_0 t + \theta_0$, then

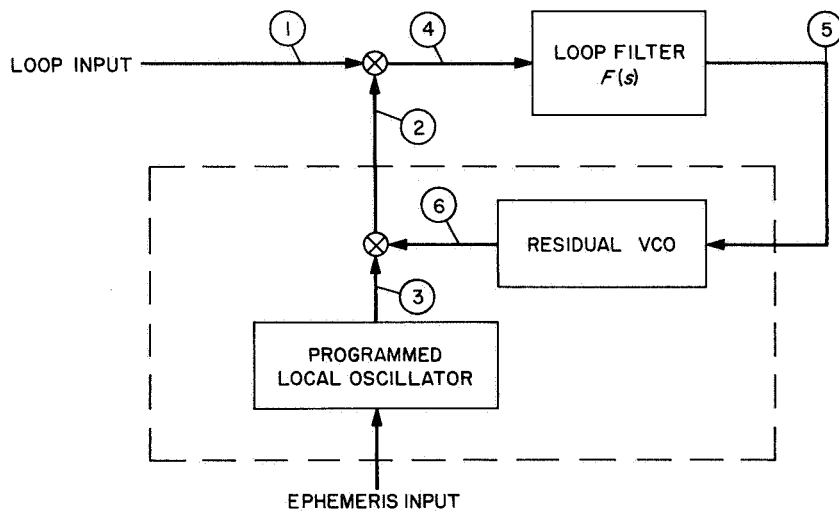
$$\dot{\theta}_{eq} = \Omega_0 \left(1 - \frac{K_{VCO}}{\hat{K}_{VCO}} \frac{\hat{\Omega}_0}{\Omega_0} \right) \quad (2)$$

a much reduced frequency offset when predictions are good. The quantity in parentheses may be termed *prediction error*, and we see that there are two ways error is produced. First, it can be caused by inaccurate estimation of Ω_0 , to give $\hat{\Omega}_0$; and second, it can be caused by an incorrect K_{VCO} value, \hat{K}_{VCO} .



- ① $x(t) = A(2)^{1/2} \sin(\omega_0 t + \theta) + n_I(t)$
- ② $v(t) = (2)^{1/2} \cos(\omega_0 t + \hat{\theta})$
- ③ $y(t) = AK_d \left[\sin(\theta - \hat{\theta}) + \frac{n(t)}{A} \right]$
- ④ $z(t) = F(p)y(t)$
- ⑤ $\theta(t) = \hat{\Omega}_0 / \hat{K}_{VCO}$

Fig. 8. Loop with simple open-loop tracking aid



- ① $x(t) = A(2)^{1/2} \sin[\omega_0 t + \theta(t)] + n_I(t)$
 - ② $v(t) = (2)^{1/2} \cos[\omega_0 t + \hat{\theta}(t)]$
 - ③ $v_{aid}(t) = (2)^{1/2} \cos[\omega_{aid} t + \theta_{aid}(t)]$
 - ④ $y(t) = AK_d \sin[\theta - \hat{\theta}] + K_d n(t)$
 - ⑤ $z(t) = F(p)y(t)$
 - ⑥ $v_r(t) = (2)^{1/2} \cos\left[\omega_r t + \frac{K_{VCO} F(p) z(t)}{p}\right]$
- $\omega_0 = \omega_{aid} + \omega_r$

Fig. 9. Tracking loop with ephemeris aid and PLO

The latter of these difficulties can be eliminated by the mechanization in Fig. 9. Just as in the previous example, there is, in addition to the ordinary loop input, an input from a frequency ephemeris, or schedule giving the expected frequency offset at any particular time. But now there is direct frequency conversion of the predict by a programmed local oscillator (or PLO), an instrument which generates a sinusoid at the expected incoming frequency, according to ephemeris, but offset by the rest-frequency of the residual VCO. The resulting phase estimate $\hat{\theta}$ of θ is a composite of the residual VCO phase, plus that of the PLO,

$$\hat{\theta} = \theta - \phi = \theta_{aid} + \frac{AKF(p)}{P} \left[\sin \phi + \frac{n(t)}{A} \right] \quad (3)$$

Again, we see that the equivalent loop offset frequency $\dot{\theta}_{eq}$ is decreased to

$$\dot{\theta}_{eq} = \dot{\theta} - \dot{\theta}_{aid} \quad (4)$$

In the simple example $\theta = \Omega_0 t + \theta_0$ and $\theta_{aid} = \hat{\Omega}_0 t + \hat{\theta}_0$, we find

$$\dot{\theta}_{eq} = \Omega_0 \left(1 - \frac{\hat{\Omega}_0}{\Omega_0} \right) \quad (5)$$

The error, in this case, is merely dependent on how well Ω_0 can be predicted.

The function performed inside the dashed box in Fig. 9 can be synthesized many ways, but the result is equivalent to what we have shown.

3. Subcarrier Loops with Aided Track

In a locked receiver, the phase of the reconstructed carrier component often carries much information about the phase variations of any subcarriers. This is especially true when the carrier and subcarrier are coherent frequencies; but even in the incoherent case, the two may reflect the same doppler offsets, for example. Whenever a subcarrier is related to the carrier frequency, either coherently, or nearly so, the carrier-loop information can be extracted to aid the subcarrier loop. There are several ways this can be done:

a. Open loop doppler aid. First, and most obviously, the carrier frequency can be processed to extract the doppler offset; then the subcarrier VCO can be tuned accordingly, as in Fig. 10, to have its center frequency at the proper (computed) frequency. In this way, the equivalent frequency uncertainty interval is vastly reduced, allowing the use of a narrow-band subcarrier loop. This type of rate-aid is of the open-loop type, in that uncertainties in Ω_0 and K_{VCO} are not self-compensating. The analysis in this implementation follows (Eq. 1) exactly; and, in fact, Ω_0 is precisely equal to the predict $\hat{\Omega}_0$ plus the VCO rest-frequency drift.

b. Carrier-loop-aided subcarrier track. Assuming that the true carrier-to-subcarrier frequency ratio is $N = \omega_0 / \omega_{sc}$, then it follows that the carrier VCO output, when frequency-divided by N , provides a sinusoid at the subcarrier frequency with the doppler frequency offset properly scaled, but having a phase angle differing from that of the subcarrier by a constant angle, in the coherent case, and by a slowly varying one in the noncoherent case.

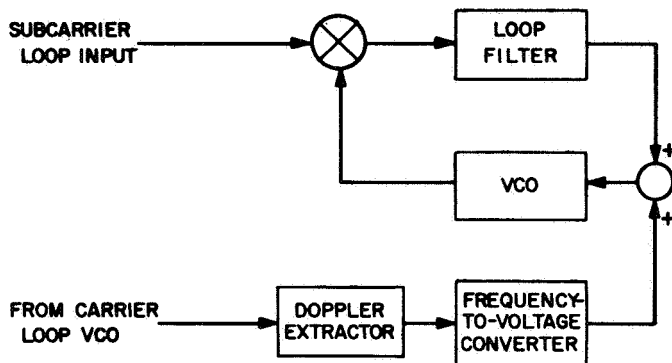


Fig. 10. Subcarrier loop with carrier-loop aid

The subcarrier loop shown in Fig. 11 detects this phase difference, and causes an appropriate phase shift to be introduced for proper tracking.

In reference to the figure, the loop operates as follows: The carrier loop VCO output $v(t)$ is frequency-divided by some number \hat{N} , approximately the true carrier-to-subcarrier ratio, to give

$$v_{aid}(t) = K_{aid}(2)^{1/2} \sin(\omega_{sc}t + \theta') \quad (6)$$

where K_{aid} is the rms divider output amplitude; $\omega_{sc} = \omega_0 / N$; and θ' contains the composite result of carrier loop phase noise, doppler phase, division by only an approximate N , etc.

$$\theta' = \hat{\theta}(t) / \hat{N} + \frac{\pi}{2} + \omega_{sc}t \left(\frac{N}{\hat{N}} - 1 \right) \quad (7)$$

The fact that \hat{N} is usually very large produces an almost noise-free θ' .

The other input to the loop is the one to be phase tracked, the subcarrier itself, in noise.

$$x_{sc}(t) = A(2)^{1/2} \sin(\omega_{sc}t + \psi) + n_i(t) \quad (8)$$

Here A represents the rms subcarrier amplitude; ψ its phase function relative to $\omega_{sc}t$ (highly correlated with θ'); and $n_i(t)$ noise from the receiver input, with spectral density N_0 . The signal appearing in Eq. (8) is phase detected as shown, filtered, and the resulting error $e(t)$ used to alter the phase of $v_{aid}(t)$, the divided-down carrier. Just as in Fig. 9, the functions inside the dashed box shown in Fig. 11 may be synthesized in various ways, but functionally they are equivalent to those shown. The voltage-controlled phase-shifter we envision is a device which alters the phase according to

$$\hat{\psi} = \psi + \frac{K_\phi}{p} e(t) \quad (9)$$

where K_ϕ represents the device gain, and $\hat{\psi}$ is the loop estimate of the subcarrier phase ψ . The loop equation is thus

$$\hat{\psi} = \psi - \phi = \theta' + \frac{AKF(p)}{p} \left[\sin(\psi - \hat{\psi}) + \frac{n(t)}{A} \right] \quad (10)$$

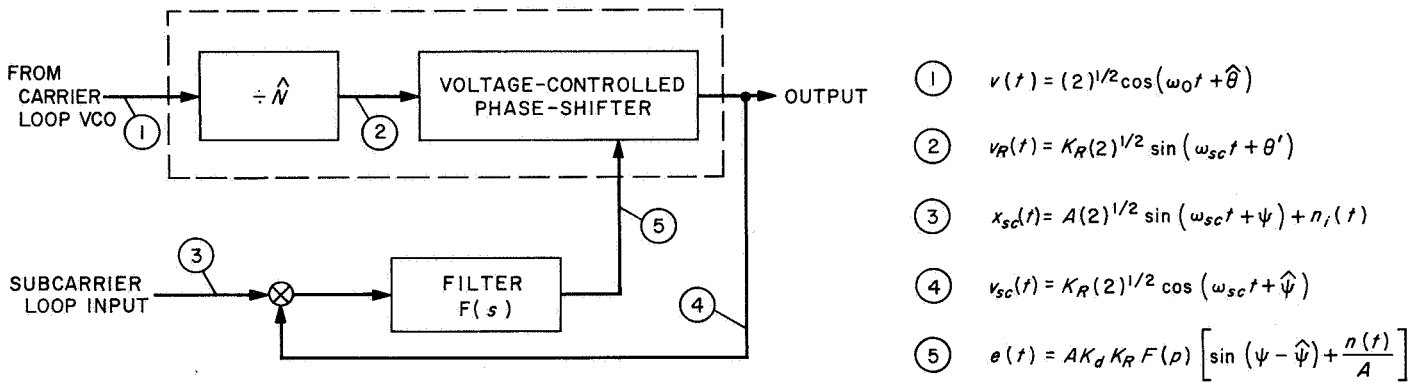


Fig. 11. Subcarrier loop with closed-loop tracking aid derived from the carrier

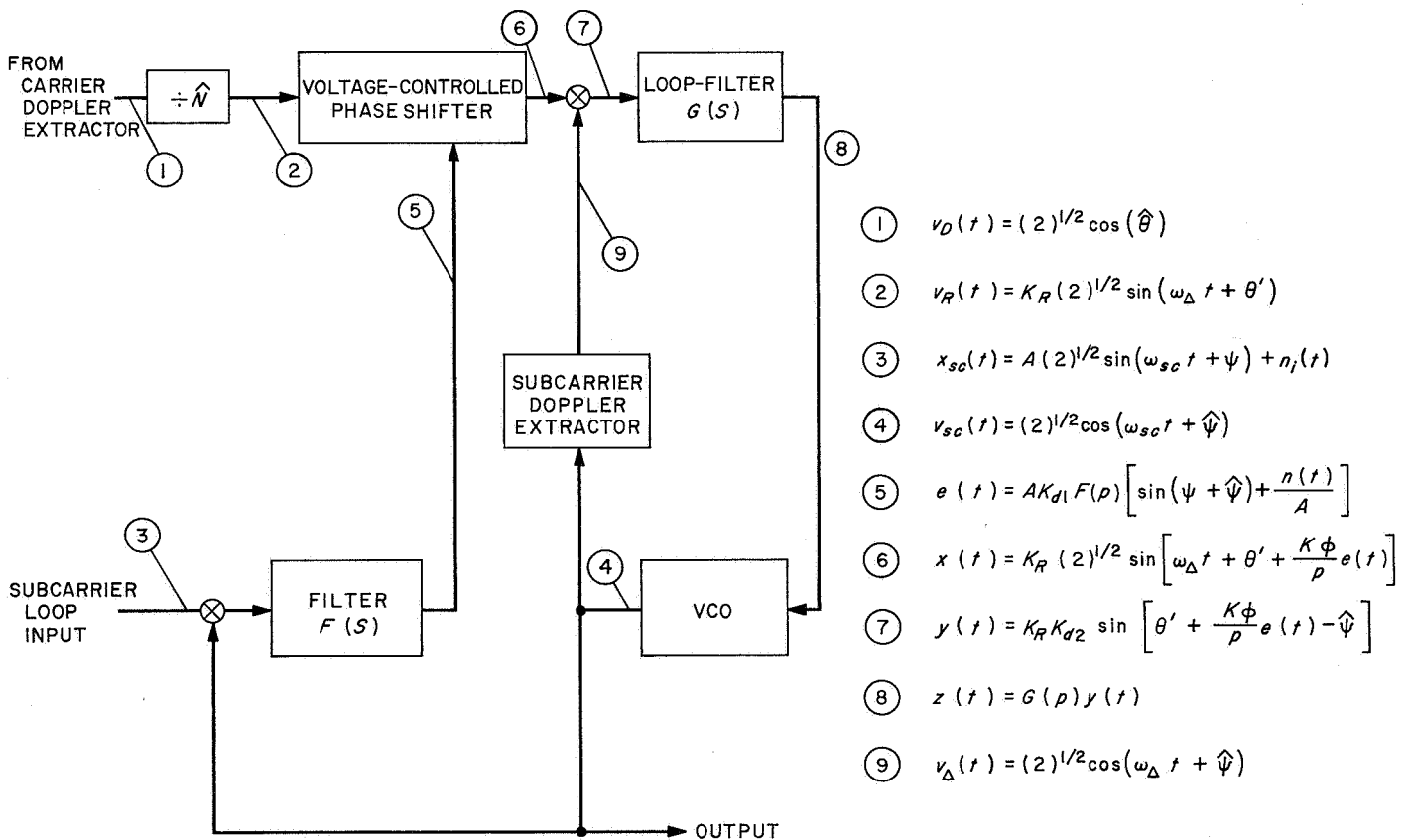


Fig. 12. Subcarrier loop with closed-loop doppler-aided track

which, with $K = K_{aid}K_dK_\phi$, is exactly the same form as Eq. (3) when ϕ is defined as $\phi = \psi - \hat{\psi}$. The equivalent loop-offset function is

$$\theta_{eq} = \psi - \theta' \quad (11)$$

and all variations in ψ common to both carrier and subcarrier are effectively removed.

c. Doppler-aided subcarrier track. In a two-way earth-spacecraft link, the uplink carrier is rebroadcast down so that coherent doppler measurements can be made. When there is also an uplink subcarrier rebroadcast to the earth (as, for example, when there is ranging onboard), coherent subcarrier doppler measurements can also be made. These two bear a very precise relationship to one another; namely, the doppler ratio is the same as the carrier-subcarrier frequency ratio. Hence, the subcarrier VCO can be made to follow the subcarrier input exactly by forcing the subcarrier doppler to follow the properly-scaled carrier doppler. A mechanization of this scheme is shown in Fig. 12. The principle is the same as the aided-track discussed in subsection 3b. above; but there is an inner loop which causes the subcarrier doppler to follow the scaled carrier doppler and an outer loop which adjusts the VCO to the proper subcarrier input phase.

The doppler-track mechanization is sometimes more useful than the carrier-track depicted in Fig. 11, in that doppler-extracted frequency is usually easier to divide by an arbitrary (or time-varying) value of N than the carrier VCO frequency is. Figure 6, for example, shows a digital doppler-scaling device; basically, it operates as follows: the carrier doppler signal is determined by counting and the resulting number divided digitally by N , to any precision desired (and the remainder retained for subsequent divisions, if greater precision is needed). This quotient, the correct frequency of the subcarrier, is the input to a number-controlled oscillator (NCO), a device which generates a waveform whose frequency is precisely the input number. A bias frequency ω_Δ can also be added, as needed, to alleviate any difficulty at zero-doppler offsets, as long as it is accounted for in the subcarrier doppler detector as well. By the mode of construction, a number inserted into the "phase-shift" input of the NCO shortens or lengthens cycles of the output, advancing or retarding its phase as desired.

With the phase-shift input disconnected, the remaining loop in Fig. 12 has virtually a noise-free input θ' . Hence, the inner loop bandwidth w_L can be made relatively

large—a possibility which reduces the effects of VCO noise to a negligible degree and guarantees almost instantaneous response of the inner loop to any phase variation at its input. Then with the outer loop intact, and with the inner loop response made very fast compared to the overall loop response, the input and reference phases into the second detector must compare, as

$$\hat{\psi} = \theta' \frac{AKF(p)}{p} \left[\sin(\psi - \hat{\psi}) + \frac{n(t)}{A} \right] \quad (12)$$

In this equation ψ is the subcarrier phase; $\hat{\psi}$ is the loop estimate of it; and the loop gain K is the product

$$K = K_{d1}K_\phi \quad (13)$$

of the gains of the first detector K_{d1} and the phase shifter K_ϕ . The reader will readily note that Eq. (12) is the same as Eq. (10) and Eq. (3), and thus that the doppler-aided loop with $w_L \ll w'_L$ performs exactly the same as the other closed-loop systems we have considered.

Solution of the double-loop system when the overall loop bandwidth w_L is not much smaller than that of the inner loop is only somewhat more complicated, but does not represent a case of wide practical interest.

D. Communications Systems Development: Signal Processing for Extended Frequency- Modulation Threshold, M. J. Malone²

1. Introduction

This article describes a technique of postdemodulation processing for extending the threshold in high-index analog frequency-modulation (FM) systems. The value of the technique is restricted largely to those cases where the use of the more common extended-threshold demodulators, such as phase-lock and frequency-feedback devices, is impractical. Typical of such cases is the recovery of analog time-division-multiplexed data from a frequency modulated subcarrier, where the character of the modulation precludes threshold improvement using feedback devices, because of the wide loop bandwidth required to track the modulation without loss of lock. Results obtained for the conventional "test" case of sinusoidal modulation indicate a threshold improvement capacity of 1½ to 2 dB, using the technique to be described.

²Weapons Research Establishment trainee.

2. Background

In the analysis of the threshold performance of FM systems, difficulties arise due to the complicated statistical and spectral properties of the system output noise. While solutions have been obtained—typically by Stumpers (Ref. 8)—for the relationship between the input (IF) signal-to-noise ratio (SNR) and the output noise power, it has long been recognized that such solutions do not tell the full story.

It has been observed that the output noise of an FM system is *apparently* separable into two very distinct components; normal noise, and a random sequence of impulses, which first appear as the IF SNR is reduced through threshold (about 10 dB), and whose average rate n increases rapidly as the IF SNR is further reduced. The explanation for this impulse phenomenon, in qualitative terms, is simple enough, the effect being due to the random 2π -anomalies which occur when an estimate of the phase of a sinusoid in narrow band noise is made via the phase of the resultant vector. In essence, an elementary FM demodulator obtains the time derivative of this phase estimate by operating on the zeros of the composite signal-plus-narrow-band-noise waveform appearing at the IF filter output. Each 2π -phase anomaly, therefore, appears as an impulse of weight 2π at the output (weight unity if output is measured in Hz).

Figure 13 illustrates the occurrence of one of these impulse events, known in FM terminology as “clicks,” or as “origin encirclements” or “cycle captures” due to the association with each event of a complete 2π -rotation of the resultant relative to the signal vector. Also indicated is the disparity in the spectral energy content during periods which do, and periods which do not, contain an impulse. Since the former spectrum is white, while the latter is essentially parabolic, at least within the modulation baseband-width B_0 , the strong impulse noise contribution to the FM threshold effect is clearly apparent.

3. Threshold Extension

Rice (Ref. 9) has recognized the inherent simplicity in the formulation of FM problems in terms of an FM output noise model, which consists of the sum of a Poisson sequence of impulses, and Gaussian noise having properties given by strong signal FM theory. He has also furnished a complete analysis of the properties of the impulse noise component in terms of the channel parameters. Using this model as a starting point we approach the possibility of threshold extension by noting the gross differences in the spectra of the two noise components

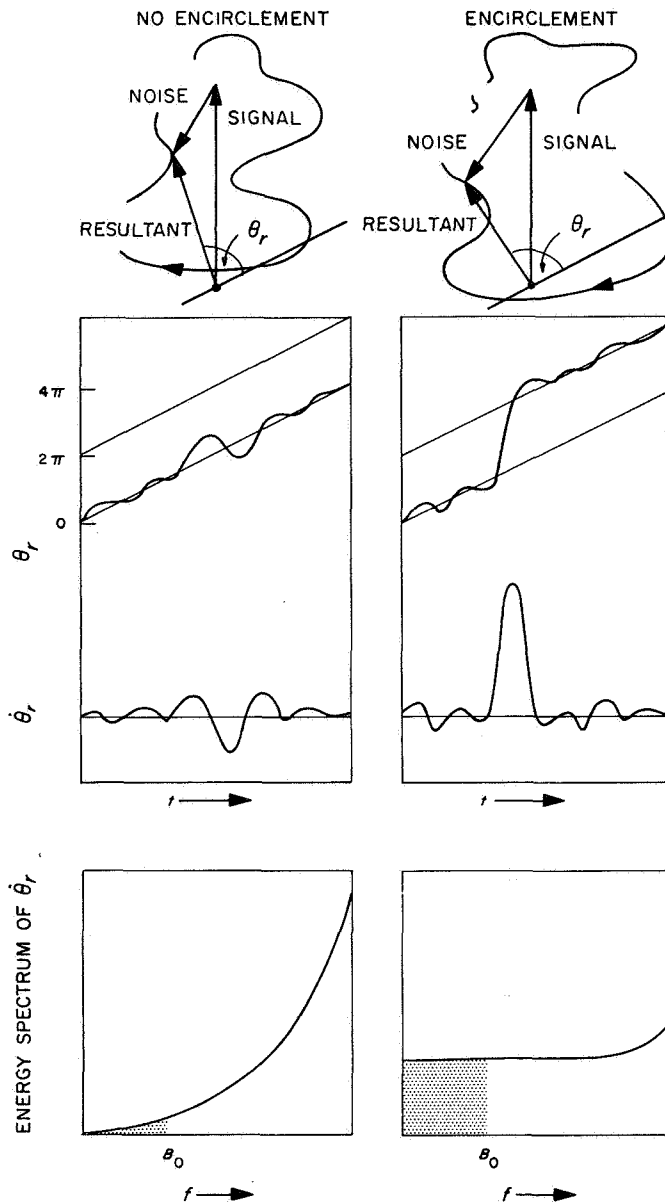


Fig. 13. FM threshold effects

and the desired baseband signal. The single-sided spectral densities are, respectively:

Gaussian noise component

$$\eta_g = \frac{f^2}{B_{IF}\rho}, \quad f \leq B_{IF/2}$$

$$= 0, \quad f > B_{IF/2}$$

Impulse noise component

$$\eta_i = 2n$$

Signal component

$$\begin{aligned} \eta_s &= k \gg \eta_i, & f &\leq B_0 \\ &= 0, & f &> B_0 \end{aligned}$$

where we have assumed a convenient flat-band limited spectrum for the signal, and where B_{IF} is the IF bandwidth; ρ is the IF SNR (power); n is the average impulse rate; and B_0 is the modulation base bandwidth. Note that the system output is measured in Hz, and this results in spectral densities having dimensions also in Hz.

Now a high index FM system has $B_{IF} \gg B_0$. Specifically, it is conventional to define a modulation index

$$m = \frac{f_d}{B_0}$$

and to fix

$$B_{IF} = 2(f_d + B_0) = 2(m + 1)B_0$$

where $2f_d$ is the extreme frequency range of the FM signal—assumed peak limited. Under conditions of $B_{IF} \gg B_0$ it is clearly possible to devise a matched filter-decision device, operating within the baseband range $0 \leq f \leq B_{IF/2}$, to indicate the occurrence of each noise impulse. The resulting information could be used to initiate some appropriate impulse-cancelling process which would operate on a delayed version of the demodulator output (delay equal to that of the matched filter). Following this, normal baseband filtering would be performed.

In the ideal world, where the validity of the FM noise model is unquestioned, this impulse cancelling technique would yield a considerable threshold extension, since in this ideal case the impulse noise bears sole responsibility for the threshold effect. The magnitude of the threshold extension would be limited largely by the impulse detection error probability becoming significant at low SNRs. However, in reality the model is less than perfect; and we have to contend not only with impulse noise but also with additional high-order noise cross-products, due to the high degree of nonlinearity evident in the transformation from signal-plus-narrow-band-noise to noise on the resultant phase angle. These additional components, although small relative to the impulse noise, make their own contribution to the departure of the FM demodulator performance from that predicted by strong-signal theory, and might be expected to limit the threshold extension practically available.

In order to test the threshold extension capacity of this scheme, a digital computer was programmed to simulate exactly—within the limitations imposed by time- and amplitude-discrete variables—the characteristics of a system in which the output is the time-derivative of the phase angle of the resultant sum of an angle modulated signal plus narrow band noise. The angle modulation was a sinusoid of frequency equal to $\frac{1}{8} B_0$, peak frequency deviation f_d , and with B_0 and f_d chosen for m equal to 1, 3, and 7. As a program check, a simulation run was performed without threshold extension; and the system output noise power (computed for various IF SNR after baseband filtering in a sharp cut-off filter of bandwidth B_0) was checked against the calculated output noise power P_m of the model, obtained from

$$\begin{aligned} P_m &= \int_0^{B_0} (\eta_i + \eta_o) df \\ &= \frac{B_0^2}{6(m+1)\rho} + 2nB_0 \end{aligned}$$

from which the system output

$$\text{SNR} = \frac{1}{3m^2(m+1)\rho} + \frac{4n}{m^2B_0}$$

Here the average impulse rate n , from Rice's Eq. (83) is

$$n \approx 2e^{-\rho} B_0 \left\{ \frac{m}{\pi} + \frac{(m+1)}{2\sqrt{3}} \frac{e^{-a\rho}}{\sqrt{\pi\rho}} I_0(a\rho) \right\}$$

where I_0 is the modified Bessel function, zero order; and a is the mean square frequency deviation normalized relative to the square of the radius of gyration of the IF noise spectrum. For the case under consideration this is

$$a = \frac{3}{2} \left(\frac{m}{m+1} \right)^2$$

As Fig. 14 indicates, the agreement is good. A number of simulation runs were then performed with threshold extension operative. The impulse cancellation was effected by deleting each detected impulse by a linear interpolation of duration $2/B_{IF}$ across the region of the impulse. This duration represents the width, between zeros, of the envelope of the IF autocorrelation function, and seems intuitively appropriate. The impulse detection

employed an approximately matched filter having "voltage"/frequency response function

$$H(f) \approx 0, \quad 0 < f \leq B_0$$

$$\approx k/f^2, \quad f > B_0, \quad k \text{ a constant}$$

followed by a decision element set for equal failure and false alarm probabilities.

4. Results

Figure 14 shows the distinct, if modest, threshold improvement obtained using the threshold extension technique described. An interesting side issue to this is that in the past some controversy has arisen over the validity of Rice's model; there being claims and counter claims to the effect that the noise-cross products mentioned earlier contribute more to the threshold noise than the impulsive component (Ref. 10). The present work would seem to indicate that the validity of the model extends

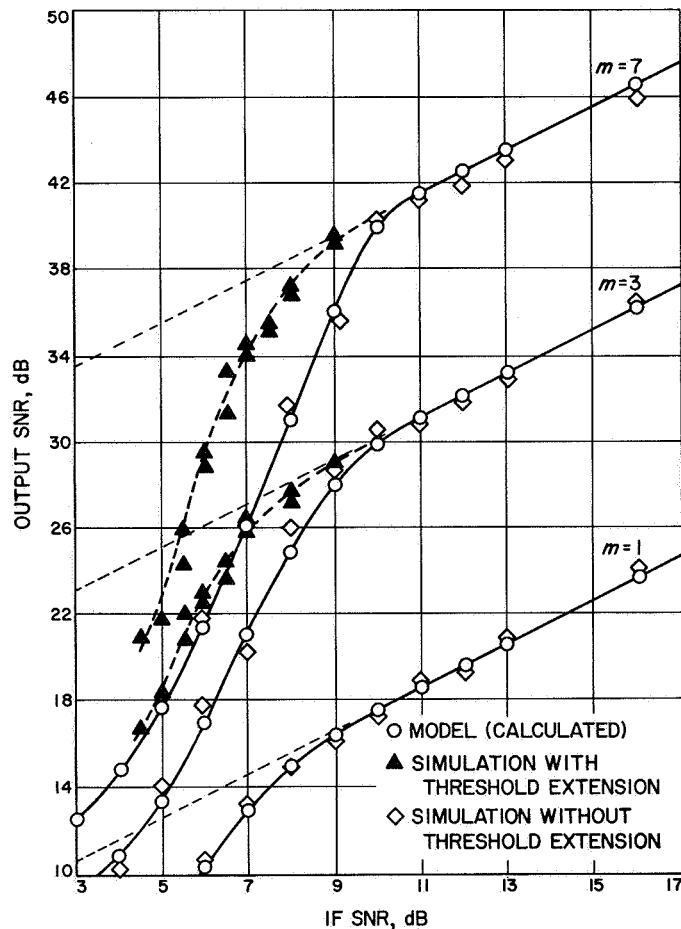


Fig. 14. FM threshold

down to about 8 dB IF SNR in the general sense, and well below this if the only concern is with the total output noise power.

E. Information Processing: Sync Error-Detecting Capability of the Deep Space Network Teletype Code

G. Solomon, E. C. Posner, and H. Fredricksen

1. Introduction

Space Programs Summary 37-45, Vol. III, pp. 32-36, contains a description of an error correcting encoder-decoder for use on Deep Space Network teletype lines. In this article, we give the arguments on the distance between code words from which the error-correcting and sync error-detecting capabilities can be computed.

2. Minimum Distance in the Code

In SPS 37-45, Vol. III, it was asserted that the (15,9) Reed-Solomon code over the 16-element field chosen for transmission of information is capable of correcting up to 3 errors in each block of 15 code symbols. This is true because the minimum distance between any pair of code words is 7.

The code words are formed by the polynomial recursion

$$F(x) = \prod_{i=0}^8 (x + \beta^i)$$

where β is a solution of $x^4 = x + 1$. This means that if a_0, \dots, a_8 are the 9 information symbols of the code, then

$$a_{k+8} = r_1 a_{k+7} + r_2 a_{k+6} + \dots + r_7 a_{k+1} + r_8 a_k, \quad 1 \leq k \leq 6$$

where

$$F(x) = x^8 + \sum_{i=1}^8 r_i x^i$$

For the code word

$$a = (a_0, \dots, a_8, a_9, \dots, a_{14})$$

associate a polynomial, as in Ref. 11, of degree at most 8

$$g_a(x) = \sum_{i=0}^8 c_i x^i$$

such that

$$g_a(\beta^j) = a_j, \quad 0 \leq j \leq 8$$

Van de Monde's determinant theorem insures that g_a exists for every a . Thus, the correspondence between (c_0, \dots, c_8) and (a_0, \dots, a_8) is unique and linear.

We claim

$$g_a(\beta^j) = a_j, \quad 9 \leq j \leq 14$$

also, so that

$$g_a(\beta^j) = a_j, \quad 0 \leq j \leq 14$$

To see this, we shall show that, with r_0 defined as 1,

$$\sum_{k=0}^8 r_k g_a(\beta^{j+k}), = 0, \quad 0 \leq k \leq 14$$

But this sum is

$$\sum_{k=0}^8 \sum_{i=0}^8 r_k c_i \beta^{ij+ik} = \sum_{i=0}^8 c_i \beta^{ij} \sum_{k=0}^8 r_k (\beta^i)^k$$

and the inner sum is 0 because the 8 roots of F are

$$\{\beta^i\}, \quad 0 \leq i \leq 8$$

So we have indeed shown that the a_j for a nonzero code word a are the values of the nonzero polynomial $g_a(x)$ as x ranges over the β^j , $0 \leq j \leq 14$, the 15 nonzero elements of the 16-element field.

Since $g_a(x)$ is of degree at most 8, it has at most 8 zeros. Therefore, $g_a(x)$ has at least 7 nonzero positions in any nonzero code word. Since the set of code words form a group, the minimum distance between any two code words is the same as the minimum number of nonzero positions in a nonzero code word. Thus, the code has minimum distance at least 7; code words of weight 7 can readily be exhibited.

3. Synchronization Error Detection

In SPS 37-45, Vol. III, it was asserted that errors of synchronization due to insertion or deletion of symbols could be detected by adding to each code word a specific vector before transmitting the code word. The vector chosen was

$$\gamma = (0,0,0,0,0,0,0,0,\beta^{13},\beta^{13},\beta,\beta^{12},\beta,\beta^8)$$

It was claimed that γ was at a distance of 6 from any vector in the code, and that $\gamma + T^i\gamma$, where $T^i\gamma$ is equal to γ shifted cyclically to the right by i positions, is also at distance 6 from any vector in the code. This is true because γ belongs to a larger code, which also contains the code F defined by $F(x)$.

Consider

$$H(x) = (x + \beta^{-1}) F(x)$$

The quantity $H(x)$ determines a cyclic code having associated polynomials

$$h_a(x) = \sum_{i=0}^9 c_i x^i$$

Since h is of degree at most 9, the minimum distance in H is ≥ 6 (and, in fact, exactly 6). So, any vector in H but not in F is at distance at least 6 from any vector in F .

Now $\delta = (\beta^{14}, \beta^{13}, \beta^{12}, \dots, \beta, 1)$ is clearly in H , since it satisfies the recursion $x + \beta^{-1}$. If we add to δ the code word ϵ in F having information symbols $\beta^{14}, \beta^{13}, \beta^{12}, \beta^{11}, \dots, \beta^6$, i.e.,

$$\epsilon = (\beta^{14}, \beta^{13}, \beta^{12}, \dots, \beta^6, \beta^7, \beta^{11}, \beta^9, \beta^7, 0, \beta^2)$$

we get $\gamma (= \delta + \epsilon)$, of weight 6 (hence, not in F). Since H is cyclic, $\gamma + T^i\gamma$ is also in H and is, therefore, distance 6 or more from code words in F . If a synchronization error occurs in transmissions, then the code word originally sent, say $\alpha^{11}(= \alpha + \gamma)$, would be received as $\alpha^{11}(= \alpha + \gamma + T^i\gamma)$ a word at distance 6 from any code word, so that the decoder will state that an uncorrectable error has occurred.

F. Information Processing: An Efficient Method for Estimating Noise Variance, E. C. Posner

1. Introduction

In the *Mariner Mars 1969* high-data rate block-coded telemetry system, the most likely waveform of 32 orthogonal waveforms and their 32 components is found by correlation techniques. That is, one correlates the noisy received word with the 32 waveforms, and determines the correlation of largest absolute value. If that correlation is positive, the word causing that largest correlation is chosen; if that correlation is negative, the negative of the dictionary word causing the largest correlation in absolute value is chosen.

When one has correct sync, the correct word correlates with a mean output of say μ , where μ is the signal; the incorrect words all have average correlation 0, with the same unknown standard deviation σ . Hence, an estimate can be used to determine whether sync still holds, for when sync is lost, the estimate of μ/σ drops, for the mean signal goes to 0. This article studies the estimation of σ .

The ground rules are as follows: To conserve equipment, σ is to be estimated from one of the nonlargest correlations. The one chosen is to be selected only by successive comparisons of the correlations in a serial system; no arithmetic operations are to be used. Furthermore, at most two of the preceding correlations are to be retained at any step.

Subject to these constraints, the estimator chosen is based on the largest of the correlations (other than the one selected as belonging to the correct word). This statistic meets the constraints. It is shown that the variance of the estimator $\tilde{\sigma}$ of σ so obtained goes to 0 with N , where $N + 1 = 32$ in this system. This statistic turns out to be most efficient, subject to the constraints. However, the present system operates with the constraint that at most one previous correlation is to be retained. Thus, the present system uses less hardware (one less register), but has a higher variance of its estimator $\hat{\sigma}$ of σ .

In the ensuing discussion, we assume that we have N Gaussian random variables y_i of known mean 0 and unknown variance σ^2 to be estimated from the knowledge only of $|y_i|$, $1 \leq i \leq N$. There is a slight effect due to the fact that the wrong word is chosen as correct. Since this probability is small even at threshold, this effect is ignored in what follows; it is a third-order effect.

2. The Extreme-Value Distribution

The estimator $\tilde{\sigma}$ of σ , which turns out to have minimum variance among the estimators satisfying the ground rules of the preceding section, is based on the statistic $x_{(1)}$, the largest of the N values x_1, \dots, x_N , where $x_i = |y_i|$, $1 \leq i \leq N$. To obtain $\tilde{\sigma}$ from $x_{(1)}$, we proceed as follows:

The random variables x_i have the common density function $h(x)$, where

$$\begin{cases} h(x) = \frac{2}{(2\pi)^{1/2} \sigma} \exp\left(-\frac{x^2}{2\sigma^2}\right), & x \geq 0 \\ h(x) = 0, & x < 0 \end{cases}$$

Define

$$H(x) = \int_{-\infty}^x h(t) dt$$

Assuming N large (10 or 20 will suffice; in our application, $N = 31, 63, \dots$) we shall find the asymptotic distribution of the largest x_i , which we call $x_{(1)}$.

We use Gumbel's extreme-value theory (Ref. 12) as follows: The random variable $x_{(1)}$ has for large N a distribution function $F(x) = \text{pr}(x_{(1)} \leq x)$ given by

$$F(x) = e^{-\exp[-\alpha(x-u)]}$$

where α and u are related to h (and N) as follows:

$$\begin{cases} H(u) = 1 - \frac{1}{N} \\ \alpha = Nh(u) \end{cases}$$

In our application, we find, using the fact that for u large

$$1 - H(u) \sim \frac{2\sigma}{(2\pi)^{1/2} u} \exp\left(-\frac{u^2}{2\sigma^2}\right)$$

(Ref. 13, p. 166), that as $N \rightarrow \infty$

$$u = \sigma(2 \log N)^{1/2} + o(1)$$

$$\alpha = \frac{u}{\sigma^2} + o(1)$$

We shall use these values for u and α in what follows, since the convergence is good even at $N = 31$.

3. The Estimator Based on $x_{(1)}$

In this subsection, we estimate σ by $\tilde{\sigma}$. The estimator $\tilde{\sigma}$ is obtained from $x_{(1)}$ by estimating $E(x_{(1)})$ by $x_{(1)}$ itself, which gives the maximum-likelihood estimate for u . The expectation of $x_{(1)}$ turns out to be a linear function of σ , so that σ is readily estimated from $x_{(1)}$.

Consider $z = \alpha(x_{(1)} - u)$, which has the distribution $e^{-\exp(-z)}$. Now

$$E(z) = \gamma$$

(Ref. 12, p. 175), where γ is Euler's constant 0.57722 \dots .

Thus

$$E(x_{(1)}) = u + \frac{\gamma}{\alpha}$$

Consequently, we find the unbiased estimator

$$\tilde{\sigma} = \frac{x_{(1)} (2 \log N)^{1/2}}{2 \log N + \gamma}$$

for σ .

Let us find the variance of $\tilde{\sigma}$. It is known (Ref. 12, p. 174) that

$$\text{Var } x_{(1)} = \frac{\pi^2}{6\alpha^2} = \frac{\pi^2 \sigma^2}{12 \log N}$$

Hence

$$\begin{aligned} \text{Var } \tilde{\sigma} &= \frac{2 \log N \text{Var } x_{(1)}}{(2 \log N + \gamma)^2} \\ &= \sigma^2 \cdot \frac{1/6 \pi^2}{(2 \log N + \gamma)^2} \end{aligned}$$

Thus, for large N

$$\text{Var } \tilde{\sigma} \sim \frac{\pi^2 \sigma^2}{24 (\log N)^2}$$

which approaches 0 as $N \rightarrow \infty$. For $N = 31$, the more exact formula gives

$$\text{Var } \tilde{\sigma} = 0.0297 \sigma^2$$

4. Comparison with Minimum-Hardware Method

The minimum-hardware method uses a random waveform of the nonlargest measured correlations. Again the effect of a wrong decision on the estimation can be ignored, since the error probability is small. The random one of the N correlations is chosen by choosing the last correlation value computed; unless, with probability $N/(N+1)$, it turns out to be the largest. Then 0 is used. The effect of this replacement is easily measurable. Since a large number M of codewords are treated by either method, $M = 4096$, the variance of the estimator $\hat{\sigma}$ obtained is approximately $(N+1)/N$ what it would have been if a truly random waveform could have been chosen. For the sample size is cut, in effect, by about $N/(N+1)$, assuming N much smaller than M , as it is in the *Mariner* system.

The estimator $\hat{\sigma}$ of σ is obtained by using $|y|$, y a normal of mean 0 and variance σ^2 . We readily compute

$$E(|y|) = \frac{2}{(2\pi)^{1/2}} \sigma$$

Then the unbiased estimator $\hat{\sigma}'$ for σ is just

$$\hat{\sigma}' = \frac{(2\pi)^{1/2}}{2} |y|$$

The variance of $|y|$ is $E(|y|^2) - [E(|y|)]^2$, so

$$\text{Var } \hat{\sigma}' = \sigma^2 \left(\frac{\pi}{2} - 1 \right) = 0.571 \sigma^2$$

and of course is independent of N : $\text{Var } \hat{\sigma}$ does not approach 0 with N .

The variance of $\hat{\sigma}$, defined only for M/N large, is

$$\text{Var } \hat{\sigma} = \left(\frac{N+1}{N} \right) \text{Var } \hat{\sigma}'$$

In the *Mariner* system, then

$$\text{Var } \hat{\sigma} = 0.590 \sigma^2$$

We see that in the *Mariner* system

$$\frac{\text{Var } \tilde{\sigma}}{\text{Var } \hat{\sigma}} = 0.050$$

However, if the system using the random waveform of the nonlargest correlations does not keep track of how many times the last correlation was the largest, then another effect comes in, increasing the variance of the final estimator for σ . For, suppose one estimates σ by

$$\sigma^* = \frac{(2\pi)^{1/2}}{2} \sum_{i=1}^{M'} \frac{|y_i|}{M(1-p)}$$

Here the y_i are independent Gaussian of mean 0 and variance σ^2 . Also, $M' = M - K$, where K has a binomial distribution with probability $p = 1/(N+1)$ of success, corresponding to the last correlation being largest. Thus, $M(1-p)$ is the expected number of y_i .

It turns out that σ^* is no longer unbiased for σ . Furthermore, σ^* has a larger variance than $\hat{\sigma}$, which is the estimator of σ when M' is known. To get a good estimate for $\text{Var } \sigma^*$, we proceed as follows: The variance of σ^* is the variance of $\hat{\sigma}$ plus a term due to the uncertain denominator. Typically, M' differs from its expected value by about "one sigma" in either direction, which is $M^{1/2} N / (N + 1)$. Hence, the extra variance to be added is about

$$\left(\frac{1}{(MN)^{1/2} - 1} \right)^2 \sigma^2 \sim \frac{1}{MN} \sigma^2$$

So we use

$$\begin{aligned} \text{Var } \sigma^* &= \text{Var } \hat{\sigma} + \frac{1}{MN} \sigma^2 \\ &= \frac{N + 1}{N} \frac{1}{M} \left(\frac{\pi}{2} - 1 \right) \sigma^2 + \frac{1}{MN} \sigma^2 \end{aligned}$$

Since we are interested in the case N large (but small compared to M), we see that we can indeed not record the exact number of times that the last correlation was largest, and still not increase $\text{Var } \sigma^*$ much. In fact, for the *Mariner* system, our above estimate for $\text{Var } \sigma^*$ (with the M dropped) turns out to be

$$\text{Var } \sigma^* = 0.624 \sigma^2$$

We shall ignore this effect in what follows.

We have seen that $\tilde{\sigma}$ is more than twice as good as $\hat{\sigma}$, in the sense of variance. However, since $M = 4096$ code-words are being used in a batch (about 1.5 s at the data rate of 16.2 kilobits/s), the system is sufficiently good for its purpose even at threshold values of μ/σ . Thus, the extra register necessary to implement the extreme-value system is not justified in this case. However, because $\text{Var } \tilde{\sigma}$ does approach 0 with N , there may be telemetry systems in which estimators using extreme values will find use.

G. Astrometrics: An Integral Arising in Fourier Inversion, E. R. Rodemich and E. C. Posner

1. Introduction

In certain radar mapping techniques, one can, in effect, measure the radar brightness integrated along lines in

the map plane. To recover the brightness map, the technique is to use Fourier transforms. Consider integrals of the form

$$I(y) = \lim_{\epsilon \rightarrow 0} \int_0^{\infty} \rho G(\rho) \exp(-\epsilon \rho + i \rho y) d\rho \quad (1)$$

Here y is a parameter depending on a polar coordinate θ ; the final brightness is

$$\frac{1}{4\pi^2} \int_0^{2\pi} I[y(\theta)] d\theta$$

where the point on the plane at which the brightness is obtained depends on the function $G(\rho)$.

Here $G(\rho)$ is a complex number of absolute value 1, depending on the point of the plane, times the Fourier transform of a function $g(t)$ (which also depends on the suppressed polar coordinate angle θ). This function $g(t)$ is actually the measured data, consisting of the correlation function of a received waveform in a chirp radar at a certain chirp rate proportional to θ . Thus

$$G(\rho) = \int_{-\infty}^{\infty} g(t) e^{-i\rho t} dt \quad (2)$$

and we want to evaluate $I(y)$ in Eq. (1) from knowledge only of g in a simple manner. The final brightness map is then obtained by the sum

$$\frac{1}{4\pi^2} \sum_i I[y(\theta_i)] \Delta\theta_i$$

where the θ_i are points on the $(0, 2\pi)$ circle.

In the analysis, we assume that $g(t)$ is integrable on $(-\infty, \infty)$; vanishes outside a bounded interval corresponding to the radar target's finite diameter; and has an integrable third derivative. This third derivative is obtained from numerically differentiating the measured $g(t)$.

2. The Formula

Starting with Eq. (1), we can write

$$I[y(\theta)] = \frac{1}{2} \lim_{\epsilon \rightarrow 0} \int_{-\infty}^{\infty} |\rho| G(\rho) \exp(-\epsilon |\rho| + i |\rho| y) d\rho \quad (3)$$

where $G(\rho) = G(-\rho)$, since $g(t)$ is even. Now it happens that

$$y(-\theta) = -y(\theta)$$

Hence,

$$I[y(\theta)] + I[y(-\theta)] = \frac{1}{2} \lim_{\epsilon \rightarrow 0} \int_{-\infty}^{\infty} |\rho| G(\rho) \exp(-\epsilon|\rho|) [\exp(i\rho y) + \exp(-i\rho y)] d\rho$$

Thus, for our purposes, it suffices to calculate

$$J(y) = \frac{1}{2} \lim_{\epsilon \rightarrow 0} \int_{-\infty}^{\infty} |\rho| G(\rho) \exp(-\epsilon|\rho| + i\rho y) d\rho \quad (4)$$

and then use

$$J(y) + J(-y) = I(y) + I(-y)$$

in the final $d\theta$ integral. We then have

$$J(y) = \frac{1}{2} \lim_{\epsilon \rightarrow 0} \int_{\rho=-\infty}^{\infty} \int_{t=-\infty}^{\infty} |\rho| \exp(-\epsilon|\rho| + i\rho y) g(t) \exp(-i\rho t) dt d\rho \quad (5)$$

Now the function

$$|\rho| \exp(-\epsilon|\rho| + i\rho y - i\rho t) g(t)$$

is integrable $d\rho dt$, since $g(t)$ vanishes outside an interval, and $|\rho| \exp(-\epsilon|\rho|)$ is integrable in ρ for every $\epsilon > 0$. Thus, Fubini's Theorem can be used to write Eq. (5) as

$$J(y) = \frac{1}{2} \lim_{\epsilon \rightarrow 0} \int_{t=-\infty}^{\infty} g(t) \left\{ \int_{-\infty}^{\infty} |\rho| \exp[-\epsilon|\rho| + i\rho(y-t)] d\rho \right\} dt \quad (6)$$

The integral in braces, however, is readily evaluated in closed form to be

$$\frac{2[\epsilon^2 - (y-t)^2]}{[\epsilon^2 + (y-t)^2]^2}$$

Hence, Eq. (6) becomes the single integral

$$J(y) = \lim_{\epsilon \rightarrow 0} \int_{t=-\infty}^{\infty} \frac{\epsilon^2 - (y-t)^2}{[\epsilon^2 + (y-t)^2]^2} g(t) dt \quad (7)$$

We now integrate by parts twice

$$A(\epsilon) = \int_{-\infty}^{\infty} \frac{\epsilon^2 - (y-t)^2}{[\epsilon^2 + (y-t)^2]^2} g(t) dt = -g(t) \frac{(y-t)}{\epsilon^2 + (y-t)^2} \Big|_{-\infty}^{\infty} + \int_{-\infty}^{\infty} g'(t) \frac{(y-t)}{\epsilon^2 + (y-t)^2} dt \quad (8)$$

But the first term vanishes at $t = I\infty$, since $g(t)$ vanishes outside an interval. Continuing, we have

$$A(\epsilon) = \frac{1}{2} g'(t) \log[\epsilon^2 + (y-t)^2] \Big|_{-\infty}^{\infty} + \frac{1}{2} \int_{-\infty}^{\infty} g''(t) \log[\epsilon^2 + (y-t)^2] dt \quad (9)$$

Again, $g(t)$ vanishes at I_∞ . Then

$$\begin{aligned}
 J(y) &= \lim_{\epsilon \rightarrow 0} A(\epsilon) \\
 &= \frac{1}{2} \lim_{\epsilon \rightarrow 0} \int_{-\infty}^{\infty} g''(t) \log [\epsilon^2 + (y-t)^2] dt
 \end{aligned}
 \tag{10}$$

Now the integrable function

$$\frac{1}{2} g''(t) \log (y-t)^2 = g''(t) \log |y-t|$$

dominates the function

$$\frac{1}{2} g''(t) \log [\epsilon^2 + (y-t)^2]$$

for every $\epsilon > 0$. Hence, Lebesgue's dominated convergence theorem can be used to conclude

$$J(y) = \int_{-\infty}^{\infty} \lim_{\epsilon \rightarrow 0} g''(t) \left\{ \frac{1}{2} \log [\epsilon^2 + (y-t)^2] \right\} dt
 \tag{11}$$

Since

$$\lim_{\epsilon \rightarrow 0} \log [\epsilon^2 + (y-t)^2] = 2 \log |y-t|$$

Eq. (11) implies

$$J(y) = \int_{-\infty}^{\infty} g''(t) \log |y-t| dt
 \tag{12}$$

However, the kernel $\log |y-t|$ is not good for numerical integration, so we integrate Eq. 12 by parts to obtain

$$\begin{aligned}
 J(y) &= g''(t) [(t-y) \log |y-t| - (t-y)] \Big|_{-\infty}^{\infty} \\
 &\quad - \int_{-\infty}^{\infty} g'''(t) [(t-y) \log |t-y| - (t-y)] dt
 \end{aligned}
 \tag{13}$$

Since $g''(t)$ vanishes outside an interval, we finally obtain

$$J(y) = \int_{-\infty}^{\infty} g'''(t) (y-t) [\log |y-t| - 1] dt
 \tag{14}$$

Equation (14) is the desired answer. It expresses $J(y)$ as the convolution of $g'''(t)$ with the kernel

$$t \log |t| - t$$

Since the kernel is 0 at 0, and g vanishes outside an interval, ordinary numerical techniques easily lead to the answer. The formula also readily lends itself to an estimate of the variance of the brightness map so obtained. Previous methods were not only ad hoc, but gave no error estimate.

H. Data Compression Techniques: Entropy of a Five-Point Space, E. C. Posner and P. Slepian

1. Introduction

Let X be a compact metric space, for example, the space of functions defining possible spacecraft orbits. Define for $\epsilon > 0$ the ϵ -entropy $H_\epsilon(X)$ as follows:

$$H_\epsilon(X) = \log N_\epsilon(X)$$

where

$$N_\epsilon(X) = \inf_{U \in V} \text{card } U$$

where V is the set of all coverings of X by, say, closed sets of diameters at most ϵ . This $H_\epsilon(X)$ measures how many bits are necessary to describe all of X within ϵ by words of fixed length.

Now define the ϵ -capacity $C_\epsilon(X)$ as

$$C_\epsilon(X) = \log M_\epsilon(X)$$

where

$$M_\epsilon(X) = \sup_{W \in Y} \text{card } W$$

where Y is the set of all collections of points of X at mutual distances strictly greater than ϵ .

Then it is immediate that

$$C_\epsilon(X) \leq H_\epsilon(X)$$

for every X , $\epsilon > 0$, since no two points of X at distance greater than ϵ are in the same set of diameter $\leq \epsilon$.

Now define for every $n \geq 1$ and every compact metric space X , a space $X^{(n)}$ as follows: The point set of $X^{(n)}$ is the cartesian product of the point set of X with itself n times. And, if X has metric d , $X^{(n)}$ has metric d_n defined by

$$d_n [(x_1, \dots, x_n), (y_1, \dots, y_n)] = \sup_{1 \leq i \leq n} d(x_i, y_i)$$

General question (unsolved): Is it true that for every compact metric space X and every positive ϵ that

$$C_\epsilon(X^{(n)}) \sim H_\epsilon(X^{(n)})$$

as $n \rightarrow \infty$?

Remark: It can be shown by using the fact that $C_\epsilon(X^{(n)})$ is superadditive in n , whereas $H_\epsilon(X^{(n)})$ is subadditive in n , that the two limits

$$h_\epsilon(X) = \lim_{n \rightarrow \infty} \frac{1}{n} H_\epsilon(X^{(n)})$$

and

$$c_\epsilon(X) = \lim_{n \rightarrow \infty} \frac{1}{n} C_\epsilon(X^{(n)})$$

both exist. The first $h_\epsilon(X)$ is called the *absolute epsilon entropy* of X ; the second $c_\epsilon(X)$ is called the *absolute epsilon capacity* of X . The above remarks imply that

$$c_\epsilon(X) \leq h_\epsilon(X)$$

It can also be shown that $c_\epsilon(X)$ is 0 if and only if $h_\epsilon(X)$ is 0. For if X has a diameter greater than ϵ , then $c_\epsilon(X) \geq \log 2$. The general question can be rephrased: is $c_\epsilon(X) = h_\epsilon(X)$ for every $\epsilon > 0$, and for every compact metric space X ?

2. Possible Counterexample

Let X be the five-point metric space $\{1,2,3,4,5\}$ with

$$d(i,j) = \min [i-j, 5 - (i-j)], \quad i \geq j$$

$$d(i,j) = d(j,i), \quad i < j$$

It can be shown by a random coding argument, due to Elwyn Berlekamp,³ that

$$h_1(X) = \log \frac{5}{2}$$

Also,

$$c(X) \geq \frac{1}{2} \log 5$$

since a construction exists giving 5 points in $X \times X \times X$ at distances > 1 (i.e., ≥ 2). Furthermore, it is easy to see that

$$c_\epsilon(X) \geq \frac{1}{n} C_\epsilon(X^{(n)}); \text{ all } n, X, \epsilon > 0$$

Thus, if

$$c(X) \neq \log \frac{5}{2}$$

the general question has a negative answer. This X seems a good space to look at for a counterexample. Also, this $c(X)$ for this X has a connection with Shannon's concept of "zero error capacity" for a certain channel with five inputs and five outputs. In fact, $c_2(X)$ is equal to the zero error capacity of any channel with inputs 1, 2, 3, 4, 5 and outputs 1, 2, 3, 4, 5, such that the effect of the channel is that i goes to either i or $i + 1$ (modulo-5), and there is for every i positive probability that either will happen. The theory of zero error capacity sheds no light on the problem, however. The rest of this article studies $C_1(X^{(k)})$ for this special compact metric space X .

3. Results

Define the subset A of $X^{(k)}$, $k = 1, 2, 3, \dots$, to be *2-separated* if and only if the distance between any two distinct points of A is 2 (which is the maximum distance of any two points of $X^{(k)}$). To find $C_1(X^{(k)})$, we must find

$$\sup_{A \text{ 2-separated}} \text{card } A$$

We can prove

Theorem: $C_1(X^{(1)}) = \log 2$; $C_1(X^{(2)}) = \log 5$; $C_1(X^{(3)}) = \log 10$; $C_1(X^{(4)}) = \log 25$.

³Formerly a consultant with JPL; now employed by Bell Telephone Laboratories.

Proof: The result for $k = 1$ is trivial. For $k = 2$, Fig. 15 proves that $C_2(X^{(2)}) > \log 5$; the x 's are single knight moves apart on a toroidal chessboard.

x				
		x		
				x
	x			
			x	

Fig. 15. $C_2(X^{(2)})$

To prove $C_1(X^{(2)}) < \log 6$, suppose A were 2-separated in $X^{(2)}$ and contained 6 points. Then one column of $X^{(2)}$ would contain 2 points of A . This means that neither of the two adjacent columns could contain any points of A . In the remaining two columns, the same argument shows that there are at most 2 points of A . Hence, A has at most 4 points, and not 6 points. Thus, we have proved that $C_1(X^{(2)}) = \log 5$ and, in fact, that any A with 5 points which is 2-separated is essentially the A of Fig. 15.

The proof that $C_1(X^{(3)}) = \log 10$ is along the same lines, but with much bookkeeping. The result that

$C_1(X^{(4)}) = \log 25$ is barely doable. The details are omitted.

The methods used in the above theorem are special and depend strongly on the dimension k . They do not appear to generalize. Nevertheless, we conjecture that

$$C_1(X^{(k)}) = \begin{cases} \log(5^{k/2}), & k \text{ even} \\ \log(2 \cdot 5^{(k-1)/2}), & k \text{ odd} \end{cases}$$

The truth of this conjecture would imply that

$$c_1(X) = \frac{1}{2} \log 5$$

Hence, we would have answered the general question in the negative. However, a weaker form of the general question might still have an affirmative answer: is

$$c_\epsilon(X) \sim h_\epsilon(X)$$

as $\epsilon \rightarrow 0$, for every compact metric space X ?

References

1. Golomb, S. W., et al., *Digital Communications With Space Applications*. Prentice-Hall, New York, 1964.
2. Stiffler, J. J., *Self-Synchronizing Binary Telemetry Codes*, PhD Dissertation, California Institute of Technology, Pasadena, California, 1962.
3. Develet, J. A., Jr., "The Influence of Time Delay on the Second-Order Loop Acquisition Range," *International Telemetry Conference*, pp. 432-437, London, England, 1963.
4. Gruen, N. J., *A Simple Derivation of Pull-in Range and Pull-in Time for Second-Order Frequency and Phase-Control Loops*, Thompson Ramo Wooldridge, Inc., Canoga Park, Calif., Mar. 7, 1962.
5. Viterbi, A. J., *Principles of Coherent Communications*, McGraw-Hill Publishing Co., New York, 1967.
6. Tausworthe, R. C., *Theory and Practical Design of Phase-Locked Receivers*, Vol. I, Technical Report TR 32-819. Jet Propulsion Laboratory, Pasadena, Calif., Feb. 1966.

References (contd)

7. Jaffee, R. M., and Rehtin, E., "Design and Performance of Phase-Locked Circuits," *IRE Trans. Information Theory*, Vol. II, No. 1, pp. 66-76, Mar. 1955.
8. Stumpers, F. L. H. M., "Theory of Frequency Modulation Noise," *Proc. IRE*, Vol. 36, pp. 1081-1152, Sept. 1948.
9. Rice, S. O., "Noise in FM Receivers," in *Time Series Analysis*, Brown Univ., Providence, R.I., 1962. Edited by M. Rosenblatt. John Wiley and Sons, Inc., New York, 1963.
10. Baghdady, E. J., and Enloe, L. H., "Decreasing the Threshold in FM by Frequency Feedback," *Proc. IEEE (Correspondence)*, Vol. 52, pp. 1039-1066, Sept. 1964.
11. Solomon, G., *Introduction to Algebraic Coding Theory*. McGraw-Hill Book Co., Inc., New York (in press).
12. Gumbel, E. J., *Statistics of Extremes*. Columbia University Press, New York, 1958.
13. Feller, W., *An Introduction to Probability Theory and Its Applications, Volume I*, Second Edition. John Wiley & Sons, Inc., New York, 1957.

XX. Communications Elements Research

TELECOMMUNICATIONS DIVISION

A. Low Noise Transponder Preamplifier Research, S. Petty

A commercial tunnel diode amplifier is being evaluated for possible application as a low noise spacecraft transponder preamplifier. The tunnel diode unit, as compared with transistor and parametric amplifiers (SPS 37-45, Vol. IV, p. 321), has many advantages, provided that certain design problems can be solved:

(1) The amplifier must be small and lightweight. With presently available miniature four-port circulators, the amplifier (not including bias supply) would weigh less than 9 oz and occupy about 3.5 in.³

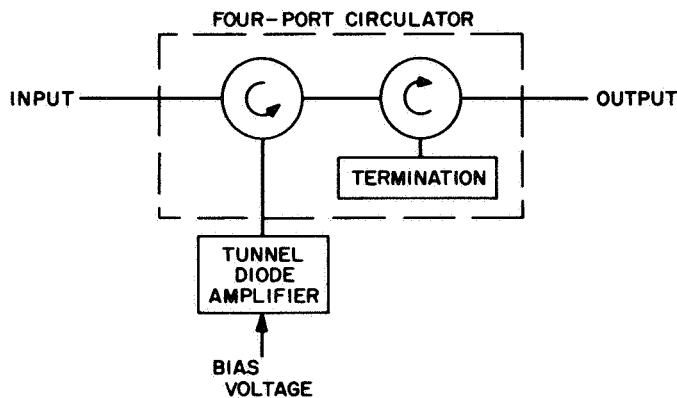


Fig. 1. Tunnel diode amplifier

(2) The amplifier must operate over a wide temperature range. The noise figure and power gain must remain at an optimum and reasonably constant level over this range.

(3) Bias power for the tunnel diode must be obtained efficiently from the spacecraft power supply.

Work in the last two areas will be described below.

A diagram of the test amplifier (Microstate Model NC-2113) is shown in Fig. 1. The ambient temperature performance of this amplifier at the spacecraft transponder frequency of 2115 MHz is described in Table 1. The particular constraints placed on a tunnel diode amplifier by the spacecraft environment would not degrade the specifications shown in the table.

Table 1. Tunnel diode amplifier performance

Signal frequency	2115 MHz
Net gain	20 dB
Temperature	25°C
Noise figure ^a	4.8 dB
Bandwidth (3 dB)	80 MHz
Bias voltage	88 mV
Input power for 1-dB gain compression	-46 dBmW

^aMeasured with ambient and cooled terminations. Includes contribution from 12.5-dB follow-up noise figure. Automatic noise figure meter measures 4.4 dB.

1. Temperature Compensation

Gain and noise figure variations as a function of temperature are undesirable and must be reduced as much as possible by inserting temperature-varying RF components in the amplifier itself, and by causing the diode bias supply to have a temperature coefficient such that these variations are minimized.

The first approach is not feasible with the present test amplifier but will be incorporated if a new tunnel diode amplifier is constructed. The second approach, diode bias compensation, has been investigated in the present test amplifier.

Figure 2 shows noise figure and power gain of the test amplifier as a function of diode bias voltage. These data are shown for each 10-deg interval of temperature between -30 and $+60^\circ\text{C}$. From these curves, the various bias voltage/temperature relationships which give the most stable gain and optimum noise figure can be plotted. All noise temperature data were obtained with automatic noise figure equipment and are approximately 0.4 dB below those measured with cold and ambient terminations. These data also include the contribution from a follow-up noise figure of 12.5 dB, thus approximating total system performance when the transponder preamplifier is followed by a diode mixer.

A linear bias voltage/temperature relationship was found to provide nearly the best compensation possible. Figure 3 shows power gain and noise figure versus temperature for the tunnel diode amplifier when the bias supply varies linearly from 111.8 mV at -30°C to 82.0 mV at $+60^\circ\text{C}$. This is compared with similar data taken with a constant bias voltage of 98.0 mV.

2. Bias Supply

A transformer-rectifier bias supply is being designed to accept spacecraft power (50 V peak square wave, 2400 Hz) and provide regulated bias voltage to the diode. Various configurations of temperature-sensitive resistive elements are being investigated to provide the linear voltage/temperature characteristics required above. Since the diode itself requires only 1 mW of bias power, the total power drain for the amplifier will be determined by transformer efficiency and dissipation in the voltage regulator and rectifier circuits. A total input power requirement of 10–40 mW is a definite possibility since the ac-powered transformer supply allows the choice of optimum dc operating voltage for the regulator circuit, with corresponding minimum power drain.

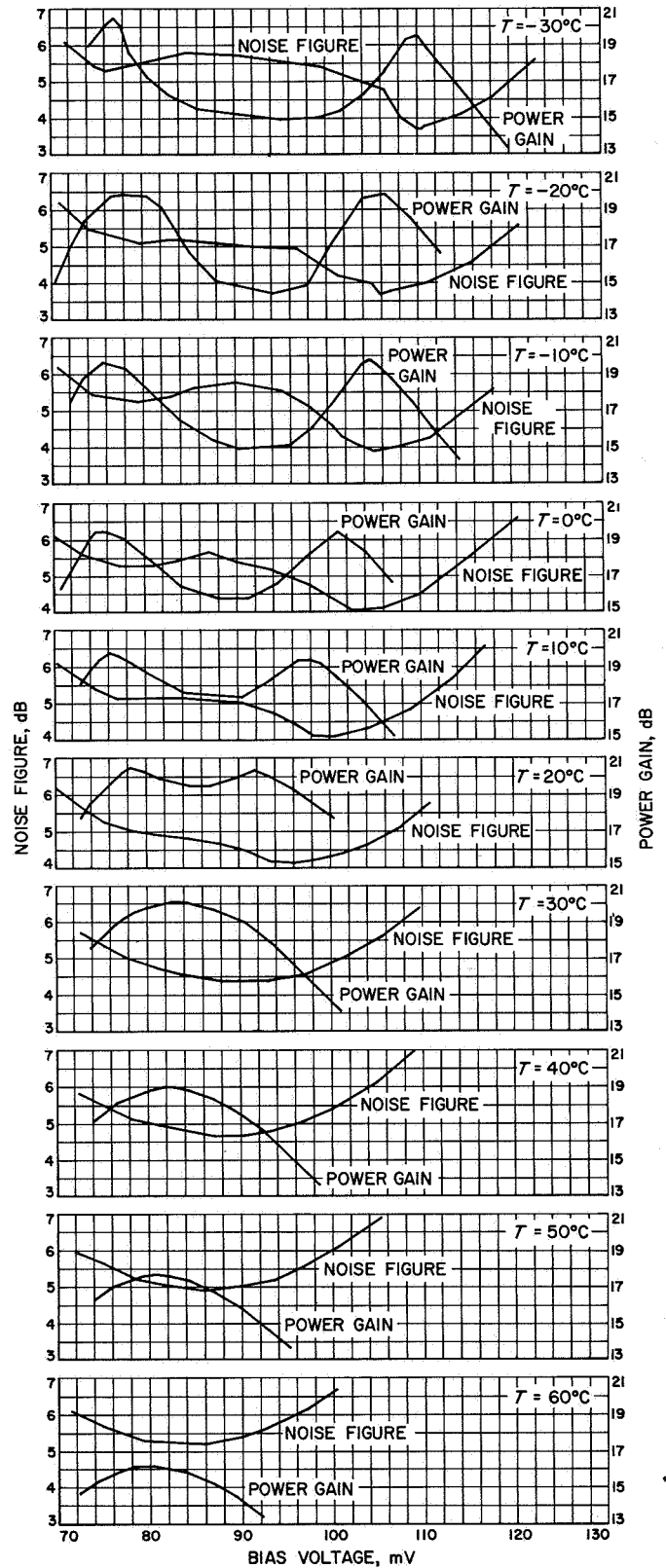


Fig. 2. Amplifier performance versus temperature

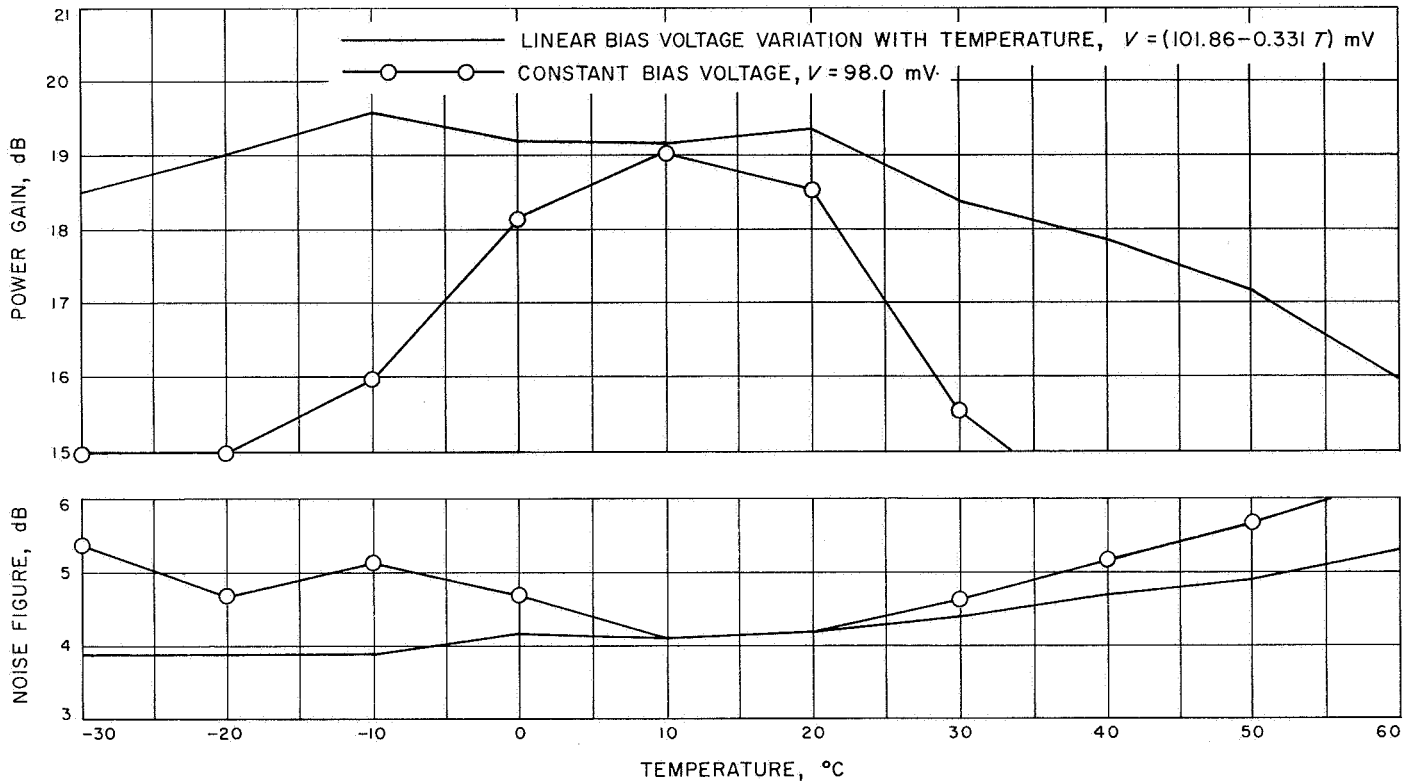


Fig. 3. Amplifier performance with and without temperature-varying bias voltage

B. Precision Calibration Techniques: Precision Rotary Vane Attenuator Calibration, C. T. Stelzried

1. Summary

The theory of microwave rotary vane attenuators with account taken for the rotor vane phase shift and attenuation is reviewed. A derivation is given for the attenuation error in terms of the parameters used in the calibration formula. These error terms are useful for design, evaluation, and calibrations. A program has been developed from this analysis for use on the IBM 7094 computer. The program listing and sample printout are given.

2. Introduction

Applications of a microwave rotary vane attenuator for primary and interlaboratory attenuation standards are well known (Ref. 1). These microwave techniques are applicable to spacecraft or ground-receiving system calibrations. A "perfect" rotary vane attenuator provides an attenuation standard because it obeys the simple precise mathematical law.

$$A = \frac{1}{\cos^4 \theta} \quad (1)$$

where

A = attenuation, power ratio

θ = rotor vane angle relative to the stators, deg

Inaccuracies of this law are caused by: (1) vane angle readout errors, (2) misalignment errors, (3) mismatch errors, and (4) transmission errors.

The angular readout error which provides the principal source of error in most rotary vane attenuators can be reduced with mechanical calibrations (SPS 37-46, Vol. III, pp. 73-82). The transmission error which is a function of rotor attenuation and phase shift can be measured and accounted for by the expanded mathematical law

$$A = \frac{1}{\cos^4 \theta + \frac{2 \cos \phi}{(L)^{1/2}} \sin^2 \theta \cos^2 \theta + \frac{1}{L} \sin^4 \theta} \quad (2)$$

where

L = the attenuation ratio between the normal and tangential power components at the rotor output

ϕ = angular phase shift difference between the normal and tangential components in the rotor, deg

It is standard practice to make the rotor attenuation ratio L as large as possible so that Eq. (2) approaches Eq. (1). The rotor attenuation ratio is then treated as an error (Ref. 1). In situations where it is not desirable to neglect L , e.g., in a precision rotary vane attenuator where the highest accuracy is required or reduced weight or size is important, Eq. (2) is especially valuable.

3. Error Analysis

An error analysis of the attenuator calibration can be obtained from Eq. (2). This analysis provides parameter specifications for the design of a rotary vane attenuator, or performance data of an existing design. Calibration accuracy information is required not only for qualitative interest but is used quantitatively as a weighting parameter for measurement data which is averaged with other calibrations (SPS 37-46, Vol. III). The probable error of A determined from Eq. (2) is given by (Ref. 2)

$$PE_A = \left[PE_\theta^2 \left(\frac{\partial A}{\partial \theta} \right)^2 + PE_L^2 \left(\frac{\partial A}{\partial L} \right)^2 + PE_\phi^2 \left(\frac{\partial A}{\partial \phi} \right)^2 \right]^{1/2} \quad (3)$$

where

PE_θ = probable error of θ , rad

PE_L = probable error of L , ratio

PE_ϕ = probable error of ϕ , rad

The rotary vane angle is given by

$$\theta = \theta_I + \alpha_1 + \alpha_2 \quad (4)$$

where

θ_I = indicated vane angle, deg

α_1 = boresight error, deg

α_2 = additional readout errors, deg

Then

$$PE_\theta = (PE_{\theta_I}^2 + PE_{\alpha_1}^2 + PE_{\alpha_2}^2)^{1/2} \quad (5)$$

where

PE_{θ_I} = probable error of θ_I , rad

PE_{α_1} = probable error of α_1 , rad

PE_{α_2} = probable error of α_2 , rad

The differentials required in Eq. (3) are

$$\left(\frac{\partial A}{\partial \theta} \right) = (2 \sin \theta \cos \theta) \left[2 \left(1 - \frac{\cos \phi}{L} \right) \times \cos^2 \theta - 2 \left(\frac{1}{L} - \frac{\cos \phi}{L^{1/2}} \right) \sin^2 \theta \right] A^2$$

$$\left(\frac{\partial A}{\partial L} \right) = \left(\frac{\sin^4 \theta}{L^2} + \frac{\cos \phi}{L^{3/2}} \sin^2 \theta \cos^2 \theta \right) A^2$$

$$\left(\frac{\partial A}{\partial \phi} \right) = (2 \sin \phi \sin^2 \theta \cos^2 \theta) \frac{A}{L^{1/2}}$$

For design and calibration purposes it is usually necessary to know not only the total error PE_A but also the individual error contributions. The individual sources of error with account taken for the effect of internal mismatch are defined by:

$PE_{A/\phi}$ (dB) = probable error of A (dB) due to the error in ϕ , dB

$PE_{A/L}$ (dB) = probable error of A (dB) due to the error in L , dB

$PE_{A/\theta}$ (dB) = probable error of A (dB) due to the error in θ , dB

$PE_{A/MM}$ (dB) = probable error of A (dB) due to the error caused by internal mismatch, dB

These errors are calculated from

$$PE_{A/\phi} \text{ (dB)} = \frac{10 \log_{10} e}{A} \left(\frac{\partial A}{\partial \phi} \right) PE_\phi$$

$$PE_{A/L} \text{ (dB)} = \frac{10 \log_{10} e}{A} \left(\frac{\partial A}{\partial L} \right) PE_L$$

$$PE_{A/\theta} \text{ (dB)} = \frac{10 \log_{10} e}{A} \left(\frac{\partial A}{\partial \theta} \right) PE_\theta$$

and (Ref. 1)

$$PE_{A/MM} \text{ (dB)} \simeq \frac{10 \log_{10} [1 + 2|\Gamma|^2 \sin^2 \theta]^2}{5}$$

where

$|\Gamma|$ = amplitude of the reflection coefficient
at the interface of the stator and rotor
resistance cards

The probable error of A in dB is then most readily given
by

$$PE_A(\text{dB}) \simeq \{ [PE_{A/\phi}(\text{dB})]^2 + [PE_{A/L}(\text{dB})]^2 + [PE_{A/\theta}(\text{dB})]^2 + [PE_{A/MM}(\text{dB})]^2 \}^{1/2} \quad (6)$$

Eq. (6) has been programmed for the IBM 7094 computer
(program CTS/29B).¹ The program listing is shown in
Fig. 4. The first sample case (Fig. 5) is appropriate to the

JPL WR 430 waveguide precision rotary vane attenuator
shown in Fig. 6. The input parameters and errors are
tabulated on the left-hand side. The computed attenua-
tion errors due to individual sources of error are tabulated
on the right-hand side. The attenuation errors are in sub-
stantial agreement with those obtained by perturbing the
operating parameters as presented in SPS 37-46, Vol. III.
The subsequent sample cases (Fig. 7) are the same as the
above except the rotor attenuation ratio and accuracy
parameters are varied. The rotor attenuation probable
error is assumed to be 1% in dB of the rotor attenuation
ratio in all cases except the last. The error due to the rotor
attenuation ratio shown graphically in Fig. 8 is minimized
at low attenuation. Accurate calibration of the rotor atten-
uation reduces this error further.

¹L. Busch, JPL, Feb. 26, 1967.

```

C      CTS 29B...PROBABLE ERROR OF ROTARY VANE ATTENUATOR
C      6/26/67 (LIB)
C
C      C=.0174532925
      TLOGE=4.342944819
15  READ(5,5) NRUN,NPTS
      K=0
20  WRITE(6,1)
      WRITE(6,2)
      N=6
25  READ(5,3) ADB,PHID,PEPHID,ELDB,PELDB,PETHID,PEA1D,PEA2D,GAMMM
      CONVERSIONS AND TRIG. FUNCTIONS.
C
26  A=10.0**(ADB/10.)
      EL=10.0**(ELDB/10.)
      PEL=EL*PELDB/TLOGE
      PHI=PHID*C
      PEPHI=PEPHID*C
      SINPHI=SIN(PHI)
      COSPHI=COS(PHI)
      PETHI=PETHID*C
      PEA1=PEA1D*C
      PEA2=PEA2D*C
      COSTH=1.0/(A**0.25)
      COSTHQ=COSTH**2
      SINTH=SQRT(1.0-COSTHQ)
      SINTHQ=SINTH**2
C
      FINAL CALCULATIONS
      PETH=SQRT(PETHI**2 + PEA1**2 + PEA2**2)
      E1=PEPHI*(2.0*SINPHI*SINTHQ*COSTHQ)* A**2/SQRT(EL)
      E2=PEL*(SINTH**4/EL**2 + COSPHI/SQRT(EL**3)*SINTHQ*COSTHQ)*A**2
      E3=PETH*(COSTHQ*(1.0-COSPHI/SQRT(EL)) - SINTHQ*(1.0/EL -COSPHI/
1  SQRT(EL)))*4.0*A**2*SINTH*COSTH
      E1DB=E1*TLOGE/A
      E2DB=E2*TLOGE/A
      E3DB=E3*TLOGE/A
      E4DB=(10.0*ALOG10((1.0+2.0*(GAMMM*SINTH)**2)**2))/5.0
      PEADB=SQRT(E1DB**2 + E2DB**2 + E3DB**2 + E4DB**2)
      PETHD=PETH*57.2957795
      WRITE(6,4) ADB,PHID,PEPHID,ELDB,PELDB,PETHID,PEA1D,PEA2D,GAMMM,
1  PETHD,E1DB,E2DB,E3DB,E4DB,PEADB
      N=N+1
      K=K+1
      IF(N.EQ.60) GO TO 20
      IF(K.EQ.NPTS) GO TO 15
      GO TO 25
C
5  FORMAT(2I5)
3  FORMAT(8E10.0)
1  FORMAT(1H1,38X52HPROBABLE ERROR OF ROTARY VANE ATTENUATOR ... CTS
129B,/)
2  FORMAT(20X2HPE,13X2HPE,5X2HPE,8X2HPE,8X2HPE,22X2HPE,5(6X2HPE),/
1  5X1HA,7X3HPI,4X3HPI,5X1HL,6X1HL,6X6HTHETA1,4X6HALPHA1,4X6HALPHA
22,3X2HMM,13X5HTHETA,3X5HA/PHI,3X3HA/L,5X7HA/THETA,1X4HA/MM,4X1HA,/
3  4X4H(DB),4X5H(DEG),2X5H(DEG),2(3X4H(DB)),3X5H(DEG),2(5X5H(DEG))),
4  5X5HGAMMA,10X5H(DEG),3X4H(DB),4(4X4H(DB)))
4  FORMAT(F10.5,4F7.2,3F10.6,F8.4,7X6F8.4)
      END

```

Fig. 4. IBM 7094 computer listing of microwave precision rotary vane attenuation error program, CTS/29B

PROBABLE ERROR OF ROTARY VANE ATTENUATOR ... CTS 29B

A	PHI	PE	PE	PE	PE	PE	PE	PE	PE	PE	PE	PE	PE	PE	PE	PE
(DB)	(DEG)	(DEG)	(DB)	(DB)	(DEG)	(DEG)	(DEG)	(DEG)	MM	THETA	A/PHI	A/L	A/THETA	A/MM	A	
										(DEG)	(DB)	(DB)	(DB)	(DB)	(DB)	
0.00001	1.00	0.12	88.00	1.00	0.000400	0.001000	0.000233	0.0150		0.0011	0.0000	0.0000	0.0000	0.0000	0.0000	
0.01928	1.00	0.12	88.00	1.00	0.000400	0.001000	0.000437	0.0150		0.0012	0.0000	0.0000	0.0000	0.0000	0.0000	
0.03898	1.00	0.12	88.00	1.00	0.000400	0.001000	0.000567	0.0150		0.0012	0.0000	0.0000	0.0000	0.0000	0.0000	
0.05384	1.00	0.12	88.00	1.00	0.000400	0.001000	0.000647	0.0150		0.0013	0.0000	0.0000	0.0000	0.0000	0.0000	
0.06498	1.00	0.12	88.00	1.00	0.000400	0.001000	0.000699	0.0150		0.0013	0.0000	0.0000	0.0000	0.0000	0.0000	
0.07874	1.00	0.12	88.00	1.00	0.000400	0.001000	0.000759	0.0150		0.0013	0.0000	0.0000	0.0000	0.0000	0.0000	
0.09860	1.00	0.12	88.00	1.00	0.000400	0.001000	0.000835	0.0150		0.0014	0.0000	0.0000	0.0000	0.0000	0.0000	
0.11911	1.00	0.12	88.00	1.00	0.000400	0.001000	0.001131	0.0150		0.0016	0.0000	0.0000	0.0001	0.0000	0.0001	
0.14363	1.00	0.12	88.00	1.00	0.000400	0.001000	0.001279	0.0150		0.0017	0.0000	0.0000	0.0001	0.0000	0.0001	
0.17375	1.00	0.12	88.00	1.00	0.000400	0.001000	0.001520	0.0150		0.0019	0.0000	0.0000	0.0001	0.0000	0.0001	
0.20991	1.00	0.12	88.00	1.00	0.000400	0.001000	0.001790	0.0150		0.0021	0.0000	0.0000	0.0002	0.0001	0.0002	
0.25266	1.00	0.12	88.00	1.00	0.000400	0.001000	0.001993	0.0150		0.0023	0.0000	0.0000	0.0002	0.0001	0.0002	
0.29556	1.00	0.12	88.00	1.00	0.000400	0.001000	0.002152	0.0150		0.0024	0.0000	0.0000	0.0003	0.0001	0.0003	
0.34075	1.00	0.12	88.00	1.00	0.000400	0.001000	0.002206	0.0150		0.0025	0.0000	0.0000	0.0003	0.0001	0.0003	
0.38510	1.00	0.12	88.00	1.00	0.000400	0.001000	0.002519	0.0150		0.0027	0.0000	0.0000	0.0004	0.0001	0.0004	
0.43142	1.00	0.12	88.00	1.00	0.000400	0.001000	0.002556	0.0150		0.0028	0.0000	0.0000	0.0004	0.0002	0.0005	
0.47921	1.00	0.12	88.00	1.00	0.000400	0.001000	0.002598	0.0150		0.0028	0.0000	0.0000	0.0005	0.0002	0.0005	
0.52748	1.00	0.12	88.00	1.00	0.000400	0.001000	0.002599	0.0150		0.0028	0.0000	0.0000	0.0005	0.0002	0.0005	
0.57404	1.00	0.12	88.00	1.00	0.000400	0.001000	0.002565	0.0150		0.0028	0.0000	0.0000	0.0005	0.0002	0.0006	
0.61604	1.00	0.12	88.00	1.00	0.000400	0.001000	0.002462	0.0150		0.0027	0.0000	0.0000	0.0006	0.0003	0.0006	
0.65375	1.00	0.12	88.00	1.00	0.000400	0.001000	0.002318	0.0150		0.0026	0.0000	0.0000	0.0006	0.0003	0.0007	
0.69400	1.00	0.12	88.00	1.00	0.000400	0.001000	0.001878	0.0150		0.0022	0.0000	0.0000	0.0006	0.0003	0.0007	
0.73288	1.00	0.12	88.00	1.00	0.000400	0.001000	0.001294	0.0150		0.0017	0.0000	0.0000	0.0005	0.0004	0.0006	
0.76923	1.00	0.12	88.00	1.00	0.000400	0.001000	0.000635	0.0150		0.0013	0.0000	0.0000	0.0004	0.0004	0.0006	
0.80200	1.00	0.12	88.00	1.00	0.000400	0.001000	0.000462	0.0150		0.0012	0.0000	0.0001	0.0004	0.0005	0.0006	
0.83121	1.00	0.12	88.00	1.00	0.000400	0.001000	0.001218	0.0150		0.0016	0.0000	0.0001	0.0007	0.0005	0.0008	
0.85211	1.00	0.12	88.00	1.00	0.000400	0.001000	0.002107	0.0150		0.0024	0.0000	0.0001	0.0011	0.0005	0.0012	
0.86165	1.00	0.12	88.00	1.00	0.000400	0.001000	0.003936	0.0150		0.0041	0.0000	0.0001	0.0021	0.0006	0.0022	
0.86699	1.00	0.12	88.00	1.00	0.000400	0.001000	0.005689	0.0150		0.0058	0.0000	0.0002	0.0035	0.0006	0.0036	
0.86919	1.00	0.12	88.00	1.00	0.000400	0.001000	0.007263	0.0150		0.0073	0.0000	0.0002	0.0051	0.0007	0.0052	
0.86302	1.00	0.12	88.00	1.00	0.000400	0.001000	0.008620	0.0150		0.0087	0.0000	0.0003	0.0069	0.0007	0.0070	
0.80310	1.00	0.12	88.00	1.00	0.000400	0.001000	0.009751	0.0150		0.0098	0.0000	0.0004	0.0089	0.0007	0.0090	
0.70419	1.00	0.12	88.00	1.00	0.000400	0.001000	0.011748	0.0150		0.0118	0.0000	0.0007	0.0147	0.0007	0.0147	
0.58366	1.00	0.12	88.00	1.00	0.000400	0.001000	0.012906	0.0150		0.0130	0.0000	0.0012	0.0217	0.0008	0.0218	
0.48028	1.00	0.12	88.00	1.00	0.000400	0.001000	0.013601	0.0150		0.0136	0.0000	0.0022	0.0308	0.0008	0.0309	
0.39948	1.00	0.12	88.00	1.00	0.000400	0.001000	0.014067	0.0150		0.0141	0.0000	0.0040	0.0427	0.0008	0.0429	
0.21186	1.00	0.12	88.00	1.00	0.000400	0.001000	0.014164	0.0150		0.0142	0.0000	0.0046	0.0462	0.0008	0.0464	
0.25285	1.00	0.12	88.00	1.00	0.000400	0.001000	0.014244	0.0150		0.0143	0.0000	0.0051	0.0494	0.0008	0.0496	
0.43735	1.00	0.12	88.00	1.00	0.000400	0.001000	0.014344	0.0150		0.0144	0.0000	0.0059	0.0533	0.0008	0.0536	
0.99959	1.00	0.12	88.00	1.00	0.000400	0.001000	0.014455	0.0150		0.0145	0.0000	0.0071	0.0588	0.0008	0.0593	
0.91299	1.00	0.12	88.00	1.00	0.000400	0.001000	0.014878	0.0150		0.0149	0.0000	0.0126	0.0809	0.0008	0.0819	
0.96424	1.00	0.12	88.00	1.00	0.000400	0.001000	0.015491	0.0150		0.0155	0.0000	0.0227	0.1138	0.0008	0.1160	
0.06493	1.00	0.12	88.00	1.00	0.000400	0.001000	0.016490	0.0150		0.0165	0.0000	0.0417	0.1653	0.0008	0.1705	

Fig. 5. Computer printout of errors pertinent to the JPL precision WR 430 waveguide rotary vane attenuator

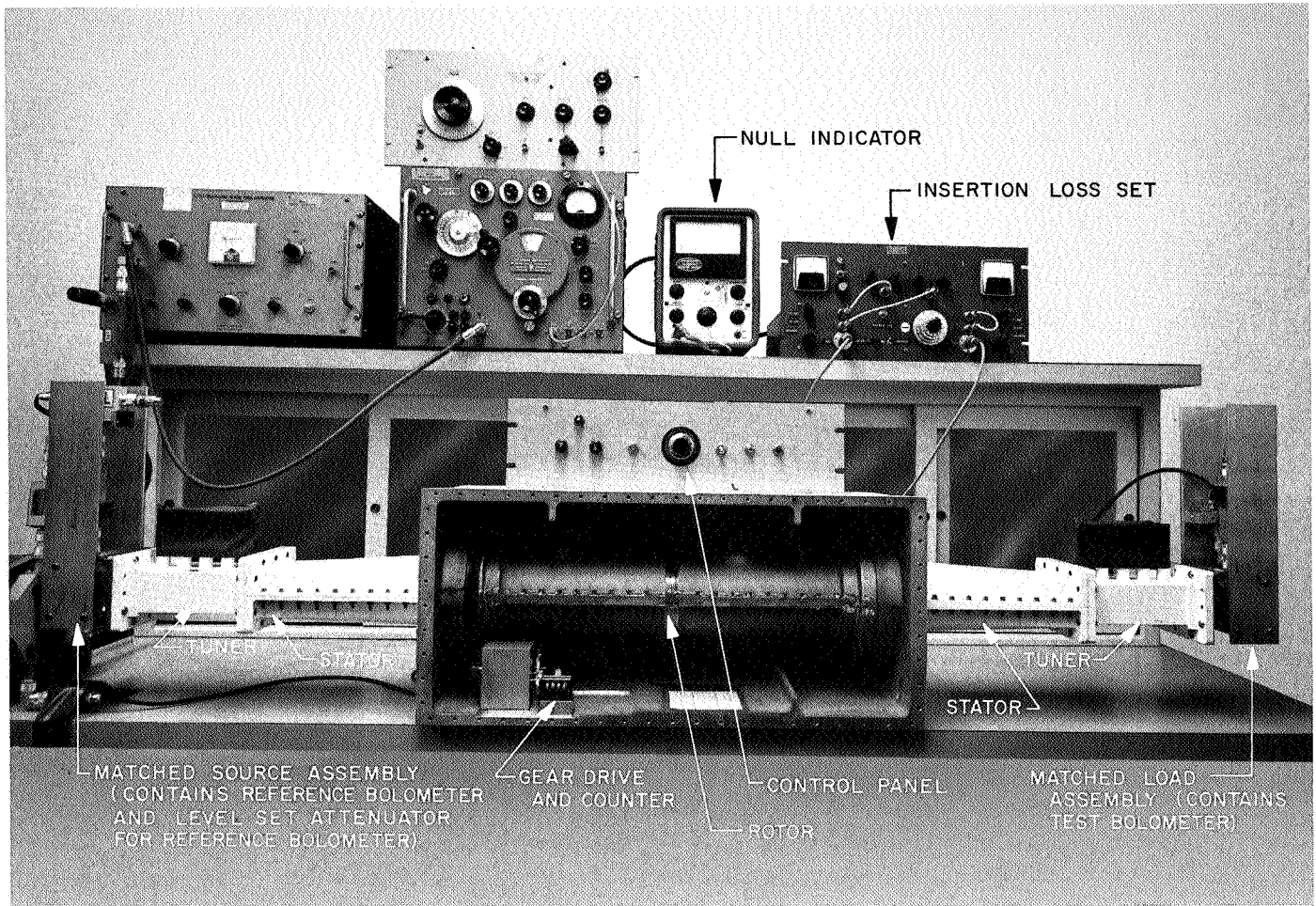


Fig. 6. WR 430 waveguide precision rotary vane attenuator

PROBABLE ERROR OF ROTARY VANE ATTENUATOR ... CTS 298

A (DB)	PHI (DEG)	PE PHI (DEG)	L (DB)	PE L (DB)	PE THETA (DEG)	PE ALPHA1 (DEG)	PE ALPHA2 (DEG)	MM GAMMA	PF THETA (DEG)	PE A/PHI (DB)	PE A/L (DB)	PE A/THETA (DB)	PE A/MM (DB)	PE A (DB)
0.00000	1.00	0.12	88.00	0.88	0.000400	0.001000	0.014000	0.0150	0.0140	0.0000	0.0000	0.0000	0.0000	0.0000
1.00000	1.00	0.12	88.00	0.88	0.000400	0.001000	0.014000	0.0150	0.0140	0.0000	0.0000	0.0015	0.0001	0.0015
3.00000	1.00	0.12	88.00	0.88	0.000400	0.001000	0.014000	0.0150	0.0140	0.0000	0.0000	0.0027	0.0002	0.0027
6.00000	1.00	0.12	88.00	0.88	0.000400	0.001000	0.014000	0.0150	0.0140	0.0000	0.0000	0.0042	0.0004	0.0043
10.00000	1.00	0.12	88.00	0.88	0.000400	0.001000	0.014000	0.0150	0.0140	0.0000	0.0001	0.0063	0.0005	0.0063
20.00000	1.00	0.12	88.00	0.88	0.000400	0.001000	0.014000	0.0150	0.0140	0.0000	0.0003	0.0128	0.0007	0.0128
40.00000	1.00	0.12	88.00	0.88	0.000400	0.001000	0.014000	0.0150	0.0140	0.0000	0.0035	0.0425	0.0008	0.0427
0.00000	1.00	0.12	60.00	0.60	0.000400	0.001000	0.014000	0.0150	0.0140	0.0000	0.0000	0.0000	0.0000	0.0000
1.00000	1.00	0.12	60.00	0.60	0.000400	0.001000	0.014000	0.0150	0.0140	0.0000	0.0001	0.0015	0.0001	0.0015
3.00000	1.00	0.12	60.00	0.60	0.000400	0.001000	0.014000	0.0150	0.0140	0.0000	0.0002	0.0027	0.0002	0.0028
6.00000	1.00	0.12	60.00	0.60	0.000400	0.001000	0.014000	0.0150	0.0140	0.0000	0.0006	0.0042	0.0004	0.0043
10.00000	1.00	0.12	60.00	0.60	0.000400	0.001000	0.014000	0.0150	0.0140	0.0000	0.0013	0.0063	0.0005	0.0064
20.00000	1.00	0.12	60.00	0.60	0.000400	0.001000	0.014000	0.0150	0.0140	0.0000	0.0054	0.0129	0.0007	0.0140
40.00000	1.00	0.12	60.00	0.60	0.000400	0.001000	0.014000	0.0150	0.0140	0.0000	0.0653	0.0465	0.0008	0.0801
0.00000	1.00	0.12	50.00	0.50	0.000400	0.001000	0.014000	0.0150	0.0140	0.0000	0.0000	0.0000	0.0000	0.0000
1.00000	1.00	0.12	50.00	0.50	0.000400	0.001000	0.014000	0.0150	0.0140	0.0000	0.0002	0.0015	0.0001	0.0015
3.00000	1.00	0.12	50.00	0.50	0.000400	0.001000	0.014000	0.0150	0.0140	0.0000	0.0007	0.0027	0.0002	0.0028
6.00000	1.00	0.12	50.00	0.50	0.000400	0.001000	0.014000	0.0150	0.0140	0.0000	0.0016	0.0042	0.0004	0.0045
10.00000	1.00	0.12	50.00	0.50	0.000400	0.001000	0.014000	0.0150	0.0140	0.0000	0.0034	0.0063	0.0005	0.0072
20.00000	1.00	0.12	50.00	0.50	0.000400	0.001000	0.014000	0.0150	0.0140	0.0000	0.0146	0.0131	0.0007	0.0196
40.00000	1.00	0.12	50.00	0.50	0.000400	0.001000	0.014000	0.0150	0.0140	0.0001	0.2055	0.0554	0.0008	0.2129
0.00000	1.00	0.12	40.00	0.40	0.000400	0.001000	0.014000	0.0150	0.0140	0.0000	0.0000	0.0000	0.0000	0.0000
1.00000	1.00	0.12	40.00	0.40	0.000400	0.001000	0.014000	0.0150	0.0140	0.0000	0.0005	0.0015	0.0001	0.0016
3.00000	1.00	0.12	40.00	0.40	0.000400	0.001000	0.014000	0.0150	0.0140	0.0000	0.0017	0.0027	0.0002	0.0032
6.00000	1.00	0.12	40.00	0.40	0.000400	0.001000	0.014000	0.0150	0.0140	0.0000	0.0040	0.0042	0.0004	0.0059
10.00000	1.00	0.12	40.00	0.40	0.000400	0.001000	0.014000	0.0150	0.0140	0.0000	0.0088	0.0063	0.0005	0.0109
20.00000	1.00	0.12	40.00	0.40	0.000400	0.001000	0.014000	0.0150	0.0140	0.0000	0.0392	0.0138	0.0007	0.0416
0.00000	1.00	0.12	30.00	0.30	0.000400	0.001000	0.014000	0.0150	0.0140	0.0000	0.0000	0.0000	0.0000	0.0000
1.00000	1.00	0.12	30.00	0.30	0.000400	0.001000	0.014000	0.0150	0.0140	0.0000	0.0012	0.0014	0.0001	0.0019
3.00000	1.00	0.12	30.00	0.30	0.000400	0.001000	0.014000	0.0150	0.0140	0.0000	0.0040	0.0027	0.0002	0.0048
6.00000	1.00	0.12	30.00	0.30	0.000400	0.001000	0.014000	0.0150	0.0140	0.0000	0.0097	0.0042	0.0004	0.0106
10.00000	1.00	0.12	30.00	0.30	0.000400	0.001000	0.014000	0.0150	0.0140	0.0000	0.0219	0.0065	0.0005	0.0229
20.00000	1.00	0.12	30.00	0.30	0.000400	0.001000	0.014000	0.0150	0.0140	0.0001	0.1097	0.0159	0.0007	0.1108
0.00000	1.00	0.12	30.00	0.03	0.000400	0.001000	0.014000	0.0150	0.0140	0.0000	0.0000	0.0000	0.0000	0.0000
1.00000	1.00	0.12	30.00	0.03	0.000400	0.001000	0.014000	0.0150	0.0140	0.0000	0.0001	0.0014	0.0001	0.0015
3.00000	1.00	0.12	30.00	0.03	0.000400	0.001000	0.014000	0.0150	0.0140	0.0000	0.0004	0.0027	0.0002	0.0027
6.00000	1.00	0.12	30.00	0.03	0.000400	0.001000	0.014000	0.0150	0.0140	0.0000	0.0010	0.0042	0.0004	0.0044
10.00000	1.00	0.12	30.00	0.03	0.000400	0.001000	0.014000	0.0150	0.0140	0.0000	0.0022	0.0065	0.0005	0.0069
20.00000	1.00	0.12	30.00	0.03	0.000400	0.001000	0.014000	0.0150	0.0140	0.0001	0.0110	0.0159	0.0007	0.0193

Fig. 7. Computer printout of errors pertinent to the JPL precision WR 430 waveguide rotary vane attenuator with various combinations of rotor attenuation ratios and errors

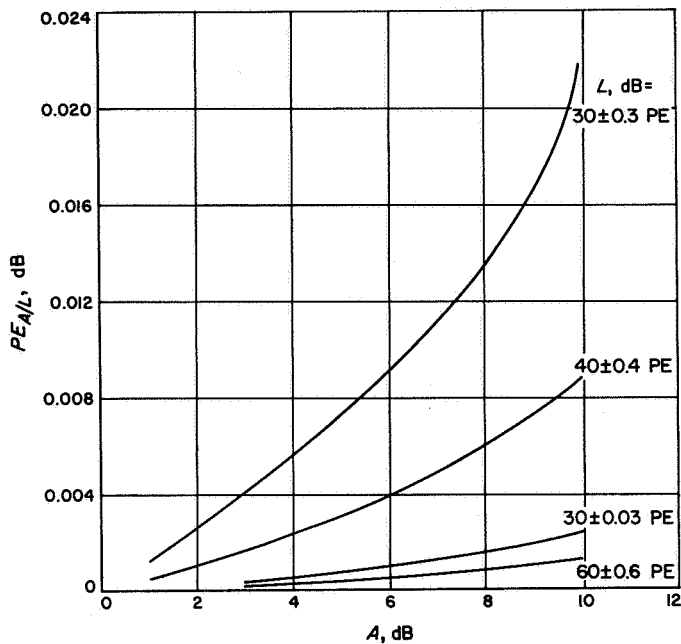


Fig. 8. Attenuation error versus attenuation setting for various combinations of rotor attenuation and accuracy relating to the JPL precision WR 430 waveguide rotary vane attenuator

4. Conclusion

A calibration formula is available to account for the rotor attenuation ratio in a microwave rotary vane attenuator. The effect of the individual sources of error on calibration accuracy can be determined from the above error analysis. Study of the individual errors is especially valuable for design applications. Considerable savings in weight and size can be obtained using a rotor with low attenuation ratios. This can be achieved without sacrifice of performance by accurately accounting for rotor attenuation in situations where low values of calibrating attenuation are applicable. A radio astronomy radiometer with a "front end" rotary vane calibration attenuator provides an excellent example. The primary advantage of a front end attenuator over an IF attenuator for this application is the elimination of nonlinearity problems in the radiometer.

C. RF Breakdown Studies, R. Woo

1. Introduction

Further results of high pressure RF breakdown in coaxial transmission lines at S-band frequencies are reported here.

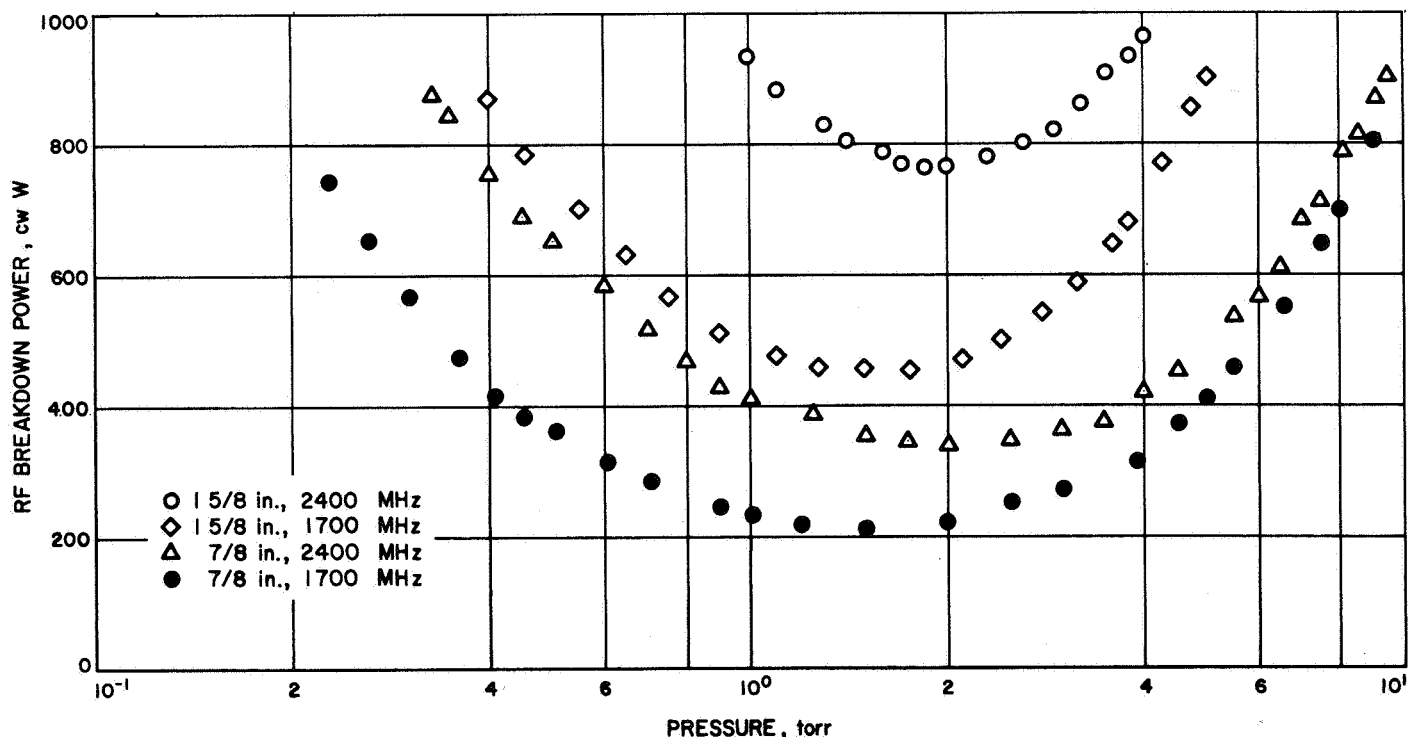


Fig. 9. RF breakdown power for 7/8- and 1-5/8-in. coaxial line at 1700 and 2400 MHz as a function of pressure

Presented in SPS 37-45, Vol. IV were breakdown data in air for 1½-in. rigid coaxial transmission line obtained in the frequency range of 1700–2400 MHz. Representation of the data by a three-dimensional surface similar to that introduced by MacDonald and Brown was discussed.

In this article we will change the $p\lambda$ axis of this three-dimensional plot (p is pressure and λ is d/π , where d is the electrode separation distance) to fd (f is frequency). Previous data and additional data obtained for 7/8-in. rigid coaxial transmission line at 1700 and 2400 MHz will be presented in this format.

2. Results and Discussion

Shown in Fig. 9 is the breakdown data in air for 7/8-in. rigid coaxial transmission line obtained at 1700 and 2400 MHz. As is expected, the power handling capability decreases with decreasing line size. Shown in Fig. 10 are these data plotted along with the theoretical curve of Gould (Ref. 3). For the case of 7/8-in. coaxial line, Gould's curve covers only pressures greater than 3.2 torr. Com-

parison of Herlin and Brown's data (Ref. 4) and our data indicated that their breakdown power levels were again approximately 10% lower.

The $p\lambda$ - $p\lambda$ plane discussed in SPS 37-45, Vol. IV is reproduced in Fig. 11. If the $p\lambda$ axis is changed to fd , it can be seen that the constant $p\lambda$ lines would represent 135-deg lines with the $p\lambda$ axis. The fd - $p\lambda$ plane, along with the various limits, is shown in Fig. 12. The main advantage of the fd - $p\lambda$ plane is that the constant fd lines are now parallel to the $p\lambda$ axis. Shown in Fig. 13 are the breakdown data for 50- Ω coaxial transmission line plotted as a function of $p\lambda$. When combined with Fig. 12, the three-dimensional surface representing breakdown can be conveniently constructed.

D. Spacecraft Antenna Research, K. Woo

1. High-Impact Square-Cup Radiator

a. Introduction. An S-band, low-gain, circularly polarized, high-impact square-cup radiator has been developed,

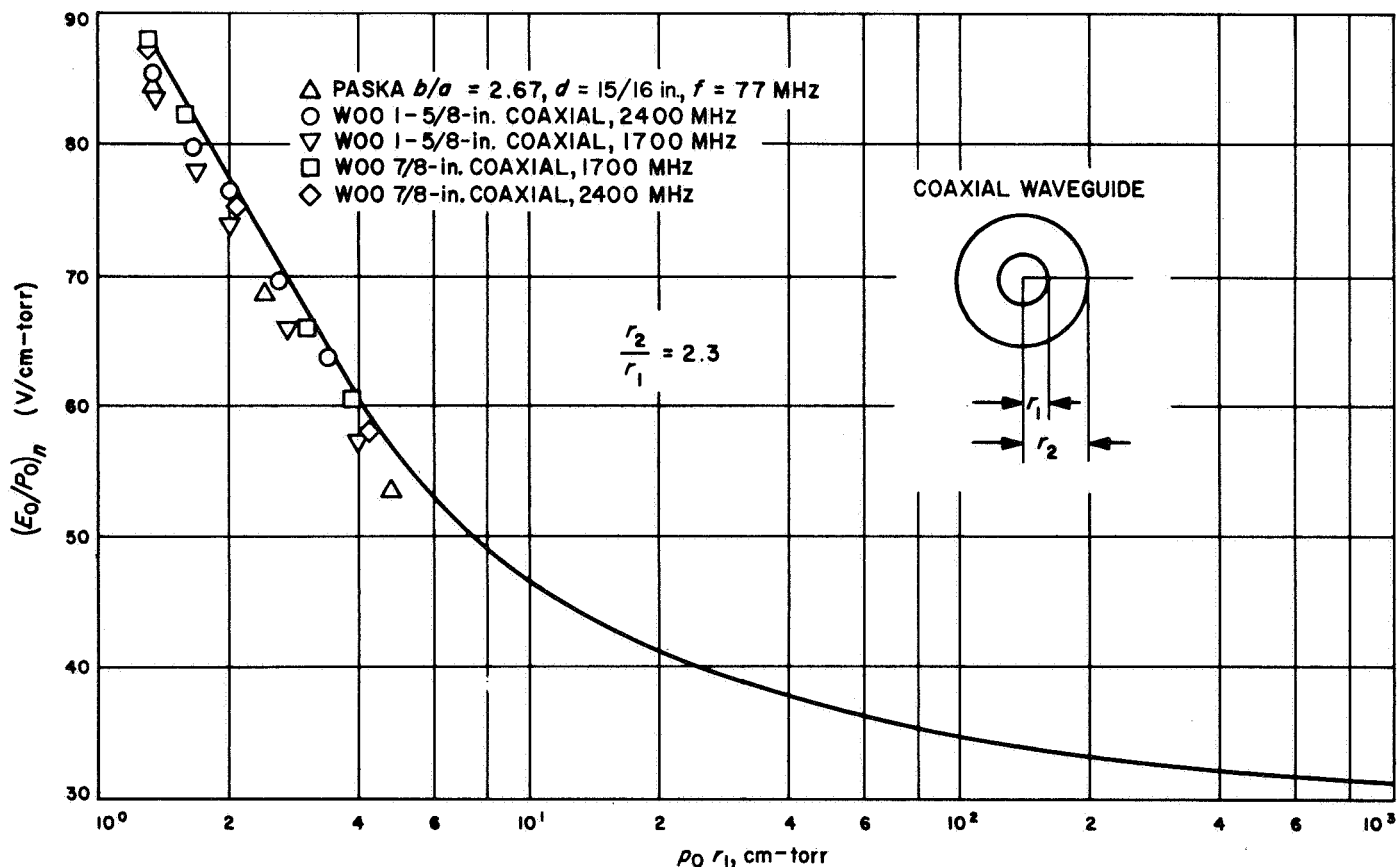


Fig. 10. Ratio of normalized cw breakdown field to pressure as a function of pressure times inner conductor radius

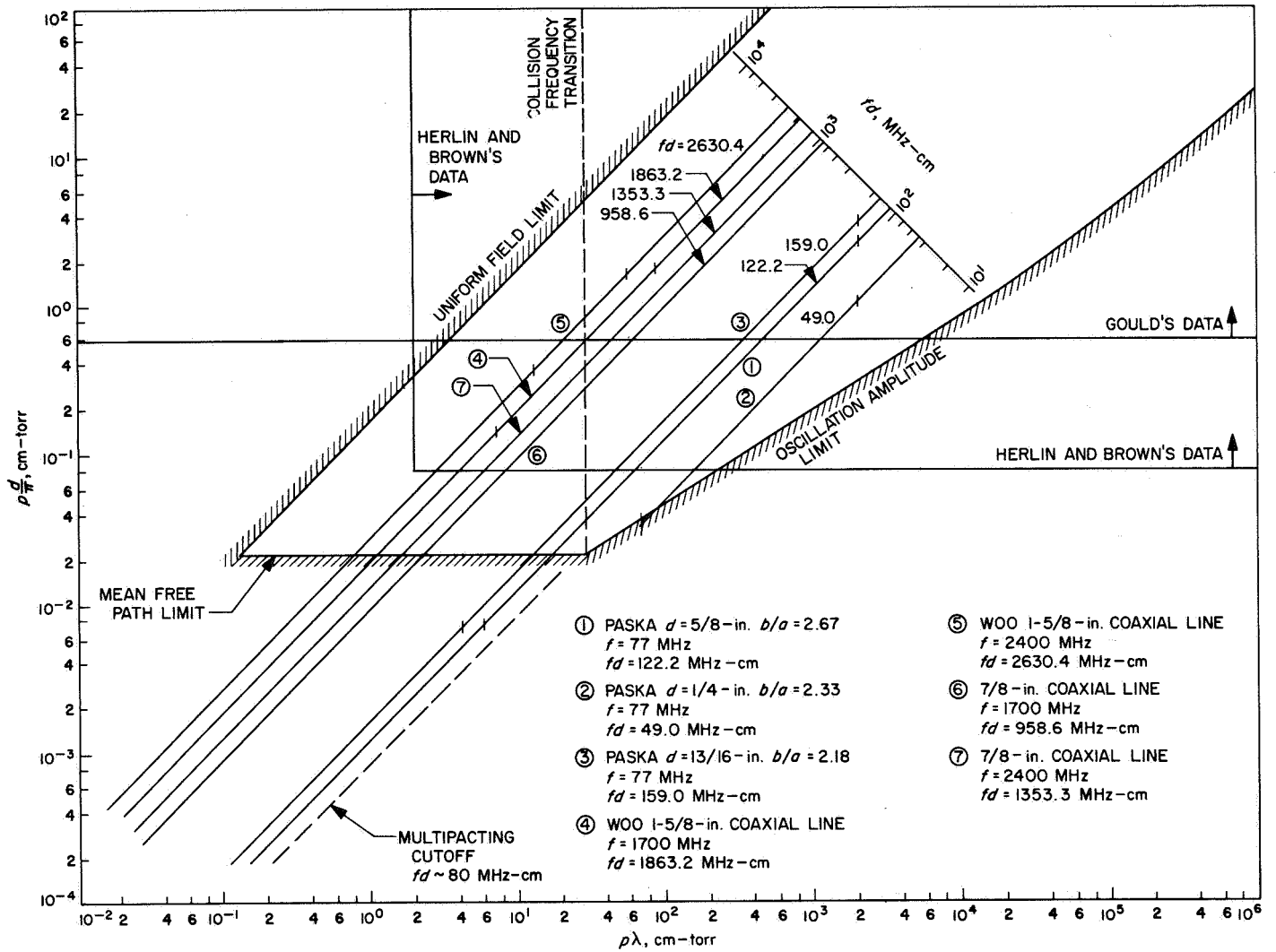


Fig. 11. The $p\Delta$ - $p\lambda$ plane

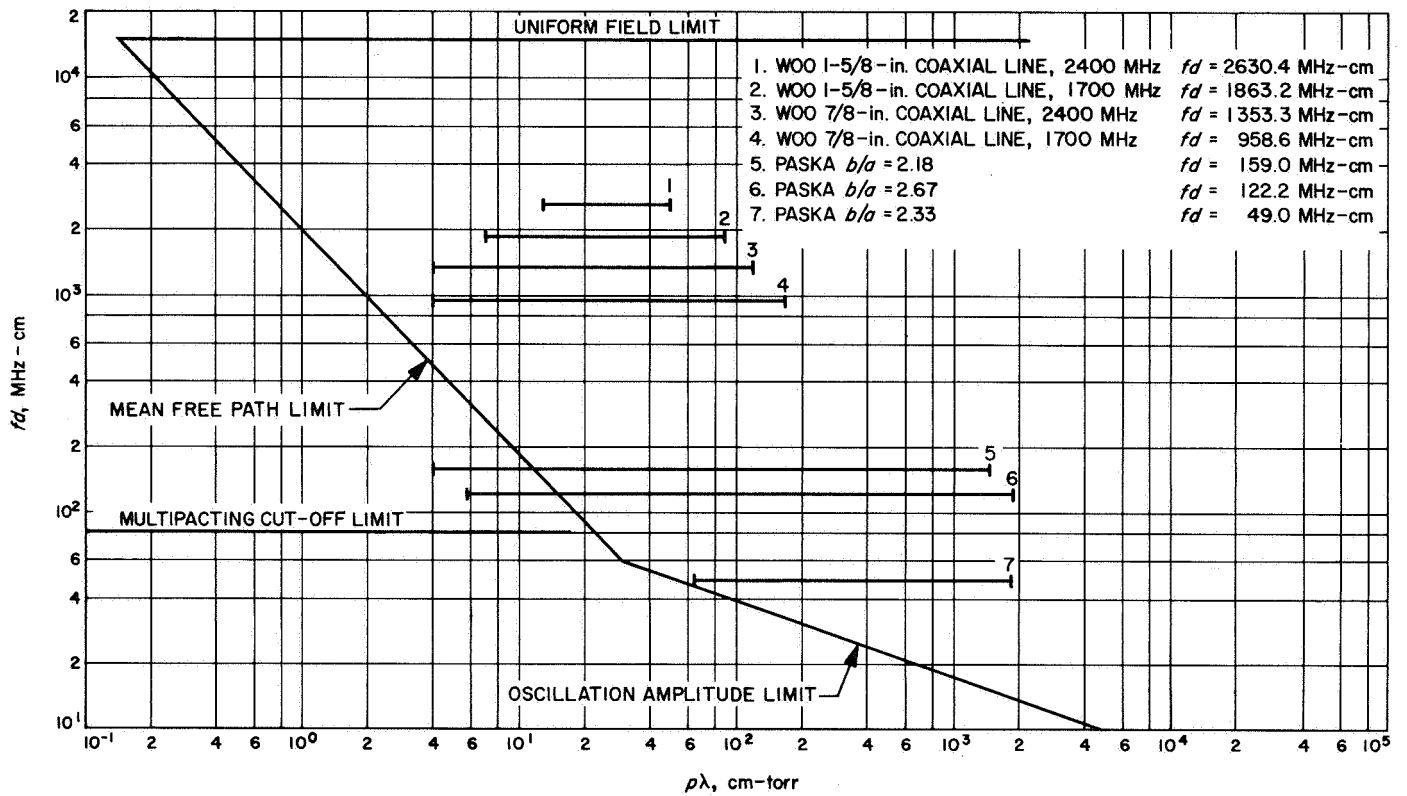


Fig. 12. The fd - $\rho\lambda$ plane

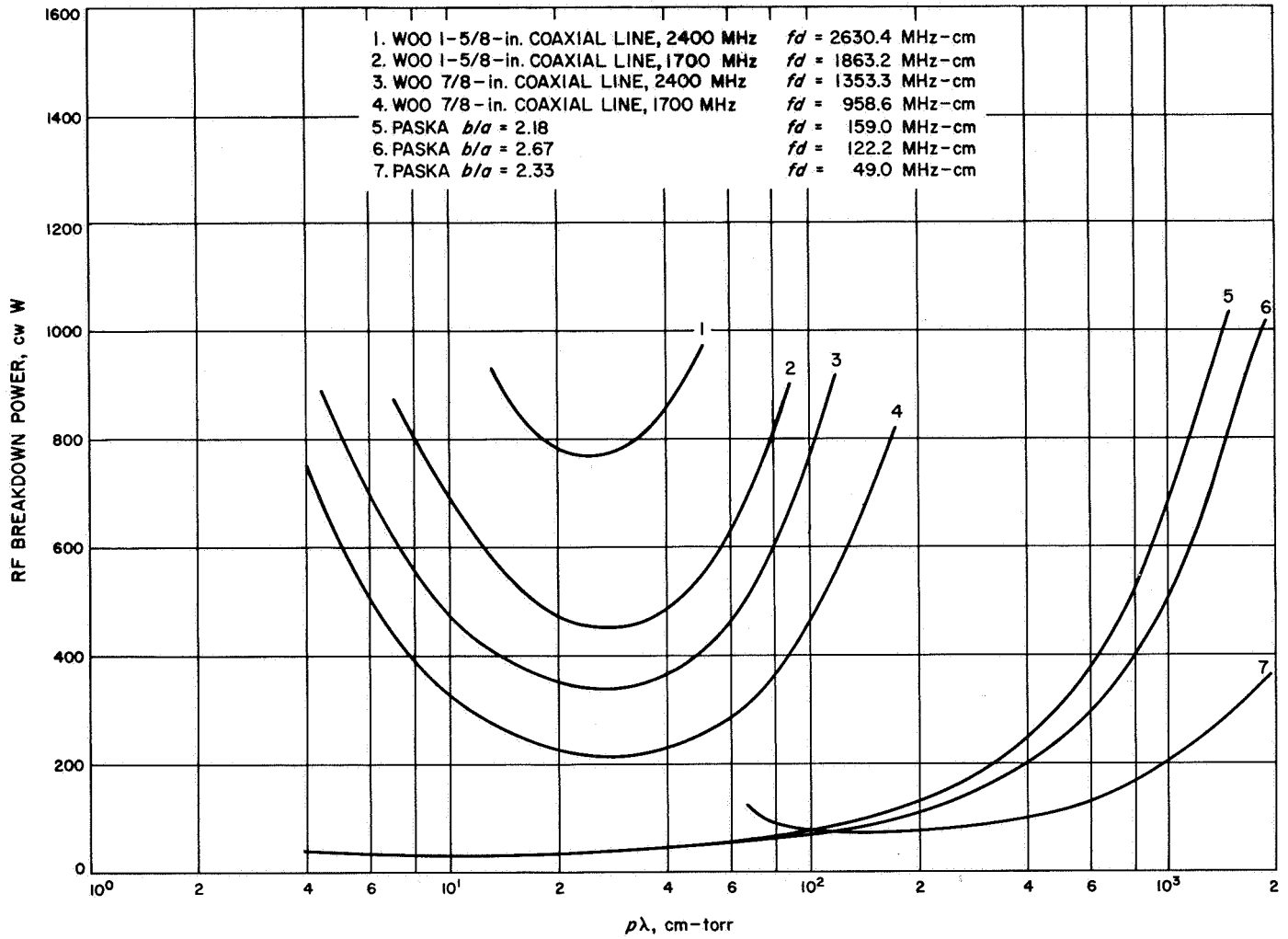


Fig. 13. Breakdown power as a function of $p\lambda$ for various values of fd

It is capable of surviving an indirect impact of 10,000 g, is relatively simple in construction, and is compact. The electrical characteristics of the antenna are similar to those of the rectangular-cup radiator (SPS 37-44, Vol. IV) except that a nearly axially symmetric beam is achieved. (Refer to SPS 37-40 to -45, Vol. IV, for other articles about high-impact antennas.)

b. Experimental model. The experimental model of the antenna is shown in Fig. 14. It consists of a ruggedized square cup (aluminum, internal dimensions $2.25 \times 2.25 \times 2.475$ in.) having ridges extending along the inside surfaces of two opposite walls, and a feed probe (beryllium copper, 3/32-in. diam) slanted between two adjacent walls, as shown in Fig. 15. The probe excites the orthogonal TE_{10}^{\square} and TE_{01}^{\square} modes, and the ridges introduce phase shift between these two modes. For sustaining high impacts, the cup is filled with low-loss foam. The foam is formed by mixing Eccofoam FP² (foam-in-place liquid resin) and catalyst. Upon curing, the foam (having density of about 26 lb/ft³) gives an all-around rigid support to the probe and the cup walls. The cup dimensions, probe

position, ridge configuration, and foam density have been properly chosen so that the antenna radiates predominantly right-hand circularly polarized waves.

c. Test results. Electrical measurements of the experimental antenna at 2298 MHz showed a gain of about 5.9 dB, and a maximum ellipticity (within ± 60 deg from the beam axis) of about 5 dB. The half-power beamwidths were respectively 92, 91, 90, and 94 deg along the 0-, 45-, 90-, and 135-deg cuts (Fig. 14a).

An indirect impact test of the antenna at 10,000 g (0.6-ms duration) was performed. The antenna was attached in a test fixture, and then the fixture was impacted against a target. There was no visible damage to the antenna or appreciable change in the electrical performance. Fig. 16 shows the radiation patterns at 2298 MHz of the right-hand and left-hand circularly polarized components before and after the impact. The input VSWR remained about the same (1.77 before impact, 1.75 after impact).

²Distributed by Emerson & Cuming, Inc.

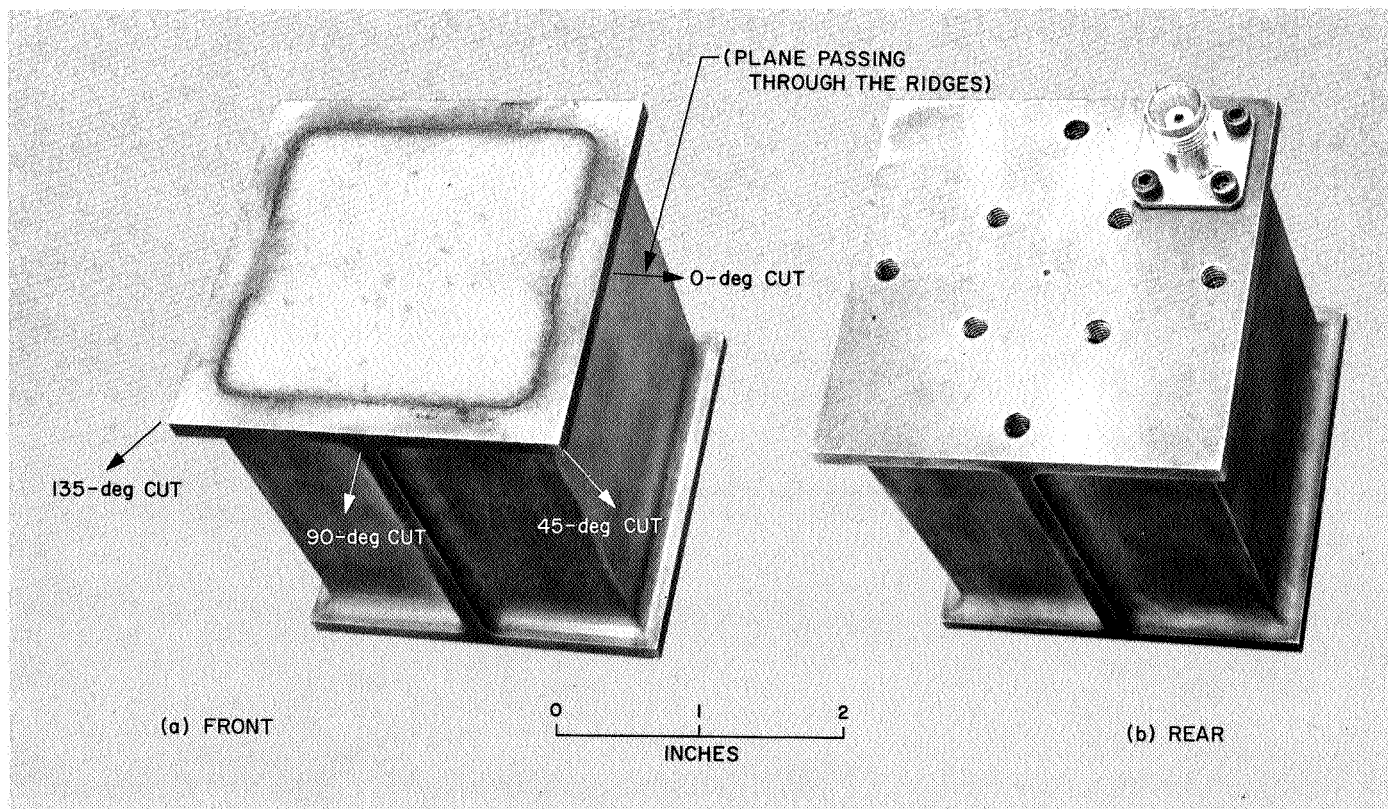


Fig. 14. High-impact square-cup radiator

Further work on the antenna is in progress. It includes:

- (1) Improving the ellipticity by optimizing the ridge configuration.

- (2) Reducing the antenna weight (present weight 0.77 lb) by further trimming the cup walls.
- (3) Investigating the power handling capability.

Fig. 15. Internal construction of square-cup radiator

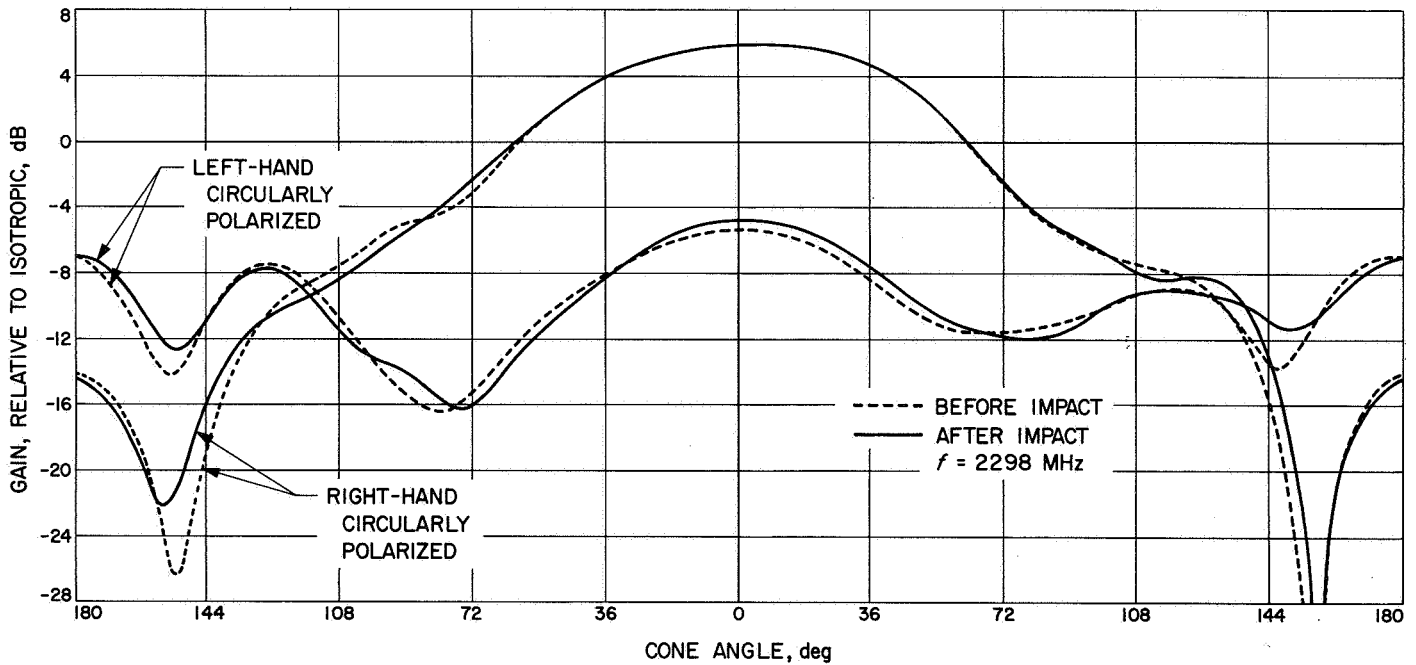
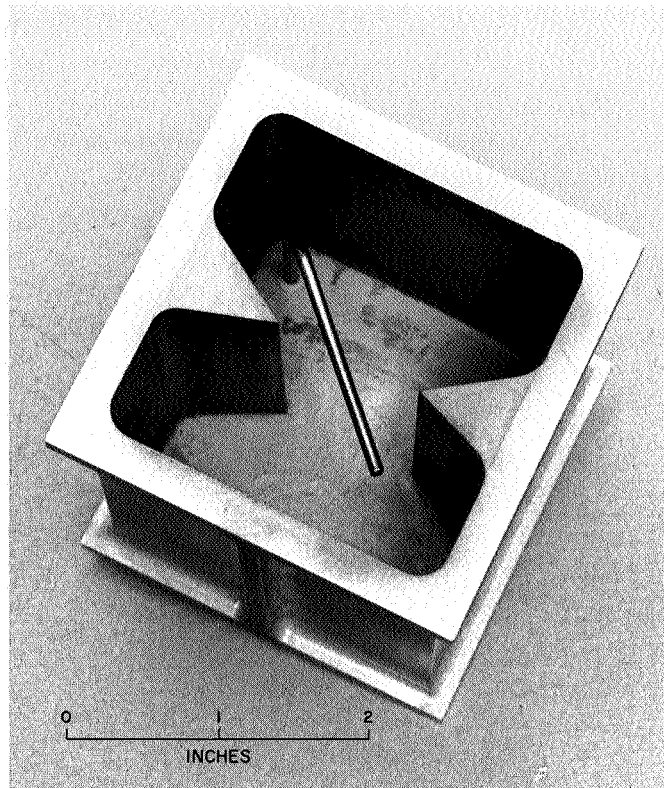


Fig. 16. Radiation patterns before and after 10,000-g indirect impact

References

1. James, A. V., "A High-Accuracy Microwave-Attenuation Standard for Use in Primary Calibration Laboratories," *IRE Trans. Instrumen.*, Vol. I-11, pp. 285-290, Dec. 1962.
2. Worthing, A., and Geffner, J., *Treatment of Experimental Data*, 9th Printing, p. 213. John Wiley & Sons, Inc., New York, 1960.
3. Gould, L., *Handbook on Breakdown of Air in Waveguide Systems*, Microwave Associates, Inc., Burlington, Mass., April 1956.
4. Herlin, M. A., and Brown, S. C., "Electrical Breakdown of a Gas Between Coaxial Cylinders at Microwave Frequencies," *Phys. Rev.*, Vol. 74, pp. 910-913, 1948.

XXI. Spacecraft Telemetry and Command

TELECOMMUNICATIONS DIVISION

A. Relay Telemetry Modulation System Development, C. Carl

1. Introduction

The overall objective of this effort is the design, development, and test of telemetry modulation systems for relay link applications, such as between a planetary entry capsule and a nearby orbiting or flyby spacecraft. Phase-shift-keyed and frequency-shift-keyed (FSK) subcarrier techniques, and transmitted versus data-derived bit synchronization techniques are among the design approaches being studied.

2. Present Activities

Currently, a breadboard of a proposed relay link for a *Mariner* 1971 type mission is being evaluated. It is a 500-bits/s binary FSK system with data-derived bit synchronization (Fig. 1). The receiver has wide (with respect to the data rate) IF bandwidths to accommodate the anticipated frequency uncertainty of the mission. The breadboard receiver is a low-frequency equivalent of the eventual RF receiver, using Q-multiplier, rather than the prospective crystal, filters. The bit synchronizer is an

early-late gate integration type, suggested by J. Layland.¹ Referring to the timing diagram in Fig. 1, the synchronizer loop error signal is an estimate of

$$\left[\int_{-T/4}^{-T/4+T} D dt \right]^2 - \left[\int_{+T/4}^{+T/4+T} D dt \right]^2$$

where D is the incoming pulse-code-modulated (PCM) data plus noise and $1/T$ is the bit rate. This error estimator is independent of data polarity and is zero for the cases of no transition in the data. Any dc bias existing on the output of the receiver is removed by the ac coupling at the synchronizer input.

The breadboard system is being evaluated to: (1) compare its results with the available analytic work with regard to data performance of FSK with large IF bandwidth-to-data-rate ratios; (2) determine acquisition time as a function of system parameters; and (3) characterize other bit synchronizer behavior, such as drift susceptibility.

¹Member of JPL Technical Section 331.

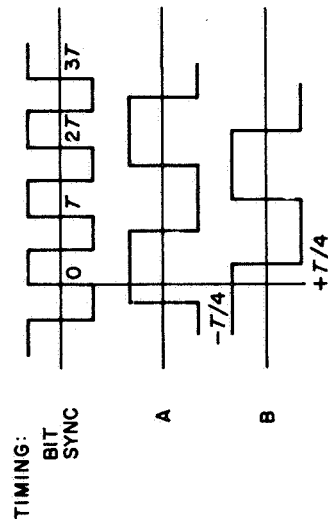
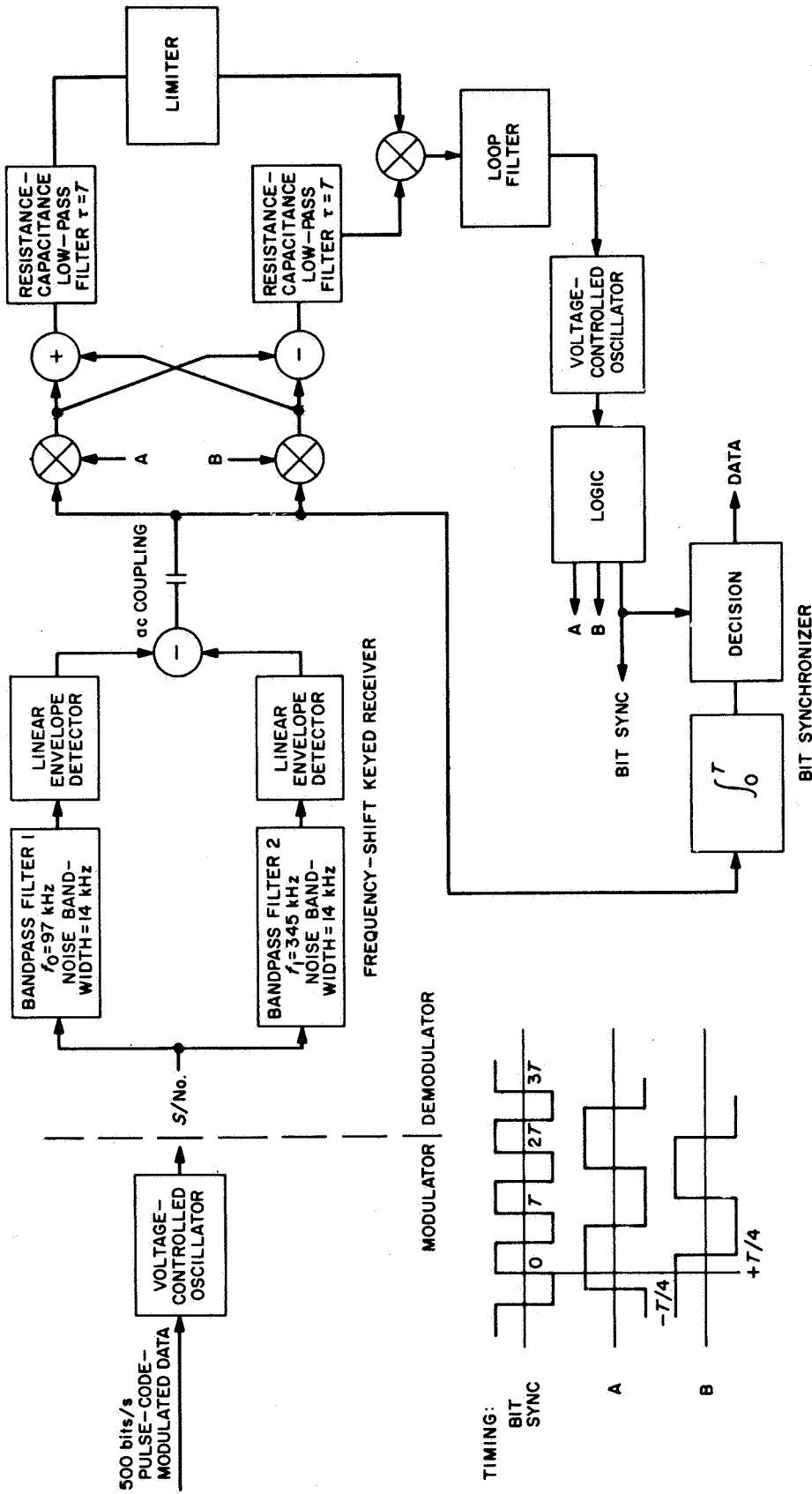


Fig. 1. Experimental FSK relay link

Data and acquisition performance are to be measured as a function of S/N_0 , the signal-to-noise-density ratio at the input to the receiver; Δf , the sync loop initial frequency offset; and $2B_L$, the sync loop noise bandwidth. As a starting point, N the IF noise-bandwidth-to-data-rate ratio is 28; the sync loop $2B_L$ is 7.5 Hz (at 200-mV signal input).

Bit-error data are taken by an accurately instrumented channel which adds spectrally-flat Gaussian noise to achieve a precise value of S/N_0 at the receiver input. Errors in the demodulated data output are detected and counted by logic circuits. Acquisition time data are taken by a closed-loop system that automatically disconnects the signal from the instrumented channel (noise remains on) when the sync loop is locked; waits 10–20 s to allow sync loop to return to rest frequency; simultaneously reapplies signal and starts a time-interval count; tests for sync loop lock-in and, when achieved, inputs that time-

interval count to a computer log program and disconnects the signal to start the process again. "In-lock" has been arbitrarily defined to be within ± 30 deg of phase-lock for 226 consecutive bit times (to insure against false-lock being announced in cases of cycle-skipping during acquisition).

The first set of acquisition and bit-error data has recently been completed. Figure 2 represents the average lock time, in bits, for various values of Δf and S/N_0 . Figure 3 is the time to acquire with probability 0.9. Each graph point is derived from 1000 samples of the respective acquisition time; computer reduction yielded the sample mean and distribution. Figure 4 shows bit-error probability performance compared against theory (Ref. 1). In both the acquisition data and bit-error data, performance is better with the 1-0 data (alternate ones and zeros) than with the PN data (pseudo-noise random data, derived from an 18-stage shift register). This is as expected for two reasons: First, the transition density for

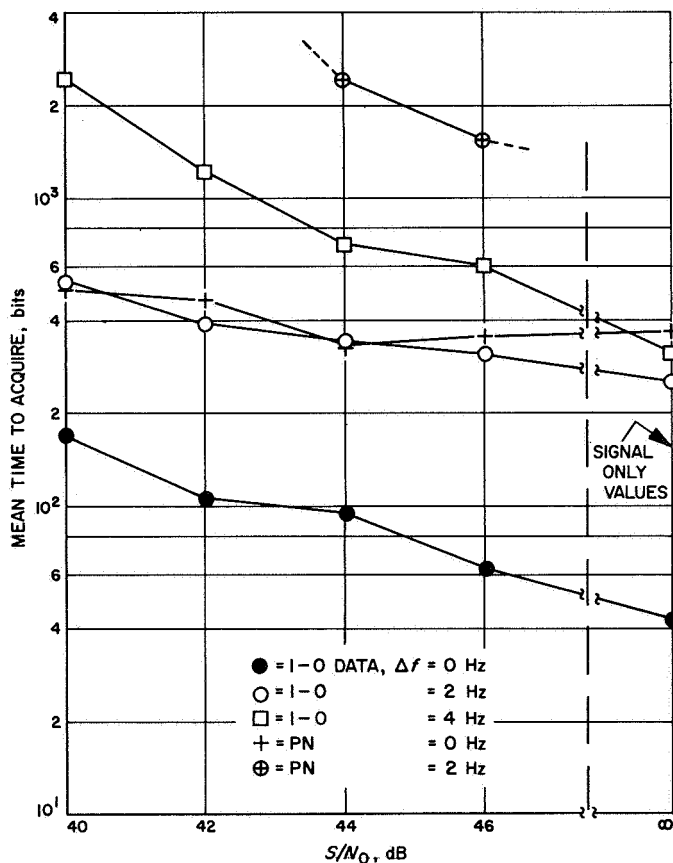


Fig. 2. Experimental FSK link acquisition time, $2B_L = 7.5$ Hz, data rate = 500 bits/s

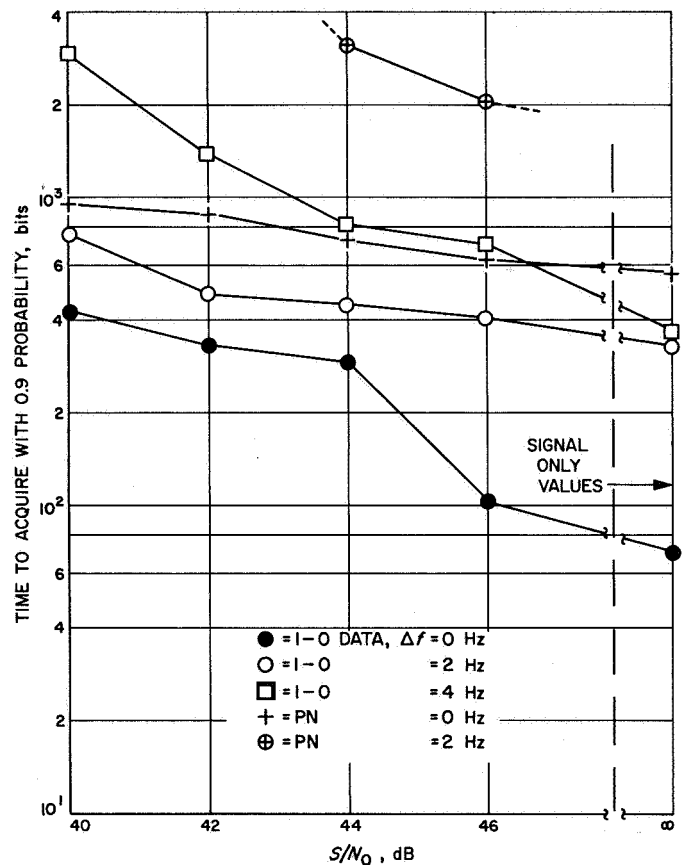


Fig. 3. Experimental FSK link acquisition time, $2B_L = 7.5$ Hz, data rate = 500 bits/s

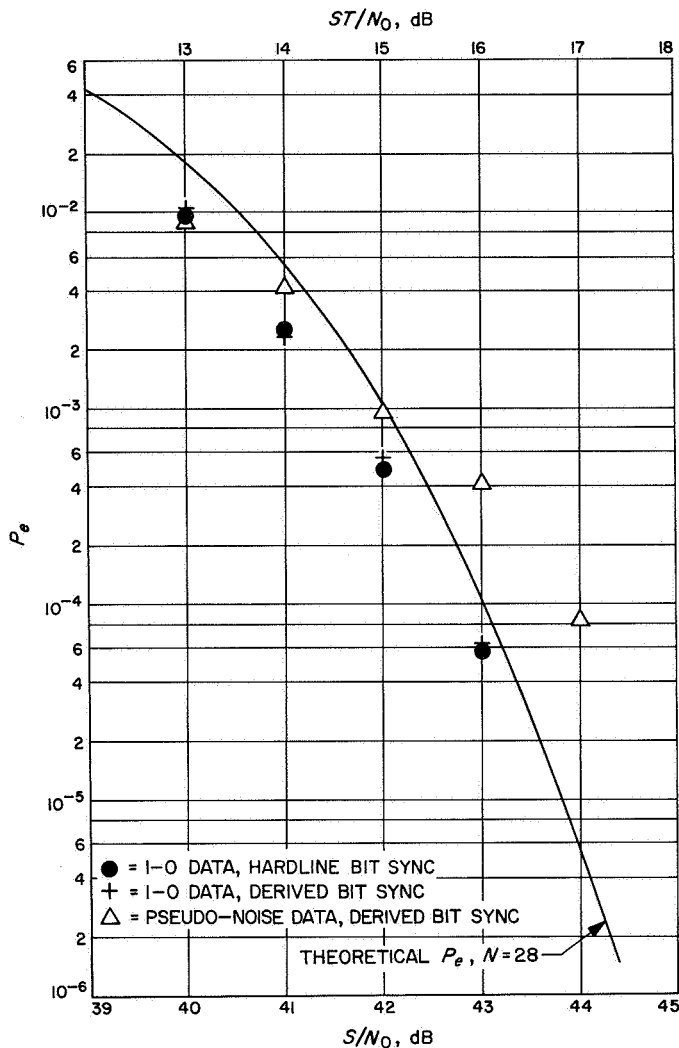


Fig. 4. Experimental FSK link bit-error probability, $2B_L = 7.5$ Hz, data rate = 500 bits/s

1-0 data is twice that for pseudo-noise data; the 1-0 data effectively give the sync loop a larger bit clock component to track. Second, PN data suffer transient distortion from the ac coupling into the synchronizer. Pronounced dc-level shifting occurs especially on long sequences of ones or zeros. This level shifting particularly affects the data detector, as indicated in Fig. 4 by the rapid departure of PN data performance from the theoretical for increasing S/N_0 .

The "better than theory" discrepancy in Fig. 4 is being investigated. It is most probably caused solely by measurement tolerances, although the theoretical curve is considered slightly pessimistic due to the central limit theorem assumption used in its derivation. In studies at the Radio Corporation of America (Ref. 2) some experimental data, particularly at $N = 100$, were also better than prediction, using the same assumption.

3. Future Plans

While these data at $2B_L = 7.5$ Hz offer a good reference point, it is felt that the acquisition times are too high for a *Mariner* 1971 application. When present data runs are completed, the bit synchronizer will be modified to a $2B_L = 25$ Hz configuration to obtain much lower acquisition times, as suggested by Viterbi's relation (Ref. 3) that time to frequency lock is

$$t \approx \frac{27(2\pi\Delta f)^2}{256 B_L^3}$$

in the no-noise case.

References

1. Boyd, D. W., *Performance of FSK Systems with Large Uncertainty in the Carrier Frequency and Linear Envelope Detectors*, Interoffice Technical Memorandum 3361-67-7. Jet Propulsion Laboratory, Pasadena, Calif., July 25, 1967.
2. *Selected Studies of VHF/UHF Communications for Planetary (Mars/Venus) Relay Links*, Final Report, Vol. 2, NASA/Ames Research Center Contract NAS 2-3772. Radio Corporation of America, Princeton, N.J., Jan. 15, 1967.
3. Viterbi, A. J., *Acquisition and Tracking Behavior of Phase-Locked Loops*, External Publication 673. Jet Propulsion Laboratory, Pasadena, Calif., July 14, 1959.

XXII. Spacecraft Radio

TELECOMMUNICATIONS DIVISION

A. Analyses of Certain Errors for d'Arsonval Movement Meters and Similar Instruments,

M. K. Tam¹ and C. E. Gilchrist

1. Introduction

This analysis is part of a continuing program in the area of telecommunication systems methodology research for determining and specifying performance margin. In SPS 37-45, Vol. IV, pp. 343-351, the first article on this program presented criteria for acceptance of a system design in which individual tolerances need not be considered. As an additional contribution to the overall program, a particular facet of the tolerance problem is discussed here.

It is the prevalent practice of the instrumentation industry that the inaccuracy of instruments such as d'Arsonval movement meters, slide-wire potentiometers, and other similar instruments with calibrated scales is summarily specified in percent of full scale. The specification of this nature is overly conservative, unrealistic, and is of little use in system tolerance evaluation, since a specific probability distribution of the instrument error

is not given. Moreover, it implies that the specific percentage error is applicable to the entire range of the instrument even though zero and full-scale adjustments are available; hence it penalizes the accuracy of the instrument unnecessarily. These difficulties prompted us to investigate the nature of error for this type of instrument from the theoretical point of view, in an attempt to obtain a more reasonable method of determining the error specifications for these instruments and other related measurement problems.

In the subsequent mathematical development and discussion, we mention almost exclusively the inaccuracy of d'Arsonval movement meters. The general concept, however, is equally applicable for slide-wire potentiometers and other similar instruments.

2. Theoretical and Mathematical Background

There are several sources contributing to the inaccuracy of a d'Arsonval meter. Among the more noticeable are the observational error, the stiction and hysteresis errors, and the inherent meter errors due to such origins as scale calibration and internal mechanism imperfection (nonlinearity). It is realized that the observational error is, by its very nature, independent of the scale position.

¹Tam Research Associates.

On the other hand, the inaccuracy due to the internal causes is to a certain extent correlated between two scale positions, simply because of the internal limitation of the construction of the meter. In other words, it is very unlikely that error indication of these types would differ drastically within two adjacent scale positions.

Let us ignore the observational, stiction, hysteresis, and other unspecified errors as being separable and consider only the errors due to the internal sources of the meter. Then, if accurate adjustments at some positions along the scale are available, it is reasonable to believe that the expected error will be a function of the scale position with respect to the positions at which adjustments are made. In the case for d'Arsonval meters, zero and full-scale adjustments are usually available.

To investigate the error function of a meter in relation to its scale position, it is necessary to imagine a scale of infinite length for which an appropriate curve fitting can be performed and a set of residuals from this curve can be generated. If an ensemble of such imaginary scales is considered, a set of curves, as shown in Fig. 1(a), will be obtained. Since the scale of a particular meter is necessarily finite, the error curve of this meter is essentially a segment of one member of the above ensemble. This segment of curve is shown in Fig. 1(b).

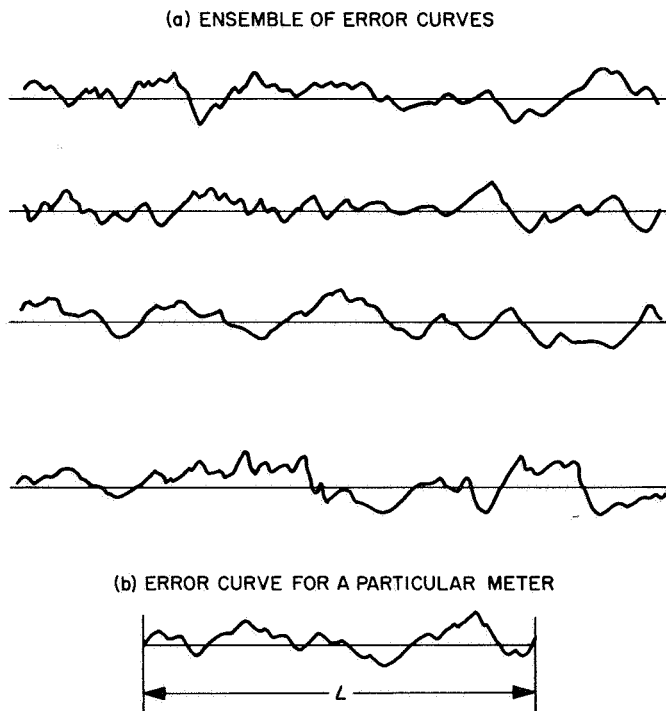


Fig. 1. Error curves for meter scales

Let us assume that for any given scale position, the error is normally distributed with zero mean and standard deviation σ . Furthermore, a correlation function $R(\ell)$ exists between any two scale positions that are separated by a distance ℓ , where $R(\ell)$ is not a delta function. Then, the joint probability density function for the two scale positions is given by

$$p(x_1, x_2) = \frac{1}{2\pi\sigma^2[1 - R^2(\ell)]^{1/2}} \times \exp\left\{-\frac{1}{2\sigma^2} \frac{x_1^2 - 2R(\ell)x_1x_2 + x_2^2}{[1 - R^2(\ell)]}\right\} \quad (1)$$

where x_1 and x_2 are random variables representing the error for the two scale positions in question.

If one of the random variables, e.g., x_1 , can be set to zero or some fixed magnitude X_1 , then, according to Bayes' theorem, one can obtain the conditional probability density function for x_2 given x_1 as follows

$$p(x_2 | x_1) = \frac{p(x_1, x_2)}{p(x_1)} = \frac{1}{(2\pi)^{1/2} \sigma [1 - R^2(\ell)]^{1/2}} \times \exp\left\{-\frac{1}{2\sigma^2} \frac{[x_2 - R(\ell)x_1]^2}{[1 - R^2(\ell)]}\right\} \quad (2)$$

The same method can be extended for n scale positions in which the values for $n - 1$ positions are given. In general, the joint probability density function for n variables each normally distributed with zero mean and standard deviation σ is given by

$$p(x_1, x_2, \dots, x_n) = \frac{1}{(2\pi)^{n/2} \sigma^n (M_n)^{1/2}} \times \exp\left[-\frac{1}{2} Q(x_1, x_2, \dots, x_n)\right] \quad (3)$$

where

$$M_n = \begin{vmatrix} \rho_{11} & \rho_{12} & \cdot & \cdot & \cdot & \rho_{1n} \\ \rho_{21} & \rho_{22} & \cdot & \cdot & \cdot & \rho_{2n} \\ \vdots & \vdots & \cdot & \cdot & \cdot & \vdots \\ \rho_{n1} & \rho_{n2} & \cdot & \cdot & \cdot & \rho_{nn} \end{vmatrix} \quad (4)$$

and

$$Q(x_1, x_2, \dots, x_n) = \frac{1}{\sigma^2 M_n} \sum_{i=1}^n \sum_{j=1}^n |M_n|_{ij} \cdot x_i x_j \quad (5)$$

In Eq. (4), the term ρ_{ij} is the correlation factor between the random variables x_i and x_j . In the case of meter scale error when the correlation function is solely dependent upon the distance between the two scale positions i and j , the following conditions become true. Namely,

$$\begin{aligned} \rho_{ij} &= \rho_{ji} \\ \rho_{ii} &= 1 \end{aligned}$$

The matrix term $|M_n|_{ij}$ in Eq. (5) is the cofactor of the term ρ_{ij} in the determinant M_n . It can be readily obtained by evaluating a reduced determinant of M_n in such a way that the row and column indicated in the subscript i and j are eliminated. The resultant quantity is then prefixed by a sign-controlling factor which is $+1$ if the sum of the subscripts is even, and -1 if this sum is odd.

The conditional probability density function for x_n given x_1, x_2, \dots, x_{n-1} can be generalized as follows

$$\begin{aligned} p(x_n | x_1, x_2, \dots, x_{n-1}) &= \frac{p(x_1, x_2, \dots, x_n)}{p(x_1, x_2, \dots, x_{n-1})} \\ &= \frac{1}{(2\pi)^{1/2} \sigma \left(\frac{M_n}{M_{n-1}} \right)^{1/2}} \\ &\times \exp \left\{ -\frac{1}{2\sigma^2} \left[\frac{1}{M_n} \sum_{i=1}^n \sum_{j=1}^n |M_n|_{ij} x_i x_j \right. \right. \\ &\quad \left. \left. - \frac{1}{M_{n-1}} \sum_{i=1}^{n-1} \sum_{j=1}^{n-1} |M_{n-1}|_{ij} x_i x_j \right] \right\} \quad (6) \end{aligned}$$

With the above basic considerations in mind, practical problems in error specifications for meters and related measurements are examined.

3. Meters With Zero Adjustment

Consider a d'Arsonval movement meter with zero adjustment only. The error curve for this case is as shown in Fig. 2. As indicated, the zero adjustment provision permits the error at the zero position of the scale to be set at any fixed magnitude X_1 . Thus, according to

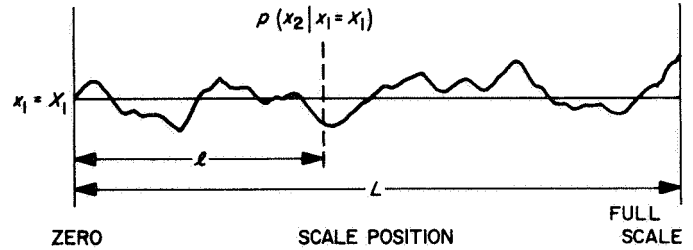


Fig. 2. Error curve for meter with zero adjustment only

Eq. (2), the conditional error distribution for any other point of the scale is given by

$$\begin{aligned} p(x_2 | x_1 = X_1) &= \frac{1}{(2\pi)^{1/2} \sigma [1 - R^2(\ell)]^{1/2}} \\ &\times \exp \left\{ -\frac{1}{2\sigma^2} \frac{[x_2 - R(\ell) X_1]^2}{[1 - R^2(\ell)]} \right\} \quad (7) \end{aligned}$$

Under the special condition when $X_1 = 0$, Eq. (7) becomes

$$\begin{aligned} p(x_2 | x_1 = 0) &= \frac{1}{(2\pi)^{1/2} \sigma [1 - R^2(\ell)]^{1/2}} \\ &\times \exp \left\{ -\frac{1}{2\sigma^2} \frac{x_2^2}{[1 - R^2(\ell)]} \right\} \quad (8) \end{aligned}$$

It can be seen from the above equations that the conditional distribution for x_2 is also normal, and that the effective mean $\overline{m_{eff}}$ and standard deviation σ_{eff} are

$$\overline{m_{eff}} = X_1 R(\ell) \quad (9)$$

$$\sigma_{eff} = \sigma [1 - R^2(\ell)]^{1/2} \quad (10)$$

Both of these parameters are a function of the correlation function $R(\ell)$, which is dependent upon the position along the scale.

The correlation function $R(\ell)$ cannot be derived by theoretical means but it must be obtained through statistical methods based on actual data. At present, let us assume that this function is exponential in terms of the scale distance ℓ . Thus,

$$R(\ell) = e^{-\ell/\lambda}, \quad 0 < \ell \leq L \quad (11)$$

where λ is the unknown characteristic constant of the meter scale.

With this assumption, the effective mean and standard deviation at a particular distance l are

$$\overline{m}_{eff}(l) = X_1 e^{-l/\lambda}, \quad 0 < l \leq L \quad (12)$$

$$\sigma_{eff}(l) = \sigma [1 - \exp(-2l/\lambda)]^{1/2}, \quad 0 < l \leq L \quad (13)$$

A sketch for the above parameters is shown in Fig. 3. The actual shape of the curves, however, is dependent upon the magnitude of the characteristic constant λ as indicated by Eqs. (12) and (13).

Notice from the above equations that when X_1 can be set at zero, the error of the meter scale is represented by Eq. (13) alone.

The results as shown in Fig. 3 are as expected. It can be reasoned that since X_1 is fixed, there should be no deviation at the zero position. Furthermore, as the scale position is further away from zero, the deviation should increase asymptotically to σ due to the decrease of the correlation factor; and the expected value should approach zero due to the regressive nature of the error curve.

4. Meters With Both Zero and Full-Scale Adjustments

To analyze this particular problem, it is appropriate to utilize the joint distribution of three random variables in which two are specifically given. The error curve diagram depicting this particular case is shown in Fig. 4.

From Eq. (6)

$$\begin{aligned} p(x_3 | x_1, x_2) &= \frac{p(x_1, x_2, x_3)}{p(x_1, x_2)} \\ &= \frac{1}{(2\pi)^{3/2} \sigma \left(\frac{M_3}{M_2}\right)^{1/2}} \\ &\quad \times \exp \left[-\frac{1}{2\sigma^2} \left(\frac{1}{M_3} \sum_{i=1}^3 \sum_{j=1}^3 |M_3|_{ij} x_i x_j \right. \right. \\ &\quad \left. \left. - \frac{1}{M_2} \sum_{i=1}^2 \sum_{j=1}^2 |M_2|_{ij} x_i x_j \right) \right] \quad (14) \end{aligned}$$

It can be shown that the conditional probability density function for x_3 , given $x_1 = X_1$ and $x_2 = X_2$, is

$$\begin{aligned} p(x_3 | x_1 = X_1, x_2 = X_2) \\ = \frac{1}{(2\pi)^{1/2} \sigma_{eff}} \exp \left[-\frac{1}{2\sigma_{eff}^2} (x_3 - \overline{m}_{eff})^2 \right] \quad (15) \end{aligned}$$

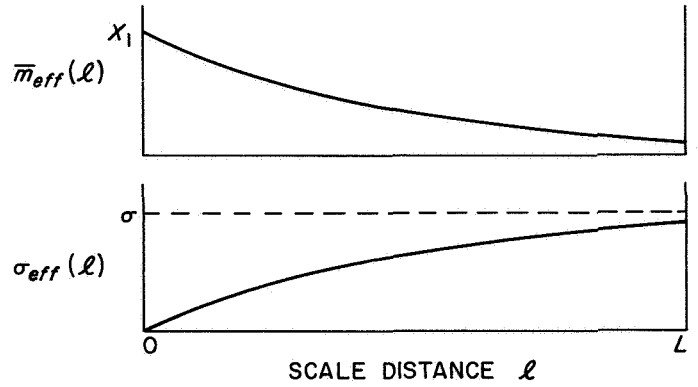


Fig. 3. \overline{m}_{eff} and σ_{eff} as a function of l

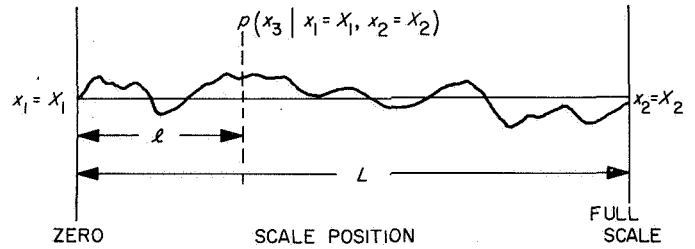


Fig. 4. Error curve for meter with independent zero and full-scale adjustments

in which

$$\overline{m}_{eff} = \frac{(\rho_{13} - \rho_{12} \rho_{23}) X_1 + (\rho_{23} - \rho_{12} \rho_{13}) X_2}{1 - \rho_{12}^2} \quad (16)$$

$$\sigma_{eff} = \sigma \left(\frac{1 + 2\rho_{12} \rho_{13} \rho_{23} - \rho_{12}^2 - \rho_{13}^2 - \rho_{23}^2}{1 - \rho_{12}^2} \right)^{1/2} \quad (17)$$

In the special case when $X_1 = 0$ and $X_2 = 0$, \overline{m}_{eff} becomes zero and

$$p(x_3 | x_1 = 0, x_2 = 0) = \frac{1}{(2\pi)^{1/2} \sigma_{eff}} \exp \left(-\frac{x_3^2}{2\sigma_{eff}^2} \right) \quad (18)$$

If the same assumption as given by Eq. (12) is adopted for various correlation factors, we have

$$\begin{aligned} \rho_{12} &= e^{-L/\lambda} \\ \rho_{13} &= e^{-l/\lambda} \\ \rho_{23} &= e^{-(L-l)/\lambda} \end{aligned}$$

and, substituting,

$$\begin{aligned} \overline{m}_{eff} &= \frac{[e^{-L/\lambda} - e^{-(2L-\ell)/\lambda}] X_1 + [e^{-(L-\ell)/\lambda} - e^{-(L+\ell)/\lambda}] X_2}{1 - e^{-2L/\lambda}} \\ &= \frac{e^{-L/\lambda}}{1 - e^{-2L/\lambda}} \\ &\quad \times \left([e^{-(L-\ell)/\lambda} - e^{-(L+\ell)/\lambda}] X_1 + [e^{\ell/\lambda} - e^{-\ell/\lambda}] X_2 \right) \end{aligned} \quad (19)$$

$$\begin{aligned} \sigma_{eff} &= \sigma \left[\frac{1 + e^{-2L/\lambda} - e^{-2\ell/\lambda} - e^{-2L/\lambda} e^{2\ell/\lambda}}{1 - e^{-2L/\lambda}} \right]^{1/2} \\ &= \sigma \left(\frac{[1 - e^{-2L/\lambda} e^{2\ell/\lambda}] [1 - e^{-2L/\lambda}]}{1 - e^{-2L/\lambda}} \right)^{1/2} \end{aligned} \quad (20)$$

The shape of the above curves depends upon the L/λ ratio. In addition, the values X_1 and X_2 also determine the shape of \overline{m}_{eff} curve. If the L/λ ratio is sufficiently large, then σ_{eff} will be equal to σ and \overline{m}_{eff} equal to zero near the middle of the scale. If this ratio is small, the maximum σ_{eff} which occurs at the middle of the scale is given by

$$\begin{aligned} \sigma_{eff(max)} &= \sigma \left[\frac{1 - e^{-L/\lambda}}{1 + e^{-L/\lambda}} \right]^{1/2} \\ &= \sigma (\tanh L/2\lambda)^{1/2} \end{aligned} \quad (21)$$

Two families of curves showing the effective mean and the effective standard deviation for various magnitudes of λ in relation to the scale length L are given in Fig. 5.

5. SNR Measurement Error

In obtaining signal-to-noise ratio (SNR), it is customary to measure the signal and the noise voltages separately with a single meter, as shown in Fig. 6. With this scheme, the errors for the two measurements are correlated to some degree, and the resultant SNR thus obtained is reasonably accurate, even though a meter of questionable accuracy is used.

The SNR can be obtained by taking the difference between the signal and the noise voltages if they are expressed in decibels. It is possible to obtain ac voltmeters with linear logarithmic (decibel) scale for which normal error distribution can be assumed. Even if conventional voltmeters are used, the region of error is usually small in comparison to the entire range of measurement and, when converted to decibels, the error

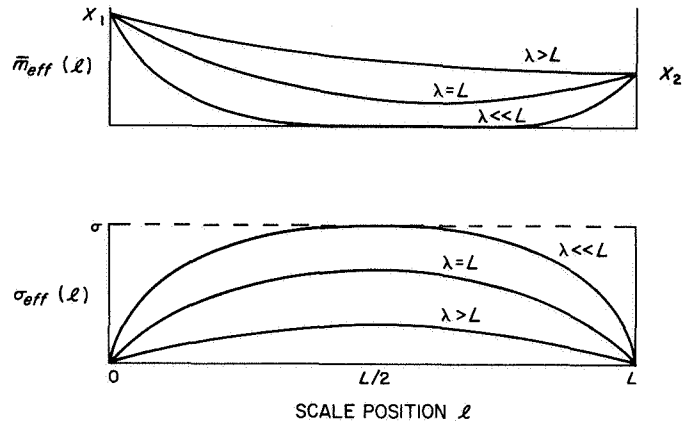


Fig. 5. Families of curves for \overline{m}_{eff} and σ_{eff}

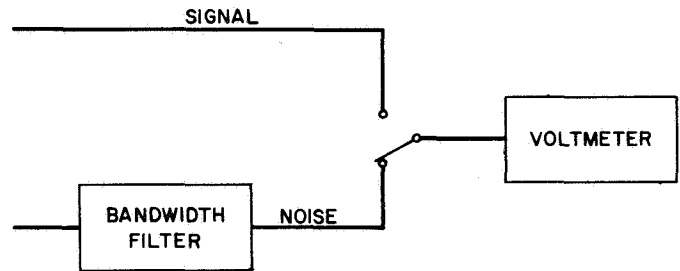


Fig. 6. Measuring SNR with a single meter

distribution is still approximately normal. With this in mind, the SNR measurement error can be expressed as

$$E = E_s - E_n \quad (22)$$

where E_s and E_n are, respectively, the error of the signal and of the noise measurement in decibels.

If E_n is given at some specific noise level, E_s will be correlated to E_n , unless the signal level is remote from the noise level at which E_n was observed. Under the normal distribution of error assumption, the SNR measurement error can be determined by utilizing the technique previously described and developed. In this particular case, four variables x_1 , x_2 , x_3 , and x_4 are involved in which the conditional distribution of x_4 given x_1 , x_2 , and x_3 is sought. Here, it is assumed that the meter is provided with zero and full-scale adjustments so that X_1 and X_2 are zero. In addition X_3 is equivalent to E_n while x_4 denotes the error for the signal measurement. Thus, the conditional distribution for x_4 given $x_1 = 0$, $x_2 = 0$, and $x_3 = X_3$ is equivalent to the distribution of E_s . It should be pointed out that, in reality, X_3 is unknown. However,

since X_1 and X_2 are zero, the average value of X_3 is also zero, as indicated by Eq. (19), irrespective of the scale

position. For generality, however, X_3 is treated as an arbitrary constant in the subsequent derivation.

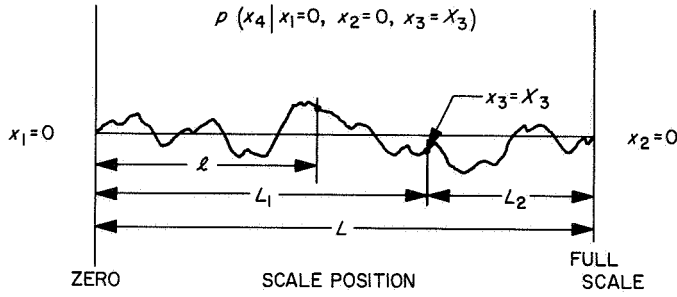


Fig. 7. Error curve for SNR measurement with common meter

Consider the error curve as shown in Fig. 7.

According to Eq. (6),

$$p(x_4 | x_1, x_2, x_3) = \frac{1}{(2\pi)^{1/2} \sigma \left(\frac{M_4}{M_3} \right)^{1/2}} \times \exp \left[-\frac{1}{2\sigma^2} \left(\frac{1}{M_4} \sum_{i=1}^4 \sum_{j=1}^4 |M_4|_{ij} x_i x_j - \frac{1}{M_3} \sum_{i=1}^3 \sum_{j=1}^3 |M_3|_{ij} x_i x_j \right) \right] \quad (23)$$

By solving the above equation and substituting with appropriate constants, it can be shown that the conditional distribution for x_4 assumes the same form as given by Eq. (15). This equation is again stated as follows:

$$p(x_4 | x_1 = 0, x_2 = 0, x_3 = X_3) = p(E_s) = \frac{1}{(2\pi)^{1/2} \sigma_{eff}} \exp \left[-\frac{1}{2\sigma_{eff}^2} (x_4 - \overline{m}_{eff})^2 \right] \quad (24)$$

where

$$\overline{m}_{eff} = \frac{-(\rho_{34} - \rho_{23}\rho_{24} - \rho_{13}\rho_{14} + \rho_{12}\rho_{13}\rho_{24} + \rho_{12}\rho_{14}\rho_{23} - \rho_{12}^2 \rho_{34})}{1 + 2\rho_{12}\rho_{13}\rho_{23} - \rho_{12}^2 - \rho_{13}^2 - \rho_{23}^2} X_3 \quad (25)$$

$$\sigma_{eff} = \sigma \left[\frac{M_4}{1 + 2\rho_{12}\rho_{13}\rho_{23} - \rho_{12}^2 - \rho_{13}^2 - \rho_{23}^2} \right]^{1/2} \quad (26)$$

in which

$$M_4 = 1 + 2(\rho_{23}\rho_{24}\rho_{34} + \rho_{12}\rho_{14}\rho_{24} + \rho_{12}\rho_{13}\rho_{23} + \rho_{13}\rho_{14}\rho_{34}) - 2(\rho_{12}\rho_{14}\rho_{23}\rho_{34} + \rho_{12}\rho_{13}\rho_{24}\rho_{34} + \rho_{13}\rho_{14}\rho_{23}\rho_{24}) + \rho_{12}^2 \rho_{34}^2 + \rho_{13}^2 \rho_{24}^2 + \rho_{14}^2 \rho_{23}^2 - (\rho_{12}^2 + \rho_{13}^2 + \rho_{14}^2 + \rho_{23}^2 + \rho_{24}^2 + \rho_{34}^2) \quad (27)$$

The probability density function for the SNR measurement error can be obtained by the familiar functional transformation method according to the following relationship.

$$E = E_s - X_3 \quad (28)$$

Thus,

$$p_E(E) = \frac{1}{(2\pi)^{1/2} \sigma_{eff}} \exp \left[-\frac{1}{2\sigma_{eff}^2} (E + X_3 + \overline{m}_{eff})^2 \right] \quad (29)$$

In the above distribution, the effective standard deviation is the same as that shown in Eq. (26) and the quantity $-(X_3 + \overline{m}_{eff})$ is the mean of that distribution. If \overline{E} denotes this quantity, then

$$\overline{E} = \left(\frac{\rho_{34} - \rho_{23}\rho_{24} - \rho_{13}\rho_{14} + \rho_{12}\rho_{13}\rho_{24} + \rho_{12}\rho_{14}\rho_{23} - \rho_{12}^2 \rho_{34}}{1 + 2\rho_{12}\rho_{13}\rho_{23} - \rho_{12}^2 - \rho_{13}^2 - \rho_{14}^2} - 1 \right) X_3 \quad (30)$$

Now, if the correlation functions in Eqs. (26), (27), and (30) are again assumed to be exponential with respect to the scale distance, then, with reference to Fig. 7,

$$\begin{aligned} \rho_{12} &= e^{-(L_1+L_2)/\lambda} \\ \rho_{13} &= e^{-L_1/\lambda} \\ \rho_{14} &= e^{-\ell/\lambda} \\ \rho_{23} &= e^{-L_2/\lambda} \\ \rho_{24} &= e^{-(L_1+L_2-\ell)/\lambda} \\ \rho_{34} &= e^{-(L_1-\ell)/\lambda}, \quad 0 \leq \ell \leq L_1 \\ &= e^{-(\ell-L_1)/\lambda}, \quad L_1 \leq \ell \leq L \end{aligned}$$

Substituting, and after some mathematical manipulation, we obtain

$$\begin{aligned} \overline{E} &= \left[\frac{e^{-L_1/\lambda}(e^{\ell/\lambda} - e^{-\ell/\lambda})}{1 - e^{-2L_1/\lambda}} - 1 \right] X_3, \quad 0 \leq \ell \leq L_1 \\ &= \left[\frac{e^{-L_2/\lambda}[e^{(L-\ell)/\lambda} - e^{-(L-\ell)/\lambda}]}{1 - e^{-2L_2/\lambda}} - 1 \right] X_3, \quad L_1 \leq \ell \leq L \end{aligned} \quad (31)$$

and

$$\begin{aligned} \sigma_{eff} &= \sigma \left(\frac{1 + e^{-2L_1/\lambda} - e^{-2\ell/\lambda} - e^{-2L_1/\lambda} e^{2\ell/\lambda}}{1 - e^{-2L_1/\lambda}} \right)^{1/2}, \quad 0 \leq \ell \leq L_1 \\ &= \sigma \left(\frac{1 + e^{-2L_2/\lambda} - e^{2(L-L_2)/\lambda} e^{-2\ell/\lambda} - e^{-2L_2/\lambda} e^{2\ell/\lambda}}{1 - e^{-2L_2/\lambda}} \right)^{1/2}, \quad L_1 \leq \ell \leq L \end{aligned} \quad (32)$$

Eq. (32) indicates that the maxima of σ_{eff} occur at the points $L_1/2$ and $L_1 + L_2/2$.

A sketch of \overline{E} and σ_{eff} versus scale position ℓ is given in Fig. 8.

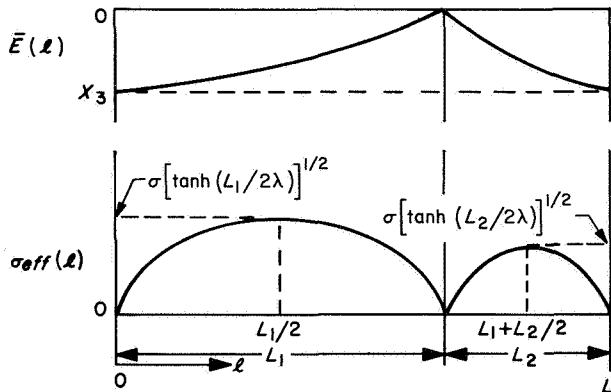


Fig. 8. Error curves \bar{E} and σ_{eff} for SNR measurement, common meter

It should be mentioned again that the average value of X_3 is zero for this particular case and the error for the SNR measurement on the average is represented by the σ_{eff} curve only.

Although the above example centered around an SNR measurement, the results can be applied to other significant examples. A notable one arises in the measurement of antenna patterns. This task is frequently accomplished on antenna ranges which utilize a standard gain horn (for reference to remove range errors) and common instrumentation. In this example, the antenna being tested and the standard gain horn are analogous to the signal and the noise measurements. This analysis gives credibility to the intuitive feeling that the accuracy is better for measured values of the antenna being tested which are close to that of the standard gain horn.

6. Interpolation and Extrapolation

Eq. (6) may be employed for interpolation and extrapolation problems. Suppose an apparatus having $n - 1$ known calibration points. We can obtain the expected value and its associated standard deviation at any position by utilizing the aforementioned equation. Unfortunately, the solution of this equation is extremely tedious for $n > 4$, and the aid of a digital computer that can handle matrices of high orders is necessary.

It can be perceived, however, that for an apparatus of this type the expected value and standard deviation curves will appear as the forms shown in Fig. 9. This is based on the results of the illustrative examples given in the preceding sections. The actual shapes for these curves, of course, depend upon the magnitude of the calibration points and the correlation functions.

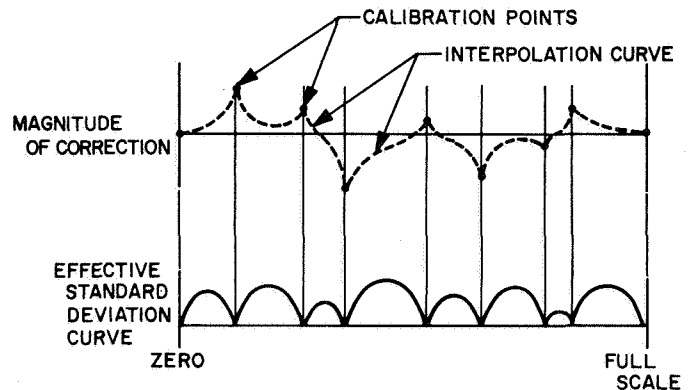


Fig. 9. Interpolative value and standard deviation curves for apparatus with numerous calibration points

As an example of extrapolation, let us consider a simple case in which two calibration points that are not the end points of a scale are given and the expected values outside of these points are desired. This problem is graphically represented in Fig. 10.

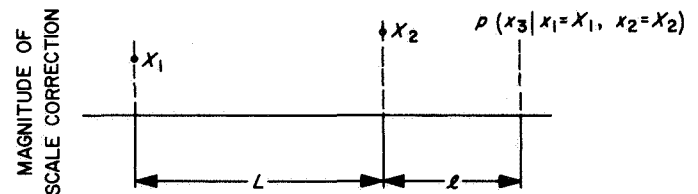


Fig. 10. Simple extrapolation problem

From Eq. (16), the expected value of x_3 is

$$\bar{X}_3 = \frac{(\rho_{13} - \rho_{12}\rho_{23})X_1 + (\rho_{23} - \rho_{12}\rho_{13})X_2}{1 - \rho_{12}^2} \quad (33)$$

If the correlation function is exponential, we have

$$\begin{aligned} \rho_{12} &= e^{-L/\lambda} \\ \rho_{13} &= e^{-(L+\ell)/\lambda} \\ \rho_{23} &= e^{-\ell/\lambda} \end{aligned}$$

It can be shown that

$$\bar{X}_3 = X_2 e^{-\ell/\lambda} \quad (34)$$

in which the magnitudes of X_1 is irrelevant. Under this condition, the extrapolation problem exhibits the characteristic of a Markov process.

This characteristic is valid for the condition when the correlation function is exponential. If the correlation function is linear with respect to the scale position, for example, the expected value X_3 will also be influenced by X_1 .

Consider a special case when $l = L$. In this case, the normalized value for \bar{X}_3 with respect to X_1 is given by

$$\bar{X}_3 = \frac{2(a-1)X_2 - 1}{2a-1}, \quad X_1 = 1.0 \quad (35)$$

where $a = \lambda/L$, the characteristic constant of the scale.

As an example, if $a = 5$, a family of extrapolation curves can be constructed for various X_2 . These curves are shown in Fig. 11.

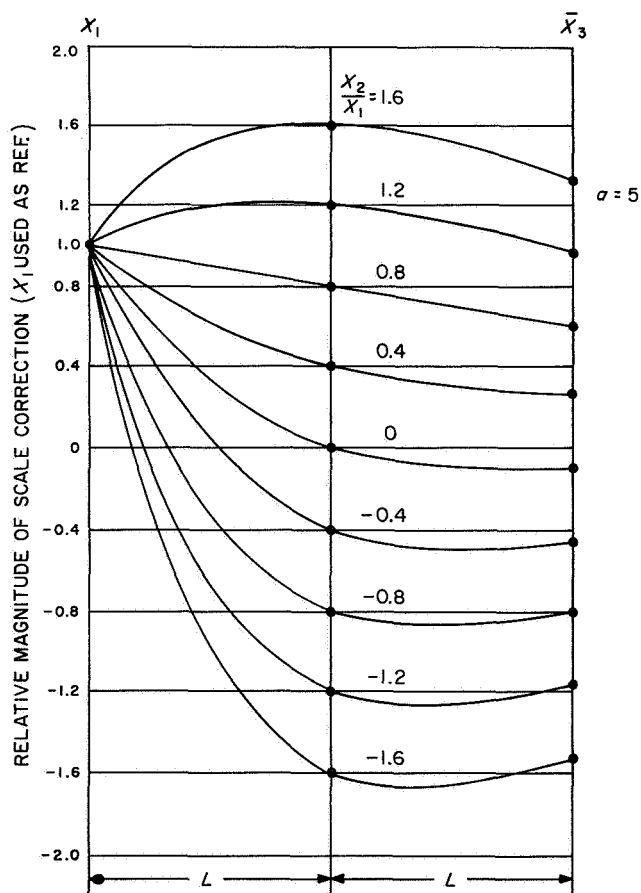


Fig. 11. Extrapolation curves for \bar{X}_3 normalized against X_1

Under certain circumstances, it is more practical to present the extrapolation curves of X_3 normalized with respect to X_2 . Thus,

$$\bar{X}_3 = \frac{2(a-1) - X_1}{2a-1}, \quad X_2 = 1.0 \quad (36)$$

This is shown in a separate diagram (Fig. 12).

The preceding analysis might be thought of as another form of curve fitting. It assumes that the randomness is in the construction of the instrument but remains fixed. Subsequent calibration of the instrument then yields the same errors. The interpolation and extrapolation curves are the expected correction values that we might obtain along the scale from those members of the ensemble of instruments whose calibration points are identical. Significantly the expected correction values are identical to

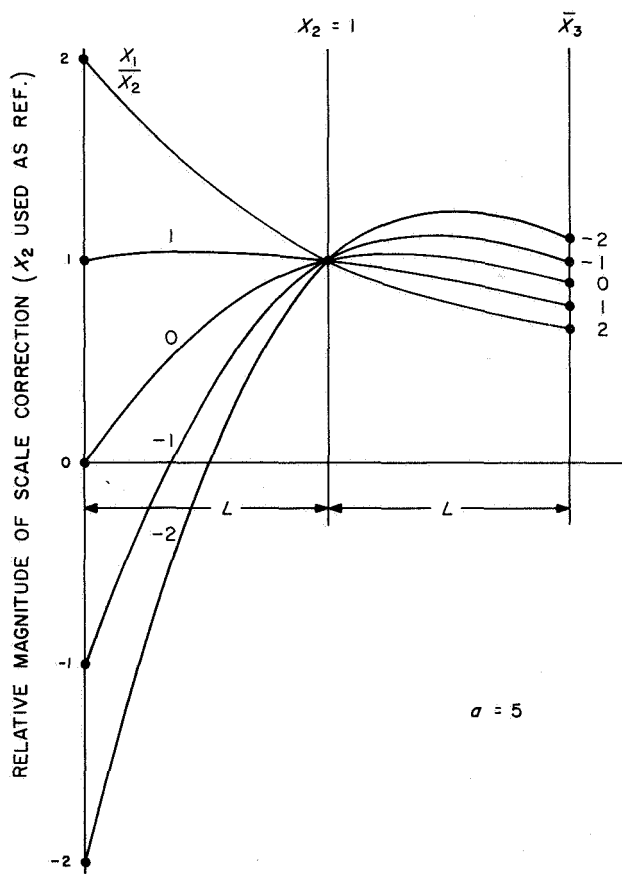


Fig. 12. Extrapolation curves for \bar{X}_3 normalized against X_2

the calibrated points at those points. Extrapolation and interpolation values have a centralizing influence which says essentially that the average correction is expected to be zero. As the distance between or beyond the calibration points becomes large with respect to the width of the correction function, \bar{X}_s approaches zero and the σ_{eff} approaches σ . Smoothing is dependent on the correlation function, and only in special cases would one expect cusps as illustrated in Fig. 9.

Least squares polynomial curve fits differ from the above example in that the randomness is usually thought of as being in the observation rather than in the construction of the instrument. The fitted curve then would not be expected to pass through the observed values. Both methods have usefulness in interpolation, extrapolation, and smoothing—depending upon the circumstances. Either method is considered to be superior to the usual unsophisticated method of straight-line interpolation between the calibration points.

7. Conclusion

The results of this study indicate that the error specifications of instruments such as d'Arsonval movement meters, slide wire potentiometers, and many others can be realistically assigned. Instead of the prevalent flat percent of full-scale error specification, one can establish a region depicting the probable error limits in relation to the scale position according to the adjustments available and to the correlation function of the scale under construction. This specification permits realistic and accurate system tolerance evaluation which, in the authors' opinion, is an important branch in the modern system engineering disciplines.

The examples used assumed correlation functions to illustrate the principles of the methods. If further use is to be made of the analysis, it is necessary to determine empirically the correlation functions for the various classes and types of instruments involved. There is nothing unusually difficult about this task; it is a fairly standard process.